ESRF

The European Synchrotron

ESRF HIGHLIGHTS
2017

ESRF
The European Synchrotron

ESRF HIGHLIGHTS 2017

Contents

Francesco Sette

DEAR ESRF USER, DEAR READER

It is a great pleasure to present to you some of the achievements of 2017 and to share some highlights of ESRF users' science over the past year. In 2017, the ESRF scientific programme continued to develop as impressively as in previous years: many new records were broken, and new infrastructure and operation features were made available. Great progress has also been made on the ongoing EBS programme and on beamline upgrades. Last September, the ESRF reached the milestone of 30 000 publications since the facility opened its doors in 1994. Among those publications are many that have since become regarded as breakthroughs. Examples of the excellence and diversity of the science carried out at the ESRF in 2017 are reported here in this latest issue of the ESRF Highlights.

User programme reaches record highs

The ESRF user programme has been vigorous, with ever-increasing interest from users: a record number of proposals received beamtime in 2017 with a record number of user visits (more than 7 000) and experimental sessions (more than 1850); a record number of proposals (more than 1 300) were submitted to our User Office by the September 10 deadline. The 2017 user programme has also greatly benefited from top-up injection using the new 4 Hz booster ramped injection power supply system, which is now fully commissioned and operational. This new top-up injection mode improves operation reliability, delivers a more stable beam and provides an increase in the average brilliance, which is very relevant for four- and 16-bunch filling modes. Top-up injection operation schemes in high current modes have been validated recently and will be implemented in 2018. The upgraded injection system is now essentially ready to be exploited in the future to fill the new EBS storage ring.

New research platforms inaugurated

During 2017, the ESRF refurbishment programme on beamlines and experiment support structures has progressed according to plan. In particular, the Cryo-Electron Microscopy Platform initiative, started in June 2015 in collaboration with our partner institutes on the EPN Campus (EMBL, IBS and ILL), was inaugurated last November with an almost perfect and unexpected concomitance with the announcement of the 2017 Chemistry Nobel prize, granted for the development of the cryo-EM technique for structural biology research. Similarly, the High Power Laser Platform for time-resolved X-ray absorption experiments on shock-waved samples has also progressed, and thanks to the procurement of the laser and the recruitment of a dedicated engineer, its initial operation phase is expected to start in early 2018. These important results improve the support to our user programme, allowing us to exploit new research opportunities provided by innovative and complementary instruments on the same site as X-ray beamlines.

Status of the EBS storage ring construction

Concerning the EBS programme, enormous advances have been made over the last three years since the project was launched. The project is so far within the initial schedule and budget and, in July 2017, the plan envisaging the start of the long shutdown in December 2018 until August 2020 was definitively retained. Nearly all parts of the new storage ring have been designed and validated by pre-series components and prototypes. They are currently being manufactured and deliveries are ongoing, with over 60% of all magnets already onsite. Major project milestones have been achieved on schedule, including, in 2017, the in-house assembly of the longitudinal gradient dipoles and the successful construction of a 'mock-up' of one of the 32 new storage ring cells. In the meantime, the assembly of the actual EBS girders with magnets, vacuum chambers and instrumentation has begun in a dedicated building.

Four new EBS flagship beamlines

While work on the storage ring progresses well, the second pillar of the upgrade, the ESRF-EBS experimental programme, has also entered a new operational phase. On 27 June 2017 the ESRF Council, representing the 22 partner nations of the ESRF synchrotron, gave the green light for the construction and commissioning of four new flagship beamlines. These new beamlines, endorsed by the ESRF SAC and designed for the full exploitation of the enhanced performance of the EBS, will address major challenges facing our society, including the development of the next generation of drugs, biomaterials and sustainable materials, as well as provide deep insights into the complex mechanisms governing living organisms. They will also elucidate our recent and ancient past, as manifested in historical artefacts and fossils. Moreover, they will provide unique opportunities for applied and innovation-driven research in material and health sciences. They complement the rich portfolio of new beamlines and instruments constructed during the ESRF Upgrade Programme Phase I (2009-2015).

EBS detector and data infrastructure programmes

Together with the new EBS beamlines, the detector and Scientific Data Analysis and Management programmes have been bolstered with the recent recruitment of key technical staff and the establishment of important collaboration initiatives with partner laboratories and synchrotron facilities.

Involvement on the international stage

In addition to its core activities in supporting its users and implementing the EBS, the ESRF is involved in many initiatives with partner laboratories and synchrotron centres, in Europe and around the world, aiming to strengthen and improve opportunities for synchrotron users at the ESRF and worldwide. Examples of this involvement are represented by the ESRF active contribution to EU-funded initiatives such as CALIPSOplus, EuCALL and CREMLIN, and by the support of the SESAME programme. Similarly, the ESRF is a member of a newly created initiative among European X-ray user facilities – LEAPS (League of Electron Accelerator-based Photon Sources) – which aims to contribute to shaping scenarios, strategies and research opportunities in X-ray science at synchrotrons and XFELs in Europe and beyond.

In 2017 India became the 22nd country to join the ESRF programme with particular emphasis on structural biology, underlining the increasing international interest in the ESRF programme.

Reaching out to the younger generation

The ESRF continues to be deeply engaged in supporting programmes to attract and train the younger generations in scientific and technological areas. Besides approximately 130 positions dedicated each year to undergraduate trainees, PhD students, post-doctoral fellows and junior scientists, the ESRF continues to support: 1) The HERCULES School for graduate students and post-doctoral fellows; 2) the ESRF-ILL summer school for undergraduate students; and 3) the programme Synchrotron@school, in partnership with the Académie de Grenoble, dedicated to pupils in scientific and technical secondary schools throughout the ESRF partner countries.

ESRF celebrates 30 years in 2018

In 2018, the ESRF will celebrate its 30th anniversary since the signature of the Intergovernmental Convention establishing the ESRF, signed in Paris in December 1988. Thirty years of ESRF users' activities, characterised by remarkable scientific discoveries and innovative technical advances, greatly contribute to the technological, health and environmental challenges facing our society. Next year, moreover, ESRF users will also witness the beginning of a new era for synchrotron science, symbolised by the end of operation of the existing storage ring and the beginning of the installation of the new one. The future ESRF operation, due to restart in September 2020 with the new storage ring and a maximum number of beamlines, will be in full swing in 2023 with the completion of the ESRF-EBS programme. By that time, the ESRF will be offering qualitatively new and worldwide unique research opportunities to the world's synchrotron community. Indeed, the new storage ring, together with the most advanced portfolio of beamlines and experimental infrastructure, will enable scientists to bring X-ray science into research domains and applications that could not have been imagined a few years ago.

The ESRF – with its mission centred on scientific excellence – continues to welcome scientists from all over the world, with their diversity in disciplines, gender, language and culture. As amply shown by the ESRF scientific publication records, the ESRF open user's programme enables many new and strong collaborations among scientists of different countries and across different disciplines, and therefore it contributes tangibly towards the study of scientific problems of global interest that know no frontiers and whose solutions are shared by all human society. The history of the ESRF shows that international scientific collaboration can create tremendous breakthroughs and build bridges between nations. Many of the scientific highlights reported here are direct testimony of how science can contribute to make a better world for everybody.

I wish to conclude by expressing my profound gratitude to our partner countries for their constant support of the ESRF programme, and to the ESRF staff for their commitment in constructing, maintaining and operating the ESRF. However, all of us at the ESRF wish to wholeheartedly thank the ESRF users, to whom the ESRF Highlights belong and are dedicated, for their wonderful scientific work at the ESRF.

FRANCESCO SETTE
Director General,
ESRF

2017 AT THE ESRF

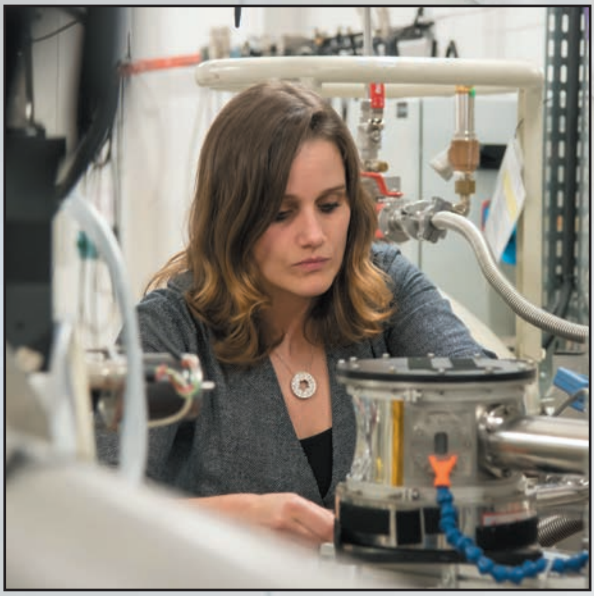

©C.ARGOUD/ESRF

Amélie Juhin Young Scientist 2017

7 February – Amélie Juhin was awarded the title of Young Scientist 2017 at the ESRF User Meeting by the ESRF User Organisation, for her experimental and theoretical studies of resonant X-ray scattering and X-ray dichroism.

Synchrotron@School goes international

March – Synchrotron@School, the ESRF's outreach programme, is now open for international students with classes from Sweden, the United Kingdom, Italy, Turkey, Greece, and Japan. More than 1300 high school students followed the course in 2017.

©S.CANDE/ESRF

©C.ARGOUD/ESRF

HERCULES specialised courses

May – Twenty-four students from 12 different countries followed the 19th HERCULES specialised course in quantitative imaging with X-rays and neutrons. HERCULES is now recognised as a successful and unique international programme to train the next generation of scientists from Europe or further afield in imaging techniques.

©S.CANDE/ESRF

Gersh Budker Prize for Pantaleo Raimondi

18 May – Pantaleo Raimondi, ESRF Accelerator & Source Director, was awarded the 2017 Gersh Budker Prize by the European Physical Society Accelerator Group (EPS-AG), for the invention of the Hybrid Multi Bend Achromat (HMBA) lattice. This design has since become the basis of most future 4th generation synchrotron sources.

India becomes 22nd country to join ESRF

19 June – India and the ESRF signed a three-year collaboration agreement making India the 22nd country to join the ESRF. Indian scientists now benefit from access to the ESRF for non-proprietary research with a focus on structural biology.

©REGIONAL CENTRE FOR BIOTECHNOLOGY, INDIA

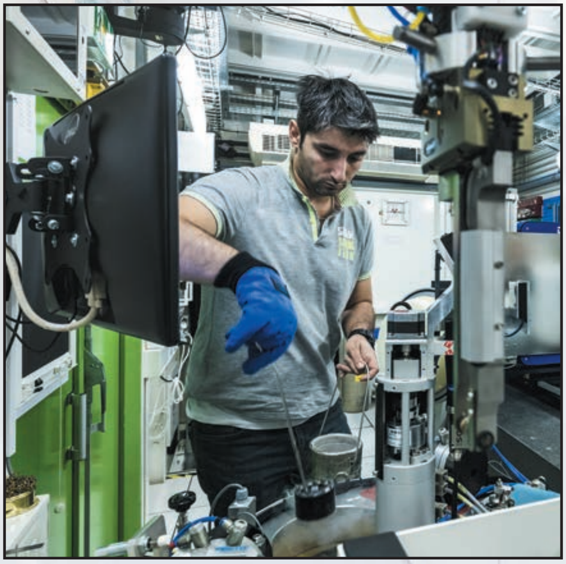

©S.CANDE/ESRF

Four new beamlines for ESRF-EBS

27 June – The ESRF Council gave the green light for the construction and commissioning of four new beamlines from 2018-2022. These new beamlines, designed for the full exploitation of the enhanced performance of the Extremely Brilliant Source, will address major challenges facing our society, including the development of the next generation of drugs, biomaterials and sustainable materials, and provide deep insights into the complex mechanisms governing living organisms.

2017 AT THE ESRF


ESRF 2017 beamtime allocation breaks all records

2409 proposals submitted

1022 proposals allocated (first time over 1000)

14752 shifts allocated

New record high for proposals received

September – A record high of 2409 proposals for beamtime were submitted in 2017, out of which 1022 experiment proposals were accepted. The proposal acceptance rate in 2017 was 42%. 2017's figures consolidate the trend for increased requests from scientific users and underline the ESRF's continued popularity among scientists.

Open SESAME: SESAME staff exchanges begin

July – Beamline scientist Mahmoud Abdellatief is the first staff member from the Synchrotron-Light for Experimental Science and Applications in the Middle East (SESAME) to come to the ESRF in the framework of OPEN SESAME, a Horizon 2020 programme coordinated by the ESRF.


©C.ARGOUD/ESRF


©Molyneux

ESRF benefits from ERC grant

September – Kristina Kvashnina was awarded a maximum level starting grant from the European Research Council for research to be carried out at the ESRF on the Helmholtz-Zentrum Dresden-Rossendorf-operated beamline, ROBL-BM20. Kvashnina can now set up her own research team and pursue ground-breaking research in the fundamental understanding of actinide and lanthanide nanomaterials.

Publications exceed 30 000

September – the ESRF reached a milestone of 30,000 publications since the facility opened its doors in 1994. Throughout the last decade, ESRF users have produced around 1800 publications per year, among which many have since become regarded as breakthroughs.

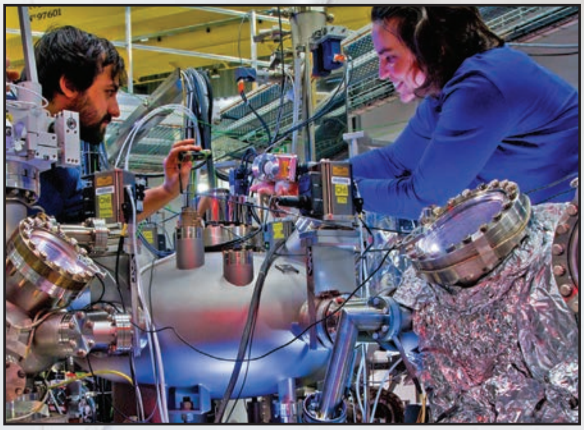
©D.MCBRIDE/ESRF

EBS mock-up is completed

October – A 'mock-up' of one of the 32 future cells of ESRF-EBS was successfully completed. The mock-up, comprised of four girders mounted with magnets, vacuum chambers, instrumentation, cooling pipes and cables, leads the way for the assembly of the EBS storage ring.

©S.CANDE/ESRF

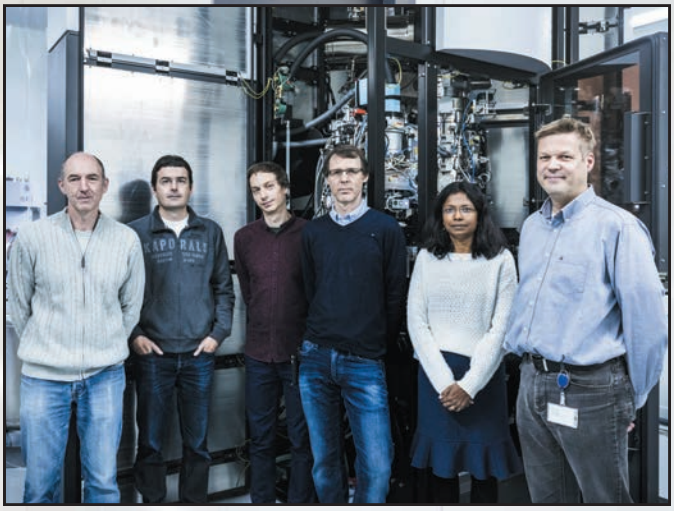

©S.CANDE/ESRF

Inauguration of Titan Krios cryo-electron microscope

10 November – A Titan Krios cryo-electron microscope was inaugurated in the presence of Ada Yonath, 2009 chemistry Nobel Prize laureate, and all the partners that jointly run the facility with the ESRF: the European Molecular Biology Laboratory (EMBL), the Institut de Biologie Structurale (IBS) and the Institut Laue-Langevin (ILL).

LEAPS

13 November – The League of European Accelerator-based Photon Sources was officially launched in Brussels. The 16 light sources in Europe that have joined forces for LEAPS aim to promote the research carried out at synchrotron sources and XFEL facilities and to share knowledge for the benefit of society worldwide.

©Courtesy of LEAPS

STATUS OF THE EBS

Three years into the EBS project, 2017 has seen the completion of many milestones, including the start of the assembly phase and the delivery of over 60% of the magnets. New flagship beamlines have been selected to take full advantage of the new source properties and upgrades are also underway.

PROJECT OVERVIEW

The past year marked the third year of the execution phase of the ESRF's Extremely Brilliant Source (EBS) project, which will see the implementation of a new lattice for the storage ring. This will reduce the natural horizontal emittance from 4 nm to about 134 pm, thus greatly increasing the brilliance and coherence of the beam, opening up new perspectives for experiments that are not conceivable today. Much of the work of the project in 2017 concentrated on the delivery of the components and equipment, as well as the start of the assembly phase. A 'mock-up' of a standard cell to be used for the new machine was successfully completed, allowing corrections to be identified and integrated into the series production. In addition to this, great efforts went into the detailed planning and organisation of the dismantling and installation phases, complex work that defines the logistical requirements, task sequences and resource needs for the next three years. Finally, the EBS storage and assembly buildings were completed and started to be put to use at the end of the year as the project entered the assembly phase. This year has seen great progress for the EBS project, and preparations are well underway for the long shutdown in 2018.

The fifth and sixth MAC (Machine Advisory Committee) meetings were held at the ESRF in April and September 2017. Committee members from various institutes came together to discuss the recent progress of the EBS project and to make recommendations for the six months ahead. In September, the MAC was impressed with the solid progress made over the year and congratulated the ESRF staff on the completion of the mock-up cell as well as the ESRF 01 building, which was delivered on time and within budget.

DIPOLE ASSEMBLY COMPLETE

A project milestone was reached in 2017 with the completion of the assembly, measurement and fine-tuning of all 128 permanent magnet dipoles, which are to be installed in the EBS storage ring in 2018. Following tests on the first two dipoles, which were assembled and measured at the end of 2016, the series assembly and measurements started at the beginning of 2017. The maximum production rate was reached at the end of March and maintained until the end of production, in October. More than six tons of samarium-cobalt permanent magnet blocks have now been assembled in 640 magnet modules.

The dipole magnets are made of five modules (**Figure 1**) with fields ranging from 0.17 T up to 0.62 T; the resulting step function field profile will contribute to the low emittance of the new EBS machine. The dipoles with longitudinal gradient (DL) were good candidates for the ESRF's well established permanent magnet technology. The permanent magnet DLs are very compact due to the absence of coils; complex coils would be needed for generating field steps along the magnet. Their zero electrical consumption, combined with the absence of power supplies and water cooling, will result in significant energy savings.

The assembly and measurement of the DLs consist of several steps. Permanent magnet blocks are first inserted into the iron yokes of the magnet modules, before measuring and trimming the field of the individual magnet modules. The modules are then assembled together to build a complete DL; the field of the complete DL is measured and the angle and trajectory offsets it gives to the electron beam are trimmed. The magnet then undergoes fiducialisation, *i.e.*

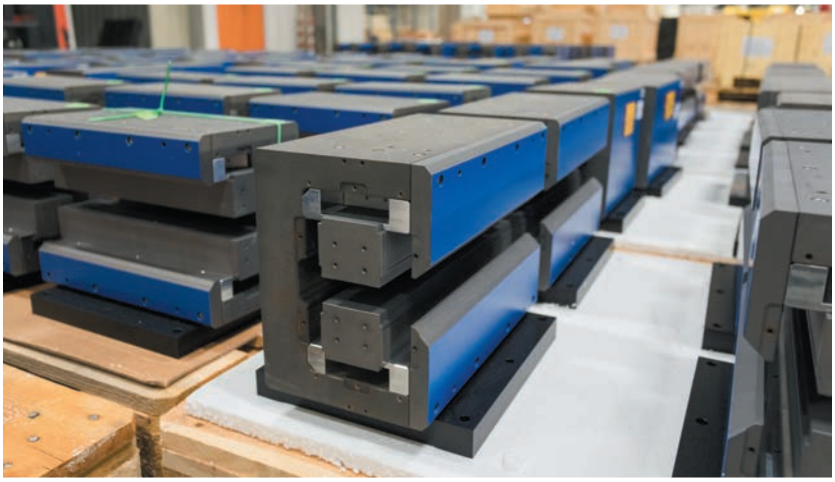

Fig. 1: Each permanent magnet module (left) weighs about 80kg and five modules are needed to make up each of the 128 complete dipoles.

measuring the coordinate of survey reference with respect to the magnetic centre. Finally, the DL is installed on its final support and stored, ready to be mounted onto the girders during the assembly phase.

MOCK-UP COMPLETED

Another major milestone was reached in September 2017; the successful completion of a mock-up of a standard cell to be used for the new machine (**Figure 2**). All magnets are now installed and aligned, all vacuum chambers have been connected together and inserted into the magnets, including front end vacuum lines, and put under vacuum. The mock-up assembly allowed staff to identify many necessary corrections, which have been integrated into the series production.

NEW BUILDINGS FOR EBS

Significant building work has taken place over 2017, and three buildings for use in the EBS project are now up and running. The beginning of June saw the mounting of buildings ESRF 02 A and B, which are now fully operational. Components for the EBS are to be stored in these two buildings before being transferred to ESRF 01 for assembly. In early September, ESRF 01, which is to be used for the assembly phase of the EBS project, was completed and inaugurated (**Figure 3**).

START OF THE ASSEMBLY PHASE

Following the delivery of the ESRF 01 assembly building in September 2017, the assembly phase of the EBS project has begun. This period, lasting from November 2017 to the end of 2018, will see 128 girders mounted with state-of-the-art magnets, vacuum chambers and instrumentation, ready to be installed in the storage ring tunnel in early 2019.

The work takes place on three assembly lines (**Figure 4**), each one dedicated to a specific task; mounting and aligning the magnets, placing the vacuum chambers inside the magnets, and finally closing the magnets for final precise alignment. Each process lasts around a week then the finished girders are placed in storage, awaiting the installation phase. Several girders have already been equipped with magnets and vacuum chambers.

Fig. 2: The completed ‘mock-up’ of an EBS cell in the Chartreuse Hall.

Fig. 3: The inauguration of ESRF 01 on 14th September. From left: Francesco Sette (ESRF Director General), Richard Walker (Chairman of the MAC), Thierry Marchial (Head of Buildings and Infrastructure), Sylvie Campillo (architect) and Dieter Einfeld (accelerator physicist).

Fig. 4: The assembly line in ESRF 01. The assembly team is being supplemented by magnet and vacuum specialists from Budker Institute of Nuclear Physics, Russia.

RF CAVITIES CONDITIONED

In preparation for installation into the EBS machine in 2018, all 12 HOM-damped cavities have now been delivered and successfully RF conditioned to 750 kV (**Figure 5**).

The manufacturing of the HOM absorbers is progressing well. The challenging brazing of the absorbing ferrite plates is being followed up very carefully by means of sophisticated qualification procedures involving ultrasonic and RF power tests. The HOM absorbers are expected to be delivered during 2018 and then installed.

The additional RF waveguides needed to power these cavities from the existing RF transmitters were ordered last October and will be delivered before June 2018. The upgrade of the klystron transmitters, including a refurbishment of the local control, is also progressing according to schedule.

Fig. 5: The RF-conditioned cavities are stored in a dedicated zone in the ESRF experimental hall.

POWERING THE EBS MAGNETS

Several large magnet powering contracts were signed in 2017, following the finalisation of the power requirements for the EBS storage ring and the launch of the procurement of more than 2100 power supplies to power the main and corrector EBS magnets. The prototypes for the main coil power converters have shown an efficiency close to the calculated values. The optimised magnets and power supply design will result in 40% overall reduction of energy consumption for the magnetic elements. The highly optimised voltage DC cabling distribution around the technical gallery is progressing well and the first test of the common sources was promising. The challenge of testing the magnetic field polarities is under preparation for smooth commissioning of the future beam.

HUMAN RESOURCES FOR THE LONG SHUTDOWN

Planning is underway to pull together the large workforce required for the dismantling and installation phases of the long shutdown in 2019. There will be a high demand for human resources during these phases and, at times, more than 100 persons will be working in different areas in the accelerator tunnel and the technical zones. It is foreseen that staff currently working on the beamlines will help with these activities and organisation charts have already been drawn up such that all roles are well attributed in advance.

PUBLIC BEAMLINE UPGRADE

Following the extraction of eight proposals for new beamlines within the EBS from 48 expressions of interest in 2017, eight Conceptual Design Reports (CDRs) were prepared:

- CDR1 – Beamline for coherence applications
- CDR2 – Beamline for hard X-ray diffraction microscopy
- CDR3 – High throughput large field phase-contrast tomography beamline
- CDR4 – Surface science beamline
- CDR5 – High-flux nano-X-ray diffraction beamline for science under extreme conditions
- CDR6 – Facility for dynamic compression studies
- CDR7 – High brilliance XAS beamline
- CDR8 – Serial crystallography beamline

After evaluation the ESRF SAC recommended to accept four CDRs for construction within the EBS (EBSL1 – CDR1, EBSL2 – CDR2, EBSL3 – CDR3, EBSL8 – CDR8), which was endorsed by Council at its meeting in June 2017. In addition, the SAC recommended to implement as many as possible of the remaining four CDRs within the regular beamline refurbishment programme (CDR4, CDR5, CDR6, CDR7). Based on this recommendation, a timetable for the construction of beamlines and refurbishment has been worked out for the period 2018-2022. Planning and design works have already started for the two flagship projects, EBSL3 and EBSL8, which will be constructed on the ports BM18 and ID29, respectively.

In parallel to the development of the EBS upgrade beamline portfolio, regular works continued to prepare the existing beamline portfolio for the new source. The refurbishment of the MX microbeam beamline ID23-2 was finished and the beamline resumed full user operation. The refurbishment of the X-ray microscopy beamline ID21 continues and is on schedule. The beamline will host the new high performance prototype scanning double crystal monochromator (DCM), which is progressing on schedule as well.

Progress has also been achieved on the two user platforms, the high power laser facility (HPLF-I) and the cryo-electron microscope (cryo-EM). The order for the high power laser has been placed and the planning for the modification of the infrastructure on beamline ID24 for the laser installation has started. The cryo-EM has been delivered and commissioned in the newly constructed premises in the Belledonne Hall between beamlines ID01 and ID02. The cryo-EM has been in full user operation since November 2017.

CRG BEAMLINE UPGRADE

The transfer of beamline BM14 to the DUBBLE consortium and preparations for the construction of a new beamline on port BM07 for the transfer of the French CRG beamline BM30A-FIP are progressing as planned. Work on the beamlines BM20 and BM28 in preparation for the new source continues on schedule as well.

INSTRUMENTATION AND DATA MANAGEMENT

The EBS project comprises an ambitious instrumentation and technology programme, which is required to gain the greatest benefit from the new source properties. In 2017 there was significant progress in data management and analysis. Version 0.6.0 of the silx toolkit (https://github.com/silx-kit), a library of common software routines for analysing data from synchrotron sources, was recently released. It includes many new features such as support for OpenGL for high speed graphics. Metadata collection is implemented on 11 beamlines and is in progress on a further six (refer to http://www.esrf.fr/datapolicy for the list of beamlines), and work has started on the long-term data archiving for 10 years, as part of the plans to complete the implementation of the ESRF data policy by 2020. A dedicated high-speed disk storage system of 2 petabytes has been purchased and is now operational for the images generated by the new cryo-EM platform.

The rotary axis of the prototype double-crystal monochromator (DCM) was assembled and is currently undergoing tests in the laboratory. In parallel, work for its implementation on ID21 is in progress and all efforts focus on installing the DCM on ID21 by the summer of 2018.

The Detector Development Plan is shaping up, with the establishment of strategic partnerships for the development of new sensor materials.

In order to strengthen expertise in mechatronics, which integrates online measurements for correction of position errors and advanced control strategies, a mechatronics task force has been created to foster synergies between the ISDD groups and provide a platform for the exchange of experience. Investments in real-time control hard- and software were made and the creation of a mechatronics laboratory is underway.

In the domain of optics and metrology, novel refractive X-ray lens optics were developed and characterised, and a new surface metrology prototype instrument based upon Shack-Hartmann sensor technology was installed and commissioned.

R. DIMPER, M. KRISCH, P. RAIMONDI,
H. REICHERT AND J. SUSINI

STRUCTURAL BIOLOGY

With several major projects aimed at improving the choices and possibilities offered to external users of our end-stations completed and the foundations laid for structural biology at the ESRF post-EBS, 2017 has been another very busy year for the ESRF Structural Biology group. Indeed, all the group's macromolecular crystallography (MX) facilities are now equipped with new generation FlexHCD sample changers, which, after initial teething troubles had been resolved, are faster, more reliable, versatile and robust than the SC3 devices they replace. Moreover, the completion of the **ID23-2** nanobeam project means that the world's first microfocus beamline dedicated to MX now provides users with a choice of two different beam sizes for experiments in micro-crystallography. However, the most high-profile project to be completed in our group in 2017 was the installation and commissioning of a Titan Krios cryo-electron microscope in the Belledonne Experimental Hall. As previously outlined, the microscope is being operated as a beamline (**CM01**) and forms part of the Partnership for Structural Biology (PSB) platform for cryo-electron microscopy (cryo-EM). Truly outstanding work by staff from the ESRF's technical support divisions ensured that the infrastructure in which the microscope is sited was delivered on time and is second to none in terms of environmental stability (temperature, vibration, magnetic field), while excellent project management guaranteed the seamless installation and commissioning of the microscope. CM01 was inaugurated on 10th November 2017 with the first external user experiments starting soon after. Although it is still too soon to fully detail the outcomes of these, initial results, including those obtained on 'test' samples (*i.e.* Tobacco Mosaic Virus), are extremely encouraging and point to a very bright future for the beamline.

While all the above was being carried out, and as has been the case for many years, the ESRF's facilities for structural biology continued to provide outstanding service to our external user community. **ID29** and **ID23-1** continue to be very productive with both end-stations delivering record numbers of depositions in the PDB (see http://biosync.sbkb.org/stats.do?stats_sec=RGNL&stats_focus_lvl=SITE&stats_site=ESRF for details). Output from the three UPBL10 MX end-stations (MASSIF-1 (**ID30A-1**), MASSIF-3 (**ID30A-3**) and **ID30B**) is also quickly ramping up, with the services they provide – particularly the 'hands-off', fully automatic data collection offered on MASSIF-1 – becoming very popular. 2017 has also seen **BM29**, the group's BioSAXS beamline, truly come of age. When BM29 was first commissioned in 2012, BioSAXS was still seen as a 'trendy', but optional, technique complementary to MX. Such has been the success of BM29 – the number of papers citing use of the beamline is rapidly approaching 100 per year – that this is no longer the case and BioSAXS is now seen as a crucial source of complementary information in integrated structural biology projects, as are the *in crystallo* spectroscopy experiments provided by the group's pioneering **ID29S** Cryobench facility, which was refurbished in 2017.

Experiments on structural biology end-stations account for ~40% of all experiments carried out at the ESRF with, as a natural consequence, external visitors (from academia and industry, remote or on-site) to these facilities making up a similar fraction of scientists carrying out experiments at the ESRF. However, we are well aware that scientific success is not purely a numbers game, and that it is quality of output that counts the most. We therefore hope that, as in previous years, the highlights reported here properly reflect the full range of the very high quality of research facilitated by experiments carried out on the Structural Biology group's end-stations. As readers will see, an increasing proportion of this research is aimed at providing structural frameworks for the design of improved therapeutic agents, including new-generation antibiotics, in the treatment of disease. In addition to an increased focus on human health, the articles presented here detail investigations of fundamental biological processes including mechanisms used in signalling (**see page 17**) and in the regulation of gene expression (**see page 20**), the discovery and characterisation of an enzyme that converts fatty acids to hydrocarbons (**see page 22**) and perhaps most fundamental of all, at least in terms of new life, the structural basis of egg coat-sperm recognition at the moment of fertilisation (**see page 29**). One article – hopefully the first of many that will appear in future editions of the *ESRF Highlights* – reminds us that the study of structural biology at the ESRF is not limited to experiments exploiting MX, BioSAXS and cryo-EM (**see page 26**).

Other techniques – in this case EXAFS experiments on BM01 – can be used to provide important structural information that helps further our understanding of the molecular mechanisms of disease.

By the time the 2018 edition of the *ESRF Highlights* appears, in January 2019, our users will have carried out the last experiments based on X-rays produced by the current ESRF storage ring. Future experiments will be carried out using ESRF-EBS (Extremely Brilliant Source), producing much brighter, more powerful X-ray beams than the current ESRF storage ring. The study of structural biology using this new source will be ensured both by the proper revision of many of our current beamlines, guaranteeing that they continue to provide state of the art end-stations (including world-leading automation and ancillary techniques) for structural biology, and by a major reconstruction, as agreed by the ESRF SAC in May 2018, of ID29. This reconstruction will provide, from late 2020, an ultra-high flux ($\sim 10^{16}$ photons/sec) micro/nanofocus facility for synchrotron serial crystallography (SSX) and time-resolved MX. Among many potential methods, the new beamline will facilitate the elucidation of SSX-derived room-temperature crystal structures that will deliver more information on the dynamics of biological macromolecules. These, combined with time-resolution on the microsecond timescale, will help provide ‘molecular’ movies of the conformational changes that are required in a multitude of biological processes.

G. LEONARD
AND C. MUELLER-DIECKMANN

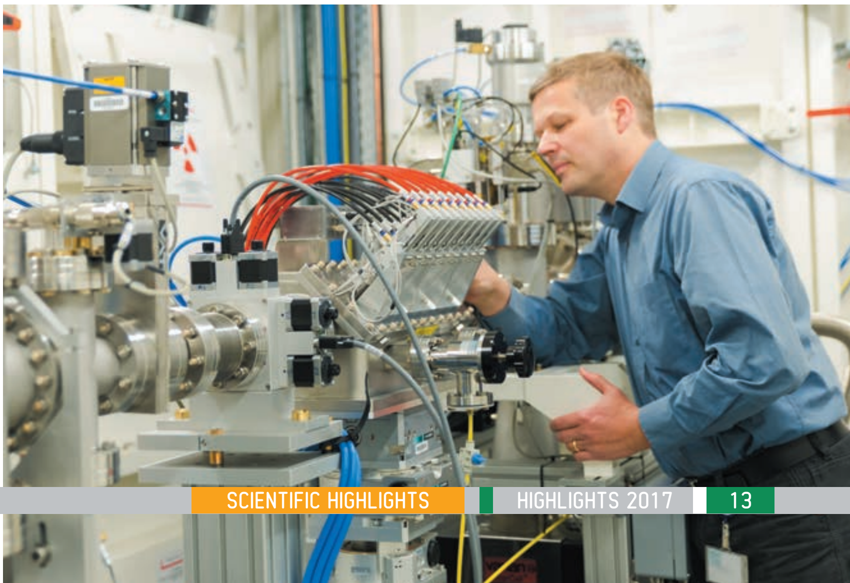

STRUCTURE OF A HUMAN EXCITATORY NEUROTRANSMITTER TRANSPORTER

Excitatory neurotransmission in the human brain requires fast removal of the transmitter glutamate from the synaptic cleft. Excitatory amino acid transporters perform this function and prevent cytotoxicity. Here, the first crystal structures of a human excitatory amino acid transporter have been solved. This has unravelled important molecular details of their function and pharmacology.

Over the last decade, the structural knowledge of human excitatory neurotransmitter transporters has been based on crystal structures of archaeal homologs that offered a first glimpse into their molecular mechanisms but fall short of explaining the functional and pharmacological complexity of human transporters. Using beamlines **ID23-1**, **ID23-2**, **ID29** and **ID30B**, among others, the X-ray crystal structures of a thermostable human excitatory amino acid transporter (EAAT1cryst) have been solved.

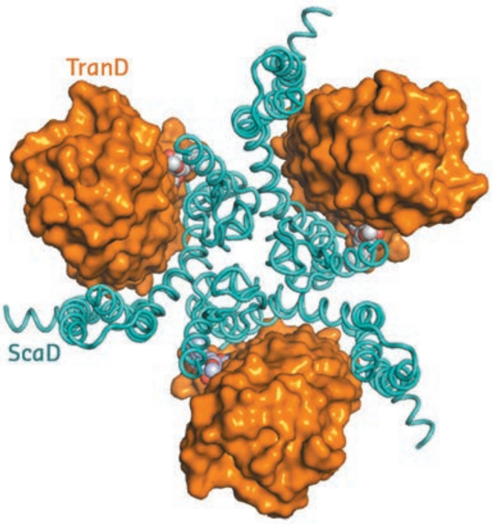

Fig. 6: Extracellular view of the EAAT1cryst trimer with the transport (TranD) and scaffold (ScaD) domains coloured orange and cyan respectively.

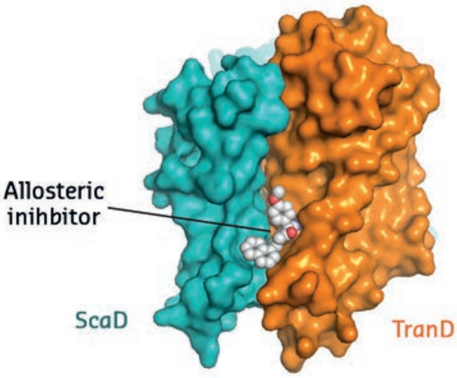

Fig. 7: Membrane view of a EAAT1cryst protomer with the allosteric compound UCPH-101 bound between the transport and scaffold domains.

The structure of EAAT1cryst shows it to be a homotrimer (~180 kDa), in which each protomer contains two domains: a scaffold domain that forms all of the inter-subunit contacts, and a transport domain that contains all the residues to coordinate the substrate and coupled sodium ions (**Figure 6**). Previous structural work on homologs showed that substrate translocation across the membrane occurs through large rigid body movements of the transport domain relative to the scaffold domain with the substrate occluded in its core **[1,2]**. The EAAT1cryst structure captures a so-called outward-facing state of the transport cycle, in which the transport domain is in the 'up-position' with the neurotransmitter-binding site facing the extracellular side of the membrane.

EAAT1cryst was crystallised in the presence of both the substrate and UCPH-101, the only known selective allosteric inhibitor of this family of proteins. Clear electron density showed the inhibitor wedged between the transport and scaffold domains of each protomer (**Figure 7**). In combination with studies of the transporter dynamics and functional assays, this crystallographic work thus unravelled the first allosteric mechanism of inhibition of excitatory neurotransmitter transporters: the allosteric compound 'glues' the transport and scaffold domains together and precludes the 'elevator-like' motions of the former that are required for transport.

This work opens the way for a better understanding of the molecular mechanisms of the function, regulation and pharmacology of an essential component of the synaptic machinery in the brain.

PRINCIPAL PUBLICATION AND AUTHORS

Structure and allosteric inhibition of excitatory amino acid transporter 1, J.C. Canul-Tec (a,b), R. Assal (a,b), E. Cirri (a,b), P. Legrand (c), S. Brier (b,d), J. Chamot-Rooke (b,d) and N. Reyes (a,b), *Nature* **544**, 446-451 (2017); doi: 10.1038/nature22064.

(a) Molecular Mechanisms of Membrane Transport Laboratory, Institut Pasteur, Paris (France)
(b) UMR 3528, CNRS, Institut Pasteur, Paris (France)
(c) Synchrotron SOLEIL, Gif-sur-Yvette (France)
(d) Structural Mass Spectrometry and Proteomics Unit, Institut Pasteur, Paris (France)

REFERENCES

[1] N. Reyes *et al., Nature* **462**, 880-885 (2009).
[2] N. Reyes *et al., Nat. Struct. Mol. Biol.* **20**, 634-640 (2013).

STRUCTURE-BASED DEVELOPMENT OF SMALL MOLECULES THAT DISRUPT GLYCOSOMAL TRANSPORT IN *TRYPANOSOMA* PARASITES

PEX14 and PEX5 are crucial to the transport of metabolic enzymes into glycosomes in *Trypanosoma* protists. Inhibition of the complex formed between these two proteins disrupts essential metabolic processes and leads to parasite death. Using a structure-based approach, the first PEX14-PEX5 protein-protein interaction inhibitors have been developed. These disrupt glycosomal transport and kill *Trypanosoma*.

Trypanosoma parasites are protozoa that cause numerous diseases including sleeping sickness and Chagas disease. Unlike for other eukaryotic cells, glycolytic processes in *Trypanosoma* parasites take place within a single organelle, the glycosome. As this organelle lacks genetic information, all the metabolic enzymes need to be imported post-translationally. The PEX14-PEX5 protein-protein interaction plays a crucial role in this pathway. Consequently, inhibiting the formation of the complex between these two proteins is a way of disrupting glycosome function, leading to accumulation of glycosomal enzymes in the cytosol which, in turn, causes adenosine triphosphate (ATP) depletion and metabolic collapse, resulting in *Trypanosoma* parasite death (**Figure 8**).

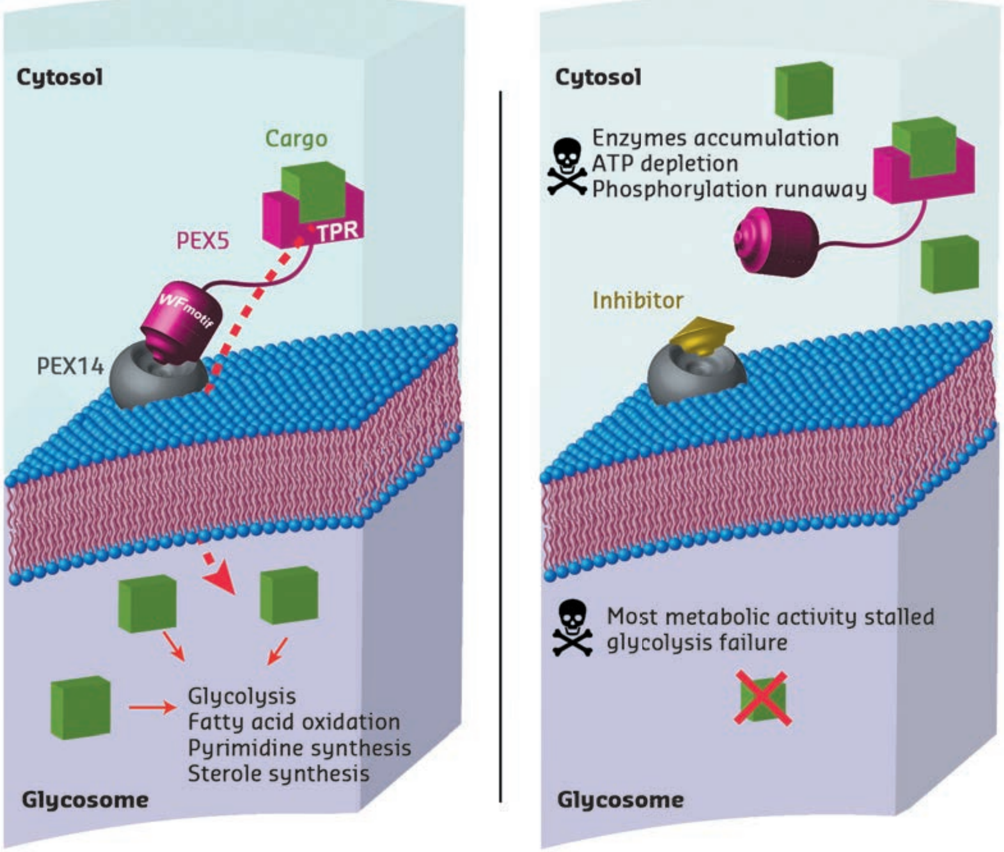

Fig. 8: Principle of the mechanism of action of PEX14 inhibitors, showing a normal cell (left) and a cell in the presence of an inhibitor (right). The inhibitor molecule interferes with PEX5 binding to the membrane-associated import factor PEX14. Instead of being transported to the glycosome, enzymes are stranded in the cytosol, multiplying damage to the cell. This disrupts major metabolic pathways in *Trypanosoma*, causing ATP depletion and, eventually, cell death.

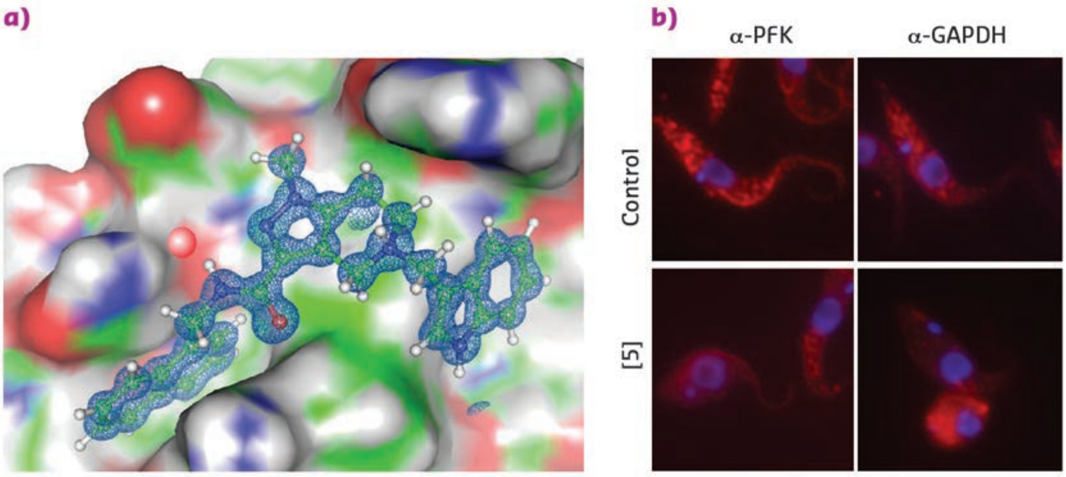

Fig. 9: a) A PEX14 inhibitor bound to trypanosomal PEX14. Very high-resolution structural data allowed the rapid optimisation of inhibitors towards enhanced potency and selectivity. b) Fluorescence microscopy reveals the disruption of the glycosomal transport system by PEX14 inhibitors. Enzymes that are localised in glycosomes in control cells (granular pattern) are spread over the entire cell volume in the presence of the inhibitor.

Existing structural information **[1]** was employed to perform a 3D pharmacophore-based *in silico* screening of a virtual compound library followed by 3D docking. This identified drug-like pyrazolo[4,3-c]pyridine derivatives that bind to PEX14 and disrupt the PEX14-PEX5 interface. Hit validation by NMR binding assays and hit optimisation based on results from NMR fragment screening led to more potent molecules that were amenable to cocrystalisation with the PEX14 protein. High-resolution X-ray data were collected at beamlines **ID29** and **ID30b** with crystals of the resulting PEX14-inhibitor complexes yielding exceptional data quality to a resolution of up to 0.86 Å (**Figure 9a**). These high-resolution structures unambiguously confirmed the *in silico* derived binding model of the inhibitors and enabled further rational compound optimisation.

A peculiarity of the cocrystal structures is the presence of a structural water molecule that mediates the interactions of ligands with the PEX14 protein and was not predicted by docking. The importance of this water molecule was evident as it could not be displaced from the protein surface by polar moieties that were tentatively attached to the ligand. Furthermore, the water molecule interacts with the side chain of Asn31, an amino acid residue that is specific to *Trypanosoma* and distinct from humans, potentially contributing to ligand specificity. Detailed analysis of the water network surrounding the protein-inhibitor complex was necessary to understand the binding energetics and optimise the ligands.

The PEX14 inhibitors that were developed show potent and selective *in vitro* activity against clinically relevant *T. brucei* and *T. cruzi* species. This activity correlates with the inhibitory effects of the ligands against PEX14-PEX5 complex formation. Together with the observed mislocalisation of glycosomal enzymes to the cytosol and decreased cellular ATP levels, this supports an on-target mode of these inhibitors (**Figure 9b**).

Many of the glycosomal enzymes have individually been successfully evaluated as trypanocidal agents in the past. This work shows an efficient way to disrupt the function of all of these enzymes simultaneously and validates the PEX14-PEX5 protein-protein interaction interface as a viable drug target for *Trypanosoma* infections.

PRINCIPAL PUBLICATION AND AUTHORS

Inhibitors of PEX14 disrupt protein import into glycosomes and kill Trypanosoma parasites, M. Dawidowski (a, b), L. Emmanouilidis (a, b), V.C. Kalel (c), K. Tripsianes (d), K. Schorpp (e), K. Hadian (e), M. Kaiser (f, g), P. Mäser (f, g), M. Kolonko (a), S. Tanghe (h), A. Rodriguez (h), W. Schliebs (c), R. Erdmann (c), M. Sattler (a, b) and G.M. Popowicz (a, b), *Science* **355**, 1416-1420 (2017); doi: 10.1126/science.aal1807.

(a) Institute of Structural Biology, Helmholtz Zentrum München, Neuherberg (Germany)
(b) Center for Integrated Protein Science Munich, Chair of Biomolecular NMR, Department Chemie, Technische Universität München, Garching (Germany)
(c) Institute of Biochemistry and Pathobiochemistry, Department of Systems Biochemistry, Ruhr University Bochum (Germany)
(d) CEITEC, Central European Institute of Technology, Masaryk University, Brno (Czech Republic)
(e) Assay Development and Screening Platform, Institute of Molecular Toxicology and Pharmacology, Helmholtz Zentrum München, Neuherberg (Germany)
(f) Swiss Tropical and Public Health Institute, Basel (Switzerland)
(g) University of Basel (Switzerland)
(h) New York University School of Medicine, Department of Microbiology, New York (USA)

REFERENCES

[1] C. Neufeld *et al.*, *EMBO J.* **28**, 745-754 (2009).

REVEALING THE MECHANISM OF BACTERIAL TRANSMEMBRANE SIGNALLING

Crystal structures of an *E. coli* sensor protein in ligand-bound and ligand-free states reveal the mechanism of transmembrane signalling employed by bacterial sensor histidine kinases.

Cellular perception of external stimuli is an ability of every living organism that is critical for survival. Sensor histidine kinases (HKs) are a large class of membrane receptor proteins that, in bacteria, are involved in different processes including pathogenicity and cell growth. This makes them attractive targets for study, particularly as various HKs of different species are expected to share a similar mechanism due to a conserved domain architecture and dimeric working state. However, despite the fact that HKs are widespread and despite the availability of some structural information, there has been no consensus concerning the molecular mechanism of sensory signal transduction through the membrane. The reason is that the available structural information is either of low resolution or from isolated domains of HK molecules, thus giving little insight into the concerted structural transformations associated with signal transduction.

In meso crystallisation and single-wavelength anomalous dispersion experiments at beamline **ID23-1** were used to determine the crystal structures in both ligand-bound and ligand-free states of a truncated construct of the *Escherichia coli* nitrate/nitrite sensor HK, NarQ. In *E. coli*, NarQ senses nitrate and nitrite ions in the periplasm and regulates the metabolism of these. This is very important as bacteria use these ions as electron acceptors in the respiratory chain in the absence of oxygen. Comparing the structures obtained reveals that binding of nitrate or nitrite to the periplasmic sensor module of NarQ causes a structural rearrangement, resulting in a symmetric displacement of ~2.5 Å of two of the four transmembrane α-helices in the HK dimer. On the cytoplasmic side, this relatively small displacement is transmitted to the amplifying HAMP domain, which undergoes a lever-like motion that results in the maximum displacement amplitude of 7 Å at the end of the HAMP output helices, likely destabilising the coiled coil phase (see **Figure 10**). The latter phenomenon is assumed to impact the stability of downstream helices, thus modulating the efficiency of kinase function.

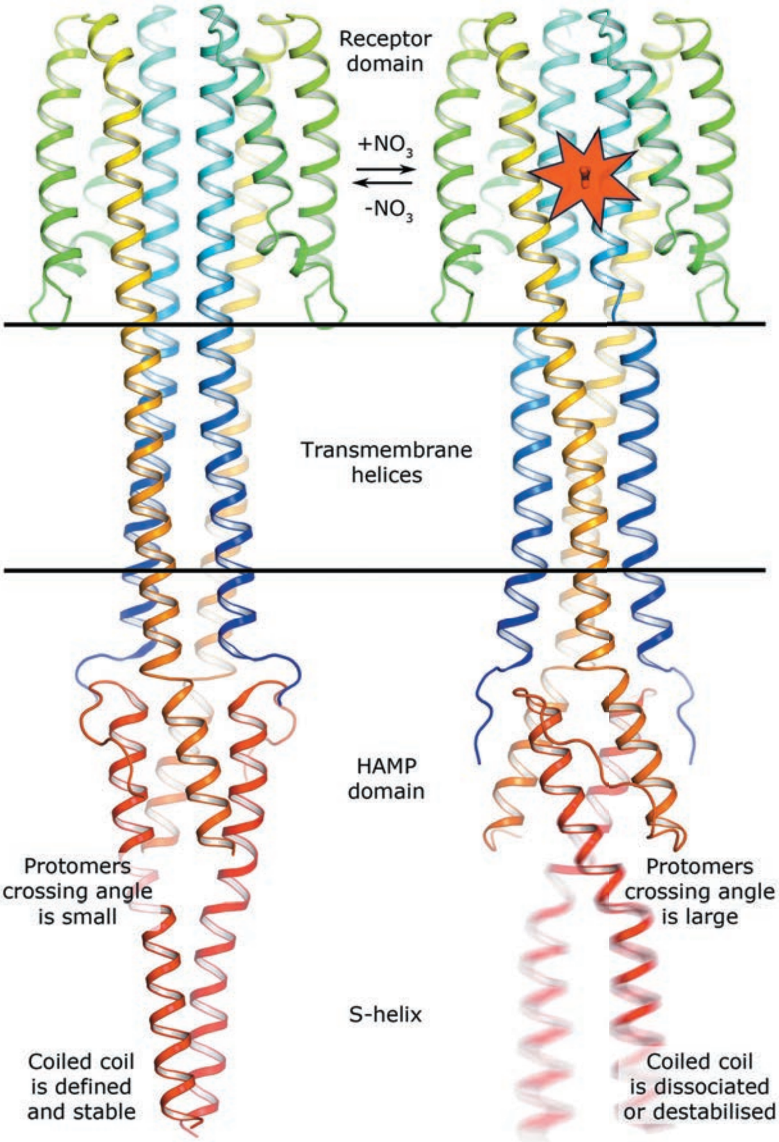

Fig. 10: Mechanism of NarQ transmembrane signalling. Binding of the ligand launches a series of structural changes including a piston-like relative displacement of the transmembrane helices towards the periplasm, consequent lever-like conformational changes in the HAMP domain and the dissociation or destabilisation of the signalling helix.

The structural similarities between HKs strongly suggest that the piston-like displacement in the transmembrane domain is an important facet in signal transduction by all HK proteins. The mechanism of the signal amplification seen for the NarQ HAMP domain also creates a framework for understanding the principles of signalling of all HAMP-containing proteins. Overall, the results show how a mechanistic signal is generated and amplified while being transduced through HKs over distances of 100 Å or more. The study may provide insights for the further understanding of signalling pathways in different species of microorganisms and, potentially, promote the production of new antimicrobial treatments other than conventional antibiotics.

PRINCIPAL PUBLICATION AND AUTHORS

Mechanism of transmembrane signaling by sensor histidine kinases, I. Gushchin (a,b), I. Melnikov (c), V. Polovinkin (a,b,d), A. Ishchenko (a,e), A. Yuzhakova (a,b), P. Buslaev (b), G. Bourenkov (f), S. Grudinin (g,h,i), E. Round (a,d), T. Balandin (a), V. Borshchevskiy (a,b), D. Willbold (a,j), G. Leonard (c), G. Büldt (b), A. Popov (c) and V. Gordeliy (a,b,d), *Science* **356**, 6342, eaah6345 (2017); doi: 10.1126/science.aah6345.

(a) Institute of Complex Systems (ICS), ICS-6: Structural Biochemistry, Research Centre Jülich (Germany)
(b) Moscow Institute of Physics and Technology, Dolgoprudniy (Russia)
(c) ESRF
(d) Université Grenoble Alpes, CEA, CNRS, IBS, Grenoble (France)
(e) Institute of Crystallography, University of Aachen (RWTH) (Germany)
(f) European Molecular Biology Laboratory (EMBL), Hamburg Outstation (Germany)
(g) Université Grenoble Alpes, LJK, Grenoble (France)
(h) CNRS, LJK, Grenoble (France)
(i) Inria, Grenoble (France)
(j) Institute of Physical Biology, Heinrich Heine University, Düsseldorf (Germany)

CONDENSIN COMPLEXES FASTEN THE BELT AROUND DNA

The crystal structure of the major DNA binding site in the eukaryotic condensin complex, which is jointly formed by the Cnd3 HEAT-repeat and Cnd2 kleisin subunits, has been determined. The DNA-bound structure indicates an unconventional 'safety belt' mechanism that anchors condensin complexes and might provide condensin with the means to form large chromatin loops.

Ever since the first observation of condensed chromosomes in dividing cells during the late 19th century scientists have been trying to understand the principles that underlie this dramatic reorganisation of chromatin fibres **[1]**. However, it took more than one hundred years before the five-subunit condensin complex was identified as the leading player in the formation of mitotic chromosomes **[2]**. Thus, despite its key role in the correct segregation of chromosomes during mitosis and meiosis, the molecular mechanisms by which condensin complexes interact with chromatin fibres and alter their topology have, so far, remained largely mysterious.

Condensin complexes share their basic architecture with other structural maintenance of chromosomes (SMC) complexes, including cohesin and SMC5/6 in eukaryotes, and different SMC-type complexes in prokaryotes. All SMC complexes play essential roles in the maintenance of a cell's genetic material during various aspects of chromosome biology, including chromosome condensation and segregation, DNA recombination and damage repair, and the organisation of chromosomal territories. The conserved basic architecture of these complexes suggests that they share a common mode of action in how they perform this array of seemingly diverse tasks.

How would such a common mechanism work? A number of different models have been suggested over the years, but recently a process called 'loop extrusion' has been championed as a simple and elegant mechanism that could explain most of the cellular tasks of SMC complexes (**Figure 11**). How these complexes might form and extend

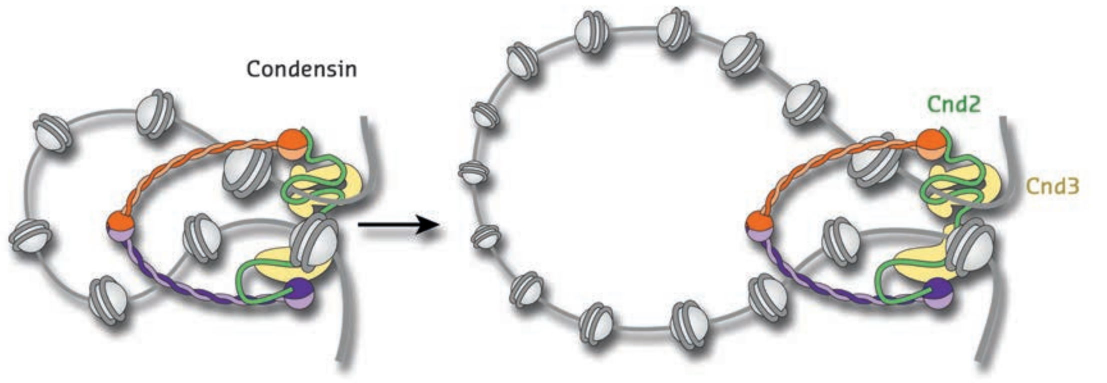

Fig. 11: Model for the extrusion of chromatin loops by the five-subunit condensin complex. The complex is thought to encircle DNA within the large ring-shaped architecture formed by its SMC2-SMC4 coiled coil subunits (orange and purple) and Cnd2 kleisin subunit (green). HEAT-repeat subunit Cnd3 (yellow) binds to the Cnd2 kleisin.

DNA loops is, however, not understood, but one precondition of any loop extrusion model is that the proteins would need to make direct contact with their DNA substrates. Since all subunits of SMC complexes are largely devoid of classic DNA-binding motifs, the nature and specificity of this interaction has remained uncertain.

Previous work had demonstrated that a ternary sub-complex consisting of two HEAT-repeat subunits and the so-called kleisin subunit can facilitate DNA binding in a sequence-unspecific manner **[3]**. To identify the DNA binding site in this ternary sub-complex, the three subunits were expressed and purified individually and tested alone or in combination for DNA binding. Neither subunit alone could bind DNA efficiently. Only the combination of the HEAT-repeat protein Cnd3 with the kleisin Cnd2 yielded a DNA-binding activity comparable to the ternary complex.

This complex was – after some additional engineering and screening – amenable to crystallisation by vapour diffusion. Following data collection at beamline **ID29**, the crystal structures from two different yeast species were determined to 2.6 and 2.8 Å resolution, respectively. The structures not only provided the molecular details of how the kleisin subunit binds along the inner surface of the harp-shaped HEAT-repeat solenoid, but also gave a clear indication of the DNA binding groove in the complex. Mutation of conserved positively charged residues in this groove confirmed its functional importance for recruiting condensin to chromosomes both *in vitro* and *in vivo*.

Additional extensive DNA screening yielded co-crystals of the sub-complex bound to DNA, for which data were collected at **ID23-2** and a structure determined to 3.0 Å by molecular replacement (**Figure 12**). The resulting structure not only confirmed that the DNA double helix passes through the positively charged groove; it also suggested that the kleisin subunit encircles the bound DNA in a manner reminiscent of the way a safety belt fastens a seated passenger. Based on *in vitro* site-specific cross-linking and DNA binding experiments, as well as chromatin co-localisation experiments, it was possible to show that this mode of interaction provides a simple and elegant mechanism to tightly bind a DNA substrate without the need for specific interactions with the DNA bases.

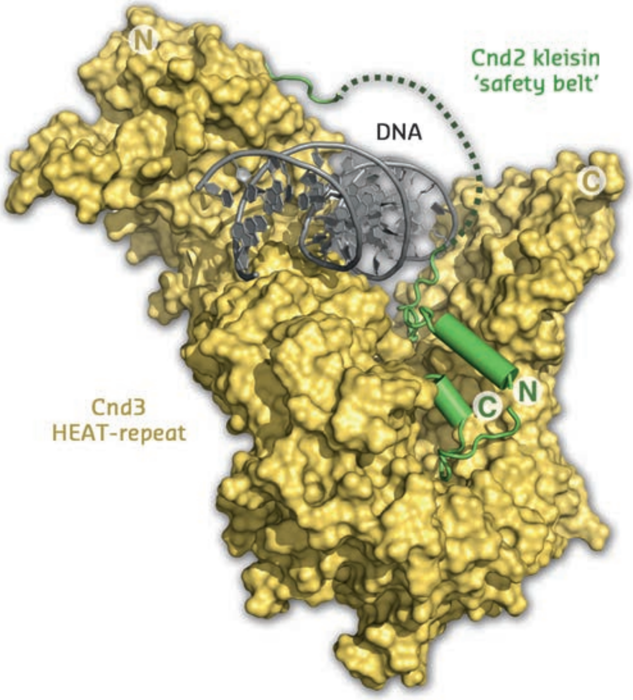

Fig. 12: Structure of the Cnd2-Cnd3 subcomplex bound to double-stranded DNA. Entrapment of the DNA helix by the Cnd2 'safety belt' is indicated by a dotted line (disordered in the crystal).

Taken together, the results provide molecular insights into the architecture of eukaryotic condensin complexes and identify a major DNA binding site, formed by Cnd3 HEAT-repeat and Cnd2 kleisin subunits in the complex. The new structures explain the preference for double-stranded DNA binding and lack of sequence specificity. The findings suggest a sophisticated DNA 'safety belt' mechanism that can be used to anchor condensin complexes to chromosomes, thereby enabling the formation of large chromatin loops as the fundamental organisational principle of higher-order chromatin structure.

PRINCIPAL PUBLICATION AND AUTHORS

Structural Basis for a Safety-Belt Mechanism That Anchors Condensin to Chromosomes, M. Kschonsak (a), F. Merkel (a), S. Bisht (a), J. Metz (a), V. Rybin (b), M. Hassler (a) and C.H. Haering (a), *Cell* **171**, 588-600 (2017); doi: 10.1016/j.cell.2017.09.008.

(a) Cell Biology and Biophysics Unit, Structural and Computational Biology Unit, European Molecular Biology Laboratory (EMBL) Heidelberg (Germany)
(b) Protein Expression and Purification Core Facility, European Molecular Biology Laboratory (EMBL) Heidelberg (Germany)

REFERENCES

[1] W. Flemming, in *Zellsubstanz, Kern und Zelltheilung* (1882).
[2] Hirano *et al.*, *Cell* **89**, 511-521 (1997).
[3] Piazza *et al.*, *Nat. Struct. Mol. Biol.* **21**, 560-568 (2014).

DNA METHYLATION AFFECTS BINDING OF MOST HUMAN TRANSCRIPTION FACTORS

The first global analysis of the effect of cytosine methylation on DNA binding specificities of human transcription factors has been carried out. The data revealed that methylation of CpG dinucleotides can influence DNA-binding of most transcription factors – often positively – and identified the molecular mechanisms behind it.

The role of both transcription factors (TFs) and DNA methylation in epigenetic inheritance is well established, and many principal mechanisms controlling gene expression are well understood. However, as the methylation changes DNA structure, it has the potential to affect binding of all TFs. To characterise this effect, the binding specificities of human TFs were analysed towards unmethylated and CpG-methylated DNA **[1, 2]**. Binding of most major classes of TFs, including bHLH, bZIP, and ETS, was inhibited by mCpG. In contrast, TFs such as homeodomain, POU, and NFAT proteins preferred to bind to methylated DNA.

Structural analysis of homeodomain proteins, using diffraction data collected at **ID29** and **ID23-1**, was used to identify the molecular mechanisms behind the preference of these TFs towards mCpG. The crystal structures of HOXB13 DBD, bound to dually methylated versions of its preferred site CTCGTAAA in the presence or absence of its heterodimeric partner MEIS1, were solved. Two regions of HOXB13 interact with DNA: the recognition helix $\alpha 3$, which tightly packs into the major groove, and the N-terminal tail interacting with the minor groove (**Figure 13a**). Analysis of the TF-DNA contacts showed that HOXB13 recognises mCpG by direct hydrophobic interactions between amino acids and the 5-methyl groups of both methylcytosines of the CpG dinucleotide: Ile262 forms a hydrophobic contact with the first methylcytosine, whereas Val269 recognises the second methylcytosine opposite to the guanine of the TCG sequence (**Figure 13a**). In addition, the aliphatic chain of Arg258 interacts with Ile262 and contributes to the hydrophobic environment of this region. These hydrophobic interactions were also present in the HOXB13:MEIS1-DNA crystal structure, indicating that the methyl groups of both cytosines are robustly recognised by HOXB13 in multiple physiologically relevant contexts (**Figure 13b**).

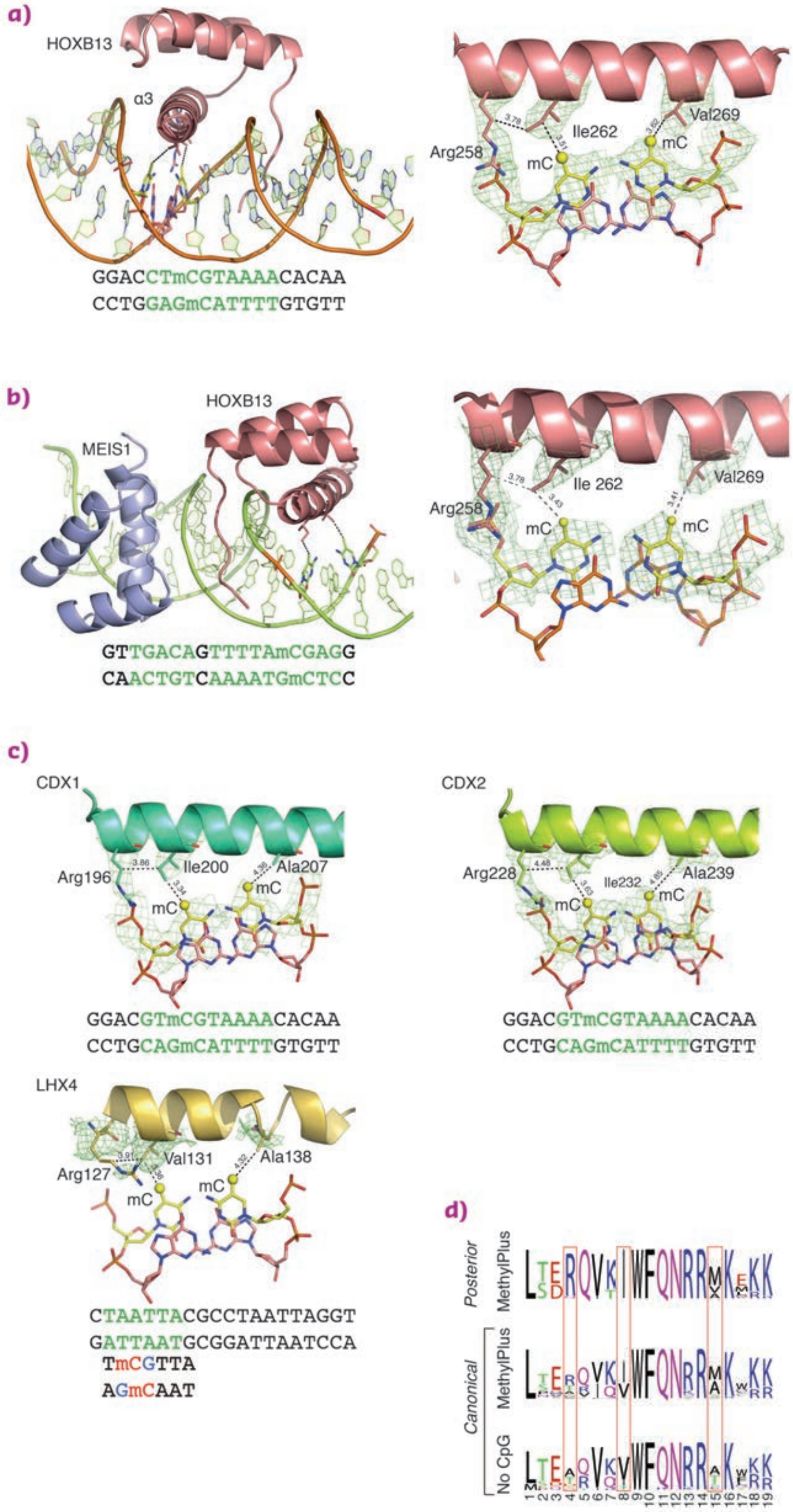

Fig. 13: Molecular basis of recognition of mCpG by homeodomain proteins.

To determine whether the mechanism of recognition of mCpG by homeodomains is general, the crystal structures of three additional proteins: CDX1, CDX2, and LHX4 were solved in their DNA-bound forms (**Figure 13c**). The crystal structures of CDX1 and CDX2 bound to their preferred GTmCGTAAA subsequence indicated that they directly recognise the 5-methyl group of methylcytosine by using amino acids in the same relative positions (**Figure 13c**). While the paraHOX proteins CDX1 and CDX2 bind strongly to mCpG in their TmCGTAAA motif, LHX4 binds to the canonical TAATTA motif and displays somewhat weaker binding to the mCpG-containing sequence TmCGTTA. The structure of LHX4 bound to a canonical TAATTA motif showed hydrophobic residues Val131 and Ala138 in positions suitable for the formation of hydrophobic contacts with methylcytosines. The aliphatic chain of Arg127 also supports a hydrophobic interaction (**Figure 13c**). These three residues are conserved in all LHX proteins, explaining their general preference towards mC. In contrast, in DLX3, a homeodomain that shows a much weaker preference for mC, the key residues corresponding to Arg127 and Ala138 were replaced by a threonine and a serine, respectively, leading to a decrease in hydrophobicity (**Figure 14a**). Furthermore, in TLX2, which does not bind to TmCGTTA, hydrophobicity of the entire binding site was lost (**Figure 14b**) **[3]**.

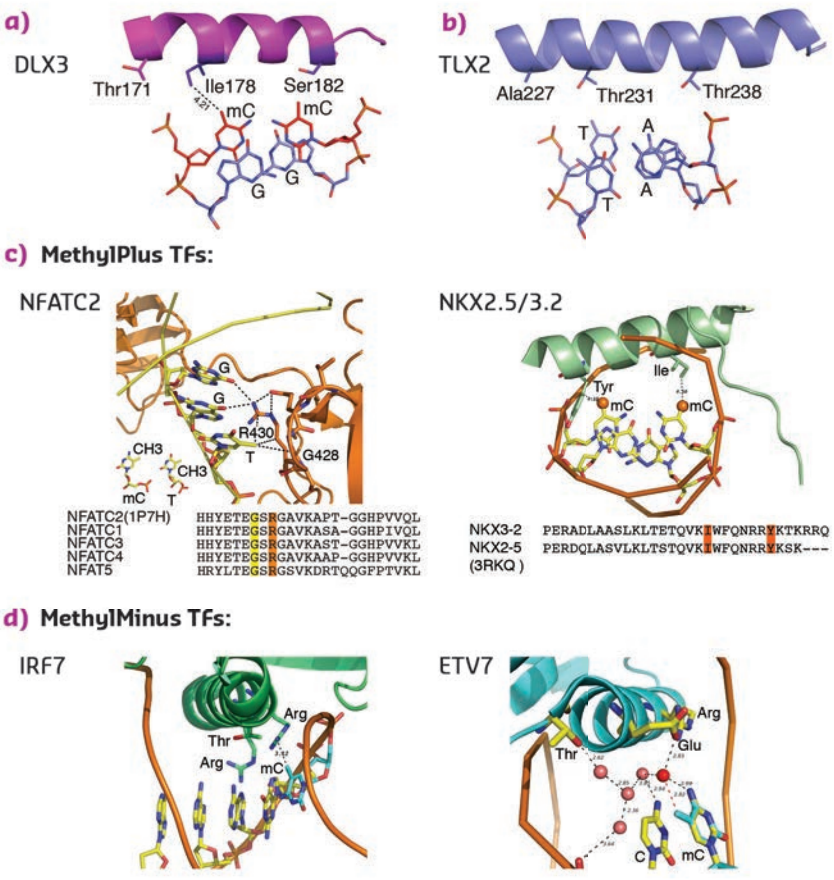

Fig. 14: Structural basis of TFs preferring methylated (a, c) or unmethylated (b, d) CpG.

Analysis of the amino acid sequences of different homeodomains that either do or do not bind to mCpG-containing sites confirmed the critical role in mCpG recognition of the three residues located at the beginning and end of the recognition helix (**Figure 13d**). Analysis of structures of the methyl-plus TFs, including some NKX- **[4, 5]** and NFAT-family proteins, confirmed that the preference for methylcytosine is based on hydrophobic interactions with the 5-methyl group (**Figure 14c**). Structural analyses also confirmed the mechanism by which methylation of cytosine inhibits TF-DNA binding; in all cases examined, the negative impact of methylation was due to steric hindrance (**Figure 14d**).

The discovery that many developmentally important TFs prefer to bind to methylated CpG sites, together with the mechanistic understanding of the increased affinity, forms a solid basis for future analyses of the role of DNA methylation on cell differentiation, chromatin reprogramming and transcriptional regulation.

PRINCIPAL PUBLICATION AND AUTHORS

Impact of cytosine methylation on DNA binding specificities of human transcription factors, Y. Yin (a), E.Morgunova (a), A. Jolma (a), E. Kaasinen (a), B. Sahu (b), S. Khund-Sayeed (c), P.K. Das (b), T. Kivioja (b), K. Dave (a), F. Zhong (a), K.R. Nitta (a), M. Taipale (a), A. Popov (d), P.A. Ginno (e), S. Domcke (e,f), J. Yan (a), D. Schübeler (e,f), C. Vinson (c) and J. Taipale (a,b), *Science* **356**, 6337, eaaj2239 (2017); doi:10.1126/science.aaj2239.

(a) Division of Functional Genomics and Systems Biology, Department of Medical Biochemistry and Biophysics, Karolinska Institutet, Stockholm (Sweden)
(b) Genome-Scale Biology Program, University of Helsinki (Finland)
(c) Laboratory of Metabolism, National Cancer Institute, National Institutes of Health, Bethesda, Maryland (USA)
(d) ESRF
(e) Friedrich-Miescher-Institute for Biomedical Research (FMI), Basel (Switzerland)
(f) Faculty of Science, University of Basel (Switzerland)

REFERENCES

[1] A. Jolma *et al.*, *Genome Res.* **20**, 861-873 (2010).
[2] A. Jolma *et al.*, *Nature* **527**, 384-388 (2015).
[3] K. Miyazono *et al.*, *Embo J.* **29**, 1613-1623 (2010).
[4] L. Pradhan *et al.*, *Biochemistry* **51**, 6312-6319 (2012).
[5] M. J. Giffin *et al.*, *Nat. Struct. Biol.* **10**, 800-806 (2003).

IDENTIFICATION AND STRUCTURE OF A NOVEL PHOTOENZYME, FATTY ACID PHOTODECARBOXYLASE

Photoenzymes are a very rare type of enzyme that require photons for their catalytic activity. In search for an enzyme responsible for the synthesis of hydrocarbons in microalgae, a flavoprotein that decarboxylates fatty acids using blue light was identified and a crystal structure in complex with a fatty acid substrate was obtained.

Besides the photosynthetic reaction centres, only two families of proteins with light-driven activity have been described: light-dependent protochlorophyllide reductases, which are involved in chlorophyll synthesis in photosynthetic organisms, and DNA photolyases, which repair UV damage in DNA in many organisms ranging from bacteria to animals and plants. While searching for an enzyme converting fatty acids to hydrocarbons, a member of the glucose-methanol-choline (GMC) family of oxidoreductases was identified and shown to be a light-driven enzyme. This novel photoenzyme was christened fatty acid photodecarboxylase (FAP).

FAP was identified in the green microalgae *Chlorella* using partial purification of fatty acid decarboxylase activity and proteomic analysis. Expression of the *Chlorella* gene encoding FAP in the bacterium *E. coli* resulted in hydrocarbon production, thus confirming its activity. Further biochemical characterisation of the recombinant protein revealed a non-covalently-bound flavine adenine dinucleotide cofactor (FAD), the release

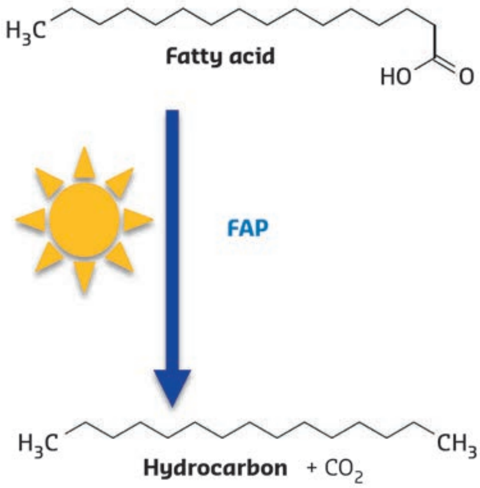

Fig. 15: Reaction catalysed by Fatty Acid Photodecarboxylase (FAP). The enzyme is not active in absence of light.

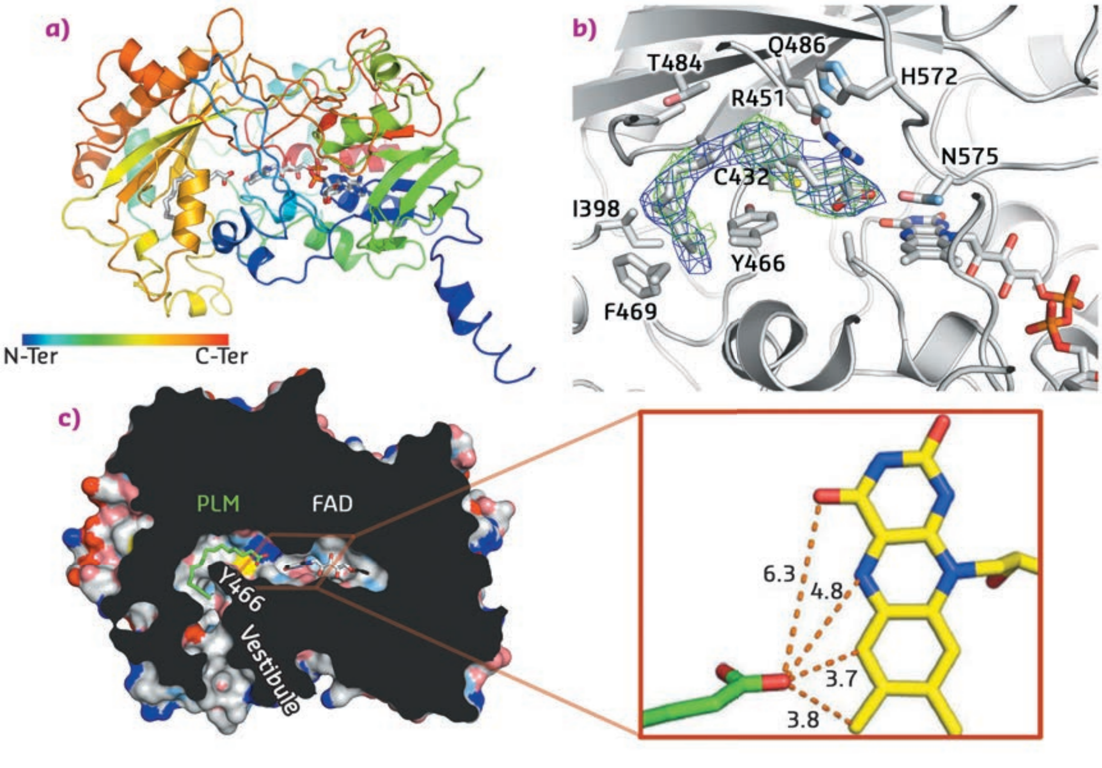

Fig. 16: Structural features of FAP. a) Overall architecture of the enzyme in complex with FAD and palmitate. b) Details of the palmitic acid binding site with the side chains of residues within 4 Å of the substrate shown as sticks. Omit map electron density associated to palmitic acid is also shown and contoured at 0.5σ (2Fo-Fc; blue) and 2σ (Fo-Fc; green). c) Slicethrough the surface representation of the fatty acid photodecarboxylase in complex with a palmitate substrate (PLM). For clarity, small cavities in the interior of the enzyme are not shown. Inset: Distances (Å) between the carboxyl groups of palmitate and FAD.

of CO_2 as a co-product and the requirement of constant illumination for activity (**Figure 15**).

In addition, the protein was successfully crystallised in presence of its fatty acid substrate. X-ray data were collected on the **MASSIF-1 ID30A-1** beamline, and the crystal structure solved at 3.15 Å resolution. Despite the fact that the crystals were twinned, the structure was solved by molecular replacement using the 3D structures of domains from two proteins of the GMC oxidoreductase family as models (*E. coli* choline oxidase and *Aspergillus flavus* glucose dehydrogenase). Accordingly, the overall architecture of the FAP is broadly similar to that of other GMC oxidoreductases with a typical two-domain fold, the first stabilising the FAD cofactor and the second participating in substrate binding. The crystal structure also revealed a narrow hydrophobic tunnel connecting the FAD cofactor to solvent. Electron density in this tunnel matches with a C16 saturated fatty acid substrate (palmitate) that wraps around the side chain of Y466 (**Figure 16**). Interestingly, the carboxylate moiety points toward the FAD cofactor. The shortest distance between FAD and the carboxylate is 3.7 Å, suggesting a direct electron transfer between substrate and FAD. Together with a time-resolved spectroscopy study, this structure enabled a mechanism to be proposed in which FAD is excited by blue light to reach an excited state that abstracts an electron from the carboxylate group of the fatty acid substrate stabilised in the hydrophobic tunnel. The radical fatty acid would then decarboxylate spontaneously to yield a hydrocarbon.

The hydrocarbon-forming microalgal enzyme FAP represents the third enzyme family that uses light directly as an energy source for catalysis. The crystal structure of FAP shows that its overall architecture is related to that of other, thermally-activated GMC oxidoreductase family members despite the unique light-driven decarboxylation activity of the FAP. The crystal structure also suggests residues that may be involved in facilitating the radical-based photochemistry after visible light excitation of the flavin cofactor.

PRINCIPAL PUBLICATION AND AUTHORS

An algal photoenzyme converts fatty acids to hydrocarbons, D. Sorigué (a), B. Légeret (a), S. Cuiné (a), S. Blangy (a), S. Moulin (a), E. Billon (a), P. Richaud (a), S. Brugière (b), Y. Couté (b), D. Nurizzo (c), P. Müller (d), K. Brettel (d), D. Pignol (e), P. Arnoux (e), Y. Li-Beisson (a), G. Peltier (a) and F. Beisson (a), *Science* **357**, 903-907 (2017);
doi: 10.1126/science.aan6349.
(a) LB3M, Biosciences and Biotechnologies Institute of Aix-Marseille, CEA, CNRS and Aix-Marseille University, Cadarache (France)
(b) Large Scale Biology Laboratory, CEA and INSERM and University Grenoble Alpes, Grenoble (France)
(c) ESRF
(d) Institute for Integrative Biology of the Cell, CEA, CNRS and Paris-Sud University, Gif-sur-Yvette (France)
(e) LBC, Biosciences and Biotechnologies Institute of Aix-Marseille, CEA, CNRS and Aix-Marseille University, Cadarache (France)

A NEW MODEL FOR THE ACTIVATION OF THE IMMUNE SYSTEM

A new model has been suggested for the activation of an important branch of the innate immune system. The activation of the large C1 protein complex is a fundamental mechanism in immunology, and this new model is likely to spur developments in immunotherapy with the aim of fighting cancer and infections.

An important part of the immune system is the so-called complement system. When the immune system detects a microorganism or other molecular signs of danger, the C1 complex is converted into an active enzyme that can cleave other proteins, thus initiating a cascade of proteolytic events. The end result of this reaction is that invading pathogenic microorganisms are more efficiently ingested by immune cells. In addition, an inflammatory response is triggered, leading to the elimination of the microorganisms. In the past few years, there has been increased focus on the C1 complex, since – in addition to its function in the immune system – it has been shown to be closely involved in the development of the nervous system and neurological disorders. One of the most exciting recent findings is that the C1 complex participates in trimming of the synapses mediating signalling between neurons.

The C1 complex circulates in an inactive state in blood and other extracellular fluids. Immunology research has so far suggested that activation of the C1 complex is due to a complicated structural change within each individual C1 complex. Such alteration of the structure was proposed to occur when the C1 complex binds to the danger-presenting object, *e.g.,* a pathogenic organism or a dying human cell. The underlying assumption

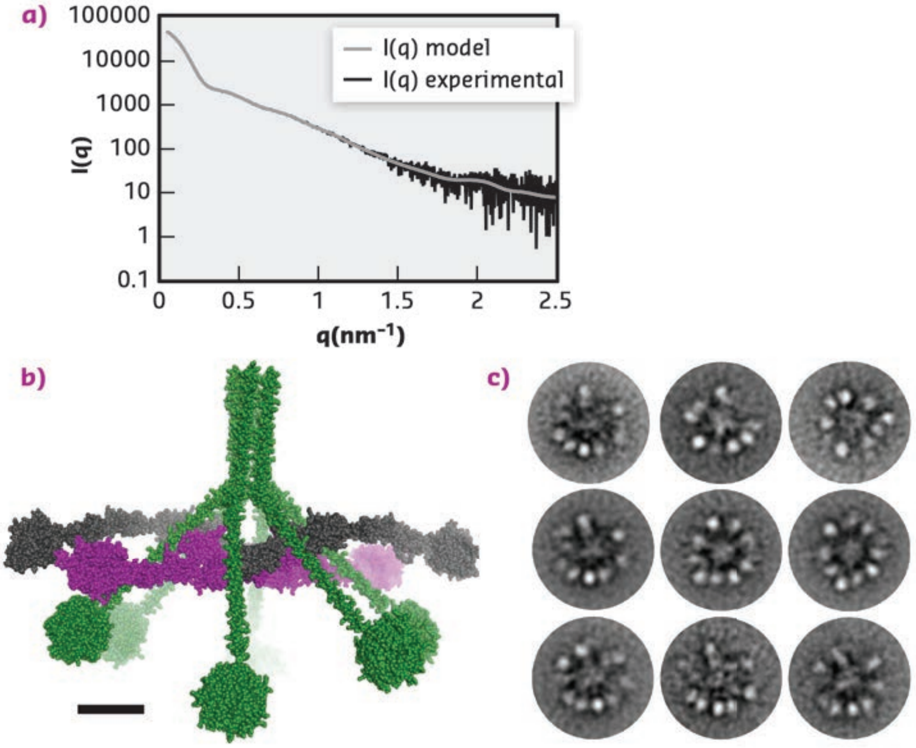

Fig. 17: The structure of the C1 complex. a) SAXS data recorded at PETRA-III, similar data were obtained at BM29. The grey curve displays how a curve calculated from the model (b) fits the experimental data. c) The 'class averages' of the C1 complex images recorded with electron microscopy. The overall architecture suggested by microscopy confirms the model obtained from the SAXS data presented in (b).

was that the C1 complex has a compact conformation that allowed the protease subunits within each individual complex to activate each other through an intramolecular activation mechanism, but this compact conformation has not yet been observed.

The MBL:MASP-1 complex resembles the C1 complex but is smaller and functions in a different branch of the complement system. Functional and structural studies showed that activation of the MBL:MASP-1 complex is an intermolecular reaction where neighbouring complexes activate each other and that the MBL:MASP-1 complex has an extended conformation with the catalytically active protease domains located at the periphery of the molecule. Whether the C1 complex also has such an extended conformation or indeed adopts a compact conformation was unknown. As the C1 complex is highly non-globular and flexible, crystallisation was deemed unlikely, instead the C1 complex and its sub-component C1r2s2 were investigated in parallel with small-angle X-ray scattering (SAXS) and Electron Microscopy (EM). SAXS data were collected for the C1 complex at **BM29** and at PETRA-III, while the data for the C1r2s2 were collected at **BM29**. For the SAXS studies, measuring the C1 complex eluting directly from a size exclusion column made it possible to remove the signal from contaminating or aggregated molecules, and was crucial for improving the quality of the data obtained. After data collection, *ab initio* modelling was used to produce a molecular envelope, showing that the C1 complex was hollow and not a compact particle. The *ab initio* model was further supported by rigid body modelling that resulted in atomic models of the C1 complex that fitted the SAXS data (**Figure 17a-b**). All these models had the protease domains present in the periphery of the C1 complex and not tightly packed in the centre of the molecule. EM micrographs confirmed this finding (**Figure 17c**).

Since these results, obtained by two orthogonal methods, suggest that the proteolytically active domains are located in the periphery and not in the core, the existing model of C1 activation as an intramolecular process needs to be reconsidered. Instead, activation is likely when two C1 complexes are located sufficiently close to each other that their protease subunits may activate each other in an intermolecular reaction. This model is also in agreement with the results obtained for the homologous MBL:MASP-1 complex **[1,2]**.

The biomedical implication of the new C1 complex activation model is that it may be sufficient to tether the C1 complex to a cancer or pathogen cell in a defined overall orientation in order to elicit an innate immune response towards a malicious cell. If this is true, a specific recognition event of molecular patterns on the surface of the offending cell is not required, and binding of the C1 complex to cells may turn out to be an attractive new approach to immunotherapy.

PRINCIPAL PUBLICATION AND AUTHORS

Structure and activation of C1, the complex initiating the classical pathway of the complement cascade, S.A. Mortensen (a), B. Sander (b), R.K. Jensen (c), J. Skov Pedersen (d), M.M. Golas (a), J.C. Jensenius (a), A.G. Hansen (a), S. Thiel (a) and G.R. Andersen (b), *PNAS* **114**, 986-991 (2017); doi: 10.1073/pnas.1616998114.

(a) Department of Biomedicine, Aarhus University (Denmark)

(b) Department of Molecular Biology and Genetics, Aarhus University (Denmark)

REFERENCES

[1] T.R. Kjaer *et al., Structure* (London, England: 1993) **23**, 342 (2014).

[2] S.E. Degn *et al., PNAS* **111**, 13445-13450 (2014).

MAKING ROD-SHAPED BACTERIA

The bacterial cell wall is a major antibiotic development target, and many pathogens require the 'elongasome' complex to guarantee its formation. MreC and PBPs form the core of the elongasome. Here, for the first time, a PBP:MreC complex has been characterised in atomic detail, revealing interaction regions that could be targeted by tailored inhibitors.

The peptidoglycan (PG) is an essential component of the bacterial cell wall, and plays a key role in shape maintenance, resistance to osmotic pressure, and cell division. Due to the central role PG plays in bacterial survival, its biosynthetic machinery has been a preferential target for antibiotic development for decades **[1]**. Proteins that are involved in PG biosynthesis associate in discrete multi-membered complexes that regulate cell division and elongation, and their inhibition or deregulation can lead to defects in cell shape and often cell wall lysis and death **[2]**.

Penicillin-binding proteins (PBPs) catalyse the two last reactions in PG biosynthesis, and have been reported to interact with several members of the cell division and elongation complexes during the bacterial cell cycle **[3]**. One of these partners is MreC, a membrane-associated protein that has been shown to form fibres in certain bacteria and is thought to serve as a scaffold for macromolecules involved in cell wall elongation. However, protein interactions within these complexes have been reported to only form at defined points in the cell cycle, thus being fleeting in nature, fragile, and difficult to isolate.

In this work, these difficulties were overcome and the PBP2:MreC core elongation complex from the human pathogen *Helicobacter pylori* was structurally and functionally characterised, as was PBP2 in its unbound form. All diffraction data were collected at beamlines **BM30A** and **ID23-2**. In the structure of PBP2 in its unbound form, its N-terminal region (blue and red in **Figure 18**) is 'closed', mimicking two clasped hands. In the structure of the PBP2:MreC complex, however, this region has undergone a conformational modification that has allowed it to open by approximately 80 Å, permitting binding of the partner molecule MreC (orange in **Figure 18**). Opening of this 'hinge' region reveals a non-polar platform that, when associated to MreC, forms a hydrophobic zipper.

The importance of the stability of the zipper was verified by introducing mutations *in vitro* and in a microbiological setting. MreC forms that carried mutations in the hydrophobic zipper did not bind to PBP2, as verified by gel filtration and ITC. In addition, *H. pylori* cells that were modified to express the same mutations in their genome lost their characteristic elongated shape and rapidly increased in diameter, indicating that the PBP2:MreC hydrophobic zipper is essential for shape maintenance in bacteria.

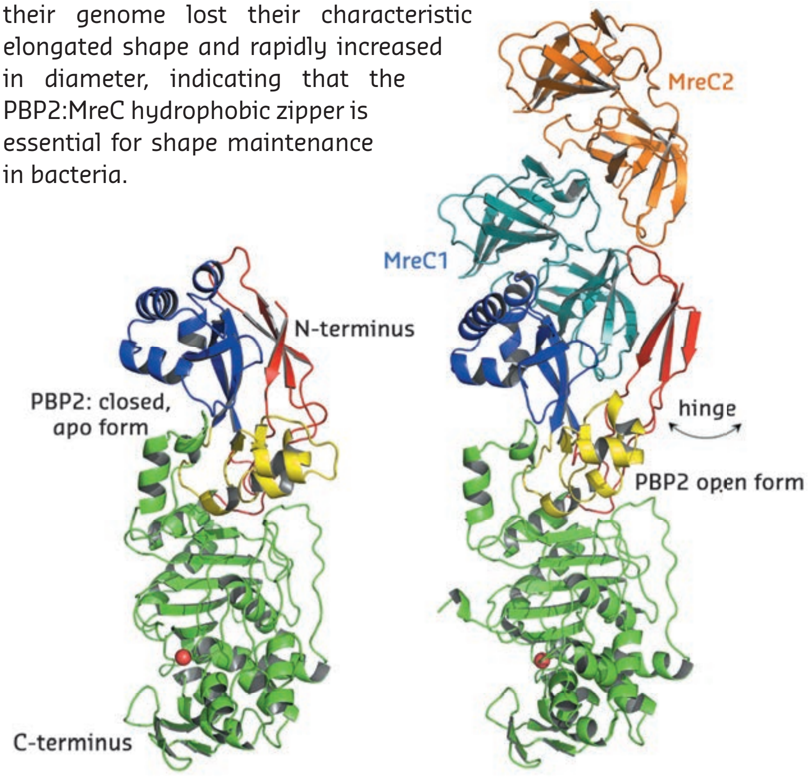

Fig. 18: Architecture and structural arrangements of PBP2 (left) and the PBP2:MreC complex (right) from *Helicobacter pylori*. In the structure of the complex, the N-terminus of PBP2 opens via a hinge region, exposing a previously hidden hydrophobic region that allows binding of MreC. The PBP2 active site, serine, is indicated as a red sphere.

This work thus provides the first visualisation of the core region of a bacterial elongation complex and reveals a novel area that could be targeted for the development of antibiotics that act by inhibiting cell wall elongation. This could lead to a generation of totally new molecules that are structurally distinct from antibiotics currently used in clinics and which face severe problems of resistance.

PRINCIPAL PUBLICATION AND AUTHORS

Molecular architecture of the PBP2:MreC core bacterial cell wall synthesis complex,
C. Contreras-Martel (a), A. Martins (b), C. Ecobichon (b), D. Maragno Trindade (c), P-J. Matteï (a), S. Hicham (b), P. Hardouin (a), M. El Ghachi (b), I. G. Boneca (b) and A. Dessen (a, c), *Nat. Commun.* **8**, 776 (2017); doi: 10.1038/s41467-017-00783-2.

(a) Institut de Biologie Structurale (IBS), CNRS, CEA, Univ. Grenoble (France)
(b) Institut Pasteur & INSERM, Paris (France)
(c) Brazilian Biosciences National Laboratory (LNBio), CNPEM, Campinas, São Paulo (Brazil)

REFERENCES

[1] L. L. Silver, *Ann N. Y. Acad. Sci.* **1277**, 29-53 (2013).
[2] T. den Blaauwen *et al.*, *FEMS Microbiol. Rev.* **32**, 321-344 (2008).
[3] P.-J. Matteï *et al.*, *Curr. Opin. Struct. Biol.* **20**, 749-755 (2010).

ZINC FASTENS TWO AMYLOID-β PEPTIDE FRAGMENTS FORMING STABLE DIMER

Binding of metal ions to amyloid-β is an initial step of the peptide transition to pathogenic forms toxic for neurons. To understand the molecular mechanisms of zinc-mediated amyloid-β aggregation, amyloid-β peptide carrying a pathogenic Taiwanese mutation was studied. Spectroscopy showed that zinc ions induce formation of a stable homodimer with a novel binuclear zinc interaction fold.

Zinc ions are crucially involved in pathogenesis of Alzheimer's Disease (AD). This neurodegenerative disorder is characterised by extracellular accumulation of amyloid-β peptide (Aβ) in proteinaceous inclusions that have characteristic supramolecular structure and are abnormally enriched by Zn, Cu and Fe ions. Aβ interacts with metal ions through its metal-binding domain, which is located in its N-terminal region (residues 1-16). Substitutions and modifications of amino acid residues in this domain critically affect the properties of A-β, facilitating dimerisation, oligomerisation and the formation of insoluble aggregates. These processes are considered essential for the initiation of Alzheimer's disease.

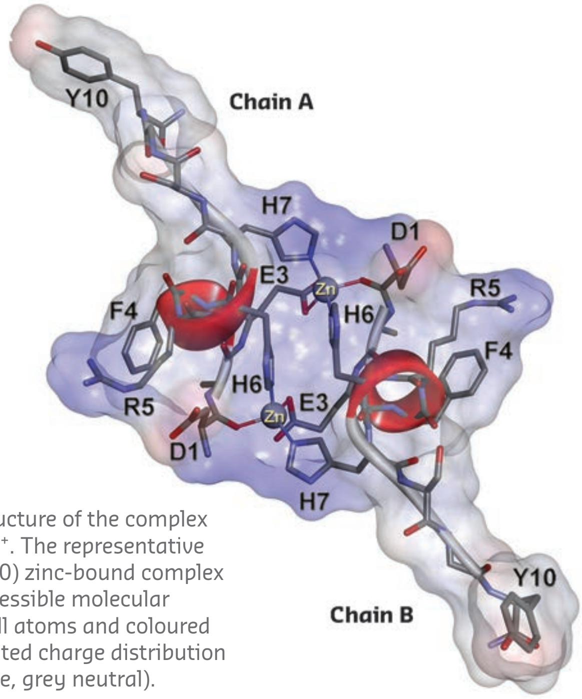

Fig. 19: NMR solution structure of the complex of D7H-Aβ(1-10) with Zn^{2+}. The representative conformer of D7H-Aβ(1-10) zinc-bound complex is shown. The solvent-accessible molecular surface is calculated for all atoms and coloured according to the interpolated charge distribution (red negative, blue positive, grey neutral).

Aβ carrying a Taiwanese mutation (D7H) stands out among all isoforms of Aβ because of the enhanced susceptibility of the peptide to the effect of Zn^{2+} or Cu^{2+} ions promoting oligomerisation **[1]**. Based on the molecular mechanism of formation of zinc-bonded dimers of different Aβ isoforms **[2]**, it was hypothesised that zinc-dependent aggregation of the metal-binding domain of Aβ with Taiwanese mutation is determined by the properties of the fragment containing residues 1-10 (D7H-Aβ(1-10)), where the relevant amino acid substitution is located.

In this study, using NMR spectroscopy, mass spectrometry, EXAFS spectroscopy on **BM31** and isothermal titration calorimetry (ITC), the behaviour of this peptide fragment in the presence of zinc ions was examined. The formation of a homodimer with a unique protein fold interlocked by two zinc ions (**Figure 19**) was observed by NMR. Most of the known examples of metal-directed peptide self-assembly are based on the formation of one or several mononuclear coordination sites. Examples of the formation of a binuclear coordination site with the participation of two zinc ions are still unknown, except when cysteine thiol groups are involved in the binding of zinc atoms.

It has been shown here for the first time that a site, with a novel topology for the coordination sphere of zinc ions, is formed upon the interaction of zinc with a relatively short fragment of A-β peptide carrying Taiwanese mutation D7H. The NMR structure determined was validated using extended X-ray absorption fine structure (EXAFS) spectroscopy, which provides information on the geometry of the metal ion chelating environment. EXAFS data give access to the nature, number, and distance of the coordinating atoms. The experimental EXAFS spectrum of the complex of D7H-Aβ(1-10) with zinc fits well to the spectrum, calculated on the basis of the coordinates of atoms determined by NMR (**Figure 20**). The scattering pathways for the atoms of the first coordination shell (D1 O, E3 Oε1, H6 Nε2 and H7 Nε2) reproduce the most intense peak at ~2 Å of the Fourier-transformed EXAFS spectrum (**Figure 20c**), while atoms of the histidine imidazole ring make a major contribution to the peaks at ~3 Å and ~4 Å.

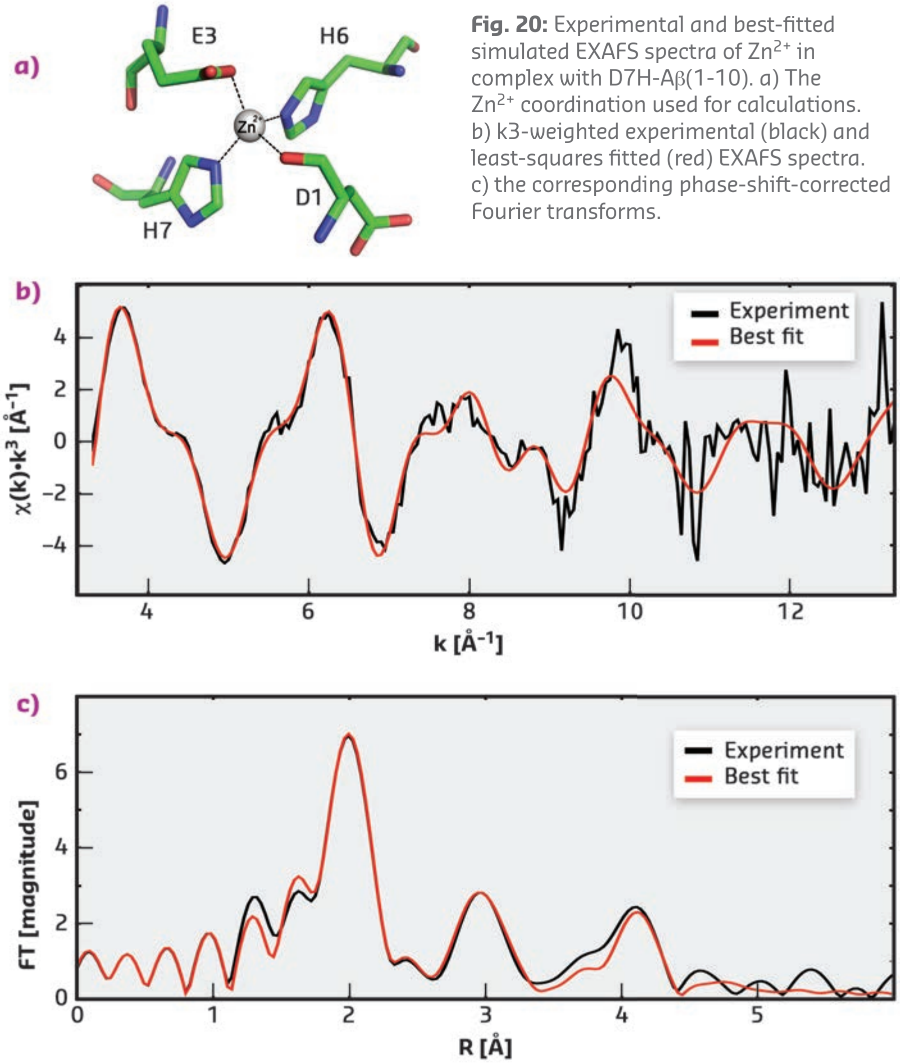

Fig. 20: Experimental and best-fitted simulated EXAFS spectra of Zn^{2+} in complex with D7H-Aβ(1-10). a) The Zn^{2+} coordination used for calculations. b) k3-weighted experimental (black) and least-squares fitted (red) EXAFS spectra. c) the corresponding phase-shift-corrected Fourier transforms.

PRINCIPAL PUBLICATION AND AUTHORS

A Binuclear Zinc Interaction Fold Discovered in the Homodimer of Alzheimer's Amyloid-β Fragment with Taiwanese Mutation D7H, V.I. Polshakov (a,b), A.B. Mantsyzov (b), S.A. Kozin (a), A.A. Adzhubei (a), S.S. Zhokhov (b), W. Van Beek (c), A.A. Kulikova (a), M.I. Indeykina (d), V.A. Mitkevich (a) and A.A. Makarov (a), *Angew. Chem. Int. Ed.* **56**, 11734-11739 (2017); doi: 10.1002/anie.201704615.

(a) Engelhardt Institute of Molecular Biology, Russian Academy of Sciences, Moscow (Russia)
(b) Faculty of Fundamental Medicine, M.V. Lomonosov Moscow State University, Moscow (Russia)
(c) SNBL, ESRF
(d) Emanuel Institute for Biochemical Physics, Russian Academy of Sciences, Moscow (Russia)

REFERENCES

[1] W.-T. Chen *et al., PLoS One* **7**, e35807 (2012).
[2] A.N. Istrate *et al., Sci. Rep.* **6**, 21734 (2016).

SMARt-420 REVERSES ANTIBIOTIC RESISTANCE IN *MYCOBACTERIUM TUBERCULOSIS*

Resistance to the current generation of antibiotics is an increasing threat to human health and strains of drug-resistant *Mycobacterium tuberculosis* have spread around the globe. SMARt-420 (Small Molecule Aborting Resistance) fully reverses the ethionamide (ETH)-acquired resistance of *M. tuberculosis* by activating an alternative ETH bioactivation pathway in the bacterium.

Antibiotic resistance is a serious, global threat to human health. Although cases of tuberculosis (TB) are decreasing by ~1.5% a year, the rise of drug resistant-TB (DR-TB), which already causes around 250,00 deaths per year (2015 figures), may reverse this and cases of TB will start to increase. Many important anti-TB therapeutics are prodrugs. Here, bacterial resistance mechanisms are often the result of mutations in the bacterial enzyme pathway targeted or the acquisition by these pathways of enzymes that modify or degrade the drug molecule introduced **[1]**. Sometimes, these resistance mechanisms can be reversed by combining the drug with other molecules (*i.e.* β-lactams plus calvulanic acid **[2]**). However, examples of this phenomenon are few and far between.

Many of the currently most efficient anti-TB antibiotics such as isoniazid (INH), pyrazinamide (PZA), p-aminosalicylic acid (PAS), ethionamide (ETH) and the recently approved delamanid (OPC-67683) are prodrugs requiring bioactivation by *M. tuberculosis*. For example, the bioactivation of ETH depends on the Baeyer-Villiger monooxygenase EthA, the production of which is regulated by the TetR-type transcriptional repressor EthR. In ETH-sensitive clinical strains of TB the effect of the prodrug can be increased during treatment by combining it with the small molecule BDM41906, which boosts the production of EthA by inhibiting the regulatory effect of EthR. However, as clinical resistance to ETH occurs via mutations in EthA, which decrease the level of ETH bioactivation, boosting the production of this mutated enzyme does not revert resistance.

A potential mechanism for reversing or attenuating drug resistance in TB is the induction of alternative bioactivation pathways. In the manuscript on which this article is based, it is shown that the Small Molecules Aborting Resistance (SMARt) family of spiroisoxazolines reverses the resistance of *M. tuberculosis* to ETH by activating alternative bioactivation pathways regulated by protein EthR2. Thermal shift assays strongly suggested that the SMARt family member SMARt-420 interacts directly with EthR2. The full details of this interaction were revealed by a series of X-ray crystallography experiments carried out in-house, at SOLEIL and at the ESRF (**ID23-1**). The crystal structures obtained (**Figure 21**) revealed EthR2 to be an archetypal TetR-type transcription regulator made up of a homodimer containing a pair of helix-turn-helix (HTH) motifs involved in the binding of EthR2 to its target DNA region. In TetR-type regulators, ligands bound to each partner of the homodimer induce a conformational change in the HTH motifs, modifying the binding of the regulator to its target DNA. The crystal structure of the EthR2–SMARt-420 complex revealed that binding of the ligand increased the distance between the HTH motifs to ~ 40.7 Å, far larger than the ±34 Å required for the efficient binding of such regulators to DNA. This observation straightforwardly provides the mechanism of action of SMARt-420.

The reversal of ETH resistance by SMARt-420 was confirmed in a series of experiments not described here. These suggest that the development of therapeutic protocols based on the switching between ETH and the "ETH + SMARt-420" combination could prove very efficient in the treatment of TB, providing the potential to eliminate populations of ETH-resistant bacteria that may emerge during treatments with this traditional anti-TB antibiotic.

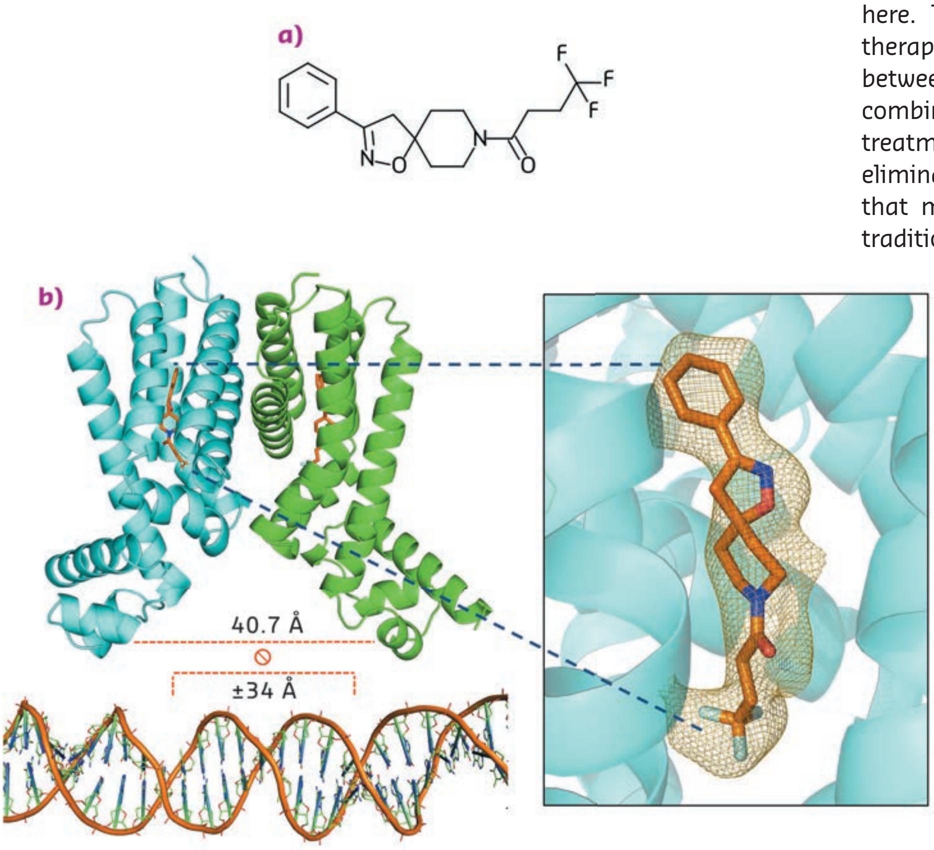

Fig. 21: a) A chemical representation of the spiroisoxazoline SMARt-420, which reverses ETH resistance in *M. tuberculosis*. b) A ribbon representation of the crystal structure of the EthR2/SMARt-420 complex. The ligands are shown as yellow sticks. The inset shows an omit map, contoured at 1.2 x r.m.s., illustrating the mode of binding of SMARt-420 to an EthR2 monomer. The binding of SMARt-420 to EthR2 increases the distance between the HTH binding motifs to 40.7 Å, sterically inhibiting the binding of EthR2 to its target DNA (bottom).

PRINCIPAL PUBLICATION AND AUTHORS

Reversion of antibiotic resistance in *Mycobacterium tuberculosis* by spiroisoxazoline SMARt-420, N. Blondiaux (a), M. Moune (a), M. Desroses (b, c) R. Frita (a), M. Flipo (b), V. Mathys (d), K. Soetaert (d), M. Kiass (d), V. Delorme (a, e), K. Djaout (a), V. Trebosc (f, g), C. Kemmer (f), R. Wintjens (h), A. Wohlkönig (i, j), R. Antoine (a), L. Huot (a), D. Hot (a), M. Coscolla (k, l), J. Feldmann (k, l), S. Gagneux (k, l), C. Locht (a), P. Brodin (a), M. Gitzinger (f), B. Déprez (b), N. Willand (b) and A. Baulard (a), *Science* **355**, 1206-1211 (2017); doi: 10.1126/science.aag1006.

(a) Université Lille, CNRS, Inserm, CHU Lille, Institut Pasteur de Lille (France)
(b) Université Lille, Inserm, Institut Pasteur de Lille, U1177–Drugs and Molecules for Living, Lille (France)
(c) Division of Translational Medicine and Chemical Biology, Department of Medical Biochemistry and Biophysics, Karolinska Institutet, Stockholm (Sweden)
(d) National Reference Center for Tuberculosis and Mycobacteria, Bacterial, Scientific Institute of Public Health (WIV-ISP), Brussels (Belgium)
(e) Tuberculosis Research Laboratory, Institut Pasteur Korea, (South Korea)
(f) Bioversys AG, Basel (Switzerland)
(g) Biozentrum, University of Basel, Basel (Switzerland)
(h) Laboratoire des Biopolymères et des Nanomatériaux Supramoléculaires, Université Libre de Bruxelles, Brussels (Belgium)
(i) VIB Center for Structural Biology, VIB, Brussels (Belgium)
(j) Structural Biology, Brussels, Vrije Universiteit Brussel (VUB), Brussels (Belgium),
(k) Swiss Tropical and Public Health Institute, Basel (Switzerland)
(l) University of Basel, Basel (Switzerland)

REFERENCES

[1] C. Walsh, *Antibiotics: Actions, Origins, Resistance* (ASM Press, 2003)
[2] C. Reading and M. Cole, *Antimicrob. Agents Chemother*. **11**, 852–857 (1977)

FIRST ATOMIC-RESOLUTION SNAPSHOTS OF EGG COAT-SPERM INTERACTION AT FERTILISATION

Crystallographic studies of egg coat components VERL and ZP2 show that a conserved protein fold mediates interaction with sperm in both invertebrates and vertebrates. Structures of VERL bound to lysin, its counterpart molecule on sperm, reveal the molecular basis of species-restricted gamete recognition, leading to a model of egg coat architecture and penetration by sperm.

By transmitting the genetic information to the next generation and marking the beginning of a new individual, the encounter between gametes at fertilisation constitutes one of the most fundamental processes of life. Although this crucial event has been studied for centuries, the molecular basis of how sperm recognises the extracellular coat of the egg at the onset of fertilisation remained unknown. Similarly, it was unclear how sperm subsequently penetrates the egg coat – called zona pellucida (ZP) in mammals and vitelline envelope (VE) in non-mammals – in order to fuse with the plasma membrane of the egg. Based on previous studies of the major ZP component ZP3 **[1]**, it was proposed that a common 'ZP-N' fold is adopted by the domain repeats of ZP2 and VERL, two sperm-interacting subunits of the mammalian ZP and mollusk VE, respectively. This suggestion had important functional implications because, whereas a binding partner of ZP2 remains to be identified, VERL is known to interact with lysin, an amphipathic sperm molecule that dissolves the VE non-enzymatically **[2]**. However, as amino acid sequence identity between ZP2 and VERL repeats is a mere 10%, this hypothesis remained highly speculative.

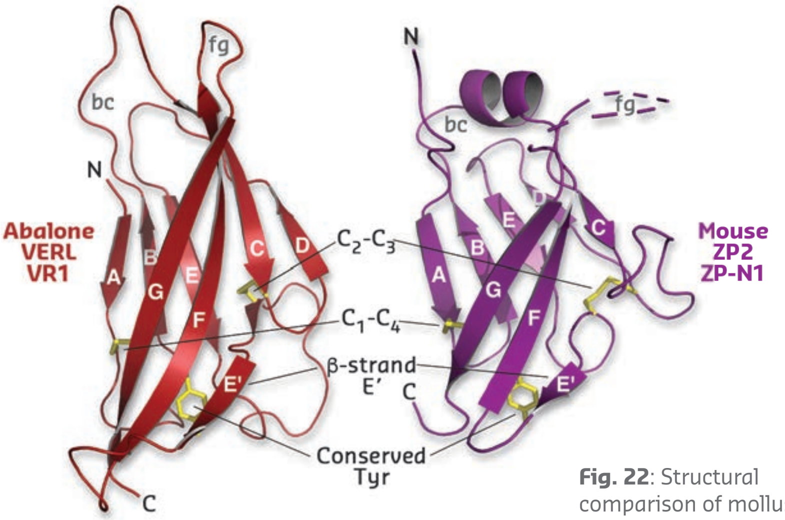

Fig. 22: Structural comparison of mollusk (left) and mammalian (right) egg coat proteins shows that their repeats share a common ZP-N domain fold, whose characteristic features are indicated.

Using diffraction data collected at beamlines **ID29** and **ID23-2**, a series of crystal structures of the first three repeats of red abalone VERL (VR1-3) and the N-terminal ZP-N1 domain of mouse ZP2 was determined (**Figure 22**). Comparison of these conclusively showed that, despite 600 million years of evolutionary divergence, mollusk and mammalian egg coat proteins use the same basic architecture to interact with sperm.

Whereas lysin and the first two repeats of VERL evolve rapidly under positive Darwinian selection, the remaining twenty repeats are homogenised by concerted evolution. To understand how this evolutionary pattern affects gamete recognition, biochemical assays of VERL-repeat-lysin interactions were performed and quantified by microscale thermophoresis. Together, these experiments showed that lysin does not bind highly sequence-divergent VR1, interacts weakly, but species-specifically, with moderately sequence-divergent VR2 (Kd ~500 nM) and forms a tight non-species-specific complex with conserved VR3 (Kd ~2 nM). Mutational analysis suggested that divergence of the N-terminal sequence of VERL inactivated VR1 and lowered the binding affinity of VR2 compared to VR3-22, thus generating species-specificity by amplifying the effect of positive selection on lysin.

To determine the molecular basis of egg coat-sperm interaction, VR2-lysin and VR3-lysin complexes were crystallised and their structures solved using datasets collected at **ID29** and **ID23-1**. VR2, which contains two additional Cys residues compared to other VERL repeats, forms an antiparallel homodimer, containing an intermolecular disulfide-bond between monomers. These hydrophobically bind two copies of lysin on the opposite faces of the dimer (**Figure 23a**). VR3 forms a similar 1:1 complex with lysin, but – consistent with a higher affinity interaction – this involves a larger number of contacts.

Taken together with VERL-VERL contacts observed in the respective crystals, the structures suggest a model whereby two intertwined VERL molecules generate a filament branch that exposes VR1 repeats on the surface of the VE (**Figure 23b**, left panel). These are followed by the covalently bound antiparallel VR2 homodimer, whose low affinity for lysin acts as a species-specific checkpoint for sperm attachment. In the absence of lysin, adjacent VERL branches are held together by interaction between their hydrophobic patches. Upon deposition of weak lysin dimers onto the VE, the sperm protein's hydrophobic interface replaces the lateral interactions between VERL branches. This results in binding of monomeric lysin to the egg coat and juxtaposition of many copies of its highly positively charged surface on the repeats of adjacent VERL branches. As supported by molecular dynamics simulations, the ensuing electrostatic repulsion then pushes the VERL branches apart and disrupts the egg coat, ultimately generating a hole for sperm penetration and fusion (**Figure 23b**, middle and right panels).

In summary, this study provides unprecedented insights into the molecular basis of the very first step of fertilisation. At the same time, considering that ZP2 ZP-N1 contains a region thought to play a crucial role in human gamete recognition **[3]**, the findings have important implications for reproductive medicine.

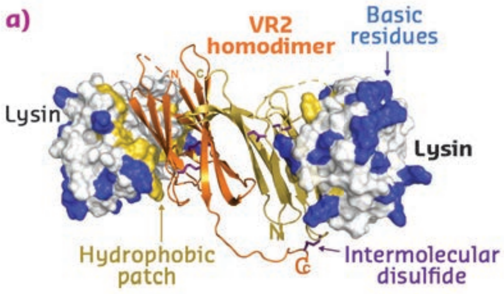

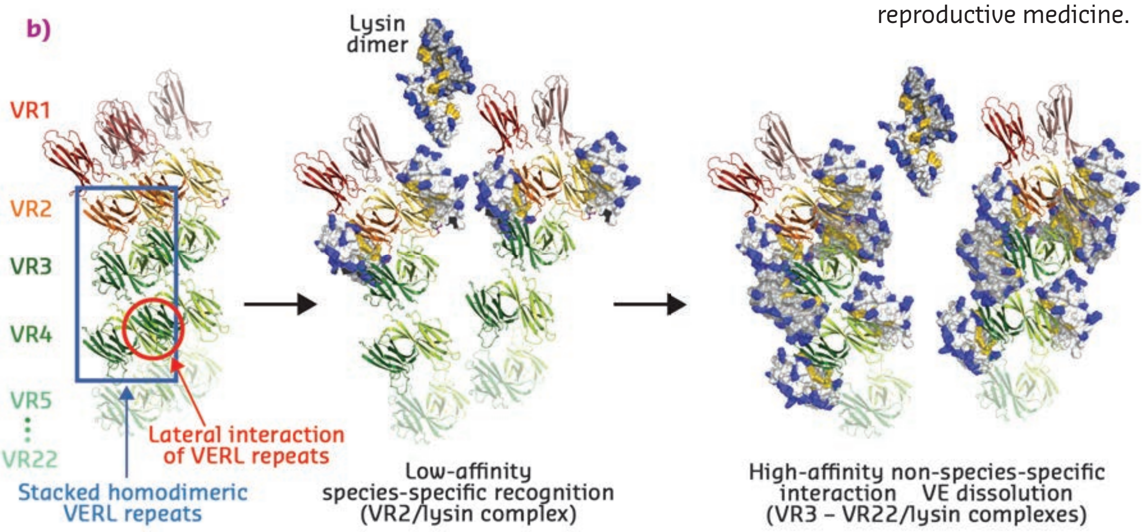

Fig. 23: a) Structure of the VERL VR2-sperm lysin complex. The VR2 homodimer is shown in cartoon representation and lysin is depicted as surface with basic and hydrophobic residues coloured blue and yellow, respectively.
b) Model of higher-order VERL organisation and its unravelling by lysin at fertilisation.

PRINCIPAL PUBLICATION AND AUTHORS

Structural basis of egg coat-sperm recognition at fertilization, I. Raj (a,c), H. Sadat Al Hosseini (a,c), E. Dioguardi (a), K. Nishimura (a), L. Han (a), A. Villa (a), D. de Sanctis (b) and L. Jovine (a), *Cell* **169**, 1315-1326 (2017); doi: 10.1016/j.cell.2017.05.033.
(a) Department of Biosciences and Nutrition & Center for Innovative Medicine, Karolinska Institutet, Huddinge (Sweden)
(b) ESRF
(c) These authors contributed equally

REFERENCES

[1] M. Monné *et al.*, *Nature* **456**, 653-657 (2008).
[2] C.A. Lewis *et al.*, *Dev. Biol.* **92**, 227-239 (1982).
[3] M.A. Avella *et al.*, *J. Cell. Biol.* **205**, 801-809 (2014).

STRUCTURES OF PAR2 COMPLEXES REVEAL NEW MODES OF MODULATION

Synchrotron radiation has been used to reveal the structure of a cell surface receptor involved in pain regulation. This has revealed new opportunities for the development of agents for pain relief.

Protease-activated receptors (PARs) are implicated in several diseases including inflammation, thrombosis, pain and cancer. These receptors are members of the G protein-coupled receptor (GPCR) family that reside in the cell membrane and include the targets for many medicines. However, PARs are unusual in not being directly activated by agonists circulating in the extracellular environment. Rather, activation occurs through extracellular proteases, which remove a short section of the polypeptide chain of the receptor, and the new end of the polypeptide chain acts as the agonist by inserting into and activating the receptor (**Figure 24**). This means of activation is commonly referred to as 'tethered agonism' and it can be mimicked by the addition of peptide corresponding to the sequence of the end of the receptor. Tethered agonists present challenges for the discovery of antagonists (which block the response), as, after proteolysis, the agonist is always adjacent to the receptor activation site, and its local concentration is far higher than for a conventional non-tethered system **[1]**. Despite the involvement of PARs in several diseases, and being the subject of drug discovery efforts in many companies, only one medicine that targets a protease-activated receptor has received regulatory approval for use in patients. Vorapaxar, which is licensed for use in patients with a risk of specific cardiovascular events, is an antagonist of protease-activated receptor 1 **[2]**.

AstraZeneca and Heptares Therapeutics embarked on a joint project to discover antagonists of protease-activated receptor 2 (PAR2) for potential development of analgesic agents. Two series of antagonists were identified from screening a library of drug-like compounds and a library of DNA-encoded molecules. Using the Heptares stabilised receptor (StaR) technology, crystal structures for the PAR2, bound to a representative of each of these series, were determined. These clearly show the binding site for one antagonist on the outside of the receptor and a site for the other adjacent to the presumed pocket for the tethered agonist. Each molecule appears to function as an antagonist by preventing the conformational changes required for the tethered agonist to bind to and activate the receptor. Using **ID29,** a structure was also obtained for PAR2 bound to a small molecule antagonist and a fragment from the monoclonal antibody MAB3949 (**Figure 25**). Loops of the heavy and light chains of the antibody bind to the extracellular face of PAR2. The epitope is comprised of the amino terminus, extracellular

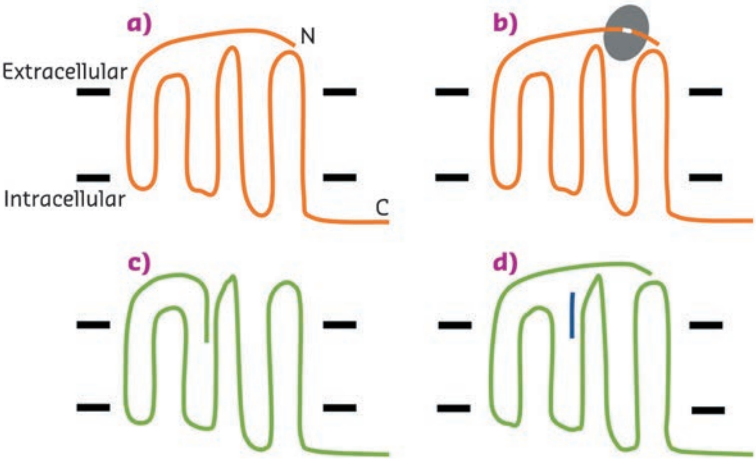

Fig. 24: Schematic representation of the activation on PARs. a) An inactive PAR (orange); the N and C-termini of the protein are labelled, and the black bars indicate the approximate location of the cell membrane. b) A protease enzyme (grey) binds to the PAR, removing a section of the N-terminus. c) The newly generated N-terminus of the PAR binds to a pocket and activates the receptor (green). d) Activation of the receptor can be mimicked without a protease by addition of a short peptide (blue).

Fig. 25: The structure of PAR2 (green) in complex with FAB3949 (heavy chain in yellow and light chain in brown). The FAB binds to the extracellular side of the receptor and the observed interaction provides a structural rationale for the antagonist activity of MAB3949.

loops 2 and 3, and the extracellular end of transmembrane helix 6. This mode of antibody binding is different from examples where the antibody targets the site that is cleaved by proteases before receptor activation. This is mirrored in assay results where the latter antibodies are able to prevent activation of the receptor after protease cleavage, but are unable to block activation by the addition of peptides. MAB3949 can prevent activation in both cases, possibly through direct competition for access to the agonist binding site.

The structural work has demonstrated three new means by which PARs can be antagonised and may pave the way for further developments for this difficult sub-group of targets.

PRINCIPAL PUBLICATION AND AUTHORS

Structural insight into allosteric modulation of protease-activated receptor 2, R.K.Y. Cheng (a), C. Fiez-Vandal (a), O. Schlenker (a), K. Edman (b), B. Aggeler (c), D.G. Brown (b), G.A. Brown (a), R.M. Cooke (a), C.E. Dumelin (d), A.S. Doré (a), S. Geschwindner (b), C. Grebner (b), N-O. Hermansson (b), A. Jazayeri (a), P. Johansson (b), L. Leong (c), R. Prihandoko (a), M. Rappas (a), H. Soutter (d), A. Snijder (b), L. Sundström (b), B. Tehan (a), P. Thornton (b), D. Troast (d), G. Wiggin (a), A. Zhukov (a), F.H. Marshall (a) and N. Dekker (b), *Nature* **545**, 112-115 (2017); doi: 10.1038/nature22309.

(a) Heptares Therapeutics (UK)
(b) AstraZeneca (Sweden, USA and UK)
(c) Bio-techne (USA)
(d) X-Chem Inc. (USA)

REFERENCES

[1] R. Ramachandran *et al., Nat Rev Drug Discov.* **11**, 69-86 (2012).
[2] B. E. Hawes *et al., Eur J Pharmacol*. **762**, 221-228 (2015).

STRUCTURAL INSIGHTS INTO A PROTEIN COMPLEX CRITICAL FOR CELLULAR NUTRIENT SENSING

A cooperative initiative of research groups from the Medical University Innsbruck have determined the crystal structure of a major cellular protein complex that has roles in sensing energy status and nutrient availability in cells and contributes to the activation of cell-growth controlling protein machinery.

The mechanistic target of rapamycin complex 1 (mTORC1) is a master regulatory protein complex for cellular growth, which responds to the availability of nutrients and associated cellular signals including energy status and other cues influenced by environmental factors **[1]**. The activity of the master regulator requires the mTORC1 complex to be recruited to the membrane of lysosomes, which are not only waste disposal systems but also mobile signalling platforms where availability of amino acids and other nutrient status determining compounds are sensed **[2]**.

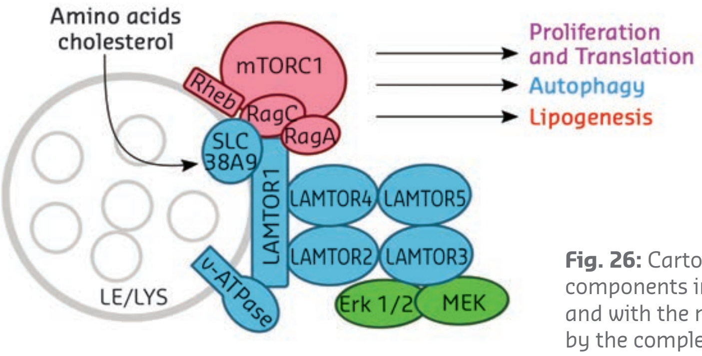

Fig. 26: Cartoon diagram showing the LAMTOR/Ragulator components in association with the late endosome/lysosome (LE/LYS) and with the mTORC1 complex. Selected cellular processes controlled by the complex are indicated.

The master regulator LAMTOR (also termed Ragulator) is a pentameric late endosomal/lysosomal scaffold complex consisting of five protein components, LAMTOR1-5 (**Figure 26**), and serving as a point of convergence/integration of nutrient status and signalling. Lipid-modified LAMTOR1 anchors the remaining subunits, LAMTOR2-5, to the limiting membrane of the organelle. Rag GTPases are Ras-related switches that exist as heterodimers sharing active GTP-bound RagA/B and inactive GDP-bound RagC/D conformations. LAMTOR/Ragulator is important for tethering these Rag-GTPases to the lysosomal membrane to meet mTORC1, depending on availability of nutrients. Indeed, Ragulator has been reported to act as a guanine nucleotide exchange factor (GEF) activating Rags for interaction with mTORC1 **[3]**.

The structure of the pentameric Ragulator complex (LAMTOR1-5), determined from data collected at beamline **ID23-2**, reveals a heterotetramer composed of two heterodimers, LAMTOR2/3 and LAMTOR4/5, apparently held together by the LAMTOR1 component, of which the helix-rich core wraps around the four 'roadblock' components in a belt-like fashion (**Figure 27**). Cellular studies with CRISPR/Cas9 edited human cells demonstrated that loss of the interactions seen in the crystal structure led to complex destabilisation and impaired mTORC1 signalling upon amino acid derived stimulation after exposure.

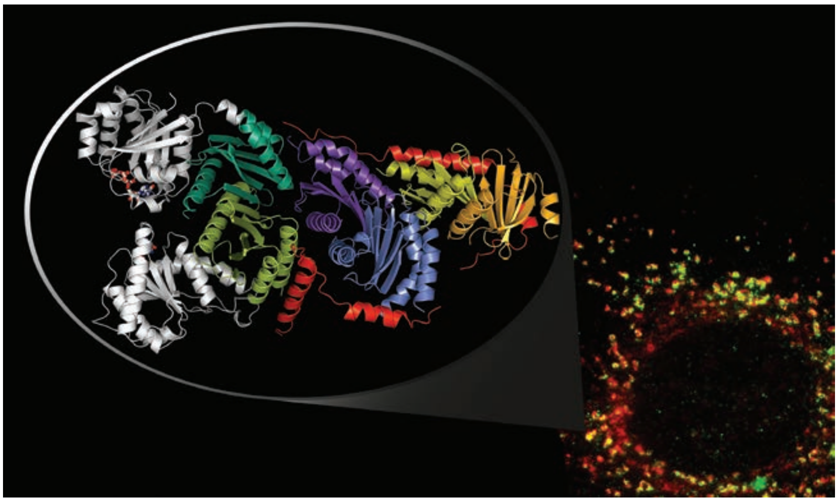

Fig. 27: Immunofluorescence image of LAMTOR components (red) and a lysosomal marker (LAMP1 in green, bottom right); co-localisation of both components is shown in yellow. The crystal structure of the truncated Rag/Ragulator complex is shown as a zoom inset (top left). Here, the belt-like LAMTOR1 component is shown in red, the G-domains (position derived from structural alignments) in grey.

Crystallisation of the heptameric Rag/Ragulator complex appeared to be challenging. However, as literature data pointed to a potential interface with the C-terminal dimerisation domains of the Rags, a complex between just those domains and Ragulator was purified and crystallised. The structure of this complex, derived from data collected at **ID29**, reveals a tight interaction between the C-terminal RagA/C roadblock dimer and the LAMTOR2/3 heterodimer. Alignment of the C-terminal roadblock domains with the crystal structure of the previously solved RagA/C homologue, Gtr1/Gtr2 (from yeast), immediately suggests a model for the full-length heptameric Rag/Ragulator complex (**Figure 27**). Most importantly, in this model the G-domains of the Rags, and thus their key nucleotide binding components (phosphate binding loop and switch regions), are exposed to the solvent rather than directly interacting with Ragulator components, as would have been expected for a canonical guanine nucleotide exchange factor.

The structural model obtained above (**Figure 27**) has been recently confirmed by a hybrid study combining crystallography of the pentameric Ragulator with cryo-electron microscopy investigations of the heptameric complex containing RagA/C heterodimers. These latter also show the Rag G-domains in an exposed position and oriented to the solvent **[4]**. Additionally, three further crystallographic studies confirmed the crystal structure of the pentameric LAMTOR/Ragulator **[5, 6, 7]** and of the G-domain truncated heptameric Ragulator complex obtained above **[4, 5, 6]**. One of these studies revealed the lack of nucleotide exchange factor activity for the recombinant Ragulator complex and raises the possibility that previously reported activity could require one (or more) additional cellular components not present in recombinantly purified complex preparations **[5]**. Future studies will investigate this issue in greater detail.

The structural knowledge about the positions of critical amino acids positions revealed in these investigations provides a basis for the development of potential new drugs that could turn off the master regulatory complex in diseases like cancer or metabolic disorders in which the mTORC1 signalling pathway is overactive.

PRINCIPAL PUBLICATION AND AUTHORS

Crystal structure of the human lysosomal mTORC1 scaffold complex and its impact on signaling, M.E.G. de Araujo (a), A. Naschberger (b), B.G. Fürnrohr (b), T. Stasyk (a), T Dunzendorfer-Matt (b), S. Lechner (b), S. Welti (b), L. Kremser (c), G. Shivalingaiah (b), M. Offterdinger (d), H.H. Lindner (c), L.A. Huber (a) and K. Scheffzek (b), *Science* **358**, 377 (2017); doi: 10.1126/science.aao1583.

(a) Division of Cell Biology, Biocenter, Medical University of Innsbruck (Austria)
(b) Division of Biological Chemistry, Biocenter, Medical University of Innsbruck (Austria)
(c) Division of Clinical Biochemistry, Biocenter, Medical University of Innsbruck (Austria)
(d) Division of Neurobiochemistry-Biooptics, Biocenter, Medical University of Innsbruck (Austria)
(e) Austrian Drug Screening Institute, Innsbruck (Austria)

REFERENCES

[1] D.M. Sabatini, *PNAS* **114**, 11818 (2017).
[2] M. Rebsamen *et al.*, *Nature* **519**, 477 (2015).
[3] L. Bar-Peled *et al.*, *Cell* **150**, 1196 (2012).
[4] M.Y. Su *et al.*, *Mol Cell* **68**, 835 (2017).
[5] T. Zhang *et al.*, *Nat Commun* **8**, 1394 (2017).
[6] R. Yonehara *et al.*, *Nat Commun* **8**, 1625 (2017).
[7] Z. Mu *et al.*, *Cell Discovery* **3**, 17049 (2017).

STRUCTURE AND CERAMIDASE FUNCTION OF ADIPONECTIN RECEPTORS

Crystal structures of adiponectin receptors (ADIPORs) are advancing understanding of the molecular mechanisms underlying their potent antidiabetic character. Here, structural data together with biochemical analyses reveal an intrinsic ceramidase activity of ADIPORs. This knowledge will facilitate structure-based drug design to treat obesity-related disease such as type 2 diabetes.

Adiponectin receptors (ADIPORs) are integral membrane proteins possessing a potent antidiabetic character, at least partly arbitrated by receptor-associated ceramidase activity, resulting in hydrolysis of ceramide to sphingosine and fatty acid.

The recent crystal structures of two adiponectin receptor subtypes, ADIPOR1 and ADIPOR2, revealed that they possess seven transmembrane (7TM) helices enclosing large unoccupied internal cavities and a zinc binding site **[1]**. However, the molecular mechanisms of ADIPOR function were still obscure. In an effort to better understand how ADIPORs function, *in meso* crystallography was used and, following data collection at beamline **ID30B**, the structure of ADIPOR2 was determined (**Figure 28a**).

Besides the 7TM architecture and the position of the zinc binding site, the new ADIPOR2 crystal structures revealed the presence of a free fatty acid (FFA) within a large internal cavity. The FFA is bound close to a putative zinc catalytic core, prompting a test of whether ADIPORs possess an intrinsic ceramidase activity. To do so, purified receptor preparations were used to determine their ability to bind and hydrolyse synthetic ceramide substrates using biochemical approaches. In addition, computational studies provided key mechanistic insights into the ceramidase function of ADIPOR2, highlighting the central role played by the zinc catalytic core and surrounding amino acids.

Structural analysis naturally led to comparisons of data with previously published work. Surprisingly, it was observed that the electron density from a recently determined ADIPOR1 crystal structure appeared to have been misinterpreted, leading to a substantial error in the structural model produced **[1]**. Using the available structure factors this crystal structure was refined using the PDB entry 3WXV as a starting point, producing a final model with much improved statistics and fit to the electron density. In stark contrast to what had been published, the corrected ADIPOR1 structure is quite distinct from the ADIPOR2 structures obtained (**Figure 28**). Specifically, no FFA molecule is bound in the ADIPOR1 structure and both the ceramide binding pocket and the putative zinc catalytic site are wide open and accessible to the inner membrane leaflet (**Figure 28b**). Because both ADIPOR1 and ADIPOR2 possess an intrinsic ceramidase activity, it is suspected that the two structures may represent key steps in this process.

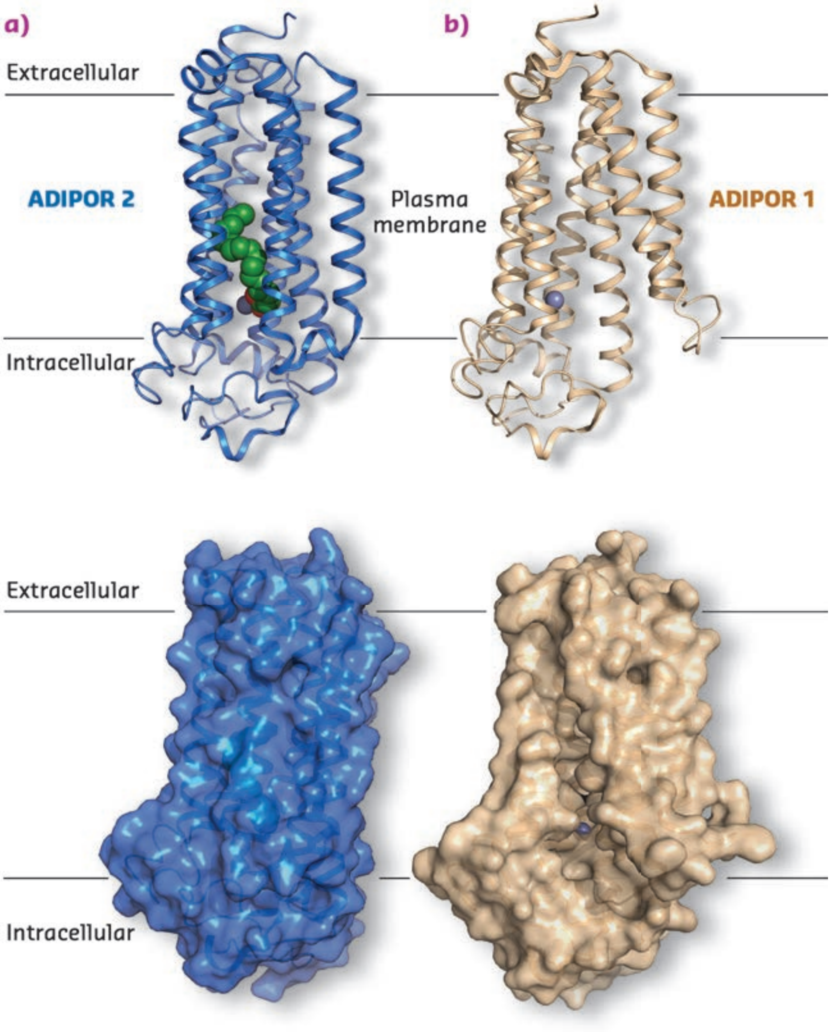

Fig. 28: a) Crystal structure of ADIPOR2, blue cartoon (top) and surface view (bottom), with free fatty acid (green spheres) and a Zn^{2+} (grey sphere) binding site.
b) Crystal structure of ADIPOR1, wheat cartoon (top) and surface view (bottom), with no free fatty acid bound and the Zn^{2+} (grey sphere) binding site exposed to the membrane environment.

In conclusion, it has been demonstrated that ADIPORs possess an intrinsic ceramidase activity (*i.e.* hydrolyse ceramide into a free fatty acid (FFA) and sphingosine) and a combination of lipidic cubic phase crystallography and computational and biochemical studies provide the molecular basis for this enzymatic activity. Since insulin resistance and type 2 diabetes correlate with increased levels of ceramides and reduced expression of ADIPORs, this study may facilitate the development of new therapeutic approaches to treat obesity-related diseases.

PRINCIPAL PUBLICATION AND AUTHORS

Structural insights into adiponectin receptors suggest ceramidase activity,
I. Vasiliauskaité-Brooks (a), R. Sounier (a), P. Rochaix (a), G. Bellot (a), M. Fortier (a), F. Hoh (b), L. De Colibus (c), C. Bechara (d), E.M. Saied (e, f), C. Arenz (e), C. Leyrat (a) and S. Granier (a), *Nature* **544**, 120-123 (2017); doi:10.1038/nature21714.

(a) Institut de Génomique Fonctionnelle, CNRS UMR-5203 INSERM U1191, University of Montpellier (France)
(b) Centre de Biochimie Structurale, CNRS UMR 5048-INSERM 1054 University of Montpellier (France)
(c) Division of Structural Biology, University of Oxford (UK)
(d) Dynamique des Interactions Membranaires Normales et Pathologiques, CNRS UMR5235, University of Montpellier (France)
(e) Institute for Chemistry, Humboldt-Universität zu Berlin (Germany)
(f) Chemistry Department, Faculty of Science, Suez Canal University, Ismailia (Egypt)

REFERENCES

[1] H. Tanabe *et al., Nature* **520**, 312-316 (2015).

TARGETING ACUTE PANCREATITIS WITH INHIBITORS OF KYNURENINE-3-MONOOXYGENASE THAT TILT THE CATALYTIC FLAVIN

X-ray crystallographic and mechanistic studies have enabled the discovery of kynurenine-3-monooxygenase (KMO) inhibitors suitable for preclinical evaluation in Acute Pancreatitis. These picomolar, long-residence-time compounds trap the catalytic flavin in an unusual tilted orientation that overcomes the mechanistic liability of stimulated hydrogen peroxide production seen with previous active site binders.

Scientists at GlaxoSmithKline (GSK) and the University of Edinburgh have worked closely together to find new inhibitors of kynurenine-3-monooxygenase (KMO) to treat Acute Pancreatitis.

Acute Pancreatitis (AP) disease is typically caused by gallstones or excessive alcohol consumption. For the majority of AP patients, symptoms resolve within a week or so. However, in approximately one in five cases, the disease progresses to multiple organ failure with a > 20% mortality rate. Currently there are no disease-modifying treatments available, highlighting the need for new therapies.

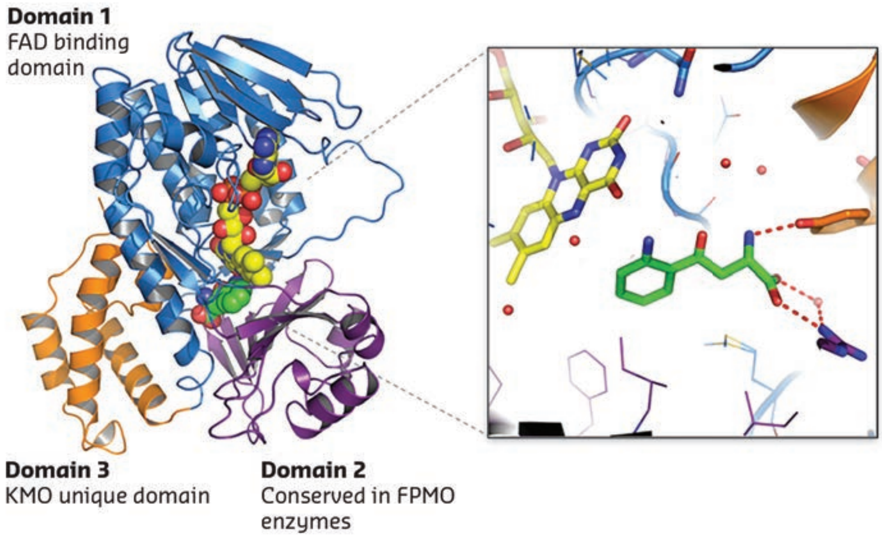

Fig. 29: 1.5 Å X-ray structure of Pf-KMO in complex with substrate.

In mammals, the major metabolic route of tryptophan degradation is via the kynurenine pathway. KMO is a class A flavoprotein monooxygenase (FPMO) that catalyses the hydroxylation of L-kynurenine (L-Kyn) using NADPH as a co-substrate. The product, 3-hydroxy kynurenine (3-HK), is a neurotoxin that can also induce apoptotic cell death in endothelial cells. Pharmacological inhibition of KMO has long been considered as a target for neurogenerative disorders such as Huntington's and Alzheimer's diseases, as well as more recently, for Acute Pancreatitis Multiple Organ Dysfunction Syndrome (AP-MODS).

Surprisingly for such an important metabolic enzyme and drug target, structural insights have so far been remarkably limited. Human KMO is a 56 kDa protein containing a tightly bound FAD co-factor and is attached to the mitochondrial outer membrane via a C-terminal region. Human KMO remains recalcitrant to crystallisation with no structure reported to date. The homologous bacterial *Pseudomonas fluorescens* enzyme, Pf-KMO, (34% sequence identity), which lacks the transmembrane region, was therefore developed as a structural surrogate.

Native Pf-KMO crystals diffracted poorly, but a double C252S/C461S Pf-KMO mutant could be optimised to yield a high resolution-diffracting monoclinic crystal form amenable for ligand soaking studies, enabling a rapid turnaround of crystal structures determined on **ID23-1**, **ID30A** and **ID30B** to drive structure-based drug design.

Many KMO inhibitors are substrate inspired. A 1.5 Å L-Kyn bound Pf-KMO structure gave the first view of how the native substrate sits within the active site (**Figure 29**). The details of this structure differ from previous computational models and represent a significant advance, allowing explanation of puzzling structure-activity relationships and providing a firm basis for novel inhibitor discovery and mechanistic analysis. This was demonstrated by the discovery of the first type-II KMO inhibitors that bind to an unprecedented tilting flavin conformation of Pf-KMO.

Carefully choreographed flavin motions are critical to multiple steps in the catalytic cycle of FPMO enzymes, controlling substrate binding, product release and regulating the reductive and oxidative steps during catalysis. Rare snapshots of flavin motion have been captured by crystallography (**Figures 30a, c**) but none of these were known to be important or benefical for inhibitor design.

GSK775 was synthesised during a structure-based optimisation of a series of oxazolidinone

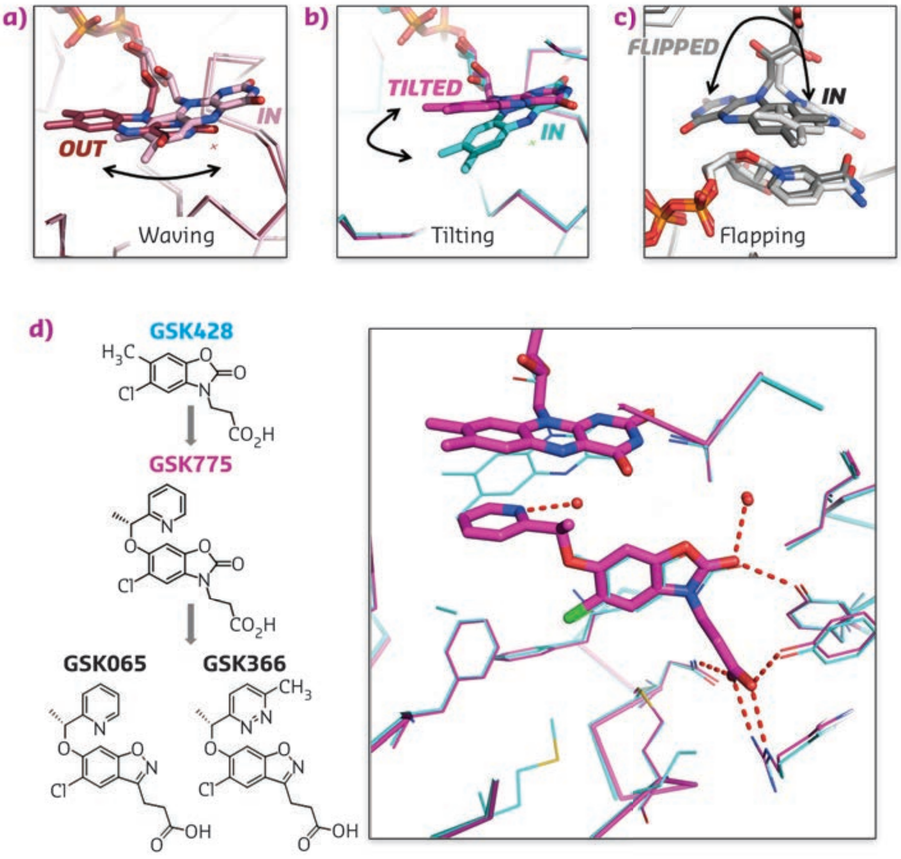

Fig. 30: a-c) Crystal structures of flavin captured in different orientations in various crystal structures. d) Chemical structures of type I inhibitor GSK428 and type II inhibitors GSK775, GSK065 and GSK366. Overlay of X-ray structures of Pf-KMO bound with GSK428 (cyan) and GSK775 (magenta).

inhibitors such as GSK428 (**Figure 30d**). The pyridine ring of GSK775 was designed to occupy space close to the flavin ring to gain additional potency. However, GSK775 was much more potent than expected and exhibited slow kinetics. Crystal structures revealed it didn't bind close to the flavin but, instead, pushed it into a tilted orientation never seen before (**Figures 30b, d**). This traps the flavin in an unproductive position that decouples substrate site binding from NAPDH reduction and flavin oxidation. The result is that type-II compounds such as GSK775 lose the mechanistic liability of stimulated hydrogen peroxide production carried by simple substrate site inhibitors such as GSK428.

Transferring this structural and mechanistic understanding to a benzisoxazole series has delivered picomolar, long residence time, type-II compounds, GSK065 and GSK366, which have the full profile of pharmaceutical and pharmacological *in vitro* and *in vivo* properties for progression to clinical evaluation in AP-MODS.

PRINCIPAL PUBLICATION AND AUTHORS

Structural and mechanistic basis of differentiated inhibitors of the acute pancreatitis target kynurenine-3-monooxygenase, J.P. Hutchinson (a), P. Rowland (a), M. Taylor (b), E.M. Christodoulou (a), C. Haslam (a), C.M. Hobbs (a), D.S. Holmes (c), P. Homes (a), J. Liddle (c), D.J. Mole (d, e), I. Uings (c), A.L. Walker (c), S.P. Webster (f), C. G. Mowat (b) and C. Chung (a), *Nat Commun* **8**, 15827 (2017); doi:10.1038/ncomms15827.

(a) Platform Technologies and Science , GlaxoSmithKline, Stevenage (UK)
(b) EastChem School of Chemistry, University of Edinburgh (UK)
(c) Discovery Partnerships with Academia, GlaxoSmithKline, Stevenage (UK)
(d) Medical Research Council Centre for Inflammation Research, Edinburgh (UK)
(e) Clinical Surgery, University of Edinburgh (UK)
(f) British Heart Foundation Centre for Cardiovascular Science, University of Edinburgh (UK)

MATTER AT EXTREMES

2017 has been a very productive year for the MEx beamlines, not only for the science performed, but also due to major advances in instrumentation and development on the beamlines.

Experiments on **ID18** and at Petra-III, in collaboration with a team from Max Planck Institute for Nuclear Physics, have led to the development of a new nuclear resonance technique, which allows a significant increase in the number of resonant photons in an X-ray pulse, leading to an enhanced intensity that will make previously impossible experiments feasible.

On **ID27**, the vertical laser heating coupled to a Soller slits system, developed in the framework of the French ANR grant "MoFlEx" is now open to users. This system, which is unique worldwide, enables the collection of high-quality XRD data of fluids and amorphous materials in the megabar regime and at several thousands of degrees. The new setup has widespread applications in physics, chemistry and Earth sciences.

On **ID24**, an energy-dispersive tomographic absorption spectroscopy variant has been developed and is now available to the user community. It sets itself apart from existing XAS tomography techniques because a full XAS spectrum with an energy range of several hundred eV can be acquired in a single measurement.

Developments at the large-volume press on **ID06** have seen a considerable acceleration following the 2016 increase in user access. Requests for this facility have leaped over 30% with respect to last year. In particular, we have seen increased use and revision of the ultrasonic setup (in collaboration with A. Thomson, UCL), giving ultrasonic data accumulation times of less than 12 s for P and S waves respectively, to be compared to three minutes previously. The 6/6 assembly has been totally reviewed, leading to a significantly improved sample alignment for deformation. Finally, the adoption of TF05 cubes has shown a 40% improvement in compression rate.

ID15B has now finished its first year of extremely successful user operation. Replacing ID09A, which closed in November 2015 after more than 20 years of successful operation, ID15B offers powder and single crystal diffraction with high resolution well into the megabar pressure range, and variable temperatures from a few to several hundred Kelvin. Recently, a setup for phase contrast imaging was tested and successfully employed in a user experiment. To cope with the very high oversubscription rate of this beamline, a second postdoc has been hired, allowing us to increase the number of shifts provided to users from 50% to 70% until the long shutdown.

Finally, on **BM23** a five-crystal analyser, funded by the French EcoX "Equipex" has been recently coupled to the microXAS station. This spectrometer will allow better separation of fluorescence lines and scattering from complex materials, and the possibility to perform high energy-resolved fluorescence detection (HERFD) on heterogeneous materials and under *in situ* conditions. It will become available to the user community after commissioning in 2020.

The preparation of the Technical Design Report for Phase I of the High Power Laser Facility (**HPLF-I**) project is running at full speed. 2017 has seen the recruitment of a laser engineer, the transfer of an ID24 scientist to this project, and the ordering of the 100 J, ns shaped pulse laser. The delivery of the front end of the laser is planned for May 2018, and first user experiments are being scheduled starting July 2018.

Following the approval by the ESRF Council in June of the upgrade of the beamline portfolio, aimed at exploiting the higher brilliance of EBS, the MEx group will participate in an intense beamline refurbishment program, planned for 2018-2022. A completely new beamline devoted to nano X-ray diffraction at extreme conditions will be constructed, extending the existing ID27 beamline from 50 to 120 m to provide a more flexible nano-focused probe that is unique in the world in terms of photon flux and focusing capabilities. Coupled with advanced tools to monitor the most extreme conditions of pressure and temperature, the upgraded capabilities will largely surpass the current barriers and open unique routes to probe new material properties. It will benefit many areas of research, from planetary science to fundamental physics, including solid-state chemistry, materials science and biology. For example, the small beam size will allow scientists to probe pressures higher than found at the centre of the Earth, while fast signals will capture information from short-lived samples, such as those held at above

3 000 K in liquids. Materials engineering and the pharmaceutical industry will also be well served.

Secondly, one branch of the existing ID24 beamline, used for energy-dispersive XAS, will be converted to an energy-scanning XAS configuration. Using the novel in-house-developed double crystal monochromator, the new branch will provide a variable spot size from 1 mm to 1 um, a variable flux up to $4*10^{14}$ photons/s, and a time resolution for a full EXAFS down to 1 s. Today *in situ* XAS applications in the geosciences are limited to conditions relevant to the Earth's lower mantle, but the new ID24 will allow investigation of the local structure of melts down to the inner core boundary at pressures and temperatures exceeding 3 Mbar and 5 000 K. Functional materials and natural samples will also be explorable at unprecedented concentrations and timescales.

Finally, feasibility studies have been launched to implement ID18 with an extreme spatial and energy resolution. By 2020, the ID18 beamline, which will evolve within the existing experimental hall, will offer a spatial resolution of 200 nm and an energy resolution of 50 μeV.

The User Meeting in February 2018 will be an excellent opportunity for our user community to be updated on these developments and to discuss future science with EBS, in particular at the User Dedicated Symposium on High Pressure. We will also continue our training programme with tutorials and hands-on practicals on nuclear resonance applications and EXAFS.

In the MEx group, we are constantly concerned with pushing the limits of the X-ray methods we use, both to maintain our beamlines at the cutting edge of synchrotron science as well as to prepare them for upcoming challenges with EBS (**see page 40**). Another major area of research in the group is in the use of high pressures and temperatures to synthesise materials with enhanced properties (**see pages 41-44**). An important area of research deals with understanding how organic and inorganic catalysts work, aiming towards a cleaner and safer chemical industry and less energy-intensive processes (**see pages 45-51**). This field bridges towards Earth and planetary science (**see pages 54-56**), passing through environmental science, sustainable development and clean energy research, of which investigations on the carbon cycle (**see page 53**) are a nice example.

S. PASCARELLI

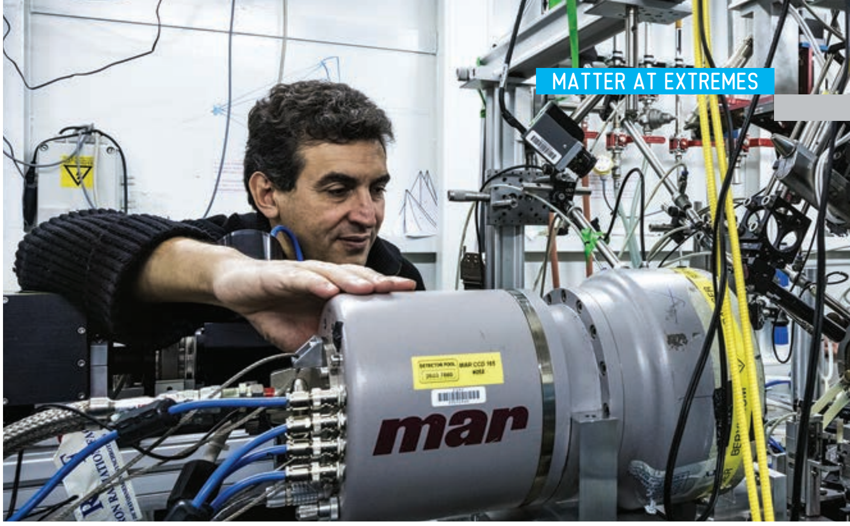

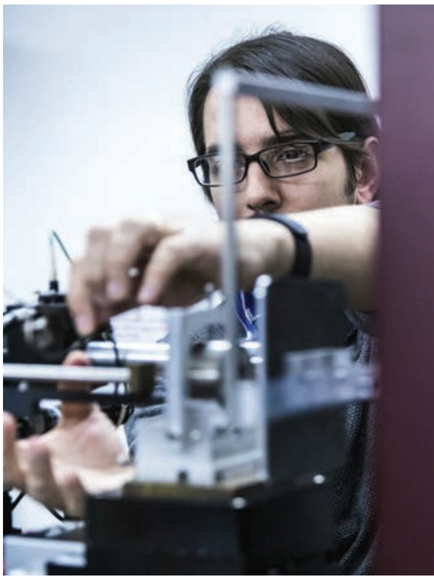

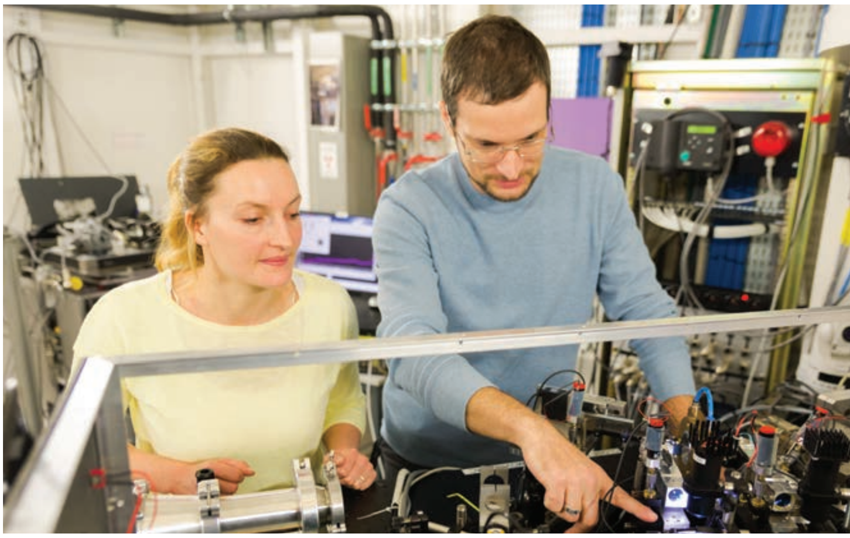

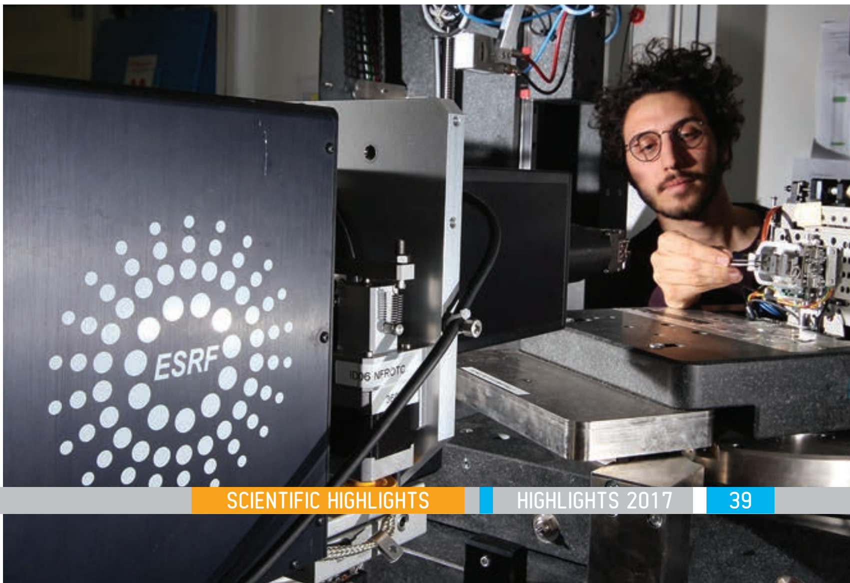

SUDDEN SHIFTS SHARPEN X-RAY PULSES

Nuclear resonance techniques use only a narrow fraction of the X-ray spectrum. By squeezing off-resonant photons onto resonance via precisely controlled motion of a resonant target, the number of resonant photons in an X-ray pulse has been significantly increased. The enhanced intensity permits previously unfeasible experiments and opens the door for new experimental possibilities.

Narrow X-ray resonances such as those of Mössbauer nuclei form the basis for a broad range of experiments based on high-precision spectroscopy and are a decisive component for novel applications in the realm of X-ray quantum optics **[1]**. However, the spectra of the short pulses delivered by modern X-ray sources are orders of magnitude broader than the narrow resonances and only a tiny fraction of the available photons interacts resonantly with the sample, while the vast majority produce an off-resonant background. This restricts the achievable spectral, spatial and temporal resolution for commonly-used narrow resonances, preventing experiments with the sharpest available resonances.

To overcome this, a novel method was developed to amplify the spectrally broad X-ray pulses of state of the art X-ray sources in a narrow spectral region. Unlike with monochromators, the undesired off-resonant photons are not simply removed, but converted into resonant ones.

Pictorially, the method works like a mechanical digger that shapes a hill out of a flat landscape by removing earth at the sides and piling it up. Analogously, the new method removes photons in off-resonant spectral regions, and piles them up in a narrow resonant spectral region. In the experiments performed at **ID18** and P01 (PETRA-III, DESY), the role of the digger is taken by a piezoelectric material that performs specific motions upon precisely characterised and controlled electric signals (**Figure 31a**). The "photon shovel" is formed by a thin iron absorber foil on the piezo, which temporarily stores X-ray photons while it performs its motion. The operation of the piezoelectric photon shovel exploits the Mössbauer effect: nuclei such as ^{57}Fe used in this experiment, when embedded in a solid-state environment, can absorb and emit X-ray photons essentially without recoil.

The working principle of the photon shovel is based on interference effects: incoming resonant X-ray photons either pass through the sample without interaction, or are temporarily absorbed (**Figure 31a**). This absorption and re-emission leads to a phase shift, such that the scattered photons destructively interfere with the non-interacting part. As a consequence, a dip due to absorption is observed in the spectrum. If instead the absorber foil is displaced by half the resonant wavelength after the non-interacting part has passed the sample, but before most absorbed photons have been re-emitted, the destructive interference can be converted into constructive interference. This way, the number of resonant photons increases. The motion not only affects the resonant light, but conversely also attenuates the X-ray pulse around the resonance. Overall, the enhancement of the resonant photon number is thus achieved by shovelling off-resonant photons onto the resonance (**Figure 31d**).

Experiments were performed with samples enriched in the isotope ^{57}Fe with its nuclear

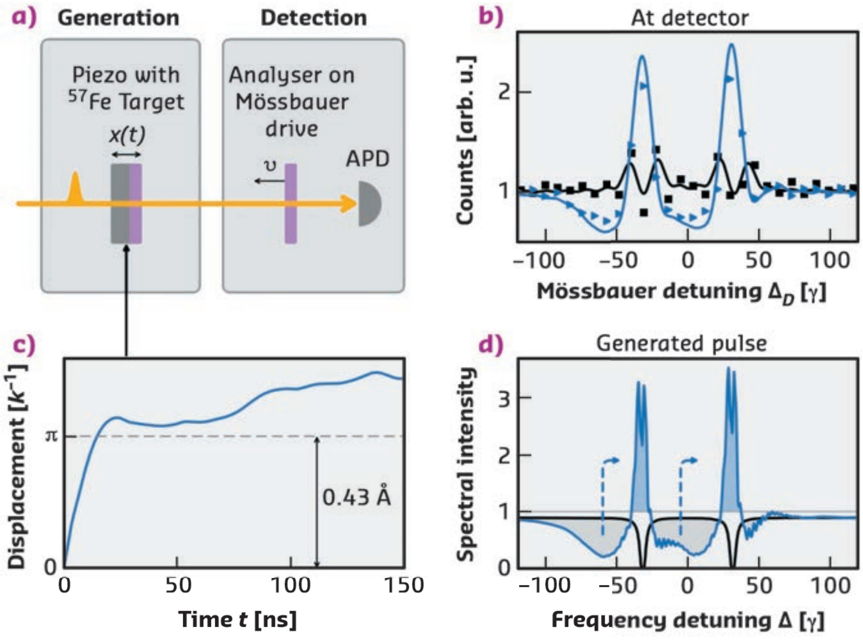

Fig. 31: a) Incoming X-ray pulses are sharpened via an iron foil mounted on a piezo drive, and subsequently their spectrum is detected. b) Experimental data together with theoretical fits. c) The piezo is displaced by 0.43 Å, half the resonant wavelength. d) Normalised X-ray spectra behind the piezo. Usual absorption of the magnetically split nuclear resonance is shown (black). The spectrum for the motion in (c) clearly exhibits the conversion into enhancement on resonance (blue).

transition at 14.4 keV. The displacement of the absorber foil was controlled to less than a tenth of a nanometre, and took place within a few nanoseconds (**Figure 31c**). The reconstruction of these motions from the measured spectra constituted a considerable part of the analysis. An enhancement by a factor of up to 4 was observed for the number of photons on resonance as compared to the incoming photon number. Theoretical calculations suggest that an enhancement by a factor of 10 should be feasible with an optimised absorber foil and corresponding motion, limited only by additional electronic attenuation due to the photon-shovel material. In a subsequent experiment, the possibility for further enhancements with multiple shovels was successfully demonstrated.

In future, this new technique could be deployed in the routine operation of beamlines at synchrotrons and free-electron lasers. The increased intensity results in shorter measurement times and enables measurements with presently too low signal rates. Also, the higher signal rates translate into better energy and spatial resolution. Using different displacement patterns enables a more general manipulation of the X-ray spectra **[2]**. Furthermore, the mechanical control of X-ray-matter interactions could become a valuable tool in X-ray quantum optics, alleviating the need for additional X-ray control fields in certain settings. Finally, the technique also opens the possibility to track motions on atomic length scales in a wide range of scientific and technological applications.

PRINCIPAL PUBLICATION AND AUTHORS

Spectral narrowing of X-ray pulses for precision spectroscopy with nuclear resonances, K.P. Heeg (a), A. Kaldun (a), C. Strohm (b), P. Reiser (a), C. Ott (a), R. Subramanian (a), D. Lentrodt (a), J. Haber (b), H.-C. Wille (b), S. Goerttler (a), R. Rüffer (c), C.H. Keitel (a), R. Röhlsberger (b), T. Pfeifer (a) and J. Evers (a), *Science* **357**, 375-378 (2017); doi: 10.1126/science.aan3512.

(a) Max-Planck-Institut für Kernphysik, Heidelberg (Germany)
(b) Deutsches Elektronen-Synchrotron DESY, Hamburg (Germany)
(c) ESRF

REFERENCES

[1] B.W. Adams *et al.*, *Journal of Modern Optics* **60**, 2 (2013)
[2] C. Ott *et al.*, *Science* **340**, 716-720 (2013)

Si-III SYNTHESIS AND CHARACTERISATION

Si-III was found to be a narrow-gap semiconductor following its high-pressure synthesis using the large-volume press at beamline ID06. The complete optical, electronic and thermal transport properties of Si-III have been determined.

Silicon is important for electronics, solar energy conversion and other technological applications. Its capacity to introduce new and unexpected physical phenomena, due to the numerous crystal structures, remains very promising for the development of future advanced applications.

The common structure of Si, called “number I” or Si-I, is that of diamond. High pressure allows new structures to be obtained and then recovered as metastable states under ambient conditions. The large-volume synthesis using both *in situ* and *ex situ* methods under high pressures of 7-13 GPa **[1]** and subsequent characterisation by diverse methods (optical and transport properties) combined with *ab initio* simulations allowed the Si-III (BC8 structure) to be unambiguously established as a semiconductor with a narrow direct band gap of ~30 meV, contrary to previous theories about its semi-metallic properties.

Metals are able to conduct free electrons, while insulators do not conduct electricity. Semiconductors, employed for electronics, can have their conductivity switched on and off, which is a very useful property. This is due to the ability of their electrons to pass from insulating states (valence band) to conductive states with higher energies (conduction band), by absorbing external energy (thermal, photons). The required

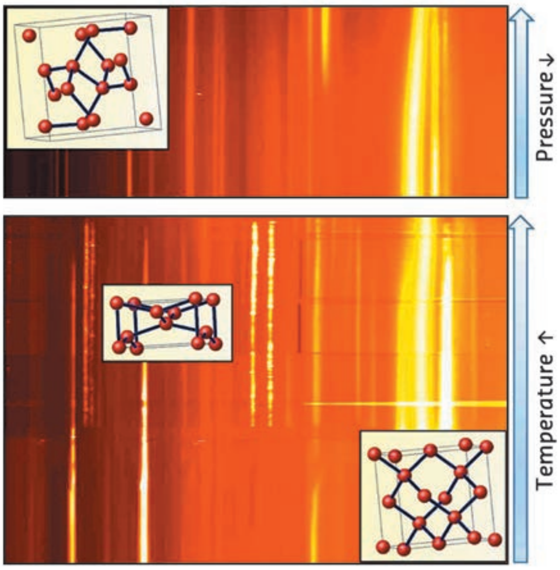

Fig. 32: Metastable silicon allotrope, Si-III, crystallises not only during decompression of the metallic Si-II allotrope with the β-tin structure stable at pressures above 10 GPa (top panel), but also forms during phase transformations as a function of temperature in Na-Si system at remarkably lower pressures, down to 7 GPa (bottom panel).

energy for such transition is called the band gap energy.

Silicon with diamond structure is a semiconductor, while most high-pressure phases are metallic (*e.g.* Si-II with β-Sn structure). On decompression of high-pressure forms, one obtains metastable Si-III rather than stable Si-I (**Figure 32**). The electronic properties of Si-III were controversial until quite recently. Earlier experimental and theoretical results suggested that Si-III is a semi-metal – with a reduced number of free electrons – without any band gap. However, phase-pure samples of sufficient size were not available for characterisation (electrical, thermal, photons).

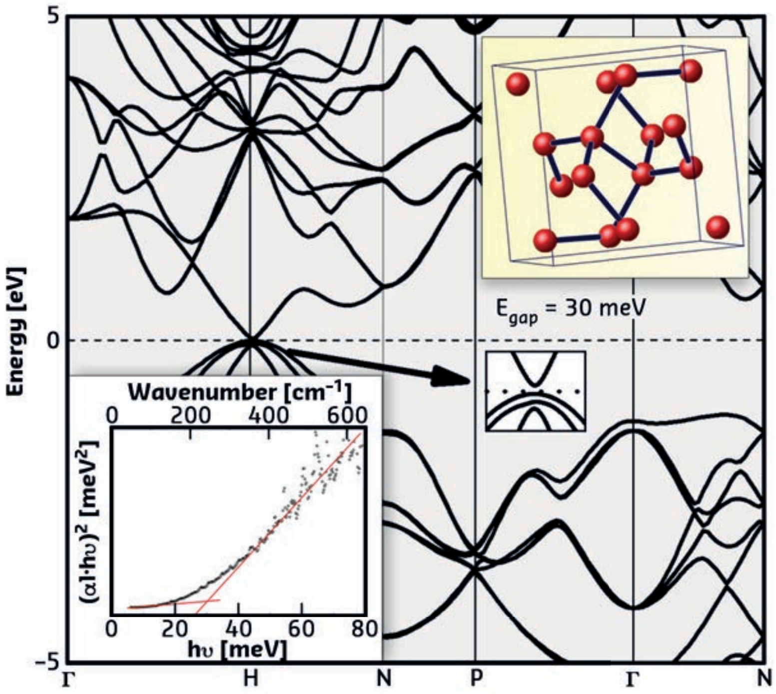

Fig. 33: Electronic structure of Si-III. Insets present the crystalline structure (upper) and the infra-red photon absorption spectra (lower).

The synthesis of pure Si-III using the large-volume press at beamline **ID06** allowed this phase to be established as a semiconductor with an extremely narrow band gap of ~30 meV, 40 times narrower than that of crystals of common Si-I (**Figure 33**). The formation of the free charge carriers (electrons) is possible by thermal activation, just like classical semiconductors. No free electrons have been observed in the 0 K limit (by heat capacity measurements). The opaque sample becomes transparent to far-infrared photons with energies lower than 30 meV (photon transmission measurements). *Ab initio* simulations allowed an accurate description of the band structure using the HSE06 hybrid functional, with levels of exact Hartree-Fock exchange mixing above 25% (an approximation more appropriate for systems with free electrons as compared to classical DFT/GW methods).

These results show that Si-III can be used beyond the traditional applications of Si where narrow gap semiconductors are used, for example, in infrared photonics, as well as the phenomena of tunnelling and confinement where heavy metal compounds are now used.

PRINCIPAL PUBLICATION AND AUTHORS

BC8 Silicon (Si-III) is a narrow-gap semiconductor, H. Zhang (a), H. Liu (a), K. Wei (b), O.O. Kurakevych (c), Y. Le Godec (c), Z. Liu (a), J. Martin (d), M. Guerrette (a), G.S. Nolas (b) and T.A. Strobel (a), *Phys. Rev. Lett.* **118**, 146601 (2017); doi: 10.1103/PhysRevLett.118.146601.

(a) Geophysical Laboratory, Carnegie Institution of Washington, Washington DC (USA)
(b) Department of Physics, University of South Florida, Tampa (USA)
(c) IMPMC, UPMC Sorbonne Universités, UMR CNRS 7590, Muséum National d'Histoire Naturelle, IRD UMR 206, Paris (France)
(d) Material Measurement Laboratory, National Institute of Standards and Technology, Gaithersburg, Maryland (USA)

REFERENCES

[1] O.O. Kurakevych *et al.*, *Inorg. Chem.* **55**, 8943-8950 (2016)

SYNTHESIS OF FeH_5 UNDER PRESSURE: DENSE ATOMIC METAL HYDROGEN STABILISED WITH Fe

FeH_5 was formed above 130 GPa in a laser-heated diamond anvil cell. It exhibits a remarkable layered structure trapping slabs of atomic hydrogen. This discovery of FeH_5 suggests a low-pressure path to make materials that approach bulk dense atomic metal hydrogen.

Pure atomic metal hydrogen is expected to have remarkable properties such as room temperature superconductivity, and other unprecedented quantum many-body properties such as a superfluid-superconductor state. Despite intensive research over the past 40 years, atomic metal hydrogen has yet to be observed unambiguously. Atomic metal hydrogen should be stable above 450 GPa. However, it is still a formidable experimental challenge to reach such a pressure and then to characterise the properties of a sample just a few µm in size.

A decade ago, N. Ashcroft suggested that the high-temperature superconductivity of atomic metal hydrogen should be observed in hydrogen-dominant metallic alloys **[1]**. Due to the chemical pre-compression effect, the attainment of these metallic alloys should be within the usual capabilities of the diamond anvil cell.

This paper has stimulated an intense theoretical structural search. A novel view on the chemical combination of hydrogen with metals under pressure has been unveiled: the solubility of hydrogen in metals drastically increases under high pressure; hydrides of metals go from interstitial complexes to compounds formed with non-traditional H stoichiometries, dubbed super-hydrides. Many of the superconductivity temperatures calculated for these super-hydrides are indeed high, some even approaching ambient temperature.

So far, only a few experimental studies have been devoted to superhydrides. Yet, the richness of this line of research has been recently confirmed by the discovery of superconductivity in hydrogen sulfide at a T_c of 203 K at 150 GPa, explained by the formation of H_3S **[2]**. However, for high hydrogen concentrations, H atoms usually form complex hydrogenic sub-lattices composed of H^-, H_2, H_3^- and cages. It remains unknown whether a super-hydride could exist that is a real analogue of metal hydrogen, *i.e.* that exhibits a dense sub-lattice of hydrogen atoms.

The discovery of FeH_5 is the first observation of such an analogue of atomic metal hydrogen. FeH_5 was synthesised by a direct reaction of Fe and H_2 above 130 GPa (a pressure of ~1.3 million atmospheres) in a diamond anvil cell. This compound consists of intercalated layers of quasi-cubic FeH_3 units and of slabs of atomic hydrogen (see **Figure 35**). The *ab initio* calculations show that no bonding exists between these H atoms. The atomic H slabs interact with the Fe atoms to stabilise dense atomic H at much lower pressure than in pure hydrogen and FeH_5 is a metal within its layers.

The experiments were performed at **ID27** using an online laser-heating set-up. Superhydrides were synthesised by compressing iron in excess hydrogen with laser heating to ease the diffusion of hydrogen into the metal. This permitted the hydride with the highest stoichiometry and stable at a given pressure to be observed. Between 3.5 and 125 GPa, the known interstitial stoichiometric compounds FeH, FeH_2 and FeH_3 were observed **[3]**. Above 130 GPa, laser heating of iron in excess of hydrogen permitted the synthesis of FeH_5 and its equation of state was

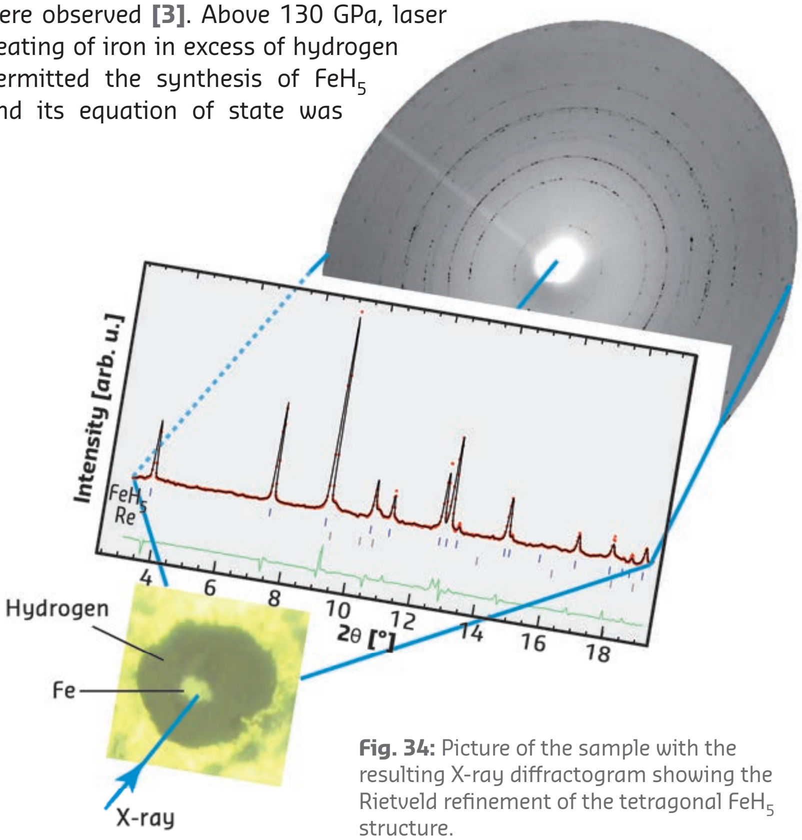

Fig. 34: Picture of the sample with the resulting X-ray diffractogram showing the Rietveld refinement of the tetragonal FeH_5 structure.

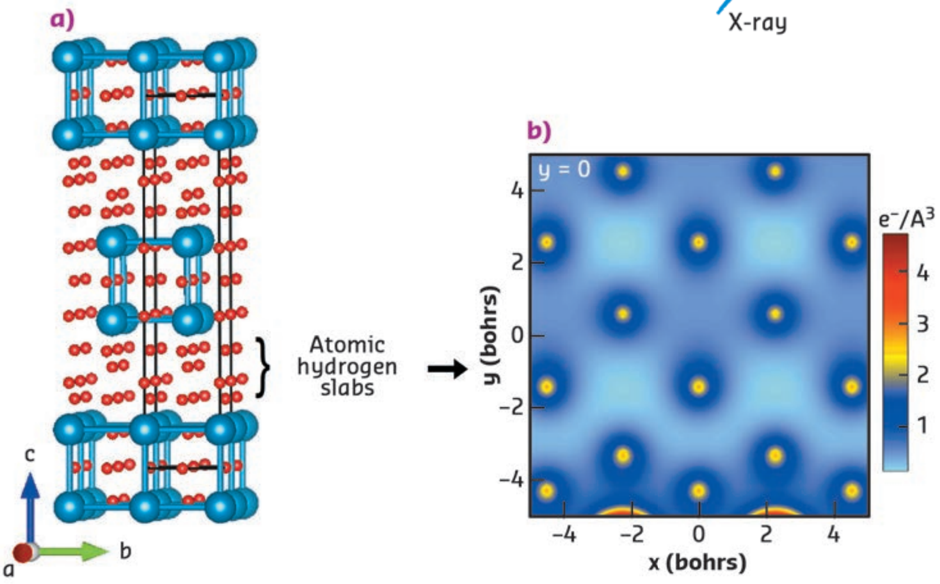

Fig. 35: a) Structure of FeH_5 showing the presence of atomic hydrogen slabs. b) Electron density map along the *c* axis: no bonds between the hydrogen atoms can be found.

measured by decreasing the pressure down to 66 GPa, after which it decomposed back to FeH_3.

Rietveld refinement of the new X-ray pattern yields a tetragonal unit cell with symmetry *I4/mmm* (**Figure 34**). Only the position of the Fe atoms can be inferred from the X-ray diffraction patterns as the low scattering power of the hydrogen atoms prevents the determination of their position. However, using volume comparisons with ideal Fe-H solutions, it is possible to propose that the stoichiometry of the new compound is that of FeH_5. *Ab initio* calculations supported the FeH_5 stoichiometry: all possible tetragonal structures with the determined Fe atom positions were tested. Among the 53 optimised structures, the one presented in **Figure 35** has the lowest enthalpy and exhibits cell parameters in good agreement with the ones measured experimentally.

These results show that the Fe-H system is an archetype of how hydrogen can combine with transition metals under pressure. At moderate pressures, structures consisting of interstitial hydrogen are formed. At higher pressure, slabs of atomic hydrogen can then be stabilised, thus suggesting a path towards bulk dense atomic hydrogen at low pressure. A little bit of Fe could do a lot to help unveil the intriguing properties of atomic metal hydrogen.

PRINCIPAL PUBLICATION AND AUTHORS

Synthesis of FeH_5: a layered structure with atomic hydrogen slabs, C. M. Pépin (a,b), G. Geneste (b), A. Dewaele (b), M. Mezouar (c) and P. Loubeyre (b)
Science **357**, 382-385 (2017);
doi: 10.1126/science.aan0961.

(a) CEA, Arpajon (France)
(b) EPSL, Institute of Condensed Matter Physics, EPFL, Lausanne (Switzerland)
(c) ESRF

REFERENCES

[1] N. W. Ashcroft, *Phys. Rev. Lett.* **92**, 187002 (2004)
[2] A. P. Drozdov *et al., Nature* **525**, 73-76 (2015)
[3] C. M. Pépin *et al., Phys. Rev. Lett.* **113**, 265504 (2014)

INTERLAYER BOND FORMATION IN BLACK PHOSPHORUS AT HIGH PRESSURE

The observation of a two-step mechanism for the A7-to-simple-cubic high-pressure phase transition in phosphorus has unveiled an intermediate pseudo-simple-cubic crystalline structure, raising the pressure limit for 2D *vs.* 3D phosphorus and explaining the long-debated anomalous pressure evolution of its T_c.

Phosphorene is a 2D corrugated monoatomic layer of phosphorus atoms that has recently gained interest from chemists, physicists and materials scientists for its fascinating properties that are related to the layered phases of phosphorus **[1]**. Black phosphorus is the starting material in the synthesis of phosphorene. The relationship between black phosphorus and phosphorene can be likened to that of graphite and graphene. Black phosphorus is one of the many solid structures of phosphorus that exist at ambient pressure and are commonly referred to by their colours (*i.e.* white, red, violet, black). They exhibit extremely diverse chemical and physical properties. Black phosphorus was first synthesised at high pressure by Bridgman in 1914 and its crystalline structure (A17) consists of stacked phosphorene layers.

The synthesis, stabilisation and functionalisation of single-layer phosphorene remain a challenge. Knowledge of the effects that stabilise the layered *vs.* non-layered structures of phosphorus and of the mechanism of interlayer bond formation that take place during the corresponding phase transitions are important for the design and synthesis of phosphorene-based materials and heterostructures.

At room temperature and under high-pressure conditions, the layered structure of black phosphorus (A17, orthorhombic) is stable up to about 5 GPa, where it transforms to rhombohedral A7, another phase with a layered structure stable up to about 11 GPa. Here, according to the literature, a transition to a non-layered simple-cubic (sc) phase occurs. This transition is particularly important because the associated bond reconstruction mechanism sets the stability limit for the layered phases of phosphorus.

Room-temperature compression of black phosphorus was performed at beamline **ID27** using X-ray diffraction to follow the phase changes between A17, A7 and sc phases. A membrane diamond-anvil cell (DAC) with He as the hydrostatic pressure-transmitting medium was used and pressures up to 27.6 GPa were reached. Two previously unreported peaks were observed in the diffraction pattern of the sc structure. These peaks persisted up to the highest investigated pressure and have led to a revision of the phosphorus phase diagram up to 30 GPa. Assuming a rhombohedral cell description ($R\bar{3}m$) for both A7 and sc structures, the two extra peaks are not expected in the diffraction pattern of an sc structure (angle α = 60.0 degree and atomic position u = 0.250), but they naturally emerge when $\alpha \approx 60.0$ degree and atomic position $u < 0.250$. This condition corresponds to a lattice distortion without atomic displacement. Rietveld refinement of the XRD data provided the experimental values of the lattice parameter a, of the angle α, of the atomic position u and of the nearest neighbour distance *nn* at each pressure point across the investigated pressure range. The experimental data, in agreement with theoretical predictions, demonstrate a two-step mechanism for the A7 to sc phase transition.

These observations imply that, in the pressure range from 10.5 up to at least 27.6 GPa, a pseudo-simple-cubic (p-sc) structure exists rather than the sc structure (**Figure 36**). The p-sc structure originates from pressure-dependent competition between a strong *s-p* orbital mixing that prevails at low pressure, which leads to the formation of lone pairs of electrons at phosphorus sites and layers in A17 and A7, and a dominating electrostatic contribution at higher density, which is responsible for the octahedral coordination in sc.

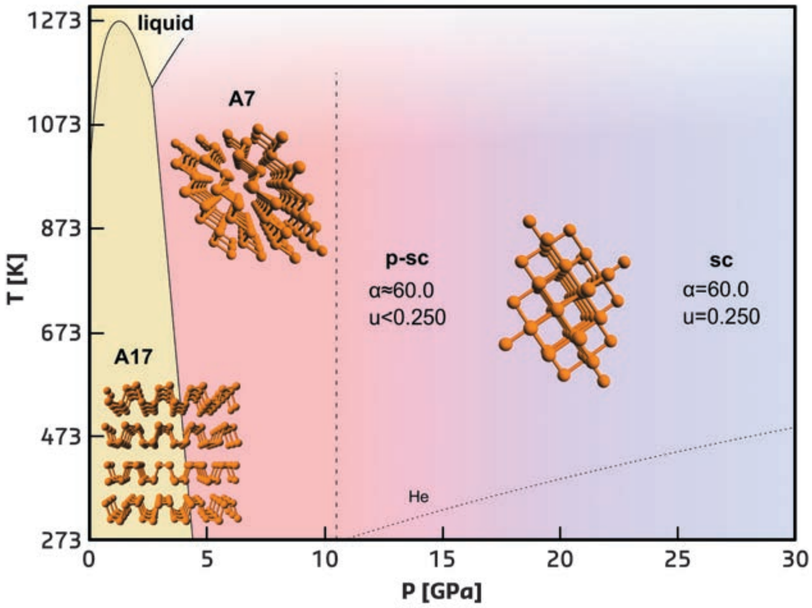

Fig. 36: Phase diagram of phosphorus between 0.0 and 30.0 GPa, showing the pressure and temperature ranges where A17 and A7 are reported to be stable. The dashed line at 10.5 GPa marks the A7-to-sc phase transition according to current literature. The room temperature data indicate that the sc phase is not achieved up to 27.6 GPa and that an intermediate pseudo-simple-cubic (p-sc) structure exists between the A7 and the sc structures. The melting line of He is also displayed (dotted line). Structures generated by the Rietveld refinement of the data in the corresponding phases are also shown, highlighting the transition between the A17 and A7 layered structures and the transformation of layered A7 to non-layered sc.

The existence of the p-sc structure has profound implications. Firstly, from a chemical point view, the presence of three shorter and three longer distances relates p-sc to A7 structurally, which significantly raises the pressure limit where the layered phases of P can exist and opens new perspectives for the synthesis, stabilisation and functionalisation of phosphorene-based systems. Secondly, concerning superconductivity, the identification of the p-sc structure in the 10-30 GPa pressure range provides new experimental evidence to explain the long-debated anomalous pressure evolution of the critical temperature T_c.

PRINCIPAL PUBLICATION AND AUTHORS

Interlayer bond formation in black phosphorus at high pressure, D. Scelta (a,b), A. Baldassarre (b,c), M. Serrano-Ruiz (a), K. Dziubek (b), A.B. Cairns (d), M. Peruzzini (a), R. Bini (a,b,c) and M. Ceppatelli (a,b), *Angew. Chem. Int. Ed.* **56**, 14135-14140 (2017); doi: 10.1002/anie.201708368.

(a) CNR-ICCOM Institute of Chemistry of OrganoMetallic Compounds, National Research Council of Italy, Sesto Fiorentino (Italy)
(b) LENS, European Laboratory for Non-Linear Spectroscopy, Sesto Fiorentino (Italy)
(c) Dipartimento di Chimica "Ugo Schiff", Università degliStudi di Firenze, Sesto Fiorentino (Italy)
(d) ESRF

REFERENCES

[1] M. Batmunkh *et al., Adv. Mater.* **28**, 8586-8617 (2016)

REDOX PROCESSES IN Fe CATALYSTS RESOLVED BY XAS AND UV/Vis SPECTROSCOPY

The iron oxidation state and local structure in a bioinspired non-heme-based catalyst used in C-H and C=C oxidation reactions was studied using energy dispersive XAS and UV/Vis spectroscopy to follow the reactions on a millisecond timescale and identify the intermediate species.

Aerobic life has evolved to depend on the oxidising power of O_2 in various metabolic pathways. Enzymes, such as non-heme iron-dependent oxygenases, catalyse the incorporation of O_2 into a wide range of biological molecules and use diverse strategies to activate their substrates. One way for

C-H activation to occur is by the hydroxylation of the C-H bond. Bioinspired non-heme aminopyridine iron complexes/H_2O_2 catalytic systems replicate the oxidation mechanism of the elaborate non-heme iron oxygenases with simple iron coordination complexes. The key feature of these mechanisms is a controlled O-O bond activation that does not generate free-diffusing radical intermediates (which undermine the oxidation selectivity). This pathway is facilitated by the different oxidation states taken by iron during the catalytic cycle (from Fe^{II} up to Fe^{IV} or Fe^{V}). However, reaction conditions have great influence on the mechanistic pathway and the key intermediates are elusive to conventional spectroscopies.

Fe^{II}(tris(2-pyridylmethyl)amine), $[Fe^{II}(TPA)(CH_3CN)_2]^{2+}$ is a paradigmatic example of such non-heme iron complexes, and here its reaction with different oxidants has been studied with a simultaneous EDXAS-UV/Vis approach at beamline **ID24**. **Figure 37a** shows the evolution of the EDXAS spectra during the course of the reaction of $[Fe^{II}(TPA)(CH_3CN)_2]^{2+}$ (35 mM) with H_2O_2 (70 mM) at 25°C. The XANES spectra show both a rapid shift in the Fe K-edge position within the first 104 ms and a modification of the structural oscillations, in accordance with an initial oxidation of Fe^{II} to Fe^{III} followed by a clear rearrangement of the local structure around the metal centre, without further changes in the iron oxidation state. **Figure 37b** shows the absorbance evolution at λ = 524 nm recorded simultaneously. The increase in absorbance at this wavelength is consistent with the formation of the $[Fe^{III}(TPA)(CH_3CN)(OOH)]^{2+}$ species (λ_{max} = 538 nm). The subsequent absorbance decrease occurring between 104 and 704 ms illustrates the evolution of this intermediate to the μ-oxo dimer $[Fe^{III}_2(TPA)_2(\mu\text{-}O\ (H_2O)_2]^{4+}$ as depicted in **Figure 37d**. The XANES spectra collected at t = 0, 104, and 1984 ms are shown in **Figure 37c**. The EDXAS analysis confirms the observations made with UV/Vis and the experimental body of evidence indicates the reaction mechanism depicted in **Figure 37d**.

A second reaction of $[Fe^{II}(TPA)(CH_3CN)_2]^{2+}$ (35 mM) and CH_3COO_2H (35 mM) as the oxidant was carried out in CH_3CN/CH_3COOH 99.6:0.4 (v/v) at 25°C. **Figure 38a** shows the XANES spectra collected every 40 ms. The Fe K-edge position of the spectrum recorded after 24 ms is found to be shifted towards higher energy with respect to the

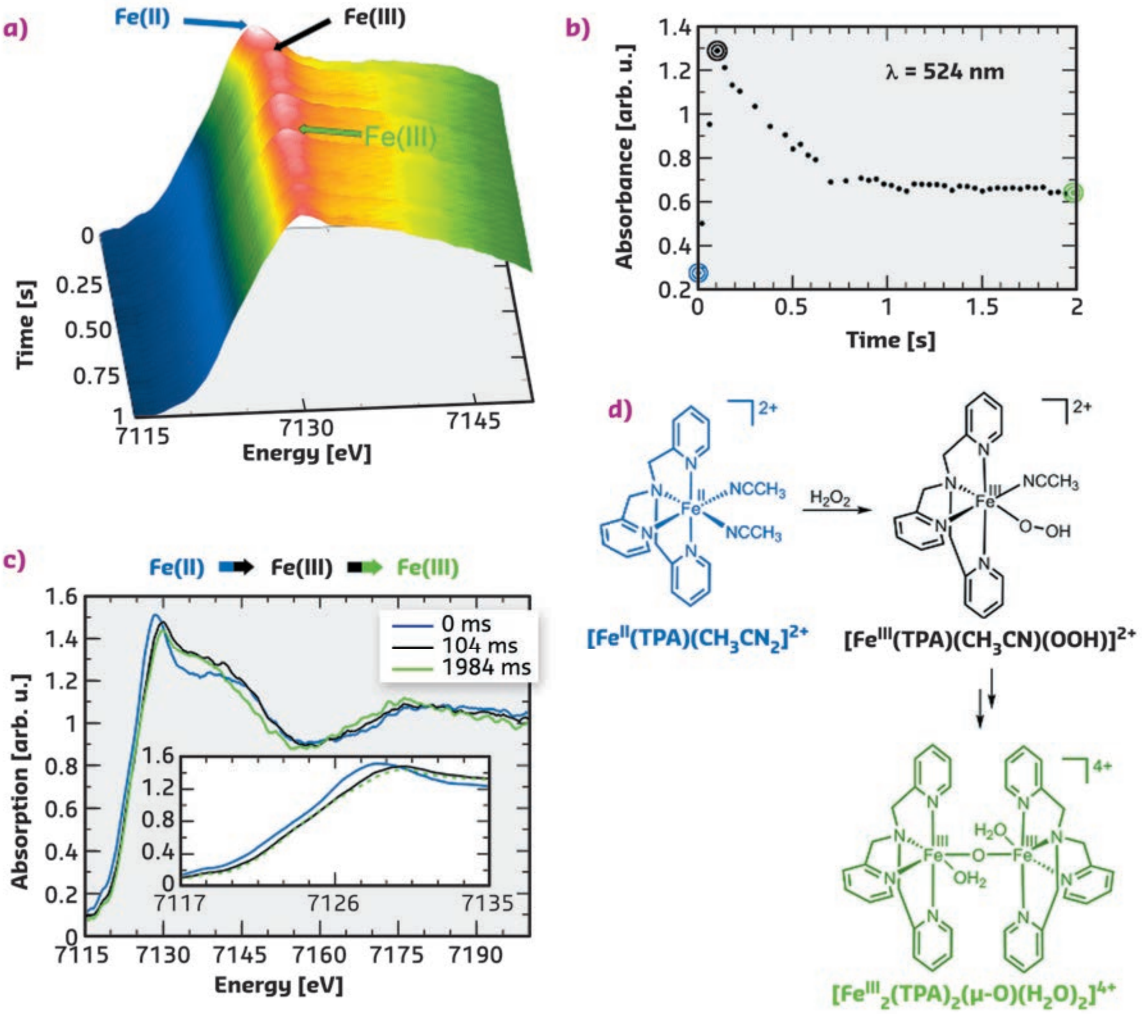

Fig. 37: a) Time evolution of the Fe K-edge EDXAS spectra of $[Fe^{II}(TPA)(CH_3CN)_2]^{2+}$ (35 mM) after addition of H_2O_2 (70 mM) in CH_3CN/H_2O 99.8:0.2 (v/v) at 25°C. b) Time evolution of the absorbance at λ = 524 nm of the same reaction mixture. c) Selected EDXAS spectra including an enlargement of the Fe K-edge region. d) Sequence of iron species compatible with the EDXAS-UV/Vis spectral evolution.

initial $[Fe^{II}(TPA)(CH_3CN)_2]^{2+}$ spectrum as evident from the selected XANES spectra reported in **Figure 38c** (compare the black and blue traces in the inset). Within the following 264 ms, the edge position is further shifted to higher energy, and then it moves back to lower energy during the subsequent 1700 ms. The time evolution of the Fe K-edge position is clearly visible in **Figure 38c**, where the XANES spectra collected at t = 0, 24, 264 and 1964 ms are reported. There is an edge shift of 0.7 eV in going from the $[Fe^{II}(TPA)(CH_3CN)_2]^{2+}$ to $[Fe^{III}(TPA\ (\kappa_2\text{-}OOAc)]^{2+}$ species and a further shift of 0.7 eV when the $[Fe^{IV}(TPA)(O)]^{2+}$ species is formed. The absorbance at 722 nm has been monitored simultaneously and its time evolution is shown in **Figure 38b**. This wavelength was chosen since the $[Fe^{IV}(TPA\ (O)]^{2+}$ complex has a characteristic pale green chromophore at λ_{max} = 720 nm, while none of its monomeric precursors show absorption in this region. A significant increase in the absorbance is evident in the first phase of the reaction (0-264 ms), while a slight decrease is observed starting from 264 ms. The observed experimental evidence strictly reproduces the mechanistic sequence of events depicted in **Figure 38d**.

The combination of energy-dispersive XAS and UV/Vis spectroscopy allowed a direct analysis of the evolution of both the oxidation states and the local structures of the Fe complexes studied here. This combined approach is a powerful tool for the characterisation of chemical reaction intermediates and will provide unique insights into reaction mechanisms involving transition metals.

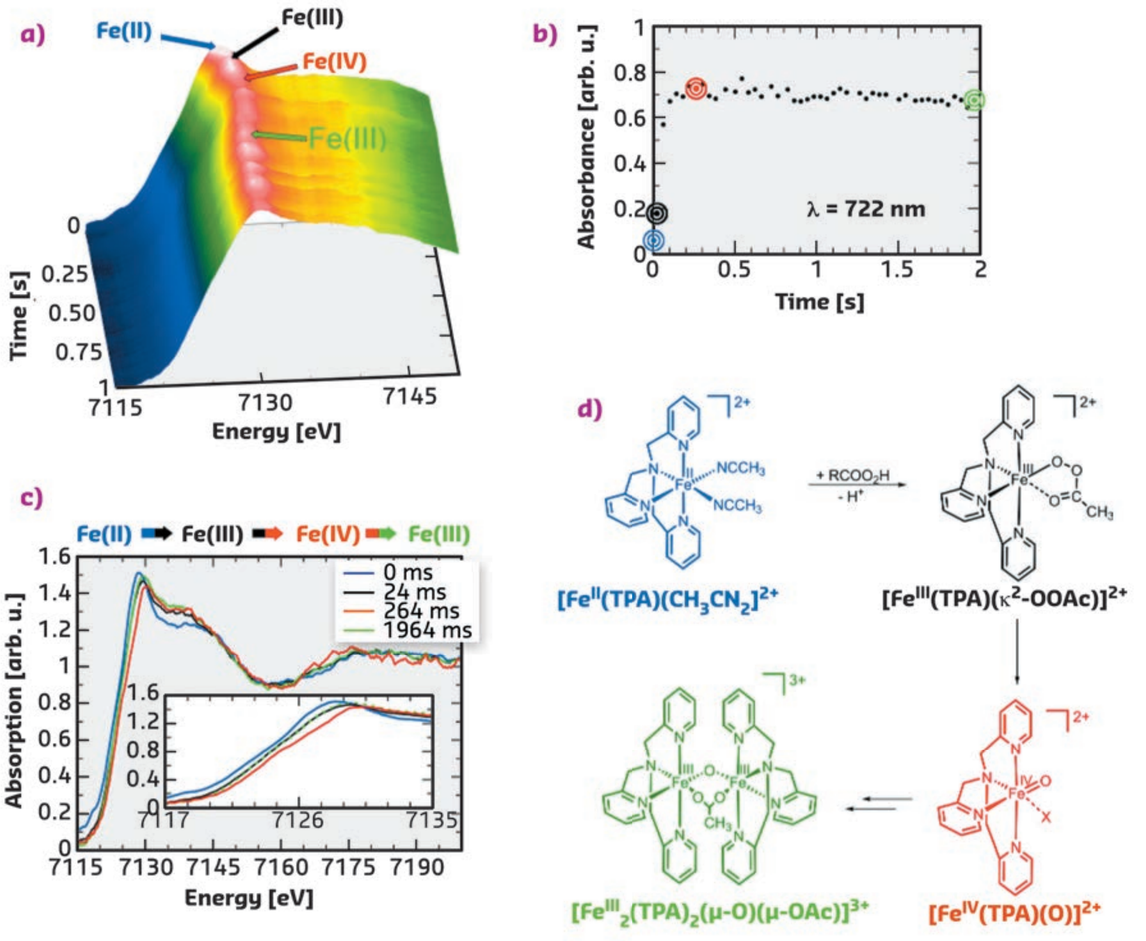

Fig. 38: a) Time evolution of the Fe K-edge EDXAS spectra of $[Fe^{II}(TPA)(CH_3CN)_2]^{2+}$ (35 mM) after addition of CH_3COO_2H (35 mM) in CH_3CN/CH_3COOH 99.6:0.4 (v/v) at 25°C. b) Time evolution of the absorbance at λ = 722 nm. c) Selected EDXAS including an enlargement of the Fe K-edge region. d) Sequence of iron species compatible with the EDXAS-UV/Vis spectral evolution (X = OAc, CH_3CN).

PRINCIPAL PUBLICATION AND AUTHORS

Following a chemical reaction on the millisecond time scale by simultaneous X-ray and UV/Vis spectroscopy, G. Olivo (a), A. Barbieri (a), V. Dantignana (a), F. Sessa (a), V. Migliorati (a), M. Monte (b), S. Pascarelli (b), T. Narayanan (b), O. Lanzalunga (a), S. Di Stefano (a) and P. D'Angelo (a), *J. Phys. Chem. Lett.* **8**, 2958-2963 (2017); doi: 10.1021/acs.jpclett.7b01133.

(a) Department of Chemistry, University "La Sapienza", Rome (Italy)
(b) ESRF

REDOX-ACTIVE MOF FOR REVERSIBLE CAPTURE AND RELEASE OF HALOGENS

Chlorine and bromine are highly toxic and corrosive. A new material that could make their storage safer has been characterised by X-ray absorption spectroscopy. This material is the first metal-organic framework able to reversibly capture and release halogens.

The extreme toxicity, corrosiveness, and volatility of chlorine and bromine pose serious challenges for the safe storage and transportation of these halogens, which play a key role in the chemical industry. Solid materials capable of forming stable non-volatile compounds upon reaction with elemental halogens may partially mitigate these issues by allowing safe halogen release on demand. In this work, elemental halogens are demonstrated to quantitatively oxidise coordinatively-unsaturated Co^{II} ions in a robust azolate metal-organic framework (MOF), Co_2Cl_2BTDD **(1)** (BTDD = bis(1H-1,2,3-triazolo[4,5-b],[4,5-i]) dibenzo[1,4]dioxin), to produce stable and safe-to-handle Co^{III} materials, namely Co_2Cl_4BTDD **(2)** and $Co_2Cl_2Br_2BTDD$ **(3)**, featuring terminal Co^{III}–halogen bonds.

The parent material **(1)** was prepared according to a previously described method **[1]**. Its crystal structure was confirmed by neutron powder diffraction (NPD), revealing infinite $-(Co-Cl)_n-$ chains coiled into threefold spirals and interconnected by the bis(triazolate) linkers, resulting in a honeycomb-like structure with one-dimensional channels (**Figure 39a**). Reaction with gaseous Cl_2 or Br_2 led to rapid oxidation of Co centres of the material from Co^{II} to Co^{III} due to the coordination of chloride or bromide ligands, resulting in the formation of **(2)** or **(3)** respectively (**Figure 39 b-d**). Consequent structural changes had noticeable but rather small effects on the X-ray diffraction pattern, since the long-range order of the material was not significantly perturbed. However, the short-range local environment of Co centres was considerably altered, which made the element-selective X-ray absorption spectroscopy (XAS) measurements, performed at beamline **BM23**, very informative. First, *ex situ* XANES spectra of the parent material **(1)** and its oxidised counterpart **(2)** exhibited a pronounced chemical shift of the Co K-edge, unambiguously confirming the 2^+ and 3^+ oxidation state of Co centres before and after treatment, respectively (**Figure 40a**). EXAFS data indicated a higher coordination number for the Co-Cl shell in **(2)**, which is direct evidence that Co centres gain one Cl extra-ligand in addition to the two Cl neighbours that are part of the framework (**Figure 40 b,c**).

The reversibility of the Cl_2 adsorption process was demonstrated by *in situ* XAS measurements performed upon heating **(2)** to 290°C (**Figure 40 a-c**). EXAFS data show a gradual decrease of the coordination number for the Co-Cl shell, while XANES spectra evidence reduction of Co centres. Importantly, both EXAFS and XANES spectra of **(2)** at the final stage of thermal treatment are very close to those of the parent material **(1)**, proving the reversibility of Cl_2 uptake on the local scale. Cl_2 release was quantified by linear combination analysis of the *in situ* XANES spectra, using the spectra of **(1)** and **(2)** at room temperature as references. It indicated almost complete conversion of Co^{III} sites back to Co^{II}, but the elevated R-factor at the final stages of treatment suggested the formation of a minor fraction of unreacted Co in a slightly distorted environment. Based on experimental evidence and subsequent DFT calculations, a probabilistic model of Cl

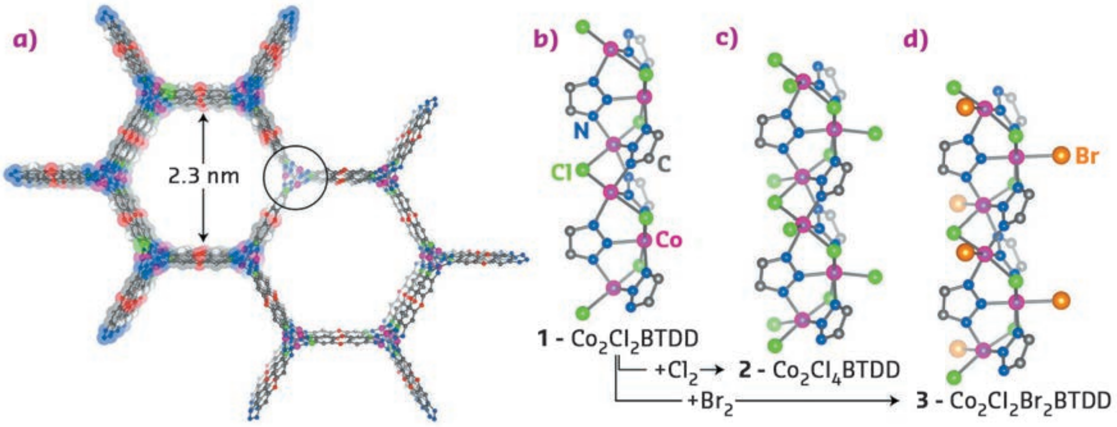

Fig. 39: Structural data. a) A portion of the structure of the parent Co^{II} MOF Co_2Cl_2BTDD **(1)** projected along the c axis. b–d) Secondary building unit (SBU) structures and local coordination environments of the Co centres in **(1)**, **(2)** and **(3)**, respectively, as determined by NPD.

release by **(2)** was constructed. With the only initial criterion being pairwise vicinal removal of halogens, this model predicts a residual Co^{III}–Cl content of 13.5%, corresponding to halogen release of 86.5% of the theoretical maximum.

These results demonstrate the ability of a Co^{II} azolate MOF to uptake and release elemental halogens reversibly, and pave the way to the design of other porous materials geared toward the capture and storage of toxic, corrosive gases through reversible chemisorptive mechanisms.

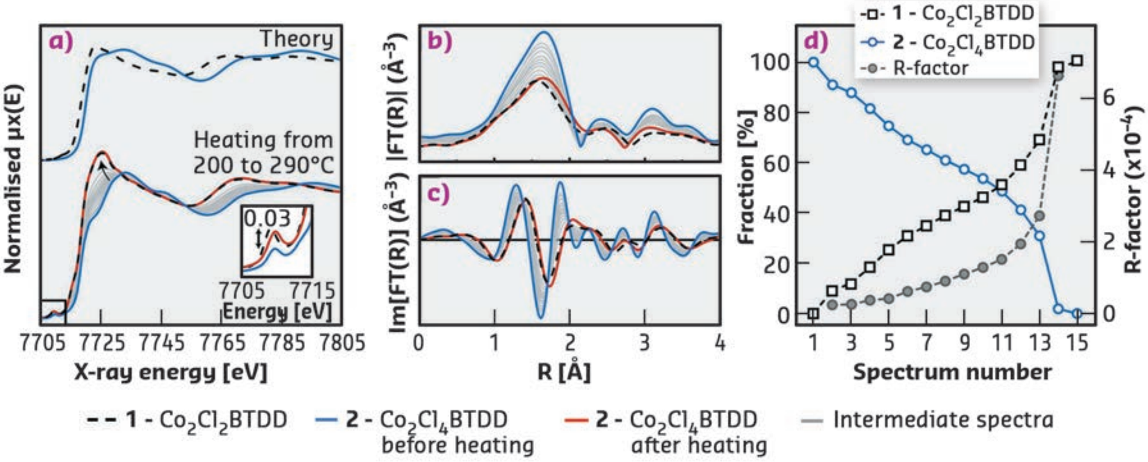

Fig. 40: Co K-edge XAS characterisation of **(1)** and **(2)**. a) (top) Theoretical XANES spectra for **(1)** and **(2)** calculated from the NPD structures using the FDMNES code **[2]**. (bottom) Experimental XANES spectra at room temperature for **(1)**, **(2)**, **(2)** after heating, and intermediate states collected *in situ* in the 200-290°C range during the thermal treatment of **(2)**. b) Magnitudes and c) imaginary parts of the phase-uncorrected Fourier transformed k^2-weighted EXAFS spectra. d) Linear combination analysis of the whole series of *in situ* XANES spectra using the spectra of **(1)** and **(2)** at room temperature as references: relative fraction (open symbols) and fit quality factor (solid symbols).

PRINCIPAL PUBLICATION AND AUTHORS

Reversible capture and release of Cl_2 and Br_2 with a redox-active metal-organic framework, Y. Tulchinsky (a), C.H. Hendon (a), K.A. Lomachenko (b,c), E. Borfecchia (d), B.C. Melot (e), M.R. Hudson (f), J.D. Tarver (f,g), M.D. Korzyński (a), A.W. Stubbs (a), J.J. Kagan (h), C. Lamberti (c,d), C.M. Brown (f) and M. Dincă (a), *J. Am. Chem. Soc.* **139**, 5992-5997 (2017); doi: 10.1021/jacs.7b02161.

(a) Department of Chemistry, Massachusetts Institute of Technology, Cambridge (USA)
(b) ESRF
(c) IRC "Smart Materials", Southern Federal University, Rostov-on-Don (Russia)
(d) Department of Chemistry, NIS, CrisDi, and INSTM Centre of Reference, University of Turin (Italy)
(e) Department of Chemistry, University of Southern California, Los Angeles (USA)
(f) Center for Neutron Research, National Institute of Standards and Technology, Gaithersburg (USA)
(g) National Renewable Energy Laboratory, Golden (USA)
(h) Department of Mathematics, Weizmann Institute of Science, Rehovot (Israel)

REFERENCES

[1] A.J. Rieth *et al.*, *J. Am. Chem. Soc.* **138**, 9401-9404 (2016)
[2] S.A. Guda *et al.*, *J. Chem. Theory Comput.* **11**, 4512-4521 (2015)

XAS REVEALS STRUCTURE-ACTIVITY RELATIONSHIPS FOR THE METHANE-TO-METHANOL CONVERSION OVER Cu-ZEOLITES

Methane-to-methanol (MTM) conversion in mild conditions represents a 'dream reaction', with an enormous impact on the energy sector and the chemical industry. Combining activity measurements with *in situ/operando* XAS, structure-activity relationships were established for the MTM process over Cu-SSZ-13 zeolites, shedding light on the nature of Cu-active sites.

A less energy-intensive process allowing methane-to-methanol (MTM) conversion would represent a major breakthrough for chemical industry, with profound energetic and environmental implications. Although nature does the work masterfully with Cu enzymes **[1]**, an industrially viable process for this conversion remains an ongoing challenge. In recent years, Cu-exchanged zeolites have been shown to possess Cu-active sites able to cleave the C–H bond of methane at temperatures ≤ 200°C, enabling its stoichiometric transformation into methanol **[2]**. The conversion is obtained through a stepwise process (**Figure 41a**), starting with a

Fig. 41: a) The stepwise process for the MTM conversion over Cu-SSZ-13 zeolite, characterised by double 6-member (6r) and 8-member (8r) rings. b) *Operando* XANES and FT-EXAFS spectra collected at the BM26A beamline after each process step on a highly productive Cu-SSZ-13 sample.

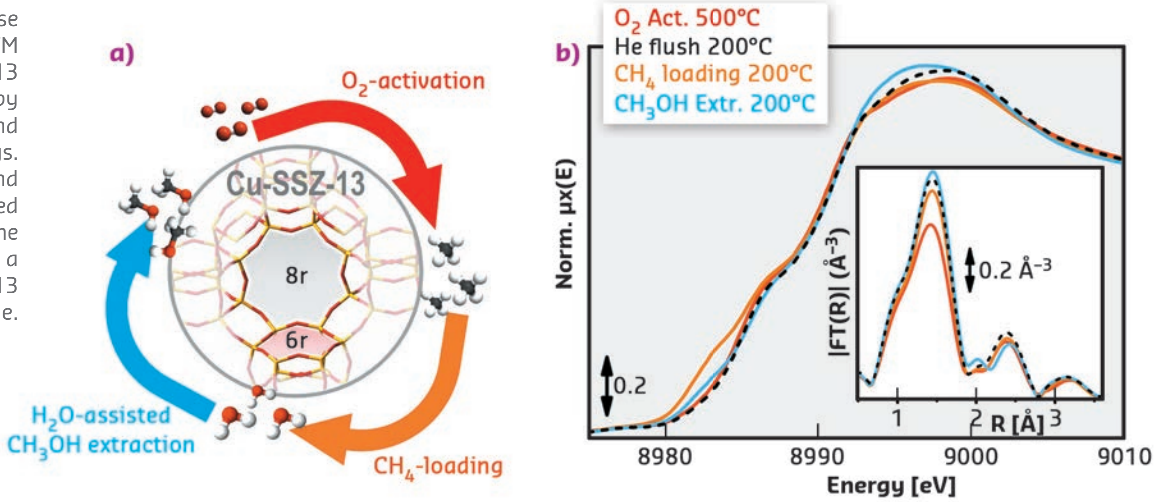

high-temperature activation in O_2 to generate the active sites. Afterwards, methane is loaded over the material at 200°C and methanol is subsequently extracted by passing steam through the reactor hydrolysing the stabilised methyl intermediates.

Laboratory activity measurements were combined with *in situ/operando* X-ray absorption spectroscopy (XAS) at beamlines **BM23** and **BM26A** to explore the MTM conversion over Cu-SSZ-13 for a wide range of materials and reaction conditions, aiming at establishing structure-activity relationships. The oxidation state and average coordination of the Cu ions in the material were tracked by *operando* XAS during each step of the process (**Figure 41b**). XAS reveals tri-coordinated framework-interacting Cu^{II} centres as the dominant species in the O_2-activated state at 500°C, while cooling to 200°C promotes an increase in the average first-shell Cu coordination number. During methane loading, XANES linear combination fit indicates the Cu^{II} to Cu^{I} reduction in 27% of the Cu sites. About half of these Cu^{I} sites (13% total Cu) undergoes re-oxidation during H_2O-assisted methanol extraction, together with the formation of 27% of mobile Cu^{II} aquo complexes.

To obtain deeper insights in the nature of the active sites, the impact of different pre-

Fig. 42: *In situ* XANES collected on the BM23 beamline for: a) Cu-SSZ-13 with Cu/Al = 0.5, Si/Al = 12 after different pre-treatments (inset: correspondent normalised CH_3OH productivities); b) He-activated Cu-SSZ-13 with Cu/Al = 0.5 and Si/Al ratio of 5, 15 and 29 (inset: linear correlation between the normalised productivity and the fraction of Cu^{I} species in the He-activated state. c) Rationalisation of the effect of composition on the productivity for the MTM conversion over Cu-SSZ-13.

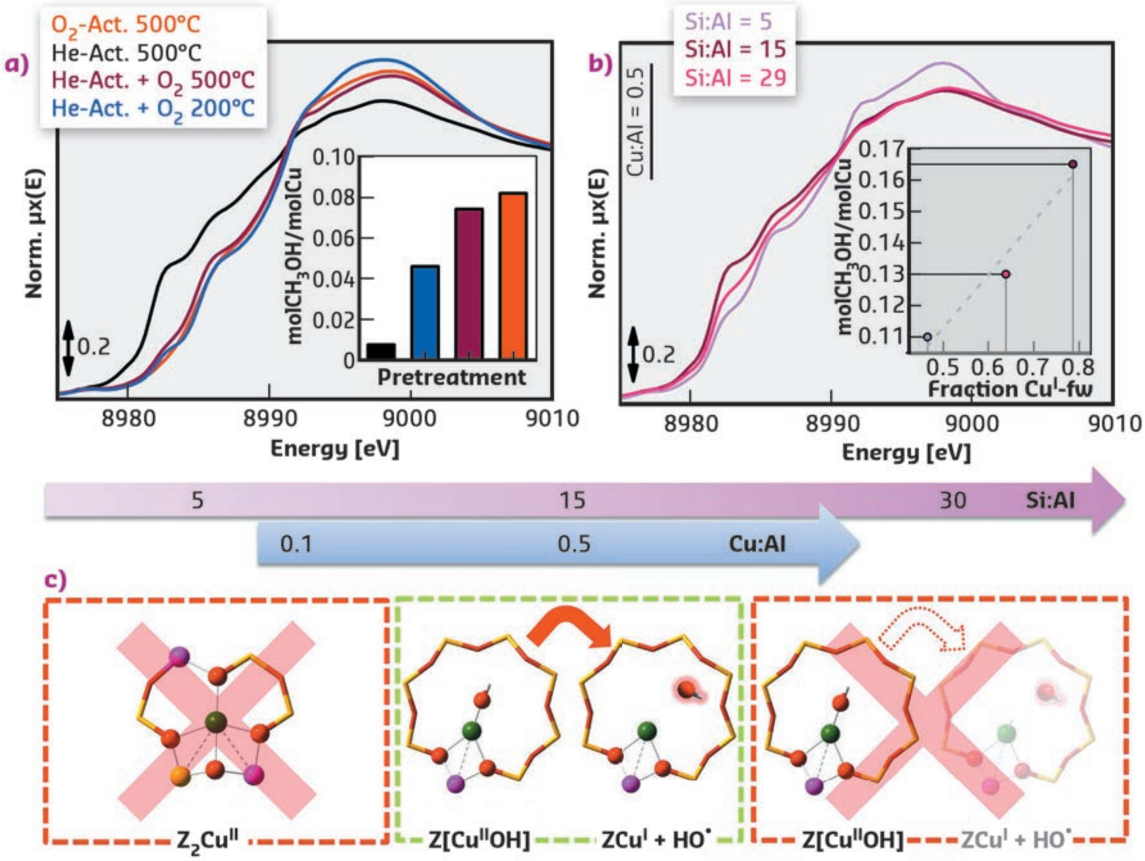

treatments was explored by coupling *in situ* XAS with activity measurements (**Figure 42a**). High-temperature reaction with O_2 is evidenced as a key requirement to form the methane-converting active sites. A positive linear correlation was also confirmed between the methanol productivity and the reducibility of the Cu centres under high-temperature treatment in He (**Figure 42b**). Here, for an accurate determination of Cu-speciation, previous results from multivariate analysis of a large composition-dependent XANES dataset were employed, also collected on **BM23** [3].

As depicted in **Figure 42c**, high populations of bare Cu^{II} sites charge-balanced by two proximal Al, favoured at low Si/Al ratios, inhibit the performance of the material by being inactive for the conversion. $[Cu^{II}OH]^+$ complexes are instead identified as the precursors to the active sites, through their ability to self-reduce, which is optimal at intermediate Si/Al ratios. As also supported by FTIR and Raman spectroscopy, $[Cu^{II}OH]^+$ species progressively deplete during high-temperature oxidative treatment, evolving towards different mono- and multimeric O_2-derived Cu^{II} moieties, among which the active sites should be researched. These results mark an important step towards an improved understanding of reactive routes in Cu-zeolites, that will lead to rationalised material synthesis and potentially to an industrially feasible MTM process.

PRINCIPAL PUBLICATION AND AUTHORS

D. K. Pappas (a), E. Borfecchia (b, c), M. Dyballa (a), I. A. Pankin (c, d), K. A. Lomachenko (d, e), A. Martini (a), M. Signorile (a), S. Teketel (b), B. Arstad (f), G. Berlier (a), C. Lamberti (c, d), S. Bordiga (a, c), U. Olsbye (a), K. P. Lillerud (a), S. Svelle (a) and P. Beato (b), Methane to methanol: structure-activity relationships for Cu-CHA, *J. Am. Chem. Soc.* **139**, 14961-14975 (2017); doi: 10.1021/jacs.7b06472.

(a) Center for Materials Science and Nanotechnology (SMN), Department of Chemistry, University of Oslo (Norway)
(b) Haldor Topsøe A/S, Kgs. Lyngby (Denmark)
(c) Department of Chemistry, NIS Centre and INSTM Reference Center, University of Turin (Italy)
(d) International Research Center "Smart Materials", Southern Federal University, Rostov-on-Don (Russia).
(e) ESRF
(f) SINTEF Materials and Chemistry, Oslo (Norway)

REFERENCES

[1] R. L. Lieberman, A. C. Rosenzweig, *Nature* **434**, 177-182 (2005)
[2] P. Tomkins *et al., Angew. Chem. Int. Ed.* **55**, 5467-5471 (2016)
[3] A. Martini *et al., Chem. Sci.* **8**, 6836-6851 (2017)

LOCALISATION AND SPECIATION OF IMPURITIES IN DEACTIVATED PETROCHEMICAL HETEROGENEOUS CATALYSTS

Fluid catalytic cracking (FCC) catalysts are key to the production of petrol from crude oil. Here, the iron species in deactivated catalysts were characterised using energy-dispersive XAS tomography.

Fluid catalytic cracking is a century-old chemical conversion process that to this day provides the majority of the world's petrol. It employs porous composites of zeolite and clay as catalyst. Owing to the harsh reaction environments and feedstock impurities, the catalysts deactivate over time. This deactivation necessitates their continuous fractional replacement with major refineries requiring up to 50 tons of fresh catalyst per day.

Using a recently developed variant of energy-dispersive X-ray absorption spectroscopy at beamline **ID24** [1], the distribution and speciation of feedstock-introduced iron impurities have been visualised in a deactivated fluid catalytic cracking catalyst. Applied to the Fe K-edge, two populations of iron impurities, with specific localisation, were identified. While ferrous iron is found in isolated areas of increased porosity, suggestive of iron particulates, ferric iron is found dominantly on the particle exterior. The latter impurities are preferentially located in the outer dense part of the particle, and suggested to contribute to the formation of an isolating amorphous silica alumina (ASA) envelope that reduces the flux to the active sites in the catalyst interior, **Figure 43**.

Considering the operational temperature range and measured impurity speciation in this outer envelope, this suggests that feedstock-introduced iron impurities contribute to the amorphisation of zeolites close to the particle exterior. Such amorphisation could lead to the formation of the apparently non-permeable ASA envelope. Both factors could contribute to the deactivation of the catalyst particle by reducing the overall number of active sites and the ease of access

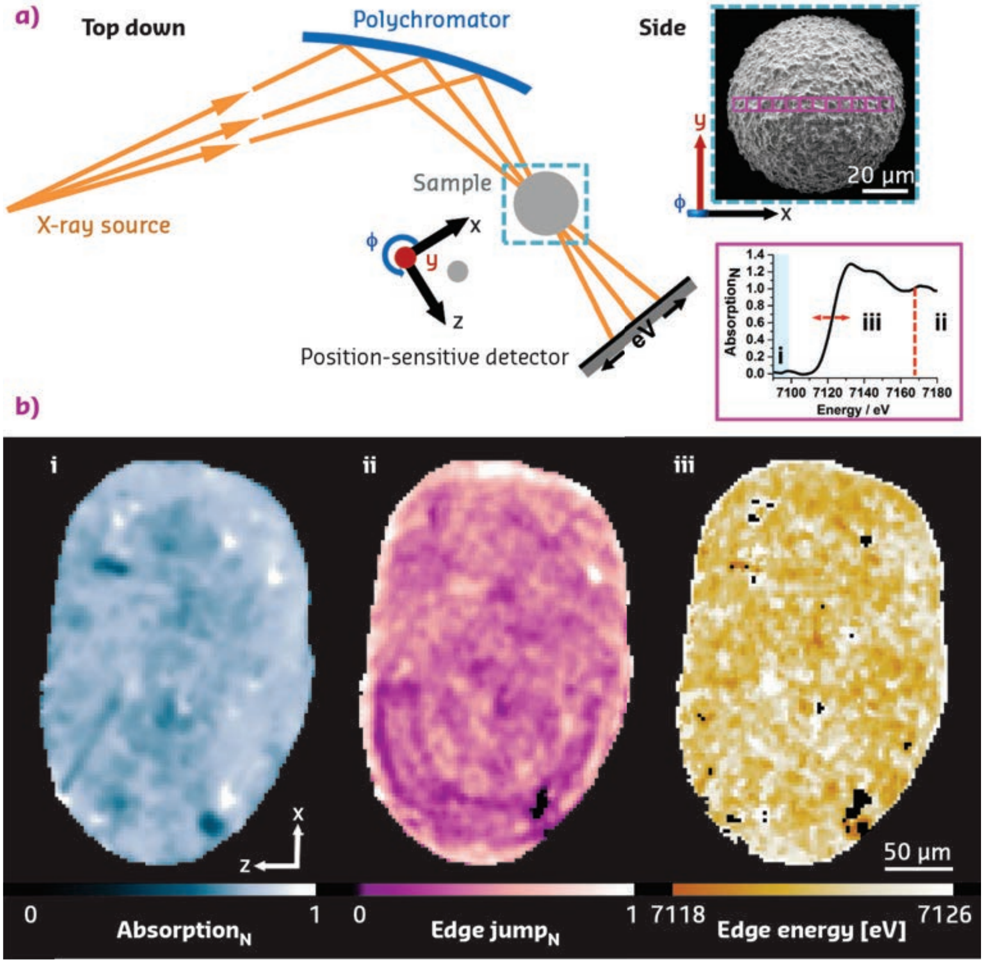

Fig. 43: Scanning energy-dispersive tomographic X-ray absorption spectroscopy of a deactivated fluid catalytic cracking (FCC) catalyst. a) Schematic of the experimental setup. Using a polychromatic fan and a position sensitive detector, a set of tomographic projections (φ) were collected. Each consisted of a line scan, step size 2 μm, central to the particle. The electron micrograph shown in the inset is representative of a typical FCC particle (probed regions indicated). Analysis of the acquired projections as a function of position and rotation allowed the construction of one sinogram per energy that can be used to reconstruct a spectro-tomographic volume in which each voxel contains a full Fe-K edge XANES spectrum (7080-7180 eV, in the present case). b) Orthoslices, slices central to the particle, each highlighting selected features in the XAS data, namely (i) absorption below the edge, indicative of density of the material, (ii) edge jump magnitude normalised with respect to the presented field of view, showing the local iron concentration, and (iii) Fe K-edge energy, revealing the iron speciation.

of the remaining active sites. Based on these observations, new conditions for catalyst regeneration and redesign are currently being explored.

The energy-dispersive tomographic absorption spectroscopy variant, currently unique to **ID24**, sets itself apart from existing XAS tomography techniques because a full XANES spectrum with an energy range of several hundred eV can be acquired in a single measurement. The method is less sensitive to temporal beam and sample instabilities compared to energy-scanning variants. Furthermore, given that a continuous XANES spectrum per voxel is retrieved, with sub-eV resolution, this method is perfectly suitable for the examination of unknown/unexpected chemical species, *i.e.* non-reliant on tabulated elemental standards. In summary, the energy-dispersive tomographic XAS variant used in this research is an attractive alternative to existing techniques for the examination of extended specimens of unknown elemental speciation with potential applications in heterogeneous catalysis, energy materials, planetary and cultural heritage research.

PRINCIPAL PUBLICATION AND AUTHORS

Localization and speciation of iron impurities within a fluid catalytic cracking catalyst, J. Ihli (a), D. Ferreira Sanchez (a), R.R. Jacob (a), V. Cuartero (b), O. Mathon (b), F. Krumeich (c), C. Borca (a), T. Huthwelker (a), W.-C. Cheng (d), Y.-Y. Shu (d), S. Pascarelli (b), D. Grolimund (a), A. Menzel (a) and J.A. van Bokhoven (a,c), *Angew. Chem. Int. Ed.* **56**, 14031-14035 (2017); doi: 10.1002/anie.201707154.

(a) Paul Scherrer Institut, Villigen (Switzerland)
(b) ESRF
(c) ETHzürich, Institute for Chemical and Bioengineering, Zurich (Switzerland)
(d) W.R. Grace, Refining Technologies, Columbia (USA)

REFERENCES

[1] D. Sanchez Ferreira *et al., Sci. Reports* **7**, 16453 (2017)

CARBON'S DESCENT INTO THE EARTH'S CORE

The presence of carbonates in the Earth's mantle is known from diamond inclusions but how carbon arrived there remains a mystery. Two new iron carbonate compounds have been synthesised and show that self-oxidation-reduction reactions could preserve carbonates in the mantle, hence becoming a potential carbon-carrier down to the Earth's core.

In the last century, the rapid increase in the amount of CO_2 in the atmosphere, together with the observed climate change, have increasingly focused scientists' attention on the carbon cycle and its evolution at the Earth's surface. The carbon cycle also extends below the surface: recent estimations locate up to 90% of the Earth's carbon budget in the Earth's mantle and core **[1]**. Due to the dynamic nature of convection and subduction, there is a constant recycling of carbon between the Earth's surface and its deep interior. Subduction is considered the only mechanism capable of carrying a significant amount of carbon into the deep Earth.

This study focuses on carbonate phases, which are the main carbon-bearing minerals in subducting slabs and, in particular, on the stability of Fe-carbonates such as $FeCO_3$ (siderite). Indeed, a previous experimental investigation on $MgCO_3$ has revealed its stability at pressures (P) and temperatures (T) down to those of the core mantle boundary (CMB) **[2]**. Motivated by the extensive solid solutions formed between $MgCO_3$ and $FeCO_3$ at ambient conditions, and the spin transition of Fe atoms at high pressures, which might influence the stability of the phase itself, high-pressure high-temperature experiments were performed on $FeCO_3$ to study its stability and determine its decomposition or transformation products at the relative P and T conditions.

Experiments were performed using synthetic $FeCO_3$ single crystals, at P and T conditions covering the entire Earth's mantle, *i.e.* reaching above 110 GPa and 2500 K, respectively. High pressures and high temperatures were achieved by means of diamond anvil cells (DACs) and by double side laser heating. $FeCO_3$ characterisation and of its derivatives required the use of microfocusing X-ray optics due to the small dimensions of the single crystals (10 μm^2). Hence, experiments were performed at the microfocus X-ray single crystal diffraction (XRSD) beamlines **ID09A** (now **ID15B**) and **ID27** as well as by the synchrotron Mössbauer source (SMS) at **ID18**. One experimental run was carried out at APS.

The results show that upon heating $FeCO_3$ to Earth geotherm temperatures at pressures up to about 50 GPa, $FeCO_3$ partially dissociates, forming different iron oxides (**Figure 44**). In particular, below and above ~25 GPa, dissociation leads to the formation of α-Fe_2O_3 (hematite) and HP-Fe_3O_4 (HP-magnetite). As reported by previous authors, α-Fe_2O_3 and HP-Fe_3O_4 form as a result of redox dissociation of liquid-$FeCO_3$ leading to dissolved Fe_3^+ and CO_2 in the carbonate melt. At pressures above ~75 GPa, two new compounds were synthesised and their structures solved – tetrairon (III) orthocarbonate; $Fe_4^{3+}C_3O_{12}$, and diiron (II) diiron (III) tetracarbonate; $Fe_2^{2+}Fe_2^{3+}C_4O_{13}$ (**Figure 45**). Both materials contain CO_4 tetrahedra and the first is characterised by a unique structure, thus indicating that high pressure carbonates may not be similar to any other compounds (including silicates). Based on a number of different datasets,

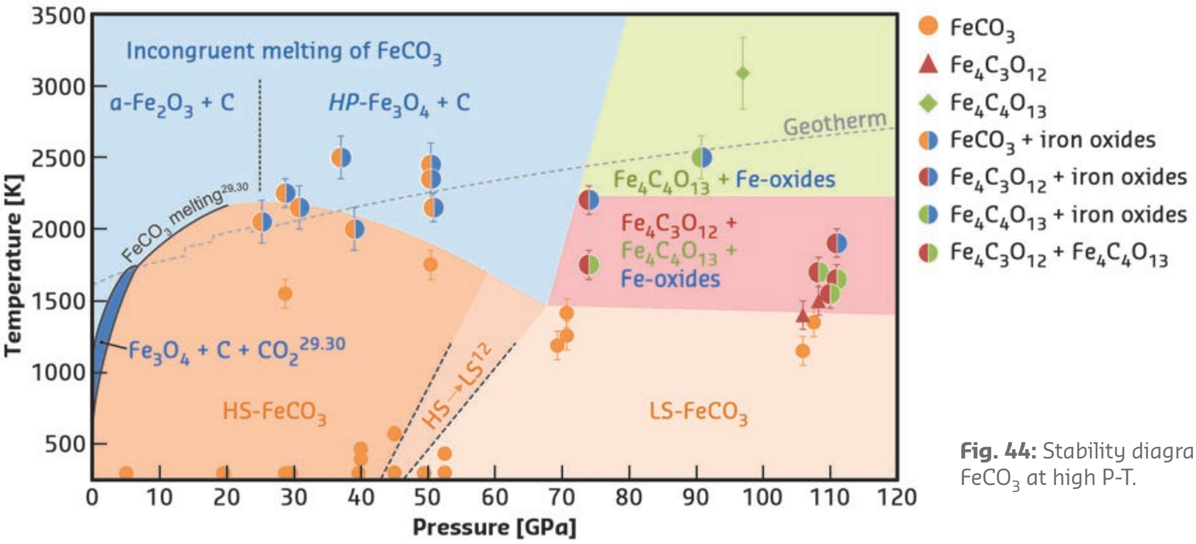

Fig. 44: Stability diagram of $FeCO_3$ at high P-T.

it is inferred that the orthocarbonate, $Fe_4C_3O_{12}$, forms directly from heating $FeCO_3$ at T > 1400 K according to the reaction $4FeCO_3 \rightarrow Fe_4C_3O_{12} + C$. The tetracarbonate, $Fe_4C_4O_{13}$, appears upon prolonged heating of $Fe_4C_3O_{12}$ above ~75 GPa but at temperatures significantly higher than those needed for the synthesis of the orthocarbonate (**Figure 44**) following the possible reaction $8Fe_4C_3O_{12} \rightarrow 6Fe_4C_4O_{13} + 4Fe_2O3 + 3O_2$. This reaction indicates that iron is reduced by oxygen, where something similar has already been observed in studies of iron(III) oxides at pressure above ~70 GPa.

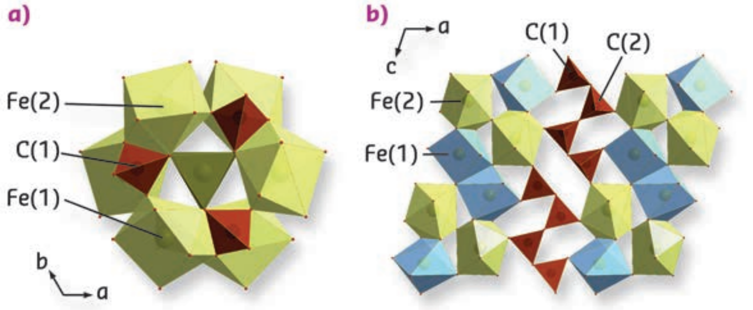

Fig. 45: Crystal structures of high-pressure carbonates a) Tetrairon (III) orthocarbonate $Fe_4C_3O_{12}$ and b) diiron (II) diiron (III) tetracarbonate $Fe_4C_4O_{13}$, at ambient temperature and 74(1) and 97(2) GPa, respectively.

Thus, it is concluded that the tetracarbonate is the product of chemical evolution of the othocarbonate and that ferrous and ferric iron plays a role in stabilising carbonates at extreme conditions. Moreover, $Fe_4C_4O_{13}$ was found to survive along the entire geotherm to the depth corresponding to at least 2500 km, demonstrating that self-oxidation-reduction reactions should not lead to the destruction of carbonates in the Earth's lower mantle.

PRINCIPAL PUBLICATION AND AUTHORS

Stability of iron-bearing carbonates in the deep Earth's interior, V. Cerantola (a), E. Bykova (b,c), I. Kupenko (a,i) , M. Merlini (d), L. Ismailova (b,e), C. McCammon (b), M. Bykov (b,f), A. I. Chumakov (a), S. Petitgirard (b), I. Kantor (a,j), V. Svitlyk (a), J. Jacobs (a), M. Hanfland (a), M. Mezouar (a), C. Prescher (g), R. Rüffer (a), V. Prakapenka (h) and L. Dubrovinsky (b), *Nat. Commun.* **8**, 15960 (2017); doi: 10.1038/ncomms15960.

(a) ESRF
(b) Bayerisches Geoinstitut, Universität Bayreuth (Germany)
(c) Deutsches Elektronen-Synchrotron, Hamburg (Germany)
(d) Dipartimento di Scienze della Terra, Università degli Studi di Milano (Italy)
(e) Skolkovo Institute of Science and Technology, Skolkovo Innovation Center (Russia)
(f) Material Modeling and Development Laboratory, National University of Science and Technology MSIS, Moscow (Russia)
(g) Institute of Geology and Mineralogy, Universität zu Köln (Germany)
(h) GSECARS, Center for Advanced Radiation Sources, University of Chicago, Argonne National Laboratory (USA)
(i) Present address: Institut für Mineralogie, Universität Münster (Germany)
(j) Present address: MAX IV Laboratory, Lund (Sweden)

REFERENCES

[1] B. Marty *et al., Rev. Mineral. Geochem.* **75**, 149-181 (2013)
[2] M. Isshiki *et al., Nature* **427**, 60-63 (2004)

CRYSTAL STRUCTURE OF SiO_2 POLYMORPH CRISTOBALITE X-I: BRIDGING THE GAP TOWARDS THE SEIFERTITE ENIGMA

Silica polymorph α-cristobalite was studied from ambient to high pressures to understand its densification mechanism and link to formation of the polymorph seifertite, only found in severely shocked meteorites. Using synchrotron radiation, the structure of an intermediate and long-disputed polymorph – cristobalite X-I – was solved, revealing the missing step in the transformation sequence.

Seiferite, α-PbO_2-type silica, is the densest known SiO_2 polymorph discovered so far. It is considered to be stable above ~80 GPa, which can either be accommodated at greater depths of planetary interiors or in the only natural samples available – severely shocked meteorites. In various shocked meteorites, low-pressure silica polymorph α-cristobalite is commonly observed in close spatial relation with seifertite. To understand the curious coexistence of these low- and high-pressure silica phases, the behaviour of α-cristobalite under pressure was systematically studied. The focus of the study was to constrain the conditions under which a controversial phase bridging α-cristobalite and seifertite – cristobalite X-I – can be formed. By revealing the crystal structure of the metastable polymorph cristobalite X-I, and the conditions under which it forms, it was possible to gain insight into the long-disputed transition mechanism from α-cristobalite to α-PbO_2-type silica.

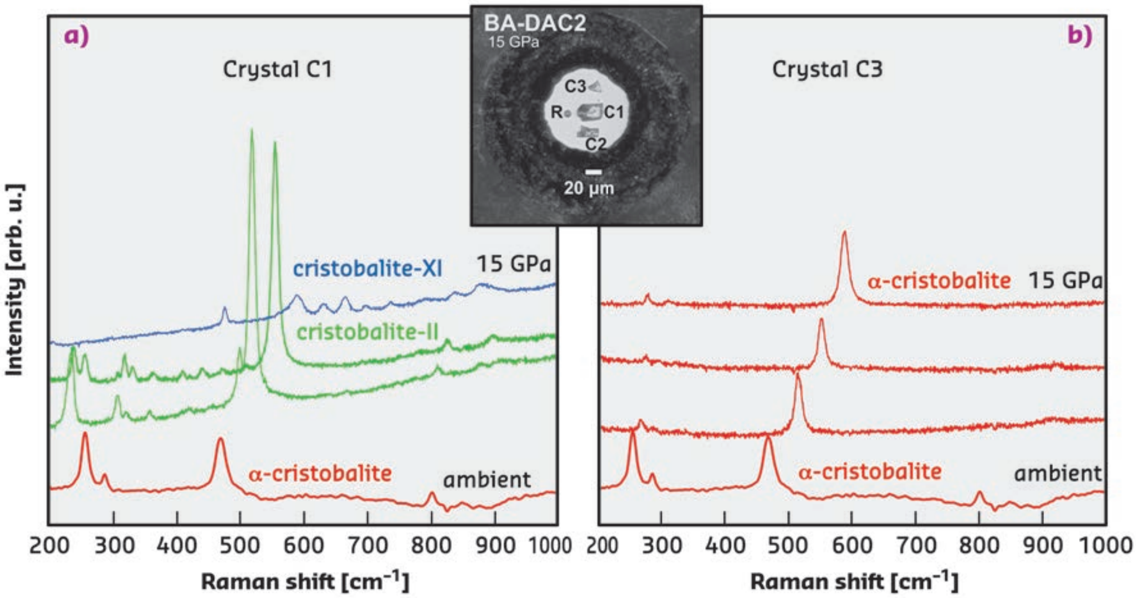

Fig. 46: *In situ* Raman spectra collected on two different single crystals of α-cristobalite at 1.1, 4.6, 8.6 and 15.0 GPa and at room temperature a) in quasi-hydrostatic conditions and b) in the case of high hydrostaticity. Inset shows the DAC pressure chamber seen at 15.0 GPa: R stands for ruby; C1, C2 and C3 for different cristobalite crystals.

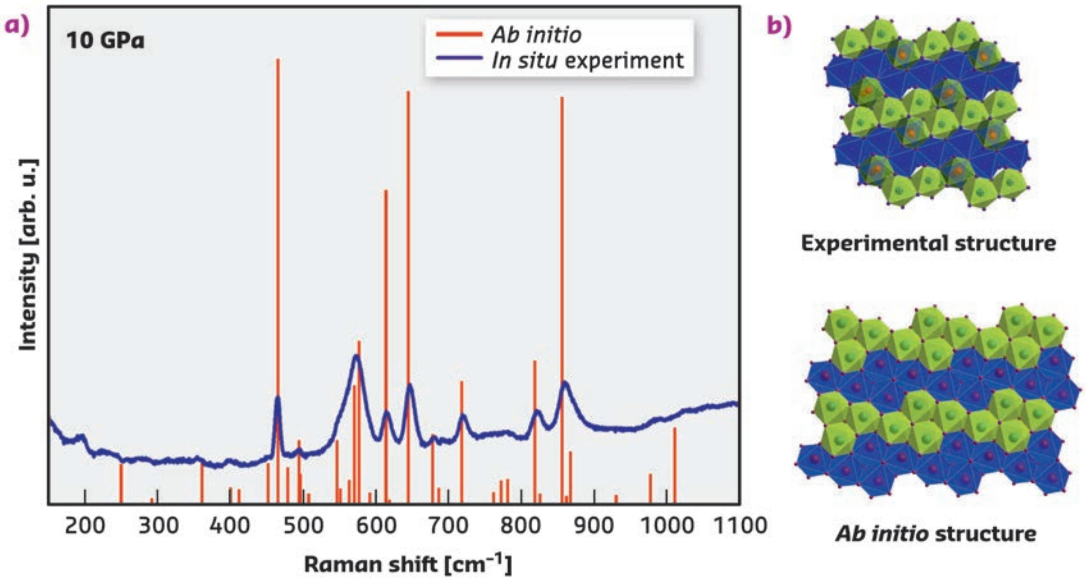

Fig. 47: a) Comparison of the Raman experimental spectrum (blue continuous line) and theoretical spectra for an ordered structural model (red vertical bars).
b) [010] projection of the structure of cristobalite X-I as obtained experimentally at ESRF (top), and used for model in *ab initio* calculations (bottom).
The experimental structure contains half-occupied octahedral positions (Si_3) shown by red spheres, and fully occupied octahedra (Si_1 and Si_2) represented by all other spheres.
The blue and the green octahedra represent different levels in the structure. The theoretical structure contains 4x4 arrangement of the fully occupied octahedra.
The blue and the green octahedra represent different levels in the structure.

High-pressure experiments were carried out on both single crystals and powders. All single-crystal experiments were conducted in quasi-hydrostatic conditions, using a pressure-transmitting medium, while powders were also studied in a non-hydrostatic environment. A starting material in the form of α-cristobalite was compressed using diamond anvil cells (DAC). *In situ* high-pressure data were obtained by Raman spectroscopy and synchrotron-based single-crystal X-ray diffraction (SCXRD) at ESRF beamlines **ID15B** and **ID27**, and also at DESY.

The mechanism that α-cristobalite adopts as response to compression was found to strongly depend on the stress conditions. Single crystals that remain surrounded by very soft neon upon compression, experiencing a (almost) hydrostatic environment, retain the structure of α-cristobalite up to at least ~15 GPa, as shown in **Figure 46**. Crystals that touch the diamond anvils upon compression, undergo a displacive phase transition to cristobalite-II near 1 GPa and further transform to cristobalite X-I just above ~10 GPa (**Figure 46**), in agreement with earlier findings **[1]**. Cristobalite X-I can be followed at least up to ~80 GPa under compression. After recovering cristobalite X-I from high-pressure experiments, it transformed back to the initial α-cristobalite. Compression experiments carried out on powders, regardless of the presence of the pressure-transmitting medium, showed identical transformation paths, ultimately resulting in the formation of seifertite-like material.

The abrupt change in Raman spectra above 10 GPa suggests that the structure of the X-I phase is quite distinct from its α- and cristobalite-II precursors (**Figures 46** and **47**). The polymorph cristobalite X-I belongs to the family of high-pressure silica phases comprising a distorted hexagonal close-packed array of oxygen ions, in which silicon atoms fully or partially occupy octahedral sites, being sixfold coordinated to oxygen (**Figure 47**). There are no other known silica polymorphs that transform to an octahedra-based structure at such low pressures upon compression at room temperature. The experimentally determined structure was then used in *ab initio* calculations to examine ordered structural models and to compute the Raman spectra and unit-cell parameters at various pressures (**Figure 47**). The theoretical study did not reveal any sign of dynamical instabilities of cristobalite X-I at pressures up to at least 100 GPa.

An increase in coordination number of silicon in cristobalite X-I from 4 to 6 occurs as low as ~10 GPa without requiring any heating, and agrees well with the results by Kubo *et al.* **[2]**. Once the thermal energy is added, cristobalite X-I transforms to the more stable arrangement – seifertite – and not to the thermodynamically stable stishovite. This could shine light onto the coexistence of α-cristobalite, formed from quenched cristobalite X-I that is only stable at high pressures, with seifertite, which is quenchable, in meteorites in which peak pressures are estimated not to have exceeded 25-30 GPa.

Based on these observations, the presence of α-cristobalite in shocked meteorites or rocks may be indicative of lower peak shock pressures.

PRINCIPAL PUBLICATION AND AUTHORS

Compressional pathways of α-cristobalite, structure of cristobalite X-I, and towards the understanding of seifertite formation,
A. Černok (a, b), K. Marquardt (a), R. Caracas (c), E. Bykova (a), G. Habler (d), H.-P. Liermann (e), M. Hanfland (f), M. Mezouar (f), E. Bobocioiu (c) and L. Dubrovinsky (a), *Nat. Commun.* **8**, 15647 (2017); doi: 10.1038/ncomms15647.
(a) Bayerisches Geoinstitut, Bayreuth (Germany)
(b) Open University, School of Physical Sciences, Milton Keynes (UK)
(c) CNRS, Laboratoire de Geologie de Lyon, Lyon (France)
(d) Department of Lithospheric Research, University of Vienna, Vienna (Austria)
(e) Deutsches Elektronen-Synchrotron (DESY), Hamburg (Germany)
(f) ESRF

REFERENCES

[1] P. Dera *et al.*, *Phys. Chem. Mineral.* **38**, 517-529 (2011)
[2] T. Kubo *et al.*, *Sci. Adv.* **1**, e1500075 (2015)

IONIC ICE MIXTURE UNDER PRESSURE

Knowing the high-pressure behaviour of water-ammonia mixtures has strong relevance for the description of giant icy planets. Here, it is demonstrated that under pressure, the equimolar mixture transforms into an unusual solid alloy composed of both molecular and ionic species, owing to a topological frustration.

Water and ammonia are simple molecules, abundant in the universe. Together with methane, they are thought to be the main constituents of the internal layers of the giant icy planets Uranus and Neptune, where extreme pressure-temperature conditions exist. It is suspected that the unusual magnetic field of these planets originates from the ionisation of such molecules at high pressures and temperatures. Previous studies have shown that for the pure ices, pressure favours the creation of ions at pressures in excess of 100 GPa at 300 K, but the presence of ionic species in ice mixtures had not been experimentally evidenced.

Experiments and first-principles simulations were used to study the solid phases of an equimolar mixture of water and ammonia, known as ammonia monohydrate (AMH). Several polymorphs had previously been disclosed below 10 GPa, all described as hydrogen-bonded molecular solids. Using Raman and synchrotron IR spectroscopies, hydroxyl (OH^-) and ammonium (NH_4^+) ion signatures were detected in the AMH samples compressed above 7.4 GPa (**Figure 48**). These spectral bands occur at frequencies close to those expected for a recently predicted P4/nmm structure. However, this structure is fully ionic, *i.e.* solely composed of hydroxyl and ammonium ions, while the presence of strong Raman and IR bands from H_2O and NH_3 molecules indicate only partial ionisation of AMH. X-ray diffraction experiments conducted at **ID27** revealed the sample was composed of two phases: a body-centred cubic (bcc) phase, representing the major part, and the P4/nmm phase. The bcc phase had been previously observed in neutron diffraction experiments and described as a disordered molecular alloy (DMA) where H_2O and NH_3 molecules are randomly distributed on the bcc lattice. The coexistence of a purely molecular alloy with a purely ionic phase was highly intriguing. Computer simulations of the bcc phase were conducted to better understand its nature.

The results showed that the bcc phase is partly ionic, containing up to 36 % $NH_4^+{\cdot}OH^-$ pairs at

10 GPa at 300 K, due to a proton transfer from a H_2O to a NH_3 molecule (**Figure 49a**). The OH^- and NH_4^+ vibrations occur at nearly the same frequencies as in the P4/nmm crystal, making it hard to distinguish the respective contributions of the two phases in the vibrational spectra. Part of the molecules does not ionise in the bcc phase (baptised disordered ionic-molecular alloy, or DIMA) due to a topological frustration: the substitutional disorder of the bcc structure implies that two NH_3 molecules can be first-neighbours, and if one of those molecules receives a proton from nearby water, then Coulombic repulsion hinders the formation of another cation in its first-neighbour shell (**Figure 49b**). Calculations also show that the DIMA phase has a higher energy than P4/nmm, indicating that the system is kinetically trapped in the DIMA phase at 300 K.

The present study demonstrates that AMH spontaneously converts into an unusual crystalline state above 7.4 GPa, where H_2O and NH_3 molecules coexist with OH^- and NH_4^+ ions. The relatively low-pressure onset for static ionisation contrasts with the extreme pressures required in the pure ices, and can be understood by the lower energy cost for the proton transfer between H_2O and NH_3. Future research will investigate the presence of a superionic phase with large proton mobility, which could exist in AMH at milder P-T conditions than in the pure ices (P > 50 GPa, T ~1000 K).

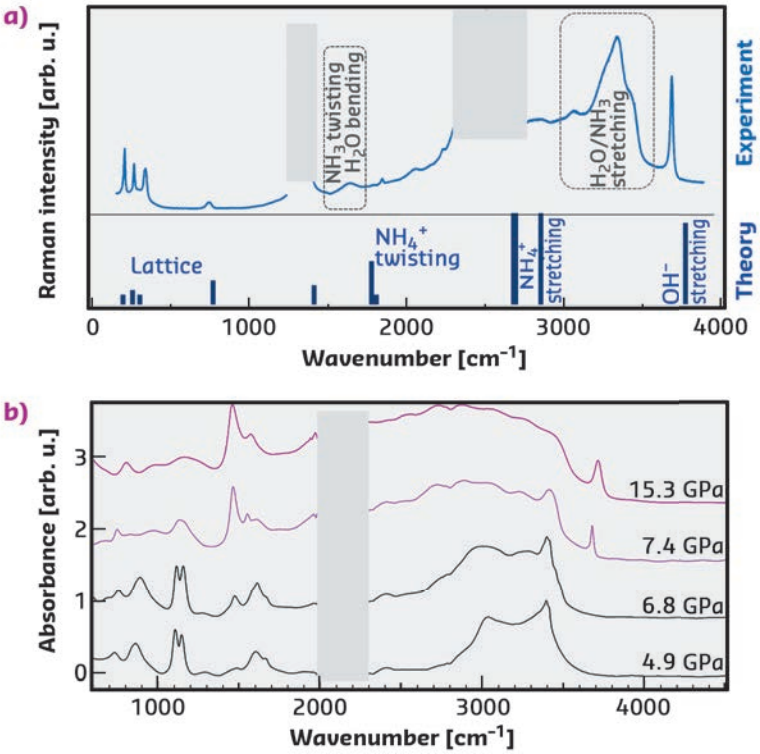

Fig. 48: a) Raman spectra of AMH at 10 GPa. The experimental spectra (collected at RT) and the theoretical one (calculated at 0 K) for the fully ionic P4/nmm structure are shown in the upper and lower panels, respectively. b) Experimental IR absorption spectra of AMH collected upon decompression at RT at SOLEIL synchrotron. Pink and black curves are spectra above and below the ionic-molecular phase transition, respectively.

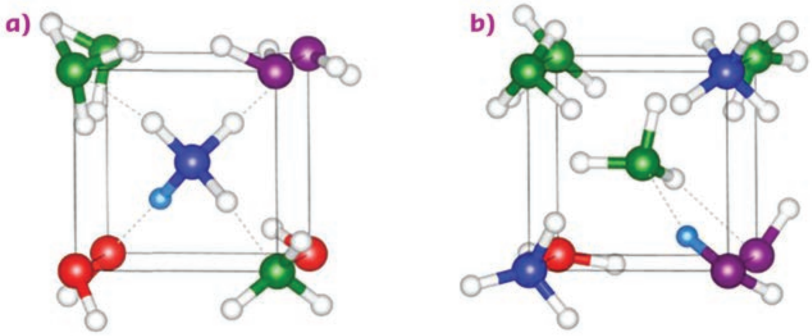

Fig. 49: Simulation snapshots showing the nearest-neighbour environment of a) an ammonium ion or b) an ammonia molecule. The H atom involved in the H-bond between the central ammonia and neighbour water molecule is rendered in cyan, the others are represented by white spheres. N atoms are in green and blue for NH_3 and NH_4^+, respectively, and O atoms are in magenta and red for H_2O and OH^-, respectively. Solid and dashed lines depict the cubic unit cell and the H-bonds, respectively.

PRINCIPAL PUBLICATION AND AUTHORS

Topologically frustrated ionization in a water-ammonia mixture, C. Liu (a, b), A. Mafety (a), J.A. Queyroux (a), C. W. Wilson (c), H. Zhang (a), K. Béneut (a), G. Le Marchand (a), B. Baptiste (a), P. Dumas (d), G. Garbarino (e), F. Finocchi (f), J.S. Loveday (c), F. Pietrucci (a), A.M. Saitta (a), F. Datchi (a) and S. Ninet (a), *Nat. Commun.* **8**, 1065 (2017); doi:10.1038/s41467-017-01132-z.

(a) Institut de Minéralogie, de Physique des Matériaux et de Cosmochimie (IMPMC), Sorbonne Université, Paris (France)
(b) Institute of Atomic and Molecular Physics and State Key Laboratory of Superhard Materials, Jilin University, Changchun (China)
(c) SUPA, School of Physics Astronomy Centre for Science at Extreme Conditions, University of Edinburgh, (UK)
(d) Synchrotron SOLEIL, Gif sur Yvette (France)
(e) ESRF
(f) Institut des Nanosciences de Paris, Sorbonne Universités, Paris (France)

COMPLEX SYSTEMS AND BIOMEDICAL SCIENCES

2017 was a very successful year for the group with the approval of two flagship beamlines for the EBS project. The first, for coherent beam experiments, will be built on ID08 and the second, for surface science, will be built on ID10. The latter will have two hutches, one for soft and one for hard surfaces. In addition, ID02, ID09 and ID17 will be upgraded with new optics and detectors.

Beamline **ID02** had a renewal of scientific staffing due to the early departure of two post docs and a second scientist. Ultra-small-angle XPCS (USA-XPCS) received a tremendous boost with the Eiger detector, which can acquire up to 20 000 frames per second. It has also been a productive year in terms of publications and industrial activity, indicating that the beamline has matured to full potential after the upgrade.

Several important innovations were implemented on **ID03**. The fast attenuators can change the attenuation, to avoid detector saturation, in less than 20 ms. Continuous scans became more efficient and the risk of damaging the detector has been eliminated. Trajectory scans in reciprocal space were also implemented with a significant reduction in acquisition time. This is particularly important for studies of slow dynamics at interfaces. Two new setups for *in situ* / *operando* electrochemical experiments were established in collaboration with University of Liverpool (UK) and University of Florence (Italy). The setups enable us to perform electrochemical experiments on ionic liquids with no oxygen/water contamination and to provide a low background environment with weak scatterers. The satellite laboratories are becoming more important. In particular, the electrochemistry laboratory supported a record number of experiments in 2017.

ID09 is dedicated to time-resolved studies of molecules on time scales from 100 picoseconds to 1 millisecond. The structure is filmed with snapshots in a pump-and-probe fashion: short laser pulses initiate a structural change and short X-ray pulses probe the change as a function of laser/X-ray delay. For chemical and biochemical reactions that cannot be triggered by a laser, a stopped-flow setup with 10-millisecond resolution was installed in July 2017. The beamline also offers time-resolved X-ray emission spectroscopy (XES) with a Johann and a Van Hamos spectrometer. The latter focuses a 100 eV spectrum into a line on a Maxipix CCD. The spectrum is therefore measured in *one* exposure, which is ideal for pump-and-probe experiments.

In preparation for the EBS, a micro focusing mirror will be installed in the former high-pressure hutch, EH1, in March 2018. The mirror will focus the pink beam in EH2 to Ø15 µm with 5 x 10^9 ph/pulse at 15 keV. Many experiments, notably serial Laue crystallography, will greatly benefit from the smaller spot. With the inauguration of the XFEL in Schenefeld (Germany) and the SwissFEL in Villigen (Switzerland), users will have access to 100-femtosecond pulses for ultra-fast experiments. With the EBS upgrade, the ESRF will continue to be an important player in picosecond science thanks to the wide energy range, superb beam stability and the greater availability for users.

2017 was a milestone for **ID10,** with the approval of a dedicated coherent beamline on the EBS, the EBSL1 project. EBSL1 will exploit the impressive increase in coherence for X-ray photon correlation spectroscopy (XPCS) and coherent X-ray diffraction imaging (CXDI). The 100-fold gain in coherent flux will extend the temporal resolution in XPCS 10 000 times, down to 100 nanoseconds. CXDI will push the spatial resolution to 5-10 µm in tomographic imaging, bridging the gap between electron and optical microscopy. ID10 will be refurbished with two hutches: the first will host a multipurpose diffractometer with a beam deflector for liquid/soft surfaces, and the second will host a setup for chemical reactions and surface dynamics. Studies of catalytic ignition and electrochemical dissolution will be possible with millisecond resolution. In addition, improved optics will open up new possibilities for studies of sub-micron objects and dynamics of buried interfaces.

The surface part of ID10, ID10SI, installed a Mythen2-1K stripe detector for GID measurements from liquid surfaces. The detector accelerated the speed of data collection 10 times! The coherent part of ID10, ID10CS, was improved with new optics, sample environments, detectors and software. In particular, the energy range for coherent experiments was extended up to 21 keV. To preserve the coherence, wavefront-preserving absorbers, made of Ge single crystals, were installed. To perform experiments in the

80-500 K range, a new cryostream, the Oxford 800 Plus, is now available. The beamline also has access to an Eiger 500 K that can run at 22 kHz, *i.e.* 60 times faster than the Maxipix. That makes it possible to track microsecond dynamics in XPCS.

ID17 is dedicated to *in vitro* and *in vivo* biomedical research. In 2017, the portfolio of detectors for micro-computed tomography was enlarged to include a double-head microscope made by Optique Peter. The detectors are designed to handle the high intensity from a pink beam. Monochromatic CT imaging in the energy range 25-150 keV can now be performed in the satellite building and pink beam CT imaging in the first experimental hutch. A FReLoN and PCO.Edge (type: 5.5) camera are used, combined with optical lenses, to define pixel sizes from 0.7 to 47 µm with fields-of-view up to 180 mm. Microbeam radiation therapy (MRT), a technique exploiting the high intensities of wiggler radiation, is used to study the tumouricidal properties of intense micro beams. MRT is frequently combined with nanoparticles or other chemotherapic adjuvants. The ultimate goal of MRT is to use it in real clinical applications. An important milestone towards this goal was reached in 2017 with conformal image-guided MRT on large targets.

2017 was also a very busy year for the **PSCM**, the Partnership for Soft Condensed Matter, which is a joint ESRF/ILL support laboratory. The number of requests for user support is steadily increasing and the PSCM is now supporting more than one hundred experiments per year from users and on-site scientists. The most requested techniques are atomic force microscopy, optical microscopy and UV-vis spectroscopy. Additional services include humidity control and 3D printing of sample environments. In particular, the PSCM is progressively specialising in 3D-printed microfluidic devices.

The results of the PSCM implementation phase 2012-2017 were reviewed in March 2017. This meeting included talks from the five current partners of the PSCM: University of Göttingen (Germany), Technical University of Berlin (Germany), Imperial College London (UK), University of Paderborn (Germany) and the University of Natural Resources and Life Sciences of Vienna (Austria). The Review Committee recommended the continuation of PSCM for the next five years, 2018-2023.

M. WULFF

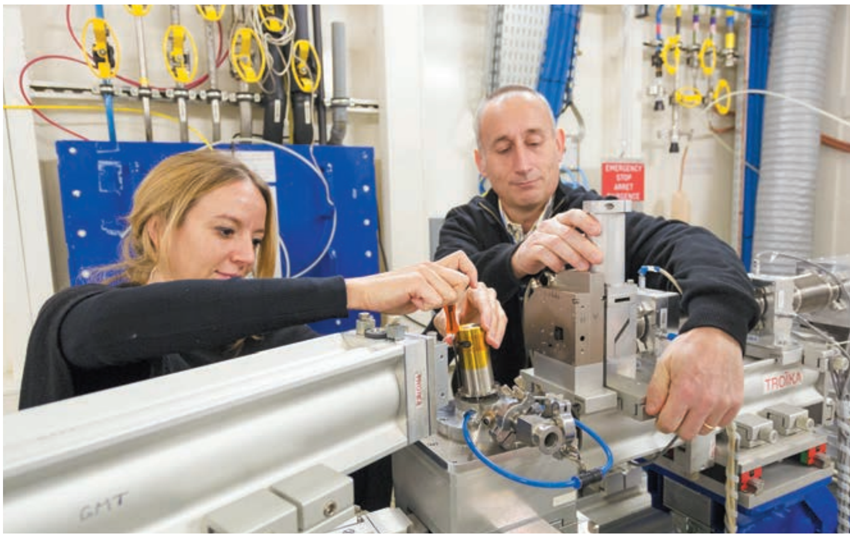

BEATING HEART EFFICIENCY REVEALED BY X-RAYS

The heart pumps blood through the vessels while keeping the pulmonary and systemic circulatory systems in balance. At the molecular level, this balance is contributed to by mechanosensing in the myosin filaments that recruit myosin motors in proportion to the load.

In the heart, a regulatory mechanism known as the Frank-Starling Law allows the pressure developed by the ventricle wall during the contraction phase (systole) to be adjusted with respect to its filling during the preceding relaxation phase (diastole). This ensures the balance between the pulmonary and systemic circulatory systems working in series. At the level of the cardiac cell (myocyte), this mechanism implies that the contractile force increases with the increase in the length of the sarcomere, the 2 µm-long structural unit. Within the sacomere, two arrays of myosin motors extending from the thick filament generate force pulling the interdigitating thin actin-containing filaments towards the centre.

In this work, the Frank-Starling law is shown to be contributed to at the molecular level by a mechanosensing-based regulation of thick filament activation. In the resting state, the myosin motors lie in their off state on the surface of the thick filament, unable to attach to the thin filament and split ATP. During contraction, the number of motors leaving the off state is adjusted to the force required to pump blood into the aorta or the pulmonary artery by mechanosensing in the thick filament. In this way, the energetic cost of the contraction is tuned to the mechanical task **[1]**.

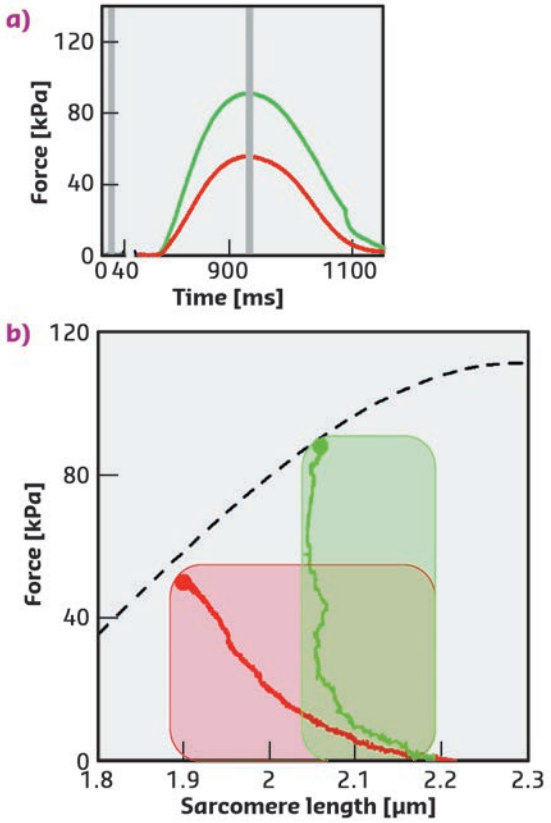

Fig. 50: a) Force of the FE (red) and LC (green) twitches. Stimulus starts at 775 ms. Grey bars: X-ray time windows. b) Relation between the peak force and the sarcomere length (dashed line) superimposed on the instantaneous force-sarcomere length plots for twitches in FE (red) and in LC (green). Filled circles, peak force. The shaded areas are the two ideal loops followed by contractions that start at sarcomere length ~2.2 µm under isometric condition and become isotonic when the force attains the same level as the twitch peak. In terms of the left ventricle beat, the dashed line is the relation between end-systolic pressure and end-systolic volume and the dashed areas are two pressure-volume loops starting from the same preload (*i.e.* end-diastolic volume) and with two different aortic pressures.

Intact trabeculae, pillars of myocytes 2-3 mm in length, were mounted between force and length transducers at beamline **ID02** to record the mechanical responses (twitches) and the X-ray diffraction signals during electrically paced contraction-relaxation cycles at different sarcomere lengths (**Figure 50a, b**). The USAXS/SAXS combination made it feasible to record, from the same trabecula, the nanometre-scale signals from the contractile proteins along the myosin and actin filaments together with the micrometre-scale changes in the length of the sarcomeres (**Figure 51a-d**).

During force development in a twitch under fixed-end conditions (FE), sarcomeres shorten against the end compliance so that, at peak force, the sarcomere length is reduced from the starting value of 2.21 µm (Dia, **Figure 51a, c**, blue) to 1.9 µm (red). Shortening during the following twitch can be largely prevented (length clamp conditions, LC) by a feedforward signal proportional to the shortening in the preceding FE twitch, so that, at peak force, the sarcomere length is 2.09 µm (green) and the force is almost twice the FE value (**Figure 50a, b**).

The myosin-based X-ray reflections marking the quasi-helical three-stranded symmetry of the myosin molecules on the thick filament are intense in diastole (Dia, **Figure 51b, d**, blue) This indicates that the myosin motors lie in helical tracks on the surface of the thick filament in their off state, in which they are unable to attach to actin and split ATP**.** At the peak of the twitch force (red and green), the intensities of the reflections decrease, due to the myosin motors leaving their helical tracks as the thick filament switches on. The M3 reflection, originating from the axial repeat of the myosin motors, exhibits a different fine structure and different increase in spacing depending on whether the contraction occurs in FE (**Figure 51b, d** red) or in LC (green). In terms of the structural model of the sarcomere **[2]**, the difference in the M3 intensity profiles indicates that, during a cardiac twitch, only

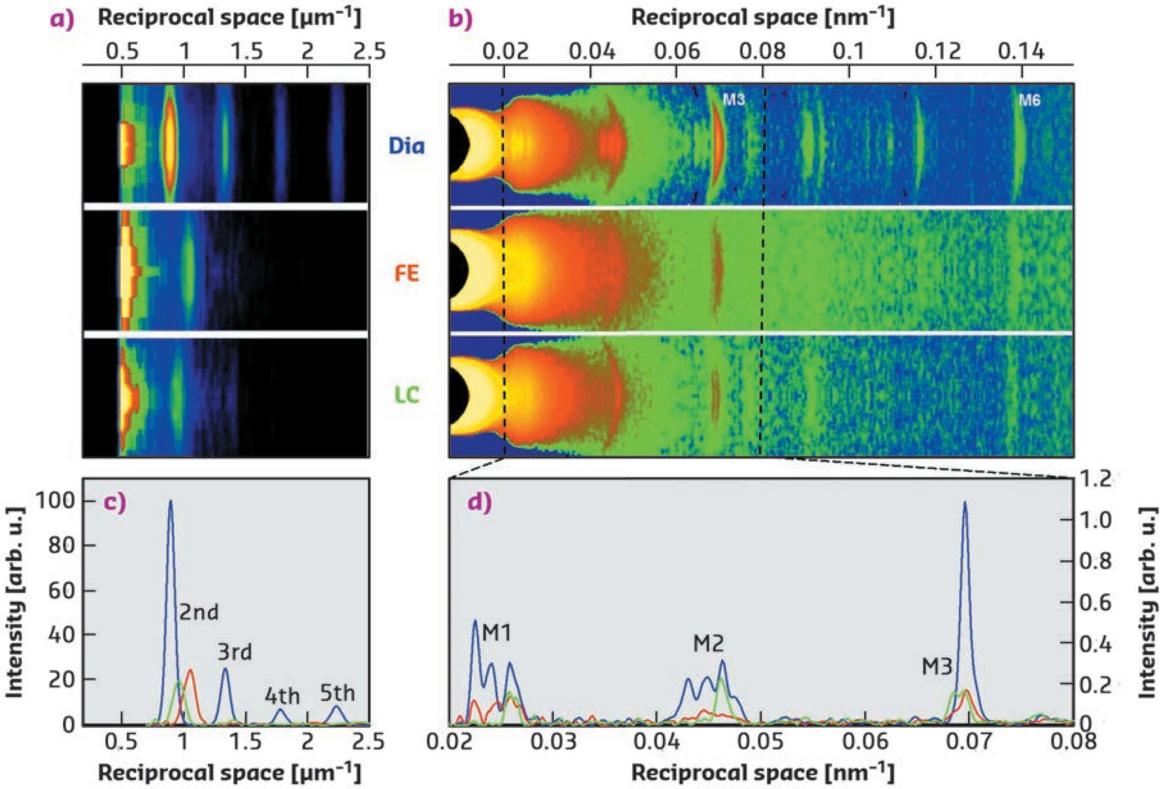

Fig. 51: a) Meridional slices of 2D X-ray patterns collected at 30 m during diastole (Dia) and at the peak force of a FE or LC twitch, showing the first orders of sarcomeric reflections. b) Meridional slices of 2D patterns, collected at 1.6 m, showing the myosin-based axial reflections (M1-M6). c) Superimposed intensity profiles from (a), starting from the second-order reflection. d) Superimposed intensity profiles from the region of (b) indicated by the dashed lines.

a fraction of the motors leaves the off state and this fraction depends on the level of the force independently of the diastolic sarcomere length. In this respect, the LC and FE twitches approximate the conditions of the left ventricle beating against a high (LC) and a low (FE) aortic pressure (**Figure 50b**).

This work provides a new integrated view of the Frank-Starling mechanism, which combines mechanical, structural and energetic aspects: independent of the end-diastolic sarcomere length (end-diastolic volume), the energetic cost of the heart beat is tuned to the ventricular end-systolic pressure-volume relation by stress-sensing in the thick filament.

PRINCIPAL PUBLICATION AND AUTHORS

Myosin filament activation in the heart is tuned to the mechanical task, M. Reconditi (a,b), M. Caremani (a), F. Pinzauti (a), J.D. Powers (a), T. Narayanan (c), G.J.M. Stienen (d), M. Linari (a,b), V. Lombardi (a) and G. Piazzesi (a), *PNAS* **114**, 3240-3245 (2017); doi: 10.1073/pnas.1619484114.

(a) PhysioLab, University of Florence (Italy)
(b) Consorzio Nazionale Interuniversitario per le Scienze Fisiche della Materia, Unità di Ricerca di Firenze, Florence (Italy)
(c) ESRF
(d) Department of Physiology, VU University Medical Center, Amsterdam (The Netherlands)

REFERENCES

[1] M. Linari *et al., Nature* **528**, 276-279 (2015).
[2] M. Reconditi *et al., PNAS* **108**, 7236-7240 (2011).

X-RAYS INDUCE DYNAMICS IN OXIDE GLASSES

High X-ray fluxes can alter the dynamical properties in hard materials, an effect that has to be considered in the analysis of X-ray data. This effect also provides an opportunity to study material properties, since the beam can probe – and even initiate – the dynamics.

Powerful X-ray sources such as diffraction-limited synchrotrons and free-electron lasers (FEL) are considered as the ultimate tools for the investigation of the microscopic properties of materials **[1]**. However, even with third-generation synchrotrons, it was realised that the intense beam can affect the material, *e.g.* biological and soft materials can suffer severe radiation damage. Despite this problem, such experiments nevertheless allow unique information to be gained about the material **[2]**. Similar effects have yet to be reported for hard materials; it has always been assumed that X-rays do not influence their properties. Now, by using X-ray photon correlation spectroscopy (XPCS) at beamline **ID10**, it has been discovered that the beam can indeed alter the properties of the sample in an important way.

The relaxation dynamics of oxide and metallic glasses were probed by varying the incoming X-ray flux. **Figure 52a** shows intensity auto-correlation curves measured in glassy SiO_2 at ambient temperature and for a wave-vector Q_p = 1.5 Å^{-1}, corresponding to the position of the maximum in the static structure factor. The curves represent a measure of the degree of correlation between two configurations separated by a lagtime t, and the decay time, τ, which is the time necessary for structural rearrangements on a length scale covering a few Å. The dynamics of oxide glasses depends strongly on the intensity, being faster – *i.e.* with shorter decay time – for higher X-ray fluxes. This is confirmed by the observation that all data collapse onto a master curve when plotted as a function of time normalised by the flux (**Figure 52b**).

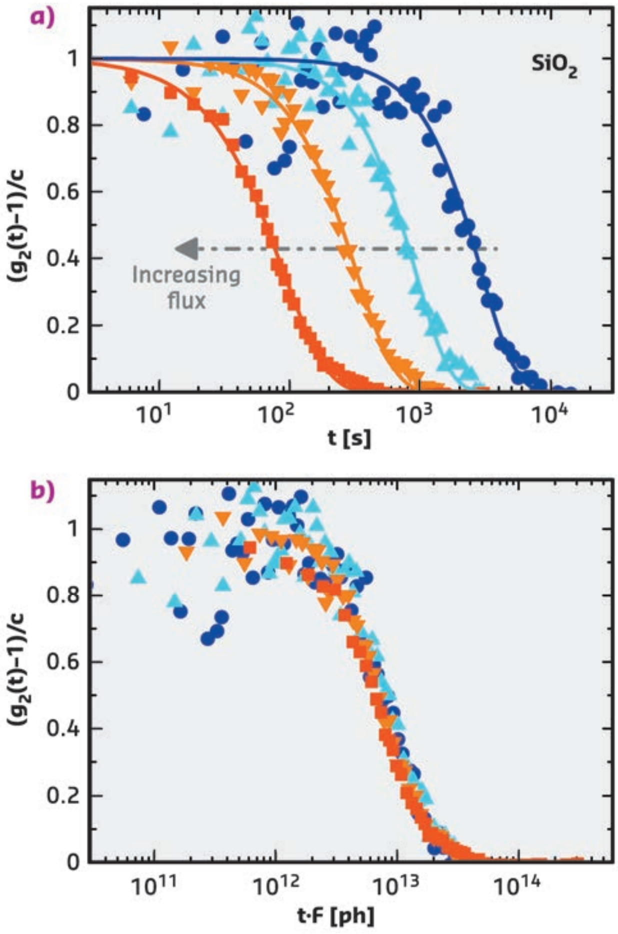

Fig. 52: a) Intensity auto-correlation functions measured in SiO_2 at T = 295 K and Q_p = 1.5 Å^{-1} for different intensities. From left to right: $F_0 \approx 1 \cdot 10^{11}$ ph/s (squares), $F_1 \approx 3 \cdot 10^{10}$ ph/s (down-triangles), $F_2 \approx 1.2 \cdot 10^{10}$ ph/s (up-triangles) and $F_3 \approx 3.6 \cdot 10^9$ ph/s (circles). b) The same data rescaled with respect to the flux.

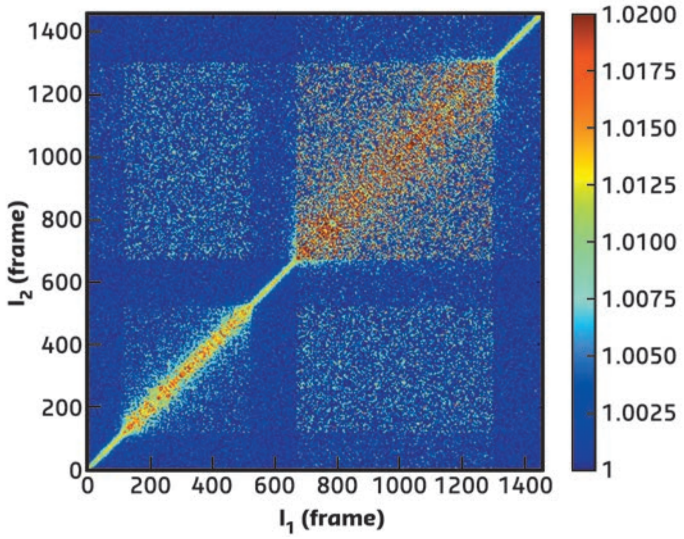

Fig. 53: Two-time correlation function measured by varying the intensity of the incoming flux. Left to right: $F_0 \approx 1 \cdot 10^{11}$ ph/s, $F_1 \approx 3 \cdot 10^{10}$ ph/s, $F_0 \approx 1 \cdot 10^{11}$ ph/s, $F_2 \approx 1.2 \cdot 10^{10}$ ph/s, and $F_0 \approx 1 \cdot 10^{11}$ ph/s. Each frame corresponds to a lagtime Δt = 6.15 s.

The observed effect cannot be classified as standard radiation damage since the induced dynamics is independent of the accumulated dose deposited on a particular sample position and the decay time is reversibly modified by changing the intensity of the beam. This is demonstrated in **Figure 53**, which shows the two-time correlation function measured while changing the beam attenuation without stopping the measurement. Each point of the two-time correlation function corresponds to the product of two images acquired at two different times **[3]**. The effect of the attenuators is signalled by the abrupt changes in the profile along the main diagonal, whose width is proportional to τ. The higher the incoming intensity, the faster the dynamics and thus the thinner the intensity profile. For a fixed incoming intensity, the profile remains constant with time thus implying that the corresponding dynamics is stationary and does not depend on the total accumulated dose.

The static structure was not affected by the X-rays, suggesting that this is not the usual radiation damage found in soft materials, but rather can be attributed to radiolysis, *i.e.* to the interaction between localised electronic excitations created by the X-rays and phonons of the material. In contrast, metallic glasses do not show this effect because their electronic excitations delocalise faster on the fs timescale.

This work demonstrates that high X-ray intensities can affect even hard materials. Therefore, high X-ray fluxes can be used to probe the material and also as a pump for the atomic motion, providing unique information on the system.

The observed behaviour is likely to occur in a variety of materials and its strength will be amplified dramatically at next generation synchrotrons and FELs **[1]**, where techniques such as XPCS that use intense coherent beams will be based on fs pulses with intensities as high as current synchrotrons provide in one second **[4]**.

PRINCIPAL PUBLICATION AND AUTHORS

Hard X-rays as pump and probe of atomic motion in oxide glasses, B. Ruta (a,b), F. Zontone (b), Y. Chushkin (b), G. Baldi (c), G. Pintori (c), G. Monaco (c), B. Rufflé (d) and W. Kob (d), *Scientific Reports* **7**, 3962 (2017);
doi: 10.1038/s41598-017-04271-x.

(a) Université Claude Bernard Lyon 1, CNRS, Institut Lumière Matière, Villeurbanne (France)
(b) ESRF
(c) Dipartimento di Fisica, Trento University, Povo (Italy)
(d) Laboratoire Charles Coulomb (L2C), UMR 5221 CNRS-Université de Montpellier (France)

REFERENCES

[1] P.G. O'Shea and H.P. Freund, *Science* **292,** 8 (2001).
[2] M. Weik *et al.*, *PNAS* **97**, 623-628 (2000).
[3] R. Neutze *et al.*, *Nature* **406**, 752-757 (2000).
[4] B. Ruta *et al.*, *Phys Rev Lett.* **109**, 165701 (2012).

OXIDATION-INDUCED NANOSCALE REORGANISATION OF Pt ELECTRODE SURFACES

X-ray scattering was used to elucidate the formation and growth of nanoscale islands on platinum electrodes during cyclic electrochemical oxidation and reduction in acid solutions. Determining this structural evolution is crucial in understanding the factors limiting the performance and longevity of fuel cells that use Pt catalysts.

Platinum is by far the most active element for a number of electrocatalytic reactions and it is the catalyst of choice for hydrogen-oxygen fuel cells for vehicle use. A problem for large-scale commercialisation is that the lifetime and performance are partly limited by the properties of the oxide that forms on the surface. The formation and removal of the oxide promotes dissolution and degradation of the catalyst particles. It is well known that repeated cycles of oxidation and oxide reduction lead to irreversible changes in the electrochemical response, which can be attributed to the formation of nanoscale islands on Pt(111) electrode surfaces (**Figure 54**). However, systematic measurements with surface sensitive techniques, which provide quantitative information on the Pt surface restructuring as a function of electrochemical parameters, were lacking.

In previous *in situ* studies of Pt(111) oxidation in liquid electrolytes by surface X-ray diffraction techniques **[1]**, the locations of the first Pt atoms that move out of their lattice sites in a place-exchange process were determined more precisely than in earlier measurements. Providing the potential is not too high, these atoms can move back to their original locations, but at higher potentials an irreversible restructuring of the surface occurs.

In studies at beamline **ID03**, the nature of this restructuring was investigated by *in situ* grazing-incidence small-angle X-ray scattering (GISAXS), which allowed monitoring of the changes in the nanoscale Pt(111) morphology induced by repeated oxidation and reduction cycles. Perchloric acid was chosen as it does not adsorb on the surface, and the number of cycles and the maximum electrode potential were systematically varied. The detector images, recorded in these GISAXS measurements, reveal characteristic diffuse peaks that grow in intensity with increasing number of potential cycles (**Figure 55a**). The positions and widths of these diffuse peaks provide quantitative information about the size distribution of the nanoscale islands evolving on the surface.

According to these studies, repetitive oxidation and oxide reduction lead to more prominent and homogeneous islands. The characteristic lateral dimensions depend on the upper limit of the cycle and only slightly increase with cycle number (**Figure 55b**). The structural evolution of the Pt

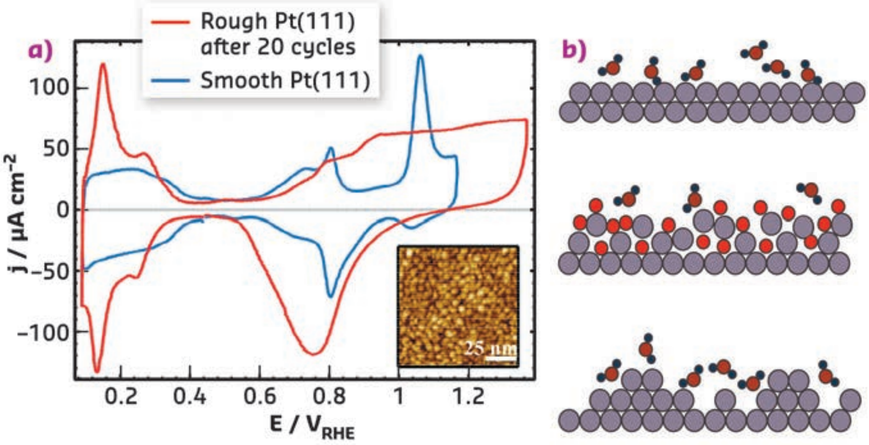

Fig. 54: a) Electrochemical current-voltage curve (cyclic voltammogram) of pristine, atomically smooth Pt(111) in 0.1 M $HClO_4$ (blue line) and of the same electrode after 20 potential cycles to 1.37 V (red line), showing the irreversible changes in the electrochemical response. The inset shows an STM image of Pt(111) after repetitive cycling. b) Schematic illustration of the structural modification induced by oxidation/oxide reduction (bright red: adsorbed O).

surface morphology strongly resembles that found in studies of Pt(111) homoepitaxial growth and ion erosion in ultra-high vacuum. This can be rationalised by considering that each potential cycle generates a population of Pt adatoms and vacancies on the electrode surface. The GISAXS data suggest that the latter obey the same surface dynamic behaviour as under vacuum conditions, resulting in a similar evolution of the nanoscale morphology.

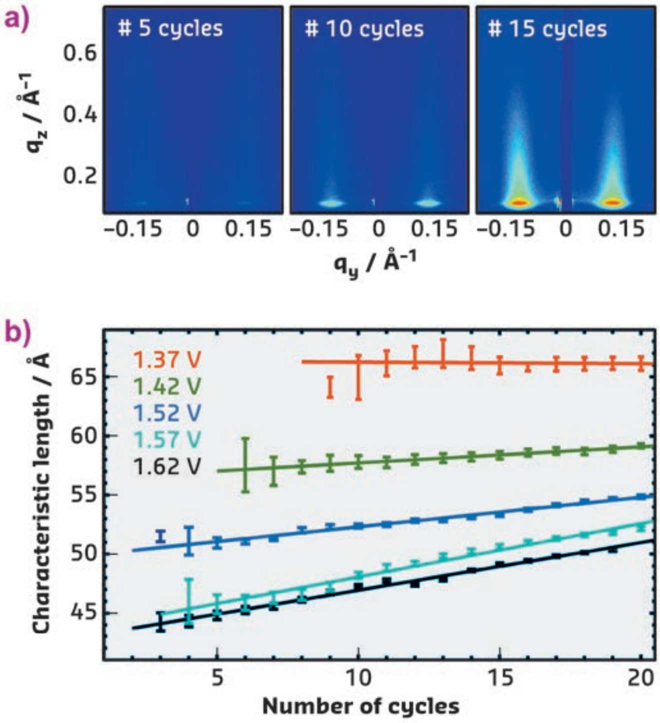

Fig. 55: a) *In situ* GISAXS images show the evolution of diffuse scattering peaks upon repeated cycles to 1.62 V. b) Quantitative studies reveal a gradual evolution of the characteristic lateral dimensions of the nanoscale islands as a function of maximum potential and number of cycles.

This remarkable similarity between the microscopic processes during electrochemical Pt(111) oxidation/reduction and those occurring in growth processes at the metal-vacuum interface is not self-evident at all. In many electrochemical systems, surface dynamic processes such as surface diffusion on terraces and across steps, attachment/detachment at steps, and nucleation strongly depend on the potential and co-adsorbed species. Apparently, these effects do not play a significant role for Pt(111) in a non-specifically adsorbing electrolyte such as perchloric acid. This is of key importance for modelling Pt oxidation, restructuring, and dissolution by *ab initio* theory and molecular dynamics simulations. Here, explicit consideration of the solvent and electrolyte at the electrochemical interface is difficult and currently not feasible for complex processes such as surface transport. The results also suggest that more technologically important cases, such as the oxidation/reduction of Pt nanoparticles, is adequately described without explicit consideration of the electrolyte.

This work shows, for the first time, the detailed quantitative evolution of a Pt surface under oxidation and reduction cycles and it should lead to a better understanding of the dissolution and catalytic degradation processes in fuel cells that are induced by surface oxidation. It also opens up the way for similar studies of oxidation in different electrolytes or of other electrode surfaces as well as for *in operando* GISAXS studies of the potential-dependent morphology during the oxidation and oxide reduction process itself **[2]**.

PRINCIPAL PUBLICATION AND AUTHORS

Structural reorganization of Pt(111) electrodes by electrochemical oxidation and reduction,
M. Ruge (a), J. Drnec (b), B. Rahn (a),
F. Reikowski (a), D.A. Harrington (c), F. Carlà (b),
R. Felici (b), J. Stettner (a) and O.M. Magnussen (a),
J. Am. Chem. Soc. **139**, 4532-4539 (2017);
doi: 10.1021/jacs.7b01039.
(a) Institut für Experimentelle und Angewandte Physik, Christian-Albrechts-Universität zu Kiel (Germany)
(b) ESRF
(c) Department of Chemistry, University of Victoria (Canada)

REFERENCES

[1] J. Drnec *et al., Electrochim. Acta.* **224**, 220-227 (2017).
[2] M. Ruge *et al., J. Electrochem. Soc.* **164**, 608-614 (2017).

REVEALING THE MOLECULAR DETAILS OF SENSOR-HISTIDINE-KINASE REGULATION BY TIME-RESOLVED X-RAY SOLUTION SCATTERING

Time-resolved X-ray solution scattering reveals the conformational changes that occur in the light-responsive histidine kinase YF1 upon blue-light absorption. These experiments provide novel insight into the regulation of the widespread sensor histidine kinases.

Sensor histidine kinases are part of the so-called two-component signalling pathways, and they are the predominant way for bacteria to gather information about their surroundings. The photoreceptor YF1 serves as a paradigm for this protein family. The homodimeric YF1 receptor consists of a blue-light-sensing light-oxygen-voltage (LOV) photosensor, an α-helical coiled-coil linker, and a histidine kinase effector. Time-resolved X-ray solution scattering data were collected at beamline **ID09**, as well as at the Advanced Photon Source and the Swiss Light Source.

Time-resolved solution scattering reports on the global conformational changes following the absorption of light. Such data were collected by exposing the YF1 protein in solution to a blue laser flash and probing the structural change by X-ray scattering at defined time intervals thereafter. The time-evolution of the difference scattering signal could be described by two sequentially populated states. The difference scattering signals arose with a time constant of 2 μs, essentially simultaneous to the formation of the chromophore photoproduct (**Figure 56**). Previous studies had shown that upon photoactivation the LOV photosensor dimer splays apart **[1,2]**. Molecular dynamics simulations were employed to analyse the conformational rearrangements. This structural refinement for full-length YF1 revealed that the separation of the photosensor feeds into the coiled-coil linker as an increase in left-handed supercoiling. A secondary event was observed in the difference scattering data at 250 ms after the laser flash. This event was determined to be an internal reorientation within the histidine kinase effector (**Figure 57**).

In summary, the study has revealed global conformational changes in the form of a rotational movement immediately following the formation of the chromophore photoproduct and a secondary rearrangement within the effector domain. The refined changes account for much of the functional data **[3]** and are in agreement with the emerging views on histidine kinase regulation.

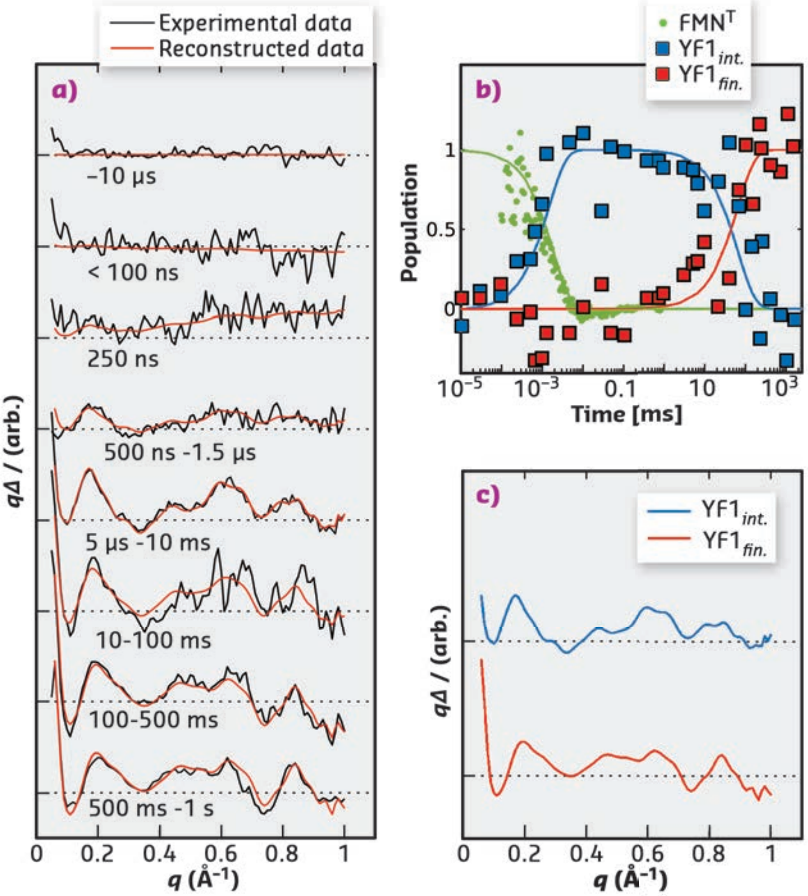

Fig. 56: Time-resolved X-ray solution scattering data (a) can be described by two intermediates following sequential kinetics (b). The time-dependent populations of the intermediates are indicated by squares, and the formation of the photoproduct state as measured by the absorbance at 715 nm is shown in green (b). Time-independent basis spectra are shown in (c).

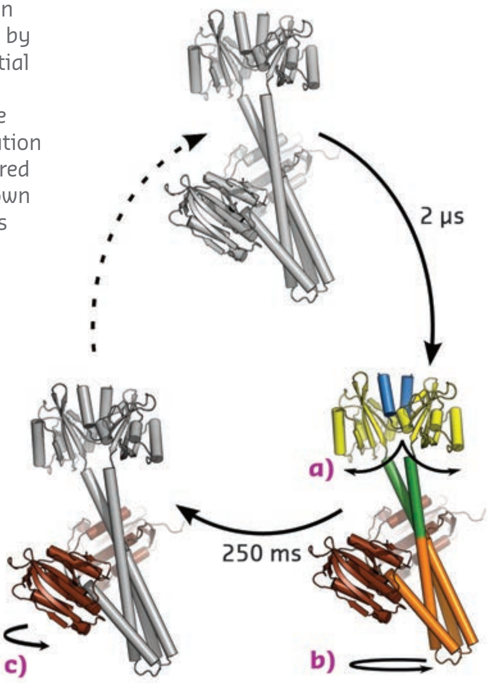

Fig. 57: Structural photocycle of YF1. Blue light causes the formation of a flavin-cysteinyl adduct in the photosensory domain. This prompts the splitting of the LOV photosensor dimer (a), which feeds into the coiled-coil linker region as a left-handed supercoiling 2 μs after photon absorption (b). After 250 ms, the effector rearranges internally as the catalytic/ATP-binding domain changes its positioning relative to the central helices (c).

PRINCIPAL PUBLICATION AND AUTHORS

Sequential conformational transitions and α-helical supercoiling regulate a sensor histidine kinase, O. Berntsson (a), R.P. Diensthuber (b), M.R. Panman (a), A. Björling (a), E. Gustavsson (a), M. Hoernke (a,c), A.J. Hughes (a), L. Henry (a), S. Niebling (a), H. Takala (a,d,e), J.A. Ihalainen (d), G. Newby (f), S. Kerruth (g), J. Heberle (g), M. Liebi (h), A. Menzel (h), R. Henning (i), I. Kosheleva (i), A. Möglich (b,j) and S. Westenhoff (a), *Nat. Commun.* **8**, 284 (2017); doi: 10.1038/s41467-017-00300-5.
(a) University of Gothenburg (Sweden)
(b) Humboldt-Universität zu Berlin (Germany)
(c) Albert-Ludwigs-Universität Freiburg (Germany)
(d) University of Jyväskylä (Finland)
(e) University of Helsinki (Finland)
(f) ESRF
(g) Freie Universität Berlin (Germany)
(h) Paul Scherrer Institut, Villigen (Switzerland)
(i) The University of Chicago (USA)
(j) Universität Bayreuth (Germany)

REFERENCES

[1] C. Engelhard *et al.*, *Sci. Reports* **7**, 1385 (2017).
[2] O. Berntsson *et al.*, *Structure* **25**, 933-938 (2017).
[3] R. Ohlendorf *et al.*, *ACS Synth Biol.* **5**, 1117-1126 (2016).

REVEALING THE INTERPLAY BETWEEN STRUCTURE AND ELECTRONIC COUPLING IN DONOR/ACCEPTOR SYSTEMS FOR ORGANIC PHOTOVOLTAICS

A comprehensive study on the charge-transfer effect in small-molecule organic semiconductor thin films has been performed. Using a combination of structural and optical methods, it was established that strong intermolecular coupling in molecular co-crystals results in new electronic properties, in particular a strong anisotropic charge-transfer transition.

One of the fundamental processes in devices based on organic semiconductors such as organic solar cells and organic light-emitting diodes is charge-transfer (CT) between electron donor (D) and electron acceptor (A) molecules at interfaces or in molecular mixed systems. A and D form a CT complex, where the energy levels of the ground and excited states depend on the overlap of the D/A wave functions, and the electronic transition to the excited state is accompanied by partial or integer charge transfer. An important question for the efficiency is the anisotropy of the CT state, *i.e.* differences in the electronic coupling in-plane *vs.* out-of-plane. The present study addresses this by complementary use of structural and spectroscopic tools. The key to success was the careful preparation of the different layer sequences and compositions, with high-precision characterisation at beamline **ID10** using surface X-ray scattering (grazing-incidence X-ray diffraction (GIXD) and reflectivity (XRR), see **Figure 58**).

Two perylene derivatives, DIP and PDIR-CN$_2$, were found to be an excellent model system to study CT effects in organic semiconductors. Three different architectures were chosen: a planar heterojunction (PHJ), a two-component mixed bulk-heterojunction film (BHJ) with different mixing ratios, and a superlattice (SL) consisting of 20 alternating monolayers as an intermediate case. The two compounds were characterised regarding structural organisation of the molecules during simultaneous or consecutive growth by organic molecular beam deposition (OMBD), as this is crucial for the formation of D/A interfaces. The result demonstrates a high miscibility between DIP and PDIR-CN$_2$ molecules, leading to the formation of a new mixed phase polymorph. Apparent changes in lattice parameters show the reorientation of D and A molecules thus creating face-to-face stacking with molecular planes parallel to each other. Despite weak crystallinity in the in-plane direction, mixed films in the absence of phase separation exhibit preferential D/A stacking, which is expected to enable CT state formation in this direction.

Spectroscopic methods were used for the characterisation of the electronic coupling (**Figure 59**). In **Figure 59a** a new emission band, emerging around 1.4 eV, was assigned to radiative recombination processes from the charge-transfer state between DIP and PDIR-CN$_2$ molecules apparently accompanied by enhanced non-radiative recombination, that was

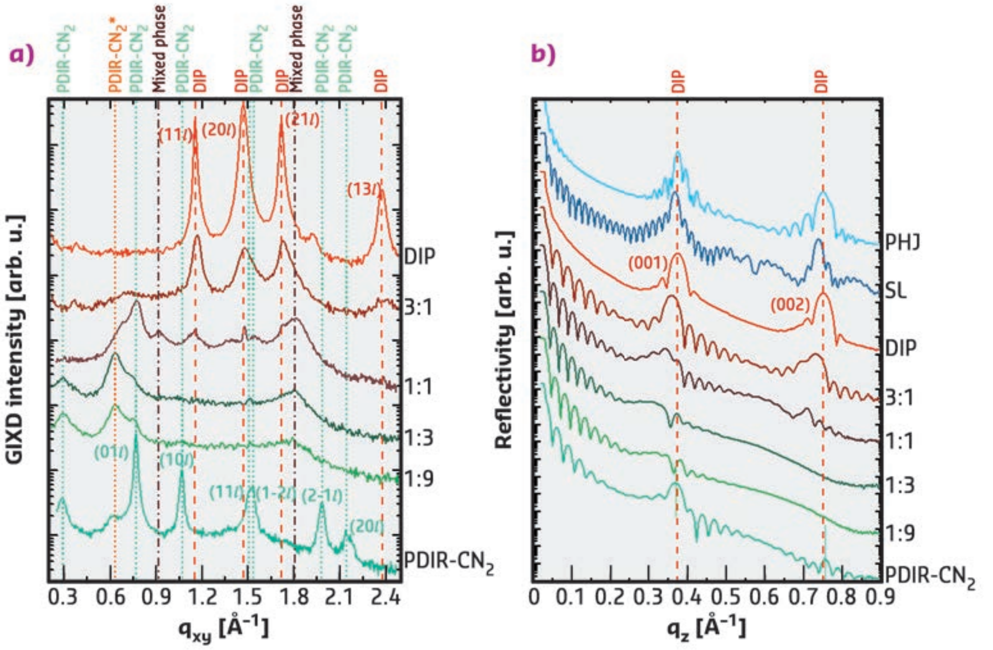

Fig. 58: a) GIXD data and b) XRR data allow the mixed phase formation to be observed. All spectra are vertically offset for clarity.

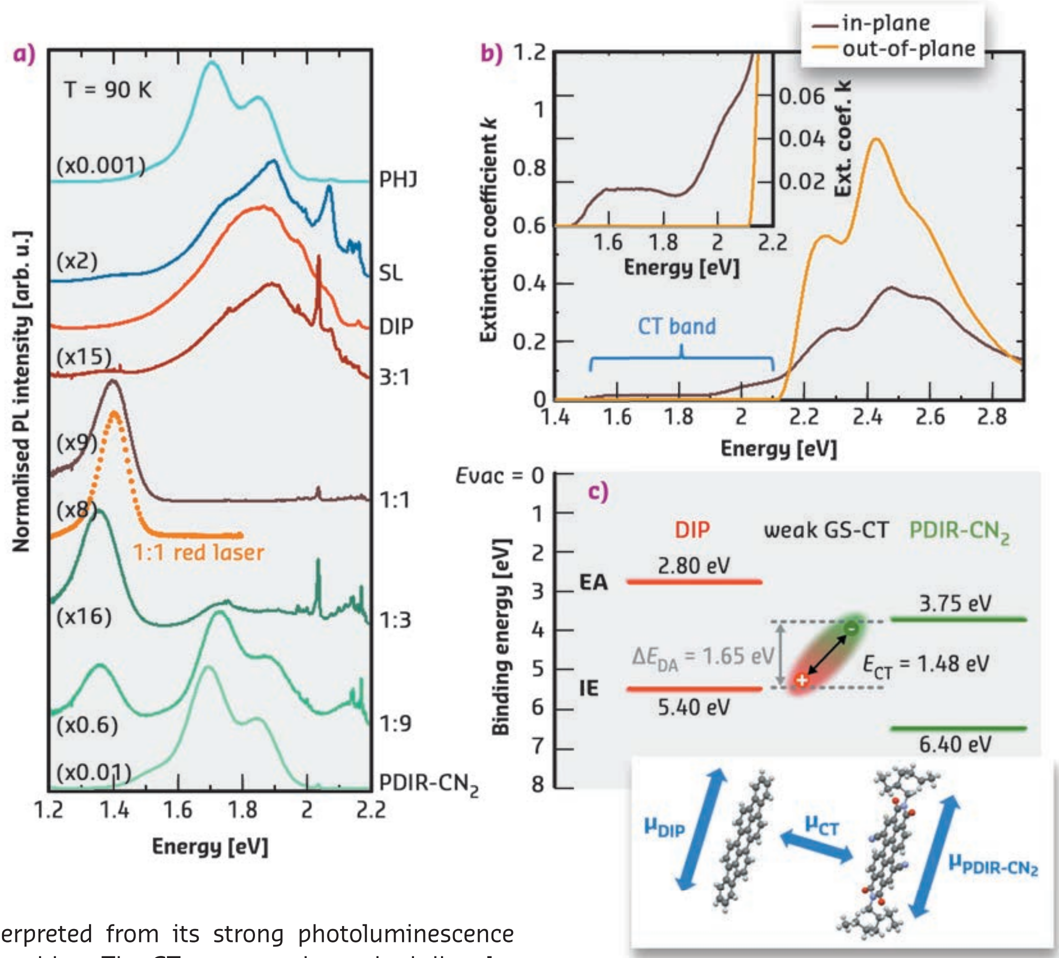

Fig. 59: a) Photoluminescence spectra. b) Anisotropic components of the extinction coefficient of the 1:1 film. The inset zooms into the range of 1.4–2.2 eV. c) Schematic energy-level diagram for the mixture DIP/PDIR-CN$_2$ (top) and orientations of transition dipole moments (bottom).

interpreted from its strong photoluminescence quenching. The CT state can be excited directly, avoiding transfer from higher-energy molecular excitons, confirmed by using a red laser. Regarding the layered samples, the PHJ exhibits strong emission dominated mainly by PDIR-CN$_2$ excitonic recombination. Emission of the SL contains features of both components, and only weak emission features from the CT states can be observed.

The absorption spectrum of the equimolar mixed film clearly reveals a broad band at photon energies below the optical gaps of the pristine materials (1.5–2.1 eV, **Figure 59b**), which originates from direct excitation of CT states. From the overlap of the absorption and emission spectra, the dominant CT state energy can be deduced. The energy-level diagram of the resulting CT complex is depicted in **Figure 59c**, where the energy gap ΔE_{DA} and the CT state energy give a CT exciton binding energy of about 0.2 eV. Spectroscopic ellipsometry allows the two anisotropic components of a 1:1 film to be distinguished as the CT band is only visible in the in-plane direction, which is the direction of the π–π interaction. Intermolecular D/A interactions are directly related to the overlap of their frontier orbitals, which is maximal in π–π stacking or face-to-face geometry (perpendicular to the molecular backbones). Therefore, the presented CT is stronger in mixed films, where molecule reorientation facilitates orbital overlap, in contrast to planar interfaces (PHJ and SL) with almost exclusively edge-on-edge stacking. The anisotropic character of the electronic transition to the excited CT state polarised in the in-plane direction is sketched in **Figure 59c** (bottom). Thus, π–π stacking is a prerequisite for efficient intermolecular coupling, while the strong intermolecular interaction itself seems to play a role as one of the driving forces for molecular (re) arrangement.

PRINCIPAL PUBLICATION AND AUTHORS

Evidence for anisotropic electronic coupling of charge transfer states in weakly interacting organic semiconductor mixtures, V. Belova (a), P. Beyer (b), E. Meister (c), T. Linderl (c), M.U. Halbich (d), M. Gerhard (d), S, Schmidt (c), T. Zechel (c), T. Meisel (b), A.V. Generalov (e), A. S. Anselmo (f), R. Scholz (h), O. Konovalov (g), A. Gerlach (a), M. Koch (d), A. Hinderhofer (a), A. Opitz (b), W. Brütting (c) and F. Schreiber (a), *J. Am. Chem. Soc.* **139**, 8474-8486 (2017); doi: 10.1021/jacs.7b01622.
(a) Institut für Angewandte Physik, Universität Tübingen (Germany)
(b) Department of Physics, Humboldt-Universität zu Berlin (Germany)
(c) Institute of Physics, Experimental Physics IV, University of Augsburg (Germany)
(d) Faculty of Physics and Material Sciences Center, Philipps-Universität Marburg (Germany)
(e) Max IV Laboratory, Lund University (Sweden)
(f) Helmholtz-Zentrum Berlin für Materialien und Energie GmbH, Berlin (Germany)
(h) Dresden Integrated Center for Applied Physics and Photonic Materials (IAPP), Technische Universität Dresden (Germany)
(g) ESRF

VIRUS-LIKE CAPSIDS FROM THE LATTICE ASSEMBLY OF NON-PEPTIDE SMALL MOLECULES

The lattice of cyclodextrin complexes self-assembles into a variety of capsid-like structures such as lamellae, helical tubes, and hollow rhombic dodecahedra. In particular, the resemblance to virus capsids goes beyond morphology and extends to structural rigidity and crystallinity – a well-defined, universal, 2D rhombic lattice of molecular arrangement.

All living organisms are self-assembled entities where two major kinds of self-assembly are involved. One is the assembly of lipids into soft, fluidic membranes mainly driven by the hydrophobic interaction. The lipid assembly is extensively reproduced and well extended by synthetic amphiphilic small molecules, polymers, and even nanoparticles to form lamellar, tubular, vesicular, and micellar structures (**Figure 60a**). The other kind is the assembly of proteins into rigid, crystalline structures driven by a combination of hydrophobic, H-bonding and electrostatic interactions. For example, virus capsids are rigid protein shells often in helical or icosahedral structures. The protein assembly that produces crystalline structures (**Figure 60b**) such as lamellae, tubules, and polyhedra is, however, largely unparalleled by synthetic or non-peptide molecules with a few notable exceptions. Looking beyond biomimetic self-assembly, one can notice that carbon allotropes share the same morphological pattern: graphite, graphene, nanotubes, and C_{60} in analogy to lamellar, tubular, and polyhedral assemblies. In this context, what has been gradually recognised is the importance of intermolecular interactions, structural flexibility/rigidity, and fluidity/crystallinity over that of morphology. A few building blocks were reported to successfully mimic protein assemblies' morphologies but cannot rival their rigidity nor well-defined crystallinity.

Seeking a synthetic system that parallels the morphology, rigidity, and crystallinity of protein assemblies or virus capsids, it was decided to study a supramolecular complex, SDS@2β-CD (one sodium dodecyl sulfate molecule inside two β-cyclodextrin molecules, **Figure 60c**). This work reports the lattice self-assembly of SDS@2β-CD into a variety of capsid-like structures such as lamellae, helical tubes, and hollow rhombic dodecahedra. The dodecahedral morphology has not hitherto been observed in self-assembly systems. The tubes can spontaneously encapsulate colloidal particles and liposomes. The dodecahedra and tubes are respectively comparable to – and much larger than – the largest known virus. In particular, the resemblance to protein assemblies is not limited to morphology but extends to structural rigidity and crystallinity – a well-defined, 2D rhombic lattice of molecular arrangement is strikingly universal for all the observed structures.

Critical to determining the capsid-like structures and molecular arrangements are the X-ray results obtained on the DUBBLE SAXS/WAXS beamline **BM26B**. The SAXS curves (**Figure 61a**) feature equally spaced, lamellar peaks that gradually vanish upon the dilution of SDS@2β-CD, indicating the increase of layer-to-layer distance and the lessening of layers in a stack. The scattering curves up to 4 nm^{-1} were fitted by a bilayer form factor and lamellar structure factor (**Figure 61b**). The corresponding electron density profile suggests a bilayer arrangement of SDS@2β-CD with its long axis perpendicular to the layer (**Figure 61c**). The scenario of a multilamellar tube diffracting X-rays is

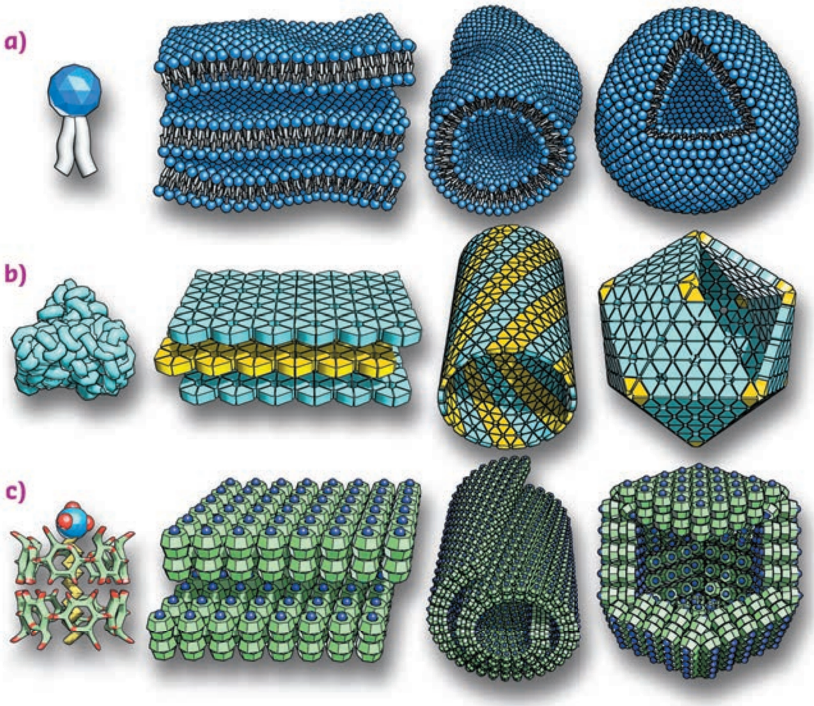

Fig. 60: Stylised view of the self-assembly of lipids, proteins, and cyclodextrin complexes.
a) Lipid molecules form lamellar, tubular, and vesicular structures, the flexibility and fluidity of which are emphasised. b) Proteins form lamellar, helical tubular, and regular icosahedral structures with rigidity and hexagonal crystallinity. c) SDS@2β-CD assembles with inherent rigidity and in-plane, rhombic crystalline nature.

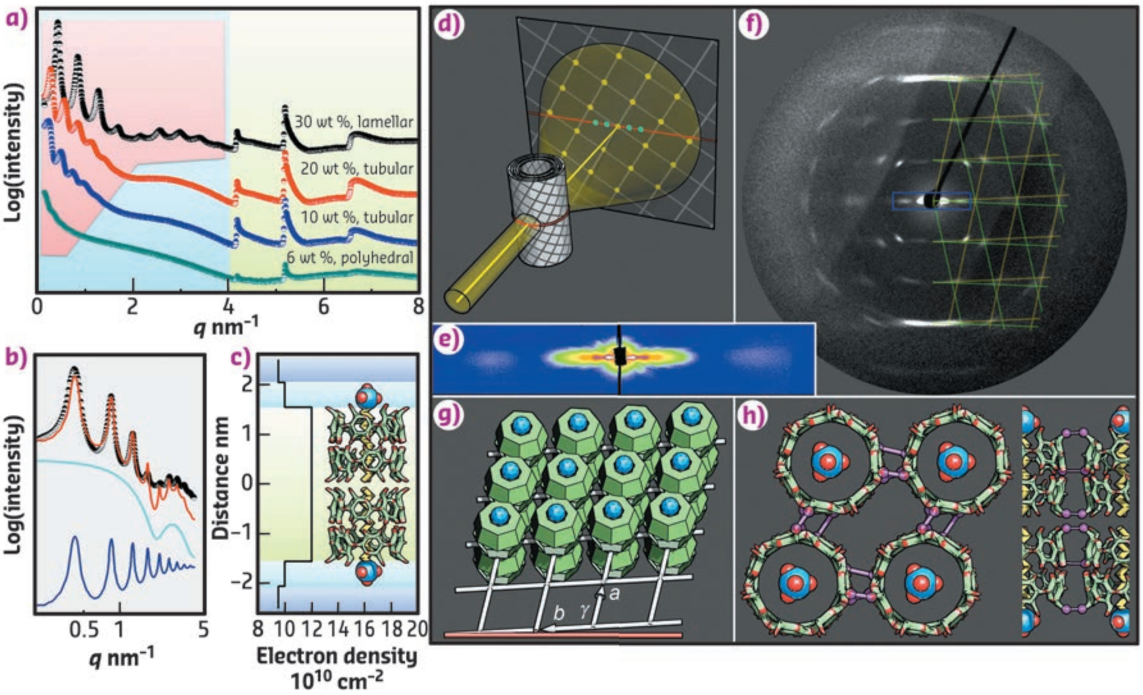

Fig. 61: X-ray scattering of the SDS@2β-CD structures.
a) SAXS curves of the lamellar, tubular, and polyhedral phases with different SDS@2β-CD concentrations.
b) The SAXS curve up to 4 nm^{-1} is fitted by a bilayer form factor (cyan line) and lamellar structure factor (blue line) with a good result (red line). c) The electron density profile across the bilayer. d) A scheme of WAXS of aligned multilamellar tubes with in-plane crystallinity.
e) Scattering pattern along the equator at small angle, corresponding to the blue box in f. f) Scattering pattern at large angle is super-positioned by the yellow and green grids.
g) The in-plane lattice.
h) Top and side views of the SDS@2β-CD lattice, highlighting the possible, inter-CD H-bonds (magenta).

schematically illustrated in **Figure 61d**. In line with this scenario, a few lamellar peaks and a broad form factor peak are located on the equator at small q (**Figure 61e**), while a well-defined diffraction pattern is observed at large q (**Figure 61f**). The pattern's symmetry along the equator and medial axis signifies a helical nature for the tubes. The pattern is perfectly matched by two mirrored lattices (green and yellow grids). The in-plane unit cell is thus resolved as a rhombus with $a = b = 1.52$ nm (comparable to β-CD diameter, 1.5 nm) and $\gamma = 104°$.

PRINCIPAL PUBLICATION AND AUTHORS

Giant capsids from lattice self-assembly of cyclodextrin complexes, S. Yang (a), Y. Yun (b), J. Huang (b), A.V. Petukhov (c, d), L.M.J. Kroon-Batenburg (c), M. Drechsler (e), C. Zhou (b), M. Tu (a), S. Granick (f) and L. Jiang (a), *Nat. Commun* **8,** 15856 (2017); doi:10.1038/ncomms15856.
(a) Jinan University, Guangzhou (China)
(b) Peking University, Beijing (China)
(c) Utrecht University, Utrecht (The Netherlands)
(d) Eindhoven University of Technology, Eindhoven (The Netherlands)
(e) University of Bayreuth, Bayreuth (Germany)
(f) Institute for Basic Science, Ulsan (Republic of Korea)

VELOCITY FLUCTUATIONS DURING PARTICLE SEDIMENTATION PROBED BY MULTISPECKLE XPCS

Settling of suspensions under the influence of gravity is an everyday experience. It is widely exploited in industrial separation processes as well as involved in geological formations. Ultra-small-angle XPCS provides new insight about the early stage of sedimentation.

Sedimentation at the colloidal scale has been extensively investigated for more than a century **[1]**. It has been identified as a powerful method for probing the interactions and dynamics in particulate suspensions **[2]**. A sedimenting suspension is an out-of-equilibrium system and many puzzles in its dynamics remain unresolved **[1]**. A particular case is when thermally driven Brownian motion is comparable to gravity-induced flow, which corresponds to the Peclet number (*Pe*) ≈ 1. If there are only a few independent particles in the suspension, their sedimentation velocity is given by the well-known Stokes law. However, in a suspension with finite concentration, the hydrodynamic back flow causes a reduction of the sedimentation velocity ($\langle V \rangle$) from the Stokes velocity. Fluctuations in the local particle number density lead to a variance in the sedimentation speed that may diverge up to the smallest container dimension **[3]**.

Nevertheless, the gravity-induced stratification may preclude observation of a divergence of velocity fluctuations **[1, 4]**. The stratification effects can be delayed by several hours using Brownian particles (*Pe* < 1). Then it becomes experimentally challenging to separate

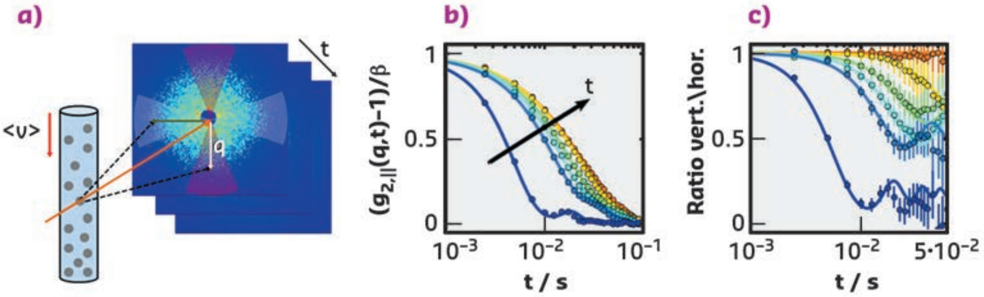

Fig. 62: a) Schematic representation of sedimentation and the scattering geometry used for multispeckle XPCS. b) Typical intensity autocorrelation functions as a function of elapsed time parallel to the sedimentation direction. c) The ratio of vertical and horizontal functions displaying the purely advective contribution and corresponding temporal evolution.

contributions of gravity-induced advective and thermal diffusive motions. Multispeckle ultra-small-angle X-ray photon correlation spectroscopy (USA-XPCS) was used at beamline **ID02** to probe the gradual transition of dynamics in suspensions of charge-stabilised Brownian particles prior to the onset of macroscopic sedimentation front. A key advantage of multispeckle XPCS is that it allows a direction-dependent analysis of the dynamics (*e.g.,* the gravity-induced advective motions along the vertical direction). The ultra-small-angle range provides access to the pertinent length scales.

Figure 62 shows the experimental scheme and typical intensity autocorrelation functions measured along the vertical direction parallel to the sedimentation. The periodic modulation in the autocorrelation function is a signature of the well-defined advective motions that dominate colloid dynamics during early stages of sedimentation. With elapsing time, these periodic modulations become indistinct, corresponding to a decay of advective currents and eventually diffusive motions become the dominating contribution in the dynamics.

Measured XPCS correlation functions can be modelled by taking into account the Doppler shifts caused by all particle pairs in the scattering volume in terms of a relatively simple velocity distribution (**Figure 62b**). The decay of the XPCS correlation function is particularly sensitive to relative velocity fluctuations and the different scattering vector (***q***) dependence permits the separation of advective contribution (linear in ***q***) from conventional diffusive part (quadratic in ***q***) as shown in **Figure 62c**. These velocity fluctuations decay over the first hour of the experiment, then measured correlation functions along vertical and horizontal directions become identical. This corresponds to the velocity fluctuations not only slowing down but also decreasing in their overall extent, *i.e.* the breakup of flow structures over time. This change of dynamic behaviour occurs on a much shorter timescale (minutes) than the appearance of the macroscopic sedimentation front (several hours). **Figure 63a** displays the sensitivity of the initial conditions on the decay of velocity fluctuations (V_{fluc}) along the height of the capillary prior to the onset of macroscopic sedimentation front. Nevertheless, once normalised by the initial V_{fluc} and the characteristic decay time (τ), all data superimpose on an exponential master curve as depicted in **Figure 63b**. A similar exponential time decay of velocity fluctuations has been observed in non-Brownian systems over larger size scales that is attributed to the concentration stratification effect mentioned above **[4]**. However, a different mechanism operates in the case of Brownian particles, likely due to the stronger coupling between advective and diffusive motions.

In summary, multispeckle USA-XPCS enabled probing velocity fluctuations over micrometre scales in colloidal sedimentation at low *Pe* regime (< 1). Well-defined advective motions are manifested as oscillations in the measured intensity autocorrelation functions that can be quantitatively described by a simple model involving velocity fluctuations around a mean sedimentation velocity. When compared to non-Brownian particles, timescales of macroscopic sedimentation and exponential decay of microscopic velocity fluctuations are well separated in the low *Pe* range. This study illustrates new capabilities offered by multi-speckle USA-XPCS to probe faster out-of-equilibrium processes in colloidal systems. Applications include self-driven active colloids and particles in a strong external flow.

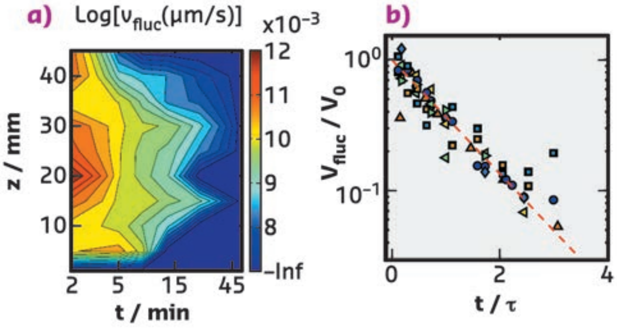

Fig. 63: a) Temporal decay of velocity fluctuations (V_{fluc}) along the height of sedimentation column (z). b) Normalised V_{fluc} (to the initial value, V_0) as a function of reduced time (with τ the characteristic decay time of velocity fluctuations) for different z and colloid concentrations.

PRINCIPAL PUBLICATION AND AUTHORS

Velocity fluctuations in sedimenting Brownian particles, J. Möller (a,b) and T. Narayanan (a), *Phys. Rev. Lett.* **118**, 198001 (2017); doi: 10.1103/PhysRevLett.118.198001.

(a) ESRF
(b) Present address: European XFEL Facility, Schenefeld (Germany)

REFERENCES

[1] S. Ramaswamy, *Adv. Phys.* **50**, 297-341 (2001).
[2] R. Piazza, *Rep. Prog. Phys.* **77**, 056602 (2014).
[3] R.E. Caflisch and J.H. Luke, *Phys. Fluids* **28**, 759 (1985).
[4] S.-Y. Tee *et al., Phys. Rev. Lett.* **89**, 054501 (2002).

ULTRA-FAST CONTROL OF NANOSCALE DEFORMATIONS IN SOLIDS

The spatio-temporal coherent control of thermal excitations in solids has been demonstrated by intersecting a sequence of optical pulses on a sample surface. Deformation control can be employed for strain-induced applications in modern nanostructures.

Density changes in the crystal lattice of nanostructures lead to modifications of physical properties, *e.g.,* band gap energy, magnetic anisotropies or electrical conductivity. Such density variations are generally described by lattice vibrations, so-called acoustic phonons that occur as incoherent or coherent superposition of modes. The former corresponds to a finite lattice temperature while the latter describes a sound wave with specific propagation speed and wave vector. Ultra-short laser pulses can generate coherent acoustic phonons on nanosecond length and picosecond timescales. Thus, they are ideal excitations for functionalisation of nanoscale systems.

At **ID19**, a new experimental method is presented that allows for full spatio-temporal control of the deformation, comprising both coherent acoustic sound waves and the incoherent thermal background. Using time-resolved X-ray reflectivity (TR-XRR), the absolute deformation amplitude *u(t)* of the surface is monitored with sub-Angstrom spatial and 100 ps temporal resolution.

As an example, a periodic surface modulation is generated by intersecting two femtosecond laser pulses that interfere on the sample surface. The sample is heated by the laser in the interference maxima and remains at the initial temperature in regions of destructive interference of the two pump pulses. On top of the thermal expansion, a surface modulation is generated by propagating surface sound waves, which are triggered by the impulsive optical excitation.

The excursion at the surface is measured by TR-XRR as depicted in **Figure 64a**. Based on the experimental data in **Figure 64b**, a quadratic dependence of the 1st order diffracted X-ray intensity *I(t)* and the square of surface amplitude *u(t)* was derived, thus allowing for an absolute measurement of the deformation. Directly after

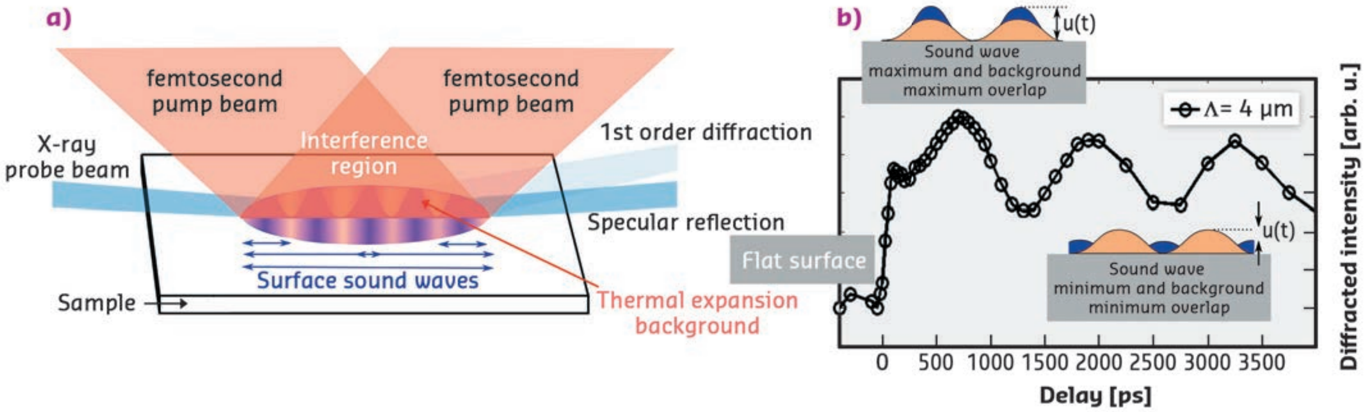

Fig. 64: a) Generation of a periodic surface modulation *u(t)* by intersecting two femtosecond laser pulses and probing by time-resolved X-ray reflectivity (TR-XRR). b) Intensity of the first diffraction order vs. time. The initial rise denotes the thermal background, the oscillation stems from propagating sound waves at the sample surface.

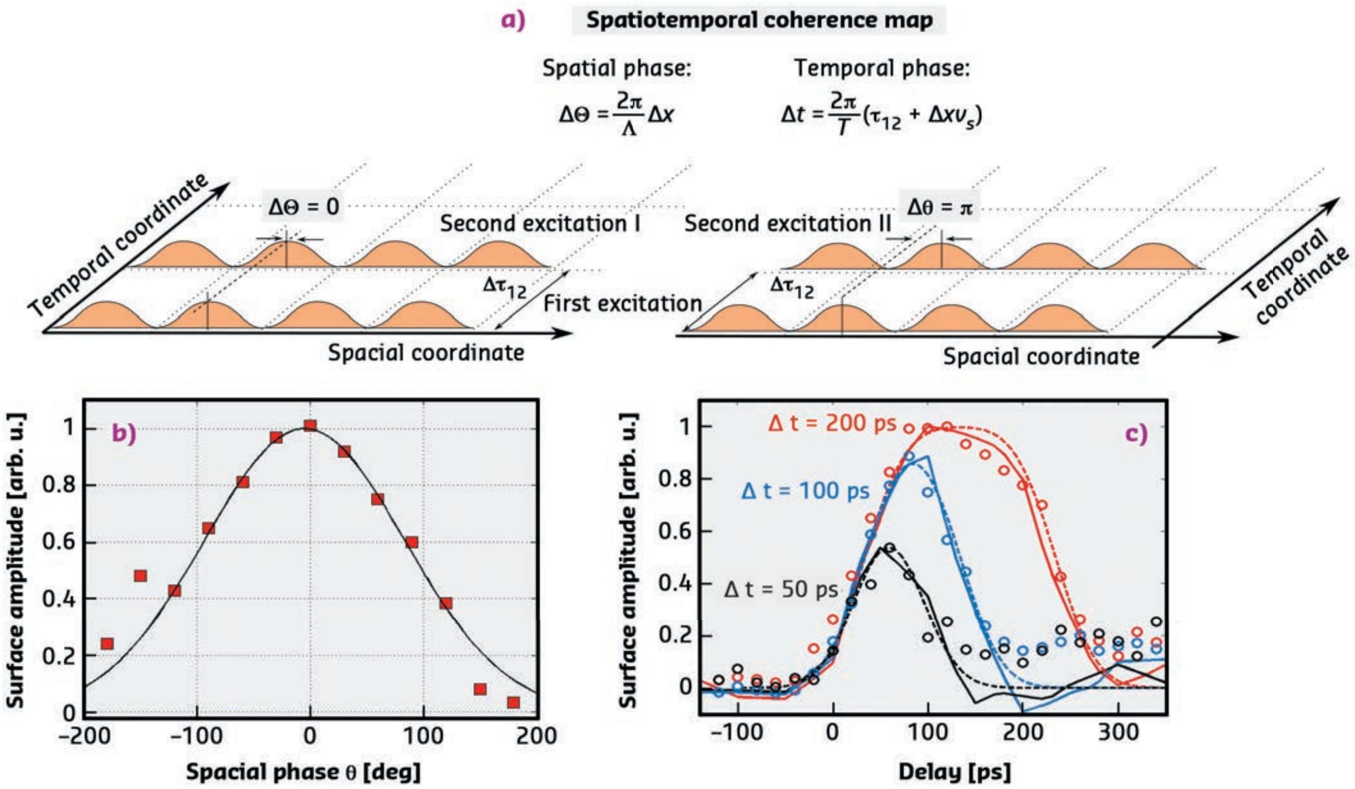

Fig. 65: a) Spatio-temporal coherence map for a spatial phase of $\Delta\theta = 0$ (left) and $\Delta\theta = \theta$ (right). b) and c) variation of the spatial and temporal phase, respectively.

the optical excitation, the diffracted intensity from the initially flat surface exhibits a step-like increase and subsequent oscillations. The oscillations stem from the modulation of the thermal background (orange) by propagating sound waves (blue) as depicted in the inset of **Figure 64b**.

To demonstrate spatio-temporal strain control, the temporal and spatial coherence is exploited as explained in **Figure 65a**. A temporal sequence of excitation pulses is employed to control the amplitude of the sound wave at the sample surface. The incoherent thermal background is controlled via the spatial periodicity of the optical excitation. The first excitation defines spatial and temporal phase. A second excitation is either spatially in phase, as in **Figure 65a** (I), or out of phase (II). Only (II) removes the thermal grating, while (I) always amplifies the thermal background. However, both excitations may remove the coherent sound waves, depending on the relative temporal phase of the second excitation.

The experimental results are shown in **Figure 65b** and **Figure 65c**. The left panel depicts the variation of the spatial phase $\Delta\theta$ in the range 0 – 2π, while the temporal phase is at $\Delta t \approx 0$. Variation of the spatial phase controls the diffracted 1st order intensity. Variation of the temporal phase Δt is shown in **Figure 65c** while the spatial phase remains $\Delta\theta = \pi$. In particular, this measurement shows that thermal background and coherent excitation are suppressed by the second excitation.

The data is the first demonstration of controlling the thermal and coherent strain in a nanostructure by a sequence of light pulses. Practical applications include employing surface deformations as control mechanisms for active X-ray optics. For example, the data in **Figure 65c** shows a switchable mirror that could be exploited as pulse picker or beam splitter in synchrotron applications. Other applications are generation and control of strain-induced processes in solid state magnetism, quantum computing or catalysis.

PRINCIPAL PUBLICATION AND AUTHORS

Spatiotemporal Coherent Control of Thermal Excitations in Solids, M. Sander (a), M. Herzog (a), J.E. Pudell (a), M. Bargheer (a, b), N. Weinkauf (c), M. Pedersen (d), G. Newby (d), J. Sellmann (e), J. Schwarzkopf (e), V. Besse (f), V.V. Temnov (f, g) and P. Gaal (b, c), *Phys. Rev. Lett.* **119**, 075901 (2017);
doi: 10.1103/PhysRevLett.119.075901.

(a) Institute for Physics and Astronomy, Universität Potsdam (Germany)
(b) Helmholtz-Zentrum Berlin for Materials and Energy GmbH, Berlin (Germany)
(c) Institute for Solid State and Nanostructure Physics, Universität Hamburg (Germany)
(d) ESRF
(e) Institute for Crystal Growth, Berlin (Germany)
(f) IMMM CNRS 6283, Université du Maine, Le Mans (France)
(g) Groupe d'Etude de la Matière Condensée (GEMaC), Université de Versailles-Saint Quentin en Yvelines, CNRS UMR 8635, Université Paris-Saclay, Versailles (France)

IN VIVO PERMEABILITY INCREASE OF BRAIN TUMOUR VESSELS INDUCED BY SYNCHROTRON MICROBEAM RADIATION THERAPY

Synchrotron microbeam radiotherapy (MRT), a spatially fractionated preclinical radiotherapy, is more efficient than broad beam irradiation (BB) at opening the blood-brain barrier of all regions of intracranial rodent glioblastomas and it might be used to obtain a better efficacy of adjuvant chemotherapy than with homogeneous radiation fields used in conventional radiotherapy.

The efficiency of blood-borne chemotherapies is hampered by a limited exposure of all the cells in the tumour mass to a sufficient drug concentration due to the anatomic/physiologic characteristics of solid tumours **[1]**. Exposure to conventional radiotherapy is known to enhance the permeability of brain tumour vessels. Microbeam radiation therapy (MRT), developed on **ID17**, might enhance vessel permeability specifically in tumours before drug

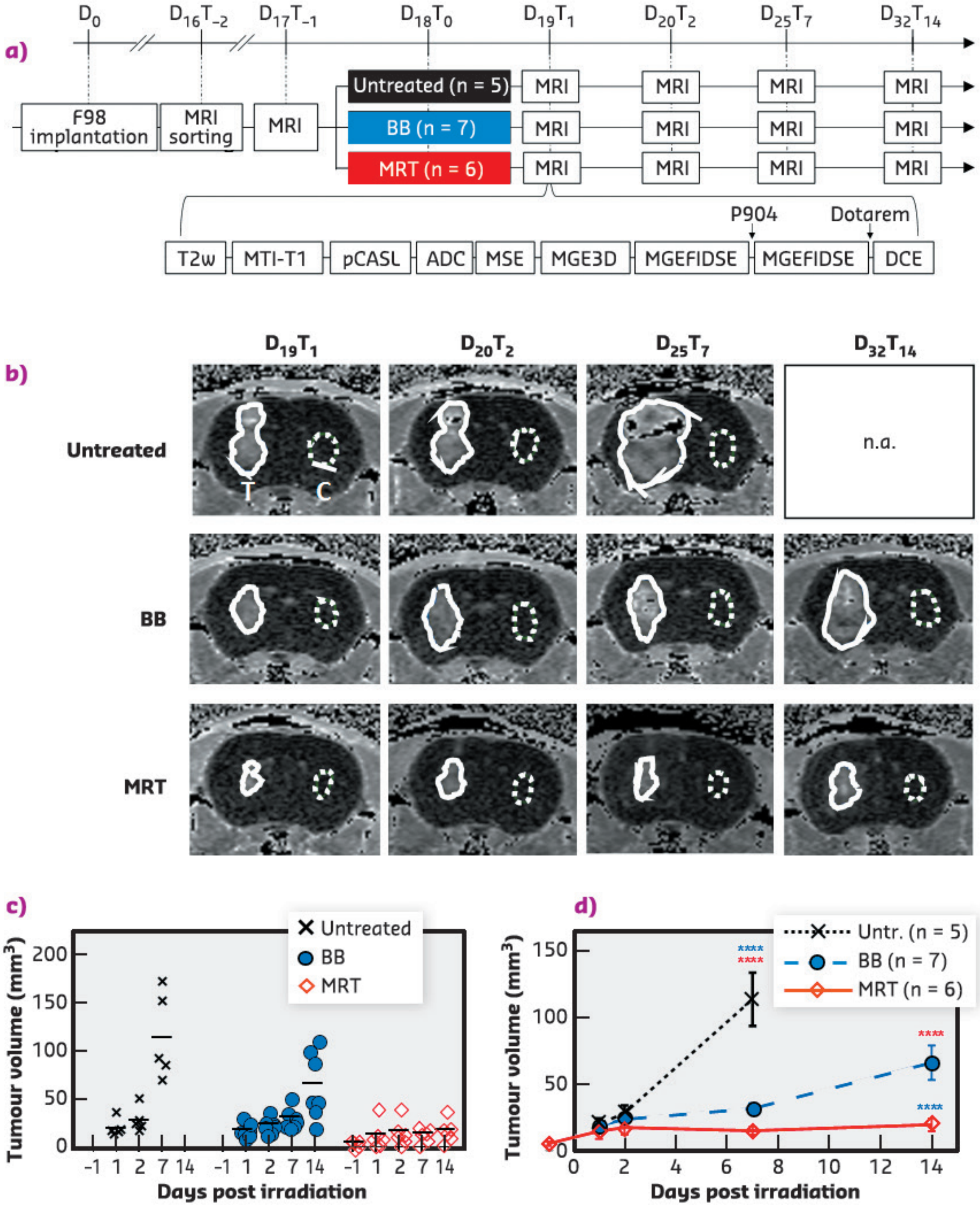

Fig. 66: a) Experimental timeline and diagram representing MRI sequences acquired for each animal at each time point. BB = Broad synchrotron X-ray beam; MRT = Microbeam Radiation Therapy. b) Tumour volume evolution after treatment. MRI follow-up, DCE-enhancement map of an untreated, BB- or MRT-treated F98-bearing rat at different delays after implantation. Solid and dotted lines delineate the tumour and the contralateral ROI, respectively. c) Individual values (plots) and means (lines) and d) means ± SEM tumour volumes measured on DCE-enhancement map at different delays after tumour irradiation for untreated (black), BB- (blue) or MRT-treated animals (red). ****: $p < 0.0001$.

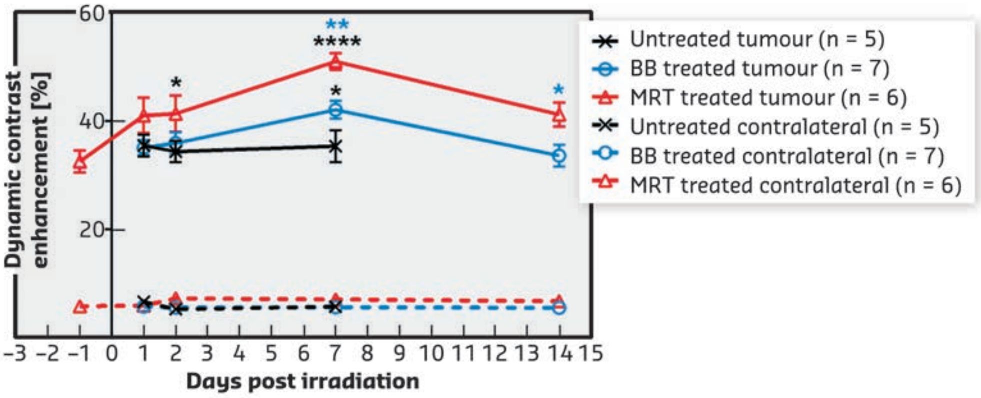

Fig. 67: Vessel permeability. Dynamic contrast enhancement (DCE) after Gd-DOTA injection measured by MRI in the F98 tumour (solid lines) and normal brain tissue in the contralateral hemisphere (dashed lines) at different times after BB- (blue) or MRT- (red) or no treatment (black). Mean ± SEM. ∗: $p < 0.05$; ∗∗: $p < 0.01$; ∗∗∗∗: $p < 0.0001$.

administration **[2,3]**. This study compares the blood-tumour barrier permeability changes induced by MRT (relying on spatial fractionation of the incident X-ray beam into parallel micron-wide beams), with a spatially non-fractionated radiotherapy.

Male rats bearing intracranial highly malignant F98 gliomas were randomised into three groups: untreated, or exposed to synchrotron microbeams (width 50 µm, 200 µm on-centre spacing, peak and valley dose: 241 and 10.5 Gy respectively) or to broad beam irradiation (BB) delivered at comparable doses (*i.e.* equivalent to MRT valley dose); both applied by two arrays, intersecting orthogonally in the tumour region. Vessel permeability was monitored *in vivo* by multiparametric magnetic resonance imaging (MRI) as previously described **[4]** one day before and one, two, seven and 14 days after treatment start. To find out whether physiological parameters influence vascular permeability, the vessel integrity has been evaluated with different cerebral blood flow, blood volume, oedema and tissue oxygenation values.

Both radiotherapy modes significantly slowed tumour growth but MRT reduced tumour growth more than BB irradiation did, *i.e.* tumours were 3.4 times smaller at $D_{32}T_{14}$ (19.5 ± 11.7 mm^3) after MRT than after BB (65.9 ± 34.2 mm^3, $p < 0.0001$) (**Figure 66**). MRT leads to a significantly higher, earlier and more continuous increase in tumour blood vessel permeability than homogeneous BB irradiation, without affecting healthy tissue (**Figure 67**). In addition, the study of permeability changes in different areas of the tumour characterised by oedema, blood volume, cerebral blood flow or tissue oxygenation revealed that MRT induces an increase in vascular permeability in all tumour areas, including those tumour areas not impacted by homogeneous irradiation. Finally, it was shown that MRT is more efficient at disrupting brain tumour vessels in the most actively proliferating area of the tumour considered as the relevant target area for adjuvant drug delivery.

High-dose microbeams could be used to facilitate the delivery of intravenously injected drugs to tumour tissue. Therefore, adjuvant chemotherapy might be more effective when coupled with MRT than with homogeneous radiation fields used in conventional radiotherapy.

PRINCIPAL PUBLICATION AND AUTHORS

Permeability of Brain Tumor Vessels Induced by Uniform or Spatially Microfractionated Synchrotron Radiation Therapies, A. Bouchet (a), M. Potez (b), N. Coquery (c), C. Rome (c), B. Lemasson (c), E. Bräuer-Krisch (d), C. Rémy (c), J. Laissue (e), E.L. Barbier (c), V. Djonov (a) and R. Serduc (b), *Int J Radiat Oncol Biol Phys.* **98**, 1174-1182 (2017);
doi: 10.1016/j.ijrobp.2017.03.025.

(a) Group Topographic and Clinical Anatomy, Institute of Anatomy, University of Bern (Switzerland)
(b) Rayonnement synchrotron et Recherche médicale, Université Grenoble Alpes (France)
(c) Team Functional NeuroImaging and Brain Perfusion, INSERM U1216, La Tronche, Institut des Neurosciences, Université Grenoble Alpes, La Tronche (France)
(d) ESRF
(e) University of Bern (Switzerland)

REFERENCES

[1] H. Holback and Y. Yeo, *Pharm Res.* **28**, 1819-1830 (2011).
[2] A. Bouchet *et al., Int J Rad Oncol Biol Phys.* **78**, 1503-1512 (2010).
[3] A. Bouchet *et al., Phys Med.* **31**, 634-641 (2015).
[4] B. Lemasson *et al., NMR Biomed.* **28**, 1163-1173 (2015).

3D QUANTIFICATION OF VASCULAR AND NEURONAL ALTERATIONS IN A MULTIPLE SCLEROSIS MODEL

X-ray phase-contrast tomography has been applied for the first time at micro- to nanoscales, with simultaneous imaging of vascular and neuronal networks, to obtain unprecedented direct 3D characterisation of the neuropathology in experimental autoimmune encephalomyelitis, the animal model for multiple sclerosis, and of the effect of mesenchymal stem cell treatment on tissue damage.

Multiple sclerosis is an autoimmune disease of the central nervous system associated with demyelination, axonal damage and neuronal loss resulting in neurological deficits. The use of appropriate animal models such as experimental autoimmune encephalomyelitis (EAE) facilitates the study of disease mechanisms and the development of new therapeutic approaches for multiple sclerosis.

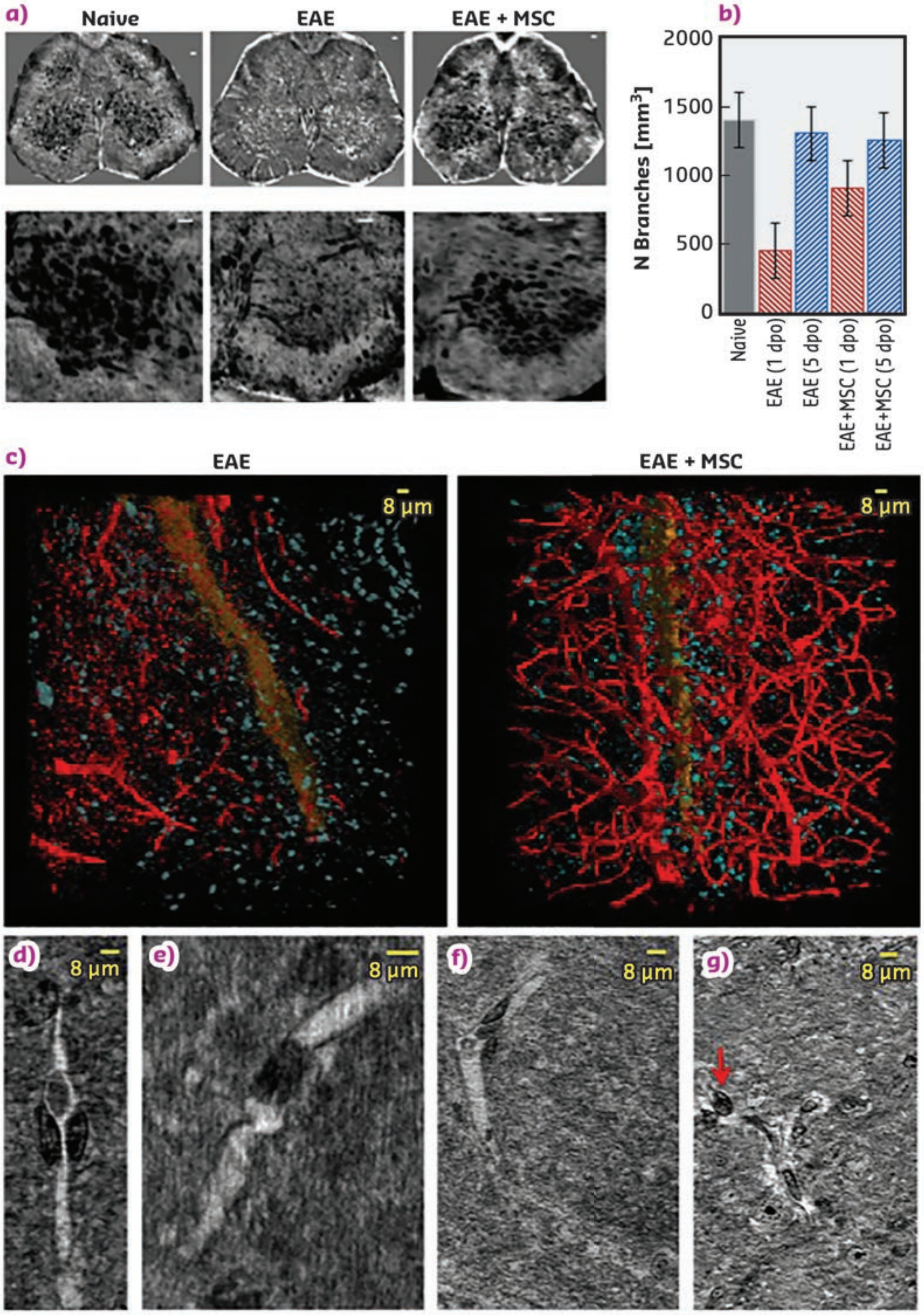

Fig. 68: Vascular alterations in EAE redeemed through MSC treatment. a) Axial projections of XPCT images of spinal cord in naive, EAE-affected, and EAE-affected MSC-treated mice. Lower panels show segmentation of the vasculature (black) of the respective upper-panels. b) Quantification of the number of vessel-branches in lumbar spinal cord at one and five days post disease onset. c) Nano-XPCT volume renderings of the capillary network (red) and cell population (blue) in spinal cord of untreated and MSC-treated EAE-affected mice at five days post disease onset. The spinal canal is rendered in orange. Nano-tomography slices of capillary alterations in EAE (d-g).

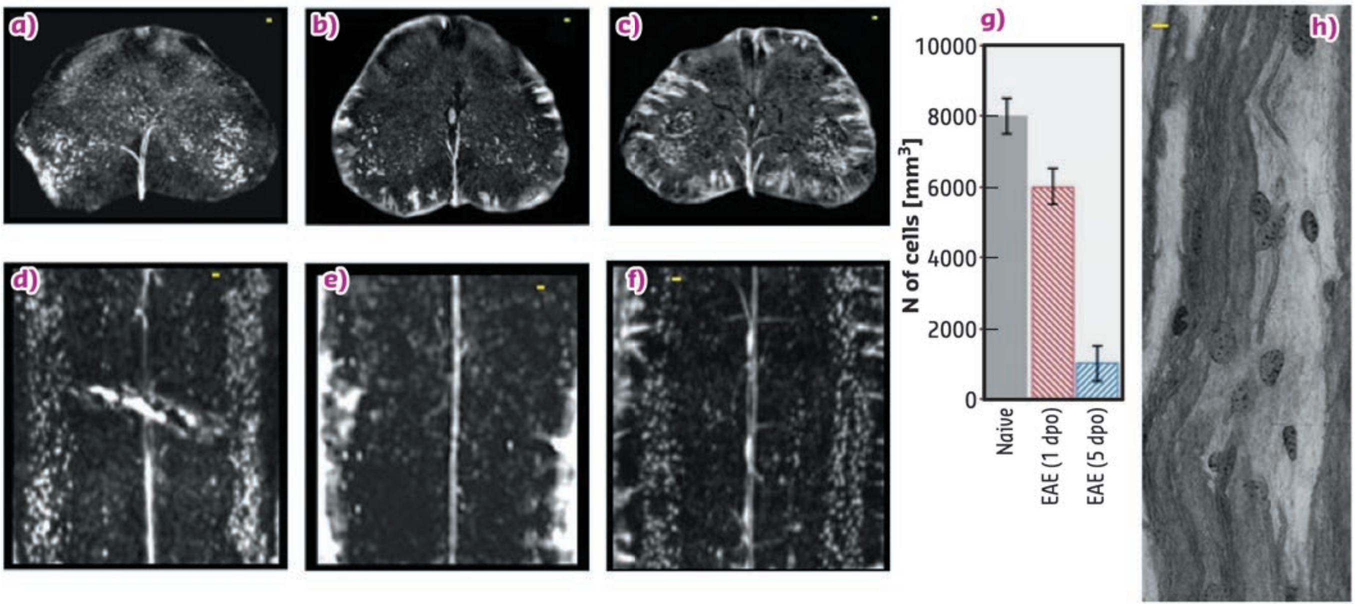

Fig. 69: Effect of MSC treatment on the altered neuronal network in EAE (a-g), scale-bar 20 µm. Nano-XPCT (scale-bar 8 µm) of myelin damage in EAE (h).

Techniques previously used to investigate damage to vascular and neuronal networks in EAE suffer from several limitations. In particular, 2D imaging restricts spatial coverage, entails destructive sample preparation, and may lead to data misinterpretation due to lack of information in the third dimension. In contrast, recent work **[1]** on naïve mouse central nervous systems demonstrated that imaging by X-ray phase-contrast tomography (XPCT) enables the study of the 3D distribution of both the vasculature and single elements of the neuronal network, without sample sectioning and specific sample preparation.

Here, multiscale XPCT images have been generated to evaluate morphological alterations in vascular and neuronal networks at relevant disease phases of EAE in affected mice and to understand how treatment with mesenchymal stem cells (MSC) modifies them. A direct 3D morphological description of EAE lesions is provided at both vascular and neuronal levels at two different length scales. Micro-XPCT was performed at beamline **ID17**, giving a 3D quantitative analysis of the vasculature and of the neurons of the entire lumbar part of the spinal cord with spatial resolution of about 7 microns (voxel size of 3.5 micron), one day and five days post disease onset, without any staining procedure. Nano-XPCT was then performed at **ID16A** to investigate the 3D capillary network and nerve fibres in a region of about 300 x 300 x 70 mm^3 with voxel size of 130 nm.

Such a multi-scale direct analysis has never been performed to understand EAE pathology and address the effect of an innovative therapeutic strategy.

Vascular alterations have been described in EAE and multiple sclerosis, and analysis indicates that vasculature density is clearly decreased at disease onset in EAE-affected mice, a decrease not observed upon treatment with MSC (**Figure 68**), suggesting a protective effect of MSC on spinal cord vasculature. Most importantly, the XPCT study revealed an alteration of the capillary network in EAE (**Figure 68**) that had not been previously described. Thus, the results strongly indicate a trend in alteration of the 10-24 micron vessels and possible occlusions in the capillaries, an observation never obtained in tissue without the use of a contrast agent. Importantly, 3D analysis demonstrated that MSC administration reduces vascular alteration of vessels.

Simultaneous 3D XPCT imaging of neuronal alterations during EAE (**Figure 69**) supports the findings **[2]** of a massive loss of lower motor neurons in multiple sclerosis patients and in mouse EAE from early disease stages, with evidence of apoptotic neuronal death. The data suggest that the angiogenesis detected at the acute phase of EAE, by 2D immunohistochemical analysis of tissue slices, is in fact not efficient, and that the massive loss of neurons observed reflects the demonstration of pyknotic neurons in EAE observed by 2D techniques.

Through XPCT, never applied before to investigate multiple sclerosis models, crucial information not obtainable with other techniques has been derived, which can be used to further study disease evolution, as well as to optimise advanced new therapies and monitor their efficacy.

PRINCIPAL PUBLICATION AND AUTHORS

X-ray phase contrast tomography reveals vascular alterations and neuronal loss in a multiple sclerosis model, A. Cedola (a), A. Bravin (b), I. Bukreeva (a), M. Fratini (a, c), A. Pacureanu (b), A. Mittone (b), L. Massimi (a), P. Cloetens (b), P. Coan (b, d), G. Campi (e), R. Spanò (f), F. Brun (a), V. Grigoryev (g), V. Petrosino (h), C. Venturi (h), M. Mastrogiacomo (f), N. Kerlero de Rosbo (f) and A. Uccelli (f), *Sci. Rep.* **7**, 5890 (2017); doi: 10.1038/s41598-017-06251-7.

(a) Nanotec-CNR, Rome (Italy)
(b) ESRF
(c) Santa Lucia Foundation, Rome (Italy)
(d) Ludwig-Maximilians-Universität, München (Germany)
(e) IC-CNR, Rome (Italy)
(f) Department of Experimental Medicine, University of Genoa, Genoa (Italy)
(g) MEPhI, Moscow (Russia)
(h) DINOGMI, University of Genoa, Genoa (Italy)

REFERENCES

[1] M. Fratini *et al. Sci Rep.* **5**, 8514 (2015).
[2] J. Vogt *et al. Ann Neurol.* **66**, 310-322 (2009).

X-RAY NANOPROBE

In 2017, imaging with nanobeams has seen an increase in the portfolio of techniques made available to users. This has been supplied both by an incremental improvement of existing techniques, making them more user-friendly to non-experts, and by the extension of available sample environments, allowing for new *in situ* or *operando* experiments. It can also be noted that important investments in new detectors and data handling strategies have had a positive impact on the acquisition rate and quality offered by the XNP beamlines.

On beamline **ID01**, a software tool for easy online data analysis of scanning diffraction data has been developed by the ESRF Data Analysis unit, allowing users to treat terabytes of data during their stay – and even during measurements – and to receive optimised feedback. This is of great utility in the perspective of higher data rates enabled by the implementation of a 2 Megapixel detector developed by the ESRF in collaboration with the PSI in Switzerland. It can record scanning data at several hundred Hz and will be able to follow acquisition rates of up to 10 kHz in the future. Furthermore, the last elements of the ID01 beamline upgrade were put into operation in 2017. A KB mirror setup, operational between 7 and 11 keV, as well as between 19 and 21 keV, supplies beams of 150 x 250 nm^2 with photon fluxes of up to 10^{11} ph/s and an energy resolution between 10^{-4} and $3{*}10^{-3}$. Full field diffraction microscopy is now offered as a new technique on ID01, the first end-station offering this technique to users.

To enable scanning micro-diffraction and micro-SAXS/WAXS with energy variation at **ID13**, a sub-micron beam (150x300 nm^2) produced by a fixed curvature KB mirror has been integrated into the beamline's microbranch in collaboration with the ESRF Optics group (R. Barrett *et al.*). It serves as an alternative focusing optics to the existing Be-CRL transfocator. The system has already been used for several very successful user experiments, mostly investigating texture effects in biomineralised or bioinspired samples. In addition, this optics has been employed for promising first tests aiming at 3D SAXS tomography with micron resolution. First successful tests of a nanobeam-compatible, *in situ* wedge-indentation sample environment have been performed in collaboration with Kubec, Keckes *et al.* (MI-1216 long-term proposal). This setup is designed to be used in transmission on thin hard condensed matter or polymer specimens. It is expected to be available for ID13 users in the second part of 2018. A second high-performance computer dedicated to online data analysis of large EIGER 4M data volumes is scheduled to be operational from the beginning of next year.

At the nanoimaging beamline **ID16A**, X-ray nanotomography is now routinely used in fluorescence, holography and ptychography mode, both at room temperature and under cryogenic conditions. All techniques exploit an intense nanofocus with a sub-13 nm size – the smallest worldwide – at a high energy of 33.6 keV. X-ray ptychography was sped up significantly at the level of acquisition and processing: software enhancements now provide optimal scanning paths and faster GPU-based reconstruction, while a GaAs pixel detector achieves lowest dose at high spatial resolution. Several studies combine the nanoimaging capabilities of the beamline with complementary techniques at other ESRF beamlines such as ID13, ID17 and ID19, or exploit correlative soft and hard X-ray microscopy. There is an increasing demand for cryo-imaging. A majority of the accepted proposals during the last round aims at imaging frozen-hydrated biological samples. This configuration has been optimised to avoid parasitic fluorescence background from the cryogenic environment. Finally, from next year on, cryo-correlative light and X-ray microscopy will complement the workflow.

The optimisation of beamline **ID16B** has been started in order to take full advantage of the future EBS. In this respect, a new seven-element XRF detector has recently been installed and tested, providing unprecedented count rate capabilities. Moreover, a new KB mirror system optimised for XAS measurements is ready to be implemented in the experimental set-up and will undoubtedly improve the beamline capabilities. *In situ/operando* experiments are now routinely performed at **ID16B**, involving most techniques available at the beamline (XRF, XRD, XEOL,XBIC, nanotomography) and many different sample environments such as high-pressure cells, furnaces, electrochemical cells, *operando* batteries, electrically connected nanowires, *etc*. After miniaturisation to fit with severe spatial constraints, more and more sophisticated environments (such as a tensile testing machine within a HT furnace) can be integrated to investigate complex dynamical phenomena by fast nanotomography.

At **ID21**, the refurbishment of the scanning X-ray microscope has started. The ultimate goal is to provide a smaller and more stable beam (~100 nm), over an extended energy range (2-11 keV), and faster XRF and XANES acquisitions. User friendliness and cryo-microscopy, which are important strengths at **ID21**, will be maintained and further developed. During a four-month shutdown (December 2017 – March 2018), the first two optics hutches will be almost emptied, and later re-equipped with new instruments, in particular a new pair of mirrors for harmonic rejection, new slits and beam viewers. Later in 2018, the first prototype of the new double crystal monochromator, specially designed for spectroscopy, will be installed and commissioned. As an unfortunate side-effect, the infrared end-station had to be definitively shut down, and the diffraction end-station will be temporarily unavailable until the refurbishment of the experiment hutch. However, some beam time will be preserved for user operation in 2018 on the scanning X-ray microscope.

T. SCHÜLLI

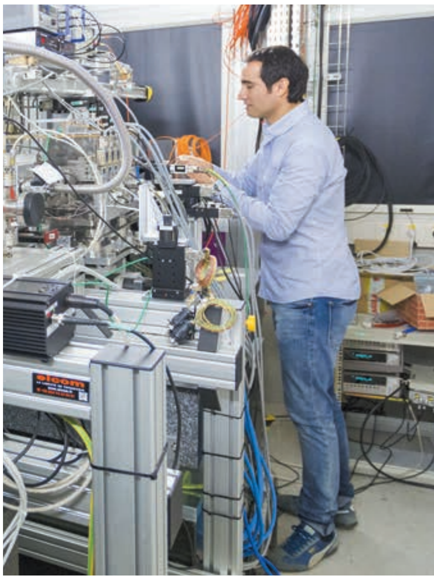

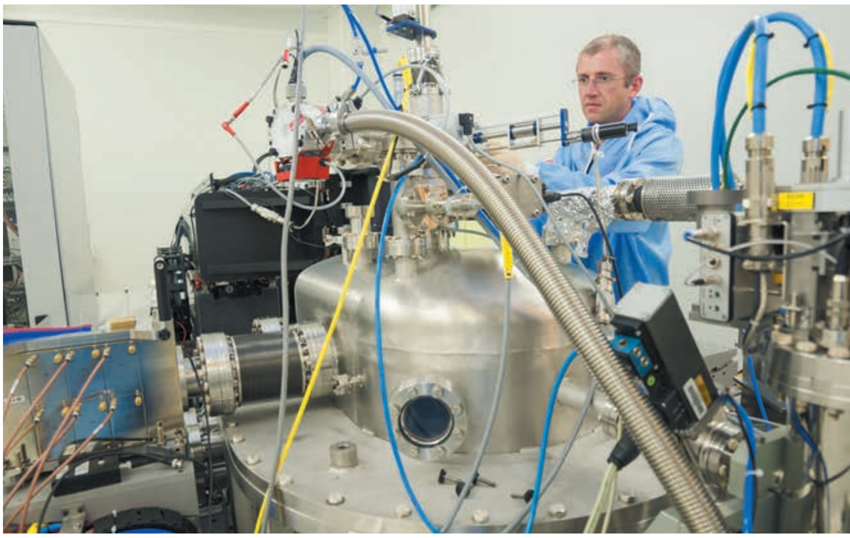

THE COMPLEX CRYSTALLINE STRUCTURE OF AN OYSTER SHELL

Biomineralisation processes produce outstandingly complex mineralised structures in living organisms. New structural features of a paradigmatic calcareous biomineral have been revealed by 3D Bragg ptychography, an X-ray microscopy method. This provides a better understanding of biomineralisation and supports recent biomineralisation models.

In many living organisms, biomineralisation processes regulate the production of the mineralised tissues such as bones, teeth and shells. Deciphering these mechanisms is of crucial importance for materials science, as it will provide bio-inspired strategies for the synthesis of nanostructured inorganic materials using soft chemistry and environmentally friendly processes. Such understanding is also important for paleoclimatology where biomineral proxies are used to perform paleoclimate reconstructions. The calcium carbonate biomineral is one of the most striking examples because theories arising from classical crystallisation (involving monomer-by-monomer addition) cannot explain the production of highly regulated calcareous crystalline biomineral structures such as those observed in sea urchin or pearl oyster. The production of this major constituent of the Earth's crust is still poorly understood.

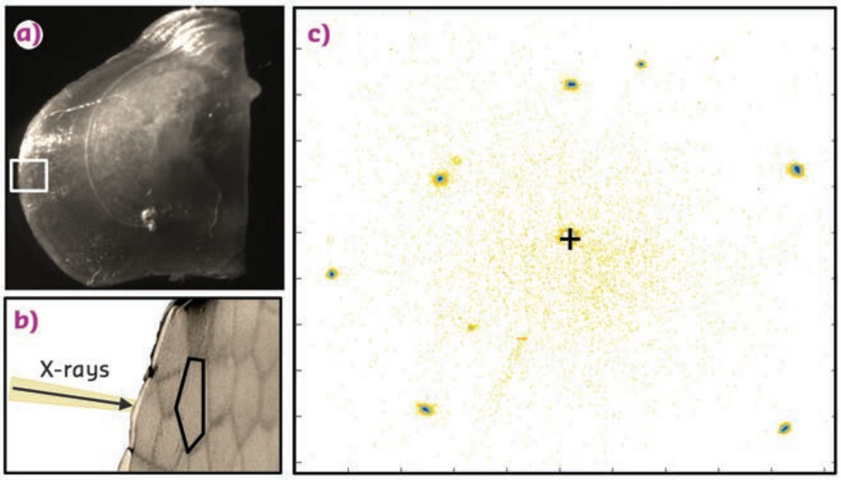

Fig. 70: a) The pearl oyster shell (*Pinctada margaritifera*) and the investigated region (white rectangle). b) Enlarged view of the shell border showing the microscopic structure of the shell constituted of calcite prisms. c) X-ray Bragg diffraction pattern acquired with the ID13 X-ray nanobeam and integrated over the full prism area. The single-crystalline behaviour of the shell produces well-defined Bragg diffraction spots.

The present study was motivated by an apparent contradiction observed in biomineral structures: while calcareous crystallising species present a remarkable architectural diversity at the macro- and microscales, their sub-micrometric scale is characterised by a granular, but crystalline, structure **[1]**. Hence, a proper description of the crystalline features at this mesoscale level, *i.e.*, over a few sub-micrometric (50-500 nm) granules, is a key to building realistic scenarios of biomineralisation. However, none of the currently used experimental approaches (electron- or X-ray-based diffraction microscopies) is able to provide access to the detailed 3D crystalline granule arrangement.

In 2011, a new approach, named Bragg ptychography, was proposed to image the crystalline properties of complex materials in 3D **[2]**. This microscopy method exploits the partially redundant information obtained by scanning a finite-size beam spot transversally to the sample, while measuring the corresponding 3D far-field intensity coherent diffraction pattern in the vicinity of a Bragg reflection. The 3D structure of the crystalline sample is further retrieved by inversion algorithms, which deliver a highly resolved image beyond the limit imposed by the size of the beam spot.

This cutting-edge synchrotron-based X-ray microscopy method was implemented at beamline **ID13** **[3]** and used to reveal the details

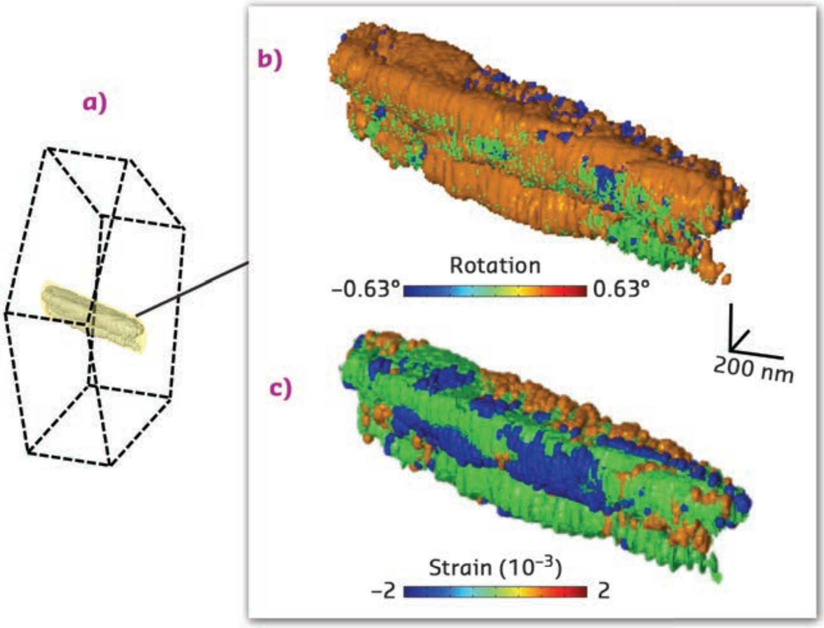

Fig. 71: Results of the 3D Bragg ptychography microscopy reconstruction. a) The retrieved volume (in yellow-grey) represents a small portion of the prism volume. b) 3D rotation and c) strain maps, showing the existence of crystalline domains within the single-crystalline-like biomineral.

of the mesocrystalline organisation in calcite prisms, the generic mineral units of the pearl oyster shell (**Figure 70**). While these prisms are usually described as single crystals, the 3D image proves the existence of large iso-oriented and iso-strained crystalline domains, slightly different one from the other (**Figure 71**). These original results call for specific non-classical crystallisation pathways: the highlighted mesocrystalline properties support recent biomineralisation models, involving the partial fusion of oriented attached primary crystalline nanoparticles **[4]** or the formation of micrometric domains arising from liquid droplet precursors, successively transformed into an amorphous and then crystalline material **[5]**.

With the unique properties of the forthcoming upgraded ESRF source combined to the new (and fast) Bragg ptychography microscopy **[6]**, the fine details of the biomineralisation processes will be soon within reach.

PRINCIPAL PUBLICATION AND AUTHORS

Revealing crystalline domains in a mollusc shell “single-crystalline” prism, F. Mastropietro (a), P. Godard (a), M. Burghammer (b), C. Chevallard (c), J. Daillant (d), J. Duboisset (a), M. Allain (a), P. Guenoun (c), J. Nouet (e) and V. Chamard (a), *Nature Materials* **16**, 946-952 (2017); doi: 10.1038/NMAT4937.
(a) Aix-Marseille Univ, CNRS, Centrale Marseille, Institut Fresnel, Marseille (France)
(b) ESRF, Grenoble (France)
(c) NIMBE, CEA, CNRS, Université Paris-Saclay, Gif-sur-Yvette (France)
(d) Synchrotron SOLEIL, Gif-sur-Yvette (France)
(e) GEOPS, Univ. Paris-Sud, CNRS, Université Paris-Saclay, Orsay (France)

REFERENCES

[1] Y. Dauphin, J. Biol. Chem. **278**, 15138 (2003); Y. Dauphin, Mineral. Mag. **71**, 247 (2008).
[2] P. Godard *et al.*, *Nature Communications* **2,** 568 (2011).
[3] V. Chamard *et al.*, *Scientific Reports* **5** 9827 (2015); A. Pateras *et al.*, *Physical Review B* **92**, 205306 (2015).
[4] A.-W. Xu *et al.*, J. Mater. Chem. **17**, 415 (2007).
[5] M. A. Bewernitz *et al.*, Faraday Discuss. **159**, 291 (2012).
[6] S.O. Hruszkewycz, *et al.*, *Nature Materials* **16**, 244 (2017).

BIOCHEMISTRY OF THE MALARIA PARASITE BY X-RAY MICROSCOPY

The distribution and concentration of chemical elements associated with heme detoxification were mapped using combined hard X-ray cryo fluorescence microscopy and soft X-ray cryo tomography study of rapidly frozen malaria parasites. These studies aim to discover ways to sabotage the detoxification of heme accumulated in the malaria parasite during its consumption of hemoglobin.

Malaria in humans is caused by the parasite *Plasmodium falciparum*. The parasite, injected by an *Anopheles* mosquito, travels the liver where it multiplies, producing thousands of new parasites. The next generation of parasites enters the blood stream and invades red blood cells, where they feed on hemoglobin (Hgb) in order to grow and multiply. After creating up to 20 new parasites, the red blood cell bursts, releasing the daughter parasites ready for new invasions. This life cycle leads to an exponential growth of the infected RBCs that may cause the death of the human host.

The aim of the research described here was to identify mechanisms critical for the parasite’s survival, thereby providing an intelligent basis for the development of drugs to interrupt the exponential growth of the infection. One such mechanism is the detoxification of heme, an iron-containing molecule that is released into the parasite upon hemoglobin degradation. The parasite neutralises heme by turning it into harmless hemozoin crystals that are built from heme dimers. Therefore, heme dimerisation and the subsequent crystallisation of the heme dimers are obvious goals for detailed experimental investigation.

Advanced X-ray methods have been used to investigate the parasite-infected red blood cells **[1-3]**. In the present study, a combination of hard X-ray cryo fluorescence microscopy at beamline **ID16A** and soft X-ray cryo tomography at MISTRAL/ALBA was used. The infected red blood cell is immobilised by rapid cooling to 80 K, leaving the intracellular water in an amorphous, so-called vitrified state. The cryo-temperature also essentially eliminates radiation damage. The tomography is based on absorption contrast just like CT scanning at a hospital, but the sample diameter is that of a single cell, about 5 micrometres in diameter. The X-ray energy was chosen to be between the absorption edges of carbon and oxygen (510 eV), rendering the vitreous ice essentially transparent, while the

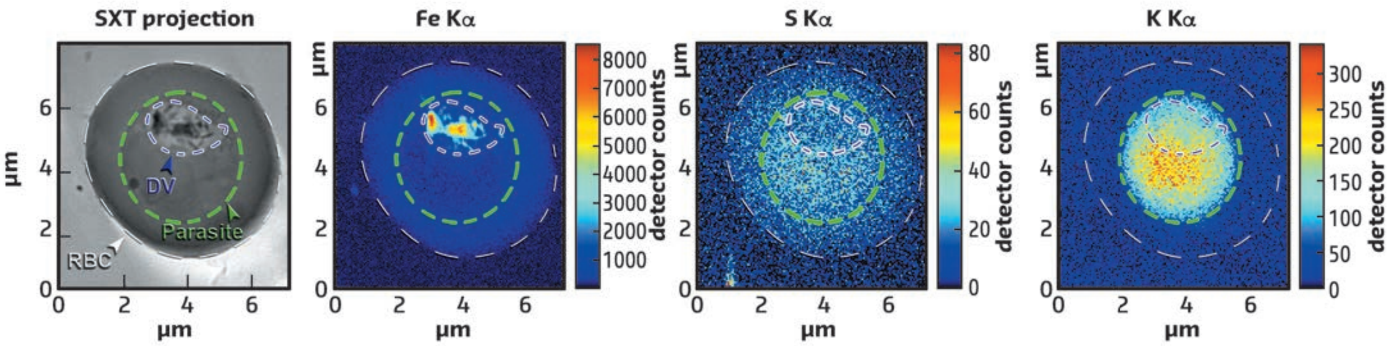

Fig. 72: Red blood cell (RBC) infected with *P. falciparum* studied by soft X-ray tomography (SXT) visualising the 3D structure of the parasite and X-ray fluorescence producing maps of iron, sulfur and potassium. The infected cell, the parasite and the digestive vacuole (DV) are outlined with white, green and blue dashed lines, respectively.

carbon content remained highly absorbing. In this way, the structure of the infected red blood cell can be mapped in three dimensions (3D) while radiation damage is avoided.

X-ray fluorescence mapping of the sample was carried out using a hard X-ray beam with a diameter of about 30 nm, permitting a sample to be scanned and the fluorescent signal registered from chemical elements ranging from sulfur (S) to iron (Fe). Fe is bound to heme and is abundant in Hgb and in the hemozoin crystals, but the concentration of Fe atoms in hemozoin is much higher than in Hgb. Furthermore, the fluorescence signal from Fe in Hgb is accompanied by the fluorescence from S since there are 12 S atoms and 4 Fe atoms in a single Hgb molecule. Thus it is possible to disentangle whether heme is bound in hemozoin crystals or in Hgb. By overlaying the 3D parasite structure and the X-ray fluorescence maps, the distribution and concentration of chemical elements can be measured within various compartments of the parasite (see **Figure 72**). Notably the potassium is relocalised to the parasite in an infected red blood cell.

The liberation of heme monomers from Hgb, their subsequent dimerisation and, finally, the crystallisation of the heme dimers, all take place in a parasite organelle called the digestive vacuole, (DV). Previous measurements of parasites that have spent between 30 and 45 hours in red blood cells have shown that there is considerable non-crystalline heme in the DV in the form of Hgb, and that *in vivo* heme crystallisation occurs at a rate of about 10^4 per second. It has been suggested that the dimerisation needed for heme crystallisation is furnished by a protein called heme detoxification protein also with a rate of about 10^4 per sec, which is determined by *in vitro* experiments. This has led to the proposal of an assembly-line model where heme liberation, dimerisation and crystallisation take place at the same rate regulated by a feedback mechanism.

Future research will include a systematic study of the evolution of heme liberation, dimerisation and detoxification with the parasite's age.

PRINCIPAL PUBLICATION AND AUTHORS

Biochemistry of malaria parasite infected red blood cells by X-ray microscopy, S. Kapishnikov (a), L. Leiserowitz (b), Y. Yang (c), P. Cloetens (c), E. Pereiro (d), F. Awamu Ndonglack (e), K. Matuschewski (e) and J. Als-Nielsen (a), *Sci Rep.* **7**, 802 (2017);
doi: 10.1038/s41598-017-00921-2.

(a) Niels Bohr Institute, University of Copenhagen (Denmark)
(b) Department of Materials and Interfaces, Weizmann Institute of Science, Rehovot (Israel)
(c) ESRF
(d) ALBA Synchrotron Light Source, Cerdanyola del Valles, Barcelona (Spain)
(e) Molecular Parasitology, Institute of Biology, Humboldt University, Berlin (Germany)

REFERENCES

[1] S. Kapishnikov *et al., PNAS* **109**, 11184-11187 (2012).
[2] S. Kapishnikov *et al., PNAS* **109**, 11188-11193 (2012).
[3] S. Kapishnikov *et al., Sci Rep.* **7**, 7610 (2017).

FAST *IN SITU* NANOIMAGING OF PARTICLE SINTERING

Neck curvature, a parameter critical to the understanding of sintering, was determined precisely for the first time for the sintering of a glass powder. This was achieved by studying the microstructure evolution during sintering by high-temperature *in situ* nanotomography using an unprecedented combination of fast scan time and high resolution.

Sintering is the consolidation and densification of a powder via the application of heat and sometimes aided by pressure. It is used to process dense or porous ceramics, metals or composites for a wide range of applications, including, for example, gears, cutting inserts, dental implants, bone substitutes, joint prosthesis and electrodes for energy conversion devices.

During the course of sintering, the system tends to reduce its specific surface, which results in neck formation and growth by material diffusion between the powder particles. Complex shapes and/or multimaterial systems are often prone to unacceptable defects. The development of models able to understand and predict the formation of such defects is crucial to avoid them **[1]**. Models require fine experimental data at the local scale to validate the underlying hypothesis. Specifically, most models assume a constant neck curvature, a hypothesis that has been questioned for some time and never clearly validated. As 2D systems are generally not representative of real cases, 3D characterisation of particle packing is needed and for this the non-destructive X-ray tomography technique is a tool of choice **[2, 3]**.

Previous experiments have focused on phenomena occurring at the scale of hundreds of particles, such as rearrangement, neck or pore evolution but no accurate measurements of neck curvature during sintering have been reported. There is an inherent difficulty in the combination of high spatial resolution, high temperature and fast scan time. In particular, a significant technical challenge is to maintain high spatial stability while heating a sample at temperatures as high as 1000 °C. Recently, a new setup dedicated to high resolution and high temperature *in situ* X-ray nanotomography has been developed at beamline **ID16B**. It relies on a specially-designed microfurnace with external water cooling and a quartz internal chamber for sample thermal stability. The first estimation of neck curvature evolution at the early stages of a sintering process in real time was obtained using this setup.

Glass particles, 40 µm in size, were heat treated at 670 °C for 105 minutes. During this time period, 90 tomography scans were recorded, each taking 33 seconds and with a pixel size of 100 nm. When compared to the state-of-the-art, this corresponds to a scan time divided by 15 and a pixel size divided by 7. Such high resolution made it possible to follow the formation and growth of micronic necks, as reported in **Figure 73**. The sizes of four necks around a selected particle were assessed to characterise growth kinetics. The classical Frenkel two-sphere model, which predicts neck size growth scaling with the square root of time, is not supported by the experiment despite being previously supported by *in situ* 2D observation. This shows that simplistic two spheres models are not applicable to complex 3D configurations of particles. The neck curvature was also measured for a selected neck and is reported in **Figure 74** as a function of the distance from the contact. The tangent circle approximation used in the Frenkel model and in many other densification models is not valid here. The neck extension is more limited but with a more pronounced curvature, especially at the very beginning of sintering.

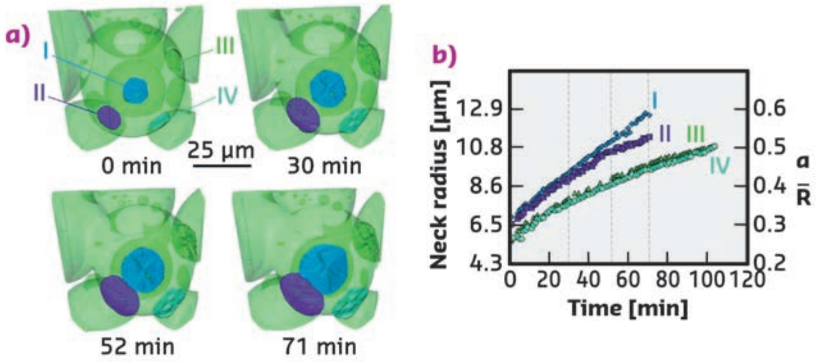

Fig. 73: a) 3D rendering of the investigated volume showing the growth of four necks (I to IV) during the sintering process at 670 °C. b) Evolution of the neck radii with time. a/R refers to the relative neck radius with neck radius: a and particle radius: R. The dashed vertical lines highlight the times when the 3D images in (a) were recorded.

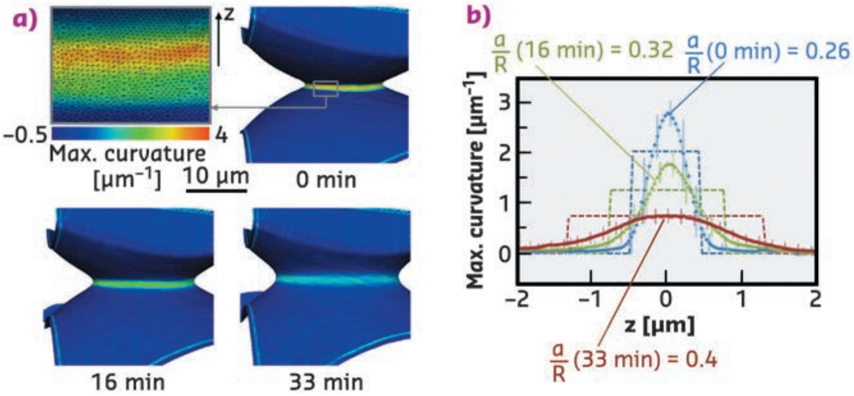

Fig. 74: a) Evolution of 3D maximum principal curvature rendering of neck IV with time. The first image is an enhanced view of the neck, highlighting the surface mesh provided by the high resolution of the experiment. b) Comparison between experimental maximum principal curvature (symbols) and the tangent-circle approximation (dashed lines) as a function of the distance z from the neck plane.

In summary, 3D *in situ* observation of particle sintering at high temperature was obtained with an unprecedented combination of high spatial resolution and fast scan time. This experiment allowed the first determination of the local neck curvature, an essential governing parameter for sintering. Future experiments target temperatures above 1000 °C and even higher resolution. High-temperature X-ray nanotomography should find applications in many other fields to reveal previously inaccessible fast phenomena, such as nucleation and growth of pores and cracks, glass synthesis, and high-temperature mineralisation processes.

PRINCIPAL PUBLICATION AND AUTHORS

Fast *in situ* 3D nanoimaging: a new tool for dynamic characterization in materials science, J. Villanova (a), R. Daudin (b), P. Lhuissier (b), D. Jauffrès (b), S. Lou (b), C.L. Martin (b), S. Labouré (a), R. Tucoulou (a), G. Martínez-Criado (a,c) and L. Salvo (b), *Mater Today* **7**, 354-359 (2017); doi: 10.1016/j.mattod.2017.06.001.
(a) ESRF
(b) University Grenoble Alpes, CNRS, SIMaP, Grenoble (France)
(c) Instituto de Ciencia de Materiales de Madrid, Consejo Superior de Investigaciones Científicas, Cantoblanco (Spain)

REFERENCES

[1] R.M. German, *Sintering: From Empirical Observations to Scientific Principles*, Butterworth-Heinemann (2014).
[2] O. Lame *et al.*, *Acta Mater*. **52**, 977-984 (2004).
[3] D. Bernard *et al.*, *Acta Mater*. **53**, 121-128 (2005).

BIOACCUMULATION OF NANOPARTICLE CuO WITHIN A TERRESTRIAL FOOD CHAIN INCREASES AFTER WEATHERING IN SOIL

Engineered nanoparticles are additives in commercial products that we consume, apply to our skin, and use in agriculture as fertilisers and pesticides. This study examined the bioaccumulation of copper nanoparticles in lettuce and possible trophic transfer to crickets, using µ-XRF and µ-XANES to map the distribution and Cu speciation upon exposure to weathered and unweathered CuO nanoparticles.

Engineered nanoparticles have been of great interest to the agricultural sector, with the most common applications being nanofertiliser and nanopesticide products for improved crop productivity **[1]**. However, the fate of these materials in the environment remains poorly understood. Nanoparticles released to soil may aggregate significantly, thereby changing their size, shape and surface chemistry over time. The aging and transformation of nanoparticles in soil during weathering processes could increase or decrease particle mobility and bioavailability within terrestrial food chains. In the present study, the impact of these transformations during nanoparticle and bulk (non-nanoparticle) CuO weathering was evaluated by means of micro X-ray fluorescence (µ-XRF) and micro X-ray absorption near-edge structure (µ-XANES) spectroscopy at beamline **ID21**. Lettuce roots were exposed to weathered (**Figure 75**) and unweathered (**Figure 76**) CuO nanoparticles at 400 mg/kg for 70 days, following which 30 µm cross sections were analysed. Additionally, crickets fed for 15 days with lettuce exposed to weathered CuO nanoparticles were depurated for 5 days and then analysed by µ-XRF.

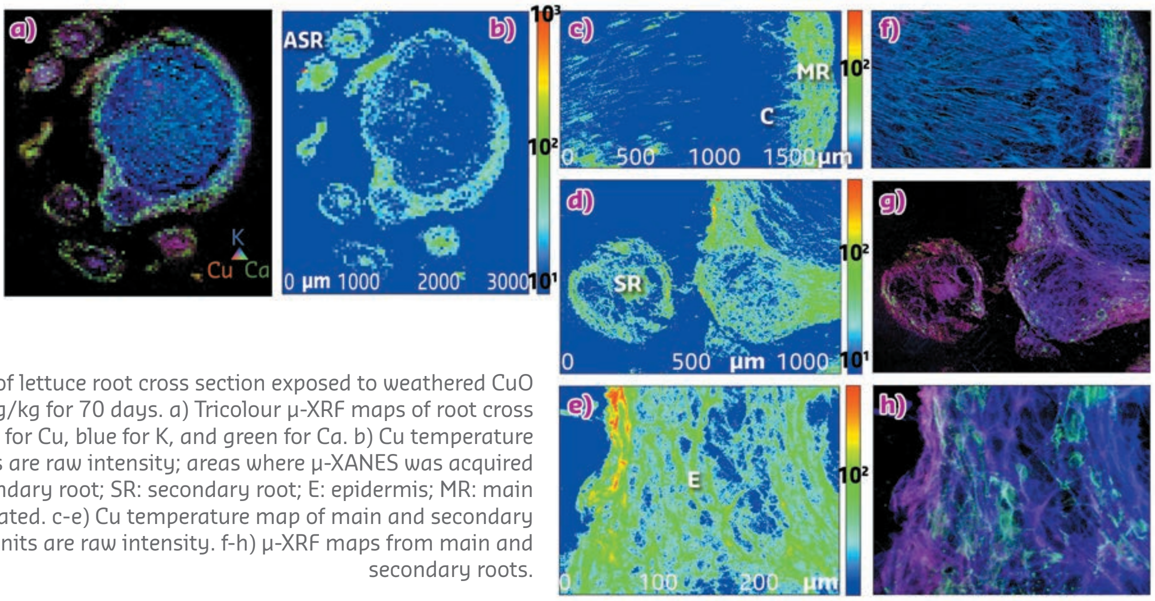

Fig. 75: Images of lettuce root cross section exposed to weathered CuO nanoparticles at 400 mg/kg for 70 days. a) Tricolour µ-XRF maps of root cross sections, red colour stands for Cu, blue for K, and green for Ca. b) Cu temperature map, colour scale units are raw intensity; areas where µ-XANES was acquired from ASR: aggregate secondary root; SR: secondary root; E: epidermis; MR: main root and C: cortex are indicated. c-e) Cu temperature map of main and secondary roots, colour scale units are raw intensity. f-h) µ-XRF maps from main and secondary roots.

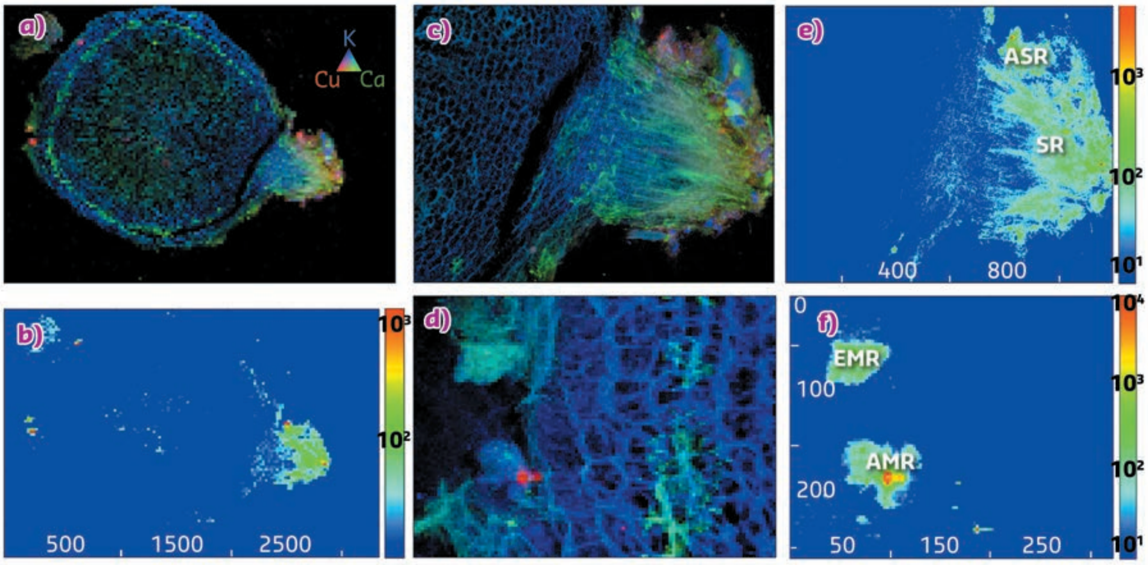

Fig. 76: Images of lettuce root cross section exposed to unweathered CuO nanoparticles at 400 mg/kg for 70 days. a) Tricolour µ-XRF maps of root cross sections, red colour stands for Cu, blue for K, and green for Ca. b) Cu temperature map, colour scale units are raw intensity. c, d) µ-XRF maps from main and secondary roots e, f) Cu temperature map of main and secondary roots from (c, d) µ-XRF maps, colour scale units are raw intensity. Areas where µ-XANES was acquired from ASR: aggregate secondary root; SR: secondary root; EMR: epidermis main root and AMR: aggregate main root are indicated.

The µ-XRF analysis results demonstrate that Cu was localised primarily in the main and secondary roots (**Figures 75a** and **76a**) of the exposed lettuce plants, regardless of weathering conditions. However, the distribution of Ca was altered due to weathering in soil, showing greater distribution within the main root for the weathered treatment (green colour, **Figure 75a**) when compared to the unweathered treatment (green colour, **Figure 76a**). Additionally, a more localised and heterogeneous Cu distribution was observed in the unweathered treatment (**Figure 76b**) as compared to the weathered exposure, where the element was homogenously distributed within root tissue (**Figure 75b**).

µ-XANES analysis of roots from weathered nanoparticle exposure demonstrated a significant Cu (II) reduction to Cu (I) compounds, including sulfidation, in all selected root areas (main, secondary, epidermis, cortex). Conversely, roots from unweathered nanoparticle treatments contained Cu mostly as the original CuO in multiple tissues, including the secondary and main roots. As such, µ-XANES analysis of the Cu K edge suggests that the reduction of CuO to Cu (I) complexes occurred in the soil during the weathering processes. Importantly, this reductive transformation of weathered nanoparticles correlated well with increased Cu in lettuce root tissues as measured by ICP-MS.

µ-XRF analysis from the trophic transfer study was used to localise Cu in the abdominal region of the primary consumer (cricket; *A. domestica*) after feeding for 15 days with lettuce exposed to weathered CuO nanoparticle treatments (data not shown). The µ-XRF results showed the homogenous distribution of P and S within the cricket's digestive system, but Cu was not associated with the digestive tract, suggesting either absorption or elimination during the depuration period. Importantly, this study demonstrated the impact of transformation processes in soil that may result in an increased availability of chemically altered nanoparticles within terrestrial food chains.

PRINCIPAL PUBLICATION AND AUTHORS

Weathering in soil increases nanoparticle CuO bioaccumulation within a terrestrial food chain, A.D. Servin (a), L. Pagano (a,b,c), H. Castillo-Michel (d), R. De la Torre-Roche (a), J. Hawthorne (a), J.A. Hernandez-Viezcas (a), R. Loredo-Portales (f,g), S. Majumdar (a), J. Gardea-Torresdey (e,h), O. Parkash Dhankher (b) and J.C. White (a), *Nanotoxicology* **11**, 98-111 (2017); doi: 10.1080/17435390.2016.1277274.

(a) Department of Analytical Chemistry, Connecticut Agricultural Experiment Station, New Haven (USA)
(b) Stockbridge School of Agriculture, University of Massachusetts, Amherst (USA)
(c) Department of Life Sciences, University of Parma (Italy)
(d) ESRF
(e) Chemistry Department, University of Texas at El Paso (USA)
(f) Universidad de Guanajuato Noria Alta (Mexico)
(g) Elettra Sincrotorone Trieste, Basovizza (Italy)
(h) University of California Center for Environmental Implications of Nanotechnology (UC CEIN), El Paso (USA)

REFERENCES

[1] A.D. Servin and J.C. White, *NanoImpact* **1**, 9-12 (2016).

ANTARCTIC SUBGLACIAL VOLCANISM, MELTWATER AND THE GLOBAL C CYCLE

Antarctica hosts a large volcanic province, but many volcanoes are under the ice. Past subglacial eruptions go undetected by ice core records, yet they could have originated large bodies of subglacial meltwaters whose discharge influenced global climate. This research provides support to a link between magmatism, the Antarctic ice sheets and climate through synchrotron-based techniques.

It has been proposed that ancient eruptions caused significant melting of the ice sheets that covered Northern Europe at the end of the last Ice Age and influenced the global climate [1]. A link between volcanism and ice sheet melting would indicate a "positive feedback" in which eruptions exacerbate melting and more melting causes more eruptions [1]. The role of ancient subglacial volcanic activity in Antarctica was investigated by mapping trace elements in subglacial carbonates via synchrotron radiation-based micro X-ray fluorescence (SR-µXRF) and X-ray absorption near-edge spectrometry (XANES) at beamline **ID21**.

Subglacial calcites grew in pockets of meltwater at the base of Boggs Valley glacier (Northern Victoria Land, East Antarctic Ice Sheet) as a result of the combination of pressure-solution and geothermal energy from 26.951 ± 0.824 to 17.054 ± 0.332 ka. The ages coincide with the last glacial maximum (LGM), when ice thickness above the now deglaciated rocks was at least 700 m. These LGM subglacial calcites yielded DNA and petrographic evidence of hydrothermally influenced subglacial discharge, most likely from a lake, which invaded a subglacial polar oasis where water existed and microbes released micronutrients, such as divalent iron, from the bedrock.

SR-µXRF maps of double-polished, 300 mm-thick wafers of the calcites were acquired by using a monochromatic beam and a large solid-state detector. The excitation energy was set at 2.6 keV and 7.5 keV to maximize the XRF yield of sulfur, which marks volcanism, and iron respectively. The fluorescence signal of sulfur in the calcites is mostly yielded by sulfate, which is mostly concentrated in detritus-rich layers (**Figure 77**), where another volcanic-related element, fluorine, was previously detected. Both sulfate and fluorine are typical of Trans Antarctic Mountain volcanisms, most of which is known to occur subglacially. XANES spectra displayed a low intensity peak at 2473.3, attributable to amino acids (*ref.* cysteine), which supports the claim that DNA data come from microbial-related organic fragments embedded in the calcites. Critically, 47 % of the DNA found in the S-rich layers accounts for thermophilic microbial taxa belonging to phylogenetic groups that thrive at temperatures above 41°C.

Other taxa are chemolithotrophs capable of releasing divalent Fe from pyrite oxidation. XANES spectra at the Fe-K edge revealed that most iron is trivalent and associated with the particulate illustrated in **Figure 77**. A small proportion is ferrous, which suggests bio-

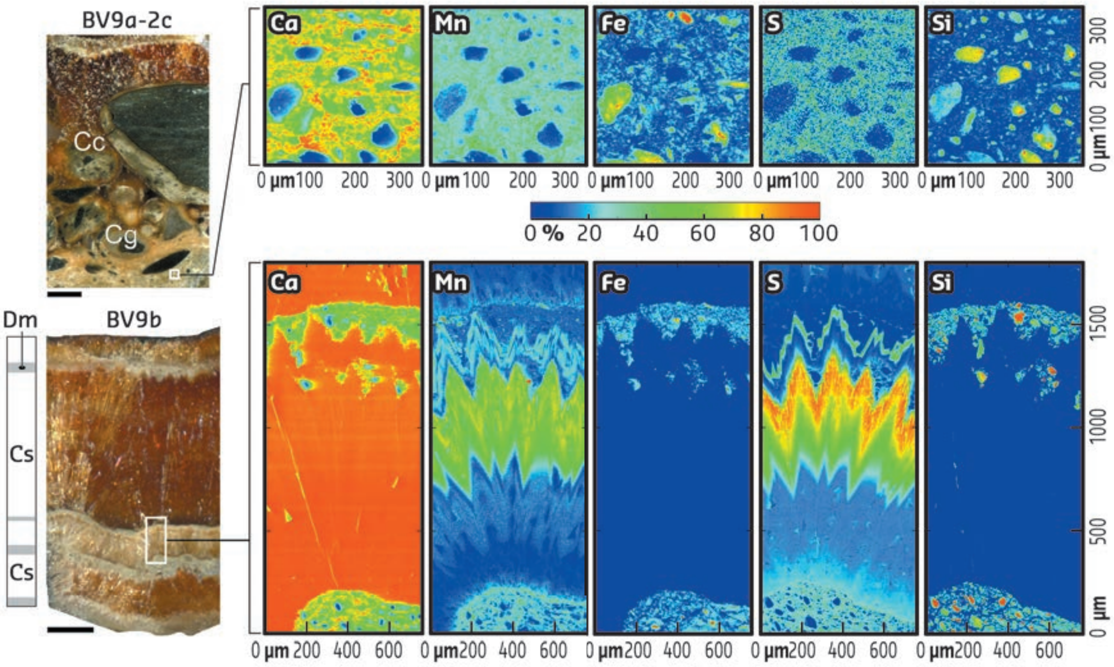

Fig. 77: SR-µXRF maps for the areas designated by a white box showing maximum concentration of S as sulfate and Fe, which is mostly present as oxy-hydroxides particulate. Scale bar for both samples is 5 mm. Elements are reported in normalised counts ranging from high (red) to low (blue) relative concentration according to the 0-100% scale bar.

weathering at the ice-bedrock interface. Yet, both forms of Fe are potentially bioavailable, with the divalent Fe more so. If transported to the Southern Ocean, bioavailable Fe boosts phytoplankton bloom, thus contributing to C sequestration by organisms that, when they die, sink to the seafloor.

A high level of sulfate and fluorine occur in calcite layers whose ages cluster around 23,500 years. They indicate that a subglacial eruption melted the ice and formed a lake, which then discharged into Boggs Valley at, or just before, 23,500 years ago. The data suggest that Fe produced subglacially in Boggs Valley was transported to the ice-sheet margin by massive drainage of such a lake. This could have triggered a series of processes that, eventually, resulted in a positive feedback, inducing further cooling during peak glacial conditions. This is one of the first demonstrations of Antarctic volcanism exacerbating global processes.

PRINCIPAL PUBLICATION AND AUTHORS

The influence of Antarctic subglacial volcanism on the global iron cycle during the Last Glacial Maximum, S. Frisia (a), L.S. Weyrich (b), J. Hellstrom (c), A. Borsato (a), N.R. Golledge (d,e), A.M. Anesio (f), P. Bajo (g), R.N. Drysdale (g,h), P.C. Augustinus (i), C. Rivard (j) and A. Cooper (b), *Nat Commun.* **8**, 15425 (2017); doi: 10.1038/ncomms15425.

(a) School of Environmental and Life Sciences, University of Newcastle, (Australia)
(b) Australian Centre for Ancient DNA (ACAD), University of Adelaide (Australia)
(c) School of Earth Sciences, University of Melbourne, Parkville (Australia)
(d) Antarctic Research Centre, Victoria University of Wellington (New Zealand)
(e) GNS Science, Lower Hut (New Zealand)
(f) Bristol Glaciology Centre, School of Geographical Sciences, University of Bristol (UK)
(g) School of Geography, University of Melbourne, Parkville (Australia)
(h) Environnements, Dynamiques et Territoires de la Montagne, UMR CNRS, Université de Savoie-Mont Blanc, Le Bourget du Lac (France)
(i) School of Environment, University of Auckland (New Zealand)
(j) ESRF

REFERENCES

[1] F. Muschitiello *et al., Nat Commun.* **8**, 1020 (2017).

3D IMAGING OF A DISLOCATION LOOP AT THE ONSET OF PLASTICITY IN AN INDENTED NANOCRYSTAL

The microstructure of a nanocrystal undergoing *in situ* mechanical loading was monitored by imaging in 3D with 13 nm resolution. Observations included the evolution of the strain field after successive loadings and the nucleation of a dislocation loop.

Understanding the stability and the mechanical response of micro and nanocrystalline materials is a long-standing topic of investigation, driven since the 1970s by efforts to reduce the length scale for functional devices in microelectronics. Strength evolution with size supports the phenomenological 'smaller is stronger' statement **[1]**, but the scaling down in length scale also reveals the intrinsic discrete nature of the strain response since each dislocation carries a quantum of deformation (the magnitude of its Burgers vector b).

Hence, for a given sample size, a large variation in mechanical response is observed experimentally at the micrometre scale **[2]**. Therefore, the mechanical behaviour of micro/nanocrystals under mechanical stimuli cannot be understood without an accurate knowledge of the microstructure (residual strain field and defect content), and a full picture of the size effect on strength can only be studied by investigating the relationship between the microstructure and the mechanical response.

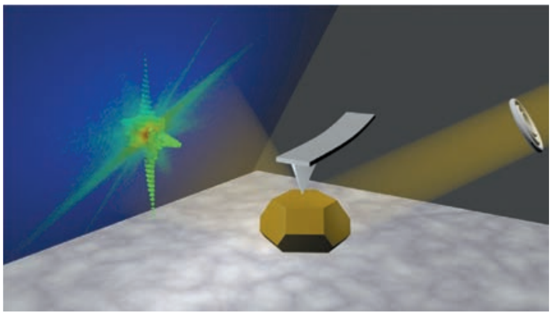

Fig. 78: Schematic illustration of the experiment.

In this work, the evolution of the microstructure of a gold nanocrystal was followed during the very first stages of its indentation. Bragg coherent diffraction imaging (BCDI) at beamline **ID01** was used to obtain quantitative 3D images of its structure at the nanoscale (**Figure 78**) **[3]**. The BCDI measurements were performed by recording the 3D intensity distribution around the 111 Bragg reflection. *In situ* mechanical stimuli were applied with a dedicated compact AFM (SFINX) **[4]** mounted on the diffractometer, and the crystal microstructure was imaged after a few indentation cycles. The reconstructed real space data after the third loading/unloading iteration reveals the presence of a dislocation loop of ~65 nm diameter nucleated during loading and trapped in the crystal. The analysis of the density and phase data, which are consistent with those around simulated dislocation loops **[5]**, allowed the unambiguous identification of the prismatic nature of the dislocation loop (**Figure 79**). The prismatic loop exits the crystallite volume after the fourth loading iteration and the reconstructed displacement fields appear to be very homogeneous, suggesting a partial relaxation of the strain field in the crystallite. To obtain a full representation of the strain field and elastic energy within the particle, FEM based calculations were carried out to complete the missing displacement components for each reconstructed configuration. The computation of the elastic stored energy revealed the same trend as the function of the applied force: an initial increase until the nucleation of the prismatic loop takes place followed by a decrease bringing the system back close to its initial state. Hence, the calculated elastic energy stored in the crystal shows clearly the footprint of the dislocation loop nucleation that relaxes the stress and brings the island back to an almost strain-free state.

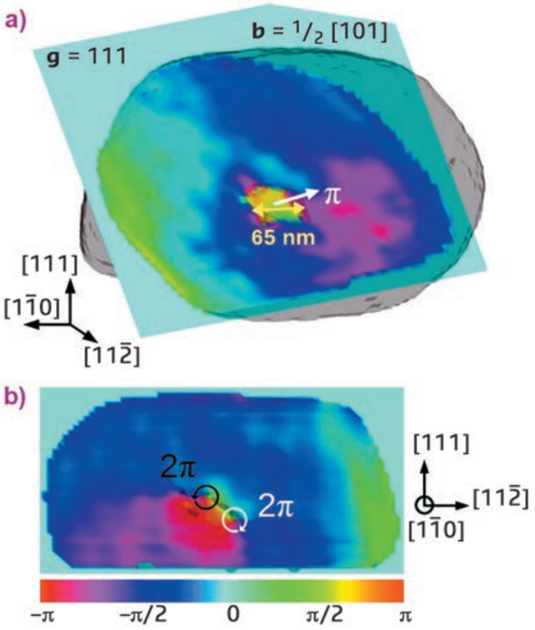

Fig. 79: a) Reconstructed experimental ϕ1 1 1 phase fields in the (1 0 1) plane normal to the glide cylinder of the prismatic loop. The electron density drawn at 21% of the maximum electron density is superimposed in transparency to indicate the position of the loop. b) Reconstructed ϕ1 1 1 phase field in the (1 $\bar{1}$ 0) plane intercepting the prismatic loop in two loci.

This work demonstrates the feasibility of monitoring and imaging in 3D the evolution of the microstructure of nanocrystals exposed to mechanical loading by BCDI. Importantly, the technique has the spatial resolution and the displacement sensitivity required to reveal the individual discrete events forming the mechanical response, such as the nucleation and disappearance of a single dislocation loop, and to relate it to the local strain field. Altogether, this approach opens a new avenue for the study of mechanical properties at the nanoscale, offering a non-invasive 3D structural microscopy for nanocrystals and with a quantitative sensitivity that outperforms electron microscopy.

PRINCIPAL PUBLICATION AND AUTHORS

3D Imaging of a dislocation loop at the onset of plasticity in an indented nanocrystal,
M. Dupraz (a), G. Beutier (a), T.W. Cornelius (b), G. Parry (a), Z. Ren (b), S. Labat (b), M.-I. Richard (b,c), G.A. Chahine (a), O. Kovalenko (d), M. De Boissieu (a), E. Rabkin (d), M. Verdier (a) and O. Thomas (b),
Nano Lett. **17**, 6696-6701 (2017);
doi: 10.1021/acs.nanolett.7b02680.
(a) Univ. Grenoble Alpes, CNRS, SIMAP, Grenoble (France)
(b) Aix Marseille Univ., Université de Toulon, CNRS, IM2NP, Marseille (France)
(c) ESRF
(d) Department of Materials Science and Engineering, Technion – Israel Institute of Technology, Haifa (Israel)

REFERENCES

[1] M.D. Uchic *et al., Science* **305**, 986-989 (2004).
[2] H. Bei *et al., Acta Mater*. **56**, 4762-4770 (2008).
[3] I. Robinson and R. Harder, *Nat. Mater*. **8,** 291-298 (2009).
[4] Z. Ren *et al., J. Synchrotron Radiat*. **21**, 1128-1133 (2014).
[5] M. Dupraz *et al., J. Appl. Crystallogr*. **48**, 621-644 (2015).

REVEALING THE PRINCIPLES OF MORPHOGENESIS OF GLASS SPICULES IN MARINE SPONGES FROM THE CLASS *DEMOSPONGIAE*

***Demospongiae* is a class of marine sponges that use amorphous glass structures, in the form of highly regular 3D microscopic spicules, to mechanically enhance their body, though the physical principles behind spicule formation had remained unknown. A model that describes the principles of spiculogenesis has been proposed.**

Microscopic silica elements called spicules (< 1 mm) are a paradigm example of symmetry in biological systems. Some of the most common examples include needle-like spicules in the shape of a simple glass fibre, tripod-like spicules with glass branches radiating from a common

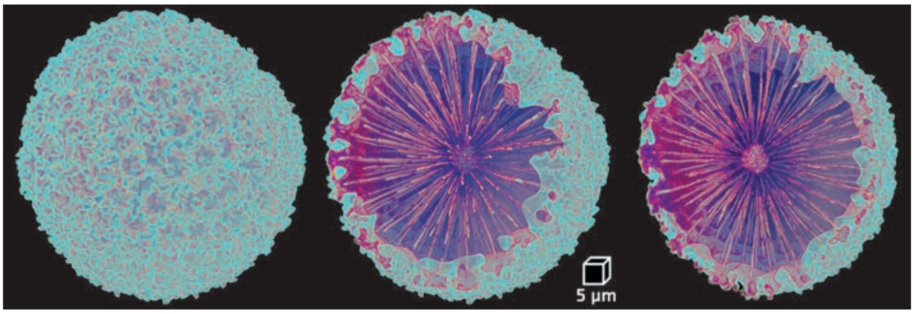

Fig. 80: 3D tomographic reconstruction of a sphere-like spicule from the sponge *Geodia cydonium*.

centre in strictly defined angles, and spicules with branches radiating in numerous random directions forming a sphere-like morphology. Each branch of a spicule contains an organic axial filament that passes through its centre. These filaments are made of enzymatically active proteins named silicateins that are responsible for silica biomineralisation and also act as a template for its deposition **[1]**. So far, the mechanisms responsible for the morphogenesis and the high regularity of the filament itself have remained unknown.

The proteins inside the axial filament are arranged in a perfectly regular mesoscopic crystalline structure **[2]** that was thought to extend through the entire spicule. It was therefore hypothesised that the highly regular shape of the filament and its branching behaviour are linked to the crystalline properties of the protein assembly. It was suggested that branching occurs on specific crystallographic planes of the protein lattice, resulting in remarkably symmetric spicule morphologies and very specific branching angles.

To corroborate this hypothesis, three types of spicules with increasing levels of spatial complexity, taken from three different sponges, were analysed: needle-shaped spicules from the sponge *Tethya aurantium*, tetrapod-like spicules from the sponge *Stryphnus ponderosus* (three branches radiating from the main shaft, each splitting into two additional branches) and sphere-like spicules from *Geodia cydonium*. To correlate between the crystalline properties of the axial filaments and their spatial distribution, the properties of the protein lattice of the axial filament and its spatial morphology in the three spicules were studied. Diffraction data, obtained at beamline **ID13**, showed that the proteins in all three spicules have a hexagonal packing with lattice parameters of a ≈ 6 nm and c ≈ 12 nm. The spatial distribution of the filament was studied using nano-tomography at **ID16A**, in the case of *Geodia cydonium* (**Figure 80**), and micro-tomography at **ID19**, in the case of *Tethya aurantium* and *Stryphnus ponderosus*.

The results demonstrate the capacity of the organism to create different templates for glass deposition by forming a variety of three-dimensionally organised filaments, using a common hexagonal unit of the protein crystal. This observation is analogous to a man-made approach to technologically relevant nanocrystalline structures **[3]**, such as rod-like, branched and hyperbranched crystals. In these structures, the branching occurs on specific crystallographic planes of the atomic lattice and the final morphology depends on growth conditions. It is asserted that the same principles apply for the morphogenesis of the axial filaments.

On the basis of this analogy, the X-ray crystallographic data, and the branching angles extracted from tomographic reconstructions, a model that describes the crystallographic directions in which spiculogenesis proceeds has been proposed. The filament in the needle-like spicule from *T. aurantium* shows no branching, which results in a needle-like morphology of the spicule. The sphere-like spicule from *G. cydonium* is hyperbranched, developing a sphere-like morphology. At the same time, the axial filament in the tripod from *S. ponderosus* shows a perfect threefold symmetry. On the basis of the known lattice parameters, it was possible to estimate the possible angles between the different arms of the spicules by assuming that the branching occurred on a specific crystallographic plane. By comparing the theoretical angle to the ones

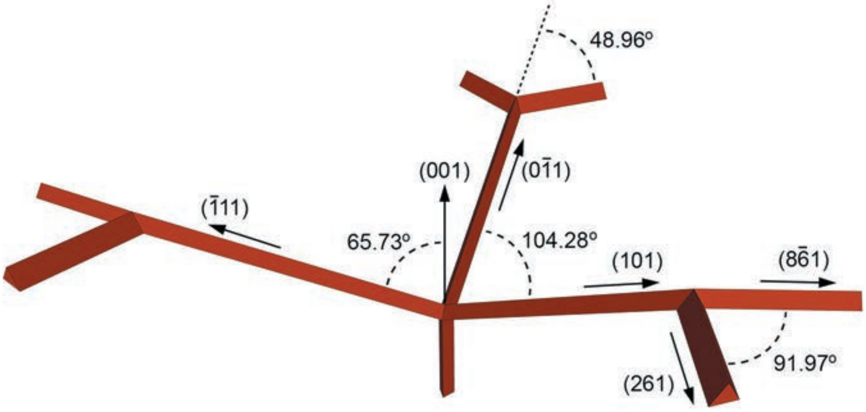

Fig. 81: 3D model of the axial filament in the spicule from *Stryphnus ponderosus* and the Miller indices of the leading crystallographic planes in the branches.

measured using the tomography data, the exact planes on which the branching proceeded was determined. For example, the angle between the main shaft (direction [001]) and the three main branches, assuming that the branching occurred on [101]-planes was calculated as 65.73°, which is close to the mean value of 66.0° ± 2.0°, measured in the spicule. The final model is summarised in **Figure 81**.

To conclude, it is astonishing that both nature and humankind converged to a similar thermodynamically driven fabrication method independently. The complexity and the high symmetry of glass architectures found in marine sponges, and the elegance with which they are formed by a living tissue, provides exciting future research opportunities.

PRINCIPAL PUBLICATION AND AUTHORS

Shaping highly regular glass architectures: A lesson from nature, V. Schoeppler (a), E. Reich (a), J. Vacelet (b), M. Rosenthal (c), A. Pacureanu (c), A. Rack (c), P. Zaslansky (d), E. Zolotoyabko (e) and I. Zlotnikov (a), *Sci. Adv.* **3**, eaao2047 (2017); doi: 10.1126/sciadv.aao2047.

(a) B CUBE–Center for Molecular Bioengineering, Technische Universität Dresden (Germany)
(b) IMBE, CNRS, Aix-Marseille Université, Université d'Avignon, IRD, Station Marine d'Endoume, Marseille (France)
(c) ESRF
(d) Julius Wolff Institute for Biomechanics and Musculoskeletal Regeneration, Berlin, (Germany)
(e) Department of Materials Science and Engineering, Technion, Haifa (Israel)

REFERENCES

[1] M.-J. Uriz, *Can. J. Zool.* **84**, 322-356 (2006).
[2] I. Zlotnikov *et al.*, *Adv. Mater.* **26**, 1682-1687 (2014).
[3] H. Li *et al.*, *Acc. Chem. Res.* **46**, 1387-1396 (2013).

A BIOLOGICAL STRATEGY FOR PRESTRESSING CRYSTALLINE CALCITE LENSES

A biostrategy has been presented for strengthening and toughening the otherwise brittle calcite optical lenses found in the brittlestar *Ophiocoma wendtii*. This intriguing process employs coherent nanoprecipitates to induce compressive stresses on the host matrix, functionally resembling the Guinier–Preston zones known in classical metallurgy, though produced at ambient conditions without heating and quenching.

Various functional materials are formed via the process of biomineralisation **[1]** and serve specific functions **[2]**. Fascinatingly, these materials are formed from limited bioavailable elements, without the possibility of heating and quenching, as is common in man-made counterparts. Instead, organisms utilise various alternative biostrategies.

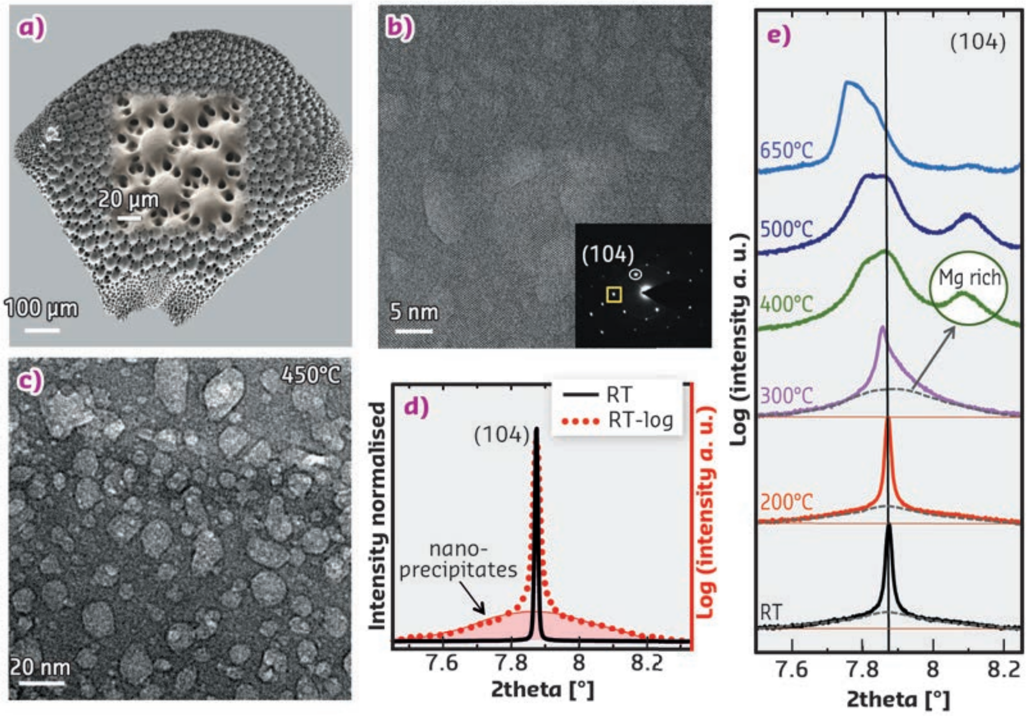

Fig. 82: a) SEM image showing an entire dorsal armplate and a higher magnification inset. b) TEM image of a thin section from a lens, revealing brighter nanodomains and their coherence with the matrix, although the FFT pattern is that of a single crystal (inset). c) Bright-field TEM image acquired during *in situ* heating at 450°C, revealing the temperature-induced growth of the nanodomains. d) The (104) diffraction peak comparing linear (black) and logarithmic (red) intensity scales, and revealing the presence of nanodomains at the base of the diffraction peak. e) Evolution of the (104) diffraction peak with temperature. At 400°C, a distinct broad diffraction peak appears owing to the loss of nanoprecipitate coherence.

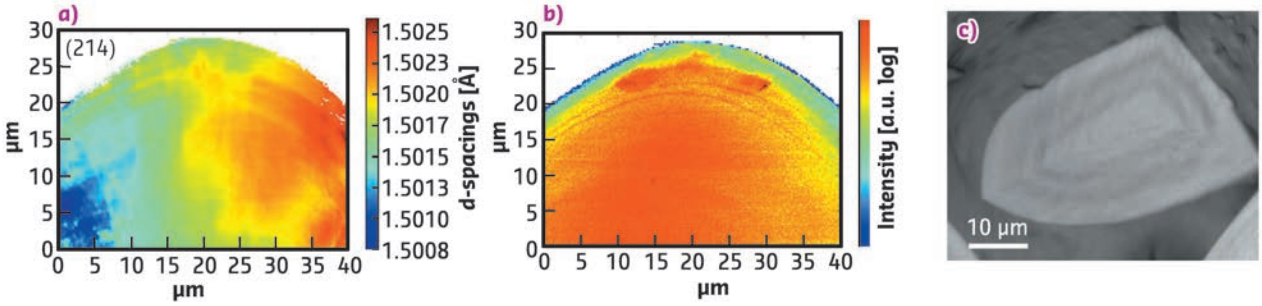

Fig. 83: a) D-spacings map of a single lens area of the (214) reflection. b) SAXS intensity map of the same lens (~2.5–16.5 nm). c) A virtual slice within a single lens produced by nanoCT, revealing alternating density layers probably owing to varying nanoprecipitate content.

A new biostrategy has been revealed in the *Ophiocoma wendtii* brittlestar, which has a unique micro-lens system made of calcite spread over its dorsal armplates (**Figure 82a**). Coherent nanoprecipitates revealed in the matrix were found to induce comprehensive compressive stresses on the host single crystal, akin to the Guinier–Preston zones known in classical metallurgy. These nanoprecipitates are rich in magnesium, which substitutes calcium in the lattice and leads to the shrinkage of lattice parameters, and this is the source of compressive stresses on the host matrix. This engineering technique strengthens and toughens ceramic materials, similar to that employed in tempered glass and prestressed concrete.

Utilising high-resolution powder diffraction on **ID22**, it was discovered that magnesium-rich nanodomains exist within the single crystal and are coherent within the matrix. This is concluded from the hump that appears at the base of each of the diffraction peaks prior to annealing (**Figure 82d**). The nanoprecipitates were also observed by aberration-corrected transmission electron microscopy (TEM), which also reveals their relatively low electron density and coherent interfaces with the matrix (**Figure 82b**). Once the sample is heated, these domains grow in size unless coherency is lost at the interface and the strain is released. This behaviour was observed both by *in situ* heating in the TEM as well as *in situ* heating on **ID22** (**Figure 82c, e**). In the latter, it was found that the diffraction peaks from the nanophase emerge only after 400°C and are shifted to higher 2-theta positions as compared to those of the matrix diffraction peaks, due to a higher magnesium concentration and hence smaller lattice parameters (**Figure 82e**).

Sub-micron diffractometry on **ID13** was used to map the variation in d-spacings and SAXS signal of a single lens. Both maps revealed structured regions slightly beneath the surface appearing in curved lines parallel to the surface (**Figure 83a, b**). These layers were also visualised via nano-computed tomography (nanoCT) measurements obtained on **ID16B**, revealing alternating layers of density, indicated by the brightness variation in phase contrast (**Figure 83c**). The alternating densities are likely due to the different concentrations of magnesium-rich nanoprecipitates, which coincides with the diffraction-mapping features.

Brittlestar lenses are formed via an amorphous precursor phase that crystallises at room temperature. This amorphous phase is supersaturated with magnesium as compared to the crystalline calcite, which drives the formation of segregated nanoprecipitates rich in magnesium after or during crystallisation. The nanometric size of the precipitates enables them to bear high tensile stresses while exerting compressive stress on the host matrix via the coherent interfaces. This is very similar to what is known in conventional metallurgy as Guinier-Preston zones, however, in contrast, biology forms this microstructure at ambient conditions without the need to heat and quench.

PRINCIPAL PUBLICATION AND AUTHORS

Coherently Aligned Nanoparticles Within a Biogenic Single Crystal: Biological Prestressing Strategy, I. Polishchuk (a), A.A. Bracha (a), L. Bloch (a) , D. Levy (a), S. Kozachkevich (a), Y. Etinger-Geller (a), Y. Kauffmann (a), M. Burghammer (b), C. Giacobbe (b), J. Villanova (b), G. Hendler (c), S. Chang-Yu (d), A.J. Giuffre (d), M.A. Marcus (e), L. Kundanati (f), P. Zaslansky (g), N.M. Pugno (f), P.U.P.A. Gilbert (d), A. Katsman (a) and B. Pokroy (a), *Science* **358**, 1294-1298 (2017); doi: 10.1126/science.aaj2156.

(a) Department of Materials Science and Engineering and the Russel Berrie Nanotechnology Institute, Technion-Israel Institute of Technology (Israel)
(b) ESRF
(c) Natural History Museum of Los Angeles County (USA)
(d) Departments of Physics, Chemistry, Geoscience, University of Wisconsin-Madison, (USA)
(e) Advanced Light Source, Lawrence Berkeley National Laboratory, California (USA)
(f) Laboratory of Bio-Inspired & Graphene Nanomechanics, University of Trento, (Italy)
(g) Department for Restorative and Preventive Dentistry, Centrum für Zahn-, Mund- und Kieferheilkunde, Charité-Universitätsmedizin Berlin, (Germany)

REFERENCES

[1] H. A. Lowenstam and S. Weiner, *On Biomineralization*, Oxford University Press (1989).
[2] J.W.C. Dunlop and P. Fratzl, *Annu. Rev. Mater. Res.* **40,** 1-24 (2010).

MICRO- AND NANOSCALE X-RAY FLUORESCENCE IMAGING REVEALS FATE AND SIZE OF TATTOO PIGMENTS IN SKIN AND LYMPH NODES

Highly sensitive X-ray fluorescence and spectroscopy methods facilitate simultaneous localisation and speciation of multiple tattoo pigment species, giving new insights on pigment distribution in the human body.

The increasing prevalence of tattoos leads to safety concerns with respect to particle distribution and effects inside the human body.

Tattoos, as well as permanent make-up, work by depositing insoluble pigments into the dermal skin layer. In conjunction with tattoos, pigmented

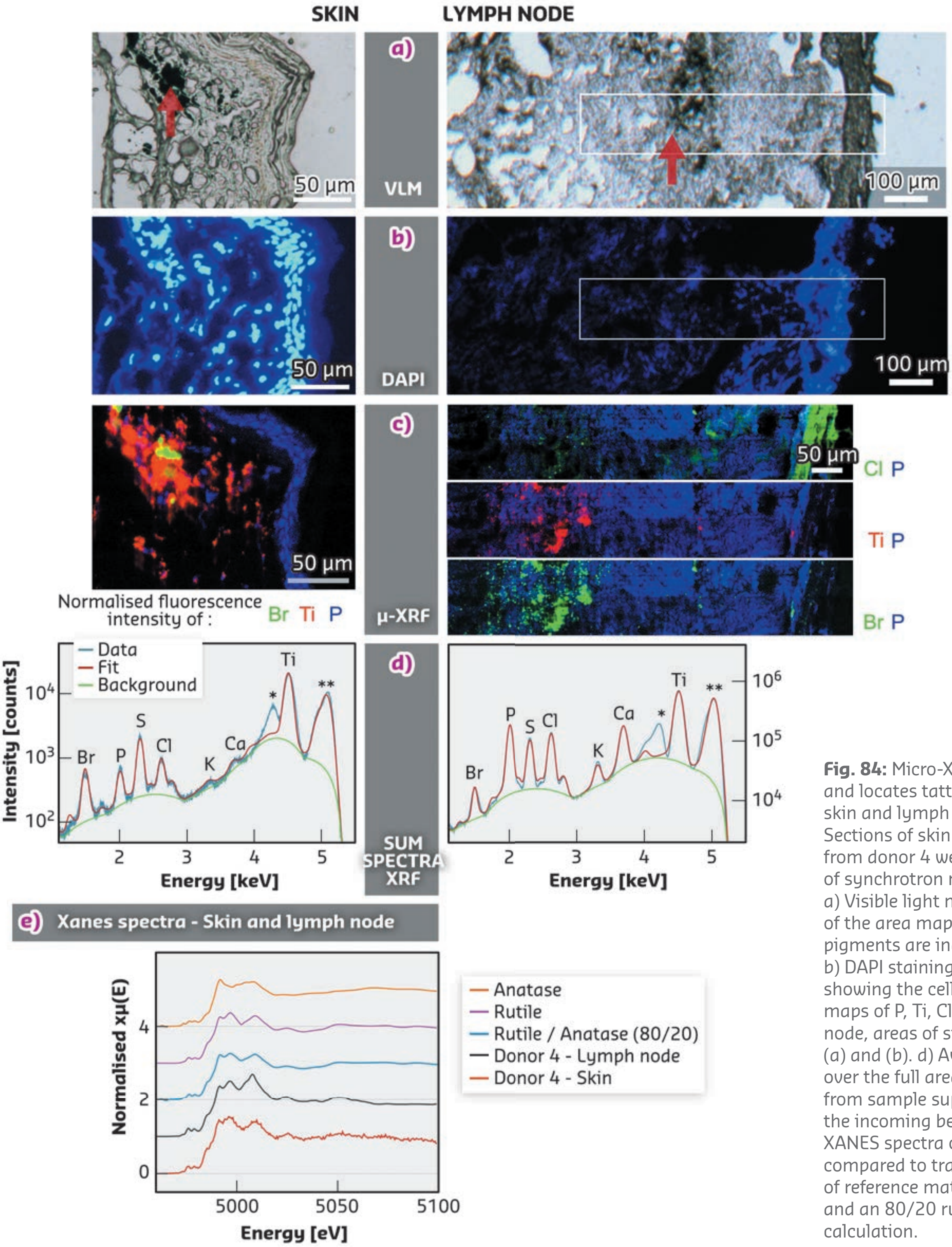

Fig. 84: Micro-XRF mapping identifies and locates tattoo particle elements in skin and lymph node tissue sections. Sections of skin and lymph node tissue from donor 4 were analysed by means of synchrotron micro-XRF at ID21. a) Visible light microscopy (VLM) images of the area mapped by micro-XRF. Tattoo pigments are indicated by a red arrow. b) DAPI staining of adjacent sections showing the cell nuclei. c) micro-XRF maps of P, Ti, Cl and/or Br. For the lymph node, areas of similar size are marked in (a) and (b). d) Average micro-XRF spectra over the full area displayed in (c) * peak from sample support; ** scatter peak of the incoming beam. e) Ti K-edge micro-XANES spectra of skin and lymph node compared to transmission XANES spectra of reference material of rutile, anatase and an 80/20 rutile/anatase mixture calculation.

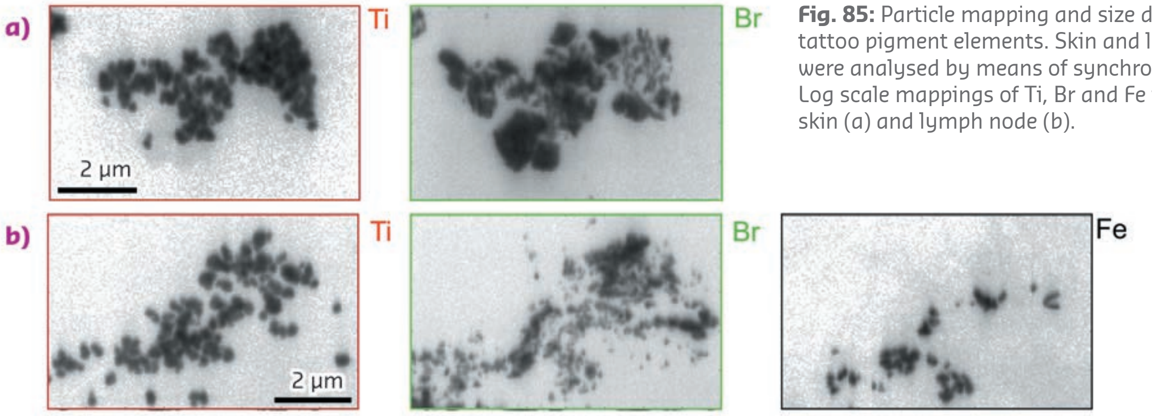

Fig. 85: Particle mapping and size distribution of different tattoo pigment elements. Skin and lymph node of donor 4 were analysed by means of synchrotron nano-XRF at ID16B. Log scale mappings of Ti, Br and Fe in the same areas in skin (a) and lymph node (b).

and enlarged lymph nodes have been noticed in tattooed individuals for years. Even though the observations leave little doubt about the origin of pigments, they have never been analytically investigated in human lymph nodes so far.

In animal studies, it has been shown that smaller particles are more easily distributed in the body. The average particle size in tattoo inks may vary from < 100 nm to > 1 µm. Therefore, most tattoo inks contain at least a small fraction of particles in the nano range. Next to the chemical identity of the pigments, the speciation of titanium dioxide (TiO_2) white pigments was investigated. TiO_2 is the second most commonly used pigment in tattoo inks. The toxicity of TiO_2 depends on its speciation (crystal structure), which can be either rutile or the more harmful photocatalytically active anatase.

This work investigated skin and lymph tissues from human corpses to address local biokinetics by means of synchrotron X-ray fluorescence (XRF) techniques. To precisely locate the different tattoo and tissue related elements in the cutaneous and lymphatic tissue sections, micro-XRF was performed at **ID21** at an energy of 5.05 keV. Additionally, Ti XANES (X-ray absorption near edge structure) spectra were collected, scanning the energy of the incoming beam from 4.95 to 5.1 keV at **ID21** to provide information on TiO_2 speciation. To assess primary particle sizes at the nanometric scale in particle mixtures, additional synchrotron-based nano X-ray fluorescence investigations were performed at **ID16B** with a pink beam of 17.5 keV.

Additional laboratory-based mass spectrometric methods demonstrated simultaneous transport of organic pigments, heavy metals and titanium from skin to regional lymph nodes. Laser desorption/ionisation mass spectrometry (LDI-MS) was used to identify organic pigments in skin and regional lymph nodes of the same donor. Inductively coupled plasma (ICP) MS was used to assess the general element load of the specimen investigated. However, these laboratory methods do not allow the localisation of the pigments in the tissues, the particle size assessment of multiple species at a time, nor the speciation of TiO_2.

In contrast, XRF-imaging at **ID21** revealed co-localisation of Ti and Br in the dermal region of the skin (**Figure 84**). Ti XANES showed that Ti can be attributed to the white pigment TiO_2 in the rutile crystal configuration (**Figure 84**). At **ID16B**, a broad range of tattoo pigment particles was found with up to several micrometres in size in human skin but only smaller than 200 nm particles in the lymph nodes (**Figure 85**). Among these compounds, the brominated organic green pigment displayed the broadest size range with smallest species preferentially reaching the lymph nodes.

With the detection of the same organic pigments and inorganic TiO_2 in skin and lymph nodes, there is strong analytical evidence for the migration of pigments from the skin towards regional lymph nodes in humans upon tattooing. The outcome of these investigations will not only be helpful in the assessment of the health risks associated with tattooing, but can also help in the judgment of other exposure scenarios, such as the entrance of TiO_2 nanoparticles present in cosmetics at the site of damaged skin or the wear-off from implant material.

PRINCIPAL PUBLICATION AND AUTHORS

Synchrotron-based ν-XRF mapping and µ-FTIR microscopy enable to look into the fate and effects of tattoo pigments in human skin, I. Schreiver (a), B. Hesse (b), C. Seim (c), H. Castillo-Michel (b), J. Villanova (b), P. Laux (a), N. Dreiack (a), R. Penning (d), R. Tucoulou (b), M. Cotte (b) and A. Luch (a), *Scientific Reports* **7**, 11395 (2017); doi: 10.1038/s41598-017-11721-z.

(a) German Federal Institute for Risk Assessment (BfR), Department of Chemical and Product Safety, Berlin (Germany)
(b) ESRF
(c) Physikalisch-Technische Bundesanstalt, Department of Temperature and Synchrotron Radiation, Berlin (Germany)
(d) Institute of Forensic Medicine, Ludwig-Maximilians University, Munich (Germany)

NUCLEATION AND GROWTH OF $CuInS_2$ NANOCRYSTALS STUDIED *IN SITU* USING SYNCHROTRON X-RAY DIFFRACTION

Synchrotron X-ray diffraction is used to monitor *in situ* the formation of $CuInS_2$ nanocrystals. SAXS measurements show that the reaction intermediate formed at 100°C presents a periodic lamellar structure. WAXS measurements of the $CuInS_2$ nanocrystals at 230°C demonstrate that their growth kinetics depend on the degree of precursor conversion achieved at 100°C.

Ternary metal chalcogenide nanocrystals (NCs) are explored for various types of applications in the fields of energy conversion (solar cells, photocatalysis, thermoelectrics), light emission and biological detection **[1, 2]**. Their optical and electronic properties can be tuned by changing the NC size (quantum confinement effect) or by varying the composition. Within this family, $CuInS_2$ (CIS) NCs are the most widely studied due to their outstanding luminescence properties and their well-established chemical synthesis. It involves mixing the metal precursors (copper iodide and indium acetate) with dodecanethiol (DDT) and heating first to 100°C (30-60 min) for complexation of the precursors and then to 230°C (15-60 min) for the growth of the NCs. Despite the simplicity of this procedure, the reaction mechanism and surface state of the obtained NCs remain elusive; they are the focus of the present study.

With the goal to monitor *in situ* the nucleation and growth stages of CIS NCs, the synthesis reaction was carried out inside a thin glass capillary. It contained the reaction intermediate obtained after heating the precursors at 100°C and was placed into a heating stage mounted on the sample goniometer at beamline **ID01** set at $\lambda = 0.774$ Å. A large q range was accessible by varying the distance of the 2D detector. The capillary was heated from room temperature to 230°C while performing SAXS and WAXS measurements. The data recorded at low temperatures (20-40°C) exhibit a distinct peak at $q = 0.18$ Å^{-1} (**Figure 86a**). As confirmed by *ex situ* SAXS measurements, this peak originates from a periodic lamellar structure with a characteristic distance of 34.9 Å, corresponding to twice the length of a DDT ligand. Additional ESI-mass spectrometry enables the hypothetical structure of the reaction intermediate to be drawn (shown in **Figure 86b**), in which metal and μ_3-bridging S atoms form a hexagonal network and alkyl chains are distributed on both sides of this slab.

During temperature increase, the SAXS peak, and hence the lamellar ordering, disappears. At around 180°C, nucleation of the CIS NCs starts but WAXS measurements do not yield any exploitable signals for heating times < 10 min at 230°C. The diffractograms obtained for longer times (**Figure 87**) correspond to CIS in the tetragonal chalcopyrite or cubic zinc blende structures, which cannot be distinguished here. Closer analysis of the peak line width using

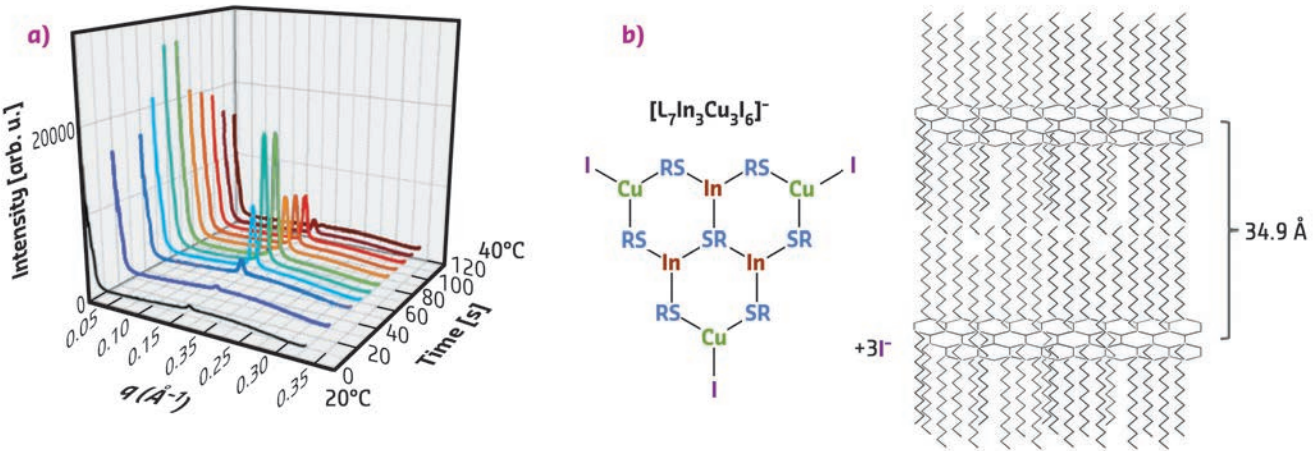

Fig. 86: a) Synchrotron *in situ* SAXS measurements performed during the heating of the CIS precursor solution in a glass capillary from 20°C to 40°C within 2 min (preheating time at 100°C: 60 min). b) Largest fragment of the reaction intermediate detected by ESI-mass spectrometry ($L = SC_{12}H_{25}^-$) and visualisation of the expected lamellar structure formed after heating the precursors to 100°C and cooling to room temperature.

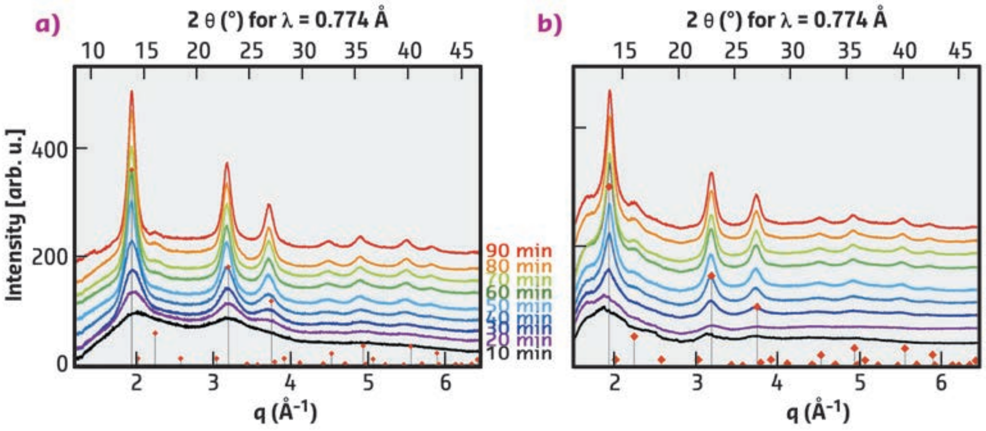

Fig. 87: *In situ* synchrotron WAXS measurements at 230°C, as a function of the preheating time at 100°C (red diamonds: diffraction pattern of chalcopyrite CIS, JCPDS: 04-002-6388). Preheating time of the precursor solution at 100°C: a) 30 min, b) 60 min.

the Scherrer formula reveals that the growth kinetics of the NCs are strongly correlated with the preheating time of the precursors at 100°C: sample A (preheating time: 30 min) grows much faster and also has a slightly larger final particle size (5.0 nm) than sample B (preheating time: 60 min, 4.2 nm). While optically the two precursor solutions do not exhibit any difference, sample A does not show the characteristic SAXS peak seen in **Figure 86a**.

An explanation for the different behaviours is as follows: In sample B the complexation of the metal precursors by thiolate molecules is accomplished. This favours cleavage of the S-C bond in dodecanethiolate, which is the only sulfur source in the system, and initially generates a large number of nuclei. In sample A the precursor conversion is not complete due to the shorter heating at 100°C. Therefore a lower number of nuclei are initially formed, which then grow to larger final particles. Beside the inorganic core, the nature, binding mode and surface density of the organic ligands capping the obtained CIS NCs are also studied using 1D and 2D proton and carbon NMR spectroscopy.

PRINCIPAL PUBLICATION AND AUTHORS

Growth Mechanism and Surface State of $CuInS_2$ Nanocrystals Synthesized with Dodecanethiol, M. Gromova (a), A. Lefrançois (b), L. Vaure (b), F. Agnese (a), D. Aldakov (b), A. Maurice (b), D. Djurado (b), C. Lebrun (2), A. de Geyer (a), T.U. Schülli (c), S. Pouget (a) and P. Reiss (b), *J. Am. Chem. Soc.* **139**, 15748-15759 (2017); doi: 10.1021/jacs.7b07401.

(a) Univ. Grenoble Alpes, CEA, INAC, MEM, Grenoble (France)
(b) Univ. Grenoble Alpes, CEA, CNRS, INAC, UMR5819 SyMMES, Grenoble (France)
(c) ESRF

REFERENCES

[1] D. Aldakov *et al.*, *J. Mater. Chem. C.* **1**, 3756-3776 (2013).
[2] M. Sandroni *et al.*, *ACS Energy Lett.* **2**, 1076-1088 (2017).

ELECTRONIC STRUCTURE, MAGNETISM AND DYNAMICS

The year 2017 started with Yves Watier joining the ESRF to lead the Sample Environment Unit that is part of the EMD group but serves all ESRF beamlines. We are excited to have Yves on board and, by January 2018, two newly recruited technicians will complete Yves' team. The ESRF Sample Environment Unit mainly develops and maintains cryostats and furnaces for *in situ* experiments. With Yves' arrival the portfolio will be extended to cover other instrumentation such as robotics. The year ended for the EMD group with the departure of Marco Moretti, who joined the ESRF in 2011 and has been in charge of beamline ID20 since 2015. Marco accepted a professorship at the Politecnico di Milano. We thank Marco for his invaluable contributions to the ESRF, wish him a wonderful career at the Politecnico and are looking forward to welcoming him at the ESRF as a scientific collaborator.

Theoretical spectroscopy is the key to understanding the experimental results obtained at the EMD beamlines. The software Crispy is a modern graphical user interface for the simulation of core-level spectra using semi-empirical multiplet theory. The code is hosted at GitHub and is released using a free and open-source license following the ESRF's policy on software development, which simplifies the integration of contributions from the user community. With the latest release it is possible to easily perform X-ray absorption (including X-ray dichroism) and resonant inelastic X-ray scattering (RIXS) simulations for transition metals and lanthanides for different site symmetries of the absorbing atom. Some support for angular-dependent calculations has also been added. In the case of non-centrosymmetric site symmetries, the inclusion of elaborate p-d mixing terms has been greatly simplified. Special attention was given to provide easy-to-use package installers for Windows and macOS operating systems in order to make the interface more accessible for non-expert users. Future developments concern other spectroscopies, such as XES and NIXS, and the extension of the interface to the analysis of density functional-based calculations.

A 5 micron-thick Si quarter wave plate was installed on **ID12** that produces a high degree of circular polarisation at photon energies in the vicinity of 2.8 keV (Brewster angle of double crystal Si [111] monochromator). Users now have the possibility of performing circular dichroism experiments at the L-edges of 4d metals and the K-edge of Cl. The beamline furthermore improved an experimental station dedicated to X-ray magnetic circular dichroism spectroscopy under a magnetic field of up to 17 Tesla and at low temperatures down to 2 K. Use of this unique instrumentation made it possible to elucidate the "non-magnetic" ground state not only in osmium ions in molecular systems (**see page 118**) but also in Pu atoms in a vortex phase of the $PuCoGa_5$ superconductor (**see page 104**).

Most of the research activities at **ID20** address problems in hard condensed matter, chemistry and material sciences. A growing number of experiments take advantage of the small X-ray spot size to explore samples under extreme pressure conditions. Developments are under way to provide, in the near future, not only the ability to manipulate precisely the polarisation of the incident X-ray beam but also the possibility to analyse the polarisation of the inelastically scattered beam. The beamline is also working toward providing a high-resolution spectrometer for non-resonant inelastic X-ray scattering. As examples for the research on ID20 we chose the unambiguous determination of the symmetry of the 5*f* ground-state wave function in URu_2S_{i2} using non-resonant inelastic X-ray scattering (**see page 98**) and a study of the evolution of magnetic order and magnetic excitations in $(Sr_{1-x}La_x)_3Ir_2O_7$ upon electron doping using high-resolution resonant inelastic X-ray scattering (**see page 114**).

The staff on **ID26** was very busy installing a new spectrometer for inelastic X-ray scattering in the tender X-ray regime between 1.5 and 5 keV. Almost 6 tonnes of steel were installed in the first experimental hutch. Eleven Johansson-type crystals select a wavelength and focus the beam onto a multi-wire proportional counter. The instrument operates between 35° and 85° Bragg angle and accepts bending radii of 500 and 1000 mm to optimise either efficiency or energy resolution. The commissioning is ongoing and the characteristics of the instrument will be presented in an upcoming publication. First experiments with users are scheduled for April 2018. This year's highlights present a study of Hg in human hair down to a few ppm concentration (**see page 99**), made possible by newly developed high-efficiency analyser crystals, and

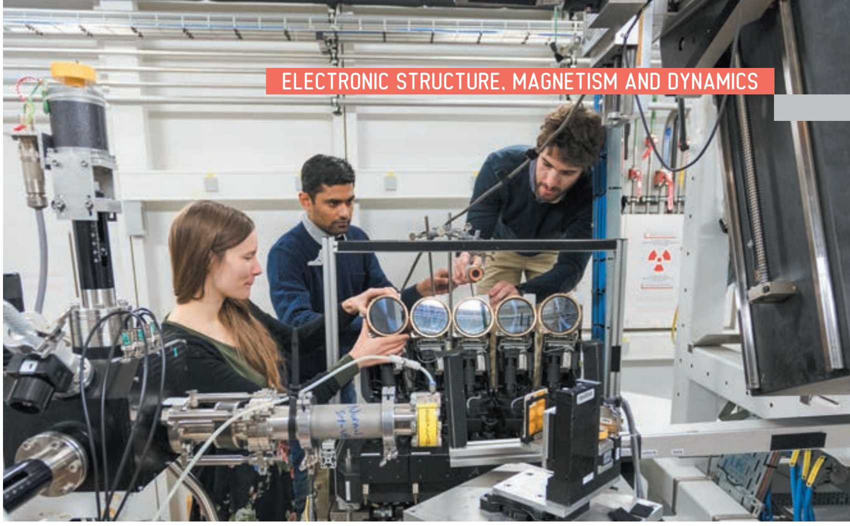

the revelation of an intermediate spin-state in proteins carrying a heme factor (**see page 112**).

Beamline **ID28** was running in 2017 with full user access to its new side station for diffuse scattering experiments. The success of the tandem operation between inelastic X-ray scattering and diffuse scattering is evident from the increasing demand for the diffraction side station. The benefit to the user community is demonstrated in this section by Wehinger *et al.* (**see page 102**). The inelastic X-ray scattering station reported the first observation of the breakdown of the Born-Oppenheimer approximation in the phonon spectra of a three-dimensional solid (**see page 105**). An interesting development for sample environment was achieved in collaboration with MPI Stuttgart, MPI Dresden and KIT: well-controlled uniaxial stress can now be applied to tiny single crystals even when the crystals are very fragile.

The past year has been an intense period for the resonant inelastic X-ray scattering branch of **ID32**. These efforts are beginning to be rewarded by interesting scientific results, as showcased in this chapter. The articles show results from the initial thrust of research on the cuprate high temperature superconductors (**see pages 103**, **107** and **115**) using the new capabilities – for example, very high-energy resolution and continuous momentum selection – presented by ID32. Such work is continuing and there is now an expansion of the application of RIXS to all the 3d transition metal elements, from titanium to copper and, in particular, their oxides, and also to the rare-earths, from cerium to samarium, where crystal field effects can be studied. This broadening of the applications of soft X-ray RIXS is very healthy and it will be very interesting to see what new scientific insights the technique will bring in the coming year.

P. GLATZEL

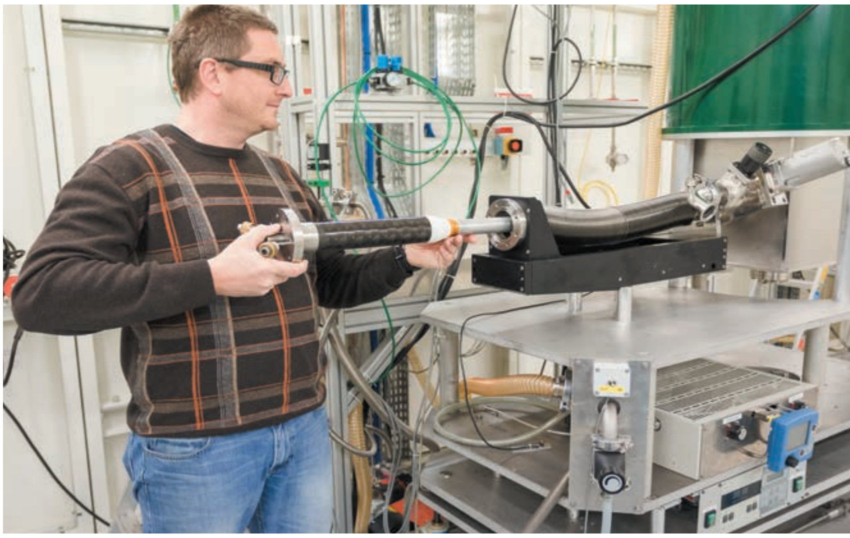

HIDDEN ORDER AND 5f ELECTRON CHARGE DENSITY IN URu_2Si_2

The symmetry of the crystal field ground state of the hidden order compound URu_2Si_2 was determined with a non-resonant inelastic X-ray scattering experiment at ID20. The strong anisotropy of the scattering signal was modelled with a full multiplet code and a quantitative result for the ground state wave function was obtained.

Thirty years ago, specific heat (entropy) measurements indicated that URu_2Si_2 undergoes a phase transition at 17 K into an electronically ordered state. Since then, this order has been investigated by many experimental and theoretical physicists worldwide but, nevertheless, both the type of order and the reason for this order have yet to be discovered. This quantum phenomenon is therefore called *hidden order* **[1-4]**.

Solving the hidden order puzzle is not only an intellectual challenge; it also advances theoretical concepts that are relevant for the design of new materials with exotic properties that may find applications in daily life. URu_2Si_2 is therefore a model material for solid state physicists in a sense that new theories and new experiments are continuously being developed to solve the hidden order.

It is generally accepted that the distribution of the electronic density of the uranium atoms at low temperatures is an important key to understand the hidden order. In the present work, the aim was to investigate the 5*f* electron density of U in URu_2Si_2. The tetragonal point symmetry of U in URu_2Si_2 splits the U $5f^2$ Hund's rule ground state into five singlets and two doublets (insets of **Figure 88a**).

A non-resonant inelastic X-ray scattering experiment (NIXS), performed at beamline **ID20**, revealed which of the seven states is the ground state. The experiment was performed at low temperature so that only the ground state was occupied. The photon-in photon-out scattering process excites a core electron to the valence band (5*d* → 5*f*). A crucial condition for such an experiment is a high incident energy (≈ 10 keV) so that large momentum transfers can be reached (≈ 10 $Å^{-1}$). The scattering signal at such high momentum transfers is dominated by higher multipole scattering terms, making the spectra excitonic and thus local. Moreover, the anisotropy of the 5*f* electron distribution (see insets in **Figure 88a**) will be reflected in a strong angular dependence; and this is what was indeed observed (see **Figure 88b**). The calculation of the *multipole selection rules* with the full multiplet code *Quanty* **[5]** gave access to the respective ground state (see **Figure 88a**). The singlets with symmetry Γ_1 or Γ_2 reproduce the observed direction dependence

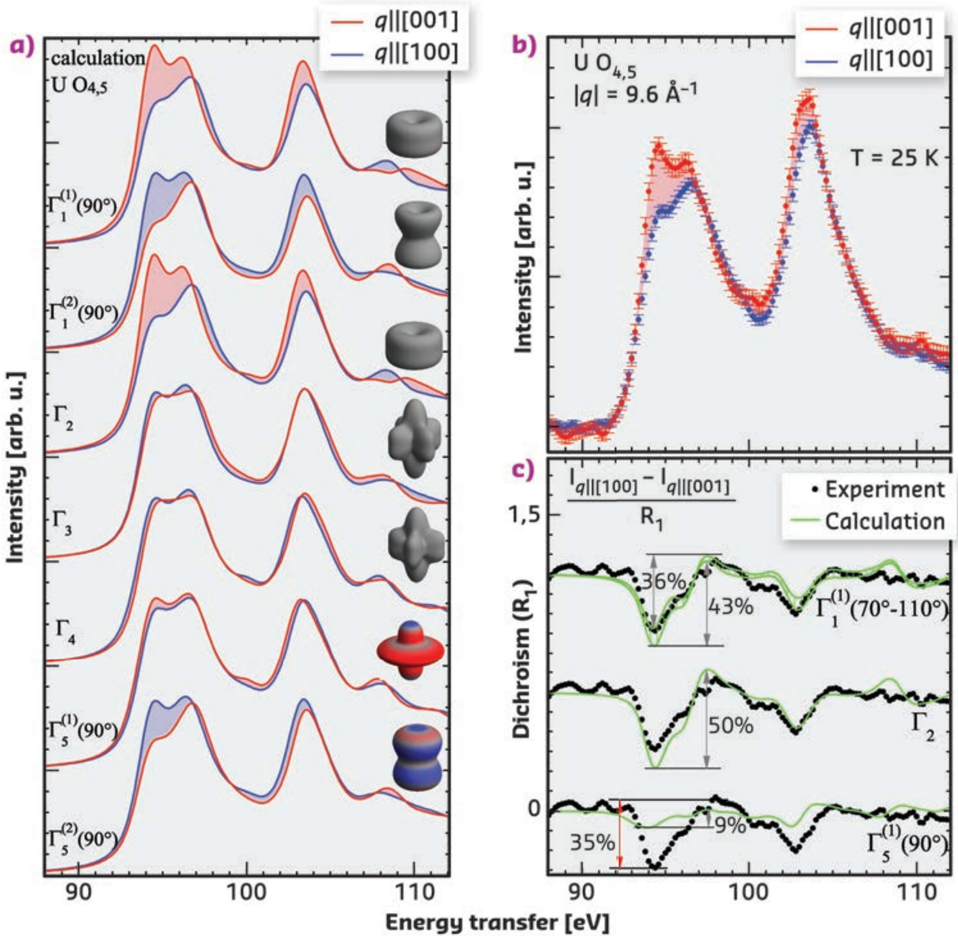

Fig. 88: a-b) Scattering function as obtained in a NIXS experiment at the U O4,5 edge for |q| = 9.6$Å^{-1}$. a) Simulation (Quanty) of the direction dependence of the $5d^{10}4f^2 \rightarrow 5d^94f^3$ transition for the seven crystal-field states. b) NIXS data for the two directions of momentum transfer. c) Comparison of difference spectra (dichroism) with calculations of Γ_1, Γ_2 and Γ_5.

(see dichroism in **Figure 88c**). Hence either of these states or both nearly degenerate are the crystal-field ground state.

These experimental results limit the number of hidden order scenarios and are therefore an important touchstone for theoretical models.

PRINCIPAL PUBLICATION AND AUTHORS

Direct bulk sensitive probe of 5f symmetry in URu_2Si_2, M. Sundermann (a,b), M.W. Haverkort (b,c), S. Agrestini (b), A. Al-Zein (d,e), M. Moretti Sala (d), Y. Huang (f), M. Golden (f), A. de Visser (f), P. Thalmeier (b), L. Hao Tjeng (b) and A. Severing (a), *PNAS* **113**, 13989-13994 (2016); doi: 10.1073/pnas.1612791113.

(a) Institute of Physics II, University of Cologne (Germany)
(b) Max-Planck Institute for Chemical Physics of Solids, Dresden (Germany)
(c) Institute for Theoretical Physics, Heidelberg University (Germany)
(d) ESRF
(e) present address: Physics Department, Faculty of Science, Beirut Arab University (Lebanon)
(f) Van der Waals-Zeeman Institute, University of Amsterdam (The Netherlands)

REFERENCES

[1] P. Oppeneer *et al.*, *Phys. Rev. B* **82**, 205103 (2010).
[2] J. Mydosh and P. Oppeneer, *Rev. Mod. Phys.* **83**, 1301 (2011).
[3] P. Chandra *et al.*, *Nature* **493**, 621 (2013).
[4] H.H. Kung *et al.*, *Science* **347**, 1339 (2015).
[5] M.W. Haverkort, *Phys. Rev. B* **85**, 165113 (2012).

HUMAN SCALP HAIR RECORDS THE SOURCE OF MERCURY EXPOSURE

HR-XANES spectroscopy was used to decipher the molecular forms of mercury in human tissue from individuals exposed inadvertently to mercury contamination. The low-Z atoms around Hg in scalp hair were identified, revealing the source of mercury exposure. In combination with nano-imaging, the timing of an exposure event was discovered.

Common sources of mercury that affect human health are methylmercury (MeHg) in fish and rice, ethylmercury (EtHg) in medical products and elemental mercury in dental amalgams (Hg^0), and mercury vapour in occupational areas. The hypothesis that the molecular forms of mercury in human hair could be an indicator of the source of the mercury was tested. Scalp hair is convenient for this purpose because it typically contains 250 times more mercury than blood, is easy to sample, and provides a history of exposure with a daily growth rate of about 40 micrometres. Mercury has a low natural abundance, at most 10 ppm (ng/mg) in the hair of fish consumers and at the ppm to sub-ppm level in the general population. Another impediment to assessing the form of mercury in hair is the proteinaceous composition of this material, therefore requiring the use of probes that can differentiate C, N, and O ligands (**Figure 89a**).

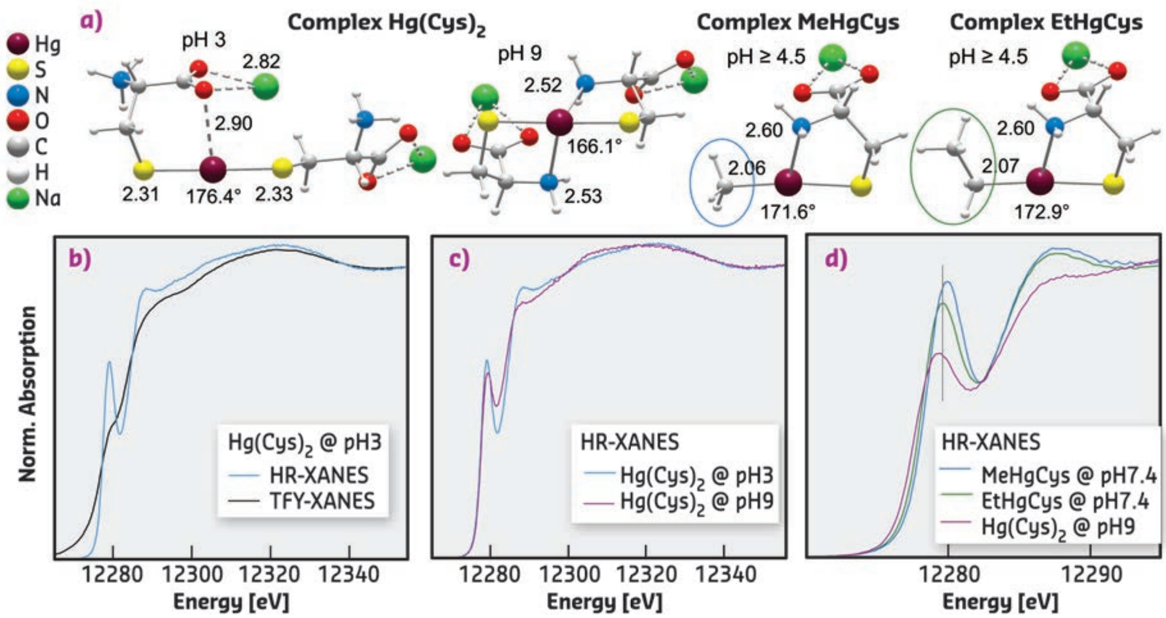

Fig. 89: a) Molecular structures of Hg-thiolate complexes optimised by MP2/TZVP-ecp calculations. Interatomic distances are in Ångstroms and S-Hg-S angle in degrees.
b-d) Hg L_3-edge HR-XANES signatures of the Hg-thiolate complexes.

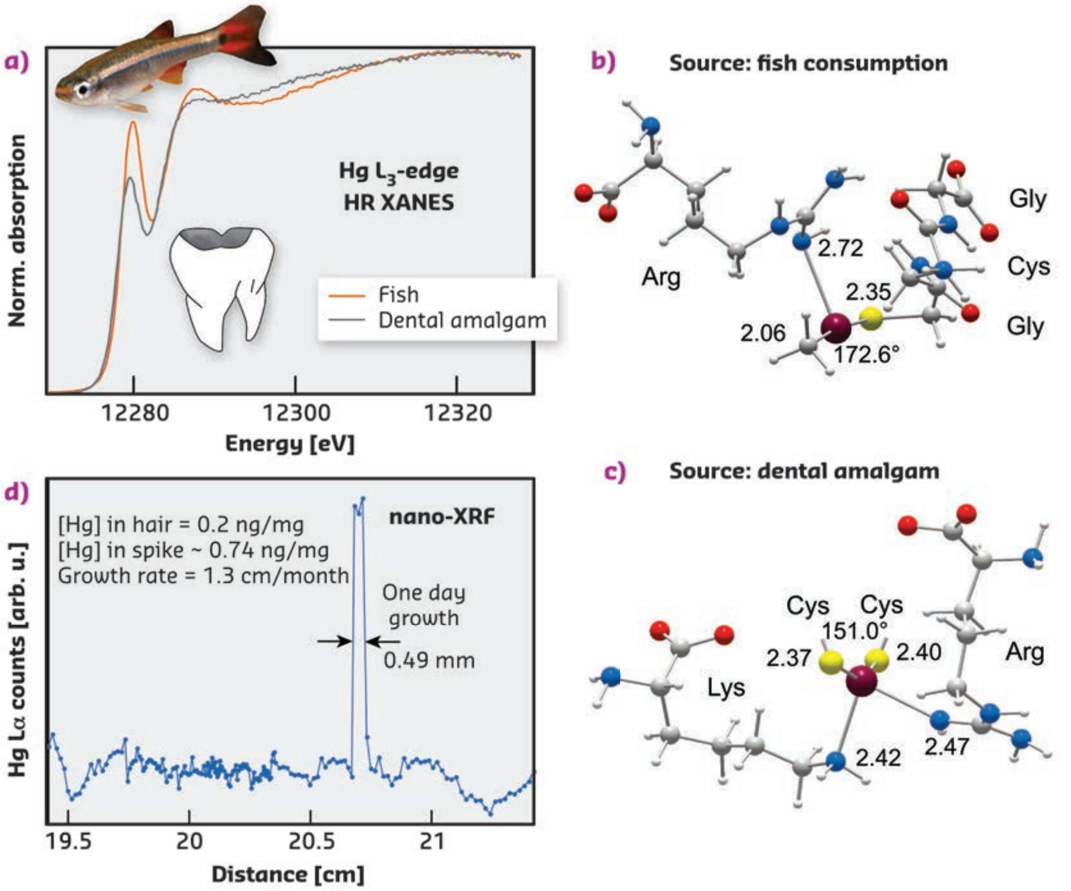

Fig. 90: a) HR-XANES signatures of two chemical forms of mercury in hair, one originating from fish consumption (MeHg) and the other from removal of a dental amalgam (Hg^0). b,c) Geometry-optimised models representing the two types of bonding environments in hair proteins (MP2/TZVP-ecp optimisation). d) Longitudinal profile of methylmercury in a single strand from an individual affected by extraction of a dental amalgam.

To tackle both detection limit and sensitivity to low-Z ligands, high-energy-resolution XANES spectroscopy was used at beamline **ID26**. HR-XANES has higher signal-to-noise (s/n) ratio than EXAFS, and also possesses better chemical-state and ligand sensitivity because of participation of unoccupied valence orbitals in the excited state **[1]**. This sensitivity was enhanced by measuring the X-ray fluorescence with analyser crystals in order to reduce the intrinsic broadening of the spectral features **[2]**.

At the Hg L_3-edge of the measurements, HR-XANES had an effective energy resolution of 3.0 eV compared to about 6.1 eV in conventional total fluorescence yield (TFY) measurement with a solid-state detector. The gain in spectral resolution is shown in **Figure 89b** with the $2p_{3/2} \rightarrow 6s/5d$ electronic transition of the bis L-cysteinate complex ($Hg(Cys)_2$) at pH 3. The linear dithiolate conformation gives a shoulder in TFY measurement and a prominent near-edge peak in HR-XANES measurement.

The whole rising region of HR-XANES contains core-to-valence features that vary in intensity and energy with the number and identity of atoms in the first and second coordination shell of Hg, and with the geometry of the bonding environment. For instance, secondary amine ligands, which bond at pH 9, give a distinctive spectral signature characterised by a less intense near-edge peak and a shift to lower energy of the HR-XANES trace beyond this peak (**Figure 89c**). Also, $Hg(Cys)_2$, MeHgCys and EtHgCys complexes are readily differentiated from the energy of the $2p_{3/2} \rightarrow 6s/5d$ transition (**Figure 89d**).

Mercury sourced from fish consumption and dental amalgam gives diagnostic HR-XANES features (**Figure 90a**) that were used to model its bonding environment in hair using first principles calculations. **Figure 90b** shows the optimised geometry of a MeHg[SR+N] coordination complex with a cysteinyl sulfur from a GlyCysGly tripeptide and a side chain guanidyl NH donor from arginine, consistent with the HR-XANES results for organic methylmercury in hair. The bending of the linear Me-Hg-SR coordination from about 180° to 172.6° constitutes a noteworthy structural marker of the Hg-N secondary bond (either through a NH or NH2 group), which gives a distinctive XANES signature.

Mercury sourced from dental amalgams is inorganic and the Hg(II) ion coordinated to two thiolate ligands (SR^-) and to two secondary N ligands in a seesaw geometry (**Figure 90c**). The timing of a particular exposure event resulting from the removal of an amalgam was determined by coupling HR-XANES at **ID26** with Hg nano-imaging at **ID16B**. The mercury spike on the longitudinal $Hg(L_\alpha)$ profile from a single strand of hair (**Figure 90d**) recorded the contamination event, and its width indicates the residence time of Hg(II) in the bloodstream, here estimated to be about one day. The dental source of Hg(II) was revealed by its Hg[$(SR)_2$+N_2] coordination in the spike area, as determined by HR-XANES.

PRINCIPAL PUBLICATION AND AUTHORS

Chemical forms of mercury in human hair reveal sources of exposure, A. Manceau (a), M. Enescu (b), A. Simionovici (a), M. Lanson (a), M. Gonzalez-Rey (c), M. Rovezzi (d), R. Tucoulou (d), P. Glatzel (d), K.L. Nagy (e) and J-P. Bourdineaud (f), *Environmental Science & Technology* **50**, 10721-10729 (2016); doi: 10.1021/acs.est.6b03468.
(a) ISTerre, Université Grenoble Alpes, CNRS, Grenoble (France)
(b) Laboratoire Chrono Environnement, Université de Franche-Comté, CNRS, Besançon (France)
(c) Laboratoire EPOC, Université de Bordeaux, CNRS, Arcachon (France)
(d) ESRF
(e) Department of Earth and Environmental Sciences, University of Illinois at Chicago (USA)
(f) Institut Européen de Chimie et Biologie, Université de Bordeaux, CNRS, Pessac (France)

REFERENCES

[1] A. Manceau *et al.*, *Inorg. Chem.* **54**, 11776-11791 (2015).
[2] P. Glatzel *et al., J. Elec. Spec. Relat. Phenom.* **188**, 17-25 (2013).

ELASTIC PROPERTIES REVEALED BY THERMAL DIFFUSE SCATTERING

The full elasticity tensor can be obtained in a single crystal diffraction experiment through measurement of thermal diffuse scattering. Both the elastic properties and the crystal structure are determined by this new approach.

Elastic moduli give important insights into the mechanical behaviour of crystalline materials. Accurate measurements of the elasticity tensor – which contains the full set of elastic moduli – are of principal interest in materials science, geophysics and condensed matter physics. Applications include superconductors, low dimensional spin systems and an improved understanding of seismological wave propagation, which, in turn, allows for decisive conclusions on composition, temperature and pressure of the Earth's interior.

The two most commonly used experimental techniques to determine the elastic tensor are ultrasound measurements and Brillouin scattering. While the former has strong limitations on small crystals and experiments under extreme conditions, the latter is difficult for opaque materials. Alternatively, information on the elasticity tensor can be obtained from inelastic scattering experiments. Now, it has been shown that the full elasticity tensor can be determined by high-precision measurements of thermal diffuse scattering from a single crystal, thus opening new perspectives in a range of scientific fields.

Thermal diffuse scattering arises from the vibrations of atoms around their equilibrium positions. In a scattering experiment these vibrations result in intensities in between Bragg reflections and are the fingerprints of the lattice dynamics. In the vicinity of Bragg reflections, the scattering intensities are dominated by acoustic phonons that correspond to elastic waves. These waves propagate with the speed of sound that can take different values depending on the composition, the crystal symmetry, direction and external influences such as temperature and pressure. The full information is given by the elasticity tensor, which can be extracted by a careful analysis of the scattering intensities.

High-quality single crystals of magnesium oxide and calcite are investigated as benchmark systems. The experimental setup is illustrated in **Figure 91**. Scattering intensities were collected at beamlines **ID29** and **BM01A**. The sample was rotated with angular steps of 0.1° with

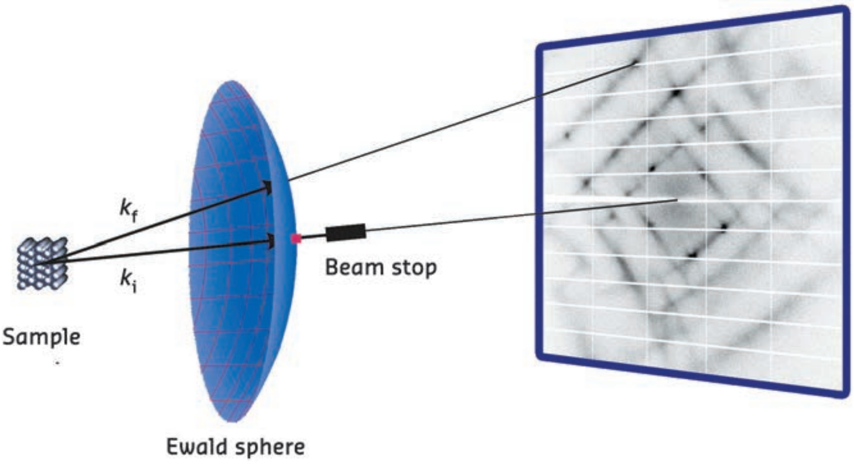

Fig. 91: Diffraction geometry for a diffuse scattering experiment in transmission **[1]**. The incoming monochromatic X-rays with wave vector k_i are scattered by the sample and diffracted onto the Ewald sphere. The area detector records the planar projection of the Ewald sphere.

	Calcite			Magnesium oxide		
	TDS	US		TDS	US	
	T = 170 K			I(T = 120 K) – I(T = 90 K)	T = 90 K	T = 120 K
C_{11}	156	155.1	C_{11}	300	306.1	305.4
C_{13}	57.0	57.69	C_{44}	151	157.2	156.9
C_{15}	21.2	21.51	C_{12}	89	94.07	94.26
C_{33}	87.6	87.12				
C_{44}	35.7	34.42				
C_{66}	48.0	47.80				

Table 1: Elastic moduli of calcite and magnesium oxide determined from thermal diffuse scattering (TDS) and ultrasound measurements (US). Values are given in GPa.

exposure times adapted to the weak diffuse scattering. Measurements were taken at various temperatures. Details of the experimental setup and the underlying theory can be found elsewhere **[1, 2]**.

The data treatment required a novel analysis technique and the development of a specialised software package, which comprises the precise reconstruction of reciprocal space and careful selection of regions in reciprocal space to be treated. The software simultaneously fits approximately 10^7 individual intensity points by taking into account the exact scattering geometry and symmetry of the crystal.

Determination of the elastic moduli from thermal diffuse scattering measured at a single temperature is demonstrated for a small calcite single crystal. Experimental scattering intensities and calculated thermal diffuse scattering intensities from the fitted elastic moduli are compared in **Figure 92**. Remarkably, the results agree within about 1% with values determined by ultrasound measurements (see **Table 1**).

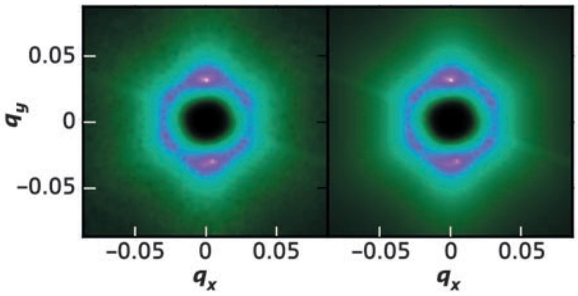

Fig. 92: Measured (left panel) and calculated (right panel) thermal diffuse scattering from calcite (T = 170 K) for momentum transfers $q \in [0.03, 0.15]$. The images show a cross-section of the reciprocal space in Cartesian coordinates, in the neighbourhood of the Bragg peak $[\bar{1}, 0, \overline{16}]$ with $q_z = 0$. The scattering intensity is shown on a linear colour scale from black (zero) to white (maximum intensity).

Absolute values of the elastic moduli can be obtained if measurements are taken at slightly different temperatures. This strategy further allows separation of the inelastic contribution from elastic scattering that may arise from disorder or imperfect surfaces. This is shown for magnesium oxide (see **Table 1**), for which accurate values in absolute units were obtained by fitting scattering intensities at two temperatures.

The new method is model-free and can be applied to very small and opaque crystals of arbitrary shape and symmetry. This implies a broad applicability in material science, geophysics and in the study of sound wave anomalies due to fundamental interactions in condensed matter physics. It is possible to measure the elastic properties together with the crystal structure in the same experiment. This is a great benefit for measurements at extreme conditions, such as high pressures, where it is often difficult to reproduce the exact experimental conditions.

PRINCIPAL PUBLICATION AND AUTHORS

Full elasticity tensor from thermal diffuse scattering, B. Wehinger (a,b), A. Mirone (c), M. Krisch (c) and A. Bosak (c), *Physical Review Letters* **118**, 035502 (2017); doi: 10.1103/PhysRevLett.118.035502.
(a) Department of Quantum Matter Physics, University of Geneva (Switzerland)
(b) Laboratory for Neutron Scattering and Imaging, Paul Scherrer Institute, Villigen (Switzerland)
(c) ESRF

REFERENCES

[1] B. Wehinger, PhD thesis, Université de Grenoble (2013), http://tel.archives-ouvertes.fr/tel-00961602.
[2] A. Bosak *et al.*, *Journal of Physics. D, Applied Physics* **48**(50), 50400 (2015).

RIXS REVEALS SIGNATURES OF PROPAGATING CHARGE DENSITY WAVE EXCITATIONS IN CUPRATES

The recent observation of a charge density wave (CDW) in high-T_c superconductors has raised the question of how it affects charge and lattice dynamics. In this study, using high-resolution resonant inelastic X-ray scattering (RIXS), the interference between phonons and CDW-related electronic excitations was observed for the first time in underdoped $Bi_2Sr_2CaCu_2O_{8+d}$.

Cuprates exhibit high-temperature superconductivity upon doping with charge carriers. Significant efforts have been made to uncover the underlying microscopic mechanism in high-T_c cuprates, which could ultimately lead to the synthesis of room temperature superconductors that would revolutionise the power transmission and electronics industries. However, this is a great challenge because cuprates are more complex than the framework of weak-coupling theories established in the last century. This complexity manifests itself in the emergence of a number of different quantum phases along with superconductivity. Clarification of the interplay among these phases is necessary to gain further insight.

Recently, experimental evidence on high-T_c cuprates revealed ubiquitous charge density wave (CDW) modulations **[1]**, which coexist with superconductivity. This is intriguing, since CDW, a state in which valence electrons tend to be localised, and superconductivity, a state in which electrons move freely, possess seemingly opposite electronic properties, implying a non-trivial relationship between the two. To gain insight into this puzzling co-existence, it is necessary to uncover how CDW interplays with other degrees of freedom. Some theories have proposed that the fluctuations of CDW, *i.e.* a form of CDW dynamics or excitations, could be important for high temperature superconductivity **[2]**, however, the experimental evidence of such CDW dynamics is lacking. With sufficient energy resolution, RIXS can be an ideal probe for CDW dynamics due to its simultaneous sensitivity to excitations (and order) of charge, spin, and orbital characters **[3]**. The soft X-ray RIXS instrument at beamline **ID32** possesses the highest ever energy resolution at the Cu L_3 edge, and provides an unprecedented opportunity to tackle this challenge.

High-resolution momentum-resolved RIXS was performed on the underdoped bi-layer cuprate $Bi_2Sr_2CaCu_2O_{8+d}$. Main results are shown in **Figure 93.** The CDW scattering peak at Q_{CDW} ~ 0.30 r.l.u. in the quasi-elastic region and a branch of phonon excitations at ~ 60 meV, attributed as the Cu-O bond-stretching modes, are clearly resolved in the RIXS intensity map. Remarkably, the phonon intensity varies non-monotonically with momentum, having a maximum near Q_A ~ 0.37 r.l.u. The RIXS phonon cross-section directly reflects the momentum-dependence of the electron-phonon coupling strength **[4]**, in stark contrast with the phonon self-energy measured by other techniques, *e.g.* inelastic neutron or non-resonant inelastic X-ray scattering. As a consequence, RIXS is also

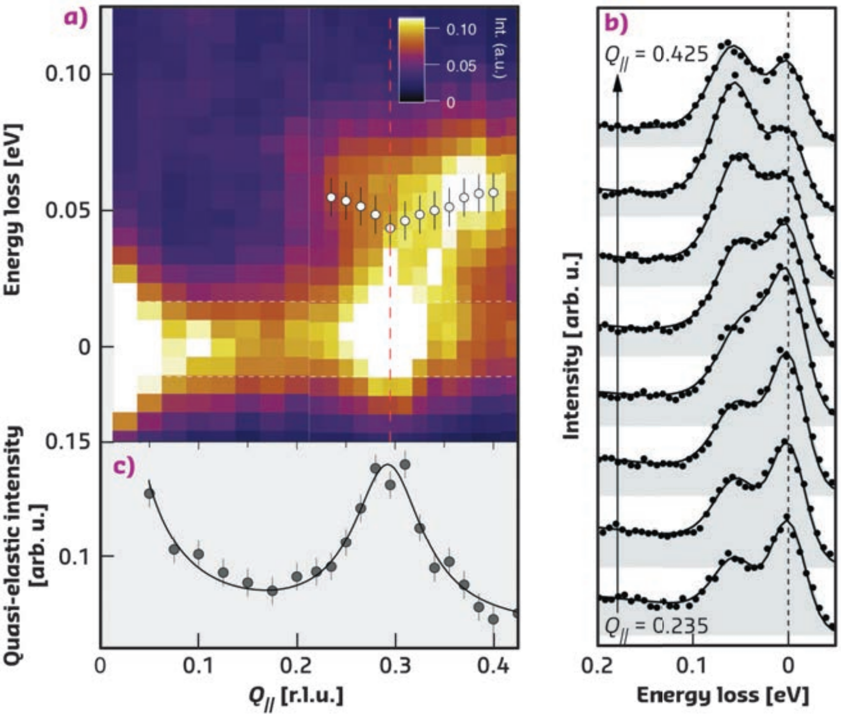

Fig. 93: a) RIXS intensity map of the high-energy resolution data (ΔE ~ 40 meV) as a function of energy loss and $Q_{//}$. The white circles represent the fitted phonon dispersion. b) Energy loss spectra at selected momentum ranging from $Q_{//}$ = 0.235 r.l.u. to $Q_{//}$ = 0.425 r.l.u. The fits (solid lines) are superimposed on the raw data (black circles). c) Averaged intensity in the quasi-elastic region, defined as the region between the two white dashed lines in (a). The solid line is a Lorentzian fit to the data with a background consisting of a constant plus a Lorentzian to account for the tail of the specular reflection peak at $Q_{//}$ = 0.

directly sensitive to the interference between phonons and underlying charge excitations, *i.e.* the Fano effect, which can manifest as an intensity anomaly. Thus, the intensity anomaly at $Q_A \neq Q_{CDW}$ provides evidence for the existence of dispersive CDW excitations that cause a strong Fano interference at the intersection with the bond-stretching phonon. Temperature-dependent measurements and theoretical calculations of RIXS phonon cross-section were also performed to support these observations.

The dispersive CDW excitations, the phonon anomaly, and the wave vector of the CDW found in this research provide a comprehensive momentum space picture of complex CDW behaviour and may point to a closer relationship with the pseudogap state. These results imply that CDW is intimately connected to the electronic structure in high-*Tc* copper oxides, in addition to the spin and phonon interactions. Future investigations to clarify the relationship among these underlying degrees of freedom would be crucial to uncover the mechanism of superconductivity in these materials.

PRINCIPAL PUBLICATION AND AUTHORS

Dispersive charge density wave excitations in $Bi_2Sr_2CaCu_2O_{8+d}$, L. Chaix (a,i), G. Ghiringhelli (b,c), Y.Y. Peng (b), M. Hashimoto (d), B. Moritz (a), K. Kummer (e), N.B. Brookes (e), Y. He (f), S. Chen (f), S. Ishida (g), Y. Yoshida (g), H. Eisaki (g), M. Salluzzo (h), L. Braicovich (b,c), Z.-X. Shen (a,f), T.P. Devereaux (a,f) and W.-S. Lee (a), *Nature Physics* **13**, 952-956 (2017); doi: 10.1038/NPHYS4157.

(a) Stanford Institute for Materials and Energy Sciences, SLAC National Accelerator Laboratory and Stanford University (USA)
(b) Dipartimento di Fisica, Politecnico di Milano (Italy)
(c) CNR-SPIN, CNISM, Politecnico di Milano (Italy)
(d) Stanford Synchrotron Radiation Lightsource, SLAC National Accelerator Laboratory, Menlo Park (USA)
(e) ESRF
(f) Geballe Laboratory for Advanced Materials, Stanford University (USA)
(g) National Institute of Advanced Industrial Science and Technology (AIST) (Japan)
(h) CNR-SPIN, Complesso Monte Sant'angelo, Napoli (Italy)
(i) present address: Laboratoire Léon Brillouin, CEA Saclay (France)

REFERENCES

[1] R. Comin *et al., Annu. Rev. Condens. Matter Phys.* **7**, 369-405 (2016).
[2] S.A. Kivelson *et al., Rev. Mod. Phys.* **75**, 1201 (2003).
[3] L.J.P. Ament *et al., Rev. Mod. Phys.* **83**, 705-767 (2011).
[4] T.P. Devereaux *et al., Phys. Rev. X* **6**, 041019 (2016).

PROBING MAGNETISM IN THE VORTEX PHASE OF AN EXOTIC PLUTONIUM SUPERCONDUCTOR

The $PuCoGa_5$ unconventional superconductor contains plutonium atoms with a nonmagnetic ground state. Yet, magnetic or virtual valence fluctuations are suspected to provide the mediating boson leading to electron pairing. Using X-ray magnetic circular dichroism, the subtle changes in the plutonium magnetism were followed across the superconducting transition.

Superconductivity is a phase of condensed matter emerging when electrons form integer-spin bound pairs and condense into a single macroscopic quantum state. For most superconductors, the short-range, isotropic attraction provided by electron-phonon coupling provides the glue for electron pairing. However, several compounds are known for which a boson field different than the one associated with the vibrations of the crystal lattice is involved. One of these compounds is $PuCoGa_5$.

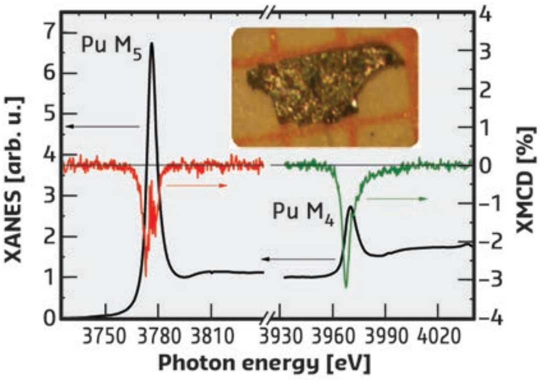

Fig. 94: XANES and XMCD spectra at the Pu $M_{4,5}$ edges in $PuCoGa_5$ at 2.1 K. Spin and orbital components of the magnetic moment are proportional to linear combinations of the integrated XMCD signals. The inset shows a picture of the single crystal sample used for the measurements.

With a critical temperature of 18.7 K, $PuCoGa_5$ represents a distinctive category of superconductor, fitting into neither the heavy-fermion nor the high-T_c superconductivity paradigms. Magnetic or virtual valence fluctuations in proximity to a quantum critical point are suspected to have an important role in stabilising its superconducting ground state. Yet, the specific nature of the electron pairing in this exotic material is not understood.

A tile of the puzzle is the nonmagnetic state of the plutonium atoms reflected by the temperature-independent paramagnetism of the normal phase. State-of-the-art electronic structure calculations show that the local 5f magnetic moment is quenched by a combination of intermediate valence and hybridisation with the surrounding cloud of conduction electrons. In this model, the Pu atoms swing between the $5f^5$ and $5f^6$ configurations and the local magnetic moment fluctuates in time. However, compensating variations in the hybridised bath maintain a constant nonmagnetic ground state. An important question in this respect is whether such a perfect dynamic balance persists in the superconducting phase. The diamagnetic response associated with the Meissner effect prevents addressing this question by macroscopic magnetometry. It was therefore decided to exploit the possibilities afforded by X-ray magnetic circular dichroism (XMCD), a technique that is not, *a priori*, sensitive to diamagnetism, to quantify the Pu properties in the normal phase and in the vortex phase below T_c.

XMCD is a well-established tool to determine spin and angular moments (μ_S and μ_L) of a given atomic shell. This is achieved by using "sum rules" that correlate the integrals of dichroic spectra measured at two spin-orbit split absorption edges. Here, data were collected in the energy range 3.7-4.1 keV, across the plutonium $M_{4,5}$ absorption edges ($3d_{3/2} \rightarrow 5f_{5/2}$ and $3d_{5/2} \rightarrow 5f_{5/2,7/2}$ transitions). The experiment was performed at the **ID12** beamline, using a single crystal containing almost isotopically pure ^{242}Pu, a long-living isotope that strongly reduces self-irradiation damage, allowing the observation of the intrinsic properties of the compound.

Figure 94 shows the spectra obtained at 2.1 K in a field of 17 T applied along the crystallographic c-axis after zero-field cooling from the normal phase. Below T_c, XMCD probes only atoms in the vortex phase, where a magnetic field that can polarise the atomic shells penetrates. Unexpectedly, the results show that μ_L increases significantly between 30 and 2 K, from 0.052(2) to 0.068(2) μ_B. The antiparallel spin component μ_S increases as well, leaving the total induced magnetic moment practically unchanged. The temperature dependence of the XMCD signal at the Pu M_4 edge is shown in **Figure 95**. This quantity, proportional to μ_L-μ_S, increases monotonically from 30 to 2 K, with no anomaly around T_c (lowered to 15.4 K by the applied field). The increase of μ_S with decreasing temperature suggests that the Kondo-like screening responsible for the Pu singlet ground state starts to break down, possibly because of a change in the hybridisation of the 5f electrons with the conduction band.

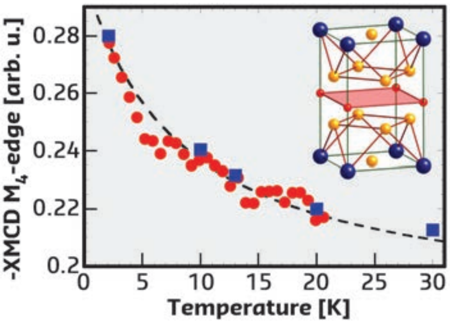

Fig. 95: Temperature dependence of the XMCD signal measured at the M_4 absorption edge. Squares correspond to the integral of the XMCD spectra, whereas circles are the value measured at the peak energy (3968 eV). The inset shows the tetragonal crystal structure of $PuCoGa_5$ (Pu: blue spheres; Co: red spheres; Ga: orange spheres).

The results validate electronic structure calculations describing $PuCoGa_5$ as a lattice of Pu Anderson impurities carrying a fluctuating local moment dynamically quenched by the hybridisation with conduction electrons. Understanding how these complex electronic dynamics are related to the formation of Cooper pairs is a significant challenge in the race towards room-temperature superconductivity.

PRINCIPAL PUBLICATION AND AUTHORS

Probing magnetism in the vortex phase of $PuCoGa_5$ by X-ray magnetic circular dichroism, N. Magnani (a), R. Eloirdi (a), F. Wilhelm (b), E. Colineau (a), J.C. Griveau (a), A.B. Shick (c), G. H. Lander (a), A. Rogalev (b) and R. Caciuffo (a), *Phys. Rev. Lett.* **119**, 157204 (2017); doi: 10.1103/PhysRevLett.119.157204

(a) European Commission, Joint Research Centre (JRC), Directorate for Nuclear Safety and Security, Karlsruhe (Germany)
(b) ESRF
(c) Institute of Physics, ASCR, Prague (Czech Republic)

NON-ADIABATIC CRYSTAL-LATTICE DYNAMICS IN SUPERCONDUCTING DIAMOND

The crystal-lattice dynamics of superconducting diamond, investigated through *ab initio* calculations and inelastic X-ray scattering, has revealed the emergence of a non-adiabatic Kohn anomaly. This result constitutes the first observation of the breakdown of the Born-Oppenheimer approximation in the phonon spectra of a three-dimensional solid.

The Kohn anomaly (KA) is one of the most striking manifestations of the influence of electron-phonon coupling on the lattice dynamics of metals **[1]**. KAs result from the screening of lattice vibrations by virtual electronic excitations, and manifest themselves through distinctive dips in the phonon dispersion relations. The existence of KAs has been confirmed by inelastic neutron scattering experiments in a number of metals, conventional superconductors, as well as superconducting semiconductors. KAs are typically well described in the adiabatic Born-Oppenheimer approximation, whereby electronic and nuclear degrees of freedom are assumed to be decoupled. This picture breaks down whenever the electronic screening takes place on timescales that are comparable to the period of lattice vibrations. Correspondingly non-adiabatic effects may arise, leading to strongly coupled dynamics of electrons and nuclei, which signals a breakdown of the Born-Oppenheimer approximation. However, it has been suggested that non-adiabatic effects might be too small to be observable in three-dimensional solids [2].

The emergence of non-adiabatic effects in the Kohn anomaly of boron-doped diamond was investigated for hole densities that make the system superconducting at low temperature. The dispersion relations of the longitudinal-optical (LO) phonons (marked in red in Figure 96e) were analysed using state-of-the-art many-body first-principles calculations and inelastic X-ray scattering (IXS) measurements. IXS spectra were measured at beamline **ID28**. The phonon dispersions have been obtained entirely from first-principles through the evaluation of the phonon self-energy and the phonon spectral function based on the many-body theory of electron-phonon coupling. The measured IXS spectra are shown in Figure 96a and b as heat maps for pristine (undoped) diamond and for a boron concentration of 10^{21} cm^{-3} for momenta along the Γ-X direction. The computed phonon dispersions are reported in Figure 96c and d, whereas the full (adiabatic) phonon dispersions are shown in Figure 96e.

The IXS spectrum of B-doped diamond reported in Figure 96b exhibits a softening of the LO phonon energy by 7 meV as compared to the dispersion measured on the pristine sample and shown in Figure 96a. The softening is further accompanied by an increase of the phonon linewidth close to Γ in the doped samples. The softening and linewidth become more pronounced with increasing hole density. Calculations based on the adiabatic Born-Oppenheimer approximation, shown in Figure 96e, fail at reproducing these features: the phonon softening is overestimated by 300%, and linewidths may not be inferred at this level of theory. Conversely, the comparison between Figure 96a and b, and Figure 96 c and d, indicates that fully non-adiabatic calculations yield phonon energies and linewidths in excellent quantitative agreement with IXS. Besides resolving the long-standing discrepancy between earlier theoretical works and measured phonon dispersions, these results demonstrate a breakdown of the adiabatic Born-Oppenheimer approximation in the phonon dispersion relations of boron-doped diamond, and reveal that these effects may be sizeable also in three-dimensional bulk compounds.

The breakdown of the adiabatic Born-Oppenheimer approximation observed in the lattice dynamics of heavily boron-doped diamond may be explained by considering the timescales involved: while LO phonons oscillate with a period τ_{ph}= 25 fs, the timescale of electronic screening τ_s is set by the plasma frequency ω_{pl} via $\tau_s = 2\pi/\omega_{pl}$, which, for a doping concentration of $1.4 \cdot 10^{21}$ cm^{-3} corresponds to τ_s = 4 fs. As screening operates on timescales that approach the characteristic phonon period, the assumptions underlying the Born-Oppenheimer approximation cease to hold, and we see the emergence of strong non-adiabatic coupling.

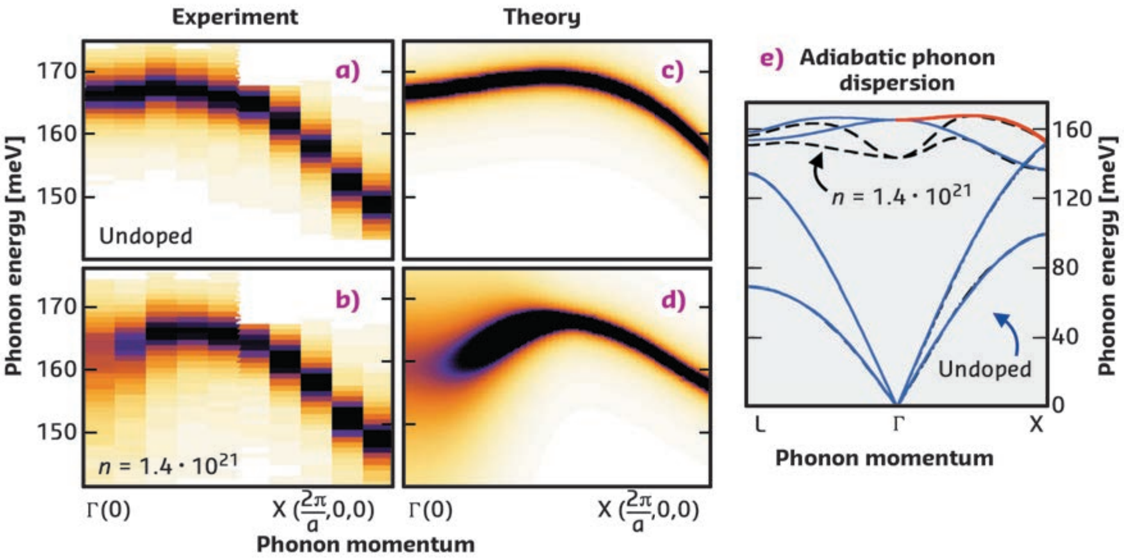

Fig. 96: Measured IXS spectra for the LO phonon (marked in red in panel (e)) of pristine (a) and B-doped (b) diamond along Γ-X. The B-doping concentration n is in units of cm^{-3}. c)-d) Non-adiabatic spectral function obtained from first-principles calculations. e) Adiabatic phonon dispersions.

In summary, by combining first-principles calculations of the electron-phonon interaction and high-resolution IXS experiments, the emergence of a non-adiabatic KA in superconducting diamond was demonstrated, and it was shown that a breakdown of the Born-Oppenheimer approximation may lead to sizeable renormalisation effects in the phonon dispersions of three-dimensional crystals. The results call for a systematic investigation of non-adiabatic effects and Kohn anomalies in the phonon dispersions of three-dimensional crystals such as doped semiconductors and transition metal oxides, and their implications on the superconducting properties of these systems. The combination of high-resolution IXS spectroscopy as provided by the **ID28** beamline and state-of-the-art *ab initio* many-body methods offers unique opportunities to explore these and other exciting new directions in the areas of crystal lattice dynamics and electron-phonon interactions.

PRINCIPAL PUBLICATION AND AUTHORS

Non-adiabatic Kohn Anomaly in Highly-Doped Diamond, F. Caruso (a,b), M. Hoesch (c), P. Achatz (d), J. Serrano (e), M. Krisch (f), E. Bustarret (d) and F. Giustino (a).
Phys. Rev. Lett. **119**, 017001 (2017);
doi: 10.1103/PhysRevLett.119.017001
(a) University of Oxford (UK)
(b) Humboldt-Universität zu Berlin (Germany)
(c) Diamond Light Source (UK)
(d) Université Grenoble Alpes (France)
(e) Yachay Tech University (Ecuador)
(f) ERSF

REFERENCES

[1] W. Kohn, *Phys. Rev. Lett.* **2**, 393 (1959).
[2] A. M. Saitta, M. Lazzeri, M. Calandra, and F. Mauri, *Phys. Rev. Lett.* **100**, 226401 (2008).

WHY APICAL OXYGENS PLAY AGAINST HIGH Tc SUPERCONDUCTIVITY

The complex intertwining of structural, magnetic and electronic properties makes the superconductivity of cuprates a 30-year-old mystery. Using resonant inelastic X-ray scattering (RIXS) to map spin-wave dispersion, out-of-plane oxygen atoms have been found to localise the in-plane electronic wave function, ultimately lowering the maximum reachable superconducting transition temperature (T_c).

Superconductivity of Cu-based layered materials is the deepest mystery of solid state physics: 30 years of intense theoretical and experimental research have not told us what really gives cuprates such a high T_c. The problem is complicated by the fact that magnetic and electronic degrees of freedom are equally important and are strongly influenced by the quasi-2D structure of the system. The superconducting CuO_2 planes are antiferromagnetic in parent compounds while their short-range spin correlation is preserved in superconducting doped materials. However, whether this has significance for the T_c is not known. Moreover, the out-of-plane coordination of Cu ions varies from family to family through the presence of apical ligands (usually oxygen). The influence of the apical ligands on the in-plane transport properties also remains a mystery. This work clarifies these two unknowns.

Resonant inelastic X-ray scattering (RIXS) at the Cu L_3 absorption edge is probably the best technique to measure spin excitations in cuprates at all doping levels across the phase diagram, from antiferromagnetic insulating parent compounds to overdoped Fermi-liquid bad metals **[1, 2]**. The ERIXS spectrometer at beamline **ID32** is currently the leading instrument for high-resolution RIXS and its unique capabilities have been fully exploited in this work. Here, the dispersion of spin-waves was carefully mapped along a symmetry-significant path in the first Brillouin zone, for three parent materials differing by the number of apical oxygen ions (see **Figure 97**, left panel): $CaCuO_2$ (CCO) no apical oxygens, $NdBa_2Cu_3O_{6+x}$ (NBCO) one apical oxygen, $Bi_2Sr_{2-x}La_xCuO_6$ (Bi2201) two apical oxygens. Data from the literature for La_2CuO_4 (LCO) with two apical oxygens was also considered **[3]**.

The comparison in **Figure 98** confirms that the "average" super-exchange Cu-Cu interaction is always very strong, making the most of the spin excitation energy ≈ 300 meV in all materials: the ubiquity of strong antiferromagnetism is confirmed again. More interestingly, it is found that the dispersion along the Brillouin zone boundary (measured by the parameter ΔE_{MBZB}) is strictly related to the number and distance of apical oxygens. The phenomenological analysis by different models confirms that apical oxygen ions tend to localise the exchange interaction to the first and second neighbours. This means that, more generally, hopping integrals follow the same rule, and that wave functions are more extended in-plane when apical ligands are farther away. Theory had previously posed that superconductivity is enhanced by larger long-range hopping integrals **[4]**, therefore here a direct link between an important structural property of cuprates and their maximum T_c is revealed.

These findings explain why tri-layer structures have the highest T_c, as they reach the best compromise between hole doping and hopping extent. In materials with larger number of layers per unit cell, the transfer of doping holes to the CuO_2 planes is strongly reduced by the absence of apical oxygens, and T_c decreases due to insufficient doping in the inner layers. Nevertheless, new ideas for engineering higher T_c superconductors may arise from these results.

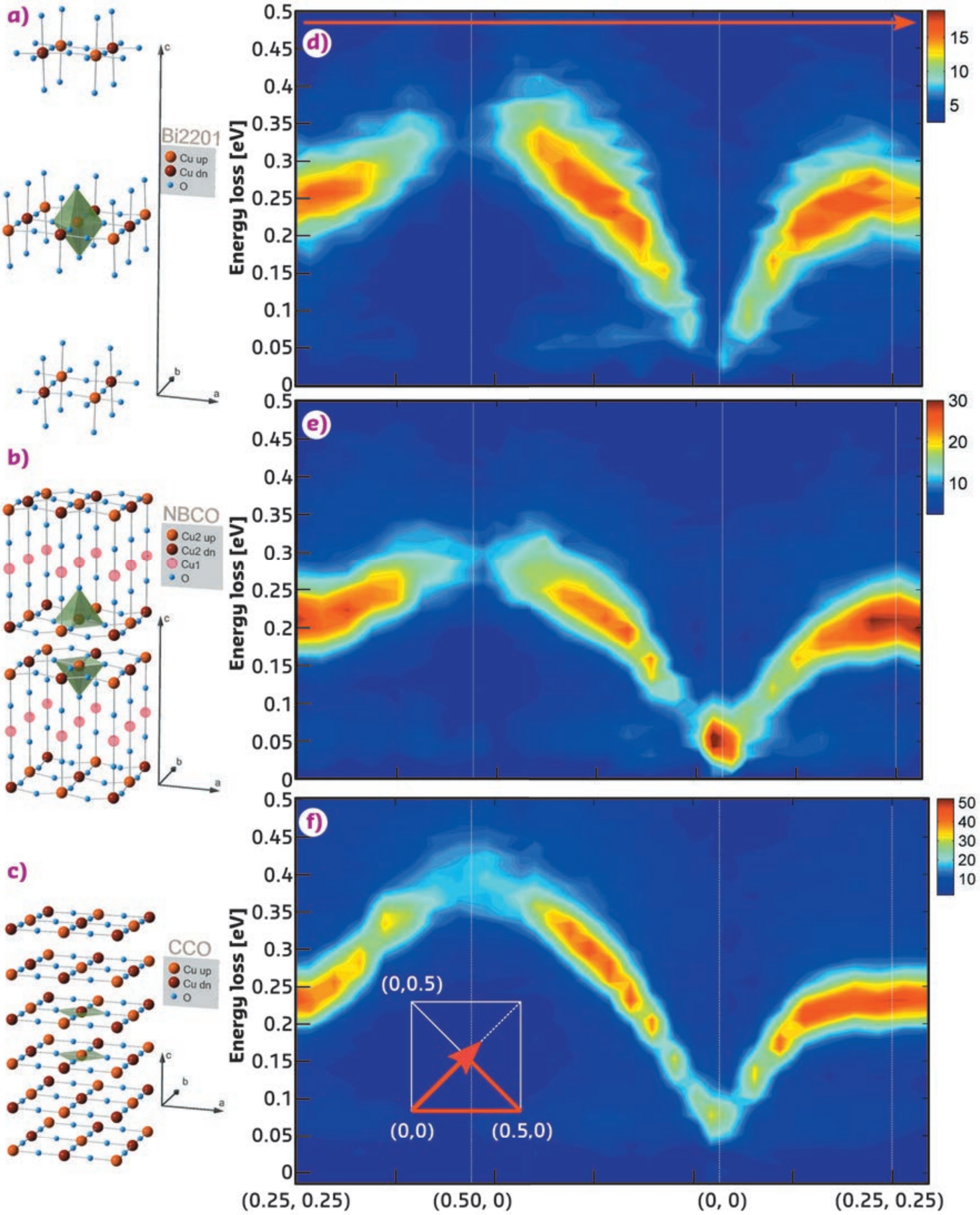

Fig. 97: In-plane momentum dependence of the magnetic excitations of antiferromagnetic layered cuprates measured by RIXS at the Cu L_3 resonance. Spin-wave dispersion of heavily underdoped $Bi_2Sr_{2-x}La_xCuO_6$, undoped $NdBa_2Cu_3O_{6+x}$, and $CaCuO_2$, respectively, along the high-symmetry momentum trajectory indicated in the inset of (f).

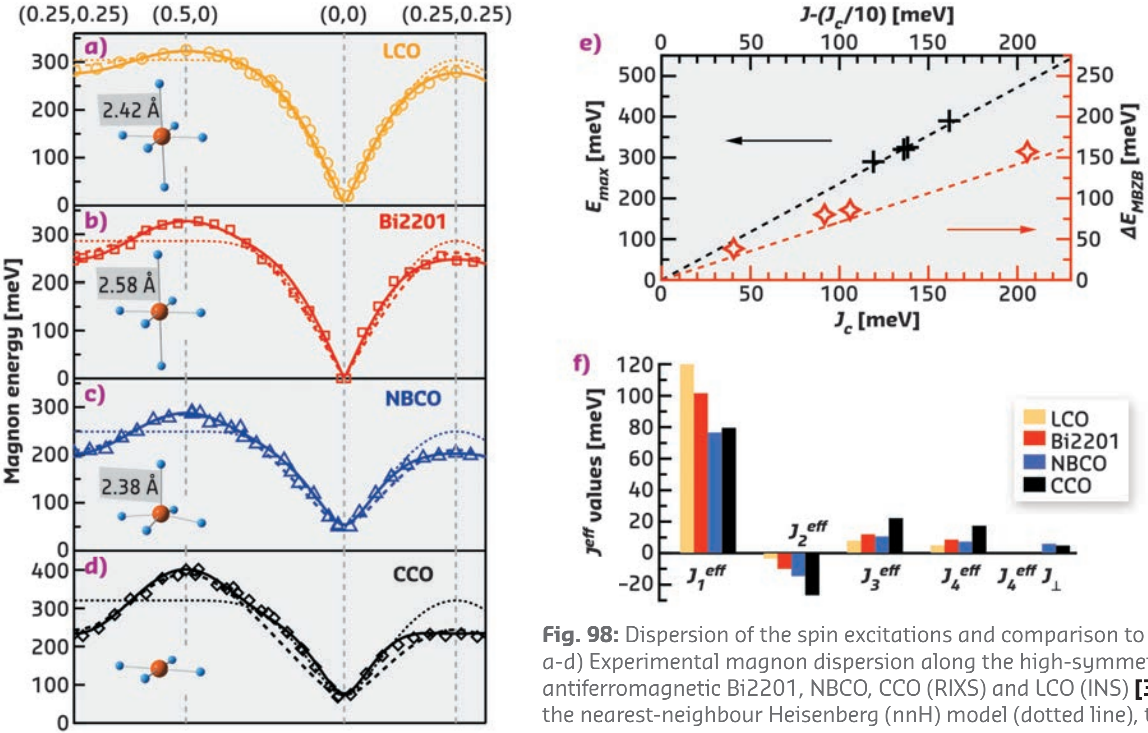

Fig. 98: Dispersion of the spin excitations and comparison to model calculations. a-d) Experimental magnon dispersion along the high-symmetry direction in antiferromagnetic Bi2201, NBCO, CCO (RIXS) and LCO (INS) **[3]**, as indicated, fitted using the nearest-neighbour Heisenberg (nnH) model (dotted line), the one-band Hubbard (1bH) model (dashed line) and the phenomenological linear spin-wave Heisenberg model with four nearest-neighbour coupling parameters ($4J^{\mathrm{eff}}$) (thick line). The respective local coordination of the Cu ions is depicted in the insets. e) Linear dependence of E_{max} and ΔE_{MBZB} versus the one-band Hubbard model parameters J and Jc. f) Effective parameters of the phenomenological spin-wave model based on four in-plane J^{eff} parameters.

PRINCIPAL PUBLICATION AND AUTHORS

Influence of apical oxygen on the extent of in-plane exchange interaction in cuprate superconductors, Y.Y. Peng (a), G. Dellea (a), M. Minola (b), M. Conni (a), A. Amorese (c), D. Di Castro (d), G.M. De Luca (e,f), K. Kummer (c), M. Salluzzo (f), X. Sun (g), X.J. Zhou (g), G. Balestrino (d), M. Le Tacon (h), B. Keimer (b), L. Braicovich (a), N.B. Brookes (c) and G. Ghiringhelli (a,i), *Nature Physics* **13**, 1201-1206 (2017); doi: 10.1038/NPHYS4248.
(a) Politecnico di Milano (Italy)
(b) Max-Planck-Institut für Festkörperforschung, Stuttgart (Germany)
(c) ESRF
(d) CNR-SPN Roma Tor Vergata (Italy)
(e) Università di Napoli Federico II (Italy)
(f) CNR-SPIN, Napoli (Italy)
(g) Institute of Physics, C.A.S. Beijing (China)
(h) Karlsruhe Institute of Technology (Germany)
(i) CNR-SPIN, Milano (Italy)

REFERENCES

[1] L. Braicovich *et al.*, *Phys. Rev. Lett.* **104**, 077002 (2010).
[2] M. Le Tacon *et al.*, *Nature Physics* **7,** 725 (2011).
[3] N.S. Headings *et al.*, *Phys. Rev. Lett.* **105**, 247001 (2010).
[4] E. Pavarini *et al.*, *Phys. Rev. Lett.* **87**, 047003 (2001).

PHOTOELECTROCHEMICAL CELL EFFICIENCY INCREASES BY PHOTOCHARGING BiVO$_4$ PHOTOANODES

Solar water splitting by a photoelectrochemical cell has potential for the sustainable production of hydrogen. The photocharging treatment of a BiVO$_4$ photoanode dramatically improves a cell's efficiency. Experiments at BM26 (DUBBLE) helped reveal that photocharging involves the surface of the electrode.

Photoelectrochemical (PEC) water splitting is an attractive route to capture, convert and store the energy from the sun in the form of chemical bonds. This approach allows for the sustainable production of solar fuels (typically H_2), and thereby addresses the challenges of new energy technologies needed for a renewable and carbon-free economy.

Solar water splitting is most efficiently performed using semiconducting photoelectrodes, which directly utilise photo-generated charge carriers to drive the water oxidation and reduction half-reactions at the corresponding solid/liquid interfaces. Metal oxides have been heavily studied as a class of photoelectrode materials for PEC devices due to their low cost and stable operation. Specifically, bismuth vanadate (BiVO$_4$) has proven to demonstrate impressive activity as a photoanode material. However, due to its inherent bulk- and surface-related limitations, complex strategies such as doping or co-catalysts are typically necessary for $BiVO_4$ to reach high yields for O_2 production.

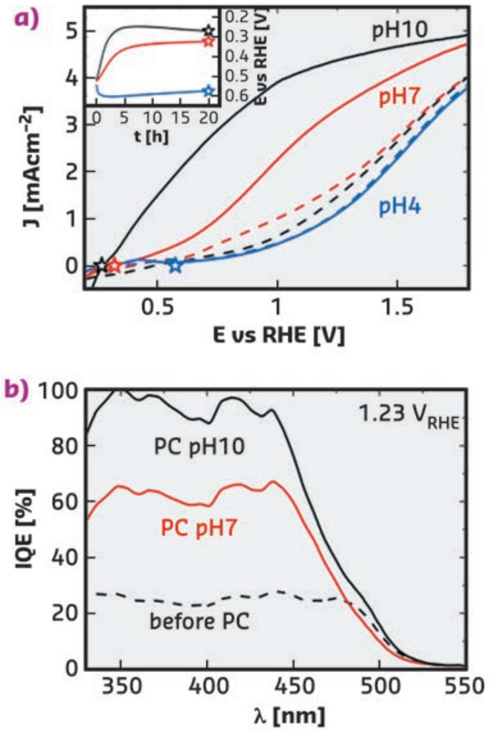

Fig. 99: a) Current vs. potential curves of $BiVO_4$ in PBA buffer at pH 4, 7 and 10; a stable tenth anodic scan is shown in each case. Dashed curves are untreated films, solid curves are photocharged films. b) Internal quantum efficiency measurements of 200 nm $BiVO_4$ in PBA buffer at pH 7 and 10 before and after photocharging (PC) collected at 1.23 V vs. RHE (reversible hydrogen electrode, a reference electrode).

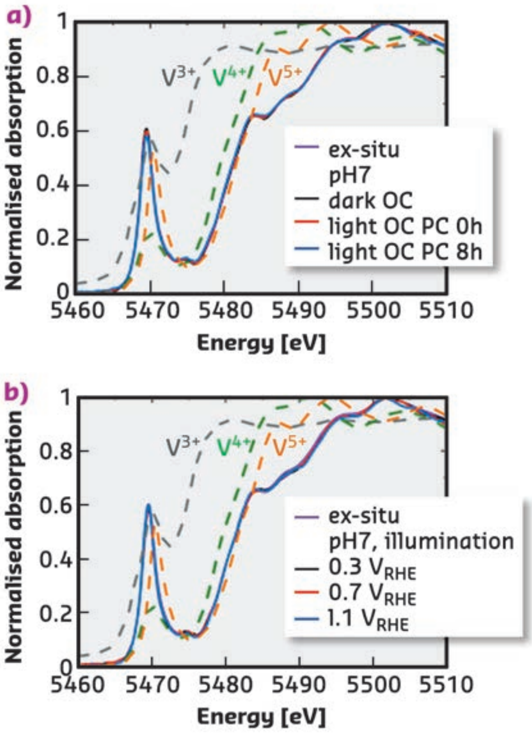

Fig. 100: Vanadium K-edge XAS spectra collected (a) *ex situ* and *in situ* while photocharging (PC) under open circuit (OC) conditions, in the dark and under illumination (b) *ex situ* and under illumination and with applied bias potential.

Herein, photocharging has been investigated, which is a simple and novel treatment that can dramatically improve the water splitting capabilities of $BiVO_4$ **[1]**. It was demonstrated that illumination combined with alkaline conditions alters the chemistry at the semiconductor-electrolyte interface to form a $BiVO_4$ surface with superior activity for the oxygen evolution reaction (see **Figure 99**).

The improvement in performance using the photocharging technique is so dramatic that both bulk and surface phenomena could be responsible for this enhancement. To investigate any possible impact of the photocharging treatment on the chemical and structural properties of bulk $BiVO_4$, specifically to identify any changes in the average bulk oxidation state of vanadium and in the local environment, an *in situ* XAS study at beamline **BM26** was carried out (**Figure 100**). This provided critical insight into photocharging that allowed a model to be built to understand the improved behaviour of the photoelectrodes.

As neither the photocharging treatment nor applying bias potential (0.3 – 1.1 V_{RHE}) alters the structure/chemistry of the bulk of $BiVO_4$ films it was concluded that the films do not display any signatures of changes in the average bulk vanadium oxidation state, despite significantly different PEC properties. The XAS experiments provided evidence that bulk vanadium in the films always remains in the +5 oxidation state. Complimentary data using XPS and electrochemical impedance spectroscopy (EIS) revealed that the surface becomes slightly reduced, resulting in vanadium in a slightly lower oxidation state, which leads to a significantly higher rate of catalysis, due to either lower surface recombination or enhanced water oxidation kinetics (**Figure 101**).

In conclusion, photocharging enhances the efficiency of $BiVO_4$ through surface reaction pathways at the semiconductor-liquid junction. It is directly correlated with the electrochemical environment in which the treatment is applied. The photocharging technique can potentially be applied to other photo-electrode materials.

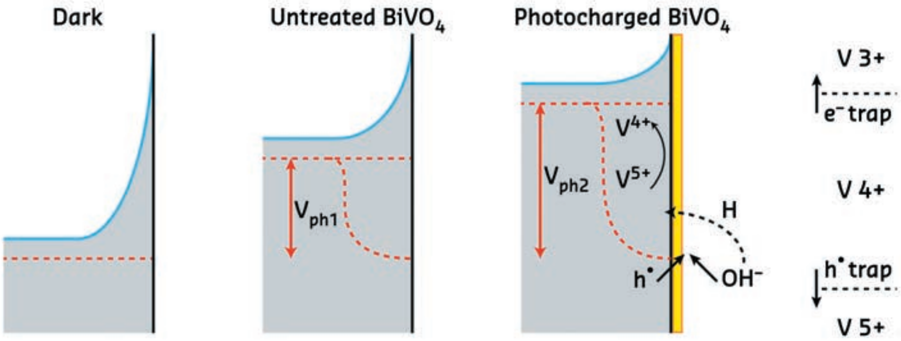

Fig. 101: Energy band diagrams of $BiVO_4$ in the dark and under illumination before and after the photocharging treatment, including the simplified photocharging mechanism model.

PRINCIPAL PUBLICATION AND AUTHORS

Near-complete suppression of surface losses and total internal quantum efficiency in $BiVO_4$ photoanodes, B.J. Trześniewski (a), I.A. Digdaya (a), T. Nagaki (a), S. Ravishankar (b), I. Herraiz-Cardona (b), D.A. Vermaas (a), A. Longo (c,d), S. Gimenez (b) and W.A. Smith (a), *Energy Environ. Sci.* **10**, 1517-1529 (2017); doi: 10.1039/c6ee03677e.
(a) Materials for Energy Conversion and Storage (MECS), Delft University of Technology, Delft (The Netherlands)
(b) Institute of Advanced Materials (INAM), Universitat Jaume I, Castelló de la Plana (Spain)
(c) Netherlands Organization for Scientific Research (NWO), ESRF, Grenoble (France)
(d) ISMN-CNR, UOS Palermo, Palermo (Italy)

REFERENCES

[1] B.J. Trześniewski and W.A. Smith, *J. Mater. Chem.* **A 4**, 2919-2926 (2016).

NICHE CHEMICAL BONDING MODEL FOR ACTINIDES COULD BE A GENERAL RULE

Scientists at Manchester, Lancaster, Nottingham, Dresden and Grenoble have published research reporting a surprise finding about the nature of lanthanide and actinide chemical bonding which suggests that an important – but previously considered niche – bonding model that controls chemical structure and reactivity may be a more general rule.

The arrangement of ligand groups at metal centres in metal complexes is crucial to determining their reactivity. For example, cis-platin is very effective at treating cancerous tumours whereas trans-platin is ineffective; both compounds have the same formula with a central platinum ion bonded to two chloride and two ammonia ligands all in the same plane in the shape of a cross, but in the former the chlorides are next to each other and in the latter they are opposite each other. The phenomenon that electronically controls to a large extent the arrangement of ligands at metal centres is known as the trans-influence (TI), which originates from the fact that some ligands bind to metals more strongly than others so ligands will avoid being opposite stronger donor ligands. This effect is observed right across the periodic table.

In contrast, at the bottom of the periodic table, things can be quite different, and for actinides a phenomenon known as the inverse-trans-influence (ITI) operates. Here, ligands that would normally do everything they could to avoid being opposite each other at a metal actually do everything they can to be oppositely disposed, and rather than this destabilising the ligands they actually mutually reinforce each other. However, the ITI was previously limited only to early actinides in their maximum or close-to-maximum oxidation states. A famous example of this is uranyl, UO_2^{2+}, which is naturally prevalent in the environment and nuclear waste, and where the two oxygen atoms reside opposite each other and are bonded very strongly to uranium. This makes the uranyl moiety very important, but also the universal view that the ITI was a niche concept of limited applicability dominated because it was restricted to high oxidation state actinides like uranium.

So whether this phenomenon was a niche rule or hinted at a broader underpinning role, in an area that famously has few rules, had been a question that endured for decades.

One reason this question had been difficult to tackle was the lack of structurally comparable families of molecules from which to conduct comparative studies where lower oxidation states of metal ions could be investigated. To address this problem, the research team prepared a new family of molecules with C=M=C cores where the metal was cerium (a lanthanide), or thorium or uranium (actinides), where two carbon atoms that are known to be strong donors were forced to be opposite to one another either side of the metal (**Figure 102**).

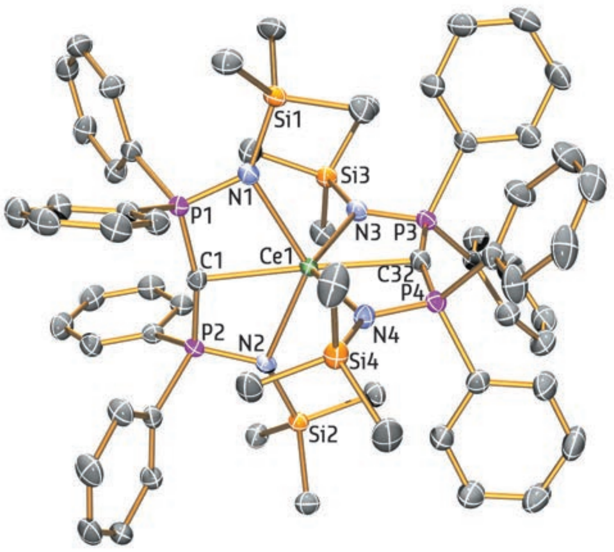

Fig. 102: Molecular structure of one of the key molecules in the study showing the linear C=M=C (M = cerium) core.

Characterisation of this family of molecules required a multi-disciplinary effort, part of which was carried out at beamline **BM20** (ROBL), combining structural, spectroscopic, and magnetic analyses to confirm the formulations of these molecules and computational chemistry to unravel their electronic structures. Surprisingly, this established that the ITI operates in these molecules that contain +4 oxidation state metal ions. The most telling observation is the fact that the two carbon atoms are bonded very closely to the metals, particularly for cerium, even though as strong donors they should be found at longer distances if the TI were operating, and this is a tell-tale sign of the presence of the ITI.

The combination of finding the ITI in +4 metal ion compounds for lanthanide as well as actinide complexes leads to the inescapable conclusion that this phenomenon is most likely of far broader reach than previously thought; if confirmed it would add a welcome rule to an area that famously lacks rules.

PRINCIPAL PUBLICATION AND AUTHORS

The inverse-trans-influence in tetravalent lanthanide and actinide bis(carbene) complexes, M. Gregson (a), E. Lu (a), D.P. Mills (a), F. Tuna (b), E.J.L. McInnes (b), C. Hennig (c,d), A.C. Scheinost (c,d), J. McMaster (e), W. Lewis (e), A.J. Blake (e), A. Kerridge (f) and S.T. Liddle (a), *Nature Communications* **8**, 14137 (2017); doi: 10.1038/ncomms14137.

(a) School of Chemistry, University of Manchester (UK)
(b) EPSRC National UK EPR Facility, School of Chemistry and Photon Science Institute, University of Manchester (UK)
(c) Helmholtz-Zentrum Dresden-Rossendorf, Institute of Resource Ecology, Dresden (Germany)
(d) ESRF
(e) School of Chemistry, University of Nottingham (UK)
(f) Department of Chemistry, Lancaster University (UK)

ACKNOWLEDGEMENTS

The project was also supported by the Royal Society, the Engineering and Physical Sciences Research Council, the European Research Council, The Universities of Manchester and Nottingham, the EPSRC UK National EPR Facility, the UK National Nuclear Laboratory, and the ESRF at Grenoble.

X-RAY SPECTROSCOPY REVEALS IRON SPIN STATE IN OXYGENATED HEMOPROTEINS

Proteins carrying a heme cofactor are essential for biological oxygen management. Advanced X-ray spectroscopy experiments have now established an effective intermediate-spin iron centre in myoglobin and hemoglobin. This has clarified the long-debated Fe-O_2 bonding situation in reversible oxygen transport.

Aerobic life on earth requires efficient management of molecular oxygen (O_2). Nature has developed proteins that bind an iron-porphyrin (heme) cofactor as versatile O_2 managers. Such hemoproteins, in particular in animals and humans, have been extensively studied, for example, establishing cooperative versus non-cooperative O_2 binding to heme iron in tetrameric hemoglobin and monomeric myoglobin, respectively. Today, rising interest in this topic stems from the ongoing discovery of globins with broad functionality in plants and microorganisms.

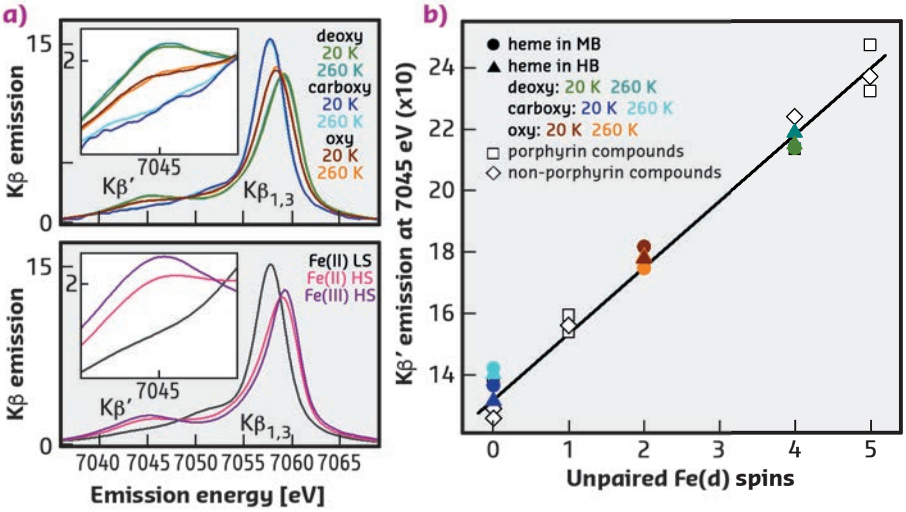

Fig. 103: X-ray spectroscopy and iron spin state. a) Normalised Kβ emission spectra of myoglobin protein (top) and porphyrin reference compounds (bottom) at 20 K and 260 K (insets: magnified Kβ´ feature). b) Correlation of Kβ´ emission intensity and formal unpaired Fe(d) spin count for myoglobin (MB), hemoglobin (HB), and model compounds. Fe(d) spins correspond to: 0, low-spin Fe(II); 1, low-spin Fe(III); 4, high-spin Fe(II), and 5, high-spin Fe(III). The line indicates that the Kβ´ intensities for oxy MB and HB placed at Fe(d) = 2 correspond to a formal intermediate-spin Fe(II).

Three physiologically-relevant heme species can be distinguished in myoglobin and hemoglobin: the ligand-free (deoxy), carbon-monoxide inhibited (carboxy), and O_2-bound (oxy) forms. Paramagnetic behaviour has established high-spin Fe(II) in deoxy whereas carboxy is diamagnetic due to low-spin Fe(II). For oxy, a diamagnetic cofactor has been proven. A controversy has remained on the nature of the iron-oxygen bonding in myoglobin and hemoglobin, dating back to the pioneering work of Pauling, Monod, and Perutz that began in the 1930s **[1]**. Pauling suggested a neutral singlet O_2 bound to a formal low-spin Fe(II), McClure and Goddard suggested a triplet O_2 and an intermediate-spin Fe(II) in an ozone-like configuration, and Weiss suggested an Fe(III) coupled to a superoxo (O_2^-) ligand **[2]**.

Core level spectroscopy is a powerful method for the electronic structure analysis of transition metal complexes. X-ray emission spectroscopy of the $K\beta$ lines probes the occupied levels via electronic decay from metal 3p to 1s levels (main line). 3p-3d spin-coupling splits the $K\beta$ main-line emission into the $K\beta'$ and $K\beta_{1,3}$ features and the $K\beta'$ intensity is a measure of metal spin state and bonding covalency. X-ray spectroscopy on hemoproteins in solution and at physiological temperature is challenging due to radiation-induced modifications and low metal concentration.

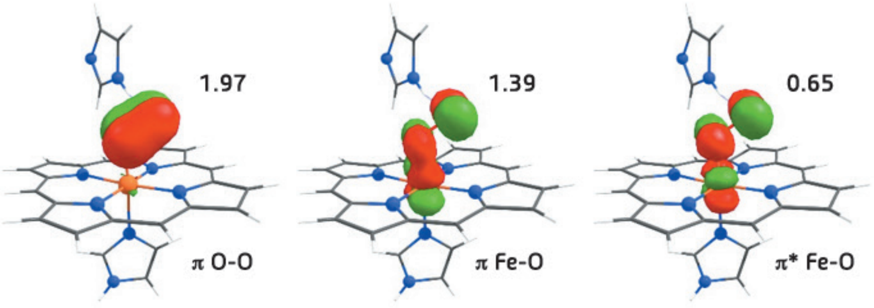

Fig. 104: Iron-oxygen bonding in heme. Comparison of molecular orbitals with non-integer electron occupation (numbers) from quantum chemical (complete active space self-consistent field) calculations shows that the effective intermediate-spin behaviour of the ferrous iron in oxy heme originates from a delocalised iron-oxygen bonding situation similar to that of ozone.

At beamline **ID26**, myoglobin and hemoglobin proteins were studied in their deoxy, carboxy and oxy forms, as well as synthetic porphyrin compounds with low-spin or high-spin Fe(II) or Fe(III) centres. $K\beta$ main-line emission spectra were collected at cryogenic (20 K) or near-ambient (260 K) temperatures (**Figure 103**). Significant line shape differences between the protein-bound heme species reflect iron spin and redox state differences. The temperature-invariant behaviour of the spectra proved the absence of spin crossover and thereby the physiological relevance of the determined spin states. Plotting of the $K\beta'$ intensities versus the formal number of unpaired Fe(d) spins revealed a linear relation. The mean $K\beta'$ amplitude for oxy heme was in best agreement with an Fe(d) spin count of two. These results strongly suggest that the high-spin Fe(II) in deoxy myoglobin and hemoglobin is converted to an effective intermediate-spin iron species upon oxygen binding to the metal.

Quantum chemical *ab initio* calculations confirmed the experimentally determined number of unpaired Fe(d) electrons. For the high-spin Fe(III) in deoxy heme, five single-occupied molecular orbitals with Fe(d) character were found and the low-spin Fe(II) in carboxy heme showed no unpaired electrons. For oxy heme, the unpaired electron density of two is the result of partial electron occupation of two orbitals representing bonding (π) and antibonding (π*) Fe-O interactions. Additional correlation with the π orbital of O_2 yields an electronic configuration in oxy heme similar to the one in ozone (**Figure 104**).

This work has helped to resolve the long-standing controversy concerning the iron-oxygen interaction and metal spin state in oxygen transporting proteins. It was achieved using quantitative correlation of advanced X-ray absorption and emission spectroscopy experiments and quantum chemical calculations. The situation in oxygenated hemoglobin and myoglobin merges the classical models into a unifying view of the Fe-O_2 bonding, which features limited radical character and delocalised backbonding stabilisation of the ligand as prerequisites in reversible biological O_2 transport. A framework has been provided to understand the tuning of hemoproteins for their numerous functions ranging from O_2 sensing and transport over activation chemistry to catalysis.

PRINCIPAL PUBLICATION AND AUTHORS

Effective intermediate-spin iron in O_2-transporting heme proteins, N. Schuth (a), S. Mebs (a), D. Huwald (b), P. Wrzolek (c), M. Schwalbe (c), A. Hemschemeier (b) and M. Haumann (a), *PNAS U. S. A.* **114**, 8556-8561 (2017); doi: 10.1073/pnas.1706527114.

(a) Freie Universität Berlin, Department of Physics, Berlin (Germany)
(b) Ruhr-Universität Bochum, Department of Plant Biochemistry, Bochum (Germany)
(c) Humboldt-Universität zu Berlin, Department of Chemistry, Berlin (Germany)

REFERENCES

[1] K.P. Kepp, *Coord. Chem. Rev*. **344**, 363-374 (2016).
[2] K.L. Bren *et al., PNAS*. **112**, 13123-13127 (2015).

TWO-DIMENSIONAL SHORT RANGE ANTIFERROMAGNETIC STATE IN HIGHLY DOPED METALLIC $(Sr_{1-x}La_x)_3Ir_2O_7$

Doping Mott insulators with charge carriers usually generates various new phases. A RIXS study of the evolution of the magnetic order and magnetic excitations reveals that electron doping drives $(Sr_{1-x}La_x)_3Ir_2O_7$ into a correlated metallic state with two-dimensional short range antiferromagnetic order and a vanishing spin gap.

High temperature superconductivity in copper oxides arises from doping charge carriers into their Mott insulating antiferromagnetic parent compounds **[1]**. In addition to superconductivity, various exotic quantum states emerge in close proximity to the metal-insulator transition. Many of the characteristic signatures of superconducting copper oxides are also realized in 5d iridium oxide-based Mott insulators. For example, Sr_2IrO_4 **[2]** is a layered perovskite iridate hosting a novel spin-orbit coupling-induced Mott insulating state **[2]**. The magnetic order, spin dynamics, and electronic structure of Sr_2IrO_4 are similar to the prototypical copper oxide La_2CuO_4 **[3]**.

In Sr_2IrO_4 collective quantum states emerge by charge-carrier doping in the strong spin-orbit coupling (SOC) limit, which suggests that electron-doped Sr_2IrO_4 is an analogous material to hole-doped La_2CuO_4 **[4]**. Compared with Sr_2IrO_4, the bilayer $Sr_3Ir_2O_7$ is similar to bilayer cuprates, which exhibit higher T_c than monolayer copper oxides **[1]**. It is a promising candidate for exploring novel phases via electron doping since it retains the $J_{eff}=1/2$ Mott state while lying close to an insulator-to-metal transition (IMT) with a small gap of $\Delta E \approx 130\,meV$. Strong interlayer coupling and magnetic anisotropy induce a c-axis G-type antiferromagnetic order (AFM) below $T_N \approx 285\,K$ and distinct magnons bearing a large magnon gap ≈ 90 meV **[5]** (**Figures 105a** and **b**). Because of the small charge gap of $Sr_3Ir_2O_7$, an IMT and a robust metallic state have been realised in $(Sr_{1-x}La_x)_3Ir_2O_7$ for $x > 0.05$ (**Figure 105c**).

Since small amounts of La dopants have little structural effect on IrO_2 layers while driving the system across the IMT, $(Sr_{1-x}La_x)_3Ir_2O_7$ provides an ideal platform for exploring novel phenomena arising from charge carrier doped novel Mott states. However, the doping evolution of $(Sr_{1-x}La_x)_3Ir_2O_7$ and the nature of the metallic state, being debated to be a Fermi liquid or a correlated metal, is still unclear. In order to address this, detailed studies of the doping-dependent magnetic order and elementary excitations are required.

In this work, the doping dependence of the magnetic order and the elementary excitations across the IMT in $(Sr_{1-x}Lax)_3Ir_2O_7$ were studied using Ir L_3 edge resonant inelastic X-ray scattering (RIXS). The experiments were carried out at **ID20** and at 27-ID-B of APS, Argonne National Laboratory. The use of the state-of-the-art hard X-ray RIXS spectrometers with very high resolution (~ 25 meV) was essential for the measurements, which enabled the tracking of the doping evolution of the magnetic order and magnetic excitations **[6]**.

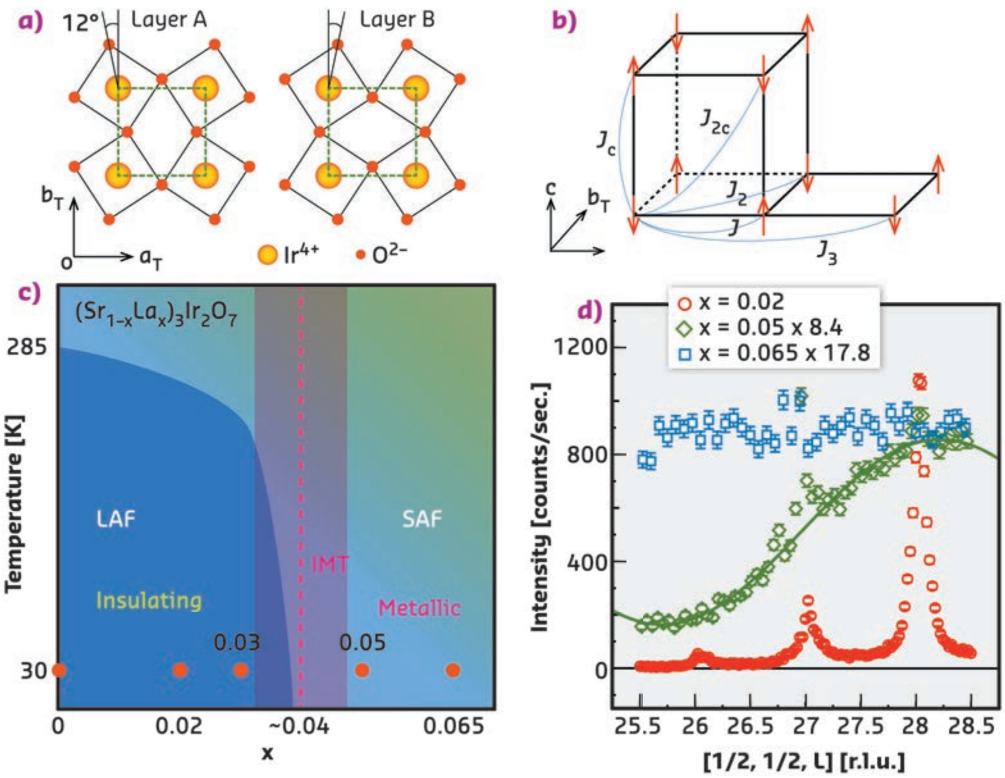

Fig. 105: a) In-plane crystal structure of $Sr_3Ir_2O_7$. b) G-type collinear antiferromagnetic order with moment along the c axis. c) Schematic phase diagram of $(Sr_{1-x}La_x)_3Ir_2O_7$. LAF and SAF are long range and short range antiferromagnetic order, respectively. d) Doping dependent L scans across the magnetic Bragg peak (1/2, 1/2, 28). The green solid curve in (d) is a fit of the L scan for x = 0.05.

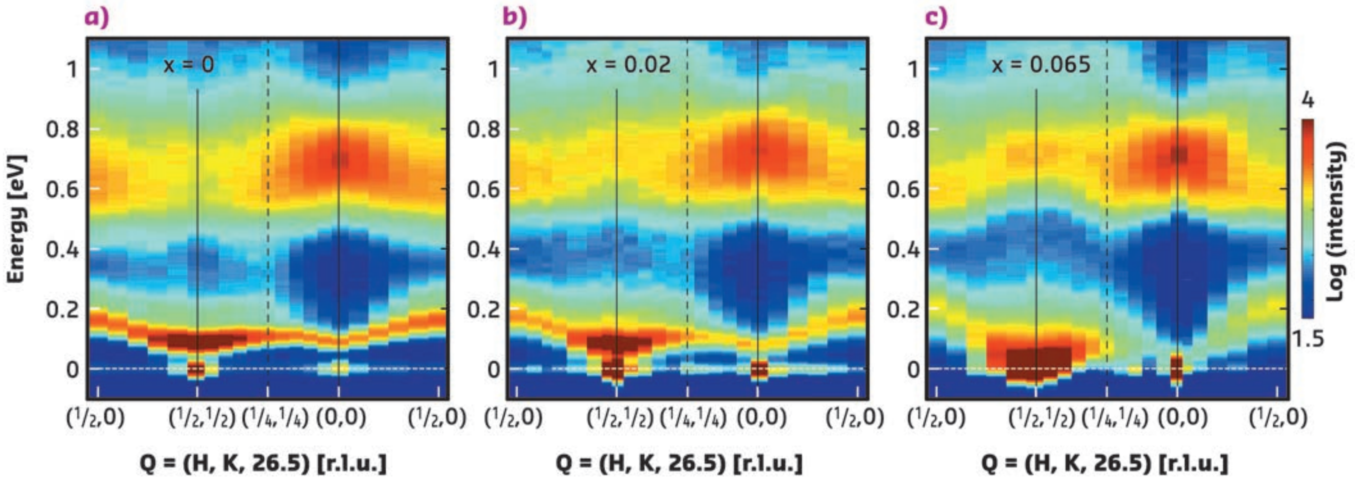

Fig. 106: a) - c) In-plane momentum dependence of RIXS spectra of $(Sr_{1-x}La_x)_3Ir_2O_7$ for x = 0, 0.02, and 0.065.

The results reveal an evolution of the AFM from three-dimensional (3D) long range AFM (LAF) ($x \leq 0.03$) to 3D short range AFM (SAF) ($x \sim 0.05$) across the IMT and subsequent 2D SAF deep in the metallic state ($x = 0.065$) (**Figures 105c** and **d**). Following the evolution of the magnetic order, **Figure 106** shows that magnetic excitations undergo damping, anisotropic softening, and gap collapse, accompanied by weakly doping-dependent spin-orbit excitons. This indicates that the emergent itinerant electrons suppress the AFM by weakening the magnetic couplings and drive the system into a 2D SAF correlated metallic state hosting strong antiferromagnetic fluctuations of the $J_{eff} = 1/2$ moments. The correlated metallic state hosting strong AFM spin fluctuations of $J_{eff} = 1/2$ in $(Sr_{1-x}La_x)_3Ir_2O_7$ provides a new platform for realising novel quantum phases by applying internal or external perturbations.

PRINCIPAL PUBLICATION AND AUTHORS

Doping Evolution of Magnetic Order and Magnetic Excitations in $(Sr_{1-x}La_x)_3Ir_2O_7$, X. Lu (a), D.E. McNally (a), M. Moretti Sala (b), J. Terzic (c,d), M.H. Upton (e), D. Casa (e), G. Ingold (f), G. Cao (c,d) and T. Schmitt (a), *Phys. Rev. Lett.* **118**, 027202 (2017), doi: 10.1103/PhysRevLett.118.027202.

(a) Synchrotron Radiation and Nanotechnology Division, Paul Scherrer Institut, Villigen PSI (Switzerland)
(b) ESRF
(c) Department of Physics and Astronomy, University of Kentucky, Kentucky (USA)
(d) Department of Physics, University of Colorado at Boulder, Colorado (USA)
(e) Advanced Photon Source, Argonne National Laboratory, Argonne, Illinois (USA)
(f) SwissFEL, Paul Scherrer Institut, Villigen PSI (Switzerland)

REFERENCES

[1] P. A. Lee *et al., Rev. Mod. Phys.* **78**, 17 (2006).
[2] J.G. Rau *et al., Annu. Rev. Condens. Matter Phys.* **7**, 195 (2015).
[3] H. Gretarsson *et al., Phys. Rev. Lett.* **117**, 107001 (2016).
[4] F. Wang and T. Senthil, *Phys. Rev. Lett.* **106**, 136402 (2011).
[5] M. Moretti Sala *et al., Phys. Rev. B* **92**, 024405 (2015).
[6] C. Donnerer *et al., ESRF Highlights 2016* ***14*** (2016).

PRECURSOR CHARGE DENSITY WAVES IN CUPRATES REVEAL SPIN-CHARGE UNLOCKED PHASE

While charge density wave (CDW) correlations are ubiquitous to cuprates [1], their microscopic mechanism and relation with spin correlations remain enigmatic. X-ray experiments revealed high-temperature precursor CDW correlations that are decoupled from spin correlations. These observations help identify the universal properties of the state from which high-temperature superconductivity emerges.

Figure 107 shows the principle of resonant inelastic X-ray scattering (RIXS) measurements on cuprates. In the presence of charge density wave (CDW) correlations, the quasi-elastic RIXS intensity is peaked at a particular momentum transfer. By measuring the position and width of this peak the CDW wave vector and correlation length was extracted from the data. In this study, Cu L_3 edge RIXS was used to achieve very high sensitivity to weak charge correlations.

This works by choosing a photon energy that resonates with a Cu 2p → 3d core level transition in order to enhance scattering from valence electrons, while using the **ID32** ERIXS spectrometer to reject the strong X-ray fluorescence that limits the sensitivity of traditional resonant soft X-ray scattering experiments. By carefully tracing the temperature dependence of the CDW peak, the CDW correlations were found to persist above the transition temperature with a correlation length that is more than ten times shorter than in the ordered phase. To distinguish between the low and high temperature CDW correlations, the CDW correlation above the phase transition are called precursor CDW correlations, as these are what order to form the low temperature phase.

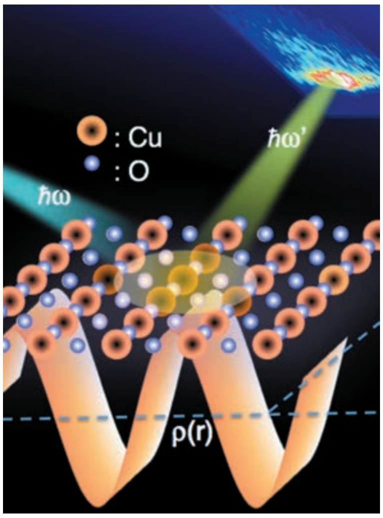

Fig. 107: Charge density waves ripple through a high-temperature superconductor. Resonant inelastic X-ray scattering experiments show that these excitations exist at temperatures above the CDW transition in the canonical stripe ordered cuprate $La_{1.875}Ba_{0.125}CuO_4$.

In **Figure 108**, the temperature dependence of the CDW correlations is plotted. The correlation length of the precursor CDW of 13(2) Å is of a similar magnitude to several other cuprate systems such as $Bi_2Sr_{2-x}La_xCuO_{6+\delta}$ (12 Å) **[2]**, $Bi_{1.5}Pb_{0.5}Sr_{1.54}CaCu_2O_{8+\delta}$ (< 24 Å) **[3]**, $La_{2-x}Sr_xCuO_4$ (LSCO) (35 Å) **[4]** and $HgBa_2CuO_{4+\delta}$ (20 Å) **[5]**, hinting that the high-temperature CDW properties may help reconcile the difference between different cuprates. Further clues are evident in the wave vector behaviour allowing the association of the high-temperature state observed here with the low-temperature behaviour of other compounds. As can be seen in **Figure 108b**, for temperatures below 55 K the incommensurability of the CDW and SDW appear to be locked by a factor of two, which is a well-known property of 214-type cuprates. Upon heating above 55 K, strong violation of this relation is seen: the CDW correlations evolve away from H ≈ 1/4 and away from twice the incommensurability of the spin density wave (SDW) (*i.e.* the CDW and SDW decouple).

These results establish shared properties between different cuprates and indicate that the wavevector of the CDW correlations may not reflect the formation mechanism of CDW, instead it is determined by a subtle balance of different competing interactions.

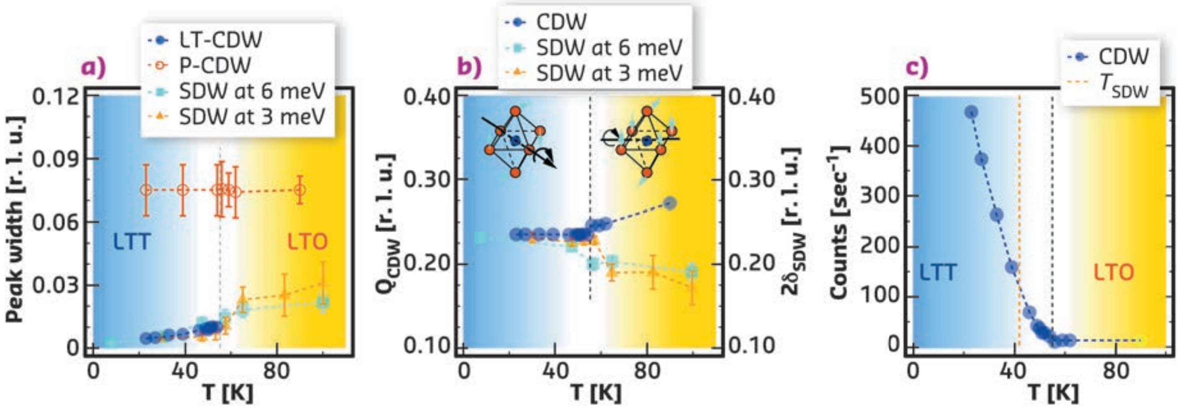

Fig. 108: Decoupling of the CDW and SDW in the high-temperature phase. a-c) The results of fitting the quasi-elastic intensity showing: a) the full width at half maximum, b) the incommensurability and c) the intensity at the peak. The black dashed line at 54 K corresponds to the low-temperature LTT-LTO structural phase transition, which is depicted in (b). Blue and yellow code temperatures below and above this threshold. The orange dashed line at 42 K in (c) represents the static SDW transition. The behaviour of the SDW, taken from inelastic neutron scattering results at 3 and 6 meV energy transfer are included on panels (a) and (b) **[6]**.

PRINCIPAL PUBLICATION AND AUTHORS

High-temperature charge density wave correlations in $La_{1.875}Ba_{0.125}CuO_4$ without spin-charge locking, H. Miao (a), J. Lorenzana (b), G. Seibold (c), Y. Y. Peng (d, e), A. Amorese (f), F. Yakhou-Harris (f), K. Kummer (f), N. B. Brookes (f), R. M. Konik (a), V. Thampy (a), G. D. Gu (a), G. Ghiringhelli (d, e), L. Braicovich (d, e) and M. P. M. Dean (a), *PNAS* **47**, 12430-12435 (2017); doi: 10.1073/pnas.1708549114.

(a) Condensed Matter Physics and Materials Science Department, Brookhaven National Laboratory, Upton, New York, (USA)
(b) ISC-CNR, Dipartimento di Fisica, Università di Roma "La Sapienza" (Italy)
(c) Institut für Physik, BTU Cottbus, (Germany)
(d) Dipartimento di Fisica, Politecnico di Milano (Italy)
(e) CNR-SPIN, Politecnico di Milano (Italy)
(f) ESRF

REFERENCES

[1] E. Fradkin *et al., Rev. Mod. Phys.* **87**, 457 (2015).
[2] R. Comin *et al., Science* **343**, 390 (2014).
[3] M. Hashimoto *et al., Phys. Rev. B* **89**, 220511 (2014).
[4] V. Thampy *et al., Phys. Rev. B* **90**, 100510 (2014).
[5] W. Tabis *et al., Nat. Commun.* **5**:5875 (2014).
[6] M. Fujita, *Phys. Rev. B* **70** 104517 (2004).

THALLIUM: A HIDDEN HAZARD WITHIN DRINKING WATER PIPELINES

Micrometre-sized aggregates of Tl_2O_3 and TlCl have been detected in rust scales in drinking water pipelines, using X-ray diffraction, scanning electron microscopy, and X-ray absorption spectroscopy. A possible mechanism is suggested for the formation of secondary sources of Tl contamination in the pipelines due to chlorine-based oxidants added at water treatment plants.

Thallium (Tl) is one of the most toxic elements for living organisms. In Pietrasanta, a small town in northern Tuscany, Italy, mineralogical and geochemical studies **[1]** had pointed out the occurrence of high Tl contents (up to 1100 µg/g) in the pyrite ores that had been exploited in the area for several decades up to the end of the 1980s. This finding emphasised the threat related to the dispersion of Tl in the environment following pyrite oxidation.

In September 2014, Tl contents up to 10 µg/L were detected in the drinking water tapped from public fountains. Once the contaminated spring had been located, it was replaced by another spring and its water, having a low Tl content (less than 0.10 µg/L), was introduced in the drinking water distribution system. Unexpectedly, the Tl content in water increased up to 80 µg/L. A new source of Tl was at the origin of the contamination and it was hypothesised that this could be due to pipeline encrustations.

Following their removal from the water distribution system, four segments of the pipeline were made available for study. Their interior was heterogeneous, with centimetre-sized patchy areas from light orange to black in colour. X-ray fluorescence (XRF) spectroscopy showed that a striking difference in the Tl content of the rust scales lining the pipeline interior occurred as a function of their position with respect to the water treatment plant: before the plant the rust scales had a low Tl content, whereas after the plant (*e.g.*, samples P#2 and P#3) Tl contents up to 5.3 wt% were measured. The difference was related to the occurrence, in the latter sample, of micrometre-sized globular aggregates of trivalent Tl(III) thallium oxide Tl_2O_3 (**Figure 109**). The rust scales were peppered with these small aggregates, as confirmed both by scanning electron microscopy observations, coupled with EDS chemical analysis, and X-ray powder diffraction.

However, since the solubility of Tl_2O_3 in water is known to be very low, it was unlikely that the high Tl concentrations in the drinking water were related to the occurrence of this Tl salt within the pipeline. In addition, leaching and drying experiments on the rust scales revealed that the precipitated salt was monovalent Tl(I) thallium chloride TlCl, a more soluble salt. The data suggested the occurrence of another source of contamination so X-ray absorption spectroscopy (XAS) measurements were taken at the CRG beamline **LISA-BM08**. **Figure 110** shows the XANES spectra measured for samples and standards. They confirmed not only the occurrence of Tl(III), related to the presence of Tl_2O_3, but demonstrated also the occurrence of a phase containing Tl(I), likely coordinated by Cl. Moreover, the XAS data collected on the leachate samples clearly supported the presence of a soluble Tl(I) compound. This finding promoted a further SEM investigation and finally micrometre-sized aggregates of nanometre-sized crystals of TlCl were identified (**Figure 109**).

The study suggests that the Tl dissolved as Tl(I) in the water from the contaminated spring was removed when the oxidants NaOCl/ClO_2 were added during the water treatment, through oxidative precipitation of Tl_2O_3 and precipitation of minor TlCl. This process has a two-fold

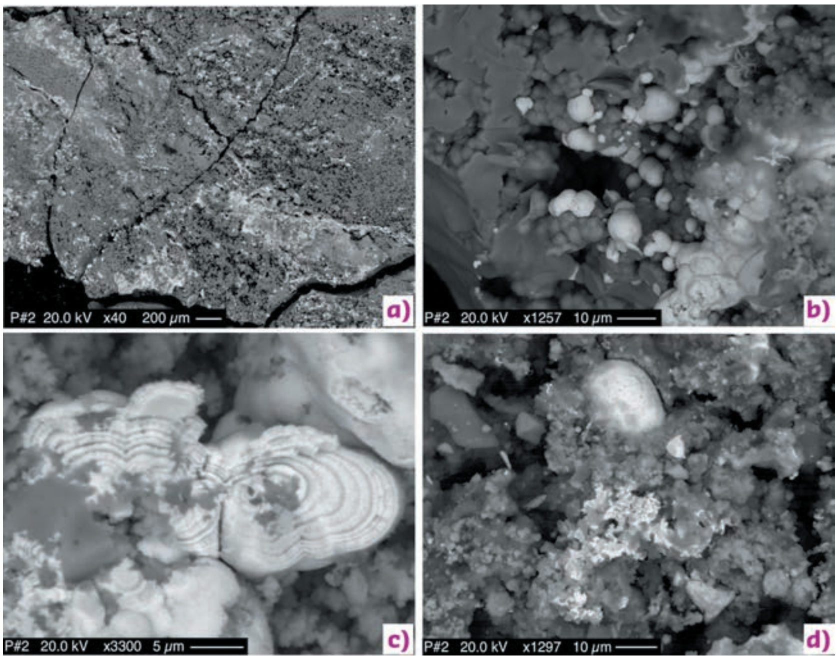

Fig. 109: Back-scattered electron images of rust scales showing details of the highly reflective, Tl-rich phases. a) Small fragment of sample P#2 showing highly reflective spots peppering the surface; b) micrometre-sized spherules of Tl_2O_3 (light grey) on Fe-hydroxides (dark grey); c) micrometre-sized spherules of Tl_2O_3 (light grey) showing their onion-shell internal structure; d) Tl_2O_3 microspherule (light grey, upper centre) close to a tiny TlCl encrustation (light grey, lower centre).

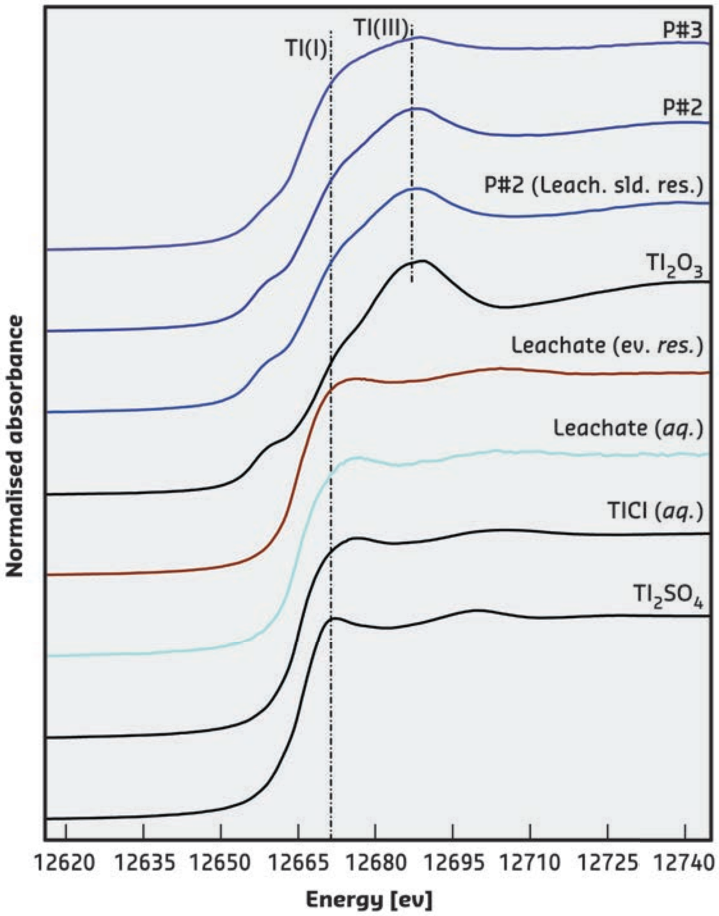

significance: it decreases the bioavailability of this element due to the precipitation of its compounds, but it favours the deposition of Tl-rich coatings within the pipelines, giving rise to a secondary and unexpected source of contamination.

Thallium is a relatively rare but widely dispersed element, and owing to its difficult detection using classical analytical methods, it is not unlikely that its passage from lithosphere to hydrosphere could be more common than thought. In addition, the thallium-rich nature of the rust scales is the result of processes integrated over a period of several years. Consequently, the presence of even low Tl concentrations could represent a hidden hazard seriously affecting the quality of drinkable water.

Fig. 110: Tl L_3-edge XANES of measured samples and model compounds. Main edge crests (dashed line) are found at ~12681 and ~12687 eV for Tl(I) and Tl(III) compounds, respectively. Samples from rust scales (from P#2 to P#3 with increasing distance from the treatment plant) are congruous with those of Tl_2O_3; the presence of a shoulder in correspondence of the Tl(I) edge position suggests the presence of two different signals from both Tl(I) and Tl(III). On the other hand, the leachate samples show the presence of the sole Tl(I).

PRINCIPAL PUBLICATION AND AUTHORS

Thallium-rich rust scales in drinkable water distribution systems: A case study from northern Tuscany, Italy, C. Biagioni (a), M. D'Orazio (a), G.O. Lepore (b), F. d'Acapito (b) and S. Vezzoni (a), *Sci Total Environ.* **587-588,** 491-501 (2017); doi: 10.1016/j.scitotenv.2017.02.177.
(a) Dipartimento di Scienze della Terra, Università di Pisa (Italy)
(b) CNR-IOM-OGG c/o ESRF-LISA CRG, Grenoble (France)

REFERENCES

[1] M. D'Orazio *et al., Mineral. Dep.* **52**, 687 (2017).

UNDERSTANDING SPIN-ORBIT ENTANGLEMENT IN MOLECULAR OSMATES

Molecular model systems may help to unravel the interplay between chemical environment and physical properties in 5d transition element-based materials. Such elements feature strong coupling of the spin of outer electrons to their orbital motion around the nucleus, which can affect physical properties, depending on atomic-level environments and metal oxidation state.

The spin-orbit interaction leads to a plethora of exotic physical properties in condensed matter. It is particularly true for 5d metal ion-based materials since this interaction gets dramatically stronger with increasing atomic number. The combined action of the crystal field and the spin-orbit interaction results in an entanglement of the spin and orbital degrees of freedom. Exotic physical properties associated to this entanglement have been recently reported in, for example, osmium-based materials **[1,2]**.

Tailoring the electronic properties of such materials would require a fundamental understanding of the spin-orbit interaction at the single-ion level. Molecular chemistry provides the methodology to spatially isolate metal ion modules and can thereby minimise or supress long-range interactions between magnetic sites present in solids, *e.g.* oxides (**Figure 111a**). However, finding molecular entities, which can realistically emulate metal ion sites in solids, is a complicated task. In nearly all oxides of the 5d elements, the metal ions are surrounded by six oxide ions (O^{2-}) placed at the corners of an octahedron. The closest, chemically attainable, molecular model of this structural motif is $[OsF_6]^{x-}$, which exists with two oxidation states of the osmium ion; $[Os^{IV}F_6]^{2-}$ and $[Os^{V}F_6]^{-}$. The possibility to switch the oxidation state between Os^{IV} and Os^{V} provided a great opportunity to elucidate the spin-orbit physics in osmates.

X-ray absorption (XAS) and X-ray magnetic circular dichroism (XMCD) were carried out at **ID12** and spectra at the $L_{2,3}$ edges of osmium in both $[Os^{IV}F_6]^{2-}$ and $[Os^{V}F_6]^{-}$ are shown in **Figure 112**. A clear XMCD signal is observed in both cases, although it is nearly two orders of magnitude larger for Os^{V} than for Os^{IV}, due to a much larger magnetic moment of the former. The combined analysis of the XAS and XMCD data offers a unique possibility to disentangle the spin and orbital contributions to the total magnetic moment. In the reported molecular osmates, the experimental results (**Figure 112**) demonstrate the van Vleck paramagnetic behaviour of the Os^{IV} centre with an orbital magnetic moment contributing to 25% of the total magnetisation. In the Curie-type paramagnetic Os^{V} system, the orbital contribution to the magnetic moment is expected to vanish due to the orbitally non-degenerate ground state. However, a finite orbital moment that did not exceed 5% of the total magnetisation was found. To further elucidate the physical origin of these magnetic moments, *ab initio* ligand field theory calculations (AILFT) were performed for the first time on a 5d metal ion complex. The calculations reproduce the experimental results and demonstrate that the orbital moment in Os^{V} originates from admixture of the electronic ground state with energetically high-lying states. Indeed this effect becomes possible only because of the interplay of the strong spin-orbit interaction with the ligand field.

Surprisingly, X-ray spectroscopic data on osmium-based materials are still scarce in literature, which is rather intriguing given the broad interest in spin-orbit entangled phenomena. This work demonstrates that the molecular chemistry approach to elucidating the relationships between oxidation state, local structure and spin-orbit entanglement is certainly a viable approach for understanding the exotic physical properties of novel 5d-based materials.

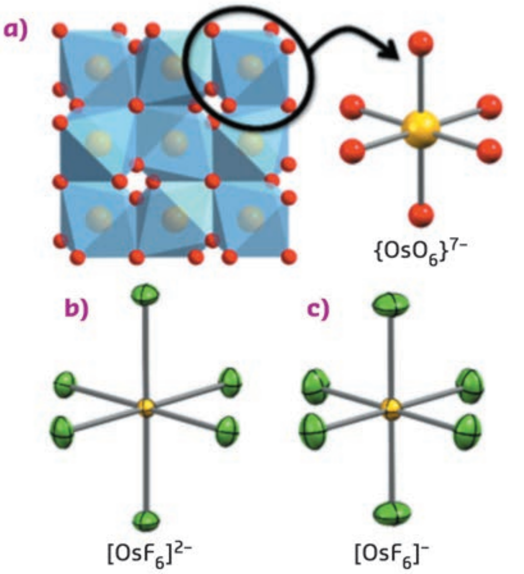

Fig. 111: Schematic illustration showing the conceptual link between osmium oxides, here represented by a) the structure of $Cd_2Os_2O_7$, b) the molecular fluoride-based analogues $[Os^{IV}F_6]^{2-}$ and c) $[Os^{V}F_6]^{-}$. Colour code: Os, yellow; O, red; F, green. Cd is omitted for clarity.

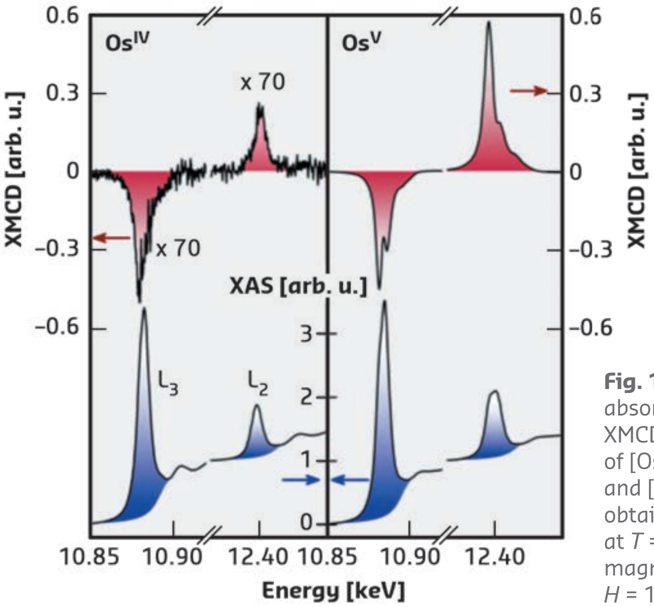

Fig. 112: X-ray absorption (blue) and XMCD (red) spectra of $[Os^{IV}F_6]^{2-}$ (left) and $[Os^{V}F_6]^{-}$ (right) obtained at ID12 at T = 3 K under a magnetic field of H = 17 T.

PRINCIPAL PUBLICATION AND AUTHORS

$[OsF_6]^{x-}$: Molecular Models for Spin-Orbit Entangled Phenomena, K.S. Pedersen (a,b,c,d,j), D.N. Woodruff (e), S.K. Singh (f), A. Tressaud (c,d), E. Durand (c,d), M. Atanasov (f,g), P. Perlepe (a,b,c,d), K. Ollefs (h,k), F. Wilhelm, (h), C. Mathonière (c,d), F. Neese (f), A. Rogalev (h), J. Bendix (i) and R. Clérac (a,b). *Chem. Eur. J.* **23**, 11244-11248 (2017); doi: 10.1002/chem.201702894.

(a) CNRS, CRPP, UMR 5031, Pessac (France)
(b) Univ. Bordeaux, CRPP, UMR 5031, Pessac (France)
(c) CNRS, ICMCB, UMR 5026, Pessac (France)
(d) Univ. Bordeaux, ICMCB, UMR 5026, Pessac (France)
(e) Department of Chemistry, University of Oxford (UK)
(f) Max-Planck Institut für Chemische Energiekonversion, Mülheim an der Ruhr (Germany)
(g) Institute of General and Inorganic Chemistry, Bulgarian Academy of Sciences, Sofia (Bulgaria)
(h) ESRF
(i) Department of Chemistry, University of Copenhagen (Denmark)
(j) DTU Chemistry, Technical University of Denmark, Kgs. Lyngby (Denmark)
(k) Faculty of Physics and Center for Nanointegration Duisburg-Essen (CENIDE), Universität Duisburg-Essen, Duisburg (Germany)

REFERENCES

[1] S. Calder *et al.*, *Nat. Commun.* **7**, 11651 (2016)
[2] L. Lu *et al.*, *Nat. Commun.* **8**, 14407 (2017)

STRUCTURE OF MATERIALS

The SoM group provides facilities for a range of X-ray scattering, imaging and spectroscopy experiments, relevant to the fields of energy research, catalysis, engineering, metallurgy, nanoscience and other fields of advanced technology. In addition to traditional technological subjects, the SoM group also covers X-ray imaging studies for biology, archaeology and palaeontology.

The materials science beamline **ID11** continues to welcome a wide range of user experiments. The new nanofocus end-station is now complete and has been used for several experiments. These include single crystal, total scattering and grain mapping experiments in several scientific areas, including metallurgy, chemistry, high pressure and geology. The ID11 team continues to develop software for grain mapping. There have been significant improvements to the MATLAB-based diffraction contrast tomography code in order to process data from twinned samples and with a greater tolerance for deformation **[1]**. Work has begun on upgrading the Fable python codes so that they can be run on python3 in the future.

ID15A is devoted primarily to *operando* studies in materials chemistry and materials engineering, with two dedicated experimental hutches. The materials chemistry hutch, operational since November 2016, is optimised for the rapid acquisition of multidimensional data on working chemical reactors, novel batteries, and other systems of interest to the chemical and energy sectors. X-ray diffraction measurements can now be combined with X-ray fluorescence measurements, absorption/phase contrast imaging, infra-red spectrometry and mass spectrometry. A gas delivery system for catalysis or other chemistry experiments is also available. Over the last few years, new software tools have been developed for the automation of data acquisition and processing, allowing users to fully exploit the rich multidimensional data collected via XRD computed tomography (XRDCT) with minimal expert intervention. A collaboration contract has been established with Finden Ltd. (UK) for the further development of XRDCT. The materials engineering station received its final instrumentation during summer 2017 and is now fully functional, offering energy or angular dispersive diffraction and ultra-fast imaging using monochromatic or pink beams, with X-ray energies up to several hundred keV. A collaboration with Manchester University (UK) has been established in the field of engineering science.

Microtomography beamline **ID19** has further expanded its capabilities, welcoming users for dynamic experiments such as shock studies or additive manufacturing. The laser safety system was installed, allowing users to perform time-resolved studies using phase contrast imaging with large propagation distances combined with laser irradiation. The pulsed laser, purchased in 2002 (Brilliant B by Quantel, 850 mJ at 1064 nm, 20 ns pulse width), was refurbished and is now equipped with frequency doubling modules as well as optical focusing elements. Within the frame of the long-term proposal MI-1252 (Eakins *et al.,* Oxford University and Imperial College London, UK) a Split-Hopkinson pressure bar was commissioned and will allow users to study the dynamic response of materials to stress. In 2017 an experiment with a two-stage gas gun demonstrated that impact velocities up to 4.7 km/s are possible for synchrotron experiments. In addition to the selected articles, one should note the paper by Hänschke *et al.* **[2]** on *in situ* imaging of dislocations in semiconductor wafers.

In January 2017 the stalwart high-precision powder diffractometer on beamline **ID22** was retired. The machine, manufactured by Rotary Precision Instruments (Bath, UK), was delivered to the ESRF in December 1994. It was tested on the Swiss Norwegian Beamline BM01B before being installed on BM16, complete with its nine-crystal multianalyser stage. SNBL, with whom the BM16 team worked in the development of the diffractometer, runs the sister machine, also acquired from RPI. The BM16 diffractometer has followed the ESRF high-resolution powder diffraction beamline around the ring, to ID31 in 2002, and to ID22 in 2014. Hundreds of papers have resulted from measurements made with this diffractometer. As part of the upgrade programme and the move from ID31 to ID22, and with a view to the EBS upgrade and developments in detector technology, a new diffractometer was procured, equipped with the latest drive electronics and advanced mechanics from LAB Motion Systems in Belgium. After a brief commissioning period the new diffractometer has been in successful user operation all year.

The high energy beamline for buried interface structures and materials processing, **ID31,** just finished its second year of operation. In order to reveal the interplay between microscopic material properties and macroscopic device performances, ID31 offers a portfolio of hard X-ray characterisation techniques combined with unique sample environment systems. For example, during 2017 first user experiments were performed using the recently acquired fuel cell test station to characterise fuel cells according to industrial standards with X-ray diffraction data during the operation. A new *operando* method for surface structure determination, transmission surface diffraction (TSD), was developed, where surface diffraction rods can be measured in transmission geometry (**see page 134**). This allows to map the local surface properties with micrometre spatial resolution. A new high throughput powder diffraction system committed mainly for industrial use was commissioned. A robotic sample changer allows the collection of diffraction data via an area detector from thousands of samples per hour with excellent powder averaging thanks to a shaker system implemented on the robot arm. The beamline is now also equipped with laser safety system for *in operando* additive manufacturing studies.

In 2017, Council selected four new EBS upgrade beamlines, including the hard X-ray diffraction microscopy project. X-ray diffraction microscopy, or dark field X-ray microscopy, is a new technique to study the hierarchical structure of materials over length scales from 1 mm to below 100 nm **[3,4]**. By using Bragg diffraction, it is sensitive to crystallographic details such as strain and grain or domain orientation that are difficult to assess with other techniques. A second EBS beamline integral to the SoM group is the **BM18** project: a high throughput large field phase contrast tomography beamline for applications from industry, materials research, engineering, biology and cultural heritage. The technical design of this beamline is already well advanced. The infrastructure work will start during the summer shutdown 2018 and will be followed by the beamline assembly phases during the long shutdown, 2019.

V. HONKIMÄKI

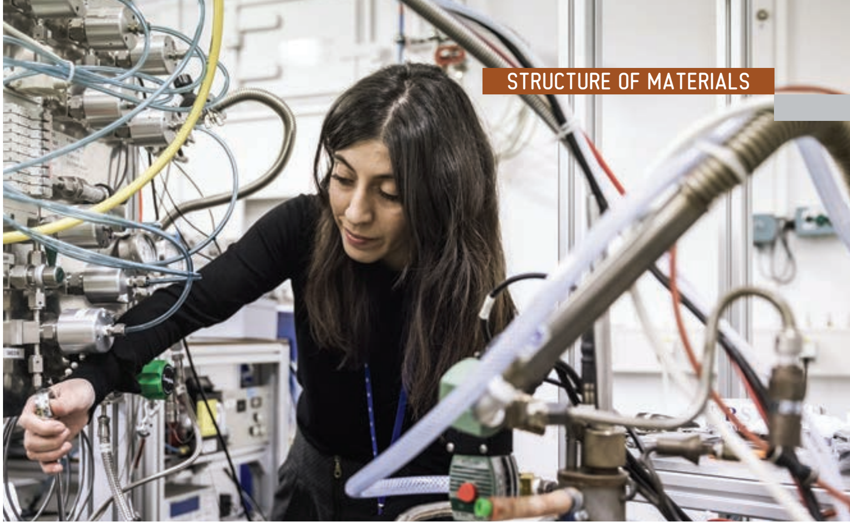

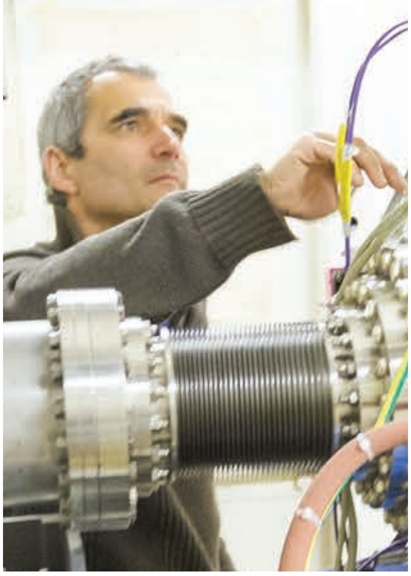

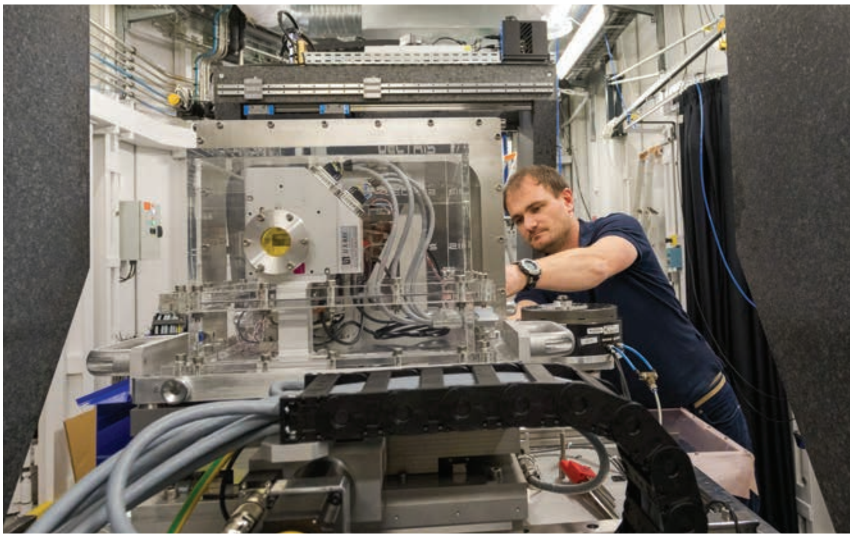

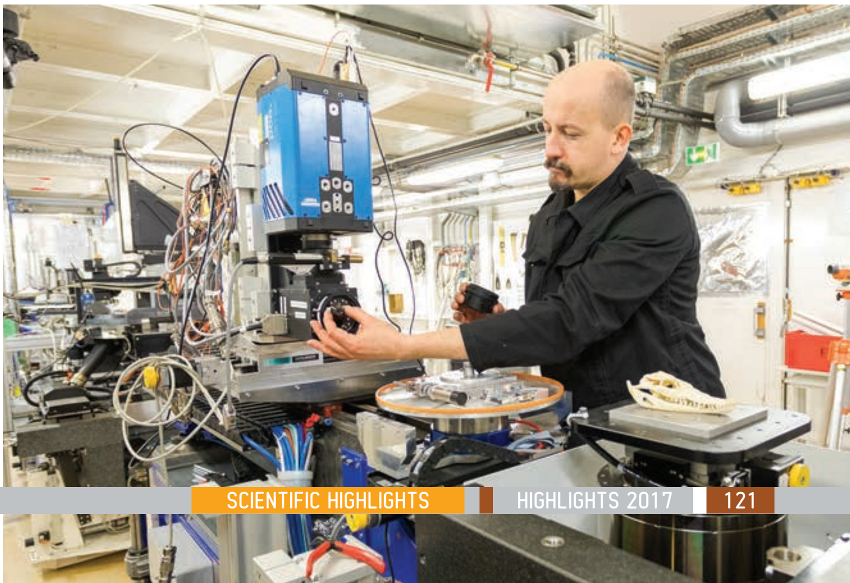

REFERENCES

[1] N. Viganò *et al.*, *Journal of Applied Crystallograpgy* **49**, 544-555 (2016).
[2] D. Hänschke *et al.*, *Phys. Rev. Lett.* **119**, 215504 (2017).
[3] H. Simons *et al.*, *MRS Bulletin* **41**, 454 (2016).
[4] H. Simons *et al.*, *Nat. Commun.* **6**, 6098 (2016).

AMPHIBIOUS BIRD-LIKE RAPTOR INTRODUCES NEW GROUP OF PREDATORY DINOSAURS

Mesozoic dinosaurs were not all stamping giants but also included the Maniraptora: a diverse group of small and agile meat-eating dinosaurs that includes all birds. The discovery of a bizarre new Cretaceous maniraptoran demonstrates that these hunters also exploited an amphibious niche.

A small, exquisitely preserved dinosaur skeleton (**Figure 113**) was poached from the famous Djadokhta Formation in southern Mongolia and resided in private collections before it was offered for palaeontological study. The fossil was partially prepared out of the Cretaceous sediment and revealed a stunning amount of detail, through which it identified itself as a member of the Maniraptora; the group of dinosaurs that includes the iconic raptors but also encompasses all birds. Nevertheless, particular properties of its morphology, preservation, and conservation also raised substantial doubts concerning the integrity of the specimen. The fact that the fossil united characteristics previously known from a diverse variety of taxa in a single individual fueled the suspicion that it may represent a chimera. This motivated a comprehensive tomographical study of the specimen to assess its integrity and to obtain more information on the skeletal elements that remained hidden inside the rock.

Hierarchical phase-contrast imaging was carried out at beamlines **BM05** and **ID19**. It was found that secondarily precipitated metallic oxides induced strong artefacts in the reconstructed volumes, which were corrected through newly designed texture enhancement and normalisation protocols. The improved data set demonstrated that the rock matrix was continuous, with original cracks propagating through the sediment and bones in unity. Furthermore, taking a certain degree of taphonomical influence into account, the important anatomical relation between the skull and neck vertebrae appears to have been conservatively retained. The left anterior limb visible on the outside of the rock was found to have been retouched during restoration but the morphology of its arm bones mirrors that of the right anterior limb still present inside the rock, which confirmed that the left arm belongs to the same individual. This observation is corroborated by the presence of a single growth line present in long bones of all four limbs, as well as in the mandible. Finally, the functional morphology of the skeleton proved internally consistent as well: adaptations in the pelvic girdle allow for a more erect posture that counteracts imbalance potentially imposed by the elongated neck.

Analyses revealed that the platyrostral snout accommodated an unexpectedly large number of tubular teeth in an intricate replacement system as well as a nervous network similar to those of crocodilians and other reptilian aquatic hunters employing a well-developed sense of mechanoreception **[1]**. The skull connects to an elongated yet flexible neck that makes up *circa* 50% of the snout-sacrum length. The ulna exhibits a certain degree of dorsoventral flattening, which is also present in modern birds that employ wing-propelled diving. The geometry of the hand is remarkable in that the lateralmost third finger is longer than the second (middle) finger, which resembles the condition in flippers of long-necked aquatic reptiles. The posterior limbs sport the hypertrophied “killing claws” shared with other raptorial dinosaurs and appear well-suited for terrestrial locomotion. This unique combination of characteristics (**Figure 114**) advocates an amphibious lifestyle: terrestrial bipedal locomotion combined with adaptations that enable aquatic piscivorous foraging and anguilliform swimming assisted by the anterior limbs. Its long neck would have enabled successful hunting in a fashion not unlike the present-day feeding tactics employed by herons.

The new species was named *Halszkaraptor escuilliei* in recognition of both the late Polish palaeontologist Halszka Osmólska, and François Escuillié who returned the poached fossil to Mongolia. This enigmatic dinosaur not only accounts for the first representative of this new species and genus, but also explains the interrelationships between two other Mongolian raptors that have proved challenging to place

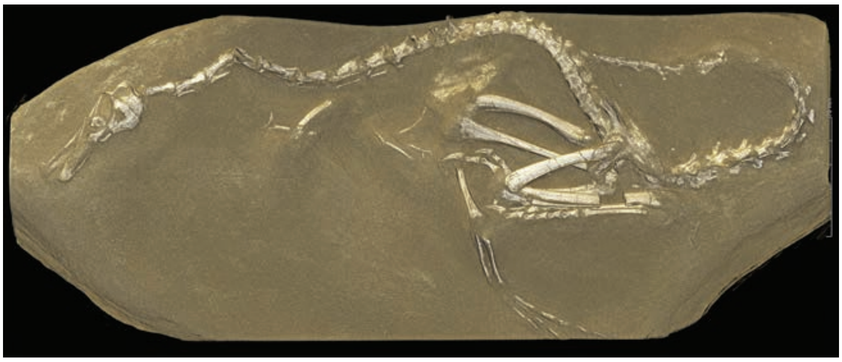

Fig. 113: 3D rendering of *Halszkaraptor escuilliei* holotype (MPC D-102/109) from synchrotron tomographic data.

before: *Halszkaraptor* allies with *Hulsanpes* and *Mahakala* in the new subfamily Halszkaraptorinae. Although future research will illuminate the potential presence of homologous amphibious adaptations in the thus-far poorly sampled genera *Hulsanpes* and *Mahakala*, *Halszkaraptor* now clearly demonstrates that maniraptoran dinosaurs not only engaged in agile terrestrial foraging and developed the capability of flight, but also exploited amphibious niches. This, in turn, not only expanded the ecological range of non-avian theropod dinosaurs **[2]**, but may also explain some of the evolutionary flexibility of Maniraptora that enabled birds to survive the end-Cretaceous mass extinction and occupy their status as the most successful class of vertebrates today.

Fig. 114: Life reconstruction of *Halszkaraptor escuilliei* (artwork by Lukas Panzarin / Andrea Cau).

PRINCIPAL PUBLICATION AND AUTHORS

Synchrotron scanning reveals amphibious ecomorphology in a new clade of bird-like dinosaurs, A. Cau (a), V. Beyrand (b, c), D. Voeten (b, c), V. Fernandez (b), P. Tafforeau (b), K. Stein (d), R. Barsbold (e), K. Tsogtbaatar (f), P.J. Currie (g) and P. Godefroit (h), *Nature* **552**, 395-399 (2017); doi: 10.1038/nature24679.

(a) Geological and Palaeontological Museum 'Giovanni Capellini', Bologna (Italy)
(b) ESRF
(c) Department of Zoology and Laboratory of Ornithology, Palacký University, Olomouc (Czech Republic)
(d) Earth System Science – AMGC Vrije Universiteit Brussel, Brussels (Belgium)
(e) Palaeontological Center, Mongolian Academy of Sciences, Ulaanbaatar (Mongolia)
(f) Institute of Palaeontology and Geology, Mongolian Academy of Sciences, Ulaanbaatar (Mongolia)
(g) Department of Biological Sciences, University of Alberta, Edmonton, Alberta (Canada)
(h) Directorate Earth & History of Life, Royal Belgian Institute of Natural Sciences, Brussels (Belgium)

REFERENCES

[1] C.T. Barker *et al., Sci. Rep.* **7**, 3749 (2017).
[2] L.E. Zanno and P.J. Makovicky, *PNAS* **108**, 232-237 (2011).

SEEING INSIDE A GROWING CATALYST

The formation and growth mechanism of hollow PtNi/C nanoparticles was unravelled using scanning transmission electron microscopy coupled to energy-dispersive X-ray spectroscopy, and *operando* high-energy wide-angle X-ray scattering. Following their formation, Ni-rich/C nanoparticles were rapidly enclosed in a $Ni_xB_yO_z$ shell and then slowly transformed into hollow PtNi/C nanoparticles.

Manipulating mono or bimetallic nanocrystallites at the atomic scale is pivotal to many domains of science. A textbook case concerns the unique optical, photo-thermal, paramagnetic and electrocatalytic properties of hollow metal nanoparticles. Indeed, in the presence of the oscillating electromagnetic field of a beam of light, the free electrons of many metal nanoparticles (in particular Au, Ag and Cu) oscillate coherently with respect to the positively charged metallic lattice, resulting in strong scattering and absorption. Bimetallic hollow nanoparticles have also demonstrated potential in the diagnosis of diseases, drug delivery and, more recently, in low temperature fuel cell electrocatalysis. However, the details and the kinetics of formation and growth of these peculiar nanomaterials remain unexplored.

Here, a combination of *operando* wide-angle X-ray scattering (WAXS) on **ID31**, scanning transmission electron microscopy (STEM) and X-ray energy dispersive spectroscopy (X-EDS) was used to reveal the formation and growth mechanism of hollow PtNi/C nanoparticles and provide the time scale at which the elementary steps of the synthesis occurred.

To synthesise hollow PtNi/C nanoparticles, a sodium borohydride solution ($NaBH_4$, a very strong reductant) was added in a dropwise manner to a solution containing the Pt and Ni

Fig. 115: X-ray energy-dispersive spectroscopy elemental maps of the different nanostructures forming during the synthesis of hollow PtNi/C nanoparticles. The images are recorded *t* = 1, 2, 3, 4, 20, 40 and 60 minutes after the addition of the first drop of the $NaBH_4$ solution. Ni atoms and Pt atoms are represented in green and red, respectively.

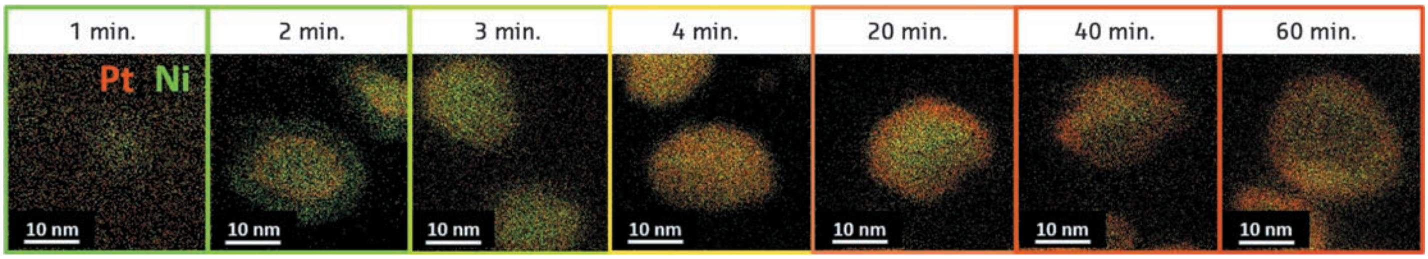

Fig. 116: *Operando* wide angle X-ray scattering patterns recorded during the synthesis of hollow PtNi/C nanoparticles. The time (t) corresponds to the time elapsed since the addition of the first drop of the $NaBH_4$ solution. Representative patterns are presented in (a), whereas (b) highlights the position and the assignment of the peaks in the $0 \leq t \leq 6.5$ min time period. Note that the raw data (energy 60.0 keV corresponding to $\lambda = 0.207$ Å) were previously converted into Cu Kα radiation ($\lambda = 1.5406$ Å) for the sake of comparison with classical X-ray diffraction.

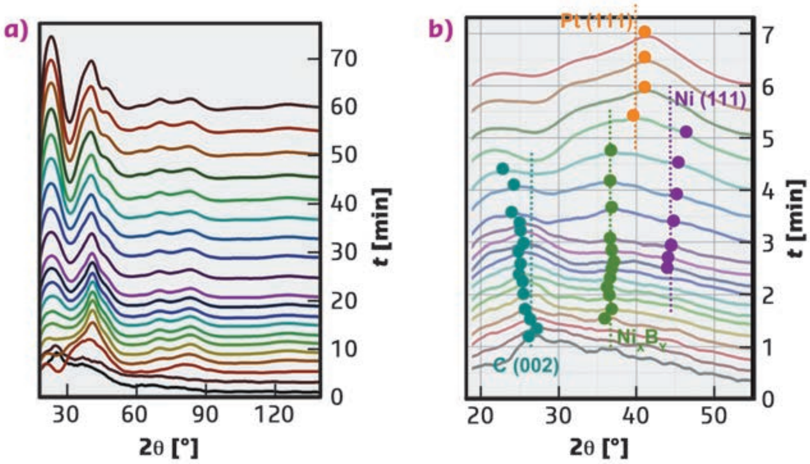

salt precursors and the high surface area carbon (Vulcan XC72). For STEM/X-EDS analyses, the synthesis was conducted in a glass reactor and sampling was performed at different time intervals after addition of the first drop of the $NaBH_4$ solution. The same experimental protocol was used for *operando* WAXS measurements but a poly(methyl methacrylate) cuvette served as reactor.

STEM/X-EDS elemental maps (**Figure 115**) and X-ray photoelectron spectroscopy analyses revealed that Ni/C nanoparticles around 5-10 nm in size formed first, before being embedded in a Ni_xByO_z shell ($t = 2$ min). This shell then served as a sacrificial template for the deposition of Pt^{2+} ions via a combination of chemical reduction and galvanic replacement (an electrochemical process in which a metallic phase is spontaneously oxidised by the ions of another metal having a higher reduction potential). Finally, in the time period $20 \leq t \leq 60$ min, the nanoscale Kirkendall (a spontaneous vacancy-mediated interdiffusion mechanism occurring in binary alloys or core@shell materials) contributed to the transformation of the solid Ni-rich core@Pt-rich shell nanoparticles into hollow alloy PtNi/C nanoparticles.

This mechanism of formation was confirmed using *operando* WAXS. Diffraction from the [002] planes of the carbon support, monoclinic NiB_3 and/or tetragonal Ni_2B, Ni(111) and Pt(111) appeared sequentially (**Figure 116**). The disappearance of the Ni(111) signal at $t \geq 6$ min confirmed that the Ni cores were corroded, or alloyed with Pt. Later in the reaction, the reflections ascribed to Pt increased in intensity, indicating enrichment in Pt in agreement with the STEM/X-EDS elemental maps displayed in **Figure 115**.

Beyond their interest for catalysis and electrocatalysis, the results provide for the first time a powerful methodology, capable of identifying the formation and growth mechanism of preferentially-shaped metal nanoparticles, core@shell nanoparticles, onion-like nanoparticles, Janus nanoparticles or a combination of all of these.

PRINCIPAL PUBLICATION AND AUTHORS

Atomic scale snapshots of the growth mechanism of hollow PtNi/C nanocatalysts for oxygen reduction reaction, R. Chattot (a,b), T. Asset (a,b), J. Drnec (c), P. Bordet (d,e), J. Nelayah (f), L. Dubau (a,b) and F. Maillard (a,b), *Nano Lett.* **17**, 2447-2453 (2017); doi: 10.1021/acs.nanolett.7b00119.
(a) Université Grenoble Alpes, LEPMI, Grenoble (France)
(b) CNRS, LEPMI, Grenoble (France)
(c) ESRF
(d) Université Grenoble Alpes, Institut Néel, Grenoble (France)
(e) CNRS, Institut Néel, Grenoble (France)
(f) Université Paris Diderot, Sorbonne Paris Cité, CNRS, Laboratoire Matériaux et Phénomènes Quantiques, UMR 7162, F-75013, Paris (France)

A STEP TOWARDS ORGANIC ZEOLITES

Hexacoordinate silicon is often seen in molecular compounds, but very rarely in crystalline silicate materials. Now, reversible Si-O chemistry has been used to assemble octahedral dianionic SiO_6 building units and anthracene derivatives into crystalline microporous silicate organic frameworks that share characteristics of both covalent organic frameworks and inorganic zeolites.

Microporous materials are used extensively in adsorption, catalysis, separation and energy storage and production. The field of microporous materials has been dominated for a long time by

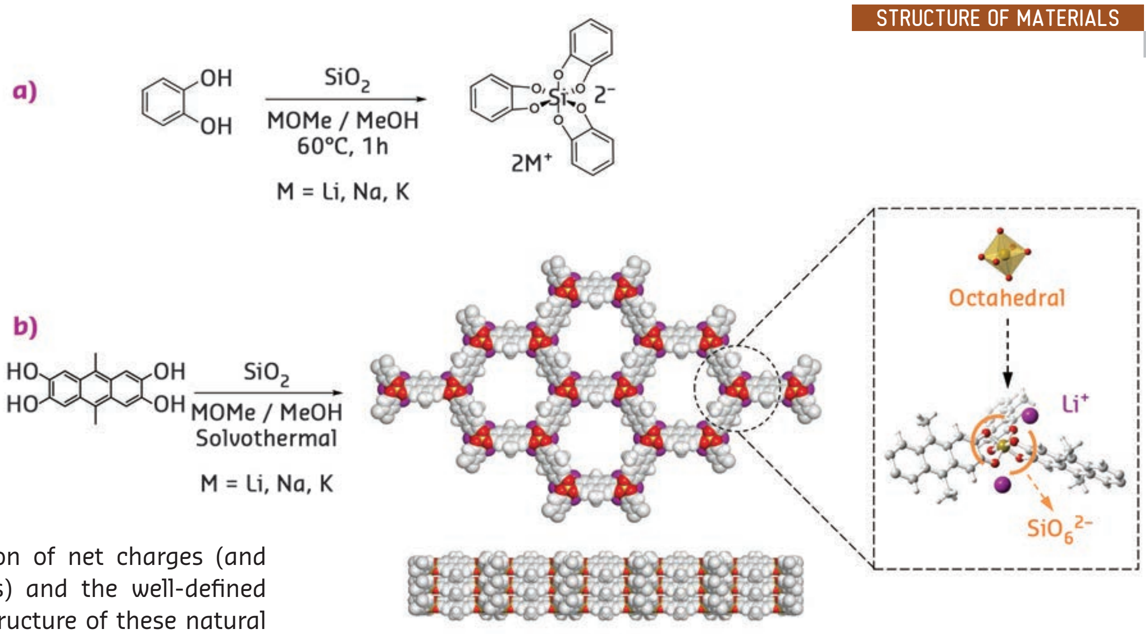

Fig. 117: a) Model condensation reaction of catechol and SiO_2 used to form tris(catecholato) silicate compounds. b) Anionic silicate covalent organic framework structure (top and side view) and formation by extending the reaction to an anthracene derivative.

zeolites. The combination of net charges (and extra-framework cations) and the well-defined crystalline framework structure of these natural and synthetic aluminosilicates are of utmost importance for their successful application as catalyst, adsorbent and ion-exchanger.

Nevertheless, there are still many applications that cannot be addressed by inorganic zeolites. A major synthetic challenge has recently been overcome with the discovery of two other classes of microporous crystalline frameworks, metal-organic frameworks (MOFs) **[1]** and covalent organic frameworks (COFs) **[2]**. These materials illustrate that microporous crystalline framework materials incorporating organic building blocks can be achieved. MOFs are hybrid 3D frameworks constructed from metal clusters and multitopic organic linkers assembled via metal-ligand coordination bonds. COFs are purely organic microporous extended crystalline frameworks composed solely of organic linkers linked through strong covalent bonds, thus holding promise for a generation of much more robust materials.

In this study, the synthesis of anionic covalent organic frameworks that bridge the gap between inorganic zeolites and COFs is reported. The frameworks were designed by exploiting the ability of silicon to form hypercoordinate compounds and by implementing reversible Si-O chemistry for the crystallisation of organic building blocks into extended crystalline frameworks. One critical step prior to the formation of a COF based on a new type of linkage consists in identifying a model compound that forms under reversible conditions and that simultaneously fulfils the criteria for the formation of extended crystalline frameworks. Catechol (1,2-dihydroxybenzene) is known to dissolve silica under basic conditions to form tris(catecholato) silicate dianions with octahedral geometry and in quantitative yields (**Figure 117a**), providing a non-polymeric compound for reference. The formation of silicates is reversible under such conditions and the synthesis of negatively charged silicate covalent organic frameworks (SiCOFs) with alkali-metal counter-ions (Li, Na, K) was successfully carried out in a simple one-pot procedure by condensation of silica and anthracene derivatives under solvothermal alkaline conditions (**Figure 117b**).

Clear evidence of the hexacoordinate environment around the silicon atoms was given by ^{29}Si nuclear magnetic resonance analysis. A single peak was observed in the ^{29}Si spectrum showing a good match with the one observed for the tris(catecholato) silicate model compound, indicating the presence of solely hexacoordinate dianionic silicon species within the network with no sign of defect (**Figure 118a**).

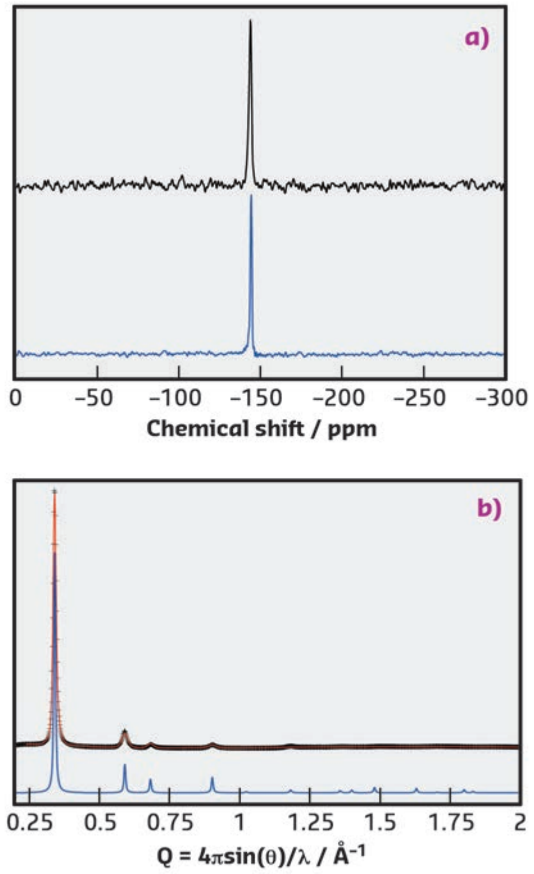

Fig. 118: a) Comparison of the ^{29}Si CP-MAS solid-state NMR spectra of SiCOF (top) and the tris(catecholato) silicate model compound (bottom) proves that solely hexacoordinate silicon species are present within the framework.
b) High-resolution powder X-ray analysis of SiCOF-Li with the observed pattern in black (λ = 0.399977 Å), the Pawley refined profile in red (Rwp = 4.40%) and the theoretical PXRD pattern in blue.

Such frameworks are synthesised as polycrystalline powders, which makes their structure solution challenging. High-resolution PXRD patterns and high-energy PXRD patterns suitable for analysis by pair-distribution function were collected at beamline **ID22** and revealed, in combination with density functional theory calculation, that SiCOFs crystallise as two-dimensional hexagonal layers stabilised in a fully-eclipsed (AA) stacking arrangement with pronounced disorder in the stacking direction (**Figures 117b** and **118b**). Microporosity with high surface area (up to 1300 $m^2 \cdot g^{-1}$) was evidenced by gas-sorption measurements and showed that the theoretical maximum surface area was nearly reached experimentally.

This work demonstrates that crystalline silicate material based on hexaoxosilicon units can form under mild reaction conditions by simple reaction of silica as a silicon source. Indeed, in silicate materials, silicon sites adopt almost exclusively a tetrahedral coordination with respect to oxygen and hexaoxosilicon centres within crystalline silicate materials have only been reported for a few high-pressure silicate phases, such as the silica polymorph stishovite.

PRINCIPAL PUBLICATION AND AUTHORS

Anionic silicate organic frameworks constructed from hexacoordinate silicon centres, J. Roeser (a), D. Prill (b), M. J. Bojdys (c), P. Fayon (d), A. Trewin (d), A. N. Fitch (e), M. U. Schmidt (b) and A. Thomas (a), *Nature Chemistry* **9**, 977-982 (2017); doi: 10.1038/nchem.2771.

(a) Department of Chemistry, Technische Universität Berlin (Germany)
(b) Institute of Inorganic and Analytical Chemistry, Goethe University, Frankfurt am Main (Germany)
(c) Department of Organic Chemistry, Charles University in Prague (Czech Republic)
(d) Department of Chemistry, Lancaster University (United Kingdom)
(e) ESRF

REFERENCES

[1] H. Furukawa *et al.*, *Science* **341**, 1230444 (2013).
[2] C. Diercks *et al.*, *Science* **355**, eaal1585 (2017).

ZOOMING IN ON SPECIFIC COMPONENTS OF A WORKING BATTERY WITH *OPERANDO* XRD/PDF COMPUTED TOMOGRAPHY

X-ray diffraction and pair distribution function computed tomography has been used to study the chemical structures of specific components in an operating battery in three dimensions, revealing the mechanism of a promising anode material. This work aims to improve the capacity and stability of batteries during many cycles of charge and discharge.

Sodium-ion batteries are a potentially important future energy storage technology. Sodium has similar chemistry to lithium and much of the established chemistry of lithium ion batteries can also be applied to sodium-ion batteries. Unfortunately, the graphite anodes used in lithium-ion batteries perform poorly with sodium, and other anode materials are required to produce sodium-ion batteries with good capacity and stability over many charge-discharge cycles. Alloying anode materials such as silicon, phosphorus, tin, antimony and bismuth offer very high capacities as they can capture several sodium ions for each anode atom **[1]**. Due to its low atomic weight, phosphorus offers the best gravimetric capacity, unfortunately its stability for battery cycling is poor. To understand the reasons for this, the chemical structure of the anode during battery

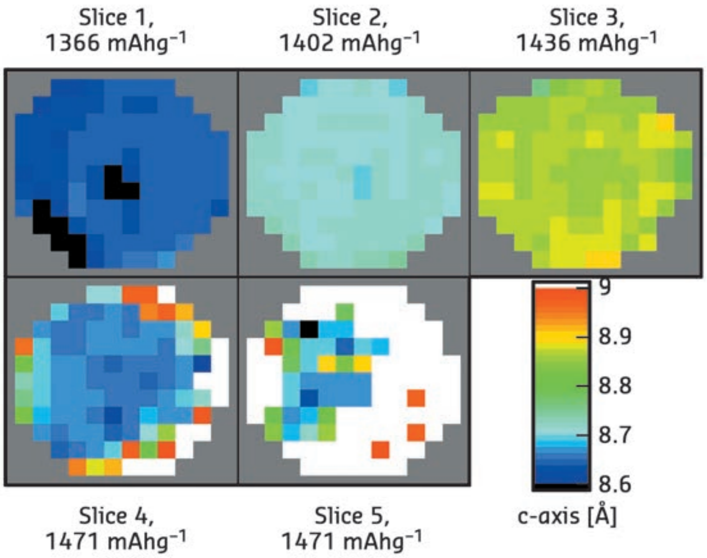

Fig. 119: Maps of selected tomographic slices from different heights in a phosphorus sodium-ion battery anode from Rietveld refinement.

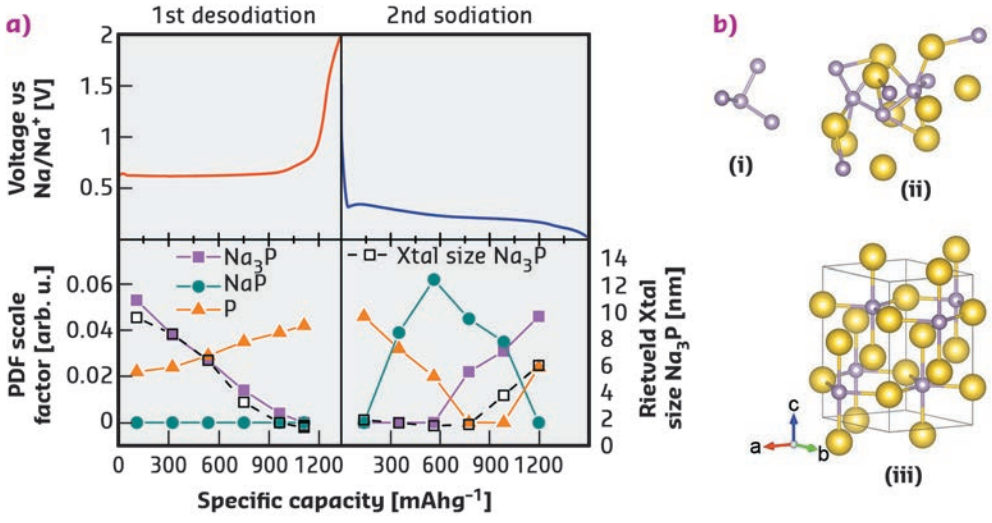

Fig. 120: a) Phases present in a phosphorus sodium-ion battery anode during cycling from PDF and Rietveld analysis. b) Structures:
(i) nano-P cluster;
(ii) nano-NaP cluster;
(iii) crystalline Na_3P.

cycling has been studied with *operando* pair distribution function and diffraction computed tomography (PDF/XRD-CT).

Phosphorus is a poor scatterer of X-rays and amorphous during most of the stages of battery cycling. This means that the normal tools of X-ray diffraction are of limited use. PDF-CT makes it possible to collect high quality PDF data on specific parts of the working battery without having to worry about background subtraction, which is one of the most problematic aspects of studying batteries with PDF methods **[2]**. Using beamline **ID15A** with a specially designed cell for battery tomography, 3D tomographic data were collected with high time resolution during cycling of the battery with a high enough energy to yield data that could be treated with both PDF and Rietveld analysis.

Comparison of the Rietveld and PDF fitting reveal that the charge and discharge of sodium in a phosphorus anode follow different structural routes and that even the crystalline phase appears first as an amorphous material. It was also possible to map the structural variation of the crystalline Na_3P phase in the anode (**Figure 119**), using several real structural parameters (unit cell axes, crystallite size, Na site occupancy) extracted by the Rietveld method. The PDF data show the first clear evidence of a NaP nanocluster intermediate phase during sodiation (discharge).

The structures present at all stages of cycling could be tracked by full fitting of all the possible phases to the PDF-CT data (**Figure 120**). Size variations at the nanoscale during cycling were clearly revealed in the PDFs: amorphous phosphorus exists in clusters of just four atoms during cycling, while the NaP forms in clusters of less than 10 Å radius.

The observations fit well with calculations that indicate a thermodynamically controlled sodiation (discharge) mechanism and kinetically controlled desodiation (charge). The kinetic mechanism is favoured despite the high formation energy of the $Na_{3-x}P$ phases due to the high mobility of sodium in crystalline Na_3P, which can maintain its layered structure as sodium is removed. During sodiation the thermodynamic path is followed through the lowest energy structures in the energy hull diagram calculated by Mayo *et al.* **[3]**.

The chemical behaviour of a sodium-ion battery was determined from XRD/PDF-CT. Also, the expansion and contraction of the anode during cycling was revealed through a combination of XRD and absorption-CT. Knowing the different chemical and macro-structural stages that phosphorus passes through while alloying with sodium during battery operation will help provide a better understanding of the battery's poor cycling stability.

PRINCIPAL PUBLICATION AND AUTHORS

Chemical structures of specific sodium ion battery components determined by *operando* pair distribution function and X-ray diffraction computed tomography, J. Sottmann (a), M. Di Michiel (b), H. Fjellvåg (a), L. Malavasi (c), S. Margadonna (d), P. Vajeeston (a), G. B. M. Vaughan (b) and D. S. Wragg (a), *Angew. Chem. Int. Ed. Engl.* **56**, 11385-11389 (2017); doi: 10.1002/anie.201704271.

(a) Department of Chemistry, University of Oslo (Norway)
(b) ESRF
(c) Department of Chemistry, University of Pavia and INSTM, (Italy)
(d) Department of Engineering, University of Swansea (UK)

REFERENCES

[1] M.N. Obrovac *et al.*, *Chemical Reviews* **114**, 11444-11502 (2014).
[2] P.K. Allan *et al.*, *J. Am. Chem. Soc.* **138**, 2352-2365 (2016).
[3] M. Mayo *et al.*, *Chem. Mater.* **28**, 2011-2021 (2016).

PROBING MECHANOCHEMISTRY WITH *IN SITU* REAL-TIME X-RAY POWDER DIFFRACTION

X-ray powder diffraction was used for real-time *in situ* monitoring of mechanochemical co-crystallisation. For the first time, the macroscopic dynamics of the powder was isolated from the chemical kinetics of the transformation. This revealed unprecedented time-dependent shifts in the kinetics of the process and rapid loss of free-flowing powder.

The use of mechanical force to induce chemical and physical transformations, *i.e.* mechanochemistry, was first used by early man, who mechanically ruptured covalent bonds to produce fire. Today, mechanochemistry is widespread, adopted by crystal engineers, physicists, materials scientists, chemists, pharmacists and industrialists. A particularly promising aspect of mechanochemistry is its ability to produce novel materials and compounds with high yields and very low environmental impact, *i.e.* solvent-free processing.

Despite the broad applications of mechanochemistry, the mechanisms that drive these processes are only poorly understood. In fact, recent work has demonstrated that different types of mechanical treatment yield different products **[1]**, and that unique reacting zones can exist even in the same milling jar **[2,3]**. This lack of control and understanding is restrictive for the further development of mechanochemical technologies in industry, where formation of undesirable and unknown products can have considerable legal and safety repercussions.

To probe the dynamics of mechanochemical co-crystallisation, a simple model system (glycine [gly] and oxalic acid dihydrate [OAD]) was studied by real-time, *in situ* X-ray powder diffraction (XRPD) at beamline **ID11**. The system represents a common situation in organic mechanochemistry, where one of the starting materials is present as a hydrate or solvate. In such situations, an additional liquid is often not required to help facilitate the reaction, greatly simplifying the system under investigation. This system was of further interest as it forms two competing products: glycinium semi-oxalate [GO] and bis(glycinium) oxalate [G2O].

A new methodology was developed to process the *in situ* XRPD patterns that were collected during the experiment. In doing so, this was the first time that critical information was obtained regarding the free-flowing powder within a milling jar. Surprisingly, powder disappeared exponentially from the path of the X-ray beam. This finding is critical to the reliability of *in situ* XRPD techniques to probe the mechanisms of mechanochemistry. The loss of powder from the beam path indicates caking of material within the ball mill, leading to a fundamental change in the composition and rheology of the system under investigation. By subsequent *ex situ* analysis, it was found that the ratio of the competing products was different in the free-flowing powder and the powder caked to the ends of the vessel. *In situ*, real-time analysis did not reflect the true situation occurring in the ball mill. A similar situation has been demonstrated by *ex situ* analysis **[2]**.

The loss of free-flowing powder also leads to a convolution of macroscopic dynamics and the kinetics of chemical conversion. In these experiments, deconvolution of these functions revealed a linear reaction profile, shown in **Figure 121**. *In situ* XRPD is incapable of resolving molecular-level mechanisms, the kinetics of which are surely not first order. However, this linear profile suggests that mixing plays a negligible role in determining reaction progress. Modelling of reaction progress in such cases

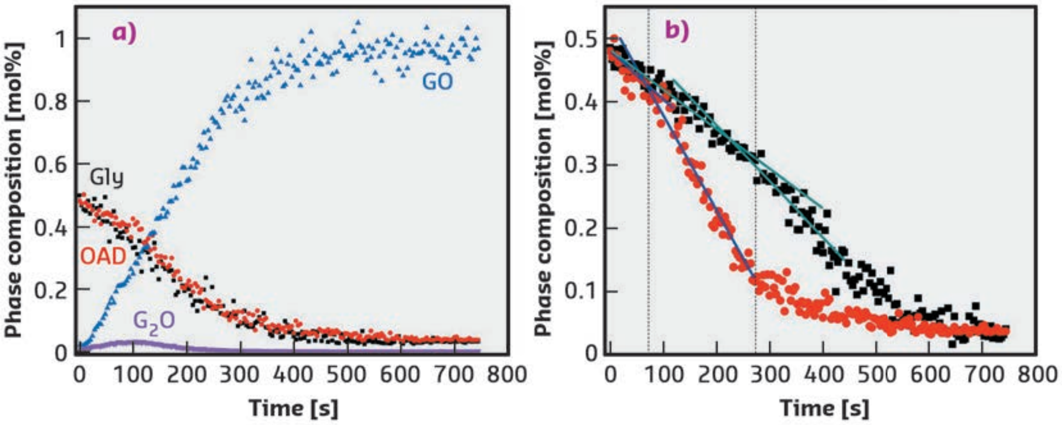

Fig. 121: Phase composition profile for the milling reaction of gly. and OAD. a) Complete phase profiles for milling reaction at 30 Hz. b) Consumption of OAD at milling frequencies 30 Hz (red) and 25 Hz (black). Change in kinetic profile is denoted by a dotted line in each case.

should be trivial, and is promising for industrial applications of mechanochemistry. Despite its apparent initial simplicity, a sudden and unexpected shift in the rate of the reaction was observed as milling progressed (**Figure 121**). This unprecedented phenomenon led to a doubling of reaction rates in some cases. The rate increase was most obvious in the rate of consumption of OAD, and likely reflects a decrease in OAD particle size, known to hasten the release of water **[4]**.

The study of mechanochemical processes is vital to the development of enhanced industrial technologies. However, without deeper understanding and control, mechanochemical techniques remain under-exploited. While *in situ* XRPD approaches are promising to investigate mechanochemical processes in real time, they remain limited by the quantity of sample that they probe. These techniques are further restricted by the level of molecular detail they offer, being restricted to the macroscopic study of kinetics and bulk composition. Despite its limitations, *in situ* real-time investigations of mechanochemical processes by XRPD remain a powerful means to obtain time-resolved information, such as dramatic shifts in kinetics, that are otherwise not observable.

PRINCIPAL PUBLICATION AND AUTHORS

Challenges of mechanochemistry: is in situ real-time quantitative phase analysis always reliable? A case study of organic salt formation, A.A.L. Michalchuk (a, b, c), I.A. Tumanov (a, d), S. Konar (b), S.A.J. Kimber (e), C.R. Pulham (b, c) and E.V. Boldyreva (a, d), *Adv. Sci.* **9**, 1700132 (2017); doi: 10.1002/advs.201700132.

(a) REC-008 Novosibirsk State University (Russian Federation)
(b) EaStChem School of Chemistry and Centre for Science at Extreme Conditions (CSEC), University of Edinburgh (UK)
(c) EPSRC Centre for Continuous Manufacturing and Crystallisation (CMAC) (UK)
(d) Institute of Solid State Chemistry and Mechanochemistry SB RAS, Novosibirsk (Russian Federation)
(e) ESRF

REFERENCES

[1] I.A. Tumanov *et al., Dokl. Chem.* **457**, 154-159 (2014).
[2] A.A.L. Michalchuk *et al., CrystEngComm* **15**, 6403-6412 (2013).
[3] A.A.L. Michalchuk *et al., Faraday Discuss.* **170**, 311-335 (2014).
[4] H. Tanaka, *J. Therm. Anal.* **29**, 1115-1122 (1984).

X-RAY GHOST IMAGING USING INDIVIDUAL SYNCHROTRON PULSES

Ghost imaging is an indirect method in which most of the X-rays used for the experiment never actually interact with the sample. The method uses two copies of the same speckled beam and the image is retrieved indirectly by correlating the two measured signals. This experiment could lead to the development of low-dose medical X-ray diagnostics and diffraction imaging at free electron lasers.

The time structure of the ESRF synchrotron beam has been used to demonstrate, for the first time ever, the X-ray version of ghost imaging, carried out at beamline **ID19**. Ghost imaging is an indirect imaging method that has received considerable attention in recent years **[1]**. In its simplest form, ghost imaging requires two identical copies of a structured (speckled) beam, as illustrated in **Figure 122**. One copy is directed on the sample and only the total intensity (not the image) transmitted or scattered by the specimen is recorded by a bucket (point) detector. The second, empty, beam is imaged by a pixel array detector, to form the reference image. In this way the sample image is never recorded directly. Remarkably though, the sample image can be reconstructed by repeating the experiment many times, each time with a different speckle pattern. The image is retrieved by correlating the bucket signals and the reference images. This can be done with an electronic correlator or, as in the case of this experiment, working offline on the whole data sequence.

Combining the special '4-bunch' filling mode of the ESRF with the intense X-ray pulses produced by the undulators at beamline **ID19**, the first proof-of-principle demonstration of ghost imaging in the hard X-ray spectral range was achieved. In 4-bunch mode, the temporal separation between the bunches is approximately 704 ns, corresponding to a frequency of about 1.42 MHz. In this experiment, the X-ray pulses were monochromatised to an energy of 20 keV by a pair of silicon crystals. The beam was then split using a thin silicon crystal in Laue diffraction, to produce the two identical copies required by the ghost imaging protocol. The sample (an X-ray opaque Cu wire) was inserted into one of the beams and both beams were detected using the same camera frame.

An ultra-fast camera was used to image the individual X-ray pulses, for an average of only a few consecutive pulses. In this way the characteristic shot noise of the synchrotron emission process is dominant and the beam contains natural speckles. In this proof-of-concept experiment, the bucket signal was calculated by summing the intensity measured in the sample beam and correlated with the reference beam image instead of using a separate bucket and reference detector.

The power spectrum of the bucket signal is shown in **Figure 123a**. The sharp peak at 0.71 MHz corresponds to half the storage ring frequency.

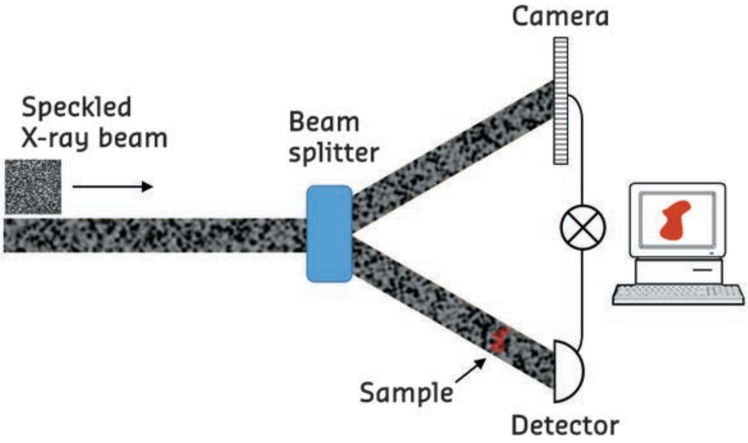

Fig. 122: Schematic diagram of a ghost-imaging experiment.

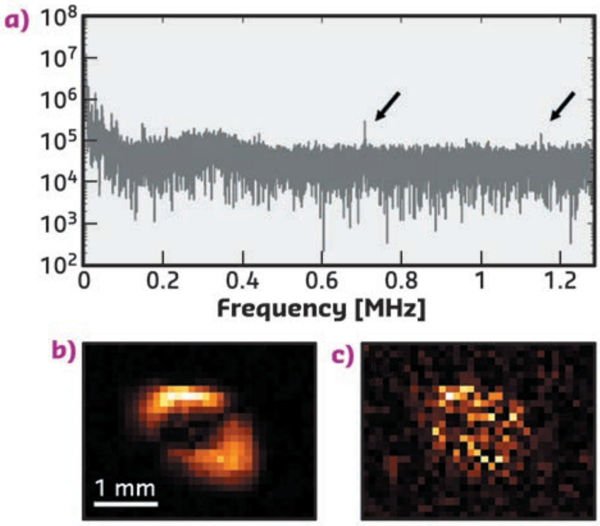

Low frequency components of the spectrum arise from mechanical vibrations of the optics (monochromator and crystal beam splitter), which are problematic. Vibrations cause small changes in the crystal orientation, which produce intensity variations in both the diffracted and transmitted beam. Such variations are actually anti-correlated and therefore obscure the genuine speckle correlation coming from the electron bunch structure.

To eliminate the effect of mechanical vibrations, Fourier filtering of the spectrum of both reference and bucket signals was performed. The true speckle correlation was isolated by windowing the 0.71 MHz peak (equivalent to taking the average of two pulses) in both reference and bucket. **Figure 123b** shows the recovered ghost image of the wire, using the filtered spectrum. **Figure 123c** shows the ghost image obtained when the window selects a nearby spectral region instead of the 0.71 MHz peak. In this latter case the speckle correlation is not present and the sample image is not recovered.

The experiment confirms that shot noise produced in the synchrotron emission of isolated electron bunches can be successfully used for correlation imaging experiments. This result might inspire new ideas on single molecule diffraction imaging at FELs. By reducing the dose of the bucket beam, a "diffraction without destruction" protocol using ghost imaging **[2]** could be devised.

X-ray ghost imaging has other potential applications that include spectroscopy, such as X-ray fluorescence, where an imaging detector generally cannot be used. Also, it could be highly beneficial for low dose radiology as most of the photons in a ghost imaging experiment never interact with the sample.

Fig. 123: a) Power spectrum of the bucket signals. Two peaks are visible in the high frequency part (marked by arrows). The actual storage ring frequency (1.42 MHz) was not resolved due to the insufficient temporal resolution of the camera. b) Ghost image of a copper wire measured by windowing the 0.71 MHz frequency component. c) By windowing the 'wrong' frequency component (in this case 0.8 MHz) the ghost image is not retrieved.

PRINCIPAL PUBLICATION AND AUTHORS

Experimental X-ray ghost imaging,
D. Pelliccia (a, b), A. Rack (c), M. Scheel (d),
V. Cantelli (e, c) and D. Paganin (f),
Phys. Rev. Lett. **117**, 113902 (2016);
doi: 10.1103/PhysRevLett.117.113902.
(a) Instruments & Data Tools Pty Ltd (Australia)
(b) RMIT University, Melbourne (Australia)
(c) ESRF
(d) Synchrotron Soleil, Gif-sur-Yvette (France)
(e) Helmholtz-Zentrum Dresden-Rossendorf, Dresden (Germany)
(f) Monash University, Melbourne (Australia)

REFERENCES

[1] B.I. Erkmen and J.H. Shapiro, *Adv. Opt. Phot.* **2**, 405-450 (2010).
[2] Z. Li *et al.*, *arXiv:*1511.05068 (2015).

SPONGE-ASSOCIATED BACTERIA MINERALISE ARSENIC AND BARIUM ON INTRACELLULAR VESICLES

Arsenic and barium are ubiquitous and toxic elements. If accumulated by organisms from their environment, they are excreted, assimilated into organic forms or mineralised. This work demonstrates that the bacterium *Entotheonella sp*. found in the Red Sea sponge *Theonella swinhoei* is capable of intracellular biomineralisation of both elements, on membrane vesicles.

Previous research found hyper-accumulation of arsenic and barium in the Red Sea sponge, *T. swinhoei* **[1]**. Fractionation of *T. swinhoei* cells and the ICP-MS elemental analysis of the resulting fractions showed that the filamentous bacteria *Entotheonella sp.* constitutes the arsenic and barium accumulating entity within its host (**Figure 124**). *Entotheonella sp.* is a filamentous bacterium described as trichomes or as chains of 4 to 20 cells. It is the most abundant bacteria found in *T. swinhoei*, comprising 3.25% of the sponge's volume.

SEM scans and EDS analysis of the *Entotheonella sp*. filaments show they contain multiple barium- and arsenic-rich spherical granules inside their cytoplasm. The average sphere volume is 0.11 ± 0.007 µm^3 (n = 121). The spheres have an organic core and are covered by an organic veneer. High-resolution synchrotron X-ray powder diffraction of freeze-dried samples obtained on **ID22** showed that barite ($BaSO_4$) was the major phase and with arsenates and phosphates as minor phases in the crystalline fraction (**Figure 125a**). Crystalline barite presence within spheres was also confirmed by high-resolution TEM examination of FIB-prepared thin section. The fast Fourier transform (FFT) of the TEM image obtained from a magnification close to an individual atomic lattice layer exhibits single crystal electron diffraction from the zone axis of barite (**Figure 125b**). Precise structural determination of the minor phases was achieved after mild thermal annealing. The resulting diffractogram clearly detects crystalline calcium arsenate ($Ca_3(AsO_4)_2$) and calcium sulfide phosphate ($Ca_{10}(PO_4)_6S$) as minor phases (**Figure 125c**).

The presence of barite and calcium arsenate were further confirmed on unprocessed flash-frozen *Entotheonella sp.* samples by synchrotron X-ray microprobe analyses performed at 95 K. The distribution of arsenic in the filaments was evident by micro-focused X-ray fluorescence (µXRF) mapping. All arsenic K edge X-ray absorption near edge structure (XANES) spectra of *Entotheonella sp*. showed As(V) as the dominant valence. Least-square linear combination fitting (LCF) of filament spectra to arsenic reference compounds was performed. Best fits were obtained using combinations of non-sulfur

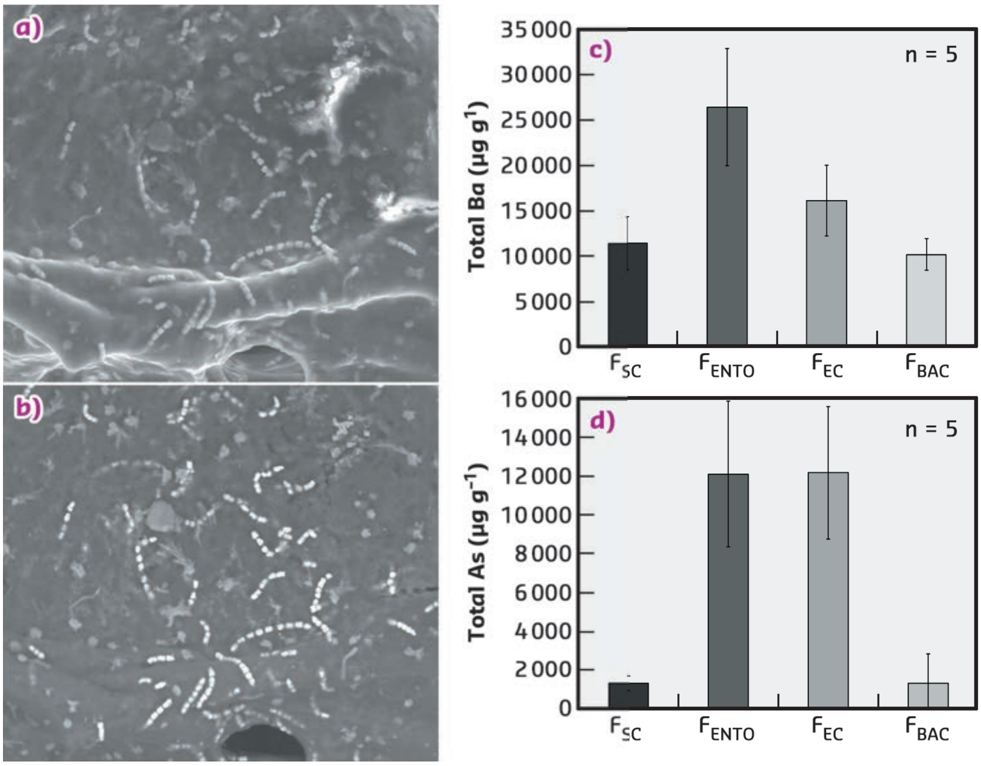

Fig. 124: SEM micrographs of *Entotheonella sp.* in sponge tissue. a) Secondary electron detection mode indicating some of the *Entotheonella sp.* filaments. Scale bar, 100 µm. b) Backscattered electron detection mode reveals *Entotheonella sp.* filaments as the most electron-dense objects in the sponge. Scale bar, 50 µm. c, d) Dry weight concentration (µg g^{-1}) of barium and arsenic (respectively) in cell-enriched fractions (n = 5). FBAC, unicellular bacterial cells; FEC, *Entotheonella sp.* with cyanobacteria; FENTO, *Entotheonella sp.* cells; FSC, sponge cells. Error bars show s.e.

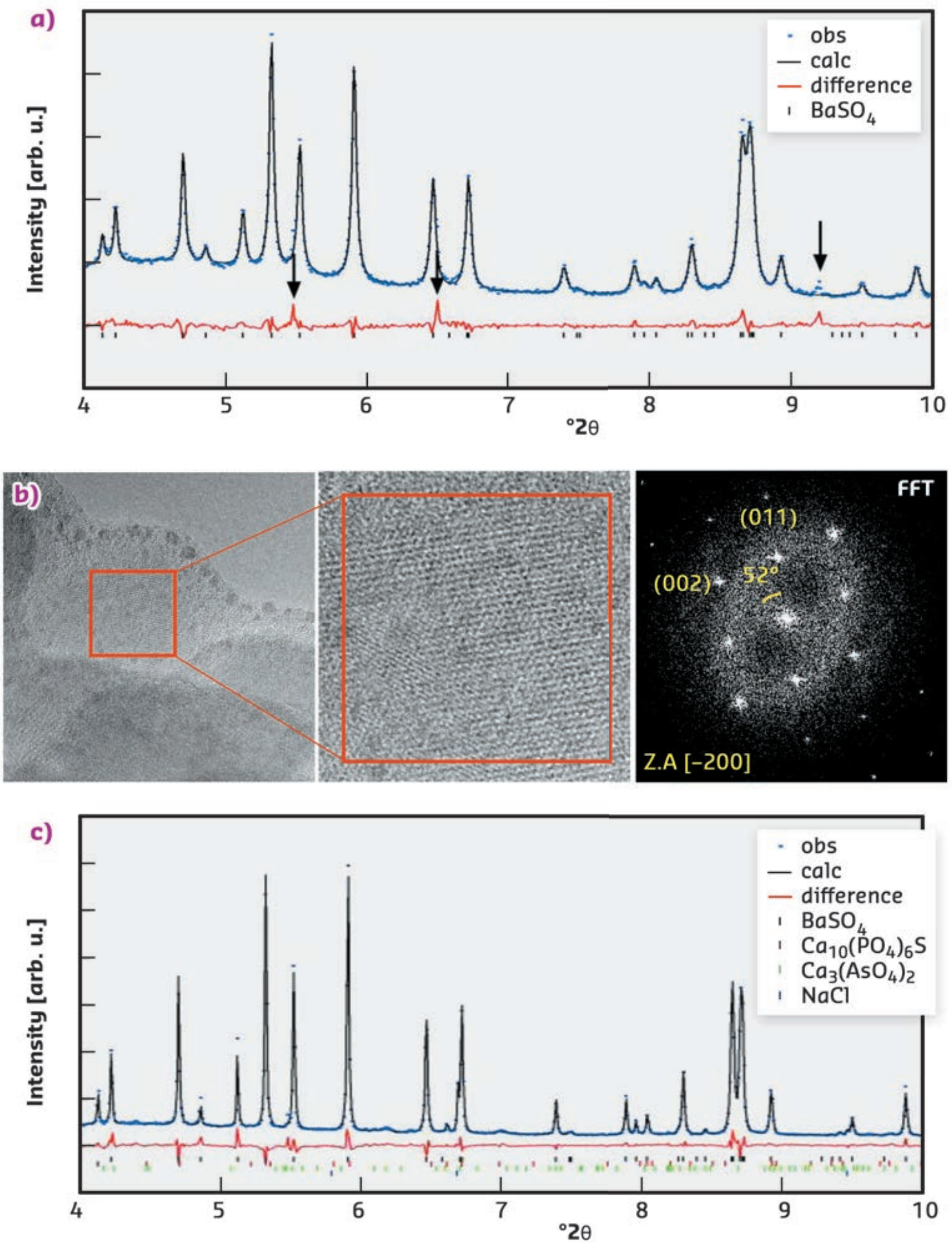

Fig. 125: XRD and TEM analysis of spheres inside *Entotheonella sp*. a) Rietveld refinement plot of preheated, freeze-dried *Entotheonella sp.* showing fit for observed (blue dots) and calculated (black line) diffraction patterns and the difference between them (red line). Black notches indicate the positions of the diffraction peaks of the major crystalline phase, barite ($BaSO_4$). Diffraction peaks highlighted by arrows in the difference curve are compatible with an arsenate or phosphate phase. b) HRTEM micrograph of a portion of the freeze-dried *Entotheonella sp.* Insert shows higher magnification image revealing the lattice, and with its fast Fourier transform (FFT). c) Rietveld refinement plot of a freeze-dried *Entotheonella sp.* after thermal annealing: minor phases of sodium chloride (NaCl), calcium arsenate ($Ca_3(AsO_4)_2$) and calcium sulfide phosphate ($Ca_{10}(PO_4)_6S$). Observed (Obs.), calculated (Calc.) and difference curves are presented in the same schematics as in (a).

As(III), calcium arsenates (mostly pharmacolite) and sodium arsenate. µXRD performed on some of the filaments' XANES locations showed the presence of pharmacolite.

These results show extraordinary concentrations of barium and arsenic in *Entotheonella sp.* (12,000 µg g^{-1} As is among the highest measured in any known organism). *Entotheonella sp.* is the only known prokaryote capable of intracellular barite mineralisation and only one other prokaryote, *Desulfotomaculum auripigmentum,* is known to intracellularly mineralise arsenic **[2]**. This is the first report of crystalline calcium arsenate, pharmacolite, as a biomineral. It is only in *Entotheonella sp.* that these elements are sequestered in a membrane-bound, organelle-like structure within the cytoplasm, and mineralised with many of the characteristics of controlled biomineralisation.

PRINCIPAL PUBLICATION AND AUTHORS

Sponge-associated bacteria mineralize arsenic and barium on intracellular vesicles, R. Keren (a), B. Mayzel (a), A. Lavy (a), I. Polishchuk (b), D. Levy (b), S.C. Fakra (c), B. Pokroy (b) and M. Ilan (a), *Nat Commun.* **8**, 14393 (2017); doi: 10.1038/ncomms14393.

(a) Department of Zoology, George S. Wise Faculty of Life Sciences, Tel Aviv University (Israel).
(b) Faculty of Materials Engineering and the Russell Berrie Nanotechnology Institute, Technion, Israel Institute of Technology (Israel).
(c) Advanced Light Source, Lawrence Berkeley National Lab, Berkeley (USA)

REFERENCES

[1] B. Mayzel *et al., PloS one* **9**, e95775 (2014).
[2] D.K. Newman *et al., Applied and Environmental Microbiology* **63**, 2022-2028 (1997).

3D RECONSTRUCTION OF NANOWIRE BENDING AND LATTICE TILT USING X-RAY DIFFRACTION

Strained core-shell nanowires have been investigated with nanofocused scanning X-ray diffraction. The bending and twisting of the nanowires was reconstructed and quantified in three dimensions. In one nanowire the shell lattice was found to be tilted with respect to the core, and the azimuthal orientation of the tilt changes along the axis.

Semiconductor nanowires have shown promising performance in a wide array of applications, such as solar cells, electronics and energy storage. A particular category of these is core-shell nanowires, which are created by first growing an axial core nanowire and then changing the conditions to promote shell growth. A lattice mismatch between core and shell creates a strained heterostructure, which can enhance carrier mobility and reduce surface recombination. While the interplay between lattice mismatch, strain and defect formation is quite well understood in strained thin film heterostructures, the thin nanowires can also accommodate strain by bending.

In this study, nano-XRD investigations were carried out of two strained GaAs-GaInP core-shell nanowires (**Figure 126a**, **b**). The nanowires were deposited from their growth substrate onto a Si_3N_4 membrane. The X-ray beam from the **ID11** beamline was focused to a size of 100 nm vertically and 6 µm horizontally. Nanowires with vertical orientation, orthogonal to the beam, were chosen and aligned in the focus. Scanning nano-XRD was performed by acquiring rocking curves, that is, small scans in rotation around the [111] Bragg angle, at points with 100 nm distance along the nanowire axis (**Figure 126c**). The scattering of the [111] reflection was mapped into reciprocal space, and the position of the Bragg peak was evaluated as a function of the axial coordinate *z*.

Nanowire A exhibits a single diffraction peak, which shows a significant variation along the nanowire axis (**Figure 126d**). A perfectly straight core-shell nanowire with constant composition would show a single vertical line in such a plot, or possibly two vertical lines for a sufficiently large lattice mismatch. The Bragg angle can vary due to variations in lattice plane distance, but also due to real-space tilting of the lattice. Since the [111] planes are orthogonal to the nanowire axis, the scattering vector is locally parallel to the tangent of the single-crystal nanowire, and the contour of the nanowire can be reconstructed by stepwise integration **[1]**. The 3D reconstruction shows that the nanowire is strongly bent in the upper half, while the lower half is straight (**Figure 126e**).

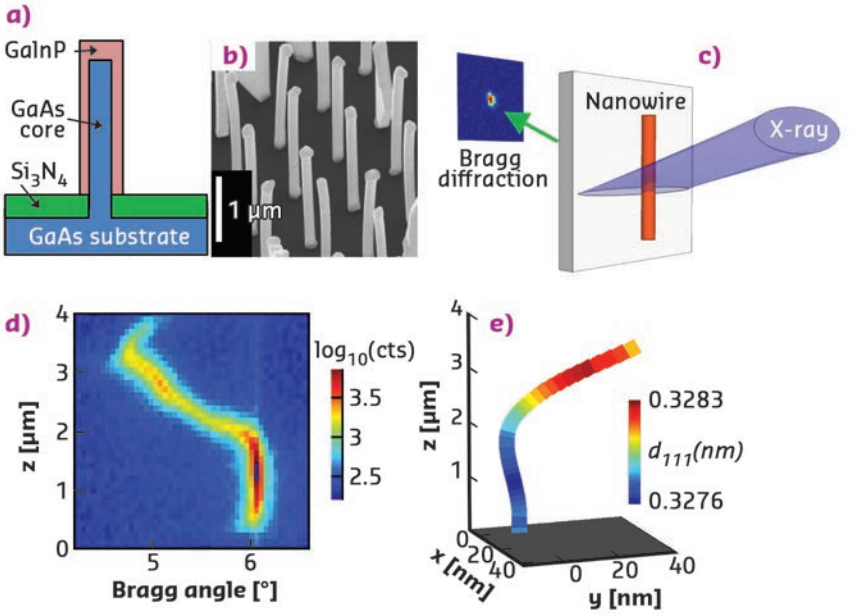

Fig. 126: Scanning X-ray nanodiffraction of nanowire A. a) Drawing of the GaAs-GaInP core-shell nanowire structure. b) SEM of the as-grown nanowires. c) Drawing of the experiment. d) Total counts in the Bragg peak on the detector, vs Bragg angle and *z*. e) 3D reconstruction of the nanowire. Note that the *x* and *y* scales are in nm and the *z* scale is in µm.

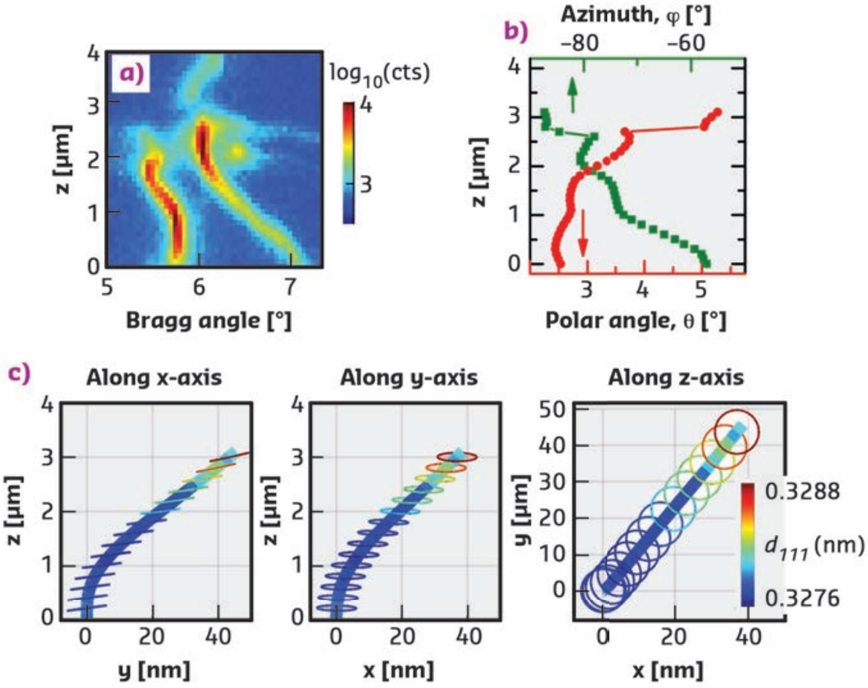

Fig. 127: Scanning X-ray nanodiffraction of nanowire B. a) Total counts of the Bragg peak on the detector, as a function of Bragg angle and z. b) The angles between the scattering vectors of the shell and the core, vs. *z*. c) 3D model of the nanowire, projected along the principal axes.

The second nanowire, B, shows two distinct Bragg peaks along most of its length (**Figure 127a**). The split in the Bragg angle is over one degree at the base of the nanowire, which is far more than the lattice mismatch could create. The reason is a difference in orientation of the core and shell lattices. The difference was quantified and converted to a spherical coordinate system, with one polar (θ) and one azimuthal (φ) angle (**Figure 127b**). To visualise the complex crystal structure, the shape of the core was first reconstructed as nanowire A, and then circles were added to represent the orientation of the shell, with the colour showing the lattice plane distance (**Figure 127c**). The tilt of the planes in the plot was magnified for better visibility.

The 3D reconstruction shows that nanowire B bends but, unlike nanowire A, it exhibits no twisting. The magnitude of the bending is similar to nanowire A. The polar θ angle represents a lattice tilt between shell and core, which increases from θ = 2° at the base to θ = 5° at the top. The relative azimuthal orientation of the tilt changes from about φ = -87° near the base, to φ = –57° at the top. Thus, the shell lattice twists around the core.

These results demonstrate how scanning nano-XRD can reveal striking differences between individual nanowires, as well as within single nanowires, which would be invisible with a lower-resolution method.

PRINCIPAL PUBLICATION AND AUTHORS

Bending and twisted lattice tilt in strained core-shell nanowires revealed by nanofocused X-ray diffraction, J. Wallentin (a, b), D. Jacobsson (b), M. Osterhoff (a), M.T. Borgström (b) and T. Salditt (a), *Nano Letters* **17**, 4143-4150 (2017); doi: 10.1021/acs.nanolett.7b00918.

(a) University of Göttingen (Germany)
(b) Lund University (Sweden)

REFERENCES

[1] J. Wallentin *et al., Adv. Mater.* **28** (9) (2016).

TRANSMISSION SURFACE DIFFRACTION

A new *operando* method for surface structure determination in an ambient environment has been developed. High-energy photons and transmission geometry are used, allowing the determination of the full in-plane surface structure with a single acquisition. By using a focused beam the local surface properties can be mapped with micrometre spatial resolution.

Processes at material interfaces to liquids or to high-pressure gases are of great interest in many technologically important areas. These include electrochemical energy storage and conversion, heterogeneous catalysis, corrosion, lithographic etching and the deposition of thin films and nanostructures. In these examples the solid material interacts with a fluid, which often leads to complex structural changes at the interface. In order to understand these changes, it is necessary to investigate these structures *in situ* under operating conditions. Only a few techniques, including synchrotron-based X-ray diffraction, are capable of such experiments.

Recent advances in surface X-ray scattering greatly speed up data acquisition by using high energy photons and large 2D detectors, which allows the measurement of large fractions of reciprocal space at once. Up to now a grazing incidence geometry was used, which has two major disadvantages; firstly, the beam spreads out over a very large area and, secondly, an extremely accurate alignment is required.

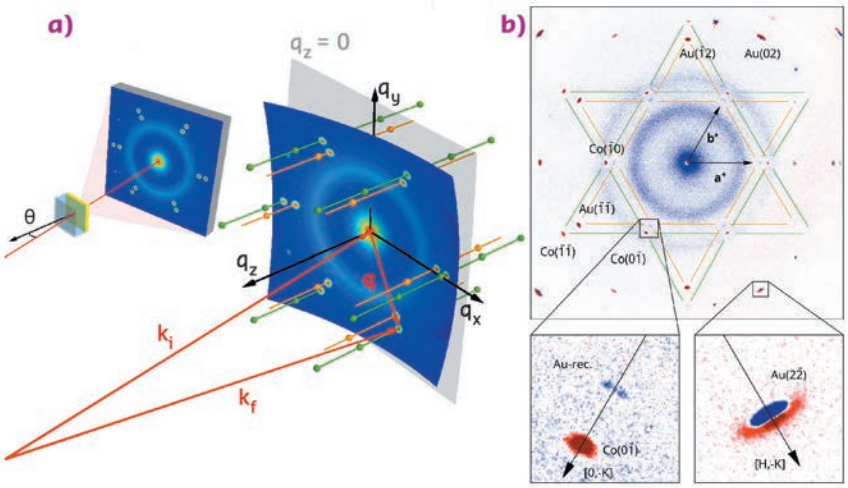

Fig. 128: a) Scattering geometry of TSD in real space (left) and reciprocal space (right). b) *In situ* TSD of a thin epitaxial film of Au(111) on Si(111) in 0.1 M $NaClO_4$ + 1.3 mM HCl + 1 mM $CoCl_2$ (40 keV, θ = 4.1°). Shown is the difference between detector images of the bare Au substrate at –0.2 $V_{Ag/AgCl}$ and after electrochemical deposition of a 20 monolayer-thick epitaxial Co(001) film at –1.05 $V_{Ag/AgCl}$. A variety of different peaks originating from the change in Co and Au diffraction rod intensity can be seen, where red colours indicate an increase and blue colours a decrease in intensity.

Transmission surface diffraction (TSD), which was developed at **ID31**, can overcome these difficulties. Here, the high-energy beam is directed perpendicular to the sample surface and passes through the solid sample and adjacent liquid. The scattered intensity is recorded with a large 2D detector located behind the sample (**Figure 128a**). This arrangement makes sample alignment fast and easy. In this geometry, the Ewald sphere is almost parallel to the surface in the region mapped by the detector, which allows the visualisation of the full in-plane structure of the sample in a single detector image (**Figure 128a**). By tilting the sample relative to the incident beam by an angle θ, out-of-plane positions along the crystal truncation rods (CTRs), which describe the surface diffraction, can be measured.

Figure 128b shows the difference between two detector images of a thin epitaxial Au(111) film on Si(111), before and after the deposition of a 20 monolayer-thick Co film. The image shows the emergence of a hexagonal diffraction pattern due to the growth of an epitaxial Co film. Furthermore, the intensity of the Au rods is altered by the deposition. A change in the Au rod position (**Figure 128b**) indicates a small change in the Au strain. The disappearance of the characteristic twin peaks near the Au rods (**Figure 128b**) shows the lifting of the Au surface reconstruction, proving the monolayer sensitivity of TSD.

The central advantage of this method is the capability of spatially resolved measurements. Contrary to grazing incidence diffraction, where the beam footprint is usually millimetres in size, the beam footprint in TSD is simply given by the focus of the beam. **Figure 129** shows maps of different surface properties of an 8 nm-thick epitaxial Co film deposited on Au(111)/Si(111) obtained in solution. The maps were created by recording 31 × 31 TSD images on a 600 × 700 μm^2 grid, using a beam size of 10 × 20 μm^2 and a photon energy of 40 keV. The tilt angle θ was 4.1°, such that a Co Bragg peak was directly on the Ewald sphere. Co film thickness, in-plane grain size and in-plane strain were determined by fitting the Co peak intensity, width and position at each of the 961 TSD detector images.

With its mapping capabilities, TSD can provide information about the heterogeneity of the surface structure that cannot be obtained with any other method. Sample alignment for TSD is simple and fast and the images are intuitive to read since they are similar to Laue diffraction and LEED. This also makes TSD a great tool for inexperienced users of synchrotron radiation.

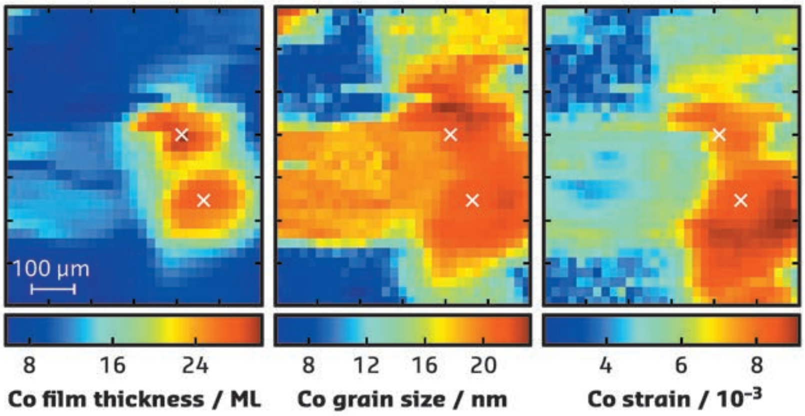

Fig. 129: TSD real space mapping (600 μm x 700 μm) of Co films on Au(111) in 0.1 M NaClO$_4$ + 1.3 mM HCl at -1.05 V$_{Ag/AgCl}$. Shown are film thickness (left), the in-plane grain size (middle) and in-plane strain (right) determined from the Co (-1 0) CTR.

PRINCIPAL PUBLICATION AND AUTHORS

Transmission Surface Diffraction for Operando Studies of Heterogeneous Interfaces,
F. Reikowski (a), T. Wiegmann (a), J. Stettner (a), J. Drnec (b), V. Honkimäki (b), F. Maroun (c), P. Allongue (c) and O.M. Magnussen (a),
J. Phys. Chem. Lett. **8**, 1067-1071 (2017);
doi: 10.1021/acs.jpclett.7b00332.
(a) Institut für Experimentelle und Angewandte Physik, Christian-Albrechts-Universität zu Kiel (Germany)
(b) ESRF
(c) Physique de la Matière Condensée, Ecole Polytechnique (France)

CARBON NANOTUBES AS TEMPLATES FOR 1D NANOSTRUCTURES VIA A ONE-REACTANT-ONE-POT METHOD

An all-in-one synthetic method has been developed, in which a single reactant, containing all the elements required for inorganic nanowires, is loaded into a carbon nanoreactor. Fluorescence-detected X-ray absorption and Raman spectroscopies in combination with transmission electron microscopy were used to monitor the transformations, revealing interactions between the nanotube and the molecules, stabilising the products.

Harnessing functional properties that emerge at the nanoscale is the key to developing superior materials for catalytic, electronic and biomedical applications. The internal cavity of single-walled carbon nanotubes (SWNTs) provides an effective template for control of the exact

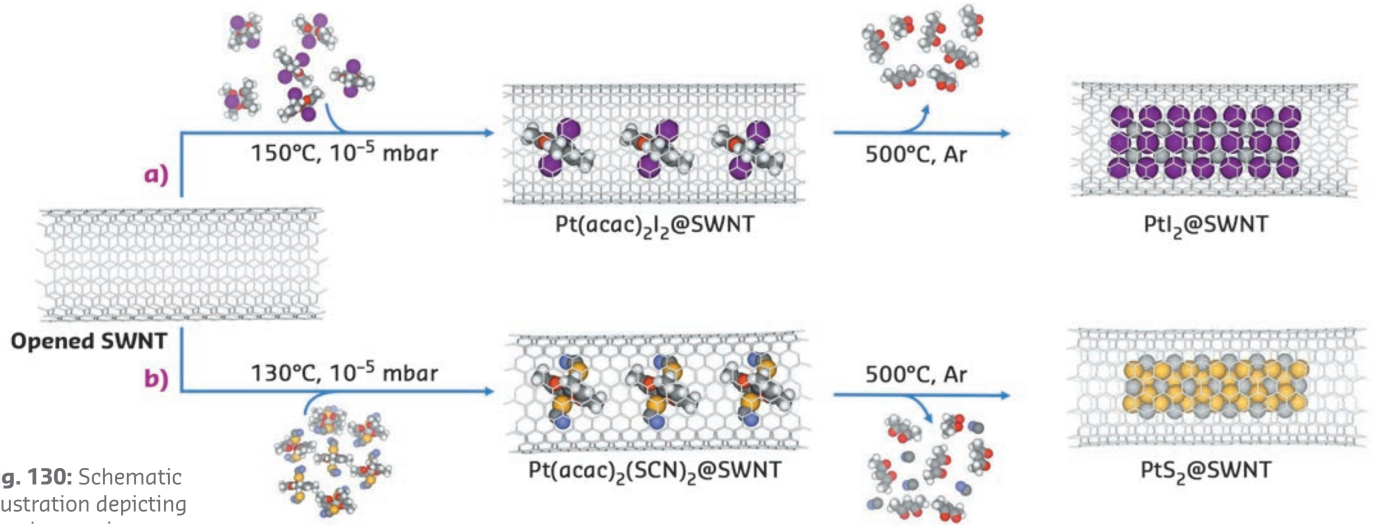

Fig. 130: Schematic illustration depicting how inorganic nanomaterials, a) PtI_2@SWNT; and b) PtS_2@SWNT, can be formed using nanotubes as templates via a one-reactant-one-pot method.

positions and orientations of molecules and atoms and has been successfully applied to the construction of nanoscale architectures from a variety of metals, **[1,2]** organic molecules, and inorganic compounds **[1,2]**. Low-dimensional inorganic materials, including transition metal chalcogenides, are of particular interest as their semiconducting properties can be precisely tuned by shaping their structures into nanoribbons. While the host nanotube can control the dimensions of the inorganic structure, the stoichiometry is much more difficult to control.

An all-in-one molecular precursor that contains all the necessary elements in the correct proportion for the desired inorganic product, encapsulated in SWNTs and subsequently converted into the inorganic material, offers a highly effective solution to this challenge. The one-pot-one-reactant synthesis involves a single step so that the stoichiometric ratio of the metal and halogen/chalcogen in the resultant material can be precisely controlled. The insertion of complexes of transition metals with ligands containing the required non-metallic elements into SWNTs is illustrated for platinum compounds containing Pt:I and Pt:S in ratios of 1:2 (**Figure 130**).

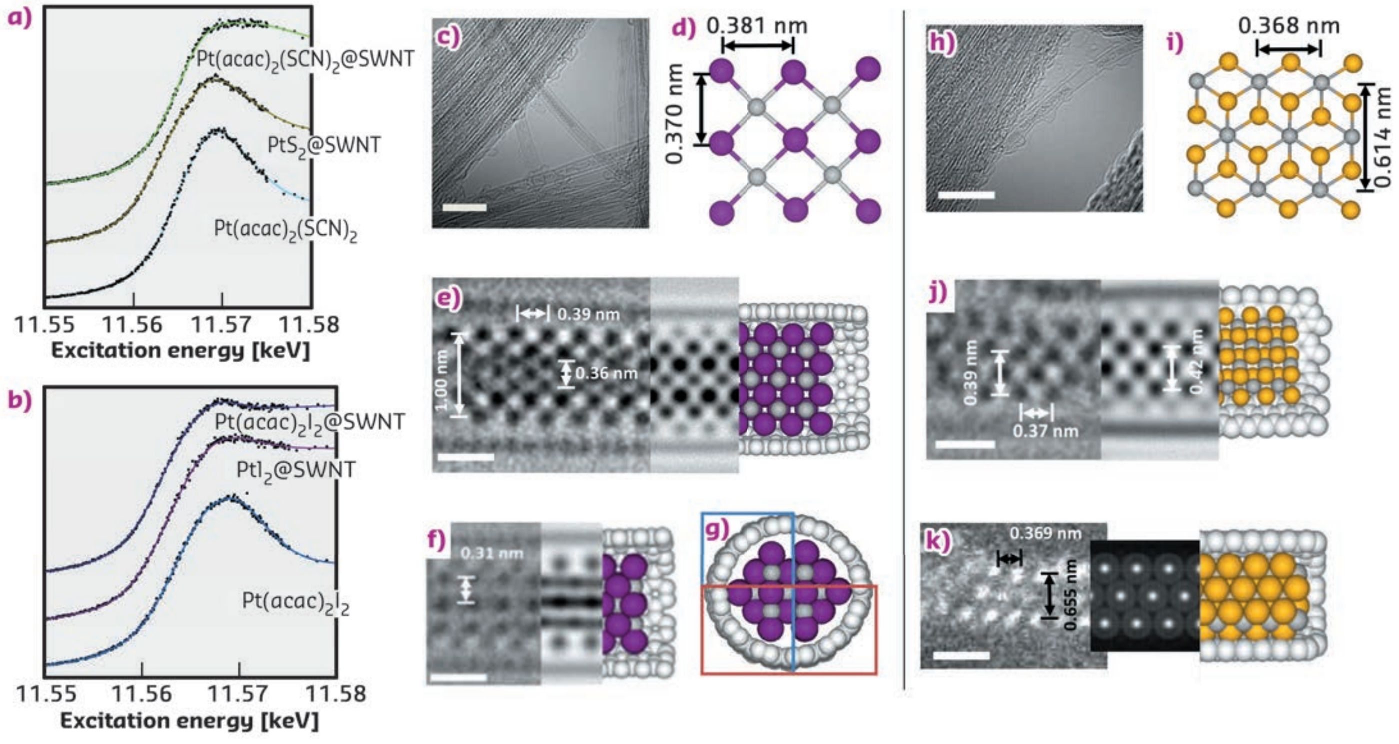

Fig. 131: a) and b) FD-XAS showing the Pt L_3 edge of materials formed in SWNTs. c) AC-HRTEM image showing a bundle of PtI_2@SWNT, the scale bar is 5 nm; d) an extended portion of the crystal structure of PtI_2 derived from the asymmetric unit of bulk PtI_2; e,f,g) two AC-HRTEM micrographs showing PtI_2@SWNT in different projections, accompanying HR-TEM simulations and computational models, the scale bars are 0.5 nm; h) an AC-HRTEM micrograph showing a bundle of nanotubes containing PtS_2 material, the scale bar is 5 nm; i) a portion of the crystal structure of bulk PtS_2; j) an AC-HRTEM image of PtS_2@SWNT with accompanying simulation and model, the scale bar is 0.5 nm; k) a HAADF-AC-STEM image PtS_2@SWNT, with accompanying simulation and model.

The L_3 edge of Pt (measured in FD-XAS at **BM28**) can be used as a probe of the oxidation state of the species inside the nanotube and can thus elucidate any transfer of electron density to or from the reactant to the nanotube upon encapsulation. Furthermore, the characteristic G-band, ubiquitously observed in the Raman spectra of graphitic nanostructures, is sensitive to strain and curvature of the nanotube, and can be used to measure any electron transfer from the nanotube to guest molecules. Interestingly, the encapsulation of $\mathrm{Pt(acac)_2I_2}$@SWNT led to a significant reduction in the absorption energy of the Pt L_3 edge, indicative of an increase of electron density onto the Pt centre as compared to free $\mathrm{Pt(acac)_2I_2}$, (**Figure 131**). This is complemented by a significant blue shift of the Raman G-band of the host SWNT, implying electron transfer from the nanotube to the guest molecule. In contrast, $\mathrm{Pt(acac)_2(SCN)_2}$@SWNT showed a decrease in the Pt edge energy in the FD-XAS and a red shift of the nanotube G-band, indicating that electron density is transferred in the opposite direction, *i.e.* from $\mathrm{Pt(acac)_2(SCN)_2}$ to SWNTs. Thermal treatment led to the facile transformation of the molecular precursors to the desired inorganic structures, $\mathrm{PtI_2}$@SWNT or $\mathrm{PtS_2}$@SWNT, with a nearly 1:2 stoichiometric metal to halogen/chalcogen composition and nanowire morphology.

AC-HRTEM imaging reveals that the atomic level structure of the $\mathrm{PtI_2}$@SWNT is different to that of the bulk (**Figure 131**), with high-coordinated I-atoms in the middle of the structure and low-coordinated I atoms located in the space between the Pt and the SWNT wall, despite the overall Pt:I ratio being the same as in the bulk crystal. Such structural changes are a result of the confined monoclinic lattice adapting to the cylindrical channel of the SWNT to maximise van der Waals interactions. In contrast, in $\mathrm{PtS_2}$@SWNT the nanowire adopts a hexagonal lattice similar to bulk $\mathrm{PtS_2}$.

PRINCIPAL PUBLICATION AND AUTHORS

A One-Pot-One-Reactant Synthesis of Platinum Compounds at the Nanoscale, C.T. Stoppiello (a), J. Biskupek (b), Z.Y. Li (c), G.A. Rance (a, d), A. Botos (a), R.M. Fogarty (e), R.A. Bourne (f), J. Yuan (g), K.R.J. Lovelock (h), P. Thompson (i, j), M.W. Fay (d), U. Kaiser (b), T.W. Chamberlain (f) and A.N. Khlobystov (a, d), *Nanoscale* **9**, 14385-14394 (2017); doi: 10.1039/c7nr05976k.

(a) School of Chemistry, University of Nottingham (UK)

(b) Central Facility for Electron Microscopy, Ulm University (Germany)

(c) Nanoscale Physics Research Laboratory, School of Physics and Astronomy, University of Birmingham (UK)

(d) The Nanoscale and Microscale Research Centre, University of Nottingham (UK)

(e) Department of Chemistry, Imperial College London (UK)

(f) iPRD, School of Chemistry, University of Leeds (UK)

(g) Department of Physics, University of York (UK)

(h) Inorganic Chemistry Laboratory, University of Oxford (UK)

(i) Department of Physics, University of Liverpool (UK)

(j) ESRF

REFERENCES

[1] T. Chamberlain *et al., ACS Nano* **11**, 2509-2520 (2017).

[2] A. Botos *et al., J. Am. Chem. Soc.* **138**, 8175-8183 (2016).

NEW INFANT APE SKULL FROM KENYA SHEDS NEW LIGHT ON APE EVOLUTION

The newly discovered most complete ape skull yet known from Napudet, Kenya, KNM-NP 59050, is dated to 13 million years. Remarkable preservation of the fossil coupled with synchrotron scanning made it possible to visualise both the external and internal morphology of the skull. The skull belongs to a new species, *Nyanzapithecus alesi*, a member of a now-extinct lineage close to the origin of the common ancestor of apes and humans.

Among living primates, humans share the same lineage with the apes, including chimpanzees, gorillas, orangutans and gibbons, and are grouped together in the superfamily Hominoidea. Our common ancestor with chimpanzees lived in Africa six to seven million years ago and many spectacular fossil finds have revealed how humans evolved since then. In contrast, the fossil record of common ancestors of living apes and humans before 10 million years ago is poor, making it difficult to find answers to two fundamental evolutionary questions: Did the common ancestor of living apes and humans originate in Africa, and, what did these early ancestors look like?

KNM-NP 59050 is a new cranium of an infant ape from the 13 million-year-old Middle Miocene site of Napudet in the Turkana Basin in Kenya **[1]**. KNM-NP 59050 is unique in that nearly all elements of external and internal morphology are preserved in a single extinct ape specimen.

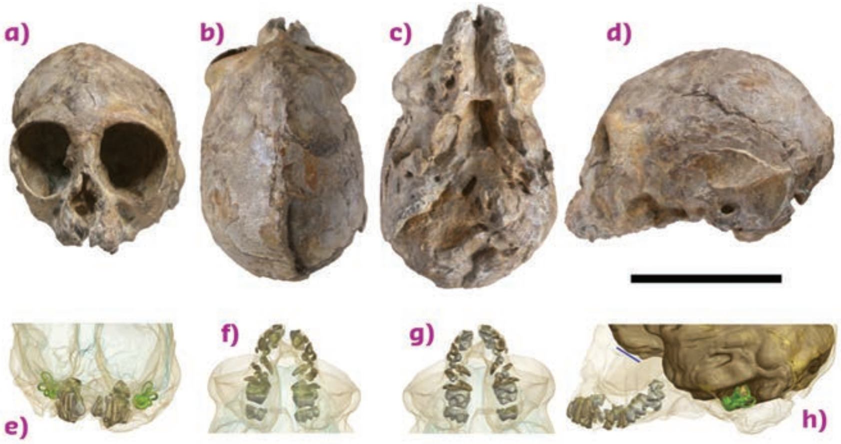

Fig. 132: KNM-NP 59050. Specimen as preserved in a) anterior view, b) superior view, c) inferior view, and d) left lateral view. e-h) 3D visualisations based on X-ray microtomography, in views matching a-d, and with the bone rendered transparent to show the deciduous dental roots (beige), the unerupted permanent tooth crowns (grey), the bony labyrinths (green) and the endocast (blue transparent in (e-g) and beige in (h); the olfactory fossa marked by the blue line placed directly underneath). Scale bar 5 cm.

Many of the most informative parts are preserved inside the fossil and, to make these visible, it was scanned at **ID19** using propagation phase contrast X-ray synchrotron microtomography (PPC-SR-μCT; **Figures 132e-h**) **[2]**. Aspects of the internal morphology available for study include the unerupted teeth, the inner ears housing the organs of hearing and balance, the middle ear (including ossicles on both sides), the nasal cavity and paranasal sinuses, and the brain endocast.

The quality of images of the unerupted adult teeth with their daily growth record lines were so fine that it could be established from the teeth that the infant was about one year and four months old at death (**Figure 133**). The volume of the brain cavity, estimated to be about 101 ml, slightly smaller than that of gibbons at the same stage of dental development, is significantly larger than the 35 ml estimates for adult monkey specimens of equivalent geological age. The lemon-sized skull, with its notably small snout, looks most like a baby gibbon. However, analyses show that this appearance is not exclusively found in gibbons, and evolved multiple times among extinct apes, monkeys, and their relatives. It was also established, based on the morphology of the unerupted adult teeth inside the infant ape's skull, that the specimen belonged to a new species, *Nyanzapithecus alesi*. A phylogenetic analysis revealed that *Nyanzapithecus alesi* belonged to a now-extinct lineage that existed in Africa for over 10 million years and was very close to the origin of humans and apes' common ancestor.

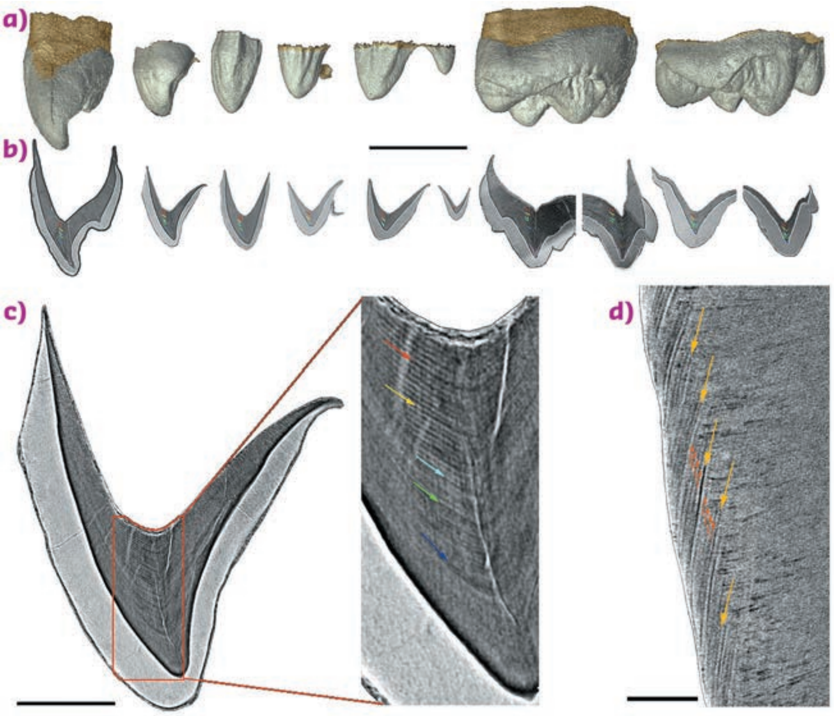

Fig. 133: Virtual histological slices of KNM-NP 59050. a) 3D rendering of the right unerupted permanent teeth germs. b) Virtual histological slices of teeth with coloured arrows showing the stress lines in dentine used for developmental cross-correlations of all the teeth and cusps. Scale bar is 5 mm. c) Detail of the Andresen lines in the dentine, and reference stress lines in the right I2 germ. Scale bar is 1 mm. d) Details of the enamel microstructure of this tooth, showing four daily lines (dark orange arrows) between consecutives Retzius lines (light orange arrows), indicating a long period line periodicity of five days. Scale bar is 100 μm.

PRINCIPAL PUBLICATION AND AUTHORS

New infant cranium from the African Miocene sheds light on ape evolution, I. Nengo (a), P. Tafforeau (b), C. Gilbert (c), J. Fleagle (d), E. Miller (e), C. Feibel (f), D. Fox (g), J. Feinberg (g), K. Pugh (c), C. Berruyer (b), S. Mana (h), Z. Engle (g) and F. Spoor (i), *Nature* **548**, 169-174 (2017); doi:10.1038/nature23456.

(a) Department of Anthropology, De Anza College and Turkana Basin Institute, Stony Brook University (USA)
(b) ESRF
(c) Department of Anthropology, Hunter College, CUNY (USA)
(d) Department of Anatomical Sciences, Stony Brook University (USA)
(e) Department of Anthropology. Wake Forest University (USA)
(f) Departments of Anthropology and Earth and Planetary Sciences Rutgers University (USA)
(g) Department of Earth Sciences, University of Minnesota (USA)
(h) Department of Geological Sciences, Salem State University (USA)
(i) Department of Cell and Developmental Biology, UCL (UK) and Department of Human Evolution Max Planck Institute (Germany)

REFERENCES

[1]. I. Nengo *et al., Nature* **548**, 169 (2017).
[2]. P. Tafforeau *et al., Appl. Phys. A-Mater.* **83**, 195 (2006).

COBALT-BASED CATALYST STRUCTURE EVOLVES ACCORDING TO PARTICLE SIZE DURING FTS

The combination of *in situ* X-ray diffraction computed tomography and pair distribution function computed tomography has been used to study a 3 mm Co/γ-Al_2O_3 catalyst for Fischer-Tropsch synthesis. This combination of techniques is very powerful for unravelling the complex Co nanoparticle phase evolution to obtain a more complete understanding of the structure-activity relationships in this catalytic system.

Fischer-Tropsch synthesis (FTS), is a catalytic process that produces long chain alkanes, alkenes or alcohols using synthesis gas (CO/H_2 mixture) and is considered one of the more viable routes to replace diesel with ultraclean fuels **[1,2]**. A popular industrial catalyst for this process comprises cobalt (Co^0) dispersed as small nanoparticles on a microporous/mesoporous structure or oxide support (Al_2O_3, SiO_2 and TiO_2). Co^0 particles are believed to be the primary active sites as they are present pre-, post- and during FTS and are thought to be necessary for high product selectivity.

The state of Co under operational conditions and in a deactivated catalyst has been of much interest and observations show an 'evolution' of the Co nanoparticle structure, including sintering, dispersion, a decrease in scattering density thought to be due to interstitial C species, as well as oxidation to form cobalt oxides; all of which in extreme cases leads to a loss in activity **[3]**. Previous *in situ* and *operando* studies utilise catalysts in powdered form but industrial catalysts should preferably be studied in their entirety to fully understand the importance of structure with function. Furthermore, today, spatially resolved chemical imaging processes as a function of time (referred to as 5D sample interrogation: 3 spatial dimensions, time and the spectral dimension) allow for a more detailed appreciation of the complex behaviour of real materials.

This work used *in situ* X-ray diffraction computed tomography (μ-XRD-CT) and pair distribution function computed tomography (μ-PDF-CT) at **ID15A** to study a 3 mm Co/γ-Al_2O_3 catalyst to understand the evolution of the Co environment during reduction and under real FT conditions (CO/H_2, ratio 1:2). The evolution of the cobalt phases was followed to determine the nature of the active species under process conditions as well as to lend insight into how to design a better performing catalyst.

Time and spatially resolved XRD-CT data are given in **Figure 134** and show a gradual evolution of Co crystalline phase from $Co_3O_4 \rightarrow CoO \rightarrow$ Co fcc metal during the pre-reaction reduction treatment in dilute flowing H_2. During reduction, Co spatial distribution is broadly retained irrespective of Co phase evolution with time/temperature. The catalytically relevant Co fcc metal phase follows a 'shrinking core' model for its formation but, interestingly, scattering intensity increases, particularly at the sample edge; this is suggestive of facile Co formation at the sample edge where oxide phases first encounter H_2. During FTS, the Co fcc phase reduces in intensity, particularly at the edge of the particle where both CoO and the Co_3O_4 phase reform. The middle of the catalyst pellet remains largely unchanged in comparison. These behavioural differences reflect a difference in particle size of the Co-containing phases present at the beginning.

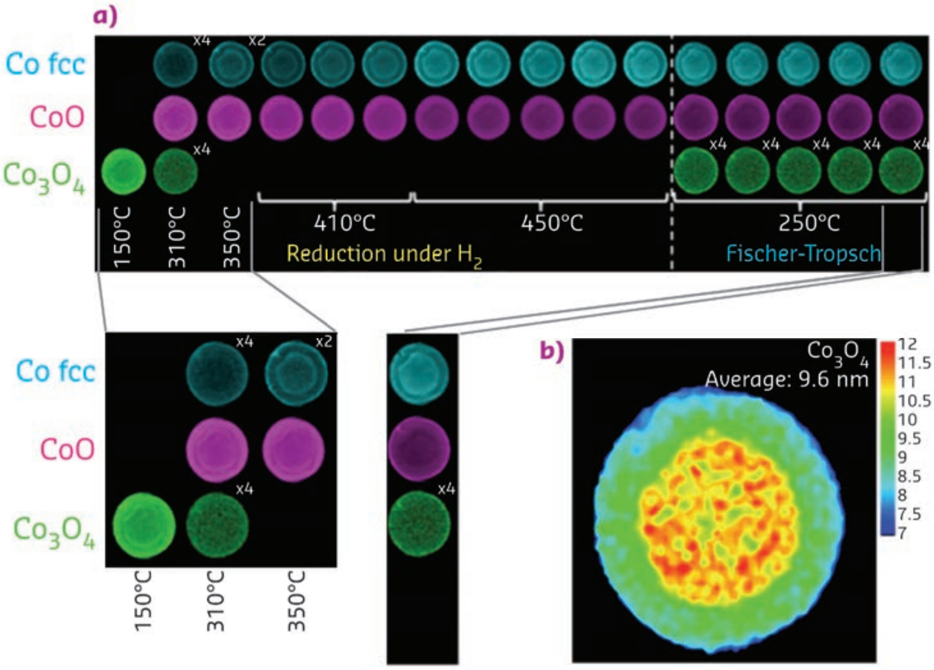

Fig. 134: a) Reconstructed 2D integrated reflection intensity maps for Co_3O_4 (220), CoO (200) and fcc Co (111) observed under reduction and during FTS conditions as a function of temperature and time. Values depicted in the right-hand corner (particularly Co_3O_4) illustrate how integrated intensity has been multiplied to enable plotting on a common intensity axis. b) Co_3O_4 (nano)particle size distribution map recorded at 150 °C during reduction in H_2.

Imperfections in the catalyst preparation process cause a range of species to be observed. These include two types of Co_3O_4 particles present at the fresh catalyst (**Figure 134b**) – well dispersed particles that interact strongly with the γ-Al_2O_3 support and poorly dispersed particles that don't. The former, when ≤ ~ 6.5 nm, cannot be fully reduced and remains as CoO during reduction treatment, whereas the latter reduces more easily. Also, μ-XRD-CT and μ-PDF-CT suggest the majority of aggregated particles are found at the edge of the sample and in the central 2.5 mm diameter of the pellet. The smaller, more numerous nanoparticles at the edge appear to reduce more quickly than the larger particles on the inside. However, these particles oxidise more readily on switchover to FTS since average metallic fcc Co particle size increase is observed at the periphery.

The results illustrate the challenge of creating a structured FTS-active Co/γ-Al_2O_3 pellet, since various Co-containing phases were detected in the sample. However, it demonstrates how μ-XRD-CT and μ-PDF-CT can put phase evolution changes into spatial context, which isn't possible via single point measurement. These techniques should eventually allow all industrial catalysts to be chemically imaged *in situ* for a more thorough evaluation of catalytic performance.

PRINCIPAL PUBLICATION AND AUTHORS

Real-Time Scattering-Contrast Imaging of a Supported Cobalt-Based Catalyst Body During Activation and Fischer Tropsch Synthesis Reveals Spatial Dependency of Particle Size and Phase on Catalytic Properties, P. Senecal (a), S.D.M. Jacques (b), M. di Michiel (c), S.A.J. Kimber (c), A. Vamvakeros (a), Y. Odarchenko (a), I. Lezcano-González (a), J. Paterson (d), E. Ferguson (d) and A.M. Beale (a), *ACS Catal.* **7**, 2284-2293 (2017); doi: 10.1021/acscatal.6b03145.

(a) Research Complex at Harwell & University College London (UK)
(b) University of Manchester, Manchester (UK)
(c) ESRF
(d) BP International Ltd (UK)

REFERENCES

[1] S.S. Aïl and S. Dasappa, *Renew. Sust. Energ. Rev.* **58**, 267 (2016).
[2] A.Y. Khodakov *et al., Chem. Rev.* **107**, 1692 (2007).
[3] J.J. Herbert *et al., Cat. Sci. Tech.* **6**, 5773 (2016).

HIGH-SPEED IMAGING OF THERMAL RUNAWAY IN LI-ION BATTERIES

Li-ion batteries have universal applications, from medical implants to grid-scale energy storage. Thermal runaway within Li-ion cells poses significant safety risks but the process is challenging to characterise. An internal short circuiting device is used in conjunction with high-speed radiography to initiate thermal runaway and record propagation through the cell to evaluate the safety of cell designs.

The use of high energy-density Li-ion batteries is ubiquitous, from powering portable electronics to providing grid-scale storage, but Li-ion batteries can and do fail, sometimes catastrophically. Although rare, recent high-profile cases of catastrophic failure highlight the importance of understanding battery failure and improving their safety; for example, the recall of Samsung's Galaxy Note 7 smartphones and the grounding of the Boeing Dreamliner aircraft fleet.

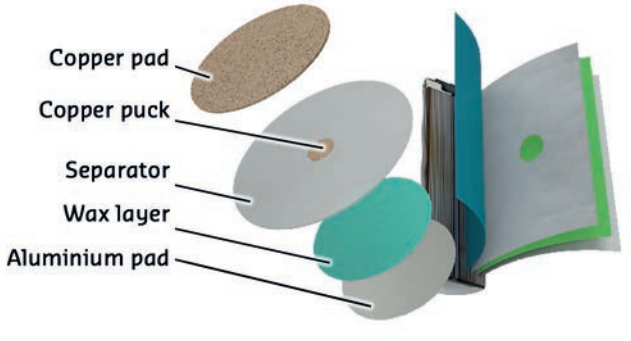

Fig. 135: Internal short-circuiting device.

Manufacturing defects and abnormal operating conditions can lead to internal short circuits in commercial Li-ion batteries, which can, in worst-case scenarios, generate enough heat to initiate a cascade of exothermic reactions in a process known as 'thermal runaway'. Internal short circuiting is of particular interest as it is thought to be responsible for a number of high-profile, real-world failures.

As highlighted in a previous study **[1]**, it is very difficult to predict when and where thermal runaway will occur due to the extreme speed of failure and uncertainty surrounding the location of initiation, making the process extremely difficult to observe and characterise. To circumvent this challenge, a device capable of generating an internal short circuit (ISC) on-demand and at a pre-determined location in Li-ion batteries was used to induce thermal runaway (**Figure 135**) **[2]**. The temperature-activated ISC device, developed by NASA and NREL **[3]**, mimics hidden defects

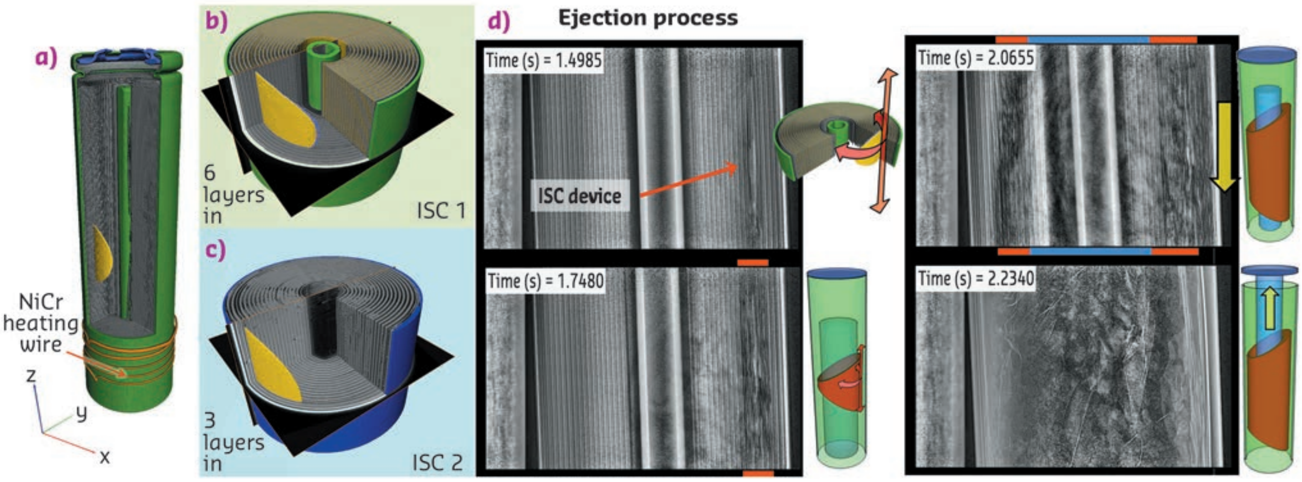

Fig. 136: a-c) Locations at which the ISC device was placed inside 18650 cells. d) Process of initiation and propagation of thermal runaway.

that can occur during battery manufacturing. Knowing when and where the cell will fail allowed characterisation of the phenomena that occur during catastrophic failure using high-speed X-ray imaging at beamline **ID19**.

The ISC device was inserted at different locations within 18650 cells (**Figure 136a-c**) to gain insight into cell design vulnerabilities with respect to the location at which thermal runaway initiates, *e.g.* an increased risk of undergoing side-wall rupturing or bursting. For the first time, the mechanism through which a short-circuit failure initiates and propagates thermal runaway inside a cell was captured in real time (**Figure 136d**). At **ID19**, high-speed X-ray imaging at 2000 fps revealed how thermal runaway spreads via a characteristic cylindrically shaped reaction zone (**Figure 136d**), where the decomposition reactions propagated fastest in the longitudinal and circumferential directions. This evolution of the reaction zone resulted in an intact core becoming surrounded by a fluidised region, reducing the shear stress on the intact electrode assembly and contributing to it shifting towards and clogging the vent, causing the cell to burst.

The ability to control the location of initiation also allowed examination of whether cells are at greater risk of undergoing side-wall rupture when thermal runaway initiates closer to the surface of the cell casing. X-ray images showed that when thermal runaway is initiated three layers deep into the cell, as opposed to six layers deep, its reaction front reaches the casing of the cell in less than 1/10th of the time. This has implications for early temperature-induced weakening of the steel casing and the formation of more favourable conditions for side-wall rupture to occur.

The results of this work demonstrate the utility of combining high-speed X-ray imaging with selective triggering of thermal runaway within similar commercial cells. By linking internal structural dynamics with external observations and thermal measurements, risks can be characterised with new insight into the internal behaviour of cells. Failure mechanisms such as cell bursting, sidewall rupture, or contained thermal runaway each pose different risks, and mechanical design of cells and their tendency to undergo such failures should be considered when assessing their suitability for powering systems. The insights achieved from high-speed X-ray imaging at **ID19** provide important information for validation of thermal runaway models as well as for informed design of next-generation lithium-ion batteries.

PRINCIPAL PUBLICATION AND AUTHORS

Characterising thermal runaway within lithium-ion cells by inducing and monitoring internal short circuits, D. P. Finegan (a), E. Darcy (b), M. Keyser (c), B. Tjaden (a), T. M. M. Heenan (a), R. Jervis (a), J. J. Bailey (a), R. Malik (d), N. T. Vo (e), O. V. Magdysyuk (e), R. Atwood (e), M. Drakopoulos (e), M. DiMichiel (f), A. Rack (f), G. Hinds (g), D. J. L. Brett (a) and P. R. Shearing (a), *Energy Environ. Sci.* **10**, 1377-1388 (2017); doi: 10.1039/c7ee00385d.
(a) Electrochemical Innovation Lab, Department of Chemical Engineering, University College London, London, (UK)
(b) NASA-Johnson Space Center, Houston, Texas (USA)
(c) National Renewable Energy Laboratory, Golden, Colorado (USA)
(d) Warwick Manufacturing Group, University of Warwick, Coventry (UK)
Diamond Light Source, The Harwell Science and Innovation Campus, Didcot (UK)
(e) ESRF
(f) National Physical Laboratory, Hampton Road, Teddington (UK)

REFERENCES

[1] D. P. Finegan *et al., Nat Commun.* **6** (2015).
[2] D. P. Finegan *et al., Energy Environ. Sci.* **10**, 1377 (2017).
[3] M. Keyser *et al., U.S. patent 9142829B2* (2015).

GUEST SPECIES SWITCHES NEGATIVE AND POSITIVE THERMAL EXPANSION IN $YFe(CN)_6$

The presence of guest ions (K^+) and molecules (H_2O) can switch thermal expansion of $YFe(CN)_6$ from negative ($\alpha_v = -33.67 \times 10^{-6}\ K^{-1}$) to positive ($\alpha_v = +42.72 \times 10^{-6}\ K^{-1}$), a range that covers thermal expansion of most inorganic compounds. This presence has a critical damping effect on transverse vibrations, thus inhibiting negative thermal expansion.

The control of thermal expansion in NTE materials is mainly achieved by chemical substitution. Since chemical substitution can have a pronounced effect on electronic structure and crystal structure, thermal expansion can be well controlled, especially in electronic-driven NTE materials, such as $PbTiO_3$-based ferroelectrics **[1]**. However, in open-framework materials, chemical substitution might not be a direct method to adjust thermal expansion, because NTE is associated with the lattice dynamics rather than the electronic structures. For example, the linear coefficient of thermal expansion (CTE, α_l) for $Zr_{1-x}M_xW_2O_{8-y}$ (M = Sc, In, Y) materials varies only over a narrow range (-7.3 to -8.7 x $10^{-6}\ K^{-1}$) **[2]**.

Figure 137 shows a $YFe(CN)_6$ entire structure with the YN_6 and FeC_6 groups bridged through CN units, and the guest molecules (H_2O) or ions (K^+) in the empty spaces of its framework structure. When $YFe(CN)_6$ is without any guest ions or molecules, a strong NTE can be observed ($\alpha_v = -33.7 \times 10^{-6}\ K^{-1}$). It is intriguing that thermal expansion of $YFe(CN)_6$ can be largely switched between negative and positive via the effect of guest K^+ ions and H_2O molecules (**Figure 138a**).

In this work, the detailed mechanism for the role of guest ions and molecules on the switched thermal expansion was investigated. Here, the phenomenon was interpreted according to both structure and lattice dynamics by joint studies using neutron powder diffraction, extended X-ray absorption fine structure (EXAFS) at beamline **BM08-LISA**, and first-principle calculations (**Figures 138b-h**). Firstly, **Figure 138b** shows correlation between atom-volume-density and CTE, that is, if there is enough space in the open-framework structure, the NTE arises due to possibly strong transverse vibrations of bridging atoms. Otherwise, the transverse vibrations are reduced and thus NTE should be restrained or switched to PTE. Secondly, there are strong anisotropic atomic displacement parameters (ADPs) in $YFe(CN)_6$ (**Figure 138c**), in which the transverse ADPs of both N and C atoms are much larger than those of longitudinal ones.

However, after the insertion of guest H_2O molecules, the ADPs are nearly identical for both transverse and longitudinal ones (**Figure 138d**), which means that the transverse Fe-C and Y-N thermal vibrations are much hindered. Thirdly, the atomic mean-square relative displacements (MSRDs) determined by Fe K-edge EXAFS measurements indicates that there is much larger transverse Fe-C vibrations in NTE $YFe(CN)_6$ than in PTE $KYFe(CN)_6$ (**Figures 138e-f**). Finally, from **Figures 138g-h**, it can be seen that most vibrational modes with negative Grüneisen parameters in $YFe(CN)_6$ switch to positive when K^+ ions are inserted, thus resulting in PTE of $KYFe(CN)_6$. The study demonstrates a potential approach to achieve adjustable CTE for those NTE framework materials and other multifunctional materials.

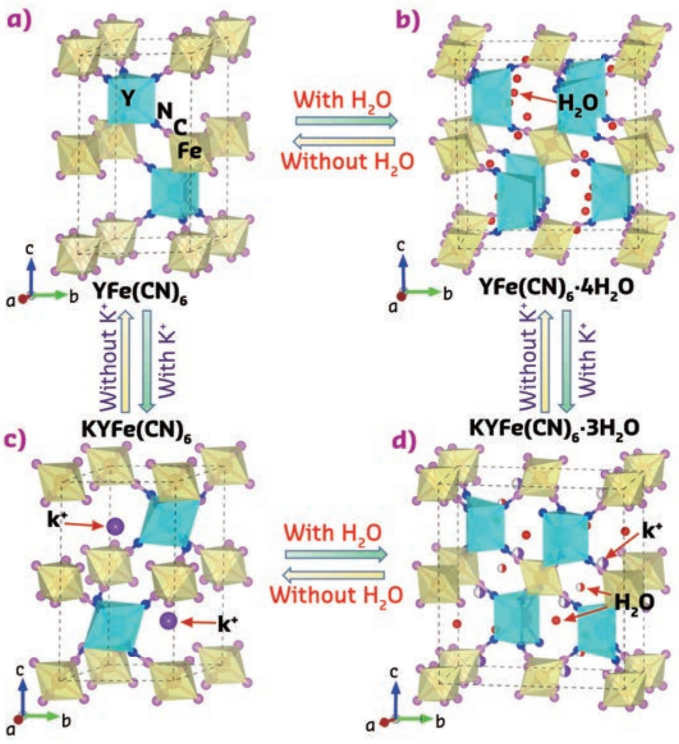

Fig. 137: Crystal structure of $YFe(CN)_6$-based Prussian blue analogues with or without guest K^+ ions and H_2O molecules. a) $YFe(CN)_6$ ($P6_3/mmc$), b) $YFe(CN)_6 \times 4H_2O$ ($Cmcm$), c) $KYFe(CN)_6$ (P-31c) and d) $KYFe(CN)_6 \times 3H_2O$ ($Pbnm$). FeC_6 and YN_6 polyhedra are in yellow and light blue colour, respectively.

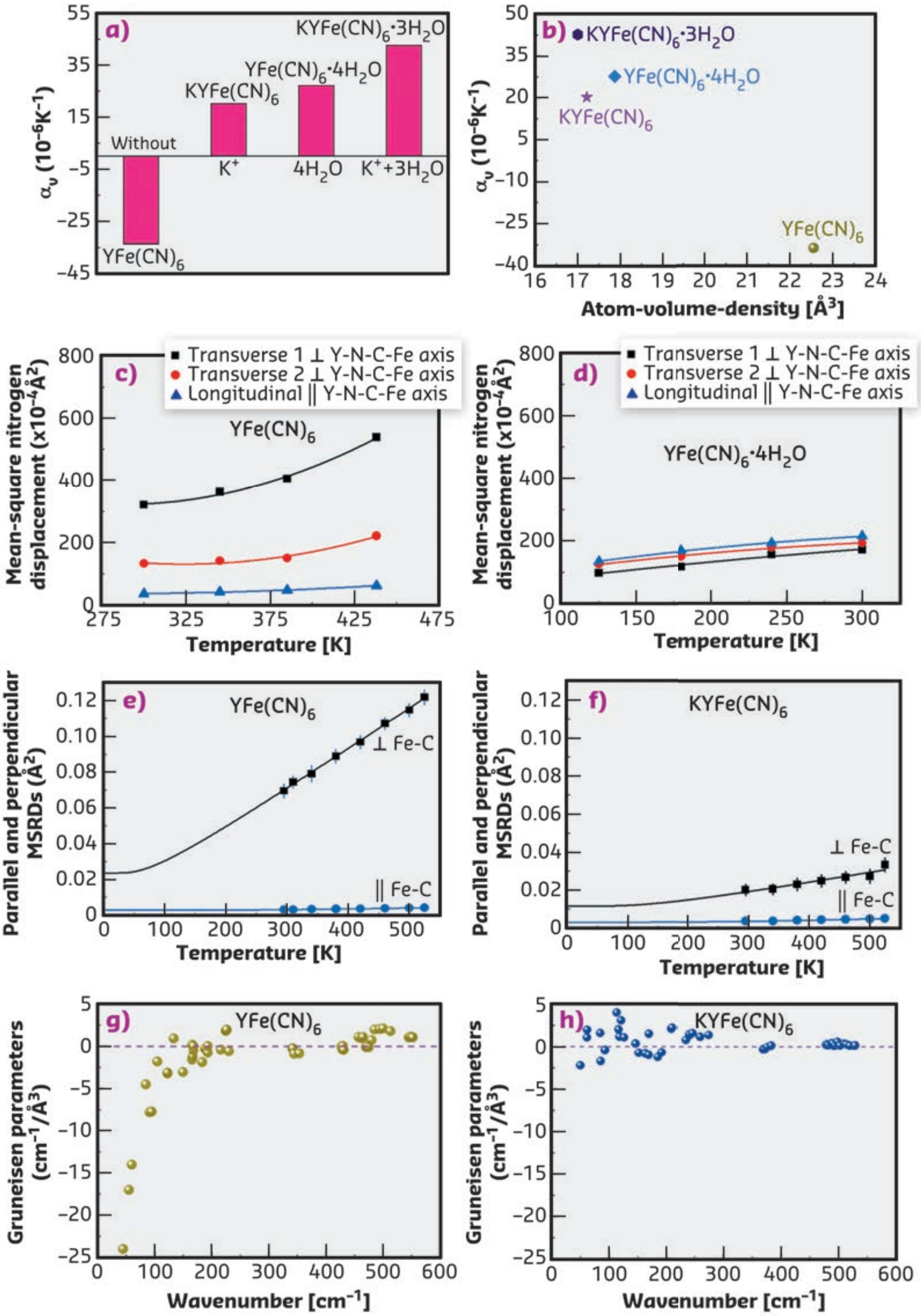

Fig. 138: a) CTE, α_V, in YFe(CN)$_6$ and related compounds. b) Correlation between atom-volume-density and α_V. Temperature variation of ADPs of the N atoms of c) YFe(CN)$_6$ and d) YFe(CN)$_6$ × 4H$_2$O, respectively. Perpendicular (squares) and parallel (circles) MSRDs of the Fe-C atomic pairs measured by EXAFS in e) NTE YFe(CN)$_6$ and f) PTE KYFe(CN)$_6$. The solid lines are the corresponding best-fit with the Einstein model. The mode Grüneisen parameters of g) NTE YFe(CN)$_6$ and h) PTE KYFe(CN)$_6$ as a function of frequency.

PRINCIPAL PUBLICATION AND AUTHORS

Switching Between Giant Positive and Negative Thermal Expansions of a YFe(CN)$_6$-based Prussian Blue Analogue Induced by Guest Species, Q. Gao (a), J. Chen (a), Q. Sun (b), D. Chang (b), Q. Huang (c), H. Wu (c), A. Sanson (d), R. Milazzo (d), H. Zhu (a), Q. Li (a), Z. Liu (a), J. Deng (a) and X. Xing (a), *Angew. Chem. Int. Ed.* 56, 9023 (2017); doi: 10.1002/anie.201702955.

(a) Department of Physical Chemistry, USTB (China)
(b)School of Physics and Engineering, ZZU (China)
(c) NIST Center for Neutron Research (USA)
(d) Department of Physics and Astronomy, University of Padova (Italy)

REFERENCES

[1] J. Chen *et al., J. Am. Chem. Soc.* **130**, 1144 (2008).
[2] N. Nakajima *et al., Solid State Commun.* **128**, 193 (2003).

From big corporations to European SMEs

Industrial research has continued to go from strength to strength at the ESRF and 2017 saw us successfully reach the goal set by the ESRF Council: to achieve 5% more commercial income than last year. This is thanks to the trust given to us by our clients worldwide who want to use our services, from international corporations to smaller companies. The work done by the scientists at the beamlines and by our expert engineers and technicians to valourise our instrumentation is crucial, as is the growing Business Development Office team, who spread the word around the world to new clients and build new collaborations. As always, the work behind the scenes involves many ESRF teams and success takes time.

This year we have achieved a milestone with one of the biggest corporations in consumer products around the world, Procter & Gamble. After many years of fruitful beam time on ID19 and ID02, the collaboration with the scientists of P&G was taken a step further. Thanks to a mutual understanding of the benefits for both P&G and the ESRF, together with the ILL, the three signed a Master Collaboration Agreement in September, making the ESRF and the ILL strategic research partners to P&G.

P&G scientists have been coming to the ESRF since 2004. The first experiments were focused on understanding and optimising the microstructure behind the hair colouring product Clairol Perfect 10. In recent years, scientists have studied diverse subjects from detergent (liquid and powder), fabric conditioner, hair and skin products, fibres (fabric, hair, nappies, wipes) to packaging, polymer films and teeth. Two P&G scientists, Eric Robles and Jeremie Gummel, are central to the studies – Gummel being a former post doc from ID02.

Gerard Baillely, Vice President of R&D Corporate Functions at P&G said, at the time of the signature: “Innovation is the lifeblood of P&G. We believe that our best innovation benefits from the most advanced sciences to precisely measure and characterise materials. Our joint work in this field with ESRF and now ILL has been very valuable to develop high quality, affordable and irresistibly superior products. This strategic partnership between P&G, ESRF and ILL will continue to help accelerate our innovation programme.”

The signature of the agreement (see photo, right) was only the starting point. Since then, scientists from both the ESRF and the ILL have travelled to the P&G headquarters in Cincinnati, where they took part in a global R&D meeting that brought P&G researchers together. This was an opportunity to showcase the science done at the European Photons and Neutrons Campus across the different divisions of P&G, opening up new possibilities of research.

Regional access to the ESRF

The ESRF, through European-supported programmes like CALIPSOplus (www.calipsoplus.eu), also wants to reach out to local companies that may want to use our synchrotron. One goal is to empower local SMEs to be able to exploit the ESRF for their product development needs and innovation-led research. In the framework of the CARAC2017 workshop, which took place in Grenoble in November, regional companies could bring their samples for free feasibility tests before carrying out full-scale measurements or experiments. We were delighted that 15 companies requested this feasibility access – with one-third of the tests carried out live during CARAC2017 itself.

This initiative to get local and regional companies interested in the opportunities of advanced materials characterisation is of utmost importance, since such companies are often highly innovative and form the core of future European competitiveness. And they can benefit from the simplicity of business within walking distance, with large-scale facilities like the ESRF and the ILL better integrated into our regional ecosystems.

At the same time, at the ESRF we need to nurture strategic alliances to keep us at the forefront of scientific industrial research. An example of this is the workshop on batteries, organised between the ESRF and its neighbouring institutes the CEA and ILL, with the sponsorship of the Business Development Office and CALIPSOplus. It brought together 150 experts working on batteries, who exchanged views and launched collaborations, building a roadmap of activities for the future to better exploit our facilities and expertise, linked with the CEA's cutting-edge applied research with industry partners.

A European-wide perspective

Europe has the best portfolio of research infrastructures in the world, offering enormous opportunities to improve links with industry. The Business Development Office is actively involved in a range of European and national projects including NFFA (www.nffa.eu), CALIPSOplus (www.calipsoplus.eu) and IRT NanoElec (www.irtnanoelec.fr). In working closely with further European projects, such as SINE2020 (www.sine2020.eu) – a consortium of European neutron sources – we have created a joint outreach programme using our Research Infrastructure Village stand, material and presentations at events and workshops across Europe. Our goal is to promote European research infrastructures to industry, opening the doors for companies to do better research and innovation and to become more competitive.

As well as outreach, we are aiming to better coordinate between research infrastructure families. In November, six European projects – CALIPSOplus, SINE2020, NFFA, EUCALL, ACCELERATE and EUSMI – got together to discuss how research infrastructures can better engage with industry through innovative joint actions now and in the future. For light sources, the LEAPS website initiative will be a strong jumping board for the future.

All in all, 2017 has been a very fruitful year, with strategic partnerships set up, a focus on local and regional access to the ESRF and new developments on the beamlines to improve our services to clients. This will continue in 2018, with more beam time available and, hopefully, more alliances to come.

E. MITCHELL
M. CAPELLAS ESPUNY

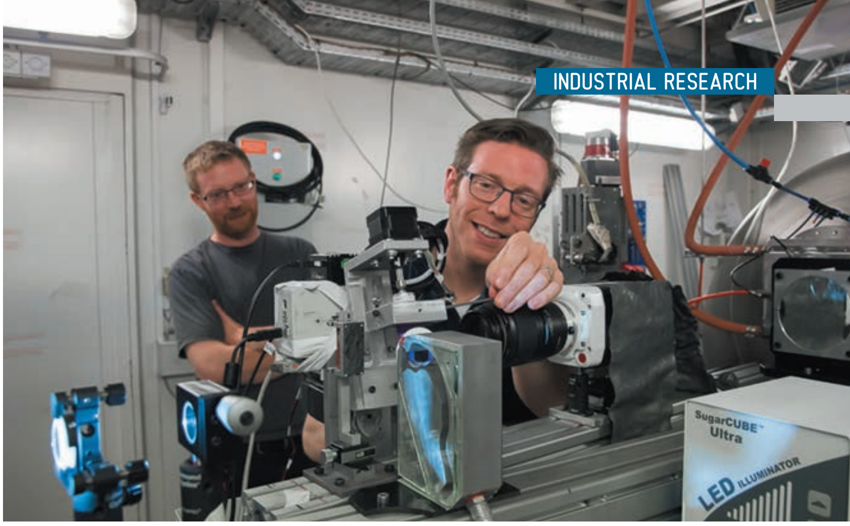

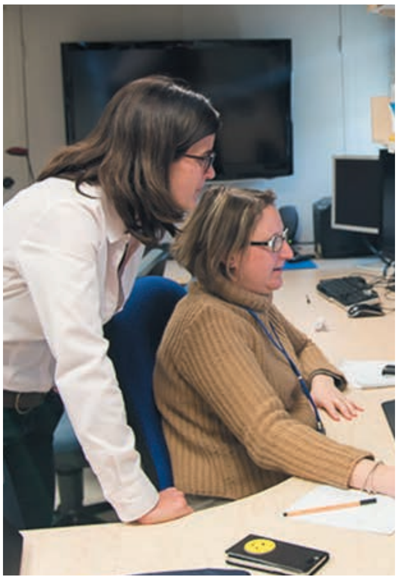

INDUSTRIAL RESEARCH ON THE BEAMLINES

Due to its proprietary nature, much of the commercial research done by industry at the ESRF in 2017 cannot be disclosed. However, sometimes companies authorise the ESRF to discuss their work and they may even publish results or access the ESRF via the public programme. Below are a few examples from 2017. Other articles linked to industrial research are published elsewhere in these Highlights, on protein crystallography (page 31 and 35), chemistry (page 49) and catalysis (page 139).

UNPRECEDENTED ULTRA-HIGH-SPEED RECORDING TO TRACK EXPLOSIONS AND CRACK PROPAGATION

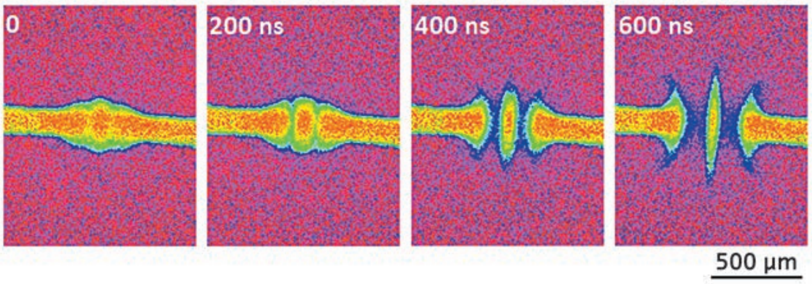

Fig. 139: A time series of X-ray radiographs during electric arc ignition of the electric fuse operation, observed with 110 ns exposure time and at 5 Mega frames per second.

The international fuse company Mersen, together with the ESRF, has managed to record exactly what happens in a fuse as it explodes, using the new technique of ultra-fast X-ray phase-contrast imaging. They recorded a time series of X-ray radiographs at ID19 during electric arc ignition of the fuse operation (**Figure 139**). The images reveal the melting of the silver metal strip and the appearance of plasma around the metal strip due to its partial vapourisation at high temperature.

PRINCIPAL PUBLICATION AND AUTHORS

MHz frame rate hard X-ray phase-contrast imaging using synchrotron radiation,
M. Olbinado *et al., Optics Express* **25**, 13857-13871 (2017); doi: 10.1364/OE.25.013857.

TOWARDS UNCOLOURED ENVIRONMENTALLY FRIENDLY CONCRETE

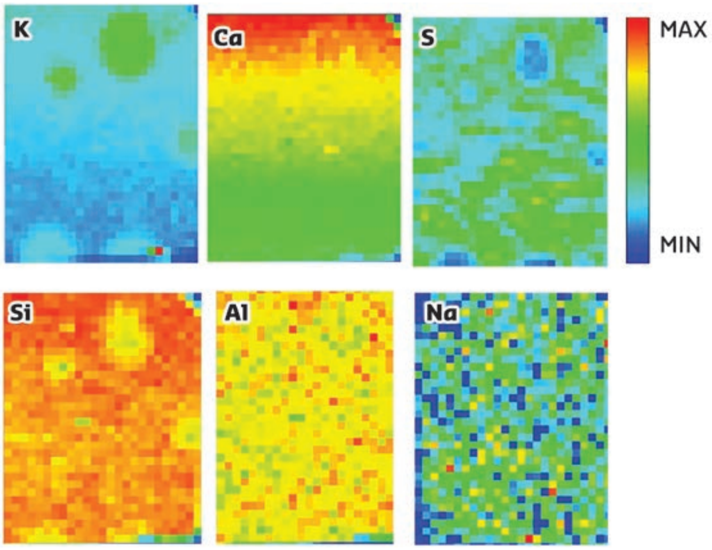

Fig. 140: Elemental distribution obtained by µ-XRF with an exciting beam of 4040 eV for K and Ca, and 2480 eV for S, Si, Al, O and Na obtained by µ-XRF with an exciting beam, map size 2.6 x 3.5 mm^2 with a step of 100 µm.

In the quest for environmentally friendly materials, the concrete company ECOCEM is using slag-rich concrete, mortar and other materials. These materials can display a blue/green colour when consolidated, which can be a concern in applications where visual aesthetics are important.

In order to find the origin of this colouration, scientists went to ID21 and used K-edge X-ray absorption near edge structure (XANES) spectroscopy to follow the evolution of the speciation of sulphur as the slag was hydrated (**Figure 140**). They found that, independently of the activating method, the blue colour was related to the presence of a pre-peak in the corresponding XANES spectrum. They linked this pre-peak to the presence of the polysulphur radical anion, S_3^-. This blue chromophore is known to be at the origin of the deep blue of the stone lapis lazuli or the ultramarine pigment.

PRINCIPAL PUBLICATION AND AUTHORS

On the origin of the blue/green color of blast-furnace slag-based materials: Sulfur K-edge XANES investigation,
M. Chaouche, XX. Gao, M. Cry, M. Cotte and L. Frouin*, J Am Ceram Soc* (2017); doi: 10.1111/jace.14670.

IMPROVING ASTHMA AND OTHER RESPIRATORY DISEASES

Prior PLM Medical, a company supporting the medical and pharmaceutical industry to develop drug delivery devices, has been studying asthma inhalers. The efficacy of inhalers is often quite poor with only 10-20% total lung deposition for most devices on the market.

At the ESRF, they used high-speed phase contrast X-ray imaging on ID19 to visualise how the dose release event from each inhaler showed the propellant mixture behaviour inside the canister and actuator (**Figure 141**). In addition, mechanical interactions could be viewed taking place. This has provided new insights and is of value as a validation method for modelling efforts.

a)

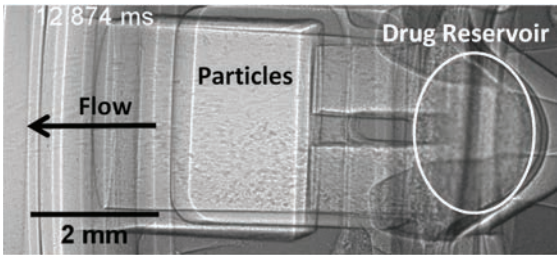

b)

Fig. 141: a) A dry powder inhaler and b) high-speed phase contrast X-ray imaging of a dosing event in a pressurised metered dose inhaler. The video can be seen at: vimeo.com/194356596.

PRINCIPAL PUBLICATION AND AUTHORS

A. McKiernan, *J Aerosol Med Pulm Drug Deliv* **30**(4):A1-A30, (2017); doi: 10.1089/jamp.2017.ab02.abstracts.

EXPLORING CHROMATOGRAPHIC FILTERING

In the global battle against cancer, the scientific community is looking into efficient solutions to effectively destroy cancer cells without harming healthy ones. A team of researchers from the University of Applied Sciences in Darmstadt (Germany), the Université de Lorraine (France) and the pharmaceutical corporation MERCK are developing new ways of separating cancerous from healthy blood cells.

They studied the technique of chromatographic filtering, which consists of flowing a cell suspension through a porous medium, which is activated by an inner surface coating. ID19 helped the scientists to delve inside the foam in an experiment reproducing the processes that take place in chromatographic filtering. The results showed that the shape of the inner surface of the foam has a considerable impact on the particle paths (**Figure 142**). The level of torsion of the surface is much smaller for slow cells moving close to the surface compared to that of fast cells, which underlines the importance of torsion for filter efficiency.

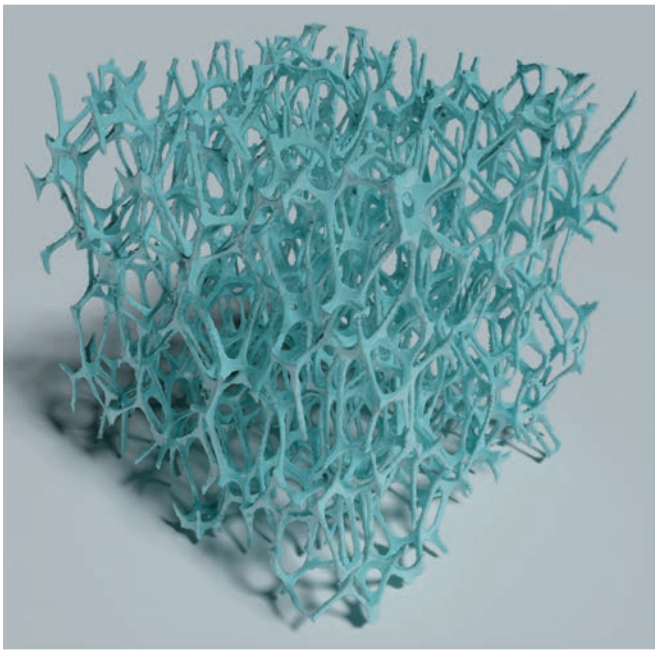

Fig. 142: Volume rendering of a tomographic data set showing a partially open foam, acquired by means of phase-contrast mathematical formula CT using synchrotron radiation.

PRINCIPAL PUBLICATION AND AUTHORS

Torsion estimation of particle paths through porous media observed by *in situ* time-resolved microtomography,
C. Blankenburg *et al., Journal of Microscopy* **266**, 141-152 (2017);
doi:10.1111/jmi.12524.

UNVEILING HOW ALUMINIUM SALTS IN DEODORANTS PLUG SWEAT PORES USING SAXS AND MICROFLUIDICS

Antiperspirant products use aluminium salts to decrease the amount of sweat delivered at the surface of skin. The mechanism of antiperspirants was previously thought to be a superficial plugging of eccrine sweat pores by the aluminium hydroxide gel formed *in situ*. Scientists from L'Oréal, LCMD (CNRS) and ESRF measured the diffusion of aluminium polycationic species in sweat counter flow using a microfluidic T-junction device. The results could open up perspectives to find new antiperspirant agents with an improved efficacy.

The device mimics sweat ducts and is designed for the real-time study of interactions between sweat and aluminium chlorohydrate under conditions that lead to plug formation. The studies were combined with small angle X-ray scattering experiments on ID02 in order to determine the structure and composition of the plug, using bovine serum albumin (BSA) as a model of sweat proteins.

The results show that pore occlusion occurs as a result of the aggregation of sweat proteins by aluminium polycations (**Figure 143**). Mapping of the device shows that this aggregation is initiated in the T-junction at the location where the flow of aluminium polycations joins the flow of BSA. The mechanism involves two stages: first, a nucleation stage in which aggregates of protein and polycations bind to the wall of the sweat duct and form a tenuous membrane, which extends across the junction; and secondly, a growth stage in which this membrane collects proteins that are carried by hydrodynamic flow in the sweat channel, and polycations that diffuse into this channel.

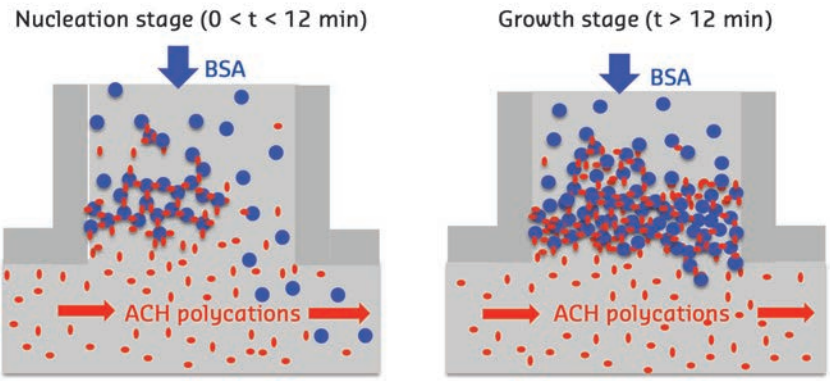

Fig. 143: A schematic, two-dimensional image of the initial membrane (left) and of a fully grown plug (right). BSA is a model of sweat proteins.

PRINCIPAL PUBLICATION AND AUTHORS

The mechanism of eccrine sweat pore plugging by aluminium salts using microfluidics combined with small-angle X-ray scattering, A. Bretagne *et al.*, *Soft Matter* **13**, 3812-3821 (2017); doi: 10.1039/c6sm02510b

KNOWLEDGE AND TECHNOLOGY TRANSFER

SCINTILLATORS: THE KEY TO A SUCCESSFUL ENDEAVOUR

Scintillators are a must-have in synchrotron sources. Utilising in-house expertise, the ESRF started producing these advanced components eight years ago and, in 2017, we achieved record sales with almost 200 scintillators sold since the start of production and an ever-increasing demand.

Beamlines on synchrotrons worldwide need many specific components in order to carry out specialised and state-of-the-art experiments. Scintillators are essential components that make X-rays visible so they can be detected with cameras.

The sub-micrometre resolution and high image contrast demanded by today's experiments require scintillator films with thicknesses in the range of 1-20 µm that also provide high optical quality and uniformity. Thin scintillators minimise degradations due to focusing defects, diffraction and spherical aberrations, therefore boosting the image contrast and spatial resolution. However, the sophisticated techniques required to grow such crystals and their high specificity means that very thin single crystal film scintillators are not commercially available.

In April 2010, the ESRF established a unique liquid phase epitaxy facility for single crystal film scintillators (**Figure 144**). Liquid phase epitaxy is a technique whereby scintillating crystal layers are grown on a solid single crystal substrate immersed in a melt. Its key appeal for synchrotrons is that it produces a homogeneous distribution of dopant activator ions within the film (the host material absorbs X-rays and the dopants emit light). Moreover, the epitaxial growth on a high-density substrate provides radiation protection for the optics of the X-ray detector system, as well as a rigid support for easy handling and cleaning.

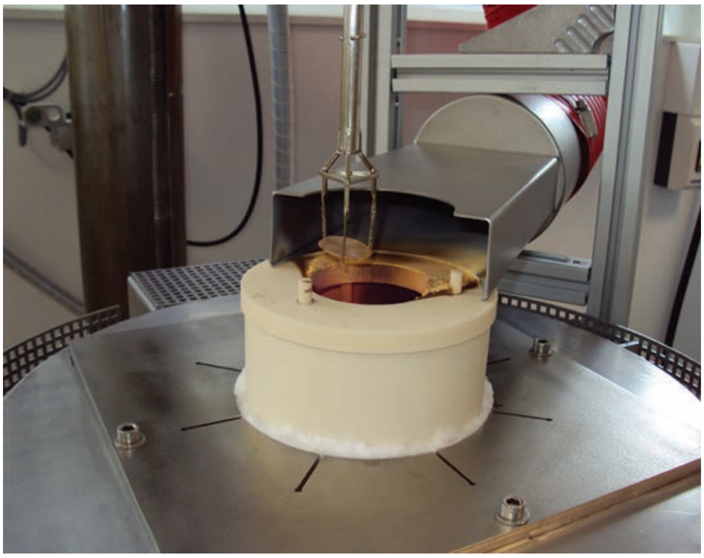

Fig. 144: A single crystal film scintillator, after growth and melt characterisation, fixed on its platinum holder.

LICENSING RF CAVITY COMBINERS

Our licensing activities have continued throughout 2017. One of the most outstanding examples is the agreement for a radio frequency (RF) cavity combiner with SigmaPhi.

SigmaPhi is a French company that designs, makes and measures magnetic systems and beam transport lines for particle accelerators. With this licence agreement, the highly experienced ESRF RF group has transferred expertise and design support for RF cavity combiners for solid-state amplifiers to SigmaPhi Electronics (formerly part of Bruker). In order to combine the power of hundreds of transistor amplifier modules for the generation of radio frequency power at the 100 kW level, complicated coaxial power combiner trees are generally used. With funding from the EU, in the frame of the FP7/ESFRI/CRISP project, Michel Langlois, from the ESRF RF Group, developed a cavity combiner that combines the power from the solid-state amplifier modules in one stage, by means of coupling loops all around the cylindrical cavity wall (**Figure 145**). It results in a much more compact and cost-effective device that minimises the combiner losses. An 85 kW prototype was successfully tested at the ESRF two years ago.

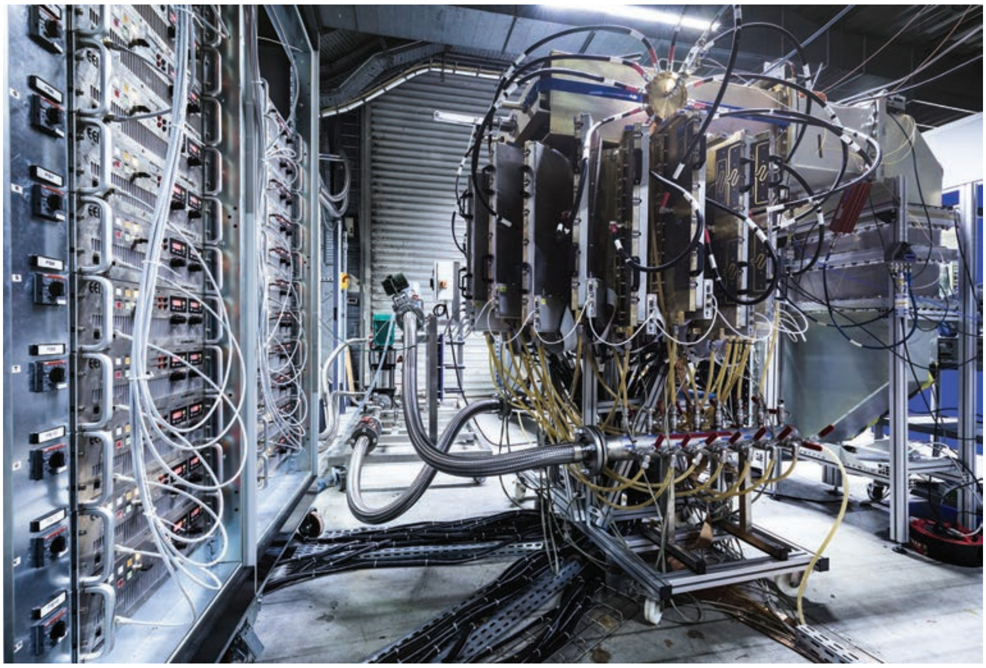

Fig. 145: The in-house-developed RF cavity combiner is licensed to SigmaPhi Electronics and could eventually become the basis for a replacement of obsolete klystron transmitters.

As in the previous two years, a substantial amount of the technological work focused on the new EBS storage ring project, which made tremendous progress in all aspects. In parallel, the beamline instrumentation programme was ramped up for the existing, to be refurbished, and new EBSL beamlines. A concise overview of these 2017 EBS activities is provided in the Status of the EBS chapter (**see page 8**).

The contributions in this chapter witness the breadth of activities in technology developments, which range from nano-focusing optics over state-of-the art precision alignment of large equipment to the ever growing challenges of data management and data analysis. The first article (**see page 152**) reports on the world-record nanofocus of less than 13 nm in the hard X-ray regime at 33.6 keV, achieved on **ID16A**. The second contribution (**see page 153**) is representative for several examples where a specific software development for one beamline (here **ID01**), based on the Silx library (http://www.silx.org), has led not only to an easy-to-use data analysis tool, but also to an almost real-time visualisation of complex data sets. Together with the last highlight on the modernisation of ISPyB (**see page 159**), the information system for protein crystallography (http://www.esrf.eu/ispyb), these two articles underline the importance of developing state-of-the-art computational frameworks, workflow and work methodologies and to deploy these between IT experts, software programmers, and scientists. The third article (**see page 155**) describes yet another X-ray imaging technique, based on speckle-tracking, where the random modulation of the X-ray beam wavefront allows the inferring of deflection by refraction in the sample. Interestingly, this approach can also be utilised at low brightness laboratory X-ray sources. The fourth contribution (**see page 156**) gives a flavour of the complexity of the alignment of the fully equipped girders for the EBS storage ring. In eight distinct survey and alignment stages, a positional uncertainty of the girder elements with respect to the electron beam of about 60 μm in the two transversal directions is reached! The fifth article (**see page 158**) describes a newly developed fast data acquisition system for real-time vacuum event analysis. This is already operational today and will be of great value during the commissioning and operation of the new storage ring.

In addition to the results presented in the Highlights articles, 2017 has witnessed many other important accomplishments and activities in various technological areas:

The PANdata (http://pan-data.eu/) Software Catalogue now has 97 entries containing contributions from ESRF, ALBA, Diamond Light Source, and ILL. This photon and neutron data infrastructure initiative brings together 13 major world-class European research infrastructures to create a fully integrated, pan-European, information infrastructure supporting the scientific process.

The first full version of OASYS (OrAnge SYnchrotron Suite), an open-source graphical environment for optics simulation software used in synchrotron facilities, was released. (http://ftp.esrf.eu/pub/scisoft/Oasys/readme.html)

The X-ray optics group was active in developing new polishing techniques and processes for the production of compound refractive lenses, and started the production of cylindrical Johann and Johannson crystals for X-ray spectroscopy.

ISDD colleagues participated in the EUCALL Annual Meeting, which took place at the ESRF in June 2017. This offered the opportunity to demonstrate RASHPA hardware features for ultra-fast data acquisition and present recent results on the X-ray wavefront analysis by the speckle tracking method. In fact, later in the year the **BM05** team successfully tested a mobile setup using the above method to characterise the X-ray beam at the European XFEL FXE beamline.

The ESRF continues to federate and coordinate joint developments with other research facilities, such as the IcePAP, TANGO, LImA, ISPyB, mxCuBE and PaNDaaS collaborations, to mention only a few. The TANGO collaboration now comprises 10 partners, thus providing sufficient critical mass to initiate software developments of common interest to all partners.

Significant progress has been made in testing cloud software for in-house and external IT provisioning. The acquired know-how will help in possible scenarios to outsource peak processing demands that cannot be covered with on-site investments. Developments will continue in the frame of the CERN-led H2020 HNSciCloud project, a pre-commercial procurement (PCP) initiative engaging IT industry and major European research infrastructures.

The implementation of the data policy is progressing according to schedule with 18 beamline end-stations already archiving metadata and raw data. This will be followed by the remaining beamlines until 2020 and is accompanied by work to restructure the way user identities are managed and how data sets can be cited in publications.

Finally, the instrumentation beamline, BM05, continued to be a strategic tool for instrumentation developments such as the characterisation of detectors, scintillators, and X-ray optical components. Together with **ID19**, it played a central role in the quality control of about 1500 beam position monitor (BPM) buttons for the new storage ring. Furthermore, a robotic film changer for industrial X-ray topography measurements was developed.

M. KRISCH
AND R. DIMPER

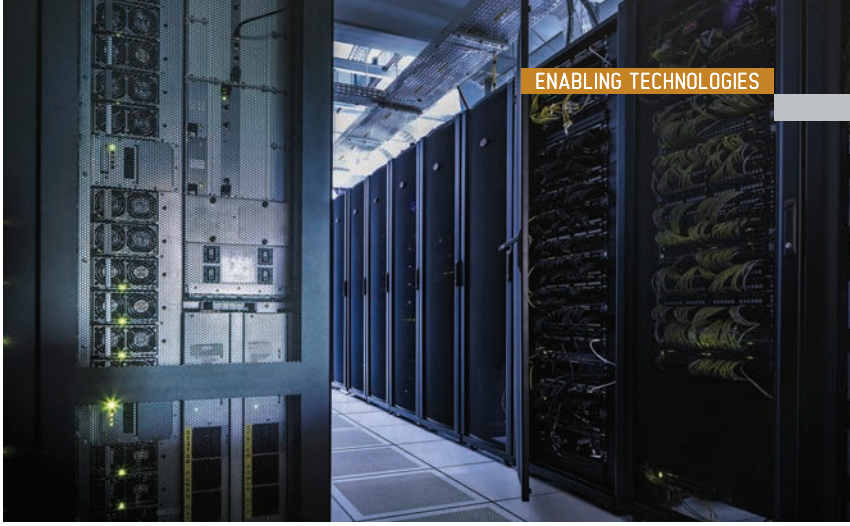

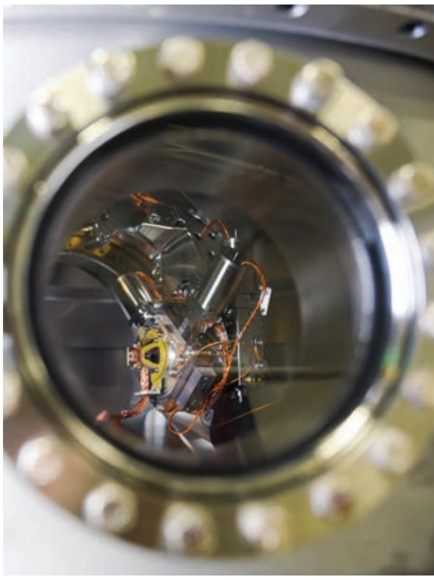

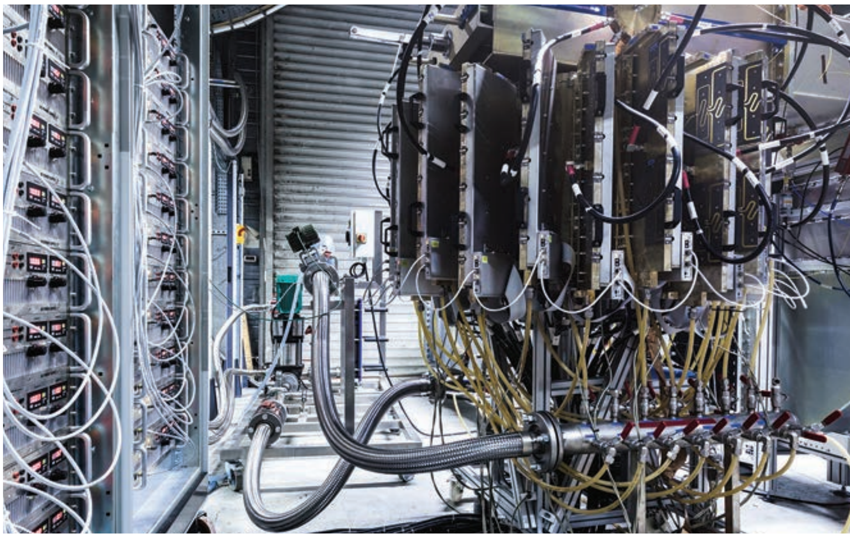

SMALLEST EVER NANOFOCUS FOR HIGH-ENERGY NANOIMAGING USING X-RAY MIRRORS

A sub-13 nm diffraction-limited X-ray focus size with six billion photons per second was reached at the ID16A nanoimaging beamline using a high precision, graded multilayer Kirkpatrick-Baez mirror system. This was made possible by significant advances in mirror fabrication technology along with a highly optimised and stable beamline optical system.

The availability of high-energy X-ray nanobeams for routine use offers new opportunities across a wide range of scientific fields. However, forming nanobeams with suitable photon flux at high-energies is an engineering challenge. As part of the newly commissioned 185 m-long **ID16A** nanoimaging beamline at the ESRF, a new optical system consisting of a pair of elliptically figured Kirkpatrick-Baez (KB) mirrors (**Figure 146**) operating at 33.6 keV delivered a sub-13 nm high-energy X-ray focus. An impressively high flux of six billion photons per second was efficiently concentrated in the focus (**Figure 147**). This is the smallest and brightest focus ever reported for energies above 20 keV.

This diffraction-limited focus was carefully characterised not only by sharp-edge X-ray fluorescence scans but also by ptychography measurements. Compared to the edge scan measurements, which tend to overestimate the focal spot size, ptychography provides a more precise evaluation of the wavefront. Thus, ptychography was used to retrieve the wavefront at the sample position, taking into consideration partial coherence effects of the beam, as shown in **Figures 147a-c**. The measurements were taken in a defocused position and the retrieved wavefront was numerically propagated back to the focus position by Fresnel propagation. To confirm the retrieved focus (**Figure 147d**), an X-ray fluorescence imaging experiment was performed on a lithographic sample in the focus position (**Figure 147e**). **Figure 147f** shows the deconvolved image using the focus determination from the ptychography measurements and shows further improvement on the image resolution (**Figure 147**).

Figure 146a shows the KB system used for X-ray focusing at the **ID16A** beamline, consisting of two mirrors: one horizontally deflecting and one vertically deflecting (**Figure 146b**). The KB system required mirrors with unprecedented surface perfection. The horizontal mirror is 36 mm long while the vertical one is 70 mm long **[1]**. The elliptical cylinder figured substrates were prepared by a commercial supplier, using polishing techniques based on technologies developed at Osaka University. The mirrors were coated at the ESRF's Multilayer Laboratory with 120 periods of W/B_4C, with a d-spacing of 2 nm. The main challenge was to coat both mirrors with a steep thickness gradient while using a 7 m-long deposition machine. The coating increases the useful numerical aperture of the optics, which reduces the diffraction-limited focus size produced by the mirrors. An in-house-designed mechanical assembly was developed to support and align the mirrors.

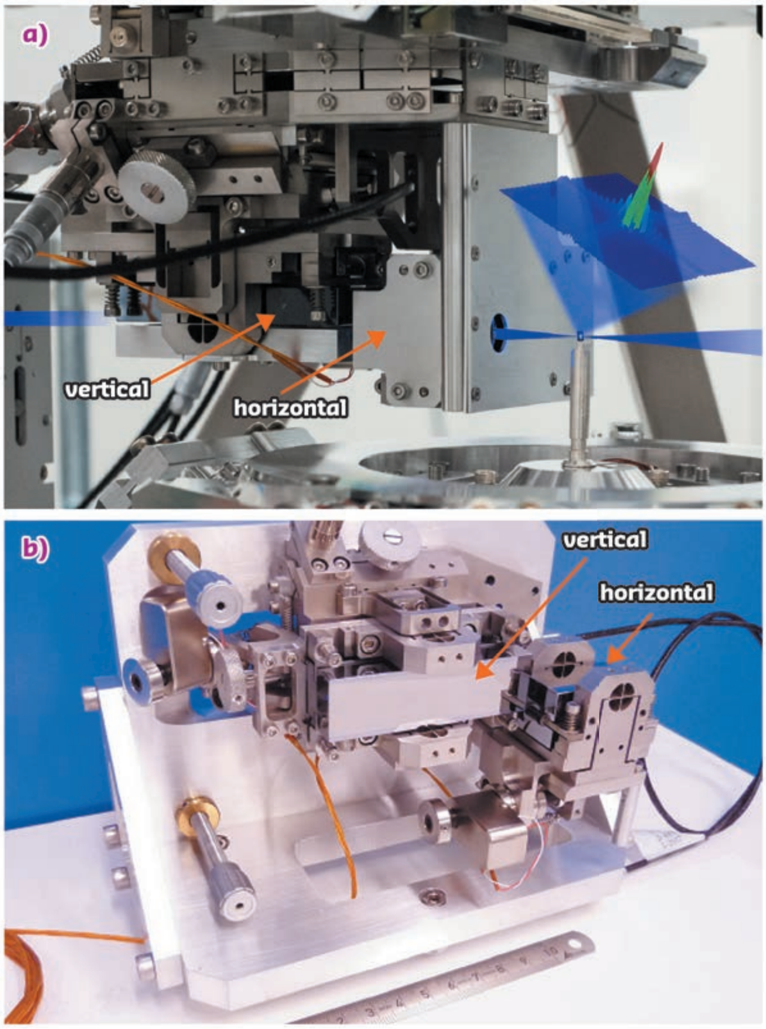

Fig. 146: The KB system on ID16A. a) Complete set-up with visualisation of the X-ray beam path (blue) and the reconstructed focal spot image. b) View of the KB mechanics including the horizontal and vertical mirrors.

The **ID16A** nanoimaging beamline was built as part of the ESRF Phase I Upgrade. The beamline features a precisely temperature-controlled environment and vibrational stability, which makes high-resolution imaging possible. A cryogenic setup is also available for radiation sensitive samples. The available techniques include full-field phase-contrast imaging, X-ray fluorescence imaging, and ptychography, all being combined with tomography to obtain 3D imaging. Applications include the study of nanotechnological materials, environmental and biological samples **[2]**.

X-ray imaging techniques, where resolution depends on the focus size, can fully benefit from the diffraction-limited nanobeam available at the **ID16A** beamline. The high energy and high flux available in such a tiny beam allows imaging of thick or highly absorbing samples with high spatial resolution, in addition to extending the range of detectable elements by X-ray fluorescence imaging **[2]**. The spatial resolution currently achievable at such a beamline offers the possibility of carrying out X-ray imaging experiments with resolution higher than that provided by super-resolution optical microscopy, without the requirement of any fluorescence markers. The present achievement is relevant not only for the X-ray optics and X-ray imaging communities, but also for many other scientific fields, which can benefit from probing samples with unprecedented precision.

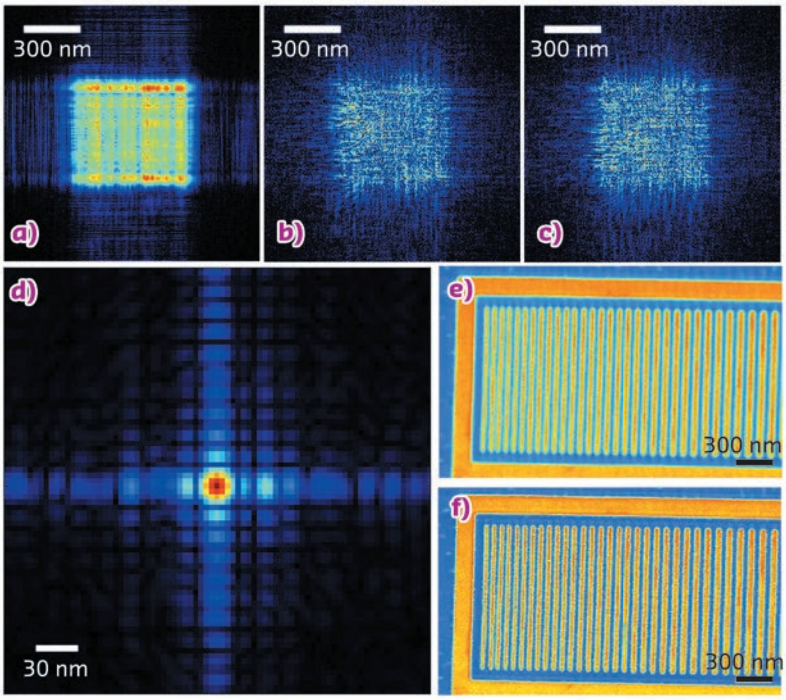

Fig. 147: The X-ray wavefront. The coherent modes of the beam retrieved by ptychography at the sample position: a) main mode (87% power), b) secondary (7% power) and c) tertiary modes (6% power). d) The retrieved focus. e) Original and f) deconvolved XRF images.

PRINCIPAL PUBLICATION AND AUTHORS

Efficient concentration of high-energy X-rays for diffraction-limited imaging resolution, J. C. da Silva (a), A. Pacureanu (a), Y. Yang (a), S. Bohic (a, b), C. Morawe (a), R. Barrett (a) and P. Cloetens (a), *Optica* **4**(5), 492-495 (2017); doi: 10.1364/OPTICA.4.000492.

(a) ESRF
(b) EA-7442 RSRM, Université Grenoble Alpes, Grenoble (France)

REFERENCES

[1] C. Morawe *et al.*, *Proc. SPIE* **9588**, 958803 (2015).
[2] J. C. da Silva *et al.*, *Proc. SPIE* **10389**, 103890F (2017).

X-SOCS – SOFTWARE AS A SERVICE OPENS NEW APPLICATIONS FOR NANOSTRAIN SCANNING

X-SOCS is a software developed at the ESRF to enable users to determine the strain and stress of their nanosamples. It allows non-expert users to analyse the huge data volumes produced during and after the experiment. X-SOCS is an example of how software is addressing the challenges of the Extremely Brilliant Source (EBS) project.

Software is a major factor for enabling users to get the most out of their data; developments in this field are therefore a relevant part of the EBS program. Within the frame of the Scientific Data Analysis and Data Management project, the ESRF has hired additional software engineers and data scientists to work on building a generic and sustainable platform for scientific software and to develop applications that are specific for scientific techniques. Thanks to funding from the NFFA (http://www.nffa.eu/) and IRT NanoElec (http://www.irtnanoelec.fr/en/) projects, a software engineer was hired to improve the X-SOCS **[1]** software on **ID01** for doing X-ray strain scanning at the nanoscale.

X-SOCS aims at retrieving strain and tilt maps of nanostructures, films, surfaces or even embedded structures. It offers the opportunity to get rapid preliminary results, giving the user the opportunity to adapt the planning of the experiments and the measurements with respect to this first set of results. This is of particular importance for the application of such fast scanning methods to *operando* studies at high temperatures or in gas or liquid environments. The ultimate goal is to offer an easy-to-use tool for visualising strain, tilt and/or a composition map for nanosamples as a remote service for users, thus opening the technique up to new user communities and applications.

The first version of the software was written by beamline scientists and users. However, the software was not time-efficient, was difficult to maintain and lacked advanced 3D visualisation capabilities. The work of the software engineer was to address these points and make the X-SOCS program maintainable in the long term. This was done by adopting and building on the newly developed Silx library (https://www.silx.org/) and, in particular, its visualisation routines for reading and writing data in common data formats. Using this library, it was possible to have advanced 3D visualisation of reciprocal space, including the definition of regions of interest, in a very short time (see **Figures 148** and **149**). Being able to define such regions of interest during an experiment makes the analysis of the treated data easier and faster. Moreover, the 3D visualisation in reciprocal space gives access to information, hidden with the 2D visualisation tools in the initial version of the software. The efficiency of the data manipulation was improved by two orders of magnitude by restructuring the code to make it more efficient, adopting HDF5 as data format and using a multi-threaded approach. The first step in the data reduction now takes minutes instead of hours. The new program is available on the ESRF cluster and for downloading, and the source code is available under an Open Source licence to facilitate contributions from other institutes. The next step is to make X-SOCS available as a remote service.

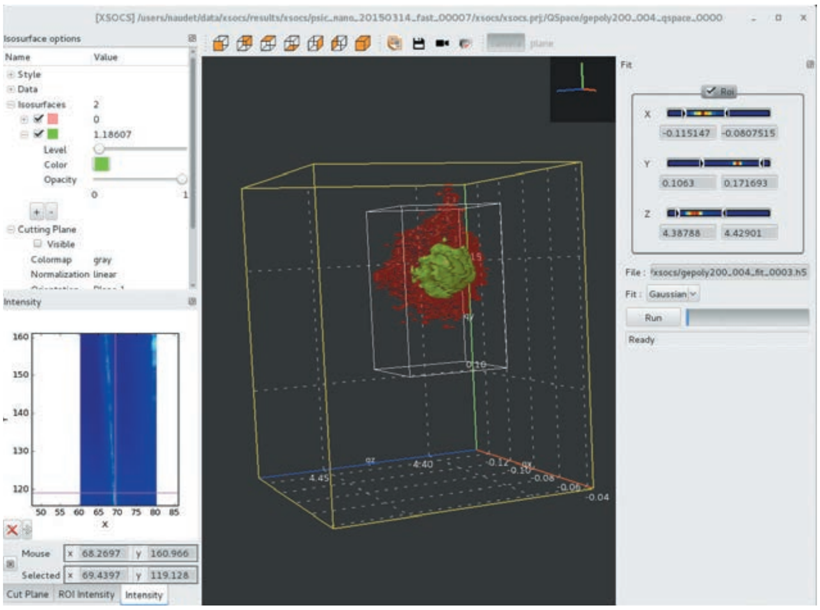

[XSOCS] /users/naudet/data/xsocs/results/xsocs/psic_nano_20150314_fast_00007/xsocs/xsocs.prj:/QSpace/gepoly200_004_qspace_0000

Isosurfaces 2
0
1.18607
Cutting Plane
Colormap gray
Normalization linear

X -0.115147 -0.0807515
Y 0.1063 0.171693
Z 4.38788 4.42901
File : /xsocs/gepoly200_004_fit_0003.h5
Fit : Gaussian
Ready

Mouse x 68.2697 y 160.966
Selected x 69.4397 y 119.128

Fig. 148: X-SOCS graphical interface: 3D view of the reciprocal space (with 2 isosurfaces).

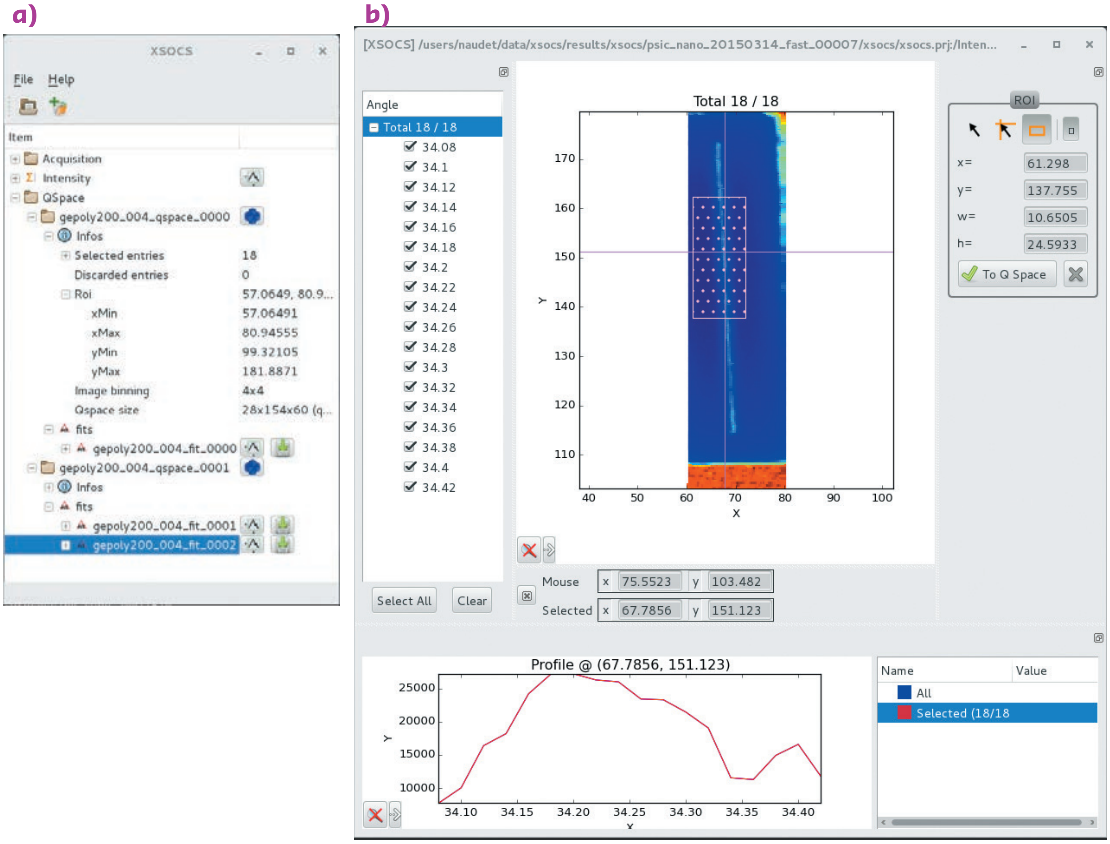

a)

XSOCS

Acquisition
Intensity
QSpace
gepoly200_004_qspace_0000
Infos
Selected entries 18
Discarded entries 0
Roi 57.0649, 80.9...
xMin 57.06491
xMax 80.94555
yMin 99.32105
yMax 181.8871
Image binning 4x4
Qspace size 28x154x60 (q...
fits
gepoly200_004_fit_0000
gepoly200_004_qspace_0001
Infos
fits
gepoly200_004_fit_0001
gepoly200_004_fit_0002

b)

[XSOCS] /users/naudet/data/xsocs/results/xsocs/psic_nano_20150314_fast_00007/xsocs/xsocs.prj:/Inten...

Angle
Total 18 / 18
☑ 34.08
☑ 34.1
☑ 34.12
☑ 34.14
☑ 34.16
☑ 34.18
☑ 34.2
☑ 34.22
☑ 34.24
☑ 34.26
☑ 34.28
☑ 34.3
☑ 34.32
☑ 34.34
☑ 34.36
☑ 34.38
☑ 34.4
☑ 34.42

x= 61.298
y= 137.755
w= 10.6505
h= 24.5933

Mouse x 75.5523 y 103.482
Selected x 67.7856 y 151.123

Profile @ (67.7856, 151.123)

Name	Value
🟦 All	
🟥 Selected (18/18	

Fig. 149: X-SOCS:
a) Workspace view and
b) acquired intensity
view / ROI selection.

The success of this project has been strongly appreciated by the **ID01** user community and, in the words of the beamline scientist, it is "a real game changer for ID01 as a user facility".

This project shows that by investing in software development major improvements can be made in user experience.

AUTHORS

D. Naudet, G. Chahine, M-I. Richard, T. Vincent, V.A. Sole, T. Schulli and A. Götz. *ESRF*

REFERENCES

[1] G.A. Chahine *et al., J. Appl. Cryst.* **47**, 762-769 (2014).

X-RAY IMAGING WITH RANDOM MODULATION: FROM THE ESRF TO LABORATORY SOURCES

By providing enhanced details of materials, phase contrast opened new perspectives for X-ray imaging at synchrotrons. To make this imaging modality accessible to a much broader community using compact laboratory sources, ESRF scientists have developed new methods to transfer phase imaging to low brightness sources.

Imaging is probably the most important application in the world of X-rays, considering its use as a non-invasive diagnostic in fields as different as medical imaging and security screening. Both 2D and 3D visualisation of samples are made possible using computed tomography due to the capacity of X-rays to penetrate matter. Very short wavelength is another property that makes X-ray imaging an invaluable probing tool to the scientific community. It permits much higher resolution than with visible light and with a greater depth of focus.

In this context, researchers are constantly looking for instrumentation and methods that could be implemented on moderate-cost X-ray laboratory equipment while simultaneously increasing the quantity and quality of information available. X-ray phase contrast imaging is a very attractive approach for this scientific case. Introduced a couple of decades ago, it showed sensitivities and signal-to-noise ratios much greater than for traditional absorption contrast employed in X-ray imaging since Röntgen's discovery. However, although phase contrast is routinely obtained at synchrotrons, it is tedious to transpose onto laboratory systems due to the much lower brightness of these sources. For instance, propagation-based phase contrast imaging is easily observed at synchrotrons and does not require the implementation of any specific instrumentation. Unfortunately, such an approach is difficult to translate to laboratory sources due to the high divergence and low monochromaticity of these sources. In comparison, wavefront modulation-based techniques are better candidate methods to be transferred to these low-brightness sources. Speckle-based techniques, which fall into this category, are considered as a candidate of choice in this endeavour.

Work conducted at the ESRF test beamline **BM05** over the last few years permitted the development of a multi-modal approach that offers the advantage of a very simple setup compatible with sources presenting short longitudinal and transverse coherence lengths. In a speckle-based method, the random modulation of the X-ray beam wavefront infers deflection by refraction in the sample. In contrast to the light experimental requirements of the approach, tracking the local displacement of the speckle modulation pattern using correlation algorithms calls for intensive numerical calculation. The random pattern, called speckle in the field of optics, is a modulation pattern very simple to obtain by

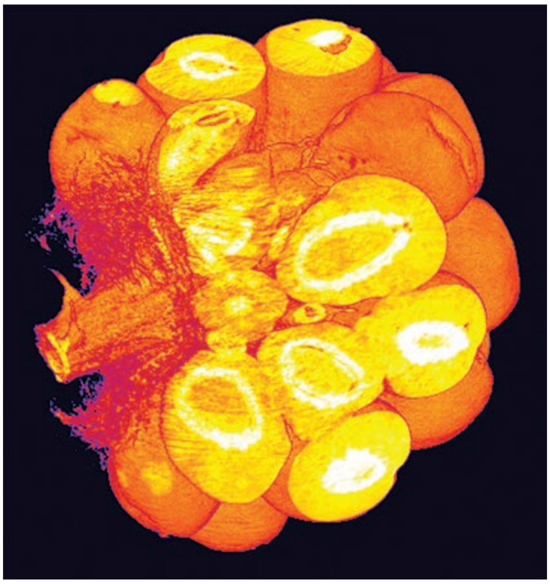

Fig. 150: Image reconstruction of a raspberry using the new speckle processing approach.

using, for instance, a random mask made of grains, or, even more easily, using coherent light. In fact, when using a coherent synchrotron light source, speckle appears by interference effects as soon as an unwanted object or dust is present in the beam path, therefore it is often labeled as noise.

Several processing approaches based on the near-field speckle have been developed over the years. In the simplest speckle approach, one can achieve moderate sensitivity and resolution with a single exposure of a sample. In a scanning processing approach, several sample exposures achieve sub-micrometre resolution and nanoradian accuracy. Unfortunately, such performance was so far only possible at the cost of many sample exposures, especially in the case of highly divergent beams, hence preventing these methods spreading beyond the synchrotron community.

With their new processing approach, scientists at the **BM05** beamline found ways to perform the speckle-based imaging methods at laboratory sources. The new concept developed **[1]** consists of building, for each pixel, an oversampled basis of speckle pattern by collecting reference data prior to the sample measurement. When the sample is inserted in the beam, only very few exposures are made during a short scan. Then, the speckle pattern distorted by sample refraction is searched for its original position within the basis built earlier. Such processing greatly reduces the overall exposure time and overall data collection time without sacrificing either the resolution or the sensitivity of the method, even with highly diverging sources. Examples of data collected at the ESRF test beamline **BM05** and processed with the new algorithm are illustrated in **Figures 150** and **151**.

These developments are expected to promote the speckle-based approach at laboratory sources so that new fields of applications may benefit from the techniques of X-ray phase contrast imaging.

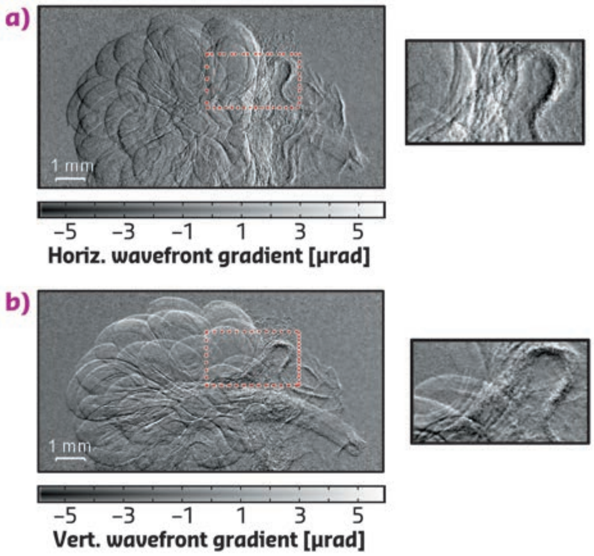

Fig. 151: a) horizontal and b) vertical wavefront gradient image of a raspberry obtained using the new speckle processing approach. The feature details in the insets show that the method used does not reduce the original resolution provided by the detector as can be the case with other wavefront modulation-based techniques.

AUTHORS

S. Berujon and E. Ziegler. *ESRF*

REFERENCES

[1] S. Berujon and E. Ziegler, *Physical Review A* **95**(6), 063822 (2017).

PRECISION CONTROL AND FIDUCIALISATION MEASUREMENTS FOR THE EBS GIRDER ASSEMBLY

The quality of the assembly, alignment and control of the key accelerator components are critical for the ultimate success of the ESRF's Extremely Brilliant Source (EBS) project. Nearly 900 magnetic accelerator elements must be aligned to within 50-80 μm of their nominal positions for the new machine to function correctly.

Alignment starts with the fiducialisation of the magnets. It is important to correctly position the magnetic centre and orientation of the magnets, however, these are not visible or accessible quantities. Fiducialisation is the process of linking the magnet centre and axis to visible references installed on the exterior of the magnet. This process is carried out on a dedicated magnet measuring bench. The magnetic axis and centre of the magnet are materialised using a stretched wire, placed in such a way as to precisely emulate the position and orientation of the electron beam. The positions of the ends of the wire and the exterior reference points on the magnet are then simultaneously measured. Thus, the electron beam trajectory is known with respect to easily visible and measureable references on the exterior of the magnet.

The fiducialised magnets are then assembled on the girders in the dedicated assembly building, ESRF 01. The assembly of the girders is a complex activity comprising the installation and precise positioning of all of the accelerator elements: principally the magnets, but also the vacuum chambers and their sub-assemblies. Alignment and control are important at several critical points.

Before any assembly starts, the girder is aligned horizontally using jacks installed specifically for this purpose. Horizontality is not a precondition for the successful assembly of a girder but it is considerably easier to work in the gravity reference frame. Once the girder is in the horizontal position, a local girder frame of reference is created using the girder's reference surfaces and survey sockets. This provides a physical and reproducible origin and orientation for the girder and all of its future sub-assemblies.

The magnets are then installed and finely aligned, a process that takes between six and eight hours to complete. This alignment consists of positioning the magnets in their nominal positions using their fiducialised references. All of the magnets, as well as the girders, have a nominal position in the EBS lattice. To establish their position on the girder, the 3D transformation of the theoretical magnet-centred coordinates of the reference points to their nominal girder-centred lattice positions is applied to the fiducialised magnet references. The positions of the magnets are then measured to ensure they are within the required positional tolerances.

Once this has been carried out, the magnets are opened and the previously assembled vacuum string is put in place. The permissible mechanical gap between the vacuum chambers and the magnet poles is very tight – less than 1 mm. To ensure these tolerances are respected, a certain percentage of the vacuum chambers are submitted to rigorous dimensional site acceptance tests (SAT) upon their arrival and all of the beam position monitor (BPM) positions are measured. This BPM fiducialisation provides 3D coordinates of the centre of the BPM buttons with respect to visible and measureable references on the exterior of the vacuum chambers. The fiducialised BPM references are then used to align the vacuum chambers on the girder and, once aligned, their positions are checked. After reassembly, the BPMs are quite difficult to access and measure.

The magnets are then reassembled and a final alignment check of everything: the magnets, vacuum chambers, absorbers and BPMs is carried out (**Figure 152**). The fully assembled girder is now ready for storage and installation in the tunnel. At this point, not only are the magnets and other elements – notably the BPMs – positioned to within a given tolerance, but their positions are also known to within a given uncertainty. This knowledge can be used very effectively to simulate the beam dynamics of the future machine.

The overall quality of the alignment is given by an expression of uncertainty. This is the quadratic sum of the uncertainties of the alignment and measurements made at all the stages of the assembly process and during the final installation. The final estimated positional uncertainty for the EBS magnets in the tunnel is given in **Table 2**.

	Ux [µm]	Uy [µm]	Uz [µm]
Fiducialisation	13	22	39
Girder rectitude	38	8	8
Magnet opening/closing	8	5	7
Alignment on girder	126	24	25
Measurement	6	7	6
Transport (estimated)	20	20	20
Alignment in tunnel (estimated)	25	15	15
Measurement in tunnel (estimated)	21	44	31
Total	**138**	**61**	**62**

Table 2: Uncertainty estimate for the final magnet alignment in the storage ring tunnel. Uncertainty as presented here is discussed in the Guide to the Uncertainty of Measurement (GUM) published through the BIPM (https://www.bipm.org/utils/common/documents/jcgm/JCGM_100_2008_E.pdf).

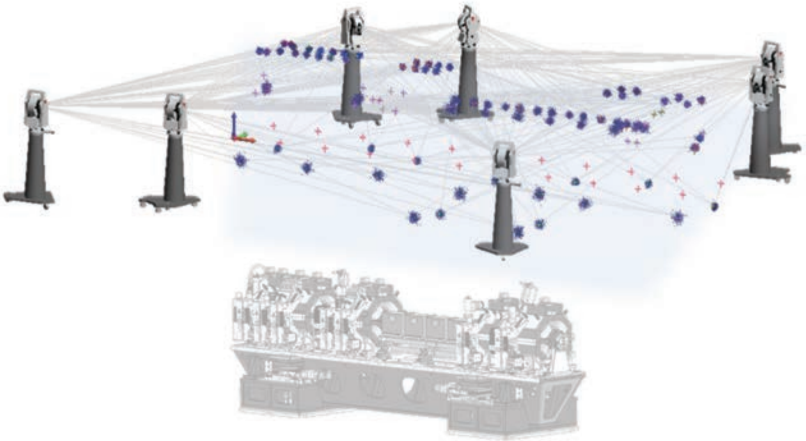

Fig. 152: To precisely determine the positions of all of the key elements on the girder, a highly redundant survey is made of all of the references installed on the magnets, vacuum chambers, BPMs, *etc*. Uncertainties of these measurements are less than 10 µm in X, Y and Z.

AUTHORS

D. Martin. *ESRF*

REAL-TIME VACUUM EVENT ANALYSIS AND LOCALISATION USING FASTVAC

A new fast data acquisition system for pressure surveying has been implemented along the ESRF storage ring. High time resolution offers new perspectives for understanding vacuum events and deeper analysis such as their precise location around the ring.

Good vacuum and an associated control system for accelerator instruments are key parameters for performance, operational reliability and safety considerations. The ultra-high vacuum (UHV) conditions are required to minimise interactions of the electron beam with residual gas molecules.

The ESRF storage ring consists of an 844 m-long assembly of vacuum chambers divided into 32 cells. Each cell is equipped with vacuum pumps (ion and getter pumps) and pressure gauges (cold cathode ionisation gauges). The gauge controller data is presently acquired through a serial interface (RS422) and archived in the hierarchical database (HDB) system at a maximum rate of one measurement per second. HDB-archived data for a typical event is illustrated in **Figure 153a**. The sampling rate is too low to allow for a detailed analysis of vacuum events lasting only a few seconds.

FastVac is a new faster data acquisition and archiving system developed to collect the analogue output signals from gauge controllers. A programmable logic controller (PLC) was deployed along the technical gallery, as illustrated in **Figure 153b**. All signals resulting from the pressure gauges of the different cells are stored in a circular buffer within the PLC. The data are processed in real time to detect any sudden pressure changes and to trigger the archiving. The time resolution is increased by 100 compared to the standard system (**Figure 153c**), thus detailed analysis becomes possible.

Since the implementation, many events (some of which were not visible with the standard system) have been detected. Different types have been identified from quantitative and qualitative analysis. Events such as electron beam-induced outgassing when gauge responses are simultaneous, instrumentation issues and local pressure outgassing with evidence of pressure wave propagation can be observed.

A semi-empirical model has thus been developed with the goal of locating initial bursts of pressure within an UHV assembly. The model is based on the main assumption that the wavefront speed, V_f, is in the first order proportional to the conductance, C and a proportional constant, A (see formula below).

$$V_f(x,t) \propto A(x_0,t_0) \bullet C(x_0,x) \qquad [1]$$

The conductance C depends on the vacuum assembly dimensions. MOLFLOW software **[1]** was used to calculate the conductance of vacuum chambers and each $C(x_0, x)$ calculated by discretisation using an average step Δx = 10 cm. Fixing the range of physically possible (x0, t0) values corresponding to the event starting position and time, and applying the formula to each gauge signal, a solution exists if there is

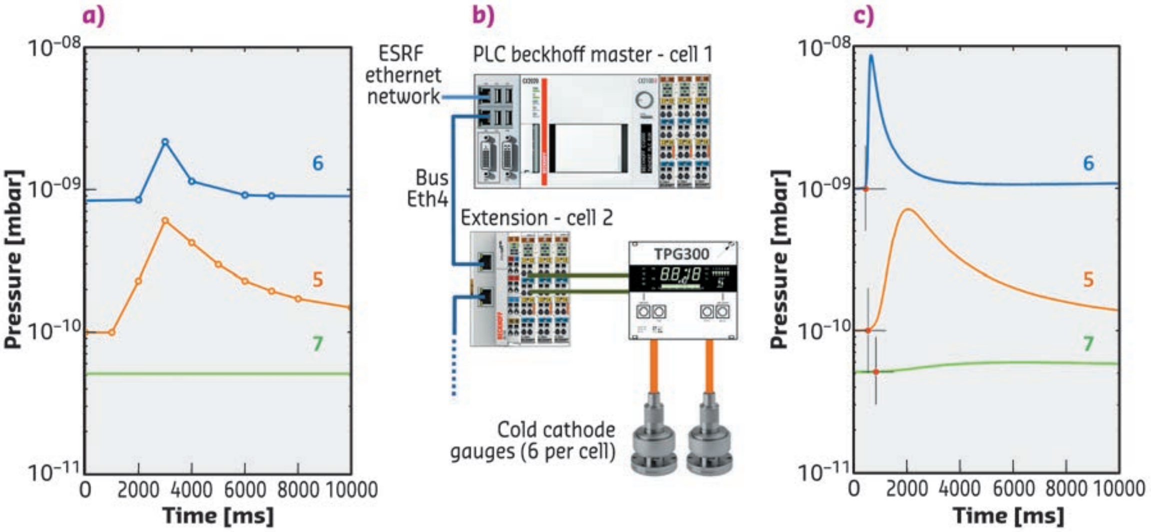

Fig. 153: a) Archived data for gauges 5, 6 and 7 of cell 11 with the standard acquisition system. b) Overview of the new hardware PLC FastVac system. c) Archived data with FastVac.

convergence of parameter *A* with a minimum of dispersion. Indeed, if *A* is a constant, its dispersion *ΔA/A* would be 0%.

This model was applied to analyse several different events recorded during User Service Mode (USM) runs and events generated in a test setup. **Figure 154** illustrates computed results corresponding to the pressure event shown in **Figure 153c**. The x_0 position has been determined with an estimated uncertainty of ± 15 cm and the ΔA/A dispersion parameter shows a strong convergence to a minimum of 1.3%. The pressure burst in that case corresponds to an outgassing resulting from the instability of RF fingers. The maximum wavefront propagation speed along the x axis is about 410 m/s and is in the order of magnitude of what is reported in literature for comparable studies **[2-5]**.

A combination of the FastVac system and a software application still under development will be very useful for real-time analysis of vacuum events during conditioning and operation of the new EBS storage ring.

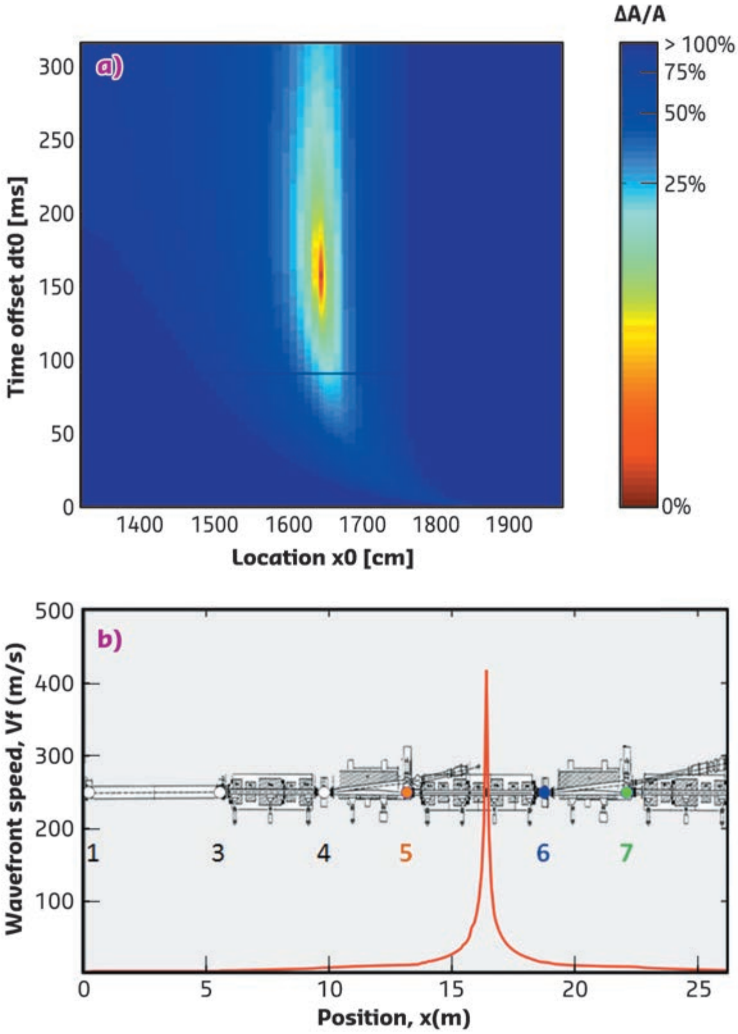

Fig. 154: Schematic layout of cell 11 of the ESRF storage ring and FastVac data analysis results for a vacuum event localisation: a) dispersion (ΔA/A) colour map for the (x0, t0) possible values and b) wavefront speed versus position along the cell.

AUTHORS

A. Meunier and E. Burtin. *ESRF*

REFERENCES

[1] R. Kersevan and J.-L. Pons, *J. of Vac. Sci. & Tech A*, **27**, 1017 (2009).
[2] M. Ady, M. Hermann *et al., IPAC2014,* WEPME039, Dresden, Germany (2014).
[3] R.C. Dhuley and S.W. Van Sciver, *Int. J. of Heat and Mass Transfer* **96**, 573-581 (2016).
[4] Y.-F. Song, C.-I. Chen *et al., Rev. of Sci. Instruments*, **57**, 3063 (1986).
[5] T. Takiya, F. Higashino *et al., J. of Vac. Sci. & Tech. A*, **17**, 2059 (1999).

MODERNISING THE ISPYB APPLICATION WITH DOCKER AND CONTINUOUS INTEGRATION

Docker containers and continuous integration are being used at the ESRF to modernise and upgrade the ISPyB web application, helping software development and IT teams work together more efficiently.

ISPyB (Information System for Protein crystallographY Beamlines) is an information management system for synchrotron macromolecular crystallography beamlines, developed as part of a joint project between the ESRF Joint Structural Biology Group (JSBG), **BM14** (e-HTPX) and the EU-funded SPINE project. The ISPyB web application is developed with Java technology, running on a JBoss application server, and supports both MySQL and Oracle databases.

Running since 2012, the project requires the input and collaboration of a number of teams at the ESRF and updating the application can often be a complicated and lengthy process. New features to be implemented by the software development team often require a new version of the server to be installed by the IT team, which itself necessitates a reinstallation of the operating system, obtaining a spare machine in case a rollback is needed, planning this with network team, backing up the data, *etc.* Unsurprisingly, the requirements of flexibility, stability, control and efficiency, are often in conflict.

To resolve this, a new set of computing practices, known as DevOps, have been used to automate the processes between software development and IT teams, in order that they can build, test, and release software faster and more reliably. The concept of DevOps is founded on building a culture of collaboration between teams that historically functioned in siloes. The promised benefits include increased trust, faster software releases, ability to solve critical issues quickly, and to better manage unplanned work.

The solution chosen to implement this was docker containers, which changes the way software is built and delivered. When an application is packed into a docker container, it is packed with part of the Operating System (OS) that is needed by the application. A Dockerfile is then written: documentation describing how to install a required program on a real machine. As a result, the container is built with simple docker commands and can be run everywhere: from a laptop to Amazon cloud services, the ESRF data centre or a beamline workstation, no matter which Linux version the machine is running.

It also offers a clear separation with the data needed for the container (or application). The containers can be given versions, so that rolling back or testing new versions of the application can be done in a matter of seconds. Docker also offers cluster features (called swarm) where automatic failover is available, and the application can be scaled up to handle more requests. This proved to be necessary for ISPyB as the JBoss server had stability issues. Docker is now able to restart the application without human intervention. Docker

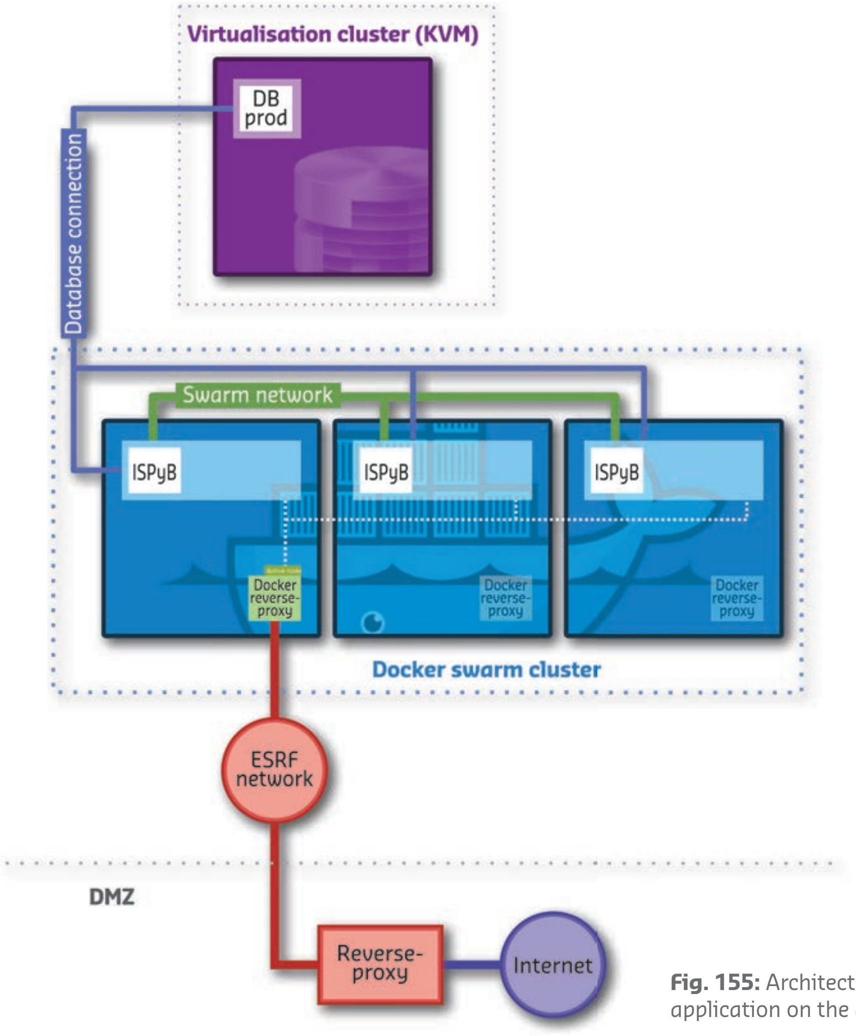

Fig. 155: Architecture diagram of the ISPyB application on the docker swarm cluster.

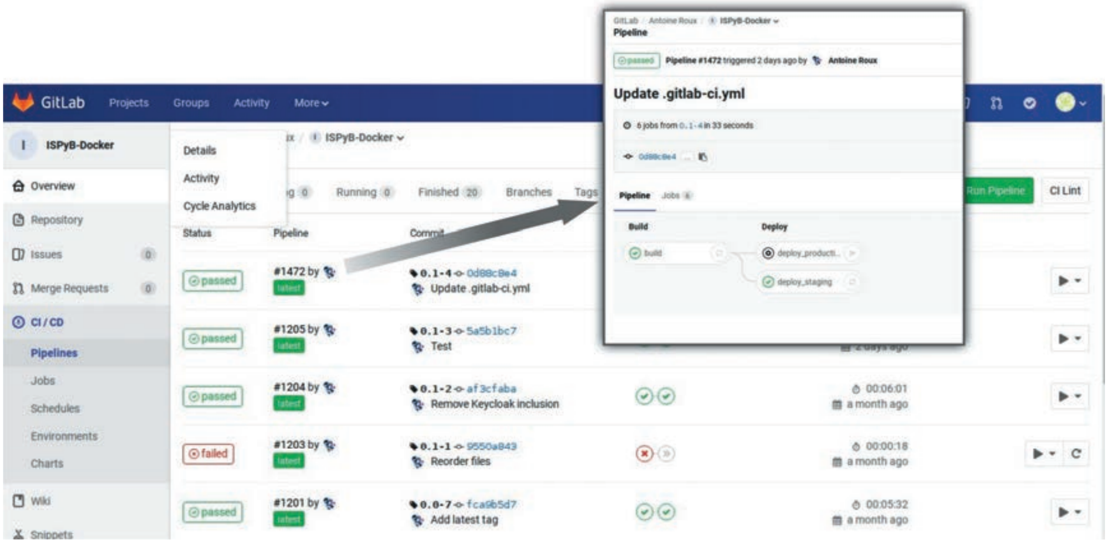

GitLab / Antoine Roux / ISPyB-Docker
Pipeline
passed Pipeline #1472 triggered 2 days ago by Antoine Roux
Update .gitlab-ci.yml
6 jobs from 0.1-4 in 33 seconds
0d88c8e4
Pipeline Jobs 6
Build: build
Deploy: deploy_producti… deploy_staging

Status	Pipeline	Commit	Stages	
passed	#1472 by latest	0.1-4 0d88c8e4 Update .gitlab-ci.yml		
passed	#1205 by latest	0.1-3 5a5b1bc7 Test		2 days ago
passed	#1204 by latest	0.1-2 af3cfaba Remove Keycloak inclusion	✓ ✓	00:06:01 a month ago
failed	#1203 by latest	0.1-1 9550a843 Reorder files	✗ »	00:00:18 a month ago
passed	#1201 by latest	0.0-7 fca9b5d7 Add latest tag	✓ ✓	00:05:32 a month ago

Fig. 156: Gitlab web interface showing the update process for the application on the production infrastructure.

containers should also eliminate application error messages that arise due to the use of old or new libraries that are not compatible with the system. There are also plenty of pre-built applications provided through Docker Hub. For instance, regarding ISPyB, pre-built containers are used with the right JBoss server version, customised to fit in-house needs (**Figure 155**).

This initiative can be extended further with continuous integration. Continuous integration is the process of automating the compilation, linking, and testing of code every time a team member commits changes to version control. This means that each time code is committed, a new container is built automatically. The software development team also has the ability to push the newly built container into production without intervention from the IT team (**Figure 156**). This is very useful as, with these methods, each team can focus on their main activity; the IT team can maintain an infrastructure with high availability, scaling abilities, monitoring, security, and high performance, and the software development team can focus on code and deliver faster, while also having full control over the release cycle in a simple way.

Docker containers and continuous integration have been successfully implemented into the workflow of the ISPyB team and now run smoothly. Of course there is a cost for all this: new tools have had to be mastered and new working methods implemented but the end result is that several teams now work together in a much more efficient manner. Container technology is not 'one tool to rule them all' but can be considered as a disruptive technology that helps deliver software in a constantly moving research infrastructure. Many major companies such as OVH, Amazon and Google are widely using these technologies today, and several initiatives have also been launched to try to adapt container techniques for very specific usage like scientific software on compute clusters, showing that this technology is only the beginning.

AUTHOR

B. Rousselle. *ESRF*

ACCELERATOR AND SOURCE

The Accelerator and Source Division (ASD) is in charge of the production of synchrotron light from the ESRF's 6 GeV storage ring. Much of the division's development work in 2017 has been focused on the ESRF-EBS, and major progress has been made in procurement and assembly, with the arrival of many more components on site and the construction of ESRF 01 and 02 A and B, as detailed in the Status of the EBS section of this report (**see page 8**). Despite the challenges faced by the increased workload of the project, the division has also continued to ensure excellent machine availability and reliability throughout 2017, including running preventative maintenance campaigns to replace ageing equipment, developing new diagnostics devices, and installing a new ramped injection power supply (RIPS) for the booster.

As a result of these efforts, the operation statistics for 2017 are very positive. A total of 5407 hours of beam was delivered out of 5502 scheduled hours, representing an availability of 98.28% and coming very close to the ESRF's all-time record (99.11%). The Mean Time Between Failures (MTBF) was high, at an average of 64.7 hours. More information on the main parameters of the storage ring can be found on **page 167**.

In May 2017, refill in top-up mode was put into operation, providing better beam stability, low vertical emittance in all filling modes and a nearly constant beam current. The implementation followed several years of upgrades and modifications to the machine, including, in 2016, a new timing sequence, the development of cleaning in the booster and the start of commissioning of the RIPS. Feedback from the beamlines is extremely positive and the new power supply will provide a crucial back-up in case of failure as well as help to reduce energy consumption at the ESRF.

This year's achievements would not have been possible without the dedication of the ASD staff and the continuous support of the other ESRF divisions. May this continue in 2018 as we face the challenges of the assembly phase of the ESRF-EBS while simultaneously ensuring optimal operating conditions for our users.

P. RAIMONDI

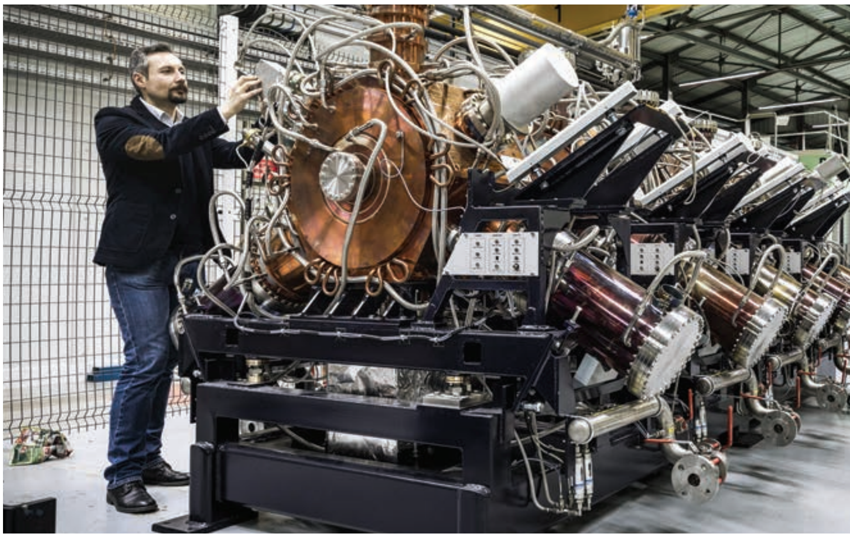

SUMMARY OF ACCELERATOR OPERATION

With one year to go before the dismantling of the storage ring, 2017 has been undoubtedly the year of highs and lows. The highs include several long weeks of deliveries, especially in top-up mode, and the lows were due to some long or repetitive failures, particularly during the final trimester of the year.

In 2017, 5407 hours of beam were delivered out of 5502 scheduled hours. This resulted in an availability of 98.28%, and a MTBF of 64.7 hours, mainly dominated by a few long-lasting failures.

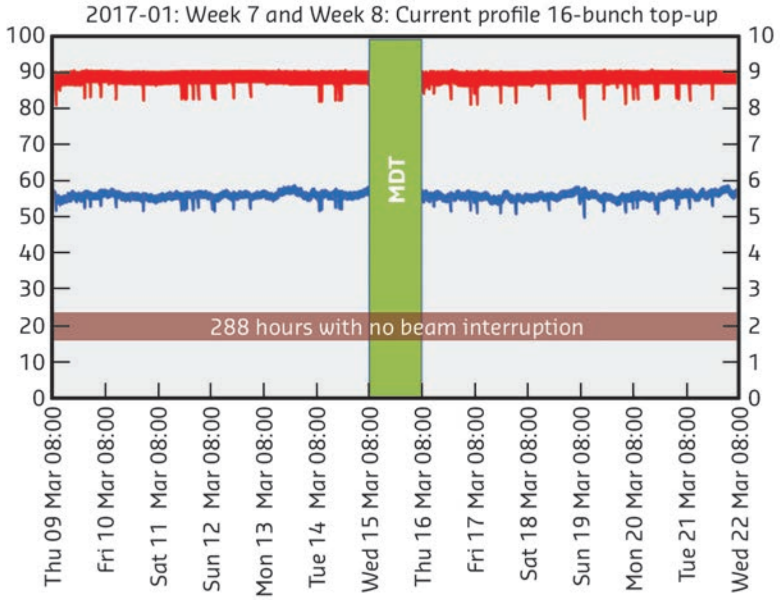

Fig. 157: Two weeks of delivery in top-up mode without a single failure.

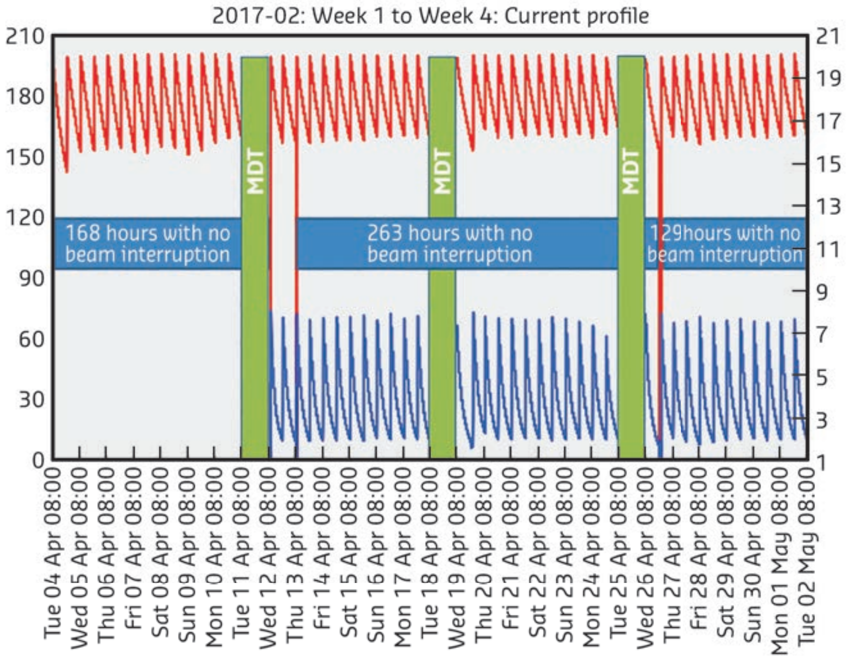

Fig. 158: Three long periods of delivery over a four-week period.

The longest beam interruption lasted more than 12 hours and occurred during the last run of the year, when a faulty valve in the water cooling system on BM20 allowed compressed air to enter the water, meaning the water network had to be switched off. This failure did not actually prevent the operation of the machine as the beam was kept stored, but the beamlines could not operate since their water network was switched off.

The second longest failure occurred the following week when a series of radio frequency arcs prevented a refill. RF experts intervened to inspect the waveguides in question and discovered severe permanent damage on some parts. Several waveguide parts were thus immediately replaced.

The third longest failure, lasting six hours, also occurred in October when the circuit breaker of a full zone of the technical gallery tripped during the night, switching off all electronic devices in this area (including vacuum controllers, gauges, *etc*.). Several side effects prevented an immediate restart and experts had to intervene during the night to be able to switch the beam back on.

Problems with the kickers in the injection system also caused two separate weeks characterised by failures. The first took place in May and was due to a faulty thyratron, causing 10 beam interruptions. The second, in September, resulted in 15 trips and was caused by an erratic side-effect of the synchronisation of the injection kickers when the injection rate was switched from 10 Hz to 4 Hz after the commissioning of the new booster ramped injection power supply (RIPS). Although the long-term solution is to redesign the associated software, a temporary solution has been implemented to fix this issue.

Aside from this, the injectors have proved their excellent reliability: more than 4000 refills took place in all modes over the year (95% of these refills were done in top-up mode). Only 3% of the refills were skipped due to minor injector problems that could be reset straight away. **Figure 157** illustrates the excellent rate of top-up delivery during the first run of 2017.

This steady injector reliability also induced several long periods of deliveries without failures during the non-top-up periods, as illustrated in **Figure 158** during the second run of 2017.

A significant improvement was made in May 2017 when the new RIPS was put into operation, replacing the former booster magnet power

RUN NUMBER	2017-01	2017-02	2017-03	2017-04	2017-05	TOTAL 2017
Scheduled beam time (h)	1172.5	1200	906.5	908	1315	**5502**
Beam available w/o refill time (h)	1151.2	1176.19	882.22	887.5	1282.4	**5379.51**
Refill time (h)	6.68	5.3	6.74	2.6	6.4	27.72
Beam available including refill time (h)	1157.88	1181.49	888.96	890.1	1288.8	**5407.23**
Availability	**98.75%**	**98.46%**	**98.07%**	**98.03%**	**98.01%**	**98.28%**
Dead time for refills	0.6%	0.4%	0.7%	0.3%	0.5%	**0.5%**
Dead time for failures	1.2%	1.5%	1.9%	2%	2%	**1.72%**
Average intensity (mA)	154	136	176	120	175	**153.1**
Number of failures	17	21	13	24	10	**85**
Mean time between failures (h)	69	57.1	69.7	37.8	131.5	**64.7**
Mean duration of a failure (h)	0.9	0.9	1.3	0.7	2.6	**1.11**

Table 3: Overview of storage ring operation in 2017.

supply system, BPSS. Among many advantages, the RIPS system does not depend upon external temperature, making it much more stable and reproducible for the electron cleaning procedure that is carried out in the booster.

It is also worth noting that during machine operation in 2017 many activities were being performed in parallel, in preparation for the EBS project. Examples include:

- CV 5000 vacuum vessel conditioning in the storage ring and cell 14
- DC-DC power supply cabling work along the technical gallery
- Installation of additional plates under some equipment in the booster in view of the circumference reduction
- Installation of a liquid nitrogen loop in the technical gallery for the cryogenic cooling of in-vacuum devices

A summary of storage ring operation in 2017 is presented in **Table 3**.

FILLING PATTERNS

The distribution of the modes did not change significantly compared to 2016, with a large preference for the 7/8 + 1 filling mode (see **Figure 159**). Today, all 4*10 mA and 16-bunch deliveries are carried out in top-up mode, with a refill every 20 minutes, allowing a very small and permanent vertical emittance in the range of 7 pm.rad, as shown in **Figure 160**. Thanks to a lot of work accomplished to minimise the disturbance during the top-up refills and to make it faster, most users declared that the refill time is now an almost or even fully transparent process.

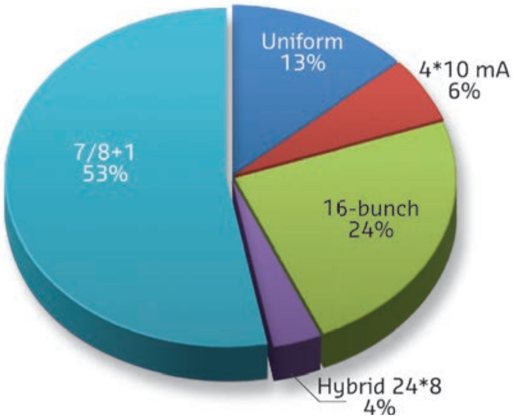

Fig. 159: Distribution of the various filling modes in 2017.

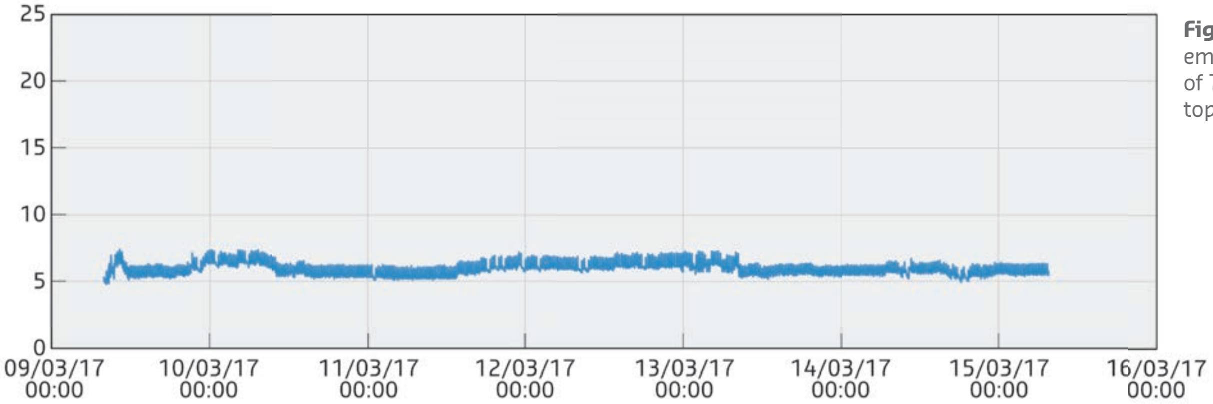

Fig. 160: Vertical emittance in the range of 7 pm.rad during top-up mode.

PROGRESS OF THE TOP-UP PROJECT

Back in April 2016, injection in top-up mode was officially launched to users, and throughout 2017 it has been fully operational in 16- and 4-bunch modes. The new mode sees the accelerators refilled with electrons every 20 minutes rather than every four to 12 hours. This results in a much higher integrated current over a 24-hour period, meaning more photons for the users and better beam stability due to smaller current variations. It also means a low vertical emittance in all filling modes. Previously, the vertical emittance would be artificially increased in some modes in order to increase the lifetime, but the nearly constant beam current provided by top-up mode means that the emittance – and the resulting brilliance and resolution for users – no longer has to be sacrificed. The top-up procedure is now well established, the sequencer fully operational, and the injection disturbance has been significantly reduced.

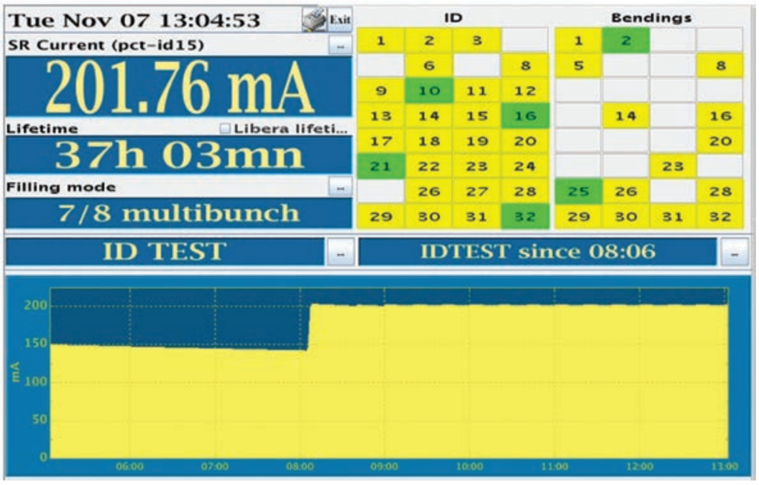

Tue Nov 07 13:04:53

SR Current (pct-id15)

201.76 mA

Lifetime ☐ Libera lifeti...

37h 03mn

Filling mode

7/8 multibunch

ID TEST

IDTEST since 08:06

ID			
1	2	3	
	6		8
9	10	11	12
13	14	15	16
17	18	19	20
21	22	23	24
	26	27	28
29	30	31	32

Bendings			
1	2		
5			8
	14		16
			20
		23	
25	26		28
29	30	31	32

Fig. 161: The control room synopsis display during tests of top-up operation in 7/8+1 filling mode in November 2017.

Top-up operation was further improved in 2017 with the installation of the new 4Hz RIPS for the booster. The switch over from the BPSS to the new RIPS system took place following the May shutdown. The switch has provided the ESRF with a crucial back-up power supply in case of failure, and has reduced the energy consumption for injection, avoiding lengthy start-up warming.

In view of the implementation of top-up in 7/8+1 filling mode, foreseen for 2018, tests were performed in collaboration with users in November 2017 (**Figure 161**). The tests evaluated the impact of injection on the more demanding beamlines, using coherence. Depending on the results, further improvements could still be envisaged in order to reduce perturbation.

REDUCTION OF BEAM DISTURBANCE AT INJECTION

In the context of the top-up project, the disturbance of the beam trajectory during injection has been drastically reduced thanks to the improvement of the injection kicker system and the addition of several active disturbance cancellation systems.

The most severe perturbation is caused by the presence of sextupole magnets inside the injection bump generated during the 2.8 ms injection revolution; these sextupoles apply an extra parasitic kick to the beam during the rise and fall of the bump amplitude. This parasitic kick has been reduced to one third of its initial amplitude by the addition of conductive shims inside the kicker magnets, introducing a non-linear field component to the normal dipole field of the kickers that partially cancels the parasitic effect of the sextupoles. The remaining parasitic horizontal kick is further reduced by the application of a set of correction kicks produced by an auxiliary kicker able to produce arbitrary shape kicks matching the residual perturbation. A vertical parasitic kick is also present, caused by some misaligment of the injection kickers. This vertical kick has been reduced by the addition of skew quadrupole magnets inside the bump and a vertical correction kicker driven by an arbitrary shape correction signal generator.

The septum magnets fired at injection also affect the stored electron beam. The fast orbit feedback has been modified by implementing a feed-forward feature. This feedforward, triggered at each injection, generates a set of correction kicks to cancel the orbit distortion.

APPENDIX 1: BEAM PARAMETERS OF THE STORAGE RING

Table 4 presents a summary of the characteristics of the storage ring electron beam in optimal conditions.

Energy	[GeV]	6.04
Maximum current	[mA]	200
Horizontal emittance	[nm]	4
Vertical emittance	[pm]	4
Revolution frequency	[kHz]	355
Number of bunches		1 to 992
Time between bunches	[ns]	2.82 to 2816

Table 4: Principal characteristics of the electron beam.

Table 5 gives the main optic functions, electron beam sizes and divergences at various source points. For insertion device source points, the beta functions, dispersion, sizes and divergences are calculated in the middle of the straight section. For bending magnets, two representative source points have been selected for each type of magnet (even or odd cell number), corresponding to magnetic fields of 0.4 T and 0.85 T. These points differ by the observation angles, of respectively 3 and 9 mrad from the entrance of the magnet.

Electron beam profiles are Gaussian and the size and divergence are presented in terms of rms values. The associated full width at half maximum sizes and divergences are 2.35 times higher. Horizontal electron beam sizes and divergences are given for the multibunch filling modes and apply to almost all filling patterns, except when the current per bunch is larger than 4.5 mA, for which a slightly larger size and divergence are attained because of the increased energy spread of the electron beam.

Vertical electron beam sizes and divergences are given for a vertical emittance of 4 pm, which is now the optimal condition for 2 x 1/3 and 7/8+1 filling modes. The vertical sizes and divergences are about 1.4 times larger in uniform filling mode (due to ion effects, which are partially corrected by the use of a vertical bunch-by-bunch feedback).

The lifetime, bunch length and energy spread mainly depend on the filling pattern. These are given in **Table 6** for a few representative patterns. Note that in 16-bunch and 4-bunch filling patterns, the energy spread and bunch length decay with the current (the value indicated in the table corresponds to the maximum current). The bunch lengths are given for the usual radiofrequency accelerating voltage of 9 MV (8 MV for 16-bunch and 4-bunch).

		Even ID (ID2, ID6...)	Odd ID (ID1, ID3...)	Even BM (ID2, ID6...) 3 mrad	Even BM (ID2, ID6...) 9 mrad	Odd BM (ID1, ID3...) 3 mrad	Odd BM (ID1, ID3...) 9 mrad
Magnetic field	[T]	Variable	Variable	0.4	0.85	0.4	0.85
Horiz. Beta function	[m]	37.6	0.35	1.33	1.06	2.12	1.61
Horiz. Dispersion	[m]	0.134	0.031	0.062	0.051	0.089	0.075
Horiz. rms e- beam size	[µm]	413	50	99	85	132	113
Horiz. rms e- divergence	[µrad]	10	107	116	114	104	99
Vert. Beta function	[m]	2.95	2.97	41.7	42	32.1	32.2
Vert. rms e- beam size	[µm]	3.4	3.4	12.9	13	11.3	11.4
Vert. rms e- divergence	[µrad]	1.17	1.16	0.50	0.50	0.36	0.36

Table 5: Beta functions, dispersion, rms beam size and divergence at the various source points.

Filling pattern		Uniform	7/8 + 1	Hybrid	16-bunch	4-bunch
Number of bunches		992	870+1	24x8+1	16	4
Maximum current	[mA]	200	200	200	90	40
Lifetime	[h]	50	45	30	16	9
Rms energy spread	[%]	0.11	0.11	0.11	0.12	0.16
Rms bunch length	[ps]	20	20	25	48	55

Table 6: Current, lifetime, bunch length and energy spread for a selection of filling modes.

FACTS AND FIGURES

MEMBERS AND ASSOCIATE COUNTRIES

(AS OF JANUARY 2018)

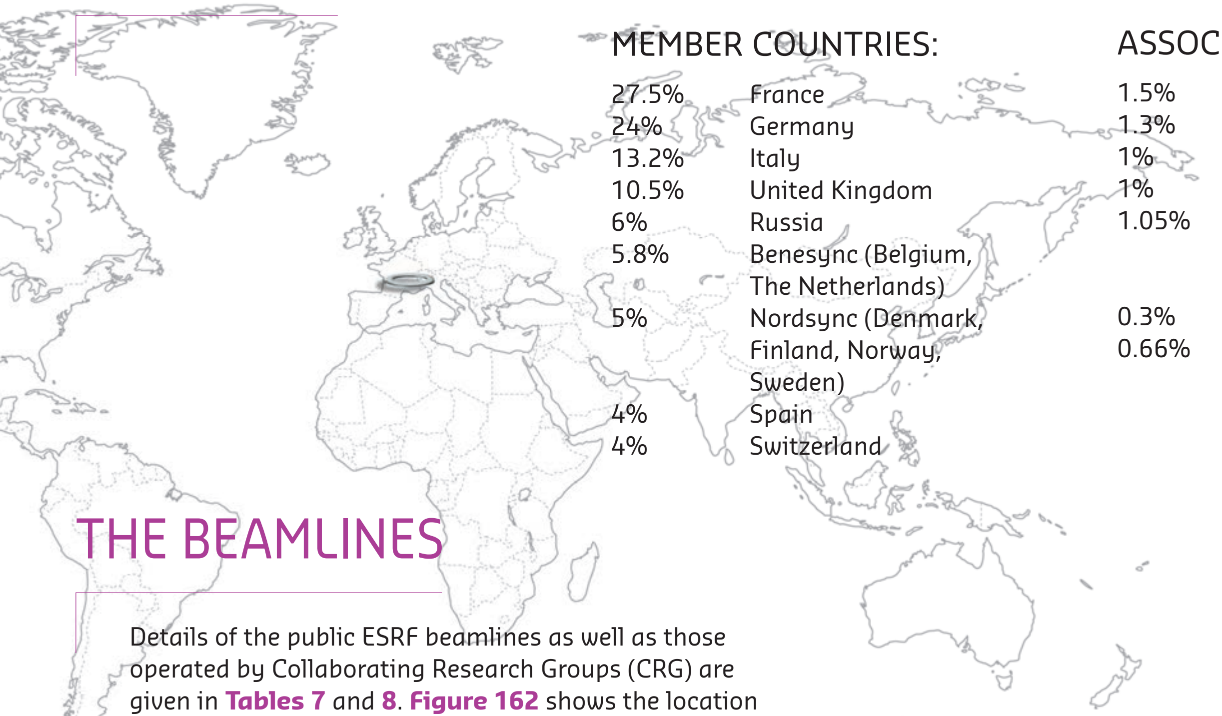

MEMBER COUNTRIES:

27.5%	France
24%	Germany
13.2%	Italy
10.5%	United Kingdom
6%	Russia
5.8%	Benesync (Belgium, The Netherlands)
5%	Nordsync (Denmark, Finland, Norway, Sweden)
4%	Spain
4%	Switzerland

ASSOCIATE COUNTRIES:

1.5%	Israel
1.3%	Austria
1%	Poland
1%	Portugal
1.05%	Centralsync (Czech Republic, Hungary, Slovakia)
0.3%	South Africa
0.66%	India

THE BEAMLINES

Details of the public ESRF beamlines as well as those operated by Collaborating Research Groups (CRG) are given in **Tables 7** and **8**. **Figure 162** shows the location of the beamlines in the experimental halls.

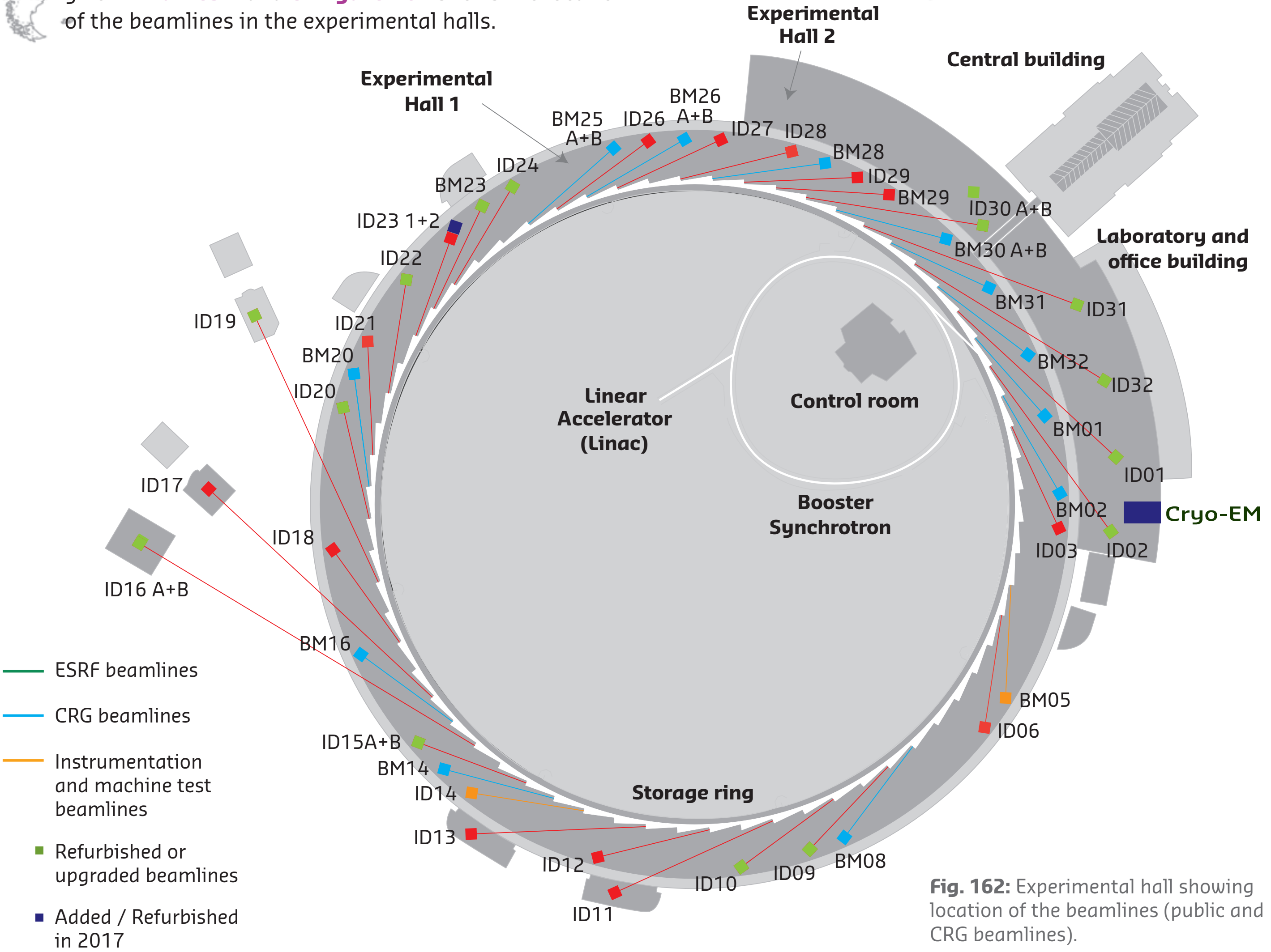

Fig. 162: Experimental hall showing location of the beamlines (public and CRG beamlines).

SOURCE POSITION	NUMBER OF INDEPENDENT END-STATIONS	BEAMLINE NAME	STATUS	
ID01	1	Microdiffraction imaging	Operational	since 12/14
ID02	1	Time-resolved ultra-small-angle X-ray scattering	Operational	since 07/14
ID03	1	Surface diffraction	Operational	since 09/94
ID06	0.4	Large volume press	Operational	since 10/13
ID09	1	Time-resolved structural dynamics	Operational	since 09/94
ID10	1	Soft interfaces and coherent scattering	Operational	since 06/12
ID11	1	Materials science	Operational	since 09/94
ID12	1	Polarisation-dependent X-ray spectroscopy	Operational	since 01/95
ID13	1	Microfocus	Operational	since 09/94
ID15A	0.7	Materials chemistry and engineering	Operational	since 11/16
ID15B	0.5	High-pressure diffraction	Operational	since 11/16
ID16A	1	Nano-imaging	Operational	since 05/14
ID16B	1	Nano-analysis	Operational	since 04/14
ID17	1	Medical	Operational	since 05/97
ID18	1	Nuclear scattering	Operational	since 01/96
ID19	1	Microtomography	Operational	since 06/96
ID20	1	Inelastic X-ray scattering	Operational	since 06/13
ID21	1	X-ray microscopy / IR spectroscopy	Operational	since 12/97
ID22	1	High resolution powder diffraction	Operational	since 05/14
ID23	2	Macromolecular crystallography MAD	Operational	since 06/04
		Macromolecular crystallography microfocus	Operational	since 09/05
ID24	1	Dispersive EXAFS	Operational	since 02/96
ID26	1	X-ray absorption and emission	Operational	since 11/97
ID27	1	High pressure	Operational	since 02/05
ID28	1	X-ray scattering II	Operational	since 12/98
ID29	1	Multiwavelength anomalous diffraction	Operational	since 01/00
ID30A	2	Macromolecular crystallography	Operational	since 07/14
ID30B	1	Macromolecular crystallography	Operational	since 04/15
ID31	1	Interfaces and materials processing	Operational	since 11/15
ID32	1	Soft X-ray spectroscopy	Operational	since 11/14
BM23	1	X-ray absorption spectroscopy	Operational	since 03/11
BM29	1	Bio SAXS	Operational	since 06/12
CM01	1	Cryo-EM	Operational	since 11/17

Table 7: List of the ESRF public beamlines.

SOURCE POSITION	NUMBER OF INDEPENDENT END-STATIONS	BEAMLINE NAME	FIELD OF RESEARCH	STATUS
BM01	1	Swiss-Norwegian BL	X-ray absorption and diffraction	Operational since 01/95
BM02	1	D2AM (French)	Materials science	Operational since 09/94
BM08	1	LISA (Italian)	X-ray absorption and diffraction	Operational since 09/94
BM20	1	ROBL (German)	Radiochemistry	Operational since 09/98
BM25	2	SPLINE (Spanish)	X-ray absorption and diffraction	Operational since 04/05
BM26	2	DUBBLE (Dutch/Belgian)	Small-angle scattering	Operational since 12/98
			EXAFS	Operational since 06/01
BM28	1	XMAS (British)	Magnetic scattering	Operational since 04/98
BM30	2	FIP (French)	Protein crystallography	Operational since 02/99
		FAME (French)	EXAFS	Operational since 08/02
BM31	1	SNBL II (Swiss-Norwegian)	X-ray absorption and diffraction	Operational since 09/16
BM32	1	IF (French)	Interfaces	Operational since 09/94
Operational in 2017:				
BM16	1	FAME-UHD (French)	EXAFS	Operational since 02/17

Table 8: List of the Collaborating Research Group beamlines.

USER OPERATION

User operation with public beam time at the ESRF in 2017 followed on from a record operation year in 2016, during which all Phase I upgrade programme beamline projects were completed. In 2017, all beamlines were fully operating with the exceptions of the X-ray microscopy beamline, ID21, and the microfocus structural biology beamline, ID23-2, which were both partially closed during this operation year for major refurbishment. BM14 also closed at the end of 2016 and will restart in 2018 as a new CRG beamline operated by the Dutch-Belgian consortium, DUBBLE. The year 2017 has been another record-breaking year in terms of both interest from the user community and provision of beamtime by the ESRF to satisfy the needs of the growing community. **Figure 163** shows the number of applications for beamtime received since 2010, and clearly demonstrates the return to full operation following Phase I of the upgrade programme as well as the unprecedented interest from the user community to use the upgraded facilities (nearly 20% increase in requests) in these post-Phase I / pre-EBS operating years.

Proposals for experiments are selected and beamtime allocations are made through peer review. As in previous years, beamtime for 2017 was allocated based on recommendations made by review committees of specialists, for the most part from the ESRF member and associate member countries. These beamline-based committees review all proposals received for a particular beamline, giving them an overview of all the projects proposed for a single beamline and flexibility to optimise the selection of proposals that will be awarded beamtime on each beamline. Proposals for experiments in 2017 were reviewed by 11 review committees, grouping the following beamlines of similar techniques or activities:

- C01 (ID01, ID03, BM25B, BM32)
- C02 (ID11, ID15A, ID22, ID31)
- C03 (ID12, ID32)
- C04 (BM08, BM16, BM20, BM23, BM25A, BM26A, BM30B, BM31)
- C05 (BM01, ID06-LVP, ID15B, ID18, ID27, ID28)
- C06 (ID17, ID19)
- C07 (ID16A, ID16B, ID21)
- C08 (ID02, ID13, BM26B)
- C09 (BM02, ID09, ID10, BM28)
- C10 (Structural biology beamlines)
- C11 (ID20, ID24, ID26)

The scientific areas of the ESRF research activities reviewed by these 11 committees are shown in **Table 9**.

The review committees met twice during the year, around six weeks after the deadlines for submission of proposals (10 September 2016 and 1 March 2017). They reviewed 2409 applications for beamtime in 2017, an all-time

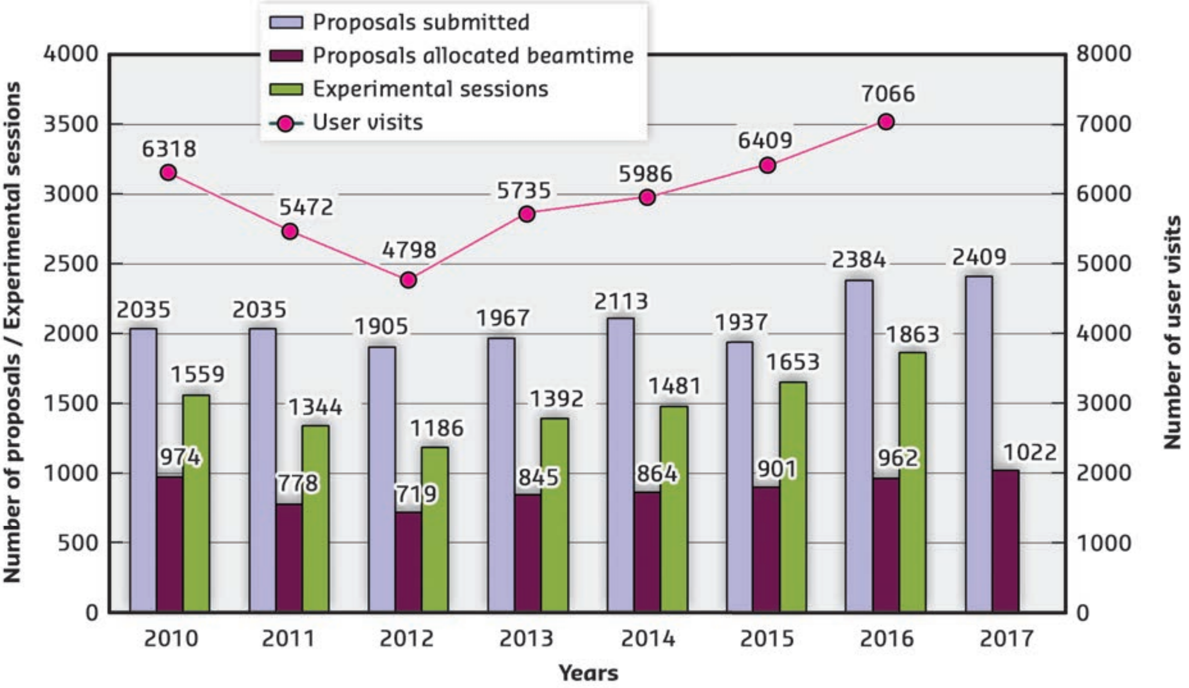

Fig. 163: Numbers of applications for beamtime, experimental sessions and user visits, 2010 to 2017.
N.B. Final numbers of experimental sessions and user visits for 2017 were not available at the time of going to press.

record, and selected 1022 (42.4%) in total. This is the highest ESRF allocation ever, and the first time that more than 1000 proposals could be allocated beam time. Requests for beamtime in 2017, which is scheduled in shifts of eight hours, totalled 34 268 shifts and, of these, 14 752 shifts (43.0%) were allocated. The distribution of shifts requested and allocated by scientific area for 2017 is shown in **Table 9**, while the number of shifts requested, allocated and delivered per year since 2010 is shown in **Figure 164**.

Table 9: Shifts of beamtime requested and allocated for public user experiments, year 2017.

Scientific field	Total shifts requested	Total shifts allocated
Chemistry	4 714	1 915
Earth Sciences	2 238	1 074
Environment	988	312
Hard Condensed Matter Science	9 464	3 354
Cultural Heritage	285	150
Life Sciences	1 755	810
Applied Materials Science	7 059	2 428
Medicine	1 159	548
Engineering	356	78
Methods & Instrumentation	539	291
Structural Biology	2 847	2 709
Soft Condensed Matter	2 864	1 083
Totals	**34 268**	**14 752**

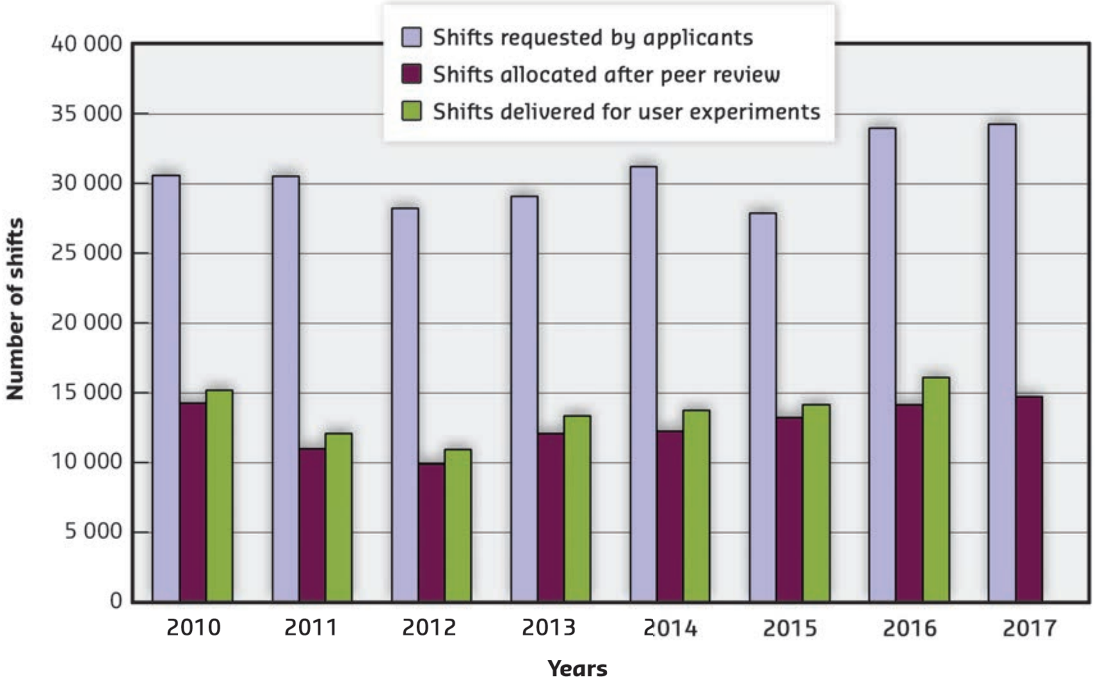

Fig. 164: Amount of beamtime requested, allocated and delivered, 2010 to 2017. N.B. The final number for beamtime delivered for 2017 was not available at the time of going to press.

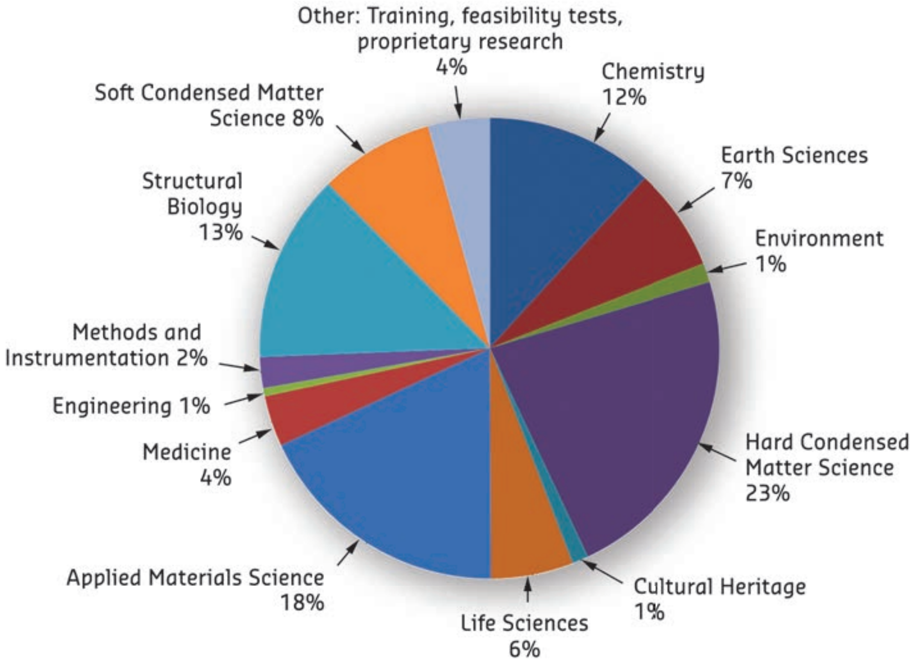

Fig. 165: Shifts delivered for experiments, March to July 2017, by scientific area, total 7663.

The breakdown of shifts delivered for public experiments by scientific area in the first half of 2017 is shown in **Figure 165**. This same period saw 3262 visits by scientists to the ESRF under the public user programme, to carry out 864 experiments. Overall, the number of users in each experimental team averaged 3.8 persons and the average duration of an experimental session was 8.5 shifts (less than three shifts for MX experiments and just over 12 shifts for non-MX experiments). Faster and more efficient experiments ensure that more proposals can be accepted, maintaining an acceptance rate of over 40% despite the increase in the number of proposals received. For this same reason, more experiments and users can be supported; the annual number of experimental sessions and user visits since 2010 is shown in **Figure 163**. Based on beamtime delivered so far in 2017, the number of public experiment sessions for the full year is expected to be close to 1900, with public user visits expected to reach 7000, while the total beamtime delivered for the public user programme is expected to reach 16 400 shifts. These beamtime usage figures are again at record levels, clearly indicating the successful outcome of the first phase of the Upgrade Programme.

One of the principal measurable output parameters of the ESRF is the number and quality of publications accepted in peer-reviewed journals. During 2017, the ESRF reached and passed the remarkable milestone of 30 000 publications resulting from data taken either wholly or partially at the ESRF since the facility first opened its doors in 1994. Yearly publication output from the ESRF has been systematically at a level of over 1800 for many years now, as shown in **Figure 166**. At the time of going to press, 1703 publications had already been registered for 2017, giving a total of 30 528 publications accepted in peer-reviewed journals, and this figure will continue to evolve with the final number for 2017 expected to again surpass 1800. Of these, around 300 every year are published in high impact factor journals. These are excellent figures, showing that the ESRF research output is maintained at a worldwide high.

User responses to questionnaires show once again that the ESRF continues to maintain its excellent reputation concerning the assistance and service given by scientists and support staff at the beamlines, and travel and administrative arrangements, in addition to the quality both of the beam and of the experimental stations. Onsite offline facilities, such as preparation laboratories and collaborative platforms offering complementary techniques and support, provide a vital contribution to the quality of user support but also to the quality of the science and results that can be achieved. Major scientific advances can be made through the collection of complete and complementary data and information on the most important scientific questions. These aspects remain key to the continuing success story of the ESRF.

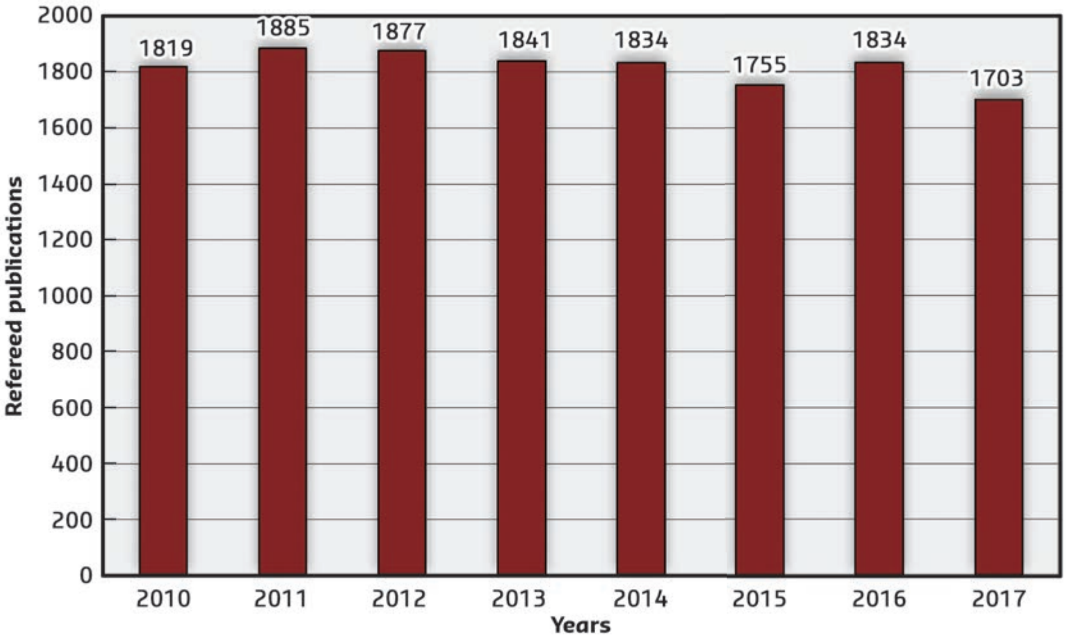

Fig. 166: Numbers of publications appearing in refereed journals reporting on data collected either partially or totally at the ESRF, 2010 to 2017. The number of publications for 2017 is not final at the time of going to press.

ADMINISTRATION AND FINANCE

The budget for 2017 includes additional contributions from Members and Scientific Associates of 10 997 kEUR dedicated to the ESRF-EBS project. The ESRF-EBS expenditure budget amounts to a total of 39 841 kEUR including 5 311 kEUR of ESRF operating budget.

Expenditure and income 2016

Expenditure		kEuro
Accelerator and Source		
Personnel		7 522.0
Recurrent		1 815.4
Operating costs	*1 597.2*	
Other recurrent costs	*218.2*	
Capital		21 101.5
Accelerator and Source developments	*21 101.5*	
Beamlines, experiments and in-house research		
Personnel		18 945.2
Recurrent		5 679.0
Operating costs	*1 648.8*	
Other Recurrent costs	*4 030.2*	
Capital		7 199.9
Beamline developments	*7 199.9*	
Beamline refurbishment		
Technical and administrative supports		
Personnel		30 983.2
Recurrent		15 158.5
Capital		4 652.2
Industrial and commercial activity		
Personnel		461.8
Recurrent		217.2
Unexpended committed funds		
Funds carried forward to 2017		4 852.0
Total		**118 587.8**

Income	kEuro
2016 Members' contributions	90 075.4
Funds carried forward from 2015	3 645.5
Other income	
Scientific Associates	5 828.5
Sale of beamtime	2 084.2
Scientific collaboration and Special projects	3 624.2
Electricity overcosts brought to account	849.0
Pre-financing / Balance	7 629.0
Funds carried forward to 2017	4 852.0
Total	**118 587.8**

Revised expenditure and income budget for 2017

Expenditure		kEuro
Accelerator and Source		
Personnel		7 256
Recurrent		3 301
Operating costs	*3 161*	
Other recurrent costs	*140*	
Capital		36 608
Accelerator and Source developments	*36 608*	
Beamlines, experiments and in-house research		
Personnel		20 143
Recurrent		5 486
Operating costs	*1 564*	
Other Recurrent costs	*3 922*	
Capital		9 982
Beamline developments	*9 982*	
Technical and administrative supports		
Personnel		31 674
Recurrent		13 739
Capital		6 743
Total		**134 932**

Income	kEuro
2017 Members' contributions	93 811
Funds carried forward from 2016	4 852
Other income	
Scientific Associates	6 740
Income from industrial co.activity	2 134
Scientific collaboration and Special projects	7 640
Balance ESRF-EBS	19 755
Total	**134 932**

Expenditure 2016 by nature of expenditure

	kEuro
PERSONNEL	
ESRF staff	55 453.9
External temporary staff	38.6
Other personnel costs	2 419.9
RECURRENT	
Consumables	9 138.1
Services	11 115.6
Other recurrent costs	2 616.2
CAPITAL	
Buildings, infrastructure	1 351.0
Lab. and Workshops	1 563.3
Accelator and Source incl. IDs and FEs	21 101.5
Beamlines, Experiments	7 199.9
Computing Infrastructure	1 671.4
Other Capital costs	66.5
Unexpended committed funds	
Funds carried forward to 2017	4 852.0
Total	**118 587.8**

Revised budget for 2017 by nature of expenditure

	kEuro
PERSONNEL	
ESRF staff	56 492
External temporary staff	20
Other personnel costs	2 561
RECURRENT	
Consumables	8 282
Services	11 864
Other recurrent costs	2 380
CAPITAL	
Buildings, infrastructure	2 279
Lab. and Workshops	2 772
Accelator and Source incl. IDs and FEs	36 608
Beamlines, Experiments	9 982
Computing Infrastructure	1 558
Other Capital costs	134
Total	**134 932**

2017 manpower *(staff members present on 31/12/2017)*

	Scientists, Engineers, Senior Administrators	Technicians and Administrative Staff	PhD Students	Total
Staff on regular positions				
Accelerator and Source*	36	43		79
Beamlines, instruments and experiments*	251	92	28	371
General technical services	35	53		88
Directorate, administration and central services	37	58		95
Sub-total	*359*	*246*	*28*	*633*
Other positions				
Short term contracts	20	16		36
Staff under “contrats de professionnalisation”		30		30
Total	**379**	**292**	**28**	**699**
Scientific collaborators and consultants	*11*			*11*

** Including scientific staff on time limited contracts.*

ORGANISATION CHART OF THE ESRF

(AS OF JANUARY 2018)

Administrative and Finance Committee
Chairperson: J. Pickett

Council
Chairperson:
B. Girard
up to 3 delegates per
Contracting Party

Science Advisory Committee
Chairperson: D. McMorrow

Machine Advisory Committee
Chairperson: R. Walker

Director General
F. Sette

DG's Services:
- **Head of DG's Office/Secretary of Council: I. Echeverria**
- **Communication Group**
- **Internal Auditor**
- **Safety Group**

ACCELERATOR AND SOURCE

Director: P. Raimondi

Beam dynamics and applications
Power supplies
Insertion devices
Front-ends
Radio frequency and linac
Diagnostics
Operation
Secretariat

ADMINISTRATION

Director: L-J. Sánchez Ortiz

Personnel
Finance
Purchasing

Joint ILL/ESRF Medical service

EXPERIMENTS

Director: J. Susini

Beamline groups:
- **Complex systems and biomedical sciences**
- **Structural biology**
- **X-ray nanoprobe**

Director: H. Reichert

Beamline groups:
- **Electronic structure, magnetism and dynamics**
- **Matter at extremes**
- **Structure of materials**

Scientific infrastructure
Theory group
User office
CRG liaison office
Business Development Office
Joint ILL/ESRF Library
Secretariat

Beam Time Allocation Panels
C01 (ID01, ID03, BM25B, BM32) Chairperson: C. Lucas
C02 (ID11, ID15A, ID22, ID31) Chairperson: A. Abakumov
C03 (ID12, ID32) Chairperson: A. Severing
C04 (BM08, BM16, BM20, BM23, BM25A, BM26A, BM30B, BM31) Chairperson: J. Van Bokhoven
C05 (ID06-LVP, ID15B, ID18, ID27, ID28, BM01) Chairperson: V. Giordano
C06 (ID17, ID19) Chairperson: E. Gouillart
C07 (ID16A, ID16B, ID21) Chairperson: F. Giannici
C08 (ID02, ID13, BM26B) Chairperson: H. Gupta
C09 (ID09, ID10, BM02, BM28) Chairperson: A. Madsen
C10 (Structural Biology Beamlines) Chairperson: M. Degano
C11 (ID20, ID24, ID26) Chairperson: M. Feiters

INSTRUMENTATION SERVICES AND DEVELOPMENT DIVISION

Head: M. Krisch

Advanced analysis and modeling
Detector and electronics
Software
X-ray optics
Mechanical engineering

TECHNICAL INFRASTRUCTURE DIVISION

Head: R. Dimper

Management information systems and web
Systems and communication
Buildings and infrastructure
EX2/CPER project team
Survey and alignment
Vacuum

Cover
Cover design by S. Lombardo

Photo credits:
C. Argoud, I. Ginzburg, P. Jayet, @StefCandé.

We gratefully acknowledge the help of:

C. Argoud, T. Baudoin, A. Bosak, J.F. Bouteille, B. Boulanger, N. Brookes, M. Capellas Espuny, J. Chavanne, D. Chenevier, K. Colvin, K. Clugnet, E. Dancer, R. Dimper, I. Echeverría, P. Gaget, S. Gerlier, P. Glatzel, L. Hardy, V. Honkimäki, J. Jacob, E. Jean-Baptiste, A. Kaprolat, M. Krisch, G. Le Bec, G. Leonard, S. Lombardo, E. Mitchell, M. Moretti-Sala, C. Mueller-Dieckmann, J. McCarthy, S. Pascarelli, E. Plouviez, P. Raimondi, H. Reichert, J.L. Revol, S. Rio, B. Roche. A. Rogalev, E. Ryan, K. Scheidt, T. Schülli, F. Sette, J. Susini, S. White, M. Wulff and all the users and staff who have contributed to this edition of the Highlights.

Editors
G. Admans and A. Joly
Layout
Pixel Project
Printing
Imprimerie du Pont de Claix

Communication Group
ESRF
CS 40 220
F38043 Grenoble Cedex 9 • France
Tel. +33 (0)4 76 88 20 56
Fax. +33 (0)4 76 88 25 42
http://www.esrf.eu